# – 12 –

# Scanning Electrochemical Microscopy

**Fu-Ren F. Fan[1], José Fernandez[1], Biao Liu[1], and Janine Mauzeroll[2]**

[1]The University of Texas at Austin, Austin, TX, USA
[2]Laboratoire d'Électrochimie Moléculaire, Université Paris 7-Denis Diderot, France

## 12.1 INTRODUCTION AND PRINCIPLES

This chapter is devoted to a concise discussion of various techniques and applications of scanning electrochemical microscopy (SECM) (1). SECM is one of the scanning probe microscopies (SPM) (2) in which three-dimensional images of surfaces are obtained by scanning a small ultramicroelectrode (UME, Chapter 6) tip across a surface (usually termed "the substrate") and recording an appropriate response. To understand the operation and response of the SECM, it is necessary to review briefly the behavior of a very small UME in an electrochemical cell. More detailed discussions of UMEs are available (Chapter 6 of this handbook). Consider a UME disk immersed in a solution containing an electrolyte and an electroactive species, Ox, as well as counter and reference electrodes. When a potential, sufficiently negative of the formal potential of the redox couple (Ox/Red), is applied to the UME, the reduction of Ox occurs at the UME at a diffusion-controlled rate, and a cathodic current passes through the UME. The current decays as a diffusion layer of Ox builds up around the electrode and attains rather quickly a steady-state value, $i_{T,\infty}$, that depends on the concentration of Ox, $C^*$, and its diffusion coefficient, $D$, and is given by (3)

$$i_{T,\infty} = 4nFDaC^* \tag{12.1.1}$$

in which $n$ is the number of electrons involved in the electrode reaction, $F$ is the Faraday constant, and $a$ is the radius of the UME. The steady-state current results from the constant flux of Ox to the electrode surface driven by an expanding, essentially hemispherical, diffusion layer around the electrode (Figure 12.1). In SECM, it is the perturbation of the tip current when the tip is brought to within a few tip diameters of a surface, which constitutes the SECM response.

Consider first when the tip is brought close to an insulating substrate (Figure 12.2a). The steady-state current flowing through the tip, $i_T$, will now be smaller than $i_{T,\infty}$ because the insulating substrate partially hinders the diffusion of Ox to the tip. Clearly, the closer the tip is to


**Handbook of Electrochemistry**
**Edited by C.G. Zoski**

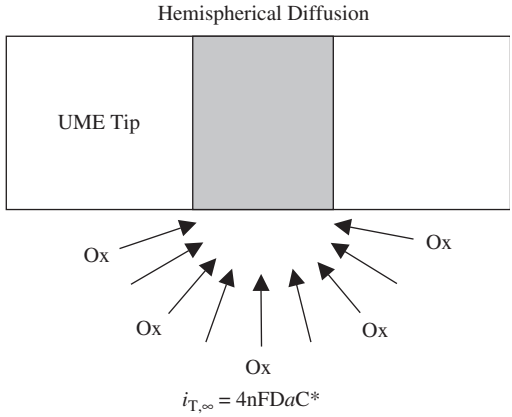


**Figure 12.1** Steady-state hemispherical diffusion at an ultramicroelectrode (UME) disk.

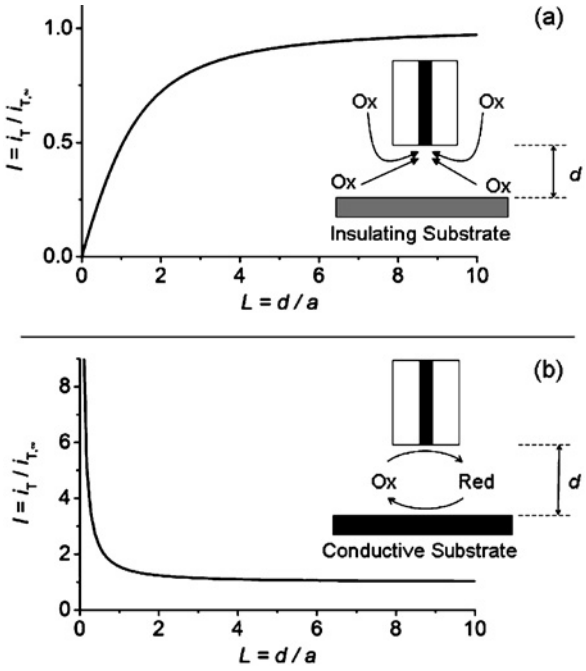


**Figure 12.2** SECM approach curves on insulating (a) and conductive (b) substrates. Negative feedback is observed on an insulating substrate and positive feedback is observed on a conductive substrate.

the insulator surface, the smaller $i_T$ will be, and with $i_T \rightarrow 0$ as the tip–substrate separation, $d$ approaches 0. This effect is termed "negative feedback." However, when the tip is close to a conductive substrate at which Red can be oxidized back to Ox, then a flux of Ox from substrate to tip occurs, in addition to some flux of Ox to the tip from the bulk solution (Figure 12.2b). This results in $i_T > i_{T,\infty}$. This flux of Ox from substrate to tip causes an increase in

$i_T$ as $d$ decreases; this is termed "positive feedback." Thus, the magnitude of $i_T$ compared with $i_{T,\infty}$ is governed by the nature of the substrate and by the tip–substrate spacing. The actual general situation can be more complicated than those two limiting cases described above, for example, when the rate of the Red $\rightarrow$ Ox + $e^-$ reaction on the substrate is governed by the rate of heterogeneous electron-transfer kinetics rather than the rate of mass transfer (diffusion) of Red to the substrate. This situation will be dealt with in Section 12.4.1.

In addition to the amperometric feedback mode described above, other amperometric operation modes are also possible. For example, in the substrate generation/tip collection (SG/TC) mode, $i_T$ is used to monitor the flux of electroactive species from the substrate and vice versa for the tip generation/substrate collection (TG/SC) mode. These operation modes will be described in Section 12.3.1.3 and are useful in studies of homogeneous reactions that occur in the tip–substrate gap (see Section 12.4.2) and also in the evaluation of catalytic activities of different materials for useful reactions, e.g., oxygen reduction and hydrogen oxidation (see Section 12.4.3). In addition to the amperometric methods, other techniques, e.g., potentiometric method is also applicable for SECM and will be discussed in Section 12.3.2. We will also update the techniques suitable for the preparation of SECM amperometric tips in Section 12.3.1.1 and potentiometric probes in Section 12.3.2.2.

The SECM can also be used as an imaging device (see Section 12.3.3), as an electrochemical tool for studies of surface reactivity of thin films (see Section 12.4.4) and as a high-resolution fabrication tool (see Section 12.4.5). Finally, the SECM can be adapted to probe the transport activity of biological systems like single cells, the ion transport across channels and enzyme activity (see Section 12.4.6).

## 12.2 INSTRUMENTATION

As SECM instrumentation has been extensively and thoroughly discussed in Chapter 2 of reference (1) and there are also commercial instruments (e.g., CH Instruments, Heka, and Uniscan) on the market, we mainly focus on experimental aspects encountered in imaging and tip positioning with SECM. Readers who are interested in the design of an SECM instrument can refer to that chapter. We also intend to include here an up-to-date account of the newly developed combined techniques so that interested individual investigators may appreciate the design of SECM-related techniques for their specific applications.

### 12.2.1 Basic SECM apparatus

An illustration of the SECM instrument is shown in Figure 12.3. An important aspect of the SECM is the positioning system, which includes the positioning elements, translation stages, and motor controllers. Equally important is the data acquisition system, which starts with the use of a bipotentiostat to amplify the tip signal. After amplification, the signal is acquired with an analog-to-digital converter (ADC) and stored on a computer which is also used to send out (through the interface modules) the controlling signals for bipotentiostat and controllers for positioning elements and translation motors. Computer software is required to control the positioning and data acquisition system as well as to display and analyze the SECM data. Other important accessories of an SECM are the probe mount

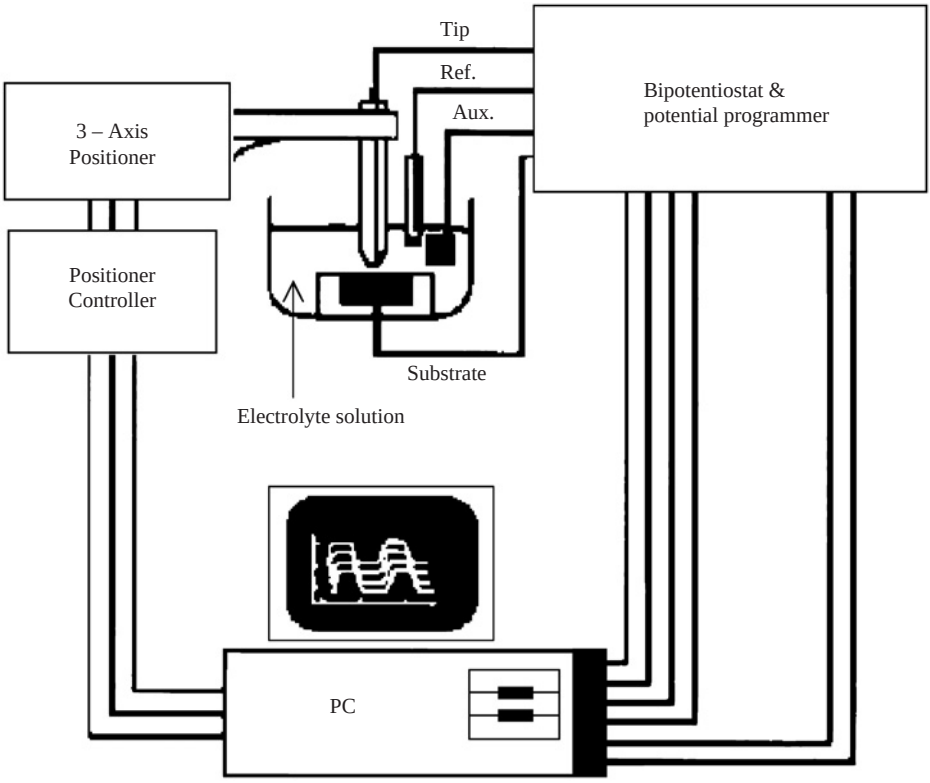


**Figure 12.3** A diagram of the SECM instrument.

system and electrochemical cells, which will be described in individual sections for different experiments. If a near-field ($d < 100$ nm) SECM experiment is performed, a vibration isolation system is required.

The SECM apparatus currently used in this laboratory is the model 900 SECM (CH Instruments) specifically designed for SECM experiments. The model 900 includes the cell and the probe positioner as well as a computer, a motor controller, and a bipotentiostat. Lateral probe scans as large as 2.5 cm are accomplished by two inchworm (or step motors for model 900B) driving crossed-roller-bearing translator stages. Vertical motion is provided by mounting the probe directly to the shaft of the third inchworm or a 3-axes piezoelectric block (for model 900B), which is mounted on the $z$-stage driven by the third motor. The 3-axes piezoelectric block can be used for fine positioning and scan, which eliminate the effect of the clamping step on the shaft movement of the inchworm motor and thus provide smooth movement. The electrochemical cell is stationary and mounted on an adjustable tilting platform to compensate for the substrate tilt. Open-loop motor control is used, and software calibration corrects scan rate, axis, and direction-dependent effects on the probe motion. The data acquisition system and bipotentiostat of the CH series-900 SECM are microprocessor based and communicate with the PC controller via

a serial data link. The bipotentiostat is suitable for analytical voltammetry and has current measurement sensitivity in the pA range. Adjustable second-order Bessel filters provide noise reduction and prevent aliasing by the ADC, which has at least 20 bits of resolution.

The software for the model series-900 SECM runs on the Windows operating system and provides all the controls necessary for positioning the probe in three dimensions and setting parameters for various electrochemical techniques. The software also supports a wide range of electrochemical experiments, graphical displays, and data processing. During probe scanning, either amperometric or potentiometric signals can be recorded. Other software features include a probe approach curve routine that automatically stops the probe when the current reaches a set level and that automatically slows the speed of approach as the probe approaches the substrate surface, helping to prevent crashing the tip. SECM imaging is normally operated at constant height mode. Graphics output during imaging and postscan is by gray-scale or color-coded plots. Further data and graphical manipulation must be done outside the main program with commercially available software packages. Closed-loop or shear force-based positioning systems as described below are also available in CH Instruments, Uniscan, or Heka apparatus.

### 12.2.2 Combining SECM with other techniques

Combining SECM with other techniques, such as atomic force microscopy (AFM), near-field scanning optical microscopy (NSOM), and electrogenerated chemiluminescence (ECL), greatly increases the difficulty of the experiment and presents challenging problems in tip preparation. However, obtaining information from two or more different techniques at the same time and at the same location can greatly increase the power of SECM (e.g., by providing independent topographical or optical data during the SECM scan).

#### *12.2.2.1 AFM/SECM*

AFM measurements made during an SECM experiment allow for an independent determination of the zero distance ($d = 0$, if the tip is not recessed) and aid in the positioning of the tip. Moreover, this combination of techniques opens the way to experiments in which changes in topography are studied by AFM as a reactant is generated electrochemically at the tip.

Several similar studies have already been reported. For example, Ludwig and coworkers (4) used a piezoelectric element attached to the tip shaft for dithering and measured the modulation by noting changes in the Fresnel diffraction pattern created with an illuminating laser beam focused on the lower part of the electrode on a split photodiode. The probe remains stationary to maintain the laser and photodiode alignment, while the substrate is scanned to make images. In the initial experiment, the probe was a 1.5-cm long section of a pulled glass capillary containing a 25-μm-diameter Pt disk electrode. The long-pulled section is necessary to produce the flexibility required for oscillation. Modulation amplitude in this experiment is about 1–2 μm, which is several orders larger than that normally used in NSOM. The large modulation amplitudes can produce a proportionately larger range of shear mode so that the probe–substrate distance, $d$, is in the μm range when shear force damping is observed. The significant perturbation of the solution near the tip can be cumbersome, especially if the tip is largely immersed in solution.

The existing SECM theory requires some modifications, as the mass transfer now is no longer purely diffusional.

An alternative is to use a cantilever-based AFM and modify the cantilever/tip to behave as an SECM tip. A conventional (not a conductive-probe AFM) cantilever is nonconductive and must be metallized to establish a conductive path to the tip (e.g., by evaporating or sputtering a thin film (~300 Å) of Pt) and then the entire conductive surface except the very end of the tip was insulated from the contacting solution. Such an arrangement was used to study a KBr crystal undergoing dissolution (5). Although the AFM imaging was not affected significantly by the metallization, the SECM performance of the tip was poor because of difficulties with simultaneously providing good tip insulation and tip configuration.

A different approach is to construct a special cantilever-type SECM tip (6). A 50-μm diameter Pt wire was bent and etched electrochemically, then flattened and insulated with electrophoretic paint. It was then epoxied to a commercial AFM chip based on the procedures as shown in Figure 12.4 (6a). Another approach used micromachining techniques (e.g., focused ion beam (FIB) and etching) to modify a silicon nitride-insulated Au-coated sharp silicon AFM cantilever into a dual AFM/SECM tip, with a UME ring surrounding the AFM probe (6b). The cantilever mount was additionally protected by an insulating varnish to prevent scratching of the silicon nitride layer. These modified cantilevers could

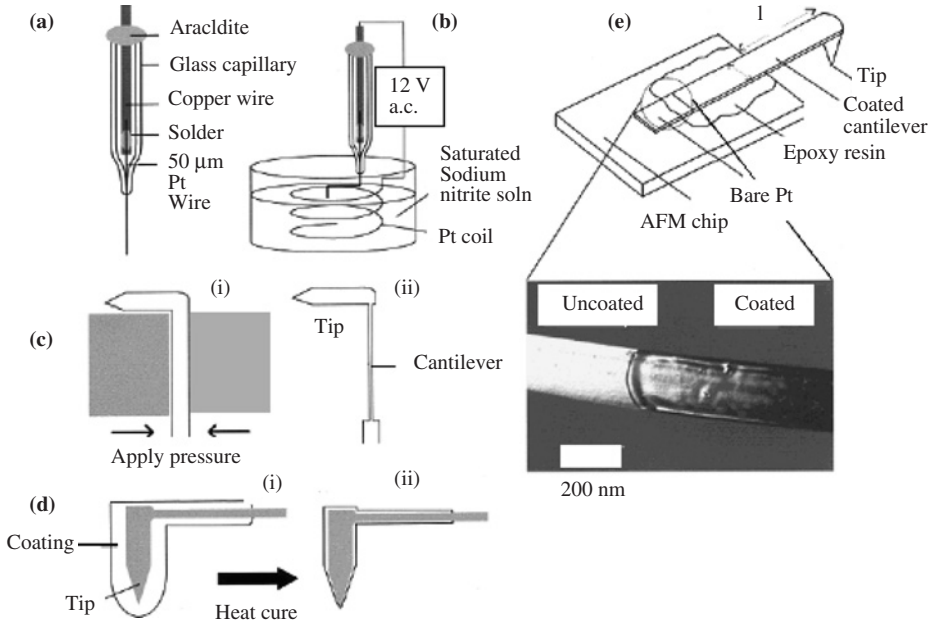


**Figure 12.4** Procedures involved in constructing an AFM/SECM tip: (a) Pt microwire inserted in holder; (b) electrochemical etching to a fine point; (c) compression to form cantilever component; (d) insulation of electrode and cantilever with electrophoretic paint followed by heating to expose the very end of the tip; and (e) attachment to a commercial AFM chip. (Adapted from reference (6a).)

then be used to replace conventional AFM cantilever used in a commercial AFM and allow for AFM and SECM measurements.

An alternative approach is the use of a tuning fork attached to an insulated SECM tip (7, 8). The SECM tip can be prepared by the procedures described in Section 12.3.1.1. A tuning fork-based SPM combined with electrochemical techniques can then be used for both topographic imaging and SECM measurements. A key issue in the application of AFM/SECM is the ability to obtain good quantitative approach curves for both insulators and conductors that agree with the theoretical treatment.

#### *12.2.2.2 NSOM/SECM*

NSOM is a SPM for obtaining high-resolution optical images and performing spectroscopic measurements. By using a fiber optic probe that has been pulled down to a very small tip (radius of curvature $< 100$ nm) and scanned along the sample surface in the near-field regime, one can obtain images whose resolution is governed by the tip diameter and placement rather than the usual diffraction limits that govern a conventional optical microscope (9). A typical NSOM tip is coated with aluminum to minimize the loss of light in passing from the laser source to the tip. For an NSOM tip to be also useful in SECM experiments, the metal coating should be electrochemically inert, such as Au or Pt, and an insulating layer must be added (usually by electrophoretic paint deposition) such that only the conducting metal ring at the end is exposed to the solution. To make NSOM tips that have a pinhole free metal layer, which promotes total internal reflection, and a pinhole free insulating layer, which yields the ring geometry, is challenging. The quality of the NSOM/SECM tip can be evaluated by lowering the tip from the air into the test solution and recording the current as the tip is immersed deeper into solution (10).

There have been several reports of the use of commercial NSOM with a W-tip coated with varnish for SECM and photoelectrochemical experiments (11). However, no SECM approach curves for these tips have been shown. Most recently, Lee and coworkers (10, 12) have demonstrated the combined tuning fork-based NSOM/SECM technique to simultaneously obtain topographic, electrochemical, and optical images of an interdigitated array electrode. Although the resolution is still on the order of μm, with the construction of a smaller tip an improved spatial resolution should be possible, leading to NSOM combined with SECM and simultaneous topography.

#### *12.2.2.3 ECL/SECM*

An alternative approach to obtain optical images with SECM is through light generation via an ECL process at the tip. The principle and various techniques of ECL are described in Chapter 13 of this handbook. Light generation at UMEs for a scanning microscope can be accomplished either by the radical ion annihilation approach (in aprotic solvents) (13) or by a coreactant route (also applicable in aqueous solutions) (14, 15). A schematic diagram showing the basic concepts of ECL generation is shown in Figure 12.5. ECL is generated at the tip as it is scanned in the *XY* plane above the sample to be imaged and collected by a detector, e.g., a photomultiplier tube (PMT) beneath the sample. An image is obtained by plotting the detector response as a function of *XY* position. The first experiments that used this technique (13, 14) (electrode radii were ~1–10 μm) relied on measurements with

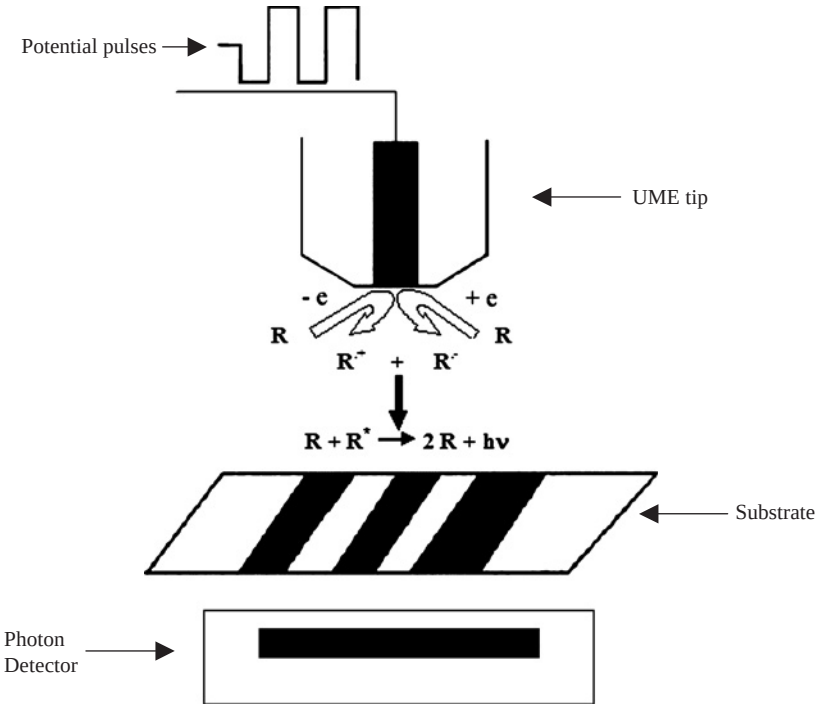


**Figure 12.5** Schematic diagram for ECL generation at an SECM tip for optical imaging. (Adapted from reference (14).)

similar *d* values and did not display high-resolution capabilities. However, the resolution obtainable by this technique, like various scanning probe techniques, depends on the UME radius and the distance, as demonstrated in later experiments (15, 16).

Maus and coworker (16) developed an interesting technique by decreasing the size of the ECL light source but still generating sufficiently strong ECL intensity ($\geq$1.8 pW) for high-resolution ECL imaging based on high-frequency alternating pulses on a conical carbon fiber electrode in benzonitrile (BN) containing 25 mM 9,10-diphenylanthacene (DPA) and 10 mM $TBAPF_6$. Square wave potentials that produce the radical cation of DPA and radical anion of BN were applied to the electrode at different frequencies. At low frequencies (e.g., 200 Hz), ECL occurred along the entire noninsulated region. As the frequency is increased, the ECL intensity increases. At higher frequencies, the area of the cone yielding the ECL emission diminishes. At the highest frequency (20 kHz), the ECL is supported only at the apex of the cone. Based on this phenomenon, a bare cone-shaped carbon fiber electrode can be used as a small light source. Submicrometer ECL light sources with similar submicrometer resolution can be achieved with this kind of technique. The results obtained so far with an ECL-based tip light source are quite promising, particularly for optical imaging of samples immersed in solution. However, to be widely applied as a laser-based NSOM used in optical imaging, the resolution, stability and intensity of ECL, and the operation speed need to be improved. Regardless of these problems, the

ECL/SECM technique can probe ECL generation restricted to small domains (e.g., biological molecules) with high spatial resolution.

## 12.3 METHODS AND OPERATIONAL MODES

### 12.3.1 Amperometric methods

SECM amperometric methods are based on the measurement of electrode currents (tip and substrate, $i_T$ and $i_S$, respectively) as a function of various parameters, including tip–substrate distance ($d$) and tip or substrate potentials ($E_T$ or $E_S$). Irrespective of the system studied (e.g., an electrode, an inert surface, a catalyst, or a living organism), the probe tip is a necessary component to perform any SECM experiment. In all cases, the amperometric tip is a UME that can be positioned in close proximity to another surface. There are two amperometric operation modes: feedback and generation/collection modes. The preparation and characterization of commonly used amperometric tips of different geometries as well as their operation modes will be described in this section.

#### *12.3.1.1 Fabrication and characterization of amperometric tips*

SECM amperometric tips are UMEs (see Chapter 6) in which insulating sheaths have been sharpened to a tip size below 10 times the effective radius, $a$, of a UME. As the UME tip needs to approach the substrate surface to within a normalized distance $L = 0.2$ ($L = d/a$) to observe significant change in its response, sharpening of the insulating sheath is necessary to prevent the edge of the insulating sheath from hampering the approach in the event of a slight tilt of the probe (and/or substrate). Because it is relatively easy to fabricate, the inlaid disk is the most commonly used SECM tip. However, other tip geometries, such as hemispheres, cones, and rings (Figure 12.6) are also used for some less extensive but specific applications.

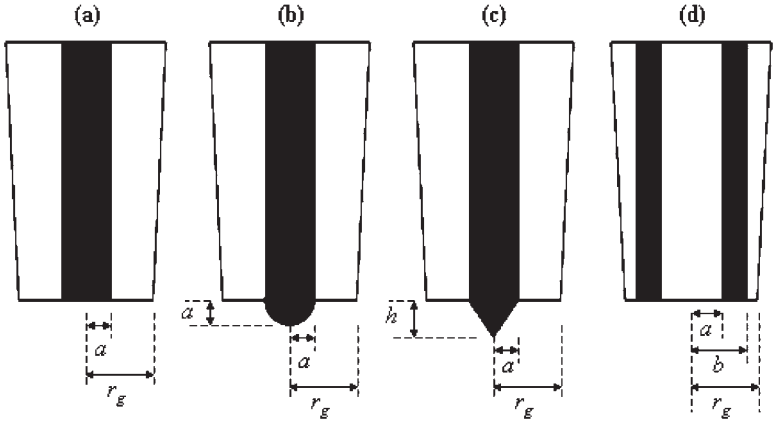


**Figure 12.6** Schematic of common tip geometries: disk (a) hemisphere (b) conical (c) and ring (d).

The fabrication of inlaid disk SECM tips (Figure 12.6a) has been described in detail in a recent review by Fan and Demaille in Chapter 3 of reference (1). Tips of varied materials like Pt, Au, and carbon can be prepared by using the conventional heat sealing and pulling methods, which are described in Section 6.3 in Chapter 6 of this handbook. Other than these techniques, there are other procedures that can be used to prepare disk-shaped SECM tips. A method widely used involves the coating of conductive fibers (metals, carbon) with insulating polymer layers (17–19). Anodic or cathodic electrophoretic deposition of polymer paints (e.g., polyacrylic acid, PAAH) is a procedure that has received widespread uses for preparing carbon and Pt disk (or flattened hemispheroid) UME tips (17, 18). The electrode fiber is immersed in an aqueous solution of the paint monomer, concentric to a Pt helix-coil counterelectrode. A positive or negative tip bias (2–7 V) is applied for 30–60 sec against the counterelectrode to evolve $O_2$ or $H_2$ with concomitant acidification or alkalinization of the electrode surface, respectively. Anodic paints will precipitate when the electrode surface is acidified, while cathodic paints will do so on alkalinized surfaces, forming a thick (~200 nm) polymeric layer covering the entire electroactive surface. After curing the layer at 140–180 °C, it becomes stable in most aqueous media, although it is unstable in most organic solvents. During curing, the layer contracts to expose the very end of the electrode and it forms a round-shaped aperture and leaves the UME disk slightly recessed. The procedure may be repeated to ensure the total insulation of the lateral walls. Sometimes, polishing may be necessary. This technique was successfully used to fabricate Pt (17) and carbon (18) tips with diameters below 100 nm. Fibers of these materials were etched down to the desired dimension either by electrochemical or thermal methods (1). These tips are only appropriate for aqueous media.

Spherical and hemispherical tips (Figure 12.6b) are less frequently used. The use of hemispherical tips is mostly related to cases where Hg UMEs are needed to extend the tip potential window to more negative values by increasing the $H_2$ evolution overpotential (20, 21). Controlled fabrication of hemispherical Hg tips has been performed by attaching a small Hg drop to a Pt or Ir UME disk by electrodeposition of Hg from $HgNO_3$ solutions (21–23), or by contacting a spinning UME tip with an Hg pool (20). Finite conical-shaped tips (Figure 12.6c) are the other preferred UME geometry for SECM amperometric probes. In fact, the optimal tip geometry is a cone with a small $H$ value ($H = h/a$), since it is possible to reach a tip–substrate distance $L = 0$ with no misalignment problems in the tip approach. The most common procedure for the fabrication of conical tips is by etching metal or carbon fibers to a sharp point and coating them with an insulating layer, such as the previously described electrophoretic paint (6, 24–26), except at the very apex (1). With this procedure, very small insulating sheath thicknesses (low RG, where $RG = r_g/a$; $r_g$ is the outer radius of the insulating sheath) can be obtained. A recent variation involves the heat sealing of etched fibers into glass capillaries (27) for making conical tips with RG values up to 5.

Ring UME tips (Figure 12.6d) have received attention only recently because of the increased interest in the combination of SECM with other techniques such as AFM (6) and optical microscopy (10). Fabrication of ring UMEs involves several steps:

(i) A cylindrical bar is coated with a layer of the metal electrode, for example, by vacuum evaporation or sputtering.
(ii) It is further insulated with a polymer film, as described previously.

Ring tips with an optic fiber core and dual ring-disk tips have been fabricated following this procedure (10, 28). Open-core ring tips, or micropipette ring tips, have also been fabricated recently with this procedure (29). Dual AFM/SECM tips with a UME ring surrounding a sharp silicon AFM probe have been fabricated by FIB-assisted microlithographic techniques (6b).

The first and most important test of the electrochemical performance of a UME is the evaluation of its voltammetric behavior, or cyclic voltammogram (CV). For all the described geometries, UMEs define stable diffusion-controlled limiting currents whose values depend on the geometric parameters of the electrodes, and are tabulated in Chapter 6 of this handbook. A good UME in a well-studied electrochemical system (e.g., ferrocenemethanol solution) will generate an S-shaped CV, with a stable and clearly defined diffusion limiting current, and small double-layer capacitance. For a well-behaved UME to be suitable as an SECM tip, it is further evaluated through the so-called SECM approach curve, as described in the following section.

#### *12.3.1.2 Feedback modes—approach curves*

The first question that one may ask is: what is the reason for carrying out an approach curve? The technical aspect of the answer is: (a) to evaluate the geometric characteristics of an SECM UME tip, and (b) to know how close the tip can be positioned with respect to the substrate surface for further experiments. Whatever the reason, the procedure is the same and is described in detail below.

An SECM approach curve (i.e., tip current as a function of distance) allows one to get a very precise value of the tip–substrate distance when the electrode reactions are diffusion controlled. This ability is a consequence of the strong effect that a surface in close proximity to the UME ($<$5 radii) has on the diffusion-controlled current. Both positive and negative feedback effects have been theoretically treated and it is possible to correlate the experimental approach curves to analytical equations to determine very accurately the position of the tip with respect to the substrate surface. Furthermore, approach curves recorded over a conducting substrate provide an additional measurement of the effective radius of the UME tip, while those recorded over insulators provide information about the effective RG of the tip. Thus, this type of experiment is very useful for the characterization of SECM tips.

Experimentally, approach curves can be recorded in a cell configuration, such as that shown in Figure 12.7a. A clean and polished Pt substrate electrode (~3 mm diameter) shown as "1" in Figure 12.7a, is placed in the hole of a Teflon cell. If the seal between the cell and the substrate electrode is not tight enough, a small quantity of Teflon tape can be used to ensure a snug fit. The Teflon cell is screwed to the SECM metal plate (Figure 12.7a, #2), which is then screwed onto the SECM head such that the cell is over the tip holder (Figure 12.7a, #3). The Teflon cell is filled with a solution containing a well-known redox system, such as 1 mM ferrocenemethanol in 0.1 M KCl solution. The base of the cell has to be inspected to ensure that the substrate electrode is snug and that the solution is not leaking out. A real sample may very likely have a different geometry, e.g., flat sheets, which need to be located at the substrate compartment. In that case, a cell configuration like that shown in Figure 12.7b is used. The substrate is tightened by a base with screws

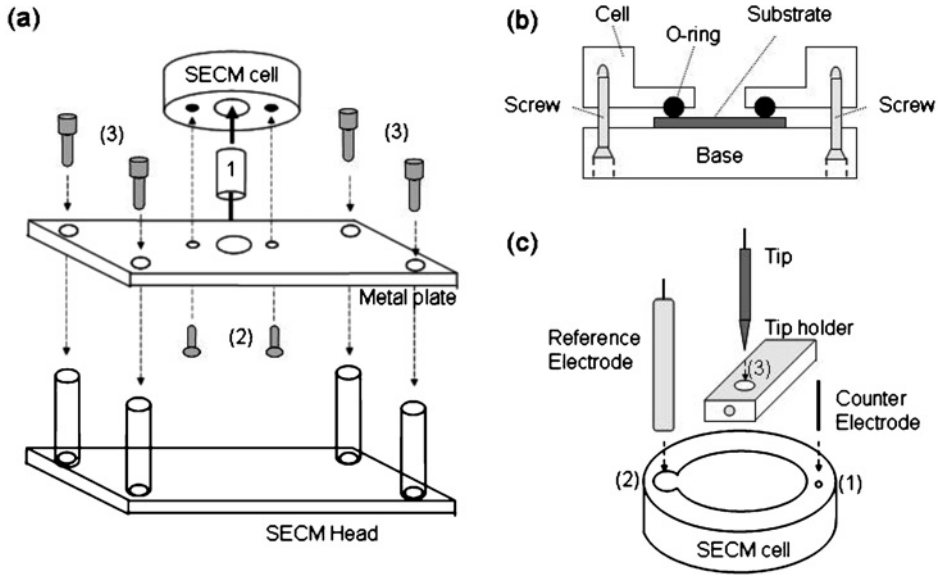


**Figure 12.7** (a) Schematic of the SECM cell assembly: inserting the substrate electrode in the SECM cell (1); screwing the cell onto the SECM metal plate (2); and screwing the metal plate onto the SECM head setup. (b) SECM cell for flat substrates. (c) Schematic of electrode setup.

from the bottom of the cell, using a Teflon or FETFE *o*-ring to prevent leakage of electrolyte. The counter (auxiliary) and reference electrodes are placed in their respective slots (Figure 12.7c, #1 and 2), and the UME is placed in the tip holder (Figure 12.7c, #3). Electrical leads are connected to the substrate, counter, reference, and UME tip electrodes.

The tip must be positioned manually about 2 mm above the substrate surface and either over the insulating sheath of the substrate or over the Pt disk electrode. The potential of the tip is held at a value where the mediator reaction occurs under diffusion-controlled condition, e.g., 0.4 V vs. Ag/AgCl for the oxidation of ferrocenemethanol, and a steady-state limiting current is obtained. Usually, a large conductive substrate at open circuit potential will regenerate the mediator by a process called substrate potential driven feedback (30). However, it is a good practice to apply a potential bias (e.g., 0 V vs. Ag/AgCl) for the reduction of tip-generated ferrocenium to carry out the substrate mediator regeneration more effectively. Of course, nonconductive substrates cannot be biased. The tip is then approached to the substrate in a fast and safe manner. A good way to accomplish this is by using a variable scan rate; that is, starting at ~50 μm $sec^{-1}$ and then decreasing to ~1 μm $sec^{-1}$ when the tip current begins to change because of the SECM feedback effect. A safe point to stop is when $i_T$ changes by about 25% of the $i_{T,\infty}$ value ($I = i_T/i_{T,\infty} = 0.75$ or 1.25 for negative or positive feedback, respectively), which gives a tip–substrate distance $L \cong 1$–2. If it is necessary to go closer, the tip can be withdrawn with a distance of $L = 10$ from this point and approached again at a slow scan rate, about 1 μm $sec^{-1}$. Typical experimental feedback approach curves ($i_T$ vs. $d_{exp}$) are shown in Figure 12.8a for a 25-μm-diameter tip approached from ~130 μm from the substrate. The expected current

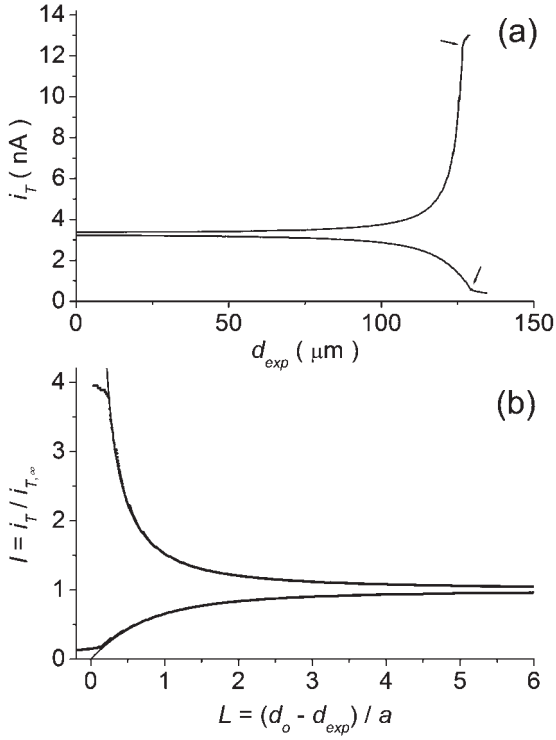


**Figure 12.8** (a) Experimental approach curves of a 25-μm Pt tip obtained in a 1 mM ferrocenemethanol−0.1 M KCl solution on a Teflon surface (lower curve) and on a 3-mm Pt electrode (upper curve) at 0 V vs. Ag/AgCl. The tip was polarized at 0.4 V vs. Ag/AgCl. Scan rate: 3 μm $sec^{-1}$. Arrows signal the point where the tip hit the substrate. (b) Best fittings of experimental approach curves (dots) using equations 12.3.1 (lower solid line) and 12.3.2 (upper solid line) with parameters for RG = 3.04. $i_{T\infty}$ = 3.29 nA in both fittings and $d_o$ = 131.0 and 129.3 μm for upper and lower curves, respectively.

for a good tip should increase to at least three times the infinite distance value ($I > 3$) for conductive substrates, or decrease to less than 25% ($I < 0.25$) for insulating surfaces, before the glass sheath of the UME hits the substrate. This event is manifested by a sudden change in the slope of the current vs. distance curve, as it is marked with arrows in the approach curves of Figure 12.8a. If the approach curve is measured just for tip characterization purposes, this is the end of the experiment and the tip can be safely withdrawn and removed from the cell. The quality and geometric characteristics of the tip will be known after fitting the approach curves. If the approach curve is performed to position the tip at a known distance from the substrate, the tip has to be stopped in a previous instance prior to hitting the substrate. The exact tip–substrate distance, corresponding to the end point of the approach curve, can be determined after fitting the measured curve with theoretical equations.

SECM theory, including amperometric feedback mode, has been recently reviewed in Chapter 5 of reference (1). Recent progress in the theoretical description of SECM include

**Table 12.1**

Dependence of coefficients $k_1$, $k_2$, $k_3$, and $k_4$ for equations (12.3.1) and (12.3.2) on the tip RG value (37)

| RG | $k_1$ | $k_2$ | $k_3$ | $K_4$ |
|---|---|---|---|---|
| Equation 12.3.1 | | | | |
| 15.2 | 0.37377 | 1.85113 | 0.61385 | −2.49554 |
| 10.2 | 0.40472 | 1.60185 | 0.58819 | −2.37294 |
| 8.13 | 0.42676 | 1.46081 | 0.56874 | −2.28548 |
| 5.09 | 0.48678 | 1.17706 | 0.51241 | −2.07873 |
| 3.04 | 0.60478 | 0.86083 | 0.39569 | −1.89455 |
| 2.03 | 0.76179 | 0.60983 | 0.23866 | −2.03267 |
| 1.51 | 0.90404 | 0.42761 | 0.09743 | −3.23064 |
| Equation 12.3.2 | | | | |
| 10.2 | 0.72627 | 0.76651 | 0.26015 | −1.41332 |
| 5.1 | 0.72035 | 0.75128 | 0.26651 | −1.62091 |
| 1.51 | 0.63349 | 0.67476 | 0.36509 | −1.42897 |

the generation of more efficient algorithms (31–33) and the report of approximate analytical expressions (34–36). Analytical approximations of the approach curves obtained by processing simulated data are shown in equations (12.3.1) and (12.3.2) for negative and positive feedback, respectively. The coefficients of these equations depend on the tip RG value and are presented in Table 12.1 (37). Note that the RG has a strong effect on the negative-feedback approach curve, which makes this dependence a good tool to estimate this parameter. The RG effect is much less pronounced in positive-feedback approach curves. To correlate these equations with the experimental curve, it is necessary to normalize the experimental variables according to equations (12.3.3) and (12.3.4). The unknown parameter is $d_o$, which is the distance between the first point of the experimental approach curve and the substrate surface, which is very close to the last point of the approach curve.

$$I = \frac{1}{\left[k_1 + \frac{k_2}{L} + k_3 \exp\left(\frac{k_4}{L}\right)\right]} \tag{12.3.1}$$

$$I = k_1 + \frac{k_2}{L} + k_3 \exp\left(\frac{k_4}{L}\right) \tag{12.3.2}$$

$$i_T \rightarrow I = i_T / i_{T,\infty} \tag{12.3.3}$$

$$d_{exp} \rightarrow L = d / a = (d_0 - d_{exp}) / a \tag{12.3.4}$$

$i_{T,\infty}$ can be estimated from the steady-state value measured when the tip is far away from the substrate. However, in the theoretical equations, $i_T$ is, in fact, normalized with respect to $i_{T,\infty}$ for a UME with infinite RG. As the limiting current is affected by the RG value when

it is lower than 10 (37), $i_{T,\infty}$ thus has some uncertainty and is treated as a variable parameter during the fitting. For example, Figure 12.8b shows the best fittings of the experimental approach curves shown in Figure 12.8a.

Different strategies to measure approach curves, their theoretical treatment, and the ways to estimate the tip dimensions when using tips having other geometries have been published for hemispherical (21, 38), conical (27), and ring or ring-disk shaped tips (39, 40).

The common characteristic of these tips is that the feedback effect in such cases is much less pronounced than that on disk-shaped tips. For example, the effect of $H$ on conical tip approach curves is shown in Figure 12.9 (27). If $H$ is sufficiently small ($H \leq 0.5$),

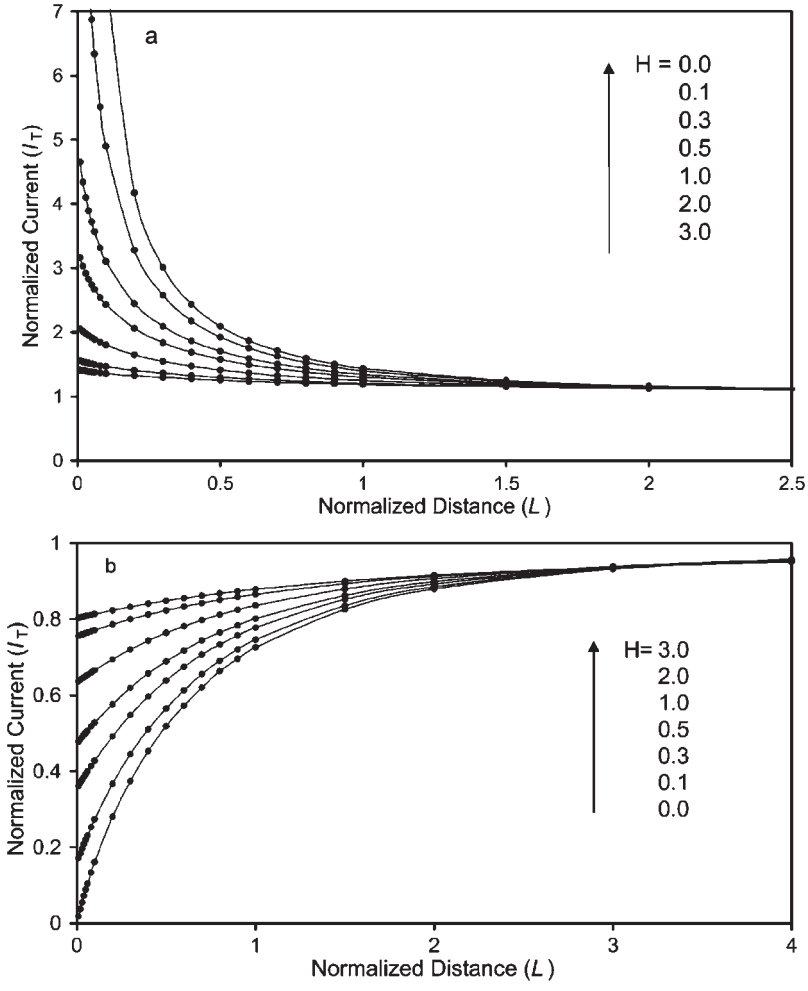


**Figure 12.9** Theoretical approach curves of conical tips at (a) a conductive and (b) an insulating substrates for different $H$ values and RG = 2 (from reference (27)). Note that the curves for $H = 0$ correspond to a disk UME.

the current at a conical tip is still very sensitive to *d*. For example, a decrease to $I = 0.5$ or an increase to $I = 3.2$ for negative and positive feedback approach curves, respectively, are expected at the substrate surface for a tip with $H = 0.5$. Thus, a conical tip with a small value of $H$ can closely approach the substrate surface and give substantial feedback.

#### *12.3.1.3 Generation/collection (G/C) mode*

The generation/collection (G/C) modes constitute a different SECM procedure that expands the applicability of the technique to a wide range of situations. In these modes, the collector (either tip or substrate) works as an amperometric sensor that collects the products produced at the generator surface (either substrate or tip, respectively). Thus, the collector potential is controlled to electrochemically react with the generator-produced species. Typical collector responses used in G/C experiments are (a) voltammetric curves, where the collector potential is swept, and (b) diffusion-controlled limiting current vs. time curves. In contrast to the feedback mode where steady-sate responses are monitored, in G/C experiments, the current–time dependence is an important set of data to evaluate. The timescale of most of G/C transient experiments is much wider, possibly up to 100 sec. Moreover, as the tip–substrate distances increase, typical coupling and distortion of transient responses are not significant.

These methods are very useful in situations where the mediator-cycling process that produces the feedback effect is somehow perturbed or just cannot be detected. Furthermore, they can be used for collection efficiency (CE) measurements of reaction products, analogous to other two-electrode geometries, such as rotating ring-disk electrode and microband arrays. Nonetheless, for similar geometric conditions, the spatial and temporal resolutions of the feedback mode are superior to those of G/C methods. Moreover, G/C methods are not useful for precise positioning of the tip, as the measured response is not very sensitive to the tip–substrate distance. Regardless of these limitations, the capabilities of the G/C modes to induce and evaluate processes in micro or even nanometer domains make them very attractive for localized studies. Importantly, G/C experiments can be performed at significant separations (up to $L \cong 20$), which is a major advantage in studies involving the reactivity of surfaces (e.g., reactivity imaging) with significant topographical geometry.

##### *(a) Substrate generation/tip collection mode*

When the collector is the tip, the mode of operation is called the SG/TC mode; the schematic is shown in Figure 12.10. In this case, the substrate may be any kind of surface that is able to generate a flux of the species to be detected at the tip, such as an electrode generating hydrogen, heterogeneous catalysts producing $H_2O_2$, or a living cell pumping out metabolites from stressing agents.

In a SG/TC experiment, the spatial and temporal mapping of concentration profiles of species coming from (or being consumed in) the studied process is performed. Classical theories for linear or hemispherical diffusion that relates concentration vs. time and spatial coordinates (3) can be used to calculate kinetic parameters of chemical and electrochemical processes, as well as mass-transport coefficients. When the substrate is a large surface, linear diffusion of the substrate-generated (or consumed) species is observed, and the

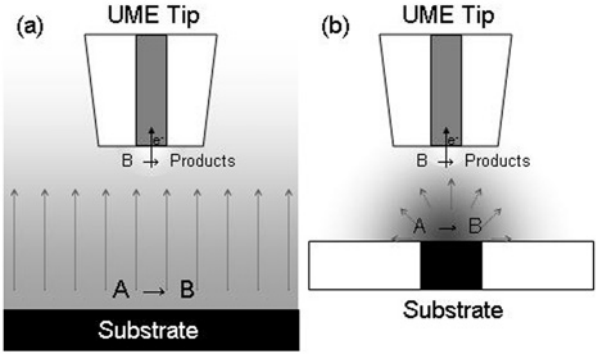


**Figure 12.10** Schematic of the SG/TC operation mode applied for studying the reaction A → B at the substrate by amperometric detection of B at the tip. (a) The substrate is a large surface (linear diffusion). (b) The substrate is a UME (hemispheric diffusion). Darker gray color indicates higher concentration of B.

diffusion layer does not reach a steady-state situation (Figure 12.10a). If the substrate is a UME disk (diameter $< 30$ μm), hemispherical diffusion of generated species is expected, which provides a quasi-steady-state concentration profile (Figure 12.10b). This latter case is very useful for electrochemical activity imaging of small conductive spots (41).

Systems that are frequently studied by SG/TC include enzymatically patterned surfaces (42). For example, the activity of immobilized *horseradish peroxidase* for reduction of $H_2O_2$ to water using ferrocenemethanol in solution as an electron-donor can be studied by amperometric detection of ferrocene methanol cations. Furthermore, the oxidation of glucose by oxygen on immobilized *glucose oxidase* can be studied by tip collection (oxidation) of $H_2O_2$, the product of oxygen reduction. The tip can be used as an amperometric oxygen sensor (by reducing $O_2$ to $H_2O$ or $H_2O_2$) to map $O_2$ concentration profiles (43). In this way, it is possible to monitor the respiration of living organisms (44, 45), and the catalytic activity for oxygen reduction of electro- and photo-catalysts (46, 47). Transport of ions and molecules through film pores has been thoroughly studied by this technique (see Chapter 9 in reference (1) for a more complete review) in view of future studies of single-pore transport processes in cell membranes. Along this line, SG/TC studies of transport activity of supported cells in a macroscopic fashion have been recently reported (48).

Probably, the main complication of this type of experiment is that the diffusion concentration profile cannot be kept unperturbed during the whole time frame of the measurement, which may be more than a minute. Even using an efficient vibration isolation table, it is very difficult to prevent natural convective processes (3). Another detail to take into account for the interpretation of SG/TC results is the effect that an amperometric tip may have on the concentration profile of the substrate, which is more important for small tip–substrate distances (49).

The CE, defined as $CE_{SG/TC} = i_T/i_S$, which is valid only when the substrate is an electrode, is a parameter of limited utility as it depends on the dimension of the substrate and generally is a very small value. In fact, the ratio $J = |i_T/i_{T,S,\infty}|$ is much more useful, where $i_{T,S,\infty}$ is the tip current when it drives the substrate reaction in the bulk solution. When

SG/TC is used in conjunction with the feedback mode, the transient response of $J$ allows the calculation of reaction rate constants for chemical reactions coupled to electrode reactions (50). Another useful ratio is $\gamma = i_{T,SG/TC}/i_{T,feedback}$ calculated at small tip–substrate distances, which allows the ratio between the diffusion coefficients of products and reactants ($\gamma = D_{product}/D_{reactant}$) (51) to be determined.

***(b) Tip generation/substrate collection mode***

In the TG/SC mode, the collector is the substrate while the tip is used to locally generate species (A), as shown in Figure 12.11a. Thus, the substrate is polarized to catalyze the electrode reaction of a species (A), which is not initially in solution. The tip is positioned in close proximity to the substrate and is controlled to generate A, which will diffuse and reach the substrate surface carrying out the electrode reaction ($A + ne^- \rightarrow B$) of interest. The faradaic substrate current is monitored as a function of time, tip–substrate distance, and substrate potential.

It is important to understand the significance of the background substrate current ($i_{S,B}$) and of the faradaic substrate current ($i_{S,F}$). The background current is the substrate current measured when the tip is not working (i.e., not generating any species). In theory, this current should be null because no solution reaction occurs. In reality, the background current can be so large and unstable that it will be impossible to perform any measurement. The origin of the background current is uncertain. Probably, it arises from the reaction of trace species in solution (e.g., oxygen) or from surface transformations (e.g., oxide electrogeneration). It is proportional to the substrate surface area and reactivity. As a rule, any TG/SC experiment should be performed on the smallest possible substrate area, and it should be preceded by a long quiescent time (up to 5 min) so that the substrate background current reaches a stable value. The background current must be measured in a blank experiment (tip off). In contrast, the faradaic current is the current exclusively from the reaction of the tip-generated species. It can be calculated from the substrate current measured when the tip is operating ($i_S$) minus the background current, $i_{S,F} = i_S - i_{S,B}$.

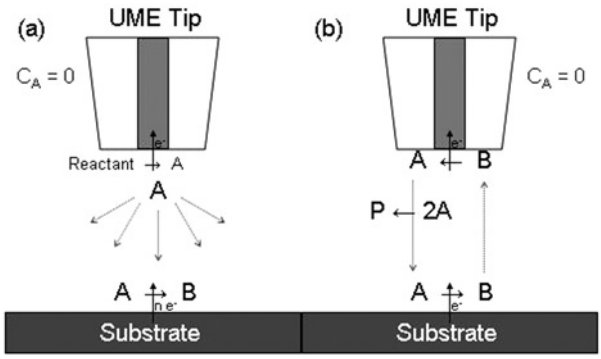


**Figure 12.11** (a) Schematic of the TG/SC operation mode applied for studying the reaction $A \rightarrow B$ at the substrate by electro-generating A at the tip by controlling either its potential or its current. (b) Schematic of TG/SC mode combined with feedback mode, applied for studying the kinetics of the chemical reaction $2A \rightarrow P$ in the tip–substrate gap.

At distances of $L < 2$, in the absence of chemical transformation in the tip–substrate gap and when the studied reaction operates under mass-transfer control, all of the tip-generated reactants reach the substrate and undergo the electrode reaction (52). Thus, the CE defined as $CE_{TG/SC} = i_{S,F}/i_T$ is close to 1. Ideally, this means that in the best case, $i_{S,F}$ will be equal to $i_T$. Note that $i_T$ will never be higher than a few nA, while $i_{S,B}$ (and $i_S$) may be as high as tens of μA. Thus, the main drawback of this method is the very low signal-to-background ratio.

This mode has been almost exclusively used in combination with feedback experiments for studying coupled homogeneous chemical reactions following electron-transfer in the tip–substrate gap (53). The CE will be affected by any side reaction in the gap (Figure 12.11b), which makes it a useful parameter to monitor and calculate chemical reaction rates. Only recently was this mode applied to the study of electrode reactions using a constant-current variant of Figure 12.11a (52, 54). The electro-reduction of dissolved oxygen on varied materials was studied using this method. The tip generates a microenvironment of $O_2$-saturated solution in a localized region close to the substrate, which allows the construction of an oxygen–reduction $I_S$ vs. $E_S$ curve (polarization curve) for that particular region. By addressing different substrate domains (e.g., spots of different materials, such as Pt and Au supported on a common conductive nonactive surface) and measuring polarization curves on them, it is possible to compare the activity of each of these materials in a single experiment (54). The imaging capability of this mode can be exploited for activity imaging on large arrays of catalyst spots, as will be detailed in Section 12.4.3, because this mode is less dependent on the tip–substrate distance.

## 12.3.2 Potentiometric method

### *12.3.2.1 Introduction*

This section deals with the fabrication of potentiometric probes and their use in SECM studies. Potentiometric probes (see Chapter 7) can detect many non-electroactive species not accessible to amperometric techniques. They are highly selective and have found widespread application in clinical chemistry, in environmental studies and the food industry. A general review of potentiometric probe fabrication has been presented previously, and several publications have demonstrated the utility of potentiometric probes in SECM studies (55). This section will provide the reader with a highlight of potentiometric probe fabrication techniques taken from the literature. The section will also include a discussion of the basic concepts, fabrication steps, necessary equipment, and characterization of ion-selective micropipettes applied in SECM studies.

Potentiometric detection is based on the detection of a membrane potential across the membrane of a probe electrode. Potentiometric probes measure a membrane potential linearly dependent on the logarithm of the activity of a primary ion. Experimentally, a typical setup would be

Outer-reference || Sample | Membrane | Internal Solution | Internal-Reference
**Ion-Selective Electrode**

The membranes used in ion-selective electrodes separate two different electrolytes and are not equally permeable to all kinds of ions. At the interface between the two electrolytes, different events contribute to the measured membrane potential. First, a diffusion potential arises from differences in mobility and concentration of ions in contact at the interface, as seen in liquid junctions. Second, a Donnan potential arises when the membrane completely prevents the diffusion of at least one species from solution to the other. Third, the exchange equilibria between the electrolyte and the membrane interface must also be considered to adequately describe the membrane potential of ion-selective electrodes with solid or liquid electrolyte membranes.

When no current is flowing, the measured cell potential ($E_{cell}$) is the sum of all potential contributions in the cell such that

$$E_{cell} = E_{IS} - E_R + E_J \tag{12.3.5}$$

where $E_{IS}$ is the potential of the ion-selective probes, $E_R$ is the potential of the reference electrode, and $E_J$ is a liquid junction potential between the sample solution and the internal solution of the reference electrode. This junction potential is often eliminated by choosing a supporting electrolyte that closely matches that of the reference electrode.

The resulting cell potential ($E_{cell}$) describes the relationship between the ion-selective membrane potential and the primary ion activity. When the membrane diffusion potential is zero, the membrane potential is defined by the Nernst equation:

$$E_{cell} = \text{Const} \pm 2.303RT/z_i F[\log(a_i)] \tag{12.3.6}$$

where Const is a constant that includes activity independent terms of the primary ion, $R$ is the gas constant, $T$ is the absolute temperature, $z_i$ is the charge of the primary ion, $F$ is the Faraday constant, and $a_i$ is the activity of the primary ion in the sample. Specific potentiometric probes should, therefore, present a Nernstian slope of about 59 mV/$z_i$/decade (25 °C). To have a relationship dependent on the concentration of the primary ion, the activity coefficient of the primary ion must be known or the experiment must be carried out under dilute conditions.

An ideal analytical sensor should specifically and quantitatively detect a single ion. This would mean that the membrane potential would be affected by only one particular ion in solution. Potentiometric probes are rarely specific to a given ion and are commonly selective to a series of ions. Their response will selectively respond to a certain type of ion but will be affected by the presence of other ions leading to interferences. In the case of a solution with only two types of ions where ion (j) would interfere with the potentiometric response of the primary ion (i), the measured cell potential can be approximated to the Nikolsky–Eisenman equation:

$$E_{cell} = \text{Const} \pm 2.303RT/z_i F\left[\log\left(a_i + \sum K_{ij}^{pot}(a_j)^{z_i/z_j}\right)\right] \tag{12.3.7}$$

where $K_{ij}^{pot}$ is the selectivity coefficient that weighs the contribution of the interfering ion, $a_j$ is the activity of the interfering ion, and $z_j$ is the charge of the interfering ion. The derivation

of this equation is reported (56); it was derived for a compact ion-exchanger membrane with a fixed concentration of equivalent active sites where an internal diffusion potential occurred.

#### *12.3.2.2 Potentiometric probe fabrication*

There are two defining groups of ion-selective electrodes: (a) solid-membrane electrodes (56, pp. 93, 96, 103, 104, 106, 107), and (b) liquid-membrane electrodes (55, pp. 408–413). In the case of solid membranes, a network of ions is immobilized in a support such that the number of active sites remains constant with time. The membranes can be homogenous (single crystal, crystalline structure, or glass) or heterogeneous (where the active sites are imbedded in a polymer matrix). In this case, the selective compound can be of opposite charge of the primary ion or a complexing agent of this ion. Liquid membrane electrodes are mutlicomponent devices whose active agents are ionized ion exchangers or electroneutral ion carriers. The measuring membranes are usually a water immiscible organic phase that contain ionophores and that can separate the sample solution from the internal filling solution. A few examples of potentiometric probe fabrication protocols that can be applied to SECM studies will be presented but the interested reader can refer to other work (57).

***(a) Ion-selective glass microelectrodes***

Glass-membrane electrodes include $H^+$, $Na^+$, $K^+$, and $Ag^+$ selective glass electrodes. The active measuring device in these electrodes is confined inside the inner walls of a pulled glass capillary. The ion selectivity is gained by choosing the appropriate glass composition. For example, glass having a weight composition of ($Na_2O$(22%); CaO(6%); and $SiO_2$(72%)) is more selective to $H^+$ ions; while a glass with a weight composition of ($Na_2O$(11%); $Al_2O_3$(18%); and $SiO_2$(71%)) is more selective toward $Na^+$ ions (56, p. 107). Glass electrodes, like the pH electrode, have a Nernstian linear response to $H^+$ up to a pH of ~11–12.

Different techniques can be employed to produce micrometer size pH probes. Generally, a thin ion-selective glass bulb needs to be combined with an insulating microcapillary stem such that the internal filling solution and Ag/AgCl reference electrode can be accommodated. To isolate the ion-selective glass at the end of the microcapillary, two approaches can be used: (a) a closed ion-selective micropipette is isolated at the end of an insulating micropipette. This can be accomplished by pulling an ion-selective micropipette and insulating the stem with an insulating material like a shellac or nail polish. Another option is to seal an ion-selective micropipette into an open-ended insulating microcapillary using a glass/glass joint (55, p. 402) or a sealing wax (55, p. 402). The glass/glass sealed pH sensor can further be pulled down with a laser puller to obtain a pH sensor on the order of 2 μm (55, p. 403). (2) The end of an open-ended microcapillary can also be coated with a thin layer of ion-selective glass (55, p. 402). This procedure can yield single and double barrel electrodes (55, p. 402).

The difficulty in combining glass membranes in SECM applications is that their fabrication is technically challenging. To our knowledge, no glass microelectrode probe has been reported in SECM experiments. As these electrodes have been applied in intracellular pH measurements, their detection limit and response time seem to be adequate for low analyte concentration measurements and seem very promising for SECM applications.

***(b) Ion-selective crystalline membrane microelectrodes***

Solid-state membrane electrodes include $H^+$, $F^-$, $CN^-$, $Cl^-$, $I^-$, $Br^-$, $H_2S$, $CN^-$, thiourea, $Pb^{2+}$, $Cu^{2+}$, and $Cd^{2+}$ selective electrodes. In this category, silver halide and silver sulphide electrodes are found. The macroscopic ion-selective electrodes made with these systems have been applied in many fields, such as medicine, food industry, and environmental studies (56, pp. 93, 96, 103, 104) but their full potential has not yet been exploited in terms of SECM studies.

Antimony microdisc electrodes used as a pH-measuring probe have been reported in SECM studies. A detailed protocol for fabrication of these tips has been published (58). Briefly, a thick-walled capillary (o.d., 10 mm; i.d., 1 mm) is filled with melted antimony using suction. The antimony filled capillary is then pulled down sequentially using glass blowing techniques or a resistor coil until a Sb microdisc (o.d., 20–30 μm; i.d., 2–3 μm diameter) is obtained. This microdisk fiber is then mechanically glued at the end of a pulled glass capillary with silver-epoxy together with a copper wire, which serves as contact.

An $Ag/Ag^+$ microelectrode has been used in SECM studies to measure $Ag^+$ and $Cl^-$ profiles (59). To build a $Ag/Ag^+$ microindicator electrode, a 1-cm long 50 μm diameter Ag wire is soldered onto a large connection wire and then inserted into the end of a Pasteur pipette. Quickset epoxy resin is then rapidly forced up as far inside the capillary as possible. Once set, the tip is sequentially sharpened to form a pencil like shape. The radius of the insulator (glass and/or epoxy resin) should be about five times that of the Ag wire. The geometry of the $Ag/Ag^+$ microelectrode has no direct influence on the measured potential, but it allows for a closer approach to the substrate and reduces shielding. The $Ag/Ag^+$ microelectrodes can also be converted into Ag/AgCl microelectrodes by briefly anodizing the Ag microelectrode in 1 mM HCl solution. The $Ag/Ag^+$ microelectrodes can be used to probe $Ag^+$ concentration profiles, while the Ag/AgCl microelectrodes can be used to monitor $Cl^-$ concentration profiles.

***(c) Ion-selective liquid membrane microelectrodes***

Liquid-membrane electrodes include classical ion-exchange, liquid ion-exchange, and electroneutral ionophore-based liquid membrane electrodes. Of particular interest are systems where the ion-exchanging compounds are dissolved macrocyclic compounds that have a strong selectivity to alkali metals. The stability of the formed complexes in nonpolar solvents far exceeds that found in water and allows for the fabrication of membrane-free micropipettes where the nonpolar/water interface is the membrane. Unfortunately, this leads to higher resistance than that exhibited by crystalline micropipettes and requires the addition of lipophilic salt to the nonpolar solvent to decrease the pipette resistance.

Most macrocycles used in the design of these electrodes are uncharged and have common properties, such as the formation of complexes with univalent ions and the ability to transport these ions across lipid membranes. The complexes have a polar cavity where the complexed ion sits and an outer lipophilic envelop that allows dissolution of the ion into the nonpolar solvent. There is a wide range of applicable macrocyclic ligands, including depsipeptides (valinomycin, enniatins A, B, and C), macrotetrolides (nonactin, monactin, dinactin, and trinactin), cyclic peptides (gramicidin S and tyrocidin A), cyclic polyethers (for example, dicyclohexyl-18-crown-6 isomers, dicyclohexyl-14-crown-4, and dibenzo-*x*-crown-*y*, where (*x*, *y*): (18, 6); (21, 7); (24, 8); (30, 10); and (60, 20)), and also some

acyclic compounds (nigericin and monensin) (56, p. 149; 55, pp. 408–413). The great advantage of using these electroneutral-based ion-selective electrodes is that their fabrication protocol differs little from one cocktail to the other.

Generally, ion-selective liquid membrane micropipettes are made from a similar procedure. The capillaries are cleaned and pulled to the desired dimensions. The interior of the pipette is silanized prior to the addition of the ion-selective cocktail. The silanization reagent concentration and time of reaction are important as the glass hydrophobicity prevents the outer aqueous solution from being drawn into the pipette. The cocktail solution is loaded from the pulled end of the pipette by capillary action and using light suction. The internal filling solution is back filled and the reference electrode (often 100 μm Ag/AgCl wire) is secured to the pipette with silicon rubber or parafilm. Two detailed fabrication protocol are given below and have been chosen on the basis that they have previously been used in potentiometric SECM studies.

***$Ca^{2+}$ ionophore sensor (60).*** To make $Ca^{2+}$-selective SECM tips, borosilicate glass capillaries (1.5-mm o.d., 0.75-mm i.d., 100-mm length) are pulled using a laser or resistor puller. The resulting micropipettes should have a 1-cm long flexible taper. Polishing of the micropipettes using a beveller coated with 1-μm sized alumina particles leads to smooth and clean openings with diameters ranging from 5 to 20 μm. The inner wall of the micropipette is then silanized using hexamethyldisilazane prior to being filled with a $Ca^{2+}$-selective liquid membrane solution like $Ca^{2+}$-ionophore, ETH129. The micropipette is back-filled with an internal electrolyte solution containing $CaCl_2$. The reference electrode, Ag/AgCl, is finally inserted as an internal electrode.

***$K^+$ ionophore sensor (61).*** To make $K^+$-selective SECM tips, borosilicate capillaries (o.d./i.d.: 1.0/0.58 mm) are cleaned in a 1:1 (v/v) mixture of concentrated sulfuric acid and 30% hydrogen peroxide overnight, washed and dried at 120 °C for 30 min. Using a laser-based pipette puller, patch clamp type pipettes are produced (orifice radius = 0.7–20 μm). The inner wall of each pipette is silanized with a toluene solution of trimethylchlorosilane (5–100% v/v). The solution is removed from the pipette after 5–30 min, emptied using a syringe, and then connected to a vacuum pump to remove any residual silanizing vapor. The experimental system can be represented by the following cell:

Ag/AgTPBCl/10 mM valinomycin + 10 mM ETH 500 (DCE) |
← aqueous sample solution/AgCl/Ag
**$K^+$ selective micropipette**

To make the $K^+$ selective micropipette, a 1,2-dichloroethane (DCE) solution of 10 mM valinomycin and 10 mM tetradodecylammonium tetrakis (4-chlorophenyl)borate (ETH 500) is used as ionophore and supporting electrolyte, respectively. Hydrophobic ETH 500 was used in the organic phase to obtain a sufficiently wide potential window and also to avoid an ion-exchange reaction between $K^+$ in the aqueous phase and the cationic electrolyte in the organic phase. The silanized pipettes are filled with the organic solution through the larger opening with a small (10 μL) syringe. A 0.25-mm silver wire coated with silver tetrakis (4-chlorophenyl) borate (AgTPBCl) by reduction of Ag in a DCE solution of

10 mM tetrabutylammonium tetrakis (4-chlorophenyl) borate and was inserted into each pipette. The top of the pipette was then closed with parafilm.

***(d) Equipment requirements***

A standard one electrode configuration for potentiometric measurements consists of the potentiometric electrode connected to a voltage follower and the reference electrode connected to electrical ground. To improve noise level and drift, a differential potentiometric mode can be carried out using a high-sensitive potentiometer in a three-electrode configuration consisting of the SECM potentiometric probe and two independent external references. For example, the potential difference between the potentiometric micropipette and a large inert Pt electrode ($\Delta E_{tip}$) is compared with the potential difference between a large reference electrode of the same nature as the potentiometric micropipette and the Pt electrode ($\Delta E_{ref}$). The Pt wire is connected to the electrical ground of the electronic circuit. High-input impedance operational amplifiers (150 fA input bias current) are used as voltage followers to buffer the input of the three electrodes (micropipette and two references). The followers should be positioned as close as possible to the electrodes. The potential differences are then compared with a precision unit-gain differential amplifier. The resulting amplified output ($\Delta E_{out} = \Delta E_{tip} - \Delta E_{ref}$) is proportional to the primary ion activity under the proper experimental conditions (60b). In such an instrument, circuit design and proper insulation connection wires are critical to limit the leakage currents. As such, the SECM head and the potentiometric circuit should be located inside a Faraday cage (55).

To perform potentiometric SECM, one needs to combine a high impedance voltmeter as described above with an SECM (homebuilt or commercial). The use of amperometric mode SECM is still desirable as it can be used to position the pipette and determine the tip–substrate distance. A more detailed discussion concerning the positioning of potentiometric probes and the acquisition of approach curves will be presented in the next section.

### *12.3.2.3 Potentiometric probe characterization*

To characterize potentiometric probes, one must evaluate their response function, selectivity coefficient, response time, and ohmic drop. The response function of a potentiometric probe is a calibration curve of the measured membrane potential with the log of the concentration (or activity) of the primary ion must be acquired. To use concentration values, the activity coefficients must be known and many of them are tabulated. Another option is to use (when possible) dilute solutions such that the activity coefficients maybe neglected.

The measured slope of the response function should be close to 59 mV/$z_i$/decade. At low primary ion concentrations, the potentiometric response can reach a steady state that can be due to impurities in the water or due to the presence of potentially interfering ions. The lower limiting value of the micropipette response at low primary ion activity can also be taken as the background for the SECM approach curves. In certain circumstances, the addition of different chelators (HEDTA, NTA, and EGTA) can be added to try to limit the effect of interfering metal ions.

Typically, ion-selective micropipettes can be used in a concentration range of $10^{-1}$ to $10^{-5}$ M and have a detection limit of about $10^{-6}$ M. As they can drift easily it is importance

that a calibration curve be performed following an experiment and compared with the initial one. This drift occurs as a result of changes in the surface structure of solid-membrane electrodes when in contact with the electrolyte and to the dissolution of the ion exchanger in liquid-membrane electrodes.

The selectivity coefficient provides fundamental information concerning the impact of various interfering ions on the performance of a given ion-selective electrode. The weaker the interference of a given ion with the primary ion, the lower is the value of the selectivity coefficient. The determination of the selectivity coefficients assumes that the behavior of the ion-selective electrode follows a nernstian behavior. As the electrode often deviates from nernstian behavior, the selectivity coefficient is often only semi-quantitative. The coefficient is dependent on the concentration of both the primary ion and the interfering ion. To determine the selectivity coefficient, a plot of the ion-selective potential vs. the logarithm of the concentration of the primary ion is obtained at a given concentration of interfering ion. This graph ideally presents two linear portions for two ions of identical charge. The intercept of these two regions is the selectivity coefficient. Many of the selectivity coefficients are tabulated and can be substituted but it should be emphasized that these coefficients roughly determine the region in which the electrode exhibits nernstian behavior and is an indication of where they can be used reliably.

The response time of an electrode describes the ion-selective electrode's sensitivity to ion activity changes. The response time is a sensitive parameter defined as the time taken by the experimental setup to reach a chosen percent of the final cell voltage following a given change in the activity of the primary ion. This definition is specific to a given experimental setup as the time response of the micropipette will vary with the type of micropipette used, the particular experimental conditions, the electronics, and the method used to cause the primary ion activity change. In terms of macro ion-selective electrode, common response times would be on the order of seconds (56, p. 70); while for ion-selective micropipettes, response times on the order of 10 ms have been reported (60). The response time of the electrode is of particular interest when close proximity measurements are made.

Liquid membrane ion-selective electrodes have a high internal resistance ($10^8 - 10^{11}\ \Omega$), which requires the use of a high-impedance voltmeter. Micropipettes with ion-exchangers tend to have impedance in the lower range, while those made with an electroneutral carrier usually exhibit impedances of $10^{11}\ \Omega$. Such high resistances require the use of a high-impedance voltage device that has an input impedance of at least $10^{13}\ \Omega$. This is necessary to avoid errors in the current input bias. Practically, the maximum current passing through the electrode multiplied by the largest resistance should not exceed 0.5 mV such that an error less than 2% is obtained on the measured activity of the primary ion (55, p. 422). Finally, to avoid contamination of the membrane potential by potentials occurring across the glass, the electrode shaft should be properly shielded.

#### *12.3.2.4 SECM potentiometric measurements*

To use potentiometric probes in SECM, it must be possible to exactly evaluate the tip–substrate distance. Different methods to evaluate the distance dependence are presented

below. None of these methods can be applied unilaterally as they are applicable to a limited number of experimental conditions or require the use of very special instrumental setups.

(1) Metal oxide electrodes have amperometric and potentiometric capabilities. $Sb/SbO_2$ electrodes can first be approached to a surface in amperometric mode using the oxygen reduction reaction (ORR). The electrode is then properly conditioned for potentiometric measurements by forming an adequate antimony oxide layer. This electrode can then be used to monitor local pH changes either in feedback or generation/collection mode. This ideal positioning and detection situation can only be applied to metal oxide electrodes because they can use dissolved oxygen as a redox couple for the initial positioning.

(2) A double barrel tip having one amperometric UME and one potentiometric probe can also be designed. To do so, theta capillaries are usually pulled down and then further modified. Fabrication of a dual barrel electrode is technically challenging. To prepare an electroneutral ionophore probe on one side of the dual barrel electrode, one of the pipette tubes must be silanized. To prevent silanization of the other compartment, nitrogen is flushed through during the silanization process. The choice of amperometric material is also limited as conventional resistance or flame sealing would also seal the end of the potentiometric probe. Liquid gallium has been used but has a limited active potential window (62). The two tips must also be separated by the smallest distance possible so that no significant error is made between the area under the amperometric probe and the potentiometric probe.

(3) For silver halides potentiometric sensors, the tip-to-substrate separation can be evaluated based on changes of solution resistance. A fixed dc potential between an AgCl micropipette and a AgCl auxiliary/reference electrode is applied and the steady-state current that passes through them is measured. This current corresponds to the formation of AgCl at the tip and dissolution of AgCl at the auxiliary electrode. This system can be modeled by an equivalent electronic circuit. As the AgCl micropipette approaches the substrate, the solution resistance increases and presents a response similar to that observed under amperometric positive feedback experiments. As with the amperometric approach curves, the solution resistance approach curves can be fitted to a derived theory to extract the true tip–substrate distance (63).

(4) An ac impedance technique based on changes in solution resistance is also available and has been applied to enzyme-coated microelectrodes (64). In this case, a sinusoidal potential is applied between the electrode and the auxiliary electrode. The measured sinusoidal current is sent to a frequency response analyzer that monitors the change of the real impedance with distance to the substrate. Using equivalent circuits, a theoretical approach curve can be obtained and fitted to the experimental solution resistance profiles with distance.

(5) Techniques 3 and 4 cannot usually be applied to electroneutral ion carrier micropipettes that have large electrode resistance. For systems under steady-state conditions, the change in concentration profile with tip–substrate distance can be used to determine the tip–substrate separation. A theory to that effect is available (58).

(6) The case of $K^+$ selective ionophore microelectrodes is of particular interest as the cell:

$$\begin{aligned}&\text{Ag / AgTPBCl / 10 mM valinomycin} \cdot \\ &\quad +10\text{ mM ETH 500 (DCE)} \,|\!\leftarrow \text{aqueous sample solution / AgCl / Ag}\end{aligned}$$

can be used in conventional voltammetric and SECM studies. At the water/DCE interface, a facilitated ion-transfer reaction occurs as follows:

$$\text{Val(DCE)} + \text{K} + \text{(water)} \rightarrow \text{Val-K}^+\text{(DCE)} \text{ (at the pipet tip)}$$

The ion-transfer processes at the microinterface between two immiscible electrolyte solutions (micro-ITIES) at the pipette tip are polarizable. The voltage, $\Delta E$, applied between the Ag/AgTPBCl electrode inside the pipette and the Ag/AgCl electrode in the aqueous phase provides the driving force for the ion transfer process. A voltammogram for $K^+$ transfer can be obtained. At sufficiently negative bias, a steady-state current is obtained and is associated with the $K^+$ transfer from water to DCE internal solution of the pipette. As seen with amperometric UMEs, the observed steady-state current is limited by spherical diffusion of $K^+$ in the outer aqueous phase to the pipette's mouth. For conditions where *the valynomicin far exceeds the $K^+$ concentration*, the steady-state current varied linearly with $K^+$ concentration and conventional approach curves of normalized current with normalized distances can be obtained.

(7) A nonelectrochemical distance control for SECM tips that permits simultaneous acquisition of topographic and electrochemical information can be used (4, 65). Briefly, two piezoelectric plates are attached to the shaft of the SECM tips. One of the plates vibrates the tip at resonance and the second plate detects the amplitude and phase of the tip oscillation. This technique can also constantly regulate the tip to sample separation during imaging experiments.

#### *12.3.2.5 Conclusions, limitations, and prospects*

The SECM potentiometric mode makes use of ion-selective micropipettes. These devices increase the range of detectable species by SECM but are technically very challenging to make and must be calibrated before and after experiments. The electronic requirements to acquire good data are very specific and must include a means to adequately evaluate the tip–substrate distance. Potentiometric detection remains underexploited in SECM studies and has great promise in terms of biological applications.

### 12.3.3 Imaging

In this section, we illustrate the application of SECM for topographic and chemical imaging. The operational principle and methodology of SECM imaging is described in Section 12.3.3.1. One example of constant height SECM imaging in bulk liquid environments is demonstrated in Section 12.3.3.2. Of particular interest is the use of SECM to perform

chemical imaging; for example, to observe differences in electrocatalytic activity of oxygen reduction or hydrogen oxidation on different materials. This will be discussed very briefly in Section 12.3.3.3. A more detailed discussion will be given in Section 12.4.3. SECM imaging for systems including enzymatic sites, corrosion pits, and other artificial patterns will also be described in individual sections.

#### *12.3.3.1 Principle and methodology of SECM imaging*

A three-dimensional SECM image is obtained by scanning the tip in the *XY* plane and monitoring the tip and/or substrate current as a function of tip location. This is the so-called constant height mode (1). The current image obtained can be converted into a plot of *Z*-height, i.e., *d* vs. *XY* position via a ($i_T$ vs. *d*) calibration plot. The current image can be presented in gray scale, where high values of current are shown in light colors and small values as dark colors, or in color code. As mentioned previously, the resolution attainable with SECM is largely governed by the tip size and the distance between tip and sample. With a very small diameter tip (e.g., diameter $< 100$ nm), scanning the tip in close proximity to the substrate surface (e.g., 100 nm above the surface), and measuring the current becomes very difficult due to stray vibrations. Irregularities in the sample surface can cause a tip crash. Thus, for high resolution, SECM must be carried out in the constant current mode (1), as is often used with STM, where the distance is adjusted by a feedback loop to the *z*-piezo to maintain $i_T$ constant. This is straightforward when the sample is either all conductive or all insulating, as the piezo feedback can be set to counter a decrease in tip current by either moving the tip closer (conductor) or farther away (insulator).

For samples that contain both types of regions, a method of recognizing the nature of the substrate must be available for designing the feedback loop. One approach is to modulate the motion of the tip normal to the sample surface and record $di_T/dz$. This is the so-called tip position modulation (TPM) technique (66). The use of TPM can improve the sensitivity and resolution of the SECM image and provide a method of distinguishing between conductive and insulating areas on the substrate surface being examined. Another more universal technique is the combined AFM/SECM technique as described in Section 12.2.2.1 topographic and SECM images to be obtained simultaneously if a proper tip is prepared.

#### *12.3.3.2 Constant height imaging*

We present one example, of a polycarbonate membrane to illustrate the important factors affecting the resolution of topographic SECM images. Figure 12.12 shows a series of constant height SECM images of polycarbonate filtration membranes having a nominal average pore size of ~14 μm. These images were taken with Pt disk tips immersed in a $KCl/K_4Fe(CN)_6$ solution. As shown in frames A–C, which are the current images taken with a 10-μm-diameter Pt disk located at different distances, the resolution of SECM images increases with decreasing distance. The gray scales of the image taken at a normalized distance ($L = d/a$) of 2.4 (frame A) are diffuse and not uniformly distributed, indicating significant overlap between the diffusion fields of the electroactive mediator around individual pores. Decreasing *d* to a normalized distance of 0.26 (frame C) resolves individual pores almost completely, although the apparent pore size is slightly larger than the

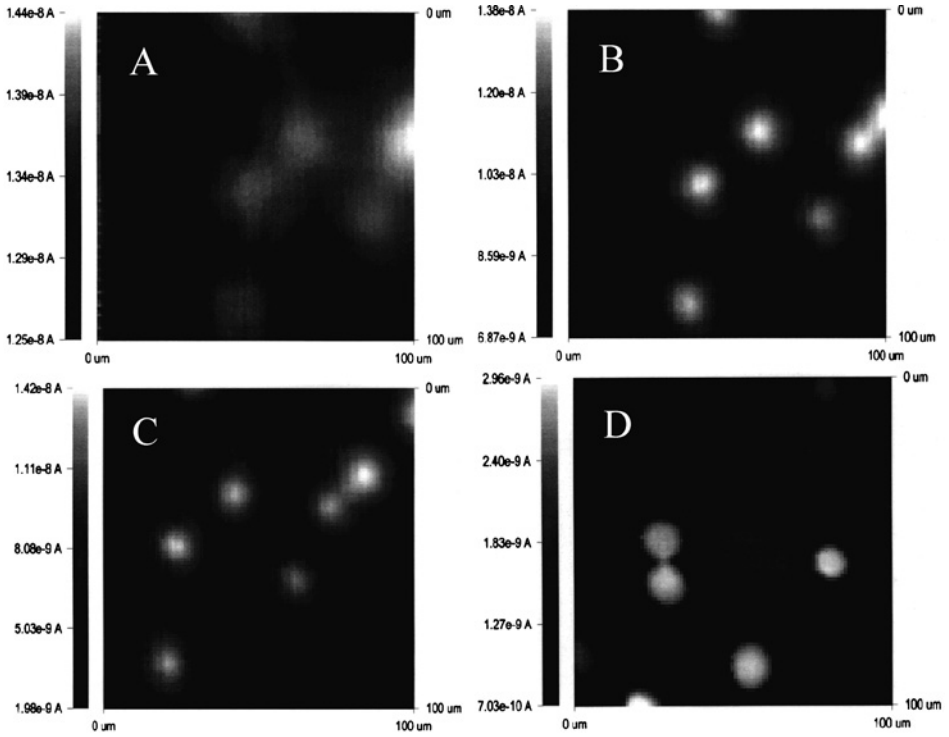


**Figure 12.12** A series of constant-height SECM images of polycarbonate filtration membranes having a nominal average pore size of ~14 μm. The scan size of each image is 100 μm × 100 μm. These images were taken with a CH series-900 SECM unit at Pt disk tips immersed in a solution containing $K_4Fe(CN)_6$ as the redox mediator and KCl as the supporting electrolyte. Images A–C for a 10-μm diameter Pt tip were taken at different normalized distances, *L*. $L = 2.4$ (A); 1.0 (B); 0.25 (C). Image D shows one SECM image of the same membrane taken with a smaller tip (2 μm diameter) at a normalized distance of 1.

nominal value and the gray scale of the image near the pores is still not uniformly distributed. Frame D shows the same membrane imaged with a smaller tip (2 μm diameter) at different location from that for frames A–C and at a normalized distance of 1. As can be seen, not only are individual pores well resolved, but also the apparent pore size is fairly close to the nominal value and the gray scale of the image near the pores is more uniformly distributed than that shown in frames A–C.

#### *12.3.3.3 Chemical imaging*

Reaction rate imaging is unique to SECM and clearly illustrates its "chemical imaging" capability. By proper choice of solution components to control the tip reaction and the electrochemistry at the substrate/solution interface by varying the electrode potential, differential reaction rates at various surfaces can be probed. For example, the location of enzyme sites in a membrane or organelle, where a particular reaction is catalyzed, can be

seen. Such enzymatic systems will be discussed in Section 12.4.6.2. Here, we choose another important reaction, the ORR on different materials in 0.5 M $H_2SO_4$, to demonstrate the capability of SECM for chemical imaging. Figure 12.13 shows several constant height images obtained by the TG/SC mode for ORR on smooth Pt (127-μm diameter, left rear) and Au (100-μm diameter, right front) disks embedded in glass (54). During imaging, two electrodes are held at the same potentials. In the region of potentials where the ORR is totally under diffusion control on both metals ($E_S \leq 0.1$ V vs. hydrogen reference electrode (HRE)), there are no significant differences between the $i_S$ values coming from each disk (see frame a), indicating no significant difference in the activity of oxygen reduction on both electrodes. In the range of $0.1 \text{ V} < E_S < 0.4$ V, the difference in electrocatalytic activity between Pt (still very active) and Au (losing substantial activity) is clearly seen (see frame b). At higher potentials ($E_S \geq 0.4$ V), the activity of Au is essentially zero,

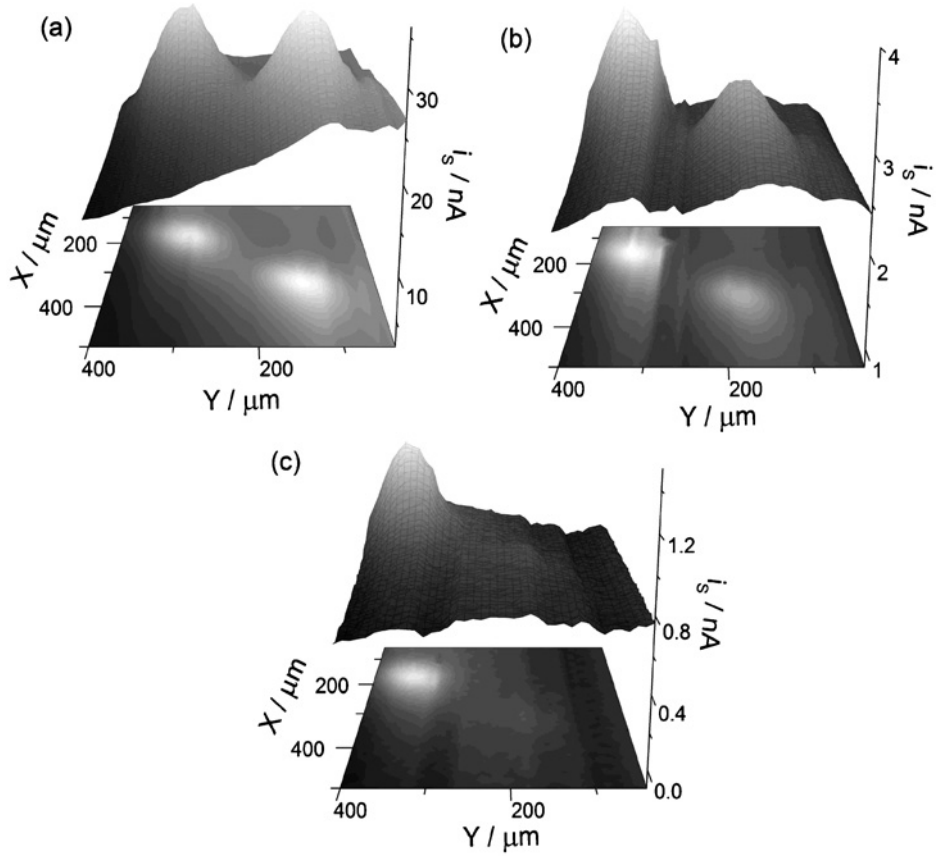


**Figure 12.13** ORR images in 0.5 M $H_2SO_4$ obtained by the TG/SC mode of smooth Pt (127-μm diameter, left rear) and Au (100-μm diameter, right front) disks electrically connected and embedded in glass: scan rate = 300 μm $sec^{-1}$; $d$ = 30 μm; $i_T$ = 15 nA; $E_S$ = 0.1 (a), 0.2 (b), 0.4 (c) V vs. hydrogen reference electrode (HRE). (Adapted from reference (54).)

while Pt still continues reducing oxygen (see frame c). When $E_S$ is positive of 0.8 V, both Pt and Au lose activity. Note that the background current also varied slightly during the scan and depended on the substrate potential. These results clearly demonstrate the chemical imaging capability of SECM and can be used to visually identify materials with different electrocatalytic activity for the ORR.

## 12.4 APPLICATIONS

### 12.4.1 Heterogeneous kinetics

It was shown in Section 12.3 that SECM approach curves allow one to obtain a very precise estimation of the tip–substrate distance and the tip geometric properties, either using negative or positive feedback. In fact, both events are limiting cases of the situation where the reaction at the substrate has a finite reaction rate (Figure 12.14a). If the reaction rate is very small, regeneration of tip reactant is negligible and the substrate behaves as an inert surface, so the approach curve resembles that of hindered diffusion. In contrast, if the substrate reaction is fast enough that it operates under mass-transfer control, total positive feedback occurs and the approach curve is insensitive to the reaction rate. When the tip approaches a substrate with a finite reaction rate, the approach curve may look as one of those shown in Figure 12.14b, depending on the value of the rate constant. This sensitivity of SECM approach curves on the substrate reaction rate, one of the most interesting

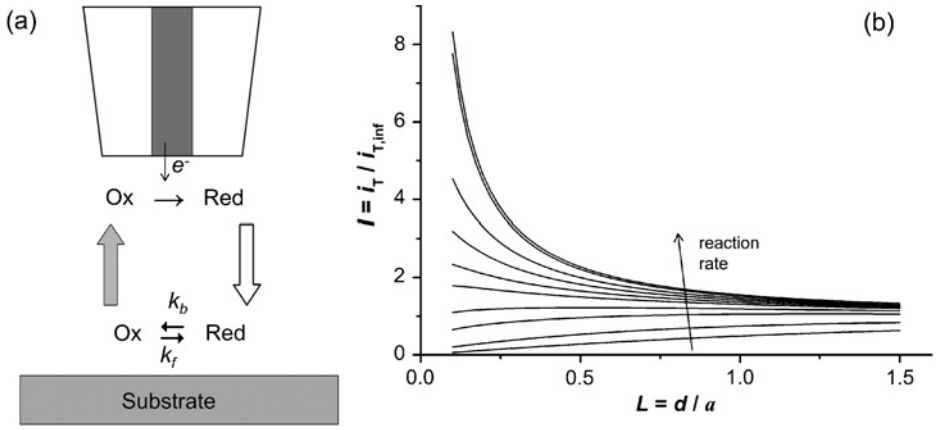


**Figure 12.14** (a) Schematic of the feedback process when the substrate reaction ( $\mathrm{Red} \rightleftharpoons \mathrm{Ox}$ ) operates under kinetic control. The tip electrode reaction ($\mathrm{Ox} + e^- \rightarrow \mathrm{Red}$) operates under diffusion control. The flux of Ox that feedbacks the tip (gray arrow) depends on the values of $k_f$ and $k_b$, the forward (reduction) and backward (oxidation) rate constants of the substrate reaction. (b) Typical kinetically controlled approach curves, where the reaction rate at the substrate increases from bottom to top. Bottom and top dashed lines are curves obtained on substrates that are insulating (negative feedback) and conductive operating under diffusion control (positive feedback), respectively.

properties of SECM, makes this technique a very powerful tool for the kinetic studies of heterogeneous reactions.

The correlation of an experimental "kinetic-controlled" approach curve with a theoretical model allows one to calculate the rate constant of the substrate reaction. To perform this operation, models involving quasireversible and irreversible (reverse reaction neglected) substrate reactions governed by a single-step Butler–Volmer equation were developed by Bard *et al.* (67) using numerical methods. Simulated values of $I$ vs. $L$ for different rate constants and substrate potentials are tabulated in Table 12.2 (67). Although it is time consuming and not very accurate, a procedure to correlate these models with experimental approach curves is by manual comparison of experimental and simulated values. This procedure was used, e.g., to study the kinetics of the $Ru(NH_3)_6^{3+}/Ru(NH_3)_6^{2+}$ couple (67), and for studies of electron-transfer processes across the liquid/liquid interface (68–70). The most common procedure for processing kinetic approach curves is through the use of an approximate analytical equation (equations (12.4.1)–(12.4.5)) (71). This equation was derived from the correlation of $I$–$L$–$\kappa$ working curves simulated for a quasireversible electron-transfer reaction at the substrate, where $\kappa = ka/D$ (where $D$ is the diffusion coefficient of tip reactant). The parameter $k$ is the rate constant of the quasireversible reaction at the substrate, which for an electrode reaction is given by equation (12.4.6), where $k^\circ$ is the standard rate constant and $E^\circ$ is the standard potential. This equation is valid in the range of distances $0.1 \leq L \leq 1.5$ and for values of rate constants in the interval $0.01 \leq \kappa \leq 1000$.

From Figure 12.14b, it can be noted that the region of highest sensitivity of these equations with respect to the value of $\kappa$ is in the interval, $0.1 \leq L \leq 0.5$. Thus, an important factor to perform reliable kinetic studies by SECM is the quality of the tip, which needs to be able to approach until the end of this distance interval.

$$I = I_S\left(1 - \frac{I_T^{ins}}{I_T^C}\right) + I_T^{ins} \tag{12.4.1}$$

$$I_T^{ins} = \frac{1}{0.15 + 1.5358/L + 0.58\exp(-1.14/L) + 0.0908\exp\left(\frac{L-6.3}{1.017L}\right)} \tag{12.4.2}$$

$$I_T^C = 0.78377/L + 0.3315\exp(-1.0672/L) + 0.68 \tag{12.4.3}$$

$$I_S = \frac{0.78377}{L + 1/\kappa} + \frac{0.68 + 0.3315\exp(-1.0672/L)}{1 + F(L,\kappa)} \tag{12.4.4}$$

$$F(L,\kappa) = \frac{(11/\kappa L) + 7.3}{110 - 40L} \tag{12.4.5}$$

$$k = k^\circ \exp\left[\frac{(1-\alpha)nF(E-E^\circ)}{RT}\right] \tag{12.4.6}$$

There is no analytical equation for a quasireversible substrate reaction. In fact, quasireversible reactions have been studied by means of approximate analytical models for the

**Table 12.2**

Normalized steady-state tip current ($I = i_T/i_{T,\infty}$) computed as a function of $L$ for a quasi-reversible substrate reaction with different values of dimensionless rate constant ($\kappa = k^\circ a/D$) and dimensionless substrate potential ($E_1 = nF\eta/RT$) (67). The Butler–Volmer relations for the forward (reduction) and backward (oxidation) rate constants are $k_f = k^\circ \exp(-\alpha E_1)$; $k_b = k^\circ \exp\left[(1-\alpha)E_1\right]$; where $\alpha$ is the transfer coefficient

| | $E_1$ | | | | | | | | | | | | | | | | | | | | |
|---|---|---|---|---|---|---|---|---|---|---|---|---|---|---|---|---|---|---|---|---|---|
| | $\kappa = 25$ | | | $\kappa = 5$ | | | $\kappa = 1$ | | | $\kappa = 0.5$ | | | $\kappa = 0.1$ | | | $\kappa = 0.05$ | | | $\kappa = 0.001$ | | |
| $L$ | 0.0 | 0.585 | 2.926 | 0.0 | 1.171 | 4.682 | 0.0 | 2.341 | 7.803 | 0.0 | 3.902 | 9.754 | 0.0 | 7.803 | 11.71 | 0.0 | 7.803 | 13.66 | 0.0 | 15.61 | 21.4 |
| 0.1 | 3.71 | 4.79 | 7.66 | 2.40 | 3.84 | 7.38 | 1.00 | 2.42 | 7.39 | 0.68 | 2.62 | 7.67 | 0.21 | 3.25 | 6.95 | 0.17 | 2.07 | 7.31 | 0.11 | 2.04 | 7.30 |
| 0.2 | 2.12 | 2.74 | 4.20 | 1.66 | 2.62 | 4.22 | 0.93 | 2.05 | 4.24 | 0.72 | 2.22 | 4.32 | 0.24 | 2.59 | 4.10 | 0.19 | 1.89 | 4.22 | 0.14 | 1.86 | 4.21 |
| 0.5 | 1.16 | 1.48 | 2.20 | 1.07 | 1.62 | 2.26 | 0.84 | 1.61 | 2.28 | 0.69 | 1.72 | 2.29 | 0.49 | 1.87 | 2.25 | 0.43 | 1.60 | 2.27 | 0.36 | 1.60 | 2.27 |
| 0.8 | 0.89 | 1.14 | 1.68 | 0.85 | 1.30 | 1.74 | 0.78 | 1.39 | 1.76 | 0.68 | 1.49 | 1.76 | 0.60 | 1.58 | 1.75 | 0.57 | 1.44 | 1.76 | 0.50 | 1.44 | 1.76 |
| 1.0 | 0.81 | 1.03 | 1.51 | 0.79 | 1.18 | 1.57 | 0.72 | 1.31 | 1.58 | 0.67 | 1.40 | 1.58 | 0.61 | 1.47 | 1.57 | 0.60 | 1.37 | 1.58 | 0.55 | 1.37 | 1.58 |
| 1.5 | 0.70 | 0.89 | 1.32 | 0.69 | 1.03 | 1.35 | 0.68 | 1.18 | 1.36 | 0.67 | 1.27 | 1.36 | 0.66 | 1.31 | 1.35 | 0.66 | 1.26 | 1.36 | 0.67 | 1.26 | 1.36 |
| 2.0 | 0.66 | 0.82 | 1.21 | 0.65 | 0.96 | 1.24 | 0.66 | 1.12 | 1.25 | 0.66 | 1.19 | 1.25 | 0.70 | 1.22 | 1.25 | 0.73 | 1.20 | 1.25 | 0.78 | 1.20 | 1.25 |
| 5.0 | 0.63 | 0.78 | 1.05 | 0.64 | 0.90 | 1.08 | 0.65 | 1.01 | 1.08 | 0.66 | 1.06 | 1.08 | 0.74 | 1.07 | 1.08 | 0.79 | 1.07 | 1.08 | 0.92 | 1.07 | 1.08 |

case where the tip reaction operates under kinetic control and the substrate reaction is mass transfer controlled (72, 73). This case has limited applicability as the electrode studied must be prepared as a UME tip. However, recently Zoski *et al.* published an approximate theory to describe SECM approach curves for quasireversible reactions based on a model combining ideal thin-layer cell geometry at close distances and linear diffusion at large tip–substrate distances (35). Although it is still approximate, this model yields a set of analytical equations that are useful for treatment of approach curves under kinetic control with a quasireversible substrate reaction. It also considers the possibility that the reaction at the substrate modifies the concentration profile of reactant in solution, the so-called shielding effect, which occurs when the backward reaction at the substrate is significant (35).

To illustrate the procedure for measuring and fitting kinetically controlled approach curves, the study of the electro-oxidation of $Fe^{2+}$ to $Fe^{3+}$ (equation (12.4.7), $E^\circ = 0.55$ V vs. Ag/AgCl) on glassy carbon, which is considered irreversible, will be described (67).

$$Fe^{2+} \rightarrow Fe^{3+} + e^- \tag{12.4.7}$$

The SECM experimental setup is identical to that described in Section 12.3.1 for measuring regular approach curves. In this example, a carbon fiber tip (in this example, a 10-μm diameter tip) is the amperometric probe that drives the reaction $Fe^{3+} + e^- \rightarrow Fe^{2+}$. At $E_T = -0.5$ V vs. Ag/AgCl, the reaction is diffusion controlled on a carbon tip in de-aerated 10 mM $Fe(NO_3)_3$/1 M $H_2SO_4$ as shown in the CV of Figure 12.15a. A large glassy carbon disk (e.g., 3-mm diameter) can be used as a substrate, with a typical CV in this solution shown in Figure 12.15b. In this CV, the oxidation of $Fe^{2+}$ occurs at $E_S > 0.6$ V vs. Ag/AgCl. Thus, a good range of potentials to study this reaction is $0.6 \leq E_S$ vs. Ag/AgCl (V) $\leq 1.3$,

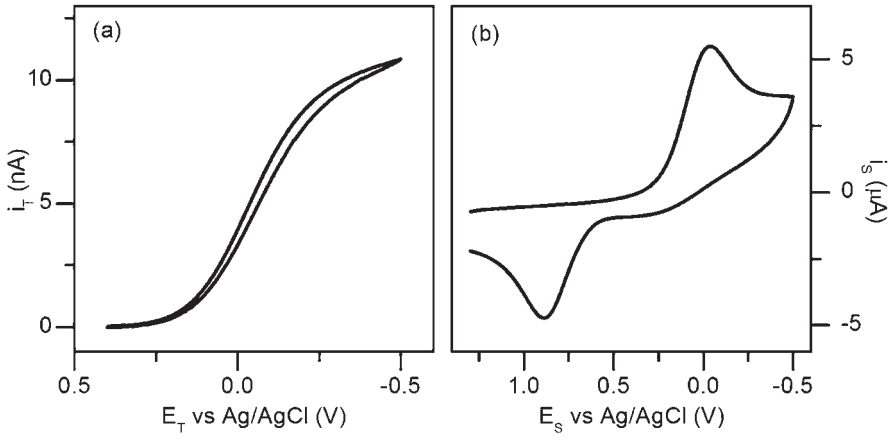


**Figure 12.15** Typical cyclic voltammograms (CV) of (a) a carbon-fiber tip (10-μm diameter) and (b) a glassy carbon substrate disk (3-mm diameter) in deaerated 10 mM $Fe(NO_3)_3$ in 1 M $H_2SO_4$. The steady-sate reduction current and the reduction peak observed on the tip and disk CVs, respectively, correspond to the $1e^-$ reduction of $Fe^{3+}$ to $Fe^{2+}$. The anodic peak observed on the disk CV comes from the $1e^-$ oxidation of surface-generated $Fe^{2+}$.

or $0.05 \leq \eta$ (V) $\leq 0.75$, where $\eta = E_S - E^\circ$. Reference and counter electrodes may be Ag/AgCl and a Pt wire, respectively.

The tip must be positioned at a tip–substrate distance $L \cong 5$–$8$ ($d \cong 25$–$40$ μm, $a = 5$ μm), from where the kinetic approach curves at different potentials will be measured. The tip can be positioned using a positive-feedback approach curve (see Section 12.3.1) by applying a sufficiently anodic potential to the substrate ($E_S = 1.4$ V vs. Ag/AgCl). When the tip is positioned at the initial place, approach curves at different substrate potentials in the range under study can be measured. For example, applying a substrate potential of 0.6 V vs. Ag/AgCl, the tip is approached at 1 μm $sec^{-1}$ and stopped when a change in the slope is observed. After the data is stored, the tip is withdrawn the approached distance, the electrode potential is changed to the next value (e.g., 0.7 V), and a new approach curve is measured. This procedure is repeated to scan the complete desired range of substrate potentials.

Fitting of the curves with equation (12.4.1) involves finding the offset distance ($d_o$) and the value of $\kappa$ simultaneously. The value of $d_o$ will affect the conversion of the experimental $i_T$ vs. $d_{exp}$ curve into the normalized curve $I$ vs. $L$ (see Section 12.3.1) that will be correlated with equation (12.4.1). A strategy to perform this operation is to plot equation (12.4.1) for different values of $\kappa$, and try to overlap the experimental $I$ vs. $L$ curve to one of these curves by manually changing the value of $d_o$. Once a good estimation of $d_o$ is obtained, it is possible to perform a fine analytical fitting to find a more accurate value of $\kappa$. Figure 12.16 shows a family of approach curves measured for the electro-oxidation of $Fe^{2+}$ to $Fe^{3+}$ on glassy carbon (equation (12.4.7)) at different potentials, correlated with

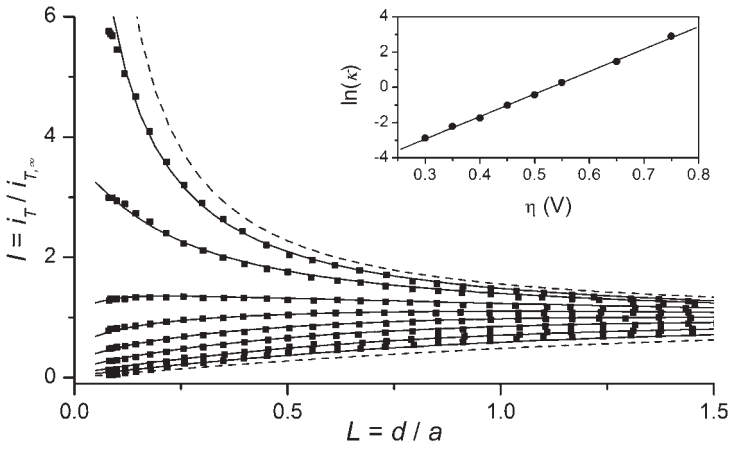


**Figure 12.16** Experimental approach curves (■) for the $Fe^{2+}/Fe^{3+}$ oxidation reaction measured on glassy carbon. The tip (10-μm diameter carbon fiber disk, RG ≅ 10) was held at a potential of −0.5 V vs. Ag/AgCl while the substrate was held at various potentials from $\eta = 0.3$ V to $\eta = 0.75$ V from bottom to top. Solid lines are the best fittings using equation 12.4.1 for the rate constant values plotted in the inset graph as a function of $\eta$ (●). Dashed lines are negative and positive feedback approach curves. Linear fit of ln ($\kappa$) vs. $\eta$ (solid line in inset graph) gives an intercept value $\ln(k^o a/D) = -6.1$ and a Tafel slope $RT/[(1 - \alpha)nF] = 81$ mV/dec, parameters that lead to a standard rate constant $k^o = 2 \times 10^{-5}$ cm $sec^{-1}$ and a transfer coefficient $\alpha = 0.7$.

equation (12.4.1) for different values of $\kappa$. Then, by plotting $\ln(\kappa)$ vs. $\eta$ (Tafel plot), it is possible to calculate kinetic parameters, such as the Tafel slope and standard rate constant, as shown in the inset of Figure 12.16. Several electrode reactions, such as oxygen reduction (74), hydrogen oxidation (75–77), electron-transfer reactions across liquid/liquid interfaces (78, 79) and on semiconductor thin films (80), and heterogeneous catalyzed reactions (81, 82) have been studied with this procedure.

### 12.4.2 Homogeneous chemical reactions

SECM is also useful for studying short-lived electrogenerated intermediates and determining the rate of a homogeneous reaction coupled to an electron-transfer reaction at an electrode. In this case, the small volume between the tip and substrate can be considered as a tiny electrochemical cell. The transient time by diffusion between the tip and substrate is $d^2/2D$. Thus, with $d = 0.1$ μm, this time is ~10 μsec. This represents the approximate half-life of electrogenerated species that can be detected in this arrangement. For a first-order homogeneous reaction following electron transfer (ET), this allows measurement of rate constants on the order of $10^5$ $sec^{-1}$, while for second-order reactions with reactant concentrations of 1 mM, rate constants on the order of $10^8$ $M^{-1}$ $s^{-1}$ are attainable. The application of SECM for studies of homogeneous chemical reactions has been discussed in detail in Chapter 7 of reference (1). It is beyond the scope of this section to provide a detailed description of the mechanics of the numerical methods that have been used to treat the general SECM problems involving coupled homogeneous kinetics. Instead, we focus on two cases for more detailed descriptions.

SECM theory has been developed for the following processes involving homogeneous chemical reactions coupled to ET: a first-order irreversible reaction ($E_rC_i$ mechanism) (50, 83), a second-order irreversible dimerization ($E_rC_{2i}$ mechanism) (53, 84) and ECE/DISP processes (85). If both heterogeneous processes at the tip and substrate electrodes are rapid (at extreme potentials of both working electrodes) and the chemical reaction (rate constant, $k_c$) is irreversible, the SECM response is a function of a single kinetic parameter $\kappa = \text{const}\, k_c/D$, and its value can be extracted from $I_T$ vs. $L$ dependencies. In the first two cases, the system of differential equations was solved numerically using the alternating-direction implicit (ADI) finite-difference method. The theory was presented in the form of two-parameter families of working curves. These curves represent steady-state tip current or CE as functions of $\kappa$ and $L$. We present here some generalizations of the theory, along with analytical approximations for the working curves. To understand this approach, we first consider a positive feedback situation with a simple redox mediator without homogeneous chemistry involved and with both tip and substrate processes under diffusion control. The total normalized steady-state tip current, given by equation (12.3.2), can be represented as the sum of two terms:

$$I_T = I_f + I_T^{ins} \tag{12.4.8}$$

where $I_f$ is the normalized feedback current coming only from the substrate and $I_T^{ins}$ is the normalized current due to the hindered diffusion of the electroactive species to the tip from

the bulk of solution, which is the tip current observed under the "negative feedback" situation and is given by equation (12.3.1). The substrate current is

$$I_S = I_f + I_d \tag{12.4.9}$$

where $I_d$ is the dissipation current (i.e., the current due to the flux of species not reaching the tip). It was shown that $I_S/I_T$ is more than 0.99 at $0 < L \leq 2$ (i.e., for any $L$ within this interval the tip and substrate currents are essentially equal to each other) (53). Thus,

$$I_d = I_T^{ins} \tag{12.4.10}$$

and

$$I_d / I_S = I_T^{ins} / I_T = f(L) \tag{12.4.11}$$

where $f(L)$ can be computed for any $L$ from equations (12.3.1) and (12.3.2).

For an electrochemical process followed by an irreversible homogeneous reaction of any order,

$$\begin{array}{ll} \text{Tip:} & \text{Ox} + \text{e} \rightarrow \text{Red} \\ \text{Gap:} & \text{Red} + \text{other reactants} \rightarrow \text{products} \\ \text{Substrate:} & \text{Red} - \text{e} \rightarrow \text{Ox} \end{array} \tag{12.4.12}$$

One can write

$$I'_T = I'_f + I_T^{ins\prime} \tag{12.4.13}$$

$$I'_S = I'_f + I'_d \tag{12.4.14}$$

$I_T^{ins\prime}$ is not affected by the occurrence of the homogeneous reaction in equation (12.4.12). Thus, $I_T^{ins\prime} = I_T^{ins}$. As the species O are stable, the fraction of these species arriving at the tip is also not affected by the homogeneous reaction in equation (12.4.12), the relation $I'_d / I'_S = f(L)$ still holds. Thus,

$$\begin{aligned} I'_T &= I_T^{ins\prime} + I'_S = I'_d \\ &= I_T^{ins} + I'_S[1 - f(L)] \end{aligned} \tag{12.4.15}$$

That is, for an SECM process with an irreversible following homogeneous chemical reaction of any order, a plot of $I'_T$ vs. $I'_S$ should be linear with a slope equal to $1 - f(L)$ and an intercept equal to $I_T^{ins}$. Thus, the TG/SC mode of the SECM for these mechanisms is equivalent to the feedback mode and any quantity, $I'_T$, $I'_S$, or the CE, $I'_T/I'_S$, can be calculated from equation (12.4.15) for a given $L$ if any other of these quantities is known.

For mechanisms with following irreversible reactions, one can expect the CE to be a function of a single kinetic parameter, $\kappa$. If this parameter is known, the SECM theory for this mechanism can be reduced to a single working curve.

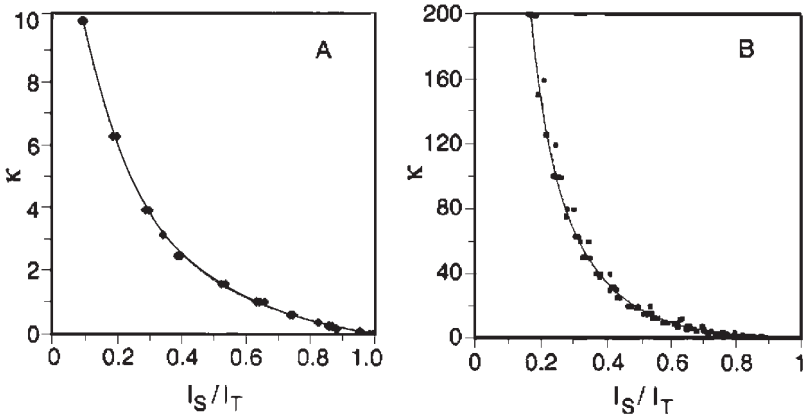


**Figure 12.17** Kinetic parameter $\kappa$ as a function of the collection efficiency (CE) ($I'_S / I'_T$). (A) $E_rC_i$ mechanism; $\kappa = k_c d^2/D$, solid line was computed from equation (12.4.16), triangles are simulated data from reference (83). (B) $E_rC_{2i}$ mechanism; $\kappa = C^* k_c d^3/aD$, solid line was computed from equation 12.4.17, squares are simulated data from reference (53). (Adapted from reference (84b).)

One has $\kappa = k_c d^2/D$ for an $E_rC_i$ mechanism (83) and $\kappa = k_c d^3 C^*/(aD)$ for an $E_rC_{2i}$ mechanism (53). Figure 12.17A shows the working curve, $\kappa$ vs. the CE, along with the simulated data for an $E_rC_i$ mechanism. The numerical results fit the analytical approximation (83):

$$\kappa = 5.608 + 9.347\exp(-7.527x) - 7.616\exp(-0.307/x) \tag{12.4.16}$$

in which $x = I'_S / I'_T$, within about 1% (84b). For the $E_rC_{2i}$ mechanism, the simulated data can be fitted to (53):

$$\kappa = 104.87 - 9.948x - 185.89/\sqrt{x} + 90.199/x + 9.389/x^2 \tag{12.4.17}$$

with an accuracy of ~5–10%, provided $0.3 \leq x \leq 0.9$ (84b) (Figure 12.17B). The invariability of $k_c$ computed from experimental points would assure the validity of the results.

To illustrate this technique, consider the dimerization of the acrylonitrile anion radical ($AN\bullet^-$) in DMF (84a). As shown in Figure 12.18A, the proposed reaction mechanism, an $E_rC_{2i}$, is

$$\begin{aligned} &AN + e \rightarrow AN\bullet^- \\ &2AN\bullet^- \rightarrow (AN)_2^{2-} \\ &(AN)_2^{2-} + 2H^+ \rightarrow (ANH)_2 \end{aligned} \tag{12.4.18}$$

As shown in Figure 12.18B, the voltammogram for the reduction of AN in a DMF/0.1 M $TBAPF_6$ solution at a gold tip ($a$ = 2.5 μm) shows a reduction wave at −2.0 V vs. a silver quasi-reference electrode (AgQRE). The tip-generated species, $AN\bullet^-$, is so unstable that when tip is far away from the Au substrate (60-μm diameter), no oxidation current

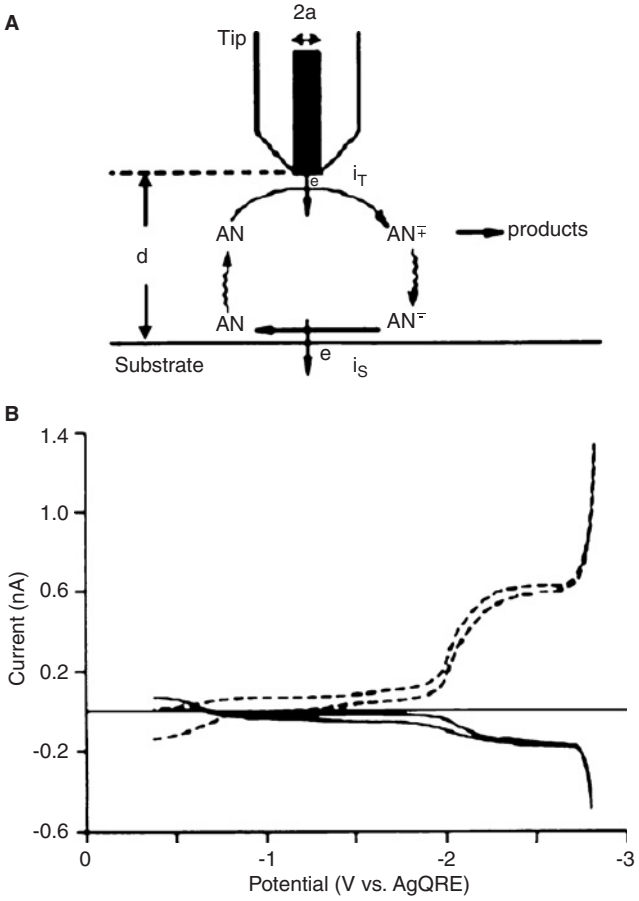


**Figure 12.18** SECM TG/SC voltammograms. (A) The tip ($a = 2.5$ μm) was spaced ~1.4 μm from a 60-μm diameter gold electrode held at a potential of −1.75 V vs. a silver QRE (AgQRE). (B) The tip potential was scanned at 100 mV $sec^{-1}$ to produce a voltammogram (dashed line) for the reduction of acrylonitrile, AN (1.5 mM) in 0.1 M $TBAPF_6$. The substrate current (solid line) shows the oxidation of the radical anion of AN generated at the tip. (Adapted from reference (84a).)

above the background current at the substrate was detected. However, when the tip is close (~1.5 μm) to the substrate, held at a potential of −1.75 V vs. AgQRE, where $AN^{\bullet-}$ is oxidized, one sees a wave for the oxidation of the radical anion as the tip is scanned through the reduction wave (see Figure 12.18B). By studying the dependence of the CE on $d$, the rate constant of reaction (12.4.18) was found to be $6 \times 10^7$ $M^{-1}s^{-1}$.

It is also possible to carry out SG/TC experiments. However, this approach to studies of homogeneous kinetics is less straightforward, since the usually larger substrate electrode does not attain a steady-state condition and also the CE for this case, is much less than unity, even in the absence of a homogeneous kinetic complication (50). However, this mode has been used to study concentration profiles above a substrate (86). SECM has also

been used to investigate more complex chemical reactions sandwiched between successive ETs, as in ECE/DISP scheme (85) discussed in Chapter 7 of reference (1).

### 12.4.3 Catalytic activity

#### *12.4.3.1 Imaging of catalytic activity by G/C modes*

In previous sections, it was shown that the SECM feedback response is highly sensitive to the intrinsic activity of the substrate material for the evaluated reaction. This fact allows one to perform kinetic studies of reactions and to determine reaction rate constants, via analysis of approach curves on varied types of materials. In Section 12.3.3, it was shown that it is also possible to image the chemical activity of heterogeneous surfaces using the sensitivity of tip current to reaction rate. Two main drawbacks of the feedback-based methodology restrict its applicability to a narrow region of conditions. The first one, which was already discussed in Section 12.3.1, is the necessity of using low mediator concentration to observe the feedback effect. The second and also important for activity imaging is the simultaneous dependence of current on activity and tip–substrate distance. Thus, to obtain SECM images that reflect only the activity of the material free of morphological effects, the catalytic surfaces must be very smooth. Moreover, the tilt of the sample, which is important when large areas are imaged, should be carefully controlled.

It was pointed out that other SECM configurations, such as the G/C modes, allow one to address systems and conditions that are inaccessible by using the feedback mode. In Section 12.3.1.3, the G/C modes were described, but very little was said about their imaging capabilities. In fact, these modes are very convenient for imaging catalytic activity of various surfaces. They have the important advantages that they are insensitive to morphological effects and are independent of feedback restrictions. The imaging abilities of these modes are discussed below, mainly focusing on their capacity to image electro-catalytic activity.

#### *12.4.3.2 Imaging by substrate generation/tip collection mode*

In this mode, the tip behaves as a passive sensor probing the concentration profile of the product of a process occurring at the substrate. The imaging capability of this mode was mainly exploited to image activity of biological materials (microorganisms, enzymes) (45, 87, 88), corrosion (89) and transport processes across membranes (Chapter 9 of reference (1)). It can also be used to image the concentration profile of oxygen photosynthetically generated from plant leaves (90) and that of electro-generated (or consumed) species at a substrate array of microelectrodes (46), as it was recently done by Zoski *et al.* to establish the quality of individually addressable electrodes (41). In that work, the rate of the reaction studied (oxidation of ferrocenemethanol) was mainly defined by the quality of each individual microelectrode, although it may be dependent on the nature of the electrode if a material-sensitive reaction is imaged. This is, for example, the case of hydrogen evolution reaction (HER) in acidic medium, which can be studied at low overpotentials ($\eta$) by this method as illustrated in Figure 12.19a. The substrate is held at a potential to reduce $H^+$ to $H_2$ at a value sufficiently small to avoid bubble formation, and the tip is

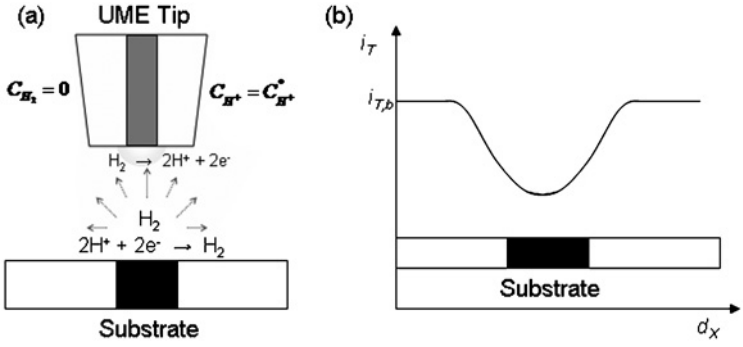


**Figure 12.19** (a) Scheme of the SG/TC mode for imaging activity of catalyst spots for the HER. (b) Expected behavior of the tip current during a SG/TC long-direction scan over a catalyst spot when imaging the activity for the HER.

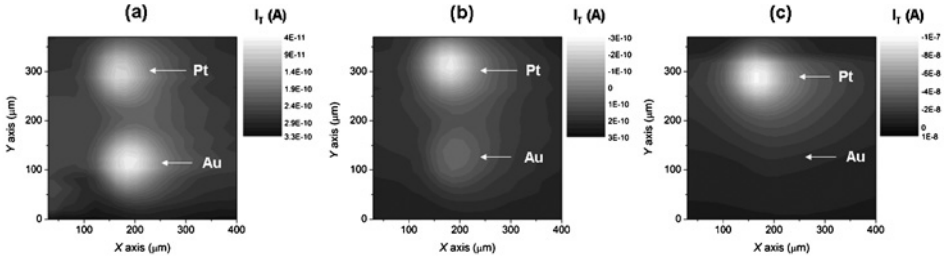


**Figure 12.20** SG/TC images of activity for the HER obtained using a 25-μm Pt tip as an amperometric probe of the $H_2$ concentration profile ($E_T$ = 0.2 V vs. HRE), over a substrate containing 100-μm diameter Pt (top) and Au (bottom) disks polarized simultaneously at −0.005 (a), −0.025 (b), and −0.065 (c) V vs. HRE. Solution: 0.5 M $H_2SO_4$. The tip current scale can be read at the top right corner of each graph.

held at a potential where the substrate-generated $H_2$ is oxidized back to $H^+$. As the reaction at the tip is diffusion controlled, the tip current is proportional to the concentration of $H_2$. In contrast, the concentration profile of $H_2$ around the substrate disk is a function of its electrocatalytic activity for HER. Thus, the mapping of this profile using the tip current provides a visual image of the activity of the substrate material for this reaction. Although the concentration profile changes in time, it reaches quasi-steady-state hemispherical diffusion in a short time if the substrate electrode is sufficiently small. The expected behavior of the tip current during the long-direction ($X$) scan is shown in Figure 12.19b. An anodic contribution (negative current) is added to the background tip current during the oxidation of the substrate-generated $H_2$. Successive long-direction scans at varied positions in $Y$ generate an image of the $H_2$ concentration profile.

As an example, Figure 12.20 shows the SG/TC images of activity for the HER of a substrate consisting of two 100-μm diameter disks, one Au (bottom) and the other Pt (top), polarized both simultaneously at three different potentials. At the lowest overpotential

($\eta$ = 0.005 V), both metals look poorly active, which is verified by the low tip current. When $\eta$ increases to 0.025 V, it is seen that the activity increases much faster on Pt than on Au (due to a larger Tafel slope), evidenced by a higher concentration of $H_2$ around the Pt disk. At $\eta$ = 0.065 V, the activity of Pt is so high compared with Au that it is only possible to see the Pt response. At higher $\eta$, $H_2$ bubbles are formed on Pt, warping the concentration profile.

#### *12.4.3.3 Imaging by tip generation/substrate collection mode*

This mode has rarely been used for imaging purposes (91) until recently, when a constant tip current was used to generate a constant flux of reactant (54). Two important facts are highlighted: very high scan rate (up to 600 μm $sec^{-1}$) and large tip–substrate distance (up to 50 μm). The effects of these two variables are much less pronounced for this case than for the feedback images. This TG/SC mode was used to image the activity of different materials for the ORR in acidic medium performing as shown in Figure 12.21a. The approach is also valid for other reactions, such as hydrogen oxidation. The substrate potential is held at a potential where oxygen is reduced to water. As the solution initially contains no oxygen, the substrate current is negligible. When a tip is placed close to the substrate and a constant oxidation current is applied to the tip, water is oxidized to oxygen on the UME and a constant flow of oxygen is generated at the tip. The tip current must be sufficiently small to prevent the saturation of the solution by oxygen and the subsequent formation of bubbles. When oxygen reaches the substrate surface, it is reduced at a reaction rate that depends on the substrate potential and its electrocatalytic activity. The substrate current is governed by the flow of oxygen from the UME tip, reacting at the substrate and being lost by lateral diffusion toward the bulk solution (54). The expected behavior of the substrate current in a long-direction ($X$) scan is shown in Figure 12.21b. In this case, a reduction current (positive) is added to the background current when the substrate reduces the tip-generated oxygen. Successive scans at different positions in $Y$ recording the substrate current produce an image of the substrate material activity for the ORR.

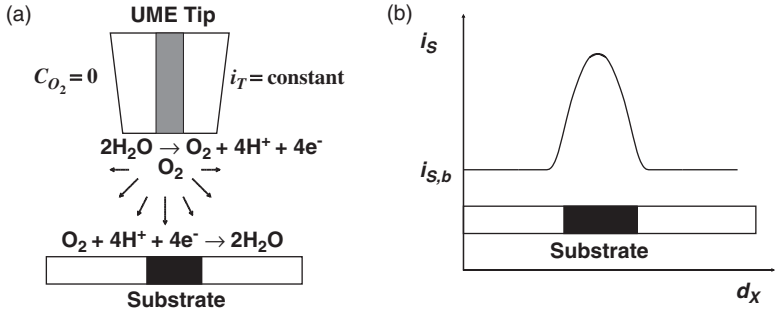


**Figure 12.21** (a) Scheme of the TG/SC mode for imaging activity of catalyst spots for the ORR in acidic medium. (b) Expected behavior of the substrate current during a TG/SC long-direction scan over a catalyst spot when imaging the activity for the ORR.

### *12.4.3.4 Activity screening of electrocatalysts*

There is a recent interest in rapid electrochemical techniques that are able to provide information about activity of a large number of electrode materials in a short period of time (92). At present, the most popular methods capable of rapid screening of electrode activity include fluorescent techniques (93) and individually addressable arrays of electrodes (94). As a technique for chemical activity imaging, SECM was applied to characterize systems in sub-micrometer ranges in varied areas including catalysis, corrosion, and microbiology. This ability was only recently exploited to analyze electrode reactions of interest in electrocatalysis, when Bard *et al.* and Hillier *et al.* addressed the study of hydrogen oxidation (75, 76) and oxygen reduction (74) by feedback SECM. After that, Hillier *et al.* (95, 96) used feedback SECM to screen the activity of arrays of individually addressable binary Pt–Ru and ternary Pt–Ru–Mo band electrodes for hydrogen oxidation. That was done by scanning a Pt tip over a 20-mm length array of catalytic bands, using the couple $H^+/H_2$ as mediator (Figure 12.22). In this study, it was rapidly demonstrated that Pt–Ru (10–50% Ru) and importantly Pt–Ru–Mo (10–25% Mo) mixtures present low overpotentials for hydrogen oxidation in the presence of CO.

Particle size effects of highly dispersed supported catalysts (Pt) on the hydrogen oxidation reaction were evaluated by the same authors using this technique (97). Moreover, electrocatalysts for oxidation of methanol were screened using a technique called scanning differential electrochemical mass spectrometry (98, 99). This method uses a capillary probe scanned over the array that allows the intake and detection by mass spectrometry of products generated locally on each electrode.

Bard *et al.* are using SECM in G/C mode to screen the activity of binary and ternary metallic arrays for electro-reduction of oxygen (54, 100, 101). They used the TG/SC described in Section 12.4.3.1 to image the activity of both multi-metallic and 'wired' enzyme catalyst spots deposited on single glassy carbon substrates (Figures 12.23 and 12.24). Different from the previous approach, the spots do not need to be individually connected

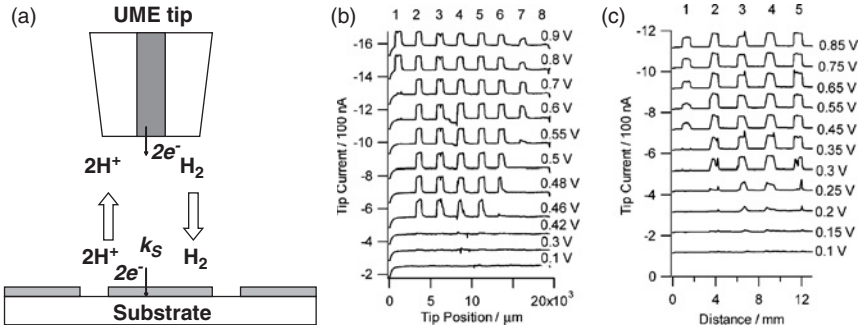


**Figure 12.22** (a) Schematic of the SECM feedback mode using the $H^+/H_2$ couple to image activity of catalyst arrays for hydrogen oxidation. SECM scans over CO-poisoned Pt–Ru (b) and Pt–Ru–Mo (c) band electrodes in 10 mM $H_2SO_4$ − 0.1 M $Na_2SO_4$, at a tip–substrate distance of 15 µm. The tip was held at −1.0 V vs. HRE to reduce $H^+$ under diffusion control. (Adapted from reference (96).)

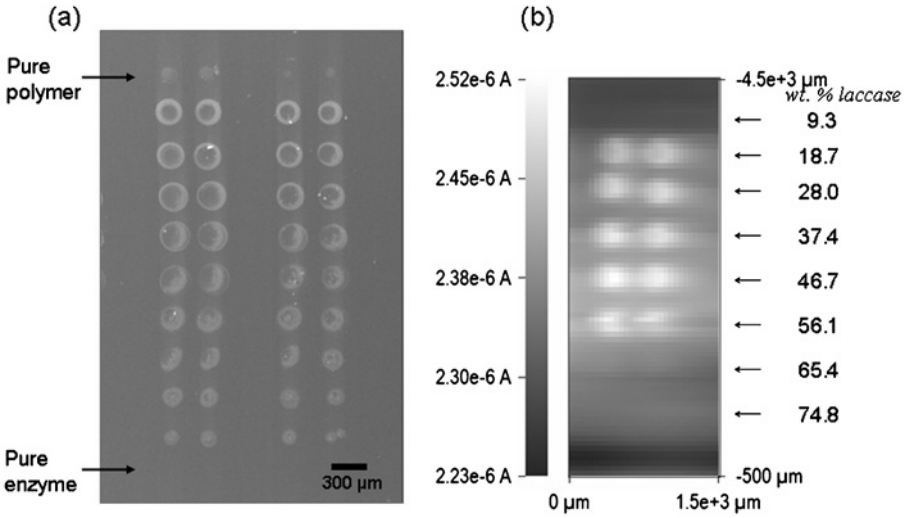


**Figure 12.23** (a) SEM photograph of two arrays of 'wired' laccase containing different compositions of enzyme and polymer (PAA-PVI-[Os(tpy)(dme-bpy)Cl]$^{1+/2+}$). (b) TG/SC SECM image of activity for the ORR obtained on one of the arrays shown in (a) polarized at 0.4 V vs. Ag/AgCl using a tip current of −240 nA and a scan rate of 300 µm sec$^{-1}$. The most active spot composition is observed at a wt.% laccase = 46.7.

as the $O_2$-generating tip addresses each spot at a time. With this technique, the optimization of the composition of "wired" enzymes used as $O_2$-cathodes in biofuel cells was performed in one single experiment, as shown in Figure 12.23 (101).

Furthermore, using this method on bi- and trimetallic catalysts it was found that Pd–Co and Pd–Co–Au electrodes (10–20% Co) present much lower overpotential for the ORR when compared with the pure components, as shown in the images of Figure12.24 (100). This fact was further verified on rotating disk electrodes of these combinations. With the idea of making this methodology useful for a wider variety of reactions, efforts to replace the reactant-generating tip by a micropipette dispenser tip are being pursued (29). This tip would allow small volumes (a few pLs) of reactant solution to be dispensed locally on a substrate with the simultaneous monitoring of the substrate current.

## 12.4.4 Surface reactivity

### *12.4.4.1 Electron transfer on self-assembled monolayers*

Understanding and controlling charge transport through molecular films of nanometer thickness is important in several areas including molecular electronics and elucidating ion and electron transport mechanisms through membranes involved in biological systems (102, 103). Self-assembled monolayers (SAMs) of organic molecules have been widely used as the model systems in this type of study. The easy preparation, high stability, and

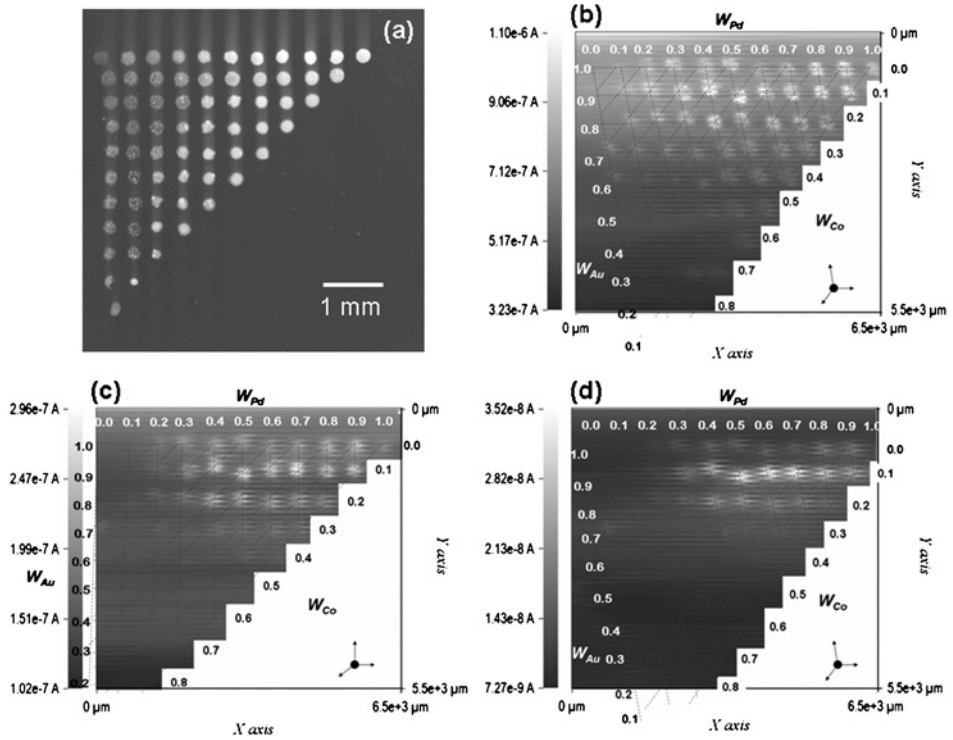


**Figure 12.24** (a) SEM photograph of a Pd–Au–Co ternary array. Top left corner is pure Au, top right is pure Pd and bottom left is Co. (b)–(d) SECM TG/SC images of oxygen reduction activity measured on Pd–Au–Co arrays in 0.5 M $H_2SO_4$. Tip–substrate distance: 30 µm, tip current = −160 nA, scan rate = 50 µm each 0.2 sec, $E_S$ = 0.4 V (b), 0.6 V (c), and 0.75 V (d) vs. HRE. $W_M$ is the atomic ratio of metal M in the spot.

the almost unlimited possibility of introducing functional groups in the monolayer make SAMs suitable models for investigating charge transport across molecular films (104).

SECM has been used for the studies of ET through monolayers supported at solid/liquid (105, 106), liquid/liquid (107–109) and air/water interfaces (110). In the case of a solid/liquid interface, the rates of ET mediated by monolayer-attached redox moieties and direct ET through the film as well as the rate of a bimolecular ET reaction between the attached and dissolved redox species have been measured using SECM (105). The monolayer may contain redox centers (Figure 12.25a) or simply act as a blocking layer (Figure 12.25b).

In Figure 12.25a, ET occurs via a bimolecular reaction between a dissolved redox species generated at the tip (R) and redox centers attached to the SAM ($M^+$) followed by the electron tunneling; while in Figure12.25b, it occurs by direct tunneling between the dissolved species, R, and the electrode. Finally, the charge transfer may occur through pinhole defects in the film. A theoretical model has been developed attempting to independently measure the rates of all of these processes (105). According to the model, provided an appropriate mediator is used and the mediator concentration is high such that the bimolecular ET is

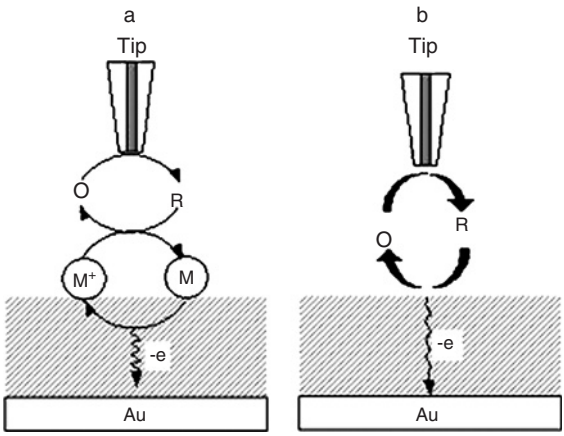


**Figure 12.25** Schematic view of the processes involved in the SECM measurements of ET across an electroactive SAM. (a) Mediated ET; (b) direct electron tunneling through monolayer. M and $M^+$ represent the reduced and oxidized forms of the monolayer bound redox moieties, respectively.

much faster than the ET through the monolayer, the rate constant of electron tunneling through the monolayer, $k_b$, is determined by equation (12.4.19):

$$k_b \cong k_{eff} C^*/\Gamma^* \tag{12.4.19}$$

where $C^*$ is the bulk concentration of the redox mediator in solution, $\Gamma^*$ is the surface coverage of the monolayer-bound redox centers, and $k_{eff}$ is the effective rate constant obtained by fitting an experimental SECM approach curve to SECM theory.

When the tip is very close to the substrate, i.e., $L \ll 1$, $L$ is the normalized tip–substrate distance ($L = d/a$, where $d$ is the distance between the tip and the substrate and $a$ is the tip radius), the mass transfer coefficient $m_o \sim D/d$, where $D$ is the diffusion coefficient, and the upper limit for measurable $k_{eff}$ is $\sim 5m_o = 5D/d$ (1). The tip can be brought down to an $L \approx 0.1$. Thus, for a 1-μm radius tip, $d = 10^{-5}$ cm. Assuming a typical diffusion coefficient $D = 10^{-5}$ cm$^2$ sec$^{-1}$, $\Gamma^* \sim 10^{-11}$ mol cm$^{-2}$ and $C^* = 2 \times 10^{-4}$ mol cm$^{-3}$, the upper limit for measurable $k_b$ is $\sim 10^8$ sec$^{-1}$, calculated using equation (12.4.19). If a nanometer-sized tip is used, a faster ET can be measured.

In contrast, if the bimolecular ET is slow compared with a electron tunneling reaction, and/or the concentration of the redox mediator in solution is low, the following equation holds:

$$k_{Ox} \cong k_{eff}(k_b + k_f)/k_b\Gamma^* \tag{12.4.20}$$

where $k_{Ox}$ is the bimolecular ET rate constant (mol$^{-1}$ cm$^3$ sec$^{-1}$), $k_b$ and $k_f$ are backward and forward electron tunneling rate constants (sec$^{-1}$), respectively. Thus, the bimolecular rate constant for ET between the monolayer-bound and dissolved redox species can be determined based on equation (12.4.20). For a 1-μm radius tip, the upper limit for measurable $k_{Ox}$ is $10^{11}$ mol$^{-1}$ cm$^3$ sec$^{-1}$ (or $10^8$ M$^{-1}$ sec$^{-1}$).

If the redox mediator is a hydrophobic species, the ET at the monolayer or bilayer modified electrodes may not occur by tunneling, but rather by diffusion through the pinholes with ET at the free sites of the electrode. This was confirmed by SECM studies of ET reactions of ferrocenemethanol at tetradecanethiol SAMs on the gold surface and at the bilayer formed by phospholipid adsorption on the first tetradecanethiol layer (106).

The quantitative SECM measurements of the heterogeneous ET at SAM modified electrodes also allows one to study the kinetics of SAMs formation on an electrode and to estimate the surface coverage and the average size of the defects in the monolayer film. For example, SECM, chronoamperometric, and cyclic voltammetric measurements suggested that the surface coverage is > 99.3 and > 99.9% for $C_{14}SH$ and $C_{18}SH$ monolayer, respectively (106, 111) and the defects in the $C_{18}SH$ film are smaller than 0.5 μm (111).

SECM was also used to study kinetics of heterogeneous ET across a monolayer of lipid adsorbed at the interface between two immiscible electrolyte solutions (107–109). The adsorption of phospholipids at the interface significantly decreases the rate of interfacial ET between two redox couples (one in each phase). The fraction of the interfacial area covered with lipid can be evaluated from the measured heterogeneous rate constants ($k_f$). The driving force dependencies of interfacial ET rates were linear, with a transfer coefficient of $\alpha = 0.5$ when the driving force for ET ($\Delta G^\circ$) was not too high and leveled off to the diffusion-controlled rate at larger overpotentials. For even higher $\Delta G^\circ$, inverted region behavior was observed, as expected from Marcus theory (107). The rate of ET decreased with the number of methylene groups in the hydrocarbon chain of adsorbed lipid suggesting that the ET reaction does not occur at defect sites in the lipid monolayer. For the monolayer consisting of two different types of lipids (e.g., phospholipids with saturated and polyconjugated hydrocarbon chains), the observed ET rate was at least two times faster through films with conjugated chains compared with those with saturated chains (108). SECM imaging of the lipid monolayer at the liquid/liquid interface also revealed the formation of the micrometer-sized domains in the monolayer (108, 109).

#### *12.4.4.2 Corrosion and passivation*

SECM is ideally suited to investigating corrosion processes as the probe UME can be used to simultaneously initiate ET reactions at the phase boundary and to monitor the response. The capability of imaging with high spatial resolution enables SECM to be a powerful tool to study the structure–activity relationship. It is especially advantageous that SECM can be used in solution under exactly the same conditions at which metal corrodes. To date, SECM has been successfully used to study the corrosion of metals and alloys, such as steel, Fe, Ti, Al, Ta, and Sn (89, 112). Some important issues, such as identifying pitting precursor sites, probing the kinetics of oxide growth and breakdown, and mapping the electronic properties of oxide films have been addressed using SECM.

Both feedback and SG/TC modes of SECM can be used to spatially resolve the electroactive sites on the metal, as illustrated schematically in Figure 12.26. In the feedback mode (Figure 12.26A), the metal substrate is bathed in a solution containing a redox mediator, R. A UME tip, poised at a potential to oxidize R at a diffusion-controlled rate, is brought close to the substrate and scanned over the substrate surface. The substrate is poised at a potential such that the tip-generated species, O, is reduced back to R at the electroactive sites.

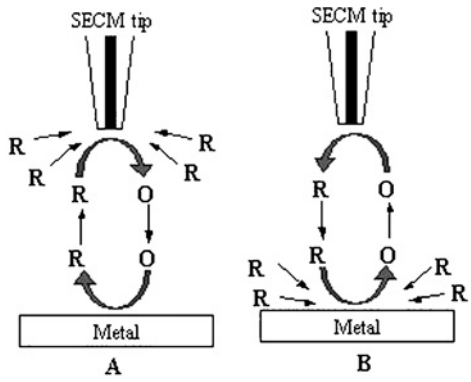


**Figure 12.26** SECM feedback (A) and substrate generation/tip collection (B) mode used in the corrosion study.

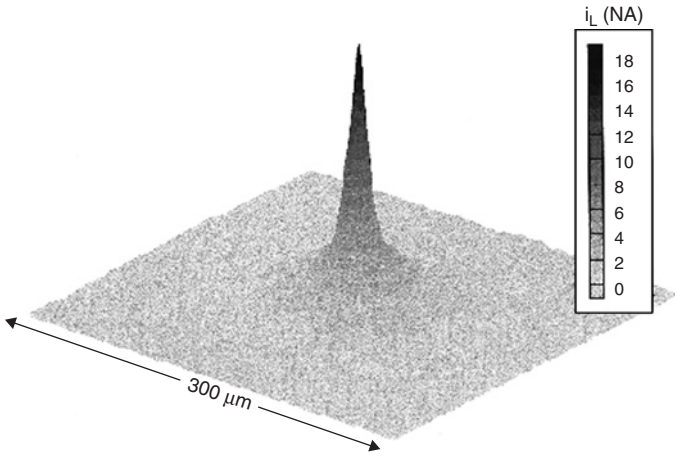


**Figure 12.27** A 300 μm × 300 μm SECM image of an electroactive site on $Ti/TiO_2$ surface obtained in a solution containing 50 mM KBr and 10 mM $H_2SO_4$. (Adapted from reference (89).)

The tip current is recorded as a function of the tip position in the *x*, *y* plane. When the tip scans above electroactive sites, higher tip currents will be observed because positive feedback occurs at these sites. Thus, SECM mapping of the substrate surface should allow one to identify electroactive sites on the metal surface. The feedback mode has been used to study the heterogeneous redox activity of aluminum alloys, such as AA2024. The SECM image showed locally high redox activity, which was attributed to second phase, intermetallic inclusions (112).

In the SG/TC mode (Figure 12.26B), the redox mediator, R, is oxidized at the electroactive sites on the substrate surface. A UME tip, brought close to the substrate and poised at a potential to reduce the substrate-generated O back to R, is scanned over the substrate surface. Thus, the areas of high electroactivity correspond to the increased cathodic tip current, measured as a function of tip position in the *x*, *y* plane. Figure 12.27 shows

a three-dimensional SECM image of an electroactive site on titanium surface obtained in the substrate generation/tip collection mode. The redox mediator used in the study was $Br•^-$ (89). Other redox mediators, such as $Fe(CN)_6^{4-}$, $I^-$, $Ru(NH_3)_6^{3+}$, and nitrobenzene have also been used at the substrate generation/tip collection mode to map the electroactivity on steel and metal surfaces. Subsequent examination of the active sites by a range of techniques (energy dispersive X-ray analysis, SEM, and confocal laser microscopy) revealed that the active sites are usually associated with the location of impurity inclusions.

Localized corrosion usually involves change in pH and chloride ion concentration around corrosion pits. Therefore, potentiometric SECM tips can be used to study corrosion processes. When a pH microsensor was used as the SECM tip for the *in situ* measurements during localized corrosion of stainless steel, it was found that pH decreases at the pit initiation stage and increases during pit growth and repassivation (113).

Alternating current scanning electrochemical microscopy (AC-SECM) was recently used to detect precursor sites for localized corrosion on lacquered tinplates (114). AC-SECM utilizes the effect of an increasing (decreasing) solution resistance as the SECM tip approaches an insulator (conductor) for mapping domains of different conductivity/electrochemical activity on surfaces immersed in electrolytes. It was demonstrated that AC-SECM could be used to visualize microscopic cracks and holes in the coating of the lacquered tinplates.

A probe consisting of an optical fiber coated with gold was used as the SECM tip to image simultaneously the electrochemical and photoelectrochemical activity of pitting precursor sites on an oxide film (11b, 115) by combining SECM with scanning photoelectrochemical microscopy (116). It was found that the area of high electrochemical activity is correlated with lower substrate photocurrent in the area.

SECM was also used to initiate pitting on steel and aluminum and to examine the pit growth and corrosion products (112a, 112b). In these studies, the UME tip was used to generate aggressive $Cl^-$ ions in close proximity to stainless steel and aluminum surfaces. The tip and substrate current were then monitored to detect corrosion events. Fluctuations in the tip and substrate current were observed, which were indicative of the breakdown of the passive film and pit initiation on the metal. SECM and CV measurements provided evidence that the large tip current fluctuations observed were caused by the reduction of $Fe^{2+}$, which was released from the iron surface in the breakdown of the passive film of iron.

### 12.4.5 Patterning

Due to the small size of the scanning tip, the versatility of tip material, and the various modes of operation, SECM has been used as a tool for the fabrication of microstructures on varieties of substrates. SECM microfabrication is based on tip-induced chemical and electrochemical reactions at the solid/liquid interfaces. So far, SECM has been used for depositing metals and other inorganic materials, etching metals and semiconductors, electropolymerizing conducting polymers, and forming patterns of organic and biomolecules (117, 118).

#### *12.4.5.1 Metal deposition and etching*

Metals such as gold, copper, silver, palladium, and cobalt may be deposited locally to form microstructures using SECM working in different modes (30, 119). In one of these modes,

the so-called direct mode, the tip, and the substrate are used as the working and counter electrodes, respectively. The electric field is focused between the tip and the substrate by bringing the tip in close proximity to the conductive substrate in a similar manner as STM. The electric field drives the electrochemical reactions at the tip and substrate, resulting in direct deposition or etching of metals. This mode requires that the tip should be very close to the substrate. To control the distance between the tip and the substrate, the substrate can be coated with a thin film of ionically conductive polymer. The tip is biased vs. the substrate. When the tip touches the polymer film, faradaic current passes through the film. The tip current is a function of the tip position in the polymer. A constant current is maintained using an electronic feedback loop to adjust the penetration of the tip into the polymer. Therefore, the tip–substrate distance can be controlled. One example of this mode is the deposition of metals in ionically conductive polymers, such as Nafion and poly (4-vinylpyridine) (119a, 119b). By changing the sign of the potential between the tip and the substrate, high-resolution deposition and etching of Au, Cu, and Ag were accomplished. The widths of the patterns were in the submicron range.

The feedback mode of SECM has also been used for metal deposition and etching. Etching via SECM feedback is straightforward, as shown in Figure 12.28. A UME tip, which is immersed in a solution containing a redox couple, e.g., $Fe(phen)_3^{2+}$ (phen = 1,10-phenanthroline), is moved close to a substrate to be etched (Cu in this case). The potential of the UME is controlled so that the redox couple is oxidized at the tip at a diffusion-controlled rate. When the tip is far away (several tip diameters) from the substrate surface, a constant steady-state current is established within several seconds. However, as the tip is brought close to the substrate, i.e., within a few tip radii, an increase in the steady-state current (a positive feedback) is observed due to the regeneration of the redox mediator via ET reaction between the strong oxidant generated at the tip and Cu. As a result, copper dissolution occurs, which is limited to the diffusion range of the oxidized mediator. As the feedback current depends on the tip–substrate separation, the distance between the tip and the substrate can be determined and controlled by measuring the changes in the tip current. The resolution of the etched patterns is governed by the tip

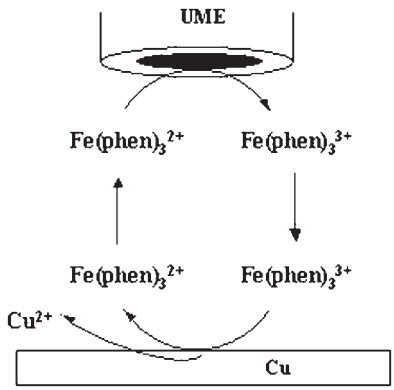


**Figure 12.28** Principles of copper etching by the SECM in the feedback mode.

diameter and tip–substrate distance (120, 121). Other parameters affecting the etching size and shape include the concentration of the redox couple and the electrolysis time.

The species generated at the tip may drive the reduction of metal ions, resulting in deposition of the metal on the substrate. Gold ($AuCl_4^-$) and palladium ($PdCl_4^{2-}$) structures are fabricated in this way and incorporated into a polymer film. $Ru(NH_3)_6^{2+}$, generated at the tip through the reduction of $Ru(NH_3)_6^{3+}$, diffuses to the substrate and drives the reduction of $AuCl_4^-$ and $PdCl_4^{2-}$ to their respective metals (119c). In another example, deposition of silver on gold is accomplished by oxidizing nitrite at the tip to lower the pH in the tip–substrate gap and introduce dissociation of $Ag(NH_3)_2^+$ in the solution. The free $Ag^+$ ions are then reduced on a negatively biased gold surface (122).

Fine silver lines can also be formed on a nonconducting substrate like a AgCl film. In this case, hydroquinone generated at the tip diffuses to an AgCl film and reduces silver cations in the vicinity of the AgCl film to form silver patterns (123). Under appropriate conditions, the line width fell below the diameter of the tip used. The high resolution resulted from the reaction of free $Ag^+$ ions in solution with hydroquinone such that the hydroquinone flux is focused on the AgCl film surface. This system is an example of a "chemical lens" that focuses the flux of the reactive species on the substrate surface. In this example, $Ag^+$ ions act as the "focusing" agent.

Another approach to metal deposition involves formation of metal ions by anodic dissolution of a microelectrode made of the same metal to be deposited (119d–119f, 124). In one example, gold patterns were fabricated in this way on indium tin oxide (124). The Au UME was anodically dissolved in bromide-containing solution to form $AuBr_4^-$ ions, which diffused to the negatively biased indium tin oxide substrate and were reduced to form micropatterns of Au.

#### *12.4.5.2 Semiconductor etching*

Similar to the metal etching, strong oxidants can be locally generated at the tip and used for etching semiconductors. One example is the etching of a GaAs wafer by tip-generated bromine (121). Bromine, generated through the oxidation of bromide at the tip, serves as an oxidant as well as the tip–substrate distance indicator, as the positive feedback is observed as the tip approaches the GaAs wafer. The parameters that affect the etching size and shape include the tip size, the distance between the tip and the substrate, and the electrolysis time. High-resolution etching of GaAs was also accomplished by the direct mode of SECM (125). Other semiconductors etched using SECM include CdTe, GaP, and Si. An interesting result from these studies was that while injection of holes into n-type semiconductors by tip-generated oxidants can effectively etch the semiconductor; injection of holes into p-type semiconductors does not lead to etching. The explanation given by the researchers is that while the injected charge can remain on the surface of n-type semiconductors leading to efficient etching, fast diffusion of the charge into the bulk of p-type semiconductors blocked the etching.

Etching resolution can be improved by using the confined etchant layer technique (CELT), which has been demonstrated by Tian and coworkers in their studies of silicon surface etching (126). The surface of silicon was etched by tip-generated bromine in a solution containing HBr. $H_3AsO_3$ was added into the etching solution to introduce a scavenging

reaction between $H_3AsO_3$ and bromine. The lateral diffusion of the etchant around the tip was suppressed by the scavenging reaction. As a result, etching pits on silicon matched closely to the tip size. This technique should be particularly useful for the slow surface etching.

#### *12.4.5.3 Deposition of conducting polymers*

Deposition of conducting polymers can be accomplished by either direct or feedback modes of SECM. In an earlier study, SECM was used to deposit polyaniline on a Pt substrate by scanning a UME tip in thin, ionically conductive Nafion films coated on the Pt surface (127). Anilinium ions were incorporated into Nafion films and the Pt substrate was biased positively, which caused the electropolymerization of aniline. The resolution of the polyaniline deposition is controlled by the tip size, the thickness of Nafion films, and the electric field distribution.

The electropolymerization of pyrrole was achieved on a gold substrate in aqueous solution (128). A potential pulse was applied to the gold substrate to obtain a high concentration of pyrrole radical cations and pyrrole oligomers within the tip–substrate gap, leading to a fast chain propagation reaction so that the chain length will reach the critical value for precipitation. Using a 10-μm diameter tip, the width of the polypyrrole lines were 50–60 μm. The aspect ratio of the microscopic deposits can be changed by controlling the tip–sample distance with an optical detection system independent from the electrochemical processes. A polypyrrole tower as high as 400 μm, with diameters of about 80 μm were fabricated (129) using this technique.

Polymerization can also be induced by the tip via an oxidation reaction. This working mode was demonstrated by Heinze and coworkers (122). The monomer 2,5-bis (1-methylpyrrol-2yl)-thiophene (NSN) was first deposited on ITO by thermal evaporation. The micropatterning was performed in an aqueous solution containing bromide. The tip oxidizes bromide to bromine, which diffuses to the surface and reacts with the monomer to form patterns of poly-NSN. The remaining monomers were removed by organic solvents. This technique can also be applied to nonconducting substrates.

The feedback mode was used to deposit polyaniline on gold, platinum, and carbon surfaces by applying a positive potential to the substrate and consuming protons at the tip to locally increase the pH in the gap between the tip and the substrate. The increased alkalinity shifts the oxidation potential of the monomer cathodically such that polymerization occurs at the substrate potential (130).

#### *12.4.5.4 Patterning of biological molecules*

SECM has been particularly promising for microfabrication and detection of biological molecules, mainly due to the mild patterning conditions and various modes of operation (see also Section 12.4.6.2.3). In contrast, conventional photolithographic techniques are usually limited due to the photoresists, organic solvents, and strong acids and bases that are necessary and are harmful to biological molecules.

Patterning of glucose oxidase was performed using a tip to electrochemically desorb alkanethiols from a SAM on a gold substrate (131). Cystamine was adsorbed on the exposed patterns of the gold surface and periodate-oxidized glucose oxidase was covalently

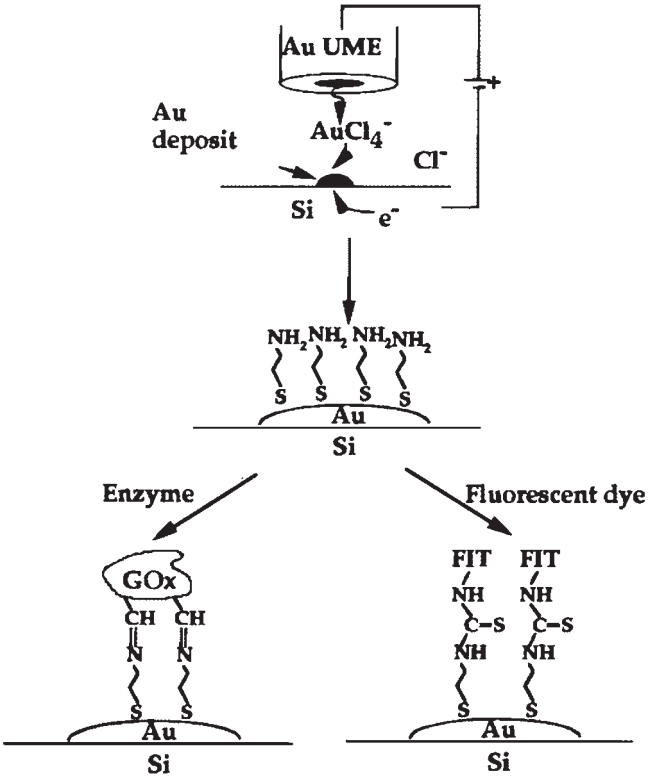


**Figure 12.29** Schematic representation of the approach for attaching organic and biological molecules onto surfaces using the SECM. (Adapted from reference (132).)

attached to the amino groups of cystamine. The enzyme activity was imaged by detection of hydrogen peroxide in the generation/collection mode.

In another method, gold patterns were deposited on silicon wafers with SECM as a result of the controlled anodic dissolution of a gold microelectrode, as described above (Section 12.4.5.1). The gold patterns were further used as microsubstrates for assembling cystamine monolayers to which either glucose oxidase or fluorescein isothiocyanate was immobilized (FIT) (Figure 12.29). The activity of the enzyme patterns was imaged using the SECM in the generation/collection mode (132).

Another approach to micropatterning of glucose oxidase is based on the fabrication of microstructures of conductive polymers (133). In this case, patterns of functionalized polypyrrole were formed on gold using the approach described above (Section 12.4.5.3). Glucose oxidase was then covalently immobilized to the polypyrrole through the reactions between the terminal amino groups of the deposited polymer and the aldehyde groups at the surface of periodate-oxidized glucose oxidase. The enzyme patterns were imaged using the enzyme-mediated positive feedback mode of SECM. The technique developed in this study could be used as a generic method for patterning of surfaces with organic and biological molecules, such as enzymes and proteins.

SECM was used for the fabrication of diaphorase-patterned surfaces (134). Diaphorase, a flavin enzyme, was immobilized on glass surfaces. The oxidation of $Br^-$ or $Cl^-$ at the tip generated a reactive species, which deactivated the enzyme molecules on glass forming unreactive patterns. The circular and linear patterns were then imaged by SECM based on the detection of catalytic current of ferrocenylmethanol coupled with oxidation of DADH.

Diaphorase patterns were also fabricated on the substrates immobilized with SAMs of different alkylsilane derivatives. A hydroxyl radical is generated at an SECM tip in a solution containing $H_2O_2$ and $Fe^{3+}$ by Fenton's reaction:

$$Fe^{3+} + e^- \rightarrow Fe^{2+}$$

$$Fe^{2+} + H_2O_2 \rightarrow Fe^{3+} + HO\bullet + HO^-$$

The hydroxyl radicals react with the SAMs and locally change the chemical and physical properties of the monolayer surface. Diaphorase patterns are then formed on the substrates by physical adsorption onto the hydrophobic area or by chemical linkage to the hydroxyl radical-attacked area (Figure 12.30). Diaphorase activity can be visualized using SECM by detecting the diaphorase-catalyzed current of ferrocenylmethanol coupled with the oxidation of reduced nicotinamide adenine dinucleotide (135). The size of the hydroxyl-radical-attacked area, which determines the resolution of the enzyme patterns, is affected by different factors, including the tip size, the concentration of $Fe^{3+}$, and the potential pulse period for generation of the hydroxyl radical.

SECM has been used to attach biotin on the surface of a carbon electrode (136). In the direct-write mode, biotin hydrazide is oxidized at the SECM tip to generate a reactive species that attaches to the carbon surface. The biotinylated region reacts further with a fluorescent avidin and can be imaged with a fluorescence microscope. Controlling the tip and substrate potential is critical in the formation of biotin patterns. The distance between the tip and the substrate surface and the speed at which the probe tip is moved are other major factors that affect the formation and resolution of patterns. The SECM probe tip can also be used as an electrochemical "eraser" cleaning off the surface attached biotin and leaving clean spots on the surface of a globally derivatized carbon surface (136).

After biotin patterns are formed on the electrode surface, biotin/avidin chemistry can be used for selective attachment of avidin-labeled biomolecules. Thus, the technique based on simple micromodification of the surface of a carbon electrode will allow the fabrication of biosensors that can potentially be tailor-made for a variety of applications.

## 12.4.6 Biological applications

### *12.4.6.1 Introduction*

SECM can be used to probe transport activity of biological systems, such as single cells, ion transport across channels, and enzyme activity. Experimentally, cells, enzymes, or ion channels are immobilized and a small size electrode (micron to nanometer size) is positioned a few microns above. By stimulating these samples with an oxidative stress agent (by the action of the substrate and cofactors, or by the presence of ions), biological

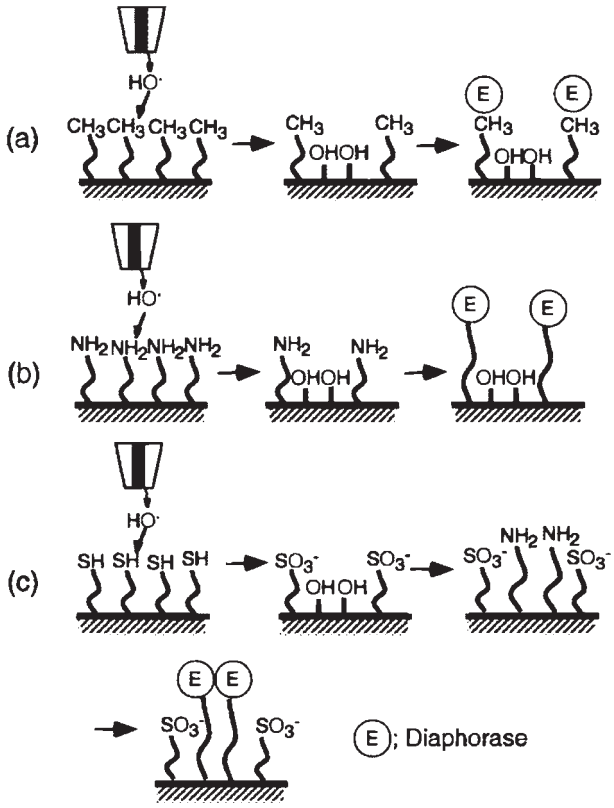


**Figure 12.30** Schematic representation of micropatterning of diaphorase at SAM-immobilized glass surfaces by electrogenerated hydroxyl radicals. (a) Diaphorase is physically adsorbed onto the hydrophobic area. (b) Diaphorase is covalently bound to the unattacked area to give a negative pattern. (c) Diaphorase is covalently bound to the hydroxyl-radical-attacked area to give a positive pattern. (Adapted from reference (135).)

metabolites, enzyme catalytic activity, and ion transport can be studied using SECM. The molecules and ions released or regenerated diffuse to the nearby tip electrode where they are detected as a current. The rate of transport or kinetic information related to these transport events can be extracted from the measure current.

This section highlights biological applications of SECM with emphasis on experimental requirements, and the difficulties/limitations involved in applying SECM to biological systems. Specifically, enzymes, ion channels, and cellular systems are considered.

### *(a) Collection mode vs. feedback mode of SECM*

When studying biological systems, one can choose between feedback and G/C (generation/collection) mode. In general, the negative feedback mode may be used to evaluate the tip–substrate distance as well as to locate biological samples based on changes in topography or blocking of a conductive layer by biofilms. Such measurements yield little information

concerning the biological activity of the substrate. Although negative feedback imaging has recently been used to image new growths emerging from PC12 dopamine releasing immortal rat cells (137), positive feedback and G/C measurements are the preferred SECM mode used in biological studies. G/C experiments use the tip electrode as a passive sensor that does not significantly perturb local concentrations. This differs from feedback experiments where the tip-generated species are actively involved in a surface reaction. As the G/C mode is independent of the substrate process, it is very flexible and different selective tips, such as amperometric, enzyme-modified, or ion-selective electrodes can be used. The quantitative characterization of this mode is often done using numerical simulations or through the development of experimentally specific models that do not reach the level of generality or ease of applicability that the feedback treatments have attained. In fact, G/C experiments often rely on independent feedback measurements for the evaluation of distances by using passive mediators or dual-barrel electrodes (138).

G/C experiments are governed by the uncontrolled mass transport of the biological specimen because, unlike the feedback experiment, they do not localize the reaction under the electrode. This implies that feedback experiments benefit from better lateral resolution and are more suited for imaging experiments. However, the G/C mode can detect lower analyte concentrations than the feedback mode because it does not have a significant background current coming from the dissolved mediator in solution. If, for example, the minimum catalytic rate, $k_{cat}$, of immobilized enzymes measured in the G/C mode was compared with that of the feedback mode, the G/C experiments could measure a $k_{cat}$ three orders of magnitude faster than that obtained via the feedback study (139). When deciding on which SECM mode to use in a biological experiment, the importance of imaging resolution against detection limits should be weighed.

#### *12.4.6.2 Enzymatic systems*

***(a) Equipment and handling requirements***

Enzymes are robust biological systems. They can be stored in the refrigerator or in the freezer for extended periods of time. Their activity under homogenous or immobilized conditions can be measured spectroscopically and electrochemically (140–142). There are no special equipment needs for SECM studies as the solid support modification is often done on electrodes or glass slides that can easily be combined with a conventional SECM setup. Most of the equipment needs are related to the patterning or immobilization of the enzymes onto solid supports.

***(b) Enzyme systems***

There is considerable literature where SECM has been used in enzymatic studies (139). Table 12.3 outlines the enzymes studied, the SECM mode used, and relevant references. These studies showed that enzyme activity could be studied using SECM and often, catalytic rates could be extracted.

The advantage of studying enzymes is that they can be regenerated by known substrates. Although they might be influenced by the enzyme turnover rate, the enzymatic substrate can sustain a level of activity that is harder to find in other interesting biological systems.

**Table 12.3**

Examples of enzyme activity studies using SECM

| Feedback mode studies | | Collection generation mode studies | |
|---|---|---|---|
| Enzyme | Reference | Enzyme | Reference |
| Glucose oxidase | (143–146) | Glucose oxidase | (64, 131) |
| NADH-cytochrome *c* reductase | (144) | Urease | (147, 148) |
| Diaphorase | (134) | NADPH-dependent oxidase | (149) |
| Horseradish peroxidase | (150) | Horseradish peroxidase | (151) |
| Nitrate reductase | (152) | Alkaline phosphotase | (153) |
| | | $NAD^+$-dependent alcohol dehydrogenase | (154) |

In antibody (150) or DNA hybridization studies, there are a finite number of events that can be detected. SECM, therefore, must turn to tagging strategies to enhance the detected signal. Recent DNA hybridization studies, for example, employed a silver staining technique to increase sensitivity that allowed detection of 30 amol of material per analyzed spot (155). This is a spectacular and unique example that is not representative of common electroactive tagging methods, which generally cannot compete with the sensitivity of current fluorescent tagging methods. There is, however, great promise in combining the SECM measurements with selective fluorescent tags in biological studies (156).

***(c) SECM imaging of enzyme features***

Enzyme-mediated feedback can be used to image enzyme patterns. To successfully image enzymatic features, tip fouling from oxide formation or adsorption from solution constituents must be avoided. The enzyme reaction at the substrate must not be inhibited by solution species. It must also be able to sustain a level of regeneration activity of the mediator that can compete with its mass transport from the bulk electrode to the tip. In the case of a glucose oxidase catalyzed reaction, a digital simulation of the positive feedback observed from this enzyme quantitatively expresses this limitation (143).

Micropatterning of enzymes has received a lot of attention because of its potential use in integrated biochemical devices, such as biosensors (see also Section 12.4.5). As the conventional lithographic techniques employ organic solvents, photoresists and conditions often unsuited for biological systems, many groups have employed different microfabrication techniques. These include enzyme-modified patterned monolayers, enzyme-modified polymer microstructures, enzyme-modified metal microstructures, and enzyme-modified insulator microstructures. A good review of the characterization of enzyme structures activity using SECM is already available (42).

An example of such patterning protocols is a piezoelectric driven dispenser able to eject picoliter-sized droplets based on the impulse movement of a piezoelectric element and a specially designed nozzle (Figure 12.31) or glass capillary (29). Using this technique, drops of enzyme solution having around 100 pL volumes can be dispensed onto a substrate following each current pulse applied on the piezoelement using a function generator. Using a positioning device like a *xyz* stage or a plotter system, the microdispenser or

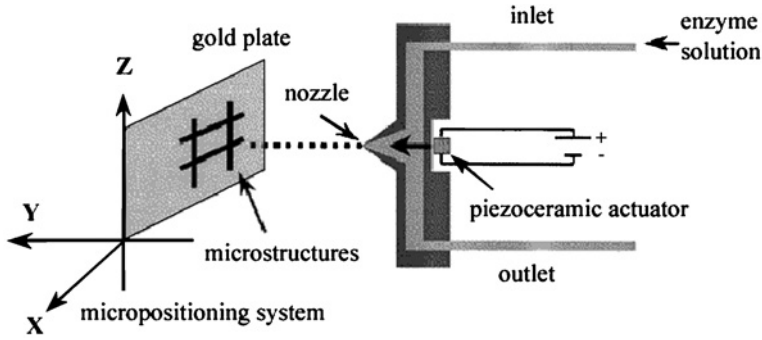


**Figure 12.31** Schematic representation of the flow-through microdispenser, gold plate, and positioning system used to obtain enzyme microstructures.

the substrate can be moved to obtain the needed enzyme pattern. Silicon wafers coated with Au (1000 Å), high quality HOPG, polymer films, and glass slides can all be used as substrates.

To immobilize enzymes on these substrates, different strategies can be adopted. In the case of glucose oxidase, catalase or multi-enzyme patterns, a drop of enzyme solution can be dispensed on SAMs of di (*N*-succinimidyl)-3, 3′-dithiodipropionate on Au (157). The formation of amide bonds between the activated ester headgroup of the SAM and the amino groups on the protein shell then takes place. Droplets of enzyme solution containing a cross-linker, such as poly(ethylene glycol) (400) diglycidyl ether (PEGDGE) can also be dispensed on clean Au plates. Polymer matrices in which the dispensed drops of enzyme are on the surface of the polymer have also been used on Au plates.

In another example applied to diaphorase patterning, microcover glasses were immersed into a 3-amino-propyl triethoxysilane/benzene solution and then patterned in three different ways (156). First, using a glass capillary (i.d. 40 mm), a diaphorase and glutaraldehyde solution is drop spotted onto the aminosilanized glass substrate. Second, a diaphorase solution is spin-coated onto the aminosilanized glass substrate, left to dry, and subjected to laser-induced patterning. Third, the SECM probe can deactivate regions of a spin-coated diaphorase substrate as above by generating highly reactive species (HOBr) at the nearby tip.

Such imaging efforts are important because they prove that SECM may be used to pattern enzymes (Figure 12.32), optimize enzyme architectures, and characterize miniaturized multi-sensor arrays. Patterning of enzymes on surfaces and the long scanning distances of SECM make this an attractive option for enzyme activity assays. In order for them to be used to extract enzyme kinetics, however, a significant amount of work remains to be done.

### *(d) Enzyme-mediated approach curves*

The diffusion-controlled feedback response at conductive and insulating surfaces, for simple solution redox couples, are represented by *normalized* current and distance plots commonly referred to as approach curves. In these situations, the approach curves for different redox couples and electrode radii can be superimposed. In the case of enzyme-mediated

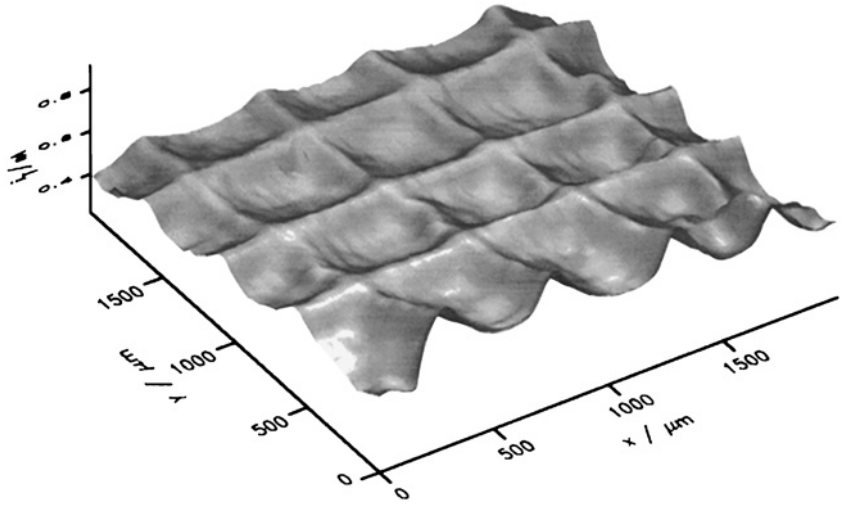


**Figure 12.32** SECM image of a GOX grid structure. Each line has a width of ~100 µm, and the distance between two lines is 500 µm. Solution dispensed to obtain the structure: 8.8 mg $mL^{-1}$ Vinnapas EP 16 and 1.2 mg $mL^{-1}$ GOX.

feedback curves, the magnitude of the current observed may depend on the enzyme turnover rate, the kinetics of the reaction between the redox couple and the enzyme, the flux of mediator to the enzyme surface, the enzyme surface coverage and the flux of the substrate to the enzyme surface. In the case of glucose oxidase, for example, it was shown that, under conditions of high glucose concentration (substrate saturation), the feedback current depended on the enzyme turnover rate of glucose, the kinetics of the sacrificial electroactive mediator (or enzyme cofactor) and the flux of the mediator to the enzyme. All of these added complications make a complete theoretical treatment of enzyme kinetics using SECM challenging.

***(e) Importance of enzyme attachment methods***

When enzymes are adsorbed onto a conductive substrate, the surface coverage of the enzyme on the substrate can be evaluated based on the catalytic currents using cyclic voltammetry (142) or by spectroscopic means (140). On an insulating substrate such as a membrane, there is no simple mathematical relationship between the surface coverage of biomolecules and the inhibition of the faradaic current that would be measured by SECM. It is, therefore, necessary to have a quantifiable means to evaluate the surface coverage of immobilized active enzyme if one wishes to extract and compare kinetic information using SECM.

In the past, Matsue *et al.* have discussed this issue in a study related to the characterization of diaphorase-patterned surfaces by SECM. Using a digital simulation based on the explicit finite difference method that considered the heterogenous enzyme reaction at the substrate, they generated steady-state current vs. distance profiles that depended on the surface concentration of the enzyme. Using these working curves, they quantified the surface concentration of the active immobilized diaphorase (134). Using, the electrochemical

oxidation of bromide or chloride at the SECM tip, they generated highly reactive species that selectively deactivated regions of the enzyme layer. By comparing the approach curves from a deactivated region to that of an untouched region, they showed that the surface concentration of the enzyme for the deactivated region was about half of that for the untreated region.

Bard *et al.* have also presented digital simulations to extract the kinetics of membrane and surface-bound glucose oxidase from feedback measurements (143). Their model included a description of the heterogeneous turnover of the mediator oxidant by immobilized glucose oxidase under a large excess of D-glucose concentrations. The limiting cases of the feedback response obtained for large and small mediator oxidant concentrations are treated. They applied this model to experimental approach curves taken from glucose oxidase immobilized in an albumin/glutaraldehyde hydrogel and showed that, at low mediator concentrations, a clear discrimination for the zero-order kinetic behavior was obtained. Their results clearly showed that the feedback response depended on the amount of immobilized enzyme, but did not quantify this relationship. They also treated the limiting cases of enzyme kinetics, but no complete SECM theoretical treatment is available at present. What is really needed is an accessible general SECM theory that can be applied to different enzymes that would facilitate comparison of results among different groups.

#### *12.4.6.3 Ion channels*

##### *(a) Equipment and handling requirements*

The special equipment requirements in SECM ion channel studies stem from lipid handling and storage problems. To perform SECM studies with ion channels, one must learn to work with lipids. Stock phospholipid solutions in organic solvents should be stored in glass containers (less than –20 °C) and the cap or closure for the vial should be lined with Teflon. When working with lipids, one should avoid contact with polymer or plastic containers (polystyrene, polyethylene, polypropylene, etc.) as impurities often leach out from such materials. Glass, stainless steel, or Teflon syringes and vials should be used to transfer and store lipids. Finally, the phase transition, miscibility, ionization constants of phospholipids, and critical micelle concentrations should always be kept in mind when working with a new lipid (158).

To facilitate and maintain lipid organization, specialized Teflon SECM cells and unusual UME arrangements have to be used. In bilayer lipid membrane (BLM) systems, for example, Teflon cells adapted to the SECM instrument usually have to be made to uniformly distribute the pressure above and below the BLM (Figure 12.33). Also, to visualize the formation of the BLM, the use of an angled microscope combined to a television facilitates the approach of the UME to the BLM (159).

For studies involving air/water interface monolayers or Langmuir-Blodgett techniques, a submarine UME is required. Such an electrode is immersed in the solution and approached to the layer from below (110, 160). The submarine electrode consists simply of a conventional UME of the desired metal and size that is fixed to a glass J tube by Teflon tape or Epoxy (Figure 12.34).

##### *(b) Previous work*

The diversity of membrane structures and transport mechanisms studied by SECM demonstrates the utility of this technique for studies of membrane transport (61, 157, 159, 161–163).

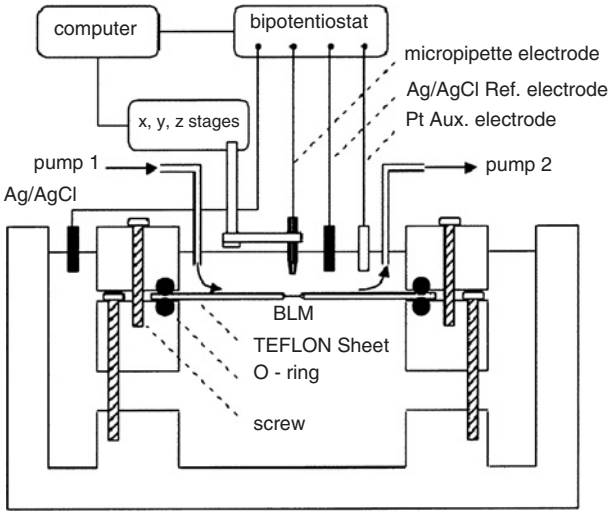


**Figure 12.33** Schematic diagram of SECM apparatus and a cell for the preparation of horizontally oriented BLM.

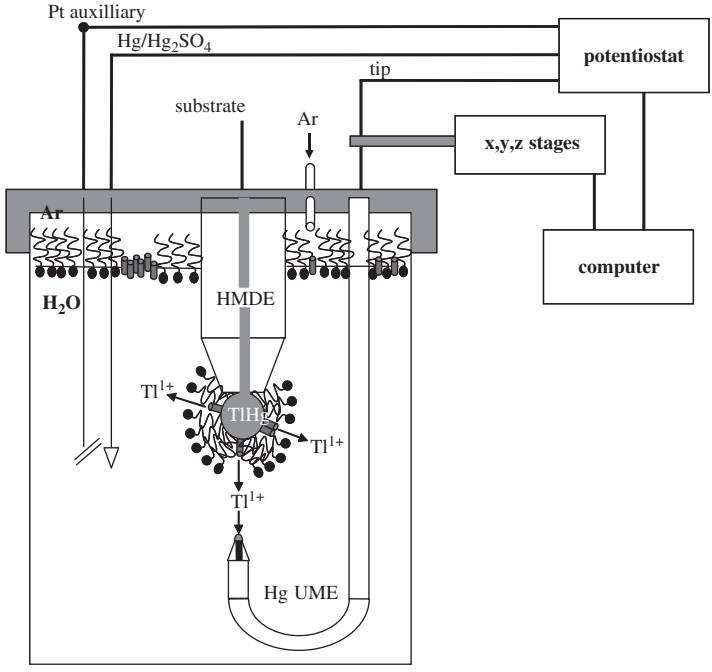


**Figure 12.34** Schematic diagram of an ion channel SECM experiment where a submarine UME is used. (Adapted from reference (20).) (for colour version: see colour section at the end of the book).

As described below, potentiometric and amperometric methods have been used to study ion channels. The $K^+$ transport across gramicidin channels imbedded in a horizontally supported BLM was studied potentiometrically, for example. In this study, a $K^+$ selective micropipette was used to acquire approach curves and measure the transport of $K^+$ across the gramicidin channel. The ion-selective micropipette electrodes consisted of silanized pulled borosilicate capillaries (i.d. 0.7–20 μm) filled with a solution of 10 mM valinomycin and 10 mM ETH 500 in dichloroethane. Characterization of the electrodes was accomplished via the steady-state tip current for $K^+$ (0.05–0.3 mM). The tips were then used in the SECM feedback and generation/collection modes to study $K^+$ transfer through gramicidin channels imbedded in a horizontal BLM of glycerol monooleate.

The difficulty with this measurement is controlling the time at which the ion transport occurs. To have a controlled release of the ion of interest, an amperometric approach can also be used but requires the use of Tl(I) as a surrogate for $K^+$. Ion transport across gramicidin channels imbedded in a dioleoylphosphatidylcholine (DOPC) monolayer adsorbed onto a Tl/Hg amalgam can be used as a membrane system. This arrangement allows one to control the release of Tl(I) into gramicidin channels by preconcentration of the Tl as an amalgam on a hanging mercury drop electrode (HMDE) with controlled oxidation of the amalgam using a potential step. An Hg/Pt submarine UME positioned close to the membrane collects the generated Tl(I) following its diffusion from the gramicidin. The tip collection response is a transient current that is fitted to numerical simulations based on finite element method or also to empirical theories. The results (21) agree well with experiments and other reported work (51). An apparent rate constant for the transport of Tl(I) from the amalgam HMDE through the channel can also be extracted (20).

***(c) Problems to tackle***

Knowing the ion channel surface coverage is important to extract the true transport rates rather than apparent rates. When the channels are adsorbed on a conductive electrode, this value can be extracted from cyclic voltamograms (164). On an insulator surface, however, this task becomes harder. As individual channels have distinct opening probabilities and are in equilibrium between the active and inactive forms, evaluating ion channel coverage remains difficult.

To reach imaging capabilities of a single channel, the lateral resolution of SECM needs to be improved and the formation of a substrate where isolated channels are present relative to the size of the electrode needs to be accomplished. Serious consideration also has to be given to current detection limitations.

#### *12.4.6.4 Cellular systems*

***(a) Equipment and handling requirements***

Though SECM studies on live cells can be performed without the use of an inverted microscope, the rough positioning of the UME over the cells is greatly facilitated if one is used. Also, the use of fluorescent viability dyes is often possible when the inverted microscope has fluorescent capabilities. This allows for simultaneous determination of cellular viability before and after the experiment. Optical micrographs of the UME positioning over the cells can also be acquired. They provide independent proof that the

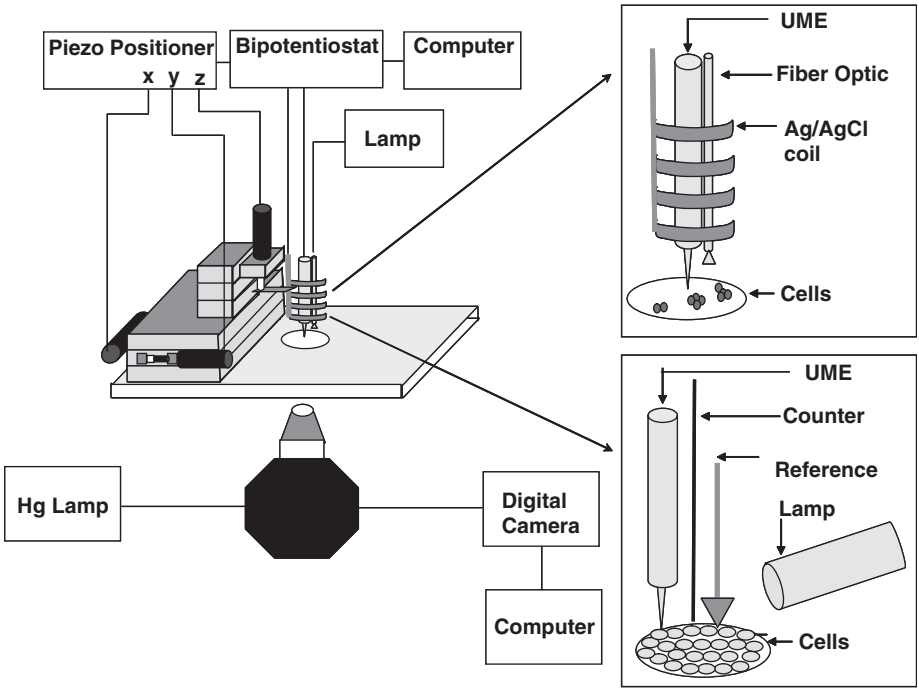


**Figure 12.35** Schematic representation of a combined SECM and inverted microscope setup. (for colour version: see colour section at the end of the book).

detected signal originates from the cells themselves and can also monitor the adhesion of the cells onto the substrate during imaging.

The SECM instrument can easily be accommodated to most inverted microscopes. By disassembling the instrument and replacing the bottom plate by a machined piece for the microscope, the SECM head can be installed on the side of the microscope. The height of the *z*-piezo often prevents the use of the illumination tower but a side halogen lamp or combined UME-fiber optic bundled can be used instead (see Figure 12.35). The UME holder must also be modified and lowered closer to the microscope optics. This can be achieved by the addition of a long cylindrical spacer between the *z*-piezo and the tip holder (165).

Biological systems are fragile and complex. They require a very controlled environment both for handling and culture conditions. As this type of research is multidisciplinary, cooperation between groups is recommended. Adhesion properties of specific cells, special electrolyte requirements, temperature, humidity, and other environmental concerns important in the design of the SECM experiments are better addressed by specialists.

***Examples of live cell systems.*** Until very recently, little work had been done on live cells. The earliest was the study of photosynthesis on the leaves of *Tradescantia fluminensis*

based on oxygen reduction profiles (90, 166) and the study of resorption of osteoclasts on bone slices using a $Ca^{2+}$ potentiometric sensor (167). Since then, a significant body of work on full cellular studies has been published.

Live cell studies have monitored respiration rate changes using oxygen reduction profiles for different cell types (44, 138, 168–170). In these experiments, oxygen is present in solution and is consumed by the living organism. Close to the cells, more oxygen is consumed and a lower oxygen reduction current is measured. The differences in oxygen reduction currents are in the ranges of 10 pA to nA. Studies have shown that the respiration rate of *in vitro* bovine embryos in the morula developmental stage are related to their quality and viability. Embryos having a higher respiration rate in the morula stage were shown to grow into larger and healthier embryos at subsequent developmental stages. Such information could be useful in supplementing the morphological data used to assess which embryos are to be used in bovine insemination.

Work has also been reported on human breast cells (171) and *Rhodobacter sphaeroides* (172). In these studies, the feedback mode of SECM was used to look at the regeneration reaction of different mediators when exposed to cells. These studies provide useful information about the permeability of the membrane to a wide variety of redox couples. A theoretical treatment enabled kinetic information about these processes (173) to be extracted. SECM has also been used to distinguish between normal and malignant human breast cells (174) with corroboration by optical and fluorescence microscopy measurements.

Other studies have focused on export pump activity of yeast and human liver cells when exposed to quinone oxidative stress. Quinones are readily transported into cells where they retain the ability to redox cycle, impose oxidative stress and form covalent adducts with important cellular species. To cope with oxidative stress, cells have enzymatic and nonenzymatic defenses, like antioxidants, that will limit the stress and damage. For example, glutathione (GSH) is the major nonprotein sulfhydryl present in cells (175) and it detoxifies cells by sacrificially reacting with quinones to limit the irreversible modification of cellular macromolecules. The thioether conjugates formed can then be degraded to other substances or actively removed from the intracellular media using an ATP-dependent pump. In the case of the menadione–glutathione conjugate, the conjugate remains intact and is transported into the extracellular media via the GS-X pump in cells (176, 177). From SECM responses, an apparent rate of transport for the uptake of menadione was extracted (48). Detection of this biological metabolite was also possible in single human liver cell. The cellular detoxification process was observed and imaged for both isolated and monolayer cultured cells (165).

***(b) Problems to tackle***

The difficulty in working at the interface of two fields like SECM and biology lies in the identification of a biologically relevant problem to address. To do so, one must often rely on collaborations. Now that ground work has been reported in full cellular SECM studies, there is a need to establish general methodologies to compare the SECM results between groups, to develop better numerical simulations adapted to the complexity of the biological system, and to apply SECM in a possible combinatorial setting.

### *12.4.6.5 Future directions*

SECM can be applied to imaging and kinetic studies of biological systems. Ground work on enzymes, ion channels, and cellular system has been reported and demonstrates SECM capabilities. To use SECM in diagnostic assays, nucleic acid analysis, biosensor, bioremediation or other biotechnological processes, SECM needs to be applied quantitatively to different biological systems. There is also a need for the development of accessible kinetic theories, the development of controlled substrate methodologies, and the fabrication of smaller well-characterized UMEs that would increase the lateral resolution of SECM.

## REFERENCES


1. A. J. Bard, M. V. Mirkin, Eds., *Scanning Electrochemical Microscopy*, Marcel Dekker: New York, 2001.
2. D. Bonnell, Ed., *Scanning Probe Microscopy and Spectroscopy, Theory, Techniques, and Applications*, Wiley-VCH: New York, 2001.
3. A. J. Bard, L. R. Faulkner, *Electrochemical Methods, Fundamentals and Applications*, John Wiley & Sons, Inc.: New York, 2001, p. 174.
4. M. Ludwig, C. Kranz, W. Schuhmann, H. E. Gaub, *Rev. Sci. Instrum.* **66**, 2857 (1995).
5. J. V. Macpherson, P. R. Unwin, A. C. Hillier, A. J. Bard, *J. Am. Chem. Soc.* **118**, 6445 (1996).
6. (a) J. V. Macpherson, P. R. Unwin, *Anal. Chem.* **72**, 276 (2000). (b) C. Kranz, G. Friedbacher, B. Mikaikoff, A. Lugstein, J. Smoliner, E. Bertagnolli, *Anal. Chem.* **73**, 2491 (2001).
7. (a) P. L. James, P. J. Moyer, L. F. Garfias-Mesias, W. H. Smyrl, *J. Electrochem. Soc.* **145**, L64 (1998). (b) M. Buchler, S. C. Kelley, W. H. Smyrl, *Electrochem. Solid-State Lett*. **3**, 35 (2000).
8. F.-R. F. Fan, A. J. Bard, Unpublished experiments.
9. (a) M. A. Paesler, P. J. Moyer, *Near-Field Optics: Theory, Instrumentation and Applications*, Wiley: New York, 1996. (b) E. Betzig, J. K. Trautman, *Science* **257**, 189 (1992).
10. Y. Lee, A. J. Bard, *Anal. Chem.* **74**, 3626 (2002).
11. G. Shi, L. F. Garfias-Mesias, W. H. Smyrl, *J. Electrochem. Soc.* **145**, 3011 (1998). (b) P. L. James, N. Casillas, W. H. Smyrl, *J. Electrochem. Soc.* **143**, 3853 (1996).
12. Y. Lee, Z. Ding, A. J. Bard, *Anal. Chem.* **74**, 3634 (2002).
13. R. G. Maus, E. M. McDonald, R. M. Wightman, *Anal. Chem.* **71**, 4944 (1999).
14. F.-R. F. Fan, D. Cliffel, A. J. Bard, *Anal. Chem.* **70**, 2941 (1998).
15. Y. Zu, Z. Ding, J. Zhou, Y. Lee, A. J. Bard, *Anal. Chem*. **73**, 2153 (2001).
16. R. G. Maus, R. M. Wightman, *Anal. Chem.* **73**, 3993 (2001).
17. J. J. Watkins, J. Chen, H. S. White, H. D. Abruña, E. Maisonhaute, C. Amatore, *Anal. Chem.* **75**, 3962 (2003).
18. S. Chen, A. Kucernak, *Electrochem. Commun.* **4**, 80 (2002).
19. P. Sun, Z. Zhang, J. Guo, Y. Shao, *Anal. Chem.* **73**, 5346 (2001).
20. J. Mauzeroll, M. Buda, A. J. Bard, F. Prieto, M. Rueda, *Langmuir* **18**, 9453 (2002).
21. J. Mauzeroll, E. A. Hueske, A. J. Bard, *Anal. Chem.* **75**, 3880 (2003).
22. I. Ciani, D. P. Burt, S. Daniele, P. R. Unwin, *J. Phys. Chem. B* **108**, 3801 (2004).
23. J. Golas, Z. Galus, J. Osteryoung, *Anal. Chem.* **59**, 389 (1987).
24. J. L. Conyers, H. S. White, *Anal. Chem.* **72**, 4441 (2000).
25. T. H. Treutler, G. Wittstock, *Electrochim. Acta* **48**, 2923 (2003).

26. A. G. Güell, I. Díez-Pérez, P. Gorostiza, F. Sanz, *Anal. Chem.* **76**, 5218 (2004).
27. C. G. Zoski, B. Liu, A. J. Bard, *Anal. Chem.* **76**, 3646 (2004).
28. P. Liljeroth, C. Johans, C. J. Slevin, B. M. Quinn, K. Kontturi, *Electrochem. Commun.* **4**, 67 (2002).
29. (a) D. A. Walsh, J. L. Fernández, A. J. Bard, C. G. Zoski, manuscript in preparation. (b) D. A. Walsh, J. Fernandez, J. Mauzeroll, A. J. Bard, *Anal. Chem.* **77**, 5182 (2005).
30. J. V. Macpherson, C. J. Slevin, P. R. Unwin, *J. Chem. Soc., Faraday Trans.* **92**, 3799 (1996).
31. Q. Fulian, A. C. Fisher, G. Denuault, *J. Phys. Chem. B* **103**, 4393 (1999).
32. O. Sklyar, G. Wittstock, *J. Phys. Chem. B* **106**, 7499 (2002).
33. T. Nann, J. Heinze, *Electrochim. Acta* **48**, 3975 (2003).
34. J. Galceran, J. Cecília, E. Companys, J. Salvador, J. Puy, *J. Phys. Chem. B* **104**, 7993 (2000).
35. C. G. Zoski, J. C. Aguilar, A. J. Bard, *Anal. Chem.* **75**, 2959 (2003).
36. L. Rajendran, S. P. Ananthi, *J. Electroanal. Chem.* **56**, 113 (2004).
37. J. L. Amphlet, G. Denuault, *J. Phys. Chem. B* **102**, 9946 (1998).
38. Y. Selzer, D. Mandler, *Anal. Chem.* **72**, 2383 (2000).
39. Y. Lee, S. Amemiya, A. J. Bard, *Anal. Chem.* **73**, 2261 (2001).
40. P. Liljeroth, C. Johans, C. J. Slevin, B. M. Quinn, K. Kontturi, *Anal. Chem.* **74**, 1972 (2002).
41. C. G. Zoski, N. Simjee, O. Guenat, M. Koudelka-Hep, *Anal. Chem.* **76**, 62 (2004).
42. G. Wittstock, *Fresenius J. Anal. Chem.* **370**, 303 (2001).
43. M. Carano, K. B. Holt, A. J. Bard, *Anal. Chem.* **75**, 5071 (2003).
44. T. Kaya, M. Nishizawa, T. Yasukawa, M. Nishiguchi, T. Onouchi, T. Matsue, *Biotechnol. Bioeng.* **76**, 391 (2001).
45. H. Shiku, T. Shiraishi, S. Aoyagi, Y. Utsumi, M. Matsudaira, H. Abe, H. Hoshi, S. Kasai, H. Ohya, T. Matsue, *Anal. Chim. Acta* **522**, 51 (2004).
46. R. C. Engstrom, B. Small, L. Kattan, *Anal. Chem.* **64**, 241 (1992).
47. S. M. Fonseca, A. L. Barker, S. Ahmed, T. J. Kemp, P. R. Unwin, *Chem. Commun.* **8**, 1002 (2003).
48. J. Mauzeroll, A. J. Bard, *Proc. Natl. Acad. Sci. U.S.A.* **101**, 7862 (2004).
49. R. C. Engstrom, R. M. Wightman, E. W. Kristensen, *Anal. Chem.* **60**, 652 (1988).
50. R. D. Martin, P. R. Unwin, *J. Chem. Soc., Faraday Trans.* **94**, 753 (1998).
51. R. D. Martin, P. R. Unwin, *Anal. Chem.* **70**, 276 (1998).
52. J. L. Fernández, A. J. Bard, *Anal. Chem.* **76**, 2281 (2004).
53. F. Zhou, P. R. Unwin, A. J. Bard, *J. Phys. Chem.* **96**, 4917 (1992).
54. J. L. Fernández, A. J. Bard, *Anal. Chem.* **75**, 2967 (2003).
55. G. Denault, G. Nagy, K. Tóth, in "*Scanning Electrochemical Microscopy*", A. J. Bard, M. V. Mirkin, Eds., Marcel Dekker, Inc.: New York, 2001, pp. 397–444.
56. J. Koryta, *Ion-Selective Electrodes*, Cambridge University Press: Cambridge, 1975.
57. D. Amman, *Ion-Selective Microelectrodes: Principle, Design & Application*, Springer Verlag: New York, 1986.
58. B. R. Horrocks, M. V. Mirkin, D. T. Pierce, A. J. Bard, G. Nagy, K. Tóth, *Anal. Chem.* **65**, 1213 (1993).
59. (a) M. H. Troise-Frank, G. Denuault, *J. Electroanal. Chem.* **354**, 331 (1993). (b) M. H. Troise-Frank, G. Denuault, *J. Electroanal. Chem.* **379**, 405 (1994).
60. (a) G. Denuault, M. H. Troise-Frank, L. M. Peter, *Faraday Discuss.* **94**, 23 (1992). (b) M. Etienne, A. Schulte, S. Mann, G. Jordan, I. D. Dietzel, W. Schuhmann, *Anal. Chem.* **76**, 3682 (2004).
61. S. Amemiya, A. J. Bard, *Anal. Chem.* **72**, 4940 (2000).
62. C. Wei, A. J. Bard, G. Nagy, K. Tóth, *Anal. Chem.* **67**, 1346 (1995).
63. C. Wei, A. J. Bard, I. Kapui, G. Nagy, K. Tóth, *Anal. Chem.* **68**, 2651 (1996).
64. B. R. Horrocks, D. Schmidtke, A. Heller, A. J. Bard, *Anal. Chem.* **65**, 3605 (1993).
65. (a) A. Hengstenberg, C. Kranz, W. Schuhmann, *Chem. Eur. J.* **6**, 1547 (2000). (b) A. Hengstenberg, A. Blöchl, I. D. Dietzel, W. Schuhmann, *Angew. Chem.Int. Ed.* **40**, 905 (2001).

66. D. O. Wipf, A. J. Bard, *Anal. Chem.* **64**, 1362 (1992).
67. A. J. Bard, M. V. Mirkin, P. R. Unwin, D. O. Wipf, *J. Phys. Chem.* **96**, 1861 (1992).
68. Z. Ding, B. M. Quinn, A. J. Bard, *J. Phys. Chem. B* **105**, 6367 (2001).
69. A. L. Barker, P. R. Unwin, J. Zhang, *Electrochem. Commun.* **3**, 372 (2001).
70. P. Liljeroth, B. M. Quinn, K. Kontturi, *Langmuir* **19**, 5121 (2003).
71. C. Wei, A. J. Bard, M. V. Mirkin, *J. Phys. Chem.* **99**, 16033 (1995).
72. M. V. Mirkin, T. C. Richards, A. J. Bard, *J. Phys. Chem.* **97**, 7672 (1993).
73. W. Miao, Z. Ding, A. J. Bard, *J. Phys. Chem. B* **106**, 1392 (2002).
74. B. Liu, A. J. Bard, *J. Phys. Chem. B* **106**, 12801 (2002).
75. J. Zhou, Y. Zu, A. J. Bard, *J. Electroanal. Chem.* **491**, 22 (2000).
76. K. Jambunathan, B. C. Shah, J. L. Hudson, A. C. Hillier, *J. Electroanal. Chem.* **500**, 279 (2001).
77. C. G. Zoski, *J. Phys. Chem. B* **107**, 6401 (2003).
78. M. Tsionsky, A. J. Bard, M. V. Mirkin, *J. Phys. Chem.* **100**, 17881 (1996).
79. Z. Zhang, Y. Yuan, P. Sun, B. Su, J. Guo, Y. Shao, H. H. Girault, *J. Phys. Chem. B* **106**, 6713 (2002).
80. S. K. Haram, A. J. Bard, *J. Phys. Chem. B* **105**, 8192 (2001).
81. Y. Selzer, I. Turyan, D. Mandler, *J. Phys. Chem. B* **103**, 1509 (1999).
82. J. L. Fernández, C. Hurth, A. J. Bard, unpublished results.
83. For example, P. R. Unwin, A. J. Bard, *J. Phys. Chem.* **95**, 7814 (1991).
84. For example, (a) F. Zhou, A. J. Bard, *J. Am. Chem. Soc.* **116**, 393 (1994). (b) D. A. Treichel, M. V. Mirkin, A. J. Bard, *J. Phys. Chem.* **98**, 5751 (1994).
85. C. Demaille, P. R. Unwin, A. J. Bard, *J. Phys. Chem.* **100**, 14137 (1996).
86. R. C. Engstrom, T. Meany, R. Tople, R. M. Wightman, *Anal. Chem.* 59, 2005 (1987).
87. (a) T. Wilhelm, G. Wittstock, Angew. Chem. *Int. Ed.* **42**, 2248 (2003). (b) C. Zhao, J. K. Sinha, C. Ajith Wijayawardhana, G. Wittstock, *J. Electroanal. Chem.* **561**, 83 (2004).
88. B. Liu, W. Cheng, S. A. Rotenberg, M. V. Mirkin, *J. Electroanal. Chem.* **500**, 590 (2001).
89. S. B. Basame, H. S. White, *J. Phys. Chem. B* **102**, 9812 (1998).
90. M. Tsionsky, Z. G. Cardon, A. J. Bard, R. B. Jackson, *Plant Physiol.* **113**, 895 (1997).
91. C. Lee, J. Kwak, F. C. Anson, *Anal. Chem.* **63**, 1501 (1991).
92. T. E. Mallouk, E. S. Smotkin, in "*Handbook of Fuel Cells—Fundamental and Applications*", W. Vielstich, A. Lamm, H. A. Gasteiger, Eds., John Wiley & Sons: Hoboken, NJ, 2003, Vol. 2, Part 3, p. 334.
93. E. Reddington, A. Sapienza, B. Gurau, R. Viswanathan, S. Sarangapani, E. S. Smotkin, T. E. Mallouk, *Science* **280**, 1735 (1998).
94. S. Guerin, B. E. Hayden, C. E. Lee, C. Mormiche, J. R. Owen, A. E. Russell, *J. Comb. Chem.* **6**, 149 (2004).
95. S. Jayaraman, A. C. Hillier, *J. Comb. Chem.* **6**, 27 (2004).
96. S. Jayaraman, A. C. Hillier, *J. Phys. Chem. B* **107**, 5221 (2003).
97. S. Jayaraman, A. C. Hillier, *Langmuir* **17**, 7857 (2001).
98. K. Jambunathan, A. C. Hillier, *J. Electrochem. Soc.* **150**, E312 (2003).
99. K Jambunathan, S. Jayaraman, A. C. Hillier, *Langmuir* **20**, 1856 (2004).
100. J. L. Fernández, D. A. Walsh, A. J. Bard, *J.Am. Chem. Soc.* **127**, 357 (2005).
101. J. L. Fernández, N. Mano, A. Heller, A. J. Bard, Angew. Chem. *Int. Ed.* **43**, 6355 (2004).
102. I. Willner, E. Katz, *Angew. Chem. Int. Ed.* **39**, 1181 (2000).
103. M. A. Fox, *Acc. Chem. Res*. **32**, 201 (1999).
104. H. O. Finklea, in "*Electroanalytical Chemistry*", A. J. Bard, I. Rubinstein, Eds., Marcel Dekker: New York, 1996, Vol. 19, pp. 109–335.
105. B. Liu, A. J. Bard, M. V. Mirkin, S. E. Creager, *J. Am. Chem. Soc.* **126**, 1485 (2004).

106. C. Cannes, F. Kanoufi, A. J. Bard, *J. Electroanal. Chem*. **547**, 83 (2003).
107. M. Tsionsky, A. J. Bard, M. V. Mirkin, *J. Am. Chem. Soc*. **119**, 10785 (1997).
108. M.-H. Delville, M. Tsionsky, A. J. Bard, *Langmuir* **14**, 2774 (1998).
109. B. Liu, M. V. Mirkin, *J. Phys. Chem. B* **106**, 3933 (2002).
110. J. Zhang, C. J. Slevin, C. Morton, P. Scott, D. J. Walton, P. R. Unwin, *J. Phys. Chem*. **105**, 11120 (2001).
111. F. Forouzan, A. J. Bard, M. V. Mirkin, *Isr. J. Chem.* **37**, 155 (1997).
112. (a) D. O. Wipf, *Colloids Surf. A* **93**, 251 (1994). (b) J. W. Still, D. O. Wipf, *J. Electrochem. Soc*. **144**, 2657 (1997). (c) C. H. Paik, H. S. White, R. C. Alkire, *J. Electrochem. Soc*. **147**, 4120 (2000). (d) M. Buchler, J. Kermino, F. Guillaume, W. H. Smyrl, *J. Electrochem. Soc*. **147**, 3691 (2000). (e) I. Serebrennikova, H. S. White, *Electrochem. Solid-State Lett*. **4**, B4 (2001). (f) I. Serebrennikova, S. Lee, H. S. White, *Faraday Discuss*. **121**, 199 (2002). (g) N. Casillas, S. Charlebois, W. H. Smyrl, H. S. White, *J. Electrochem. Soc*. **141**, 636 (1994). (h) S. B. Basame, H. S. White, *Anal. Chem*. **71**, 3166 (1999). (i) S. B. Basame, H. S. White, *Langmuir* **15**, 819 (1999). (j) Y. Zhu, D. E. Williams, *J. Electrochem. Soc.* **144**, L43 (1997). (k) D. E. Williams, T. F. Mohiuddin, Y. Zhu, *J. Electrochem. Soc*. **145**, 2664 (1998). (l) J. C. Seegmiller, D. A. Buttry, *J. Electrochem. Soc*. **150**, B413 (2003).
113. H. Tanabe, T. Misawa, *J. Mater. Sci. Lett*. **17**, 551 (1998).
114. B. B. Katemann, C. G. Inchauspe, P. A. Castro, A. Schulte, E. J. Calvo, W. Schuhmann, *Electrochim. Acta* **48**, 1115 (2003).
115. N. Casillas, P. L. James, W. H. Smyrl, *J. Electrochem. Soc*. **142**, L16 (1995).
116. R. Peat, A. Riley, D. E. Williams, L. M. Peter, *J. Electrochem. Soc*. **136**, 3352 (1989).
117. D. Mandler, in "*Scanning Electrochemical Microscopy*", A. J. Bard, M. V. Mirkin, Eds., Marcel Dekker: New York, 2001, pp. 593–627.
118. B. R. Horrocks, in "*Encyclopedia of Electrochemistry*", A. J. Bard, M. Stratmann, Eds., Wiley-VCH, 2003, Vol. 3, pp. 444–490.
119. (a) O. E. Hüsser, D. H. Craston, A. J. Bard, *J. Vac. Sci. Technol*. B **6**, 1873 (1988). (b) O. E. Hüsser, D. H. Craston, A. J. Bard, *J. Electrochem. Soc*. **136**, 3222 (1989). (c) D. Mandler, A. J. Bard, *J. Electrochem. Soc*. **137**, 1079 (1990). (d) E. Ammann, D. Mandler, *J. Electrochem. Soc*. **148**, C533 (2001). (e) Y. Yatziv, I. Turyan, D. Mandler, *J. Am. Chem. Soc*. **124**, 5618 (2002). (f) O. D. Abril, D. Mandler, P. R. Unwin, *Electrochem. Solid-State Lett.* **7**, C71 (2004).
120. D. Mandler, A. J. Bard, *J. Electrochem. Soc*. **136**, 3143 (1989).
121. D. Mandler, A. J. Bard, *J. Electrochem. Soc*. **137**, 2468 (1990).
122. K. Borgwarth, C. Ricken, D. G. Ebling, J. Heinze, *Ber Bunsenges Phys. Chem*. **99**, 1421 (1995).
123. C. Hess, K. Borgwarth, C. Ricken, D. G. Ebling, J. Heinze, *Electrochim. Acta* **42**, 3065 (1997).
124. S. Meltzer, D. Mandler, *J. Electrochem. Soc*. **142**, L82 (1995).
125. C. W. Lin, F.-R. Fan, A. J. Bard, *J. Electrochem. Soc*. **134**, 1038 (1987).
126. Y. B. Zu, L. Xie, B. W. Mao, Z. W. Tian, *Electrochim. Acta* **43**, 1683 (1998).
127. Y. M. Wuu, F.-R. Fan, A. J. Bard, *J. Electrochem. Soc*. **136**, 885 (1989).
128. C. Kranz, M. Ludiwig, H. E. Gaub, W. Schumann, *Adv. Mater*. **7**, 38 (1995).
129. C. Kranz, H. E. Gaub, W. Schumann, *Adv. Mater*. **8**, 634 (1996).
130. L. Zhou, D. O. Wipf, *J. Electrochem. Soc*. **144**, 1202 (1997).
131. G. Wittstock, W. Schumann, *Anal. Chem*. **69**, 5059 (1997).
132. I. Turyan, T. Matsue, D. Mandler, *Anal. Chem*. **72**, 3431 (2000).
133. G. Wittstock, H. Wohlschläger, W. Schumann, *Electrochim. Acta* **42**, 3105 (1997).
134. H. Shiku, T. Takeda, H. Yamada, T. Matsue, I. Uchida, *Anal. Chem*. **67**, 312 (1995).
135. H. Shiku, I. Uchida, T. Matsue, *Langmuir* **13**, 7239 (1997).
136. W. B. Nowall, D. O. Wipf, W. G. Kuhr, *Anal. Chem*. **70**, 2601 (1998).

137. J. M. Liebetrau, H. M. Miller, J. E. Baur, S. A. Takacs, V. Anupunpisit, P. A. Garris, D. O. Wipf, *Anal. Chem.* **75**, 563 (2003).
138. T. Yasukawa, T. Kaya, T. Matsue, *Anal. Chem.* **71**, 4637 (1999).
139. B. R. Horrocks, G. Wittstock, in "*Scanning Electrochemical Microscopy*", A. J. Bard, M. V. Mirkin, Eds., Marcel Dekker: New York, 2001, pp. 445–519.
140. T. Sawaguchi, T. Matsue, I. Uchida, *Bioelectrochem. Bioenerg.* **29**, 127 (1992).
141. B. Limoges, J. Moiroux, J.-M. Savéant, *J. Electroanal. Chem.* **521**, 1 (2002).
142. B. Limoges, J. Moiroux, J.-M. Savéant, *J. Electroanal. Chem.* **521**, 8 (2002).
143. D. T. Pierce, P. R. Unwin, A. J. Bard, *Anal. Chem.* **64**, 1795 (1992).
144. D. T. Pierce, A. J. Bard, *Anal. Chem.* **65**, 3598 (1993).
145. C. Kranz, G. Wittstock, H. Wohlschläger, W. Schuhmann, *Electrochim. Acta* **42**, 3105 (1997).
146. C. A. Wijayawardhana, G. Wittstock, H. B. Halsall, W. R. Heineman, *Anal. Chem.* **72**, 333 (2000).
147. B. R. Horrocks, M. V. Mirkin, D. T. Pierce, A. J. Bard, *Anal. Chem.* **65**, 1213 (1993).
148. B. R. Horrocks, M. V. Mirkin, *J. Chem. Soc. Faraday Trans.* **94**, 1115 (1998).
149. C. E. M. Berger, B. R. Horrocks, H. K. Datta, *J. Endocrinol.* **158**, 311 (1998).
150. H. Shiku, T. Matsue, I. Uchida, *Anal. Chem.* **68**, 1276 (1996).
151. H. Shiku, Y. Hara, T. Matsue, I. Uchida, *J. Electroanal. Chem.* **438**, 187 (1997).
152. J. Zaumseil, G. Wittstock, S. Bahrs, P. Steinrücke, *Fresenius J. Anal. Chem.* **367**, 352 (2000).
153. G. Wittstock, K. J. Yu, H. B. Halsall, T. H. Ridgway, W. R. Heineman, *Anal. Chem.* **67**, 3578 (1995).
154. Y. N. Antonenko, P. Pohl, E. Rosenfeld, *Arch. Biochem. Biophys.* **333**, 225 (1996).
155. J. Wang, F. Song, F. Zhou, *Langmuir* **18**, 6653 (2002).
156. D. Oyamatsu, N. Kanaya, H. Shiku, M. Nishizawa, T. Matsue, *Sens. Actuators B* **91**, 199 (2003).
157. S. Gáspár, M. Mosbach, L. Wallman, T. Laurell, E. Csöregi, W. Schuhmann, *Anal. Chem.* **73**, 4254 (2001).
158. John R. Silvius, "Thermotropic Phase Transitions of Pure Lipids in Model Membranes and Their Modifications by Membrane Proteins", in *Lipid-Protein Interactions*, John Wiley & Sons, Inc.: New York, 1982.
159. S. Amemiya, Z. Ding, J. Zhou, A. J. Bard, *Electro. Chem*. **483**, 7 (2000).
160. C. J. Slevin, J. A. Umbers, J. H. Atherton, P. R. Unwin, *J. Chem. Soc., Faraday Trans.* **92**, 5177 (1996).
161. E. R. Scott, H. S. White, J. B. Phipps, *J. Membr. Sci.* **58**, 71 (1991).
162. J. V. Macpherson, M. A. Beeston, P. R. Unwin, N. P. Hughes, D. Littlewood, *J. Chem. Soc., Faraday Trans*. **91**, 1407 (1995).
163. E. R. Scott, J. B. Phipps, H. S. White, *J. Invest. Dermatol.* **104**, 142 (1995).
164. A. Nelson, *J.Biophys.* **80**, 2694 (2001).
165. J. Mauzeroll, T. J. Monks, O. Owhadian, A. J. Bard, *Proc. Natl. Acad. Sci. U.S.A.* **101**, 17582 (2004).
166. R. B. Jackson, M. Tsionsky, Z. G. Cardon, A. J. Bard, *Plant Physiol.* **111**, 354 (1996).
167. C. E. M. Berger, H. Rathod, J. I. Gillespie, B. R. Horrocks, H. Datta, *J. Bone Miner. Res.* 16, 2092 (2001).
168. M. Nishizawa, K. Takoh, T. Matsue, *Langmuir* **18**, 3645 (2002).
169. Y. Takii, K. Takoh, M. Nishizawa, T. Matsue, *Electrochim. Acta* **48**, 3381 (2003).
170. H. Shiku, T. Shiraishi, H. Ohya, T. Matsue, H. Abe, H. Hoshi, M. Kobayashi, *Anal. Chem.* **73**, 3751 (2001).
171. B. Liu, S. A. Rotenberg, M. V. Mirkin, *Proc. Natl. Acad. Sci. U.S.A.* **97**, 9855 (2000).
172. C. Cai, B. Liu, M. V. Mirkin, H. A. Frank, J. F. Rusling, *Anal. Chem.* **74**, 114 (2002).

173. L. Biao, S. A. Rotenberg, M. V. Mirkin, *Anal. Chem.* **74**, 6340 (2002).
174. W. Feng, S. A. Rotenberg, M. V. Mirkin, *Anal. Chem.* **75**, 4148 (2003).
175. D. J. Reed, M. J. Meredith, "Cellular Defense Mechanisms Against Reactive Metabolites", in *Bioactivation of Foreign Compounds*, M. W. Anders, Ed., Academic Press: New York, pp. 71–108.
176. D. Keppler, *Free Radic. Biol. Med.* **27**(9/10), 985 (1999).
177. H. Sies, *Free Radic. Biol. Med.* **27**(9/10), 916 (1999).

# – 13 –

# Electrogenerated Chemiluminescence

**Wujian Miao**

The University of Southern Mississippi, Hattiesburg, Mississippi, USA

## 13.1 CONCEPTS AND HISTORY

Electrogenerated chemiluminescence (also called electrochemiluminescence and abbreviated ECL) is the process where species generated at electrodes undergo electron-transfer reactions to form excited states that emit light. In other words, ECL is a kind of luminescence produced by electrode reactions (1). A typical ECL system would involve a solution containing ECL precursors in a solution with supporting electrolyte in an electrochemical cell with either a single working electrode using an alternating potential, or two separate electrodes in close proximity to each other by holding one electrode at a reductive potential and the other at an oxidative potential (2). The first detailed ECL studies were described in the middle of 1960s (3–5), although reports concerning light emission during electrolysis date back to the 1920s (6, 7). After about 40 years study, ECL has now become a very powerful analytical technique and been widely used in the areas of, e.g., immunoassay, food and water testing, and biowarfare agent detection (8). ECL has also been successfully exploited as a detector of flow injection analysis (FIA), HPLC, capillary electrophoresis (CE), and micro total analysis (μTAS) (9). A time line showing various events in the development of ECL is illustrated in Figure 13.1 (10).

Various topics on ECL have been thoroughly reviewed (9, 25–57), and the first ECL monograph (8) was also published recently. In the monograph, an overview and brief history of ECL, both the experimental and theoretical aspects of ECL, a review of the behavior of coreactants, organic molecules, and metal chelates, together with the application of ECL in immunoassay, flow injection, liquid chromatography, CE, and light production and display devices are extensively presented.

## 13.2 TYPES OF LUMINESCENCE

In addition to ECL, light can be generated by a wide variety of luminescent processes (Table 13.1). Of them, both ECL and chemiluminescence (CL) involve the production of


**Handbook of Electrochemistry**
**Edited by C.G. Zoski**

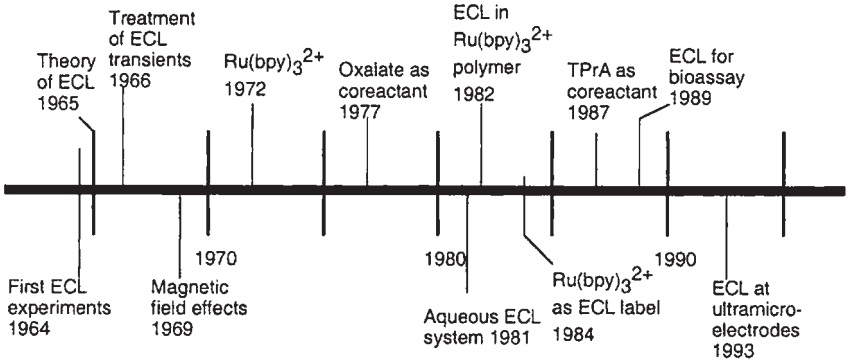


**Figure 13.1** Time line of ECL. 1964–1965: First experiments (3–5); 1965: Theory (11) ; 1966: Transients (12, 13); 1969: Magnetic field effects (14); 1972: $Ru(bpy)_3^{2+}$(15); 1977: Oxalate (16); 1981: Aqueous (17); 1982: $Ru(bpy)_3^{2+}$ polymer (18); 1984: $Ru(bpy)_3^{2+}$ label (19); 1987: Tri-*n*-propylamine (TPrA) (20, 21); 1989: Bioassay (22, 23); 1993: Ultramicroelectrodes (24) (from reference (8)).

**Table 13.1**

Different types of luminescence[a]

| Luminescence type | Caused by | References |
|---|---|---|
| Photoluminescence (PL) | Photo-excitation of compounds | (58–60) |
| Chemiluminescence (CL) | Chemical excitation of compounds | (58–82) |
| Electrochemiluminescence (ECL) | Electrogenerated chemical excitation | (9, 25–57) |
| Radiochemiluminescence | Radiation-induced chemical excitation | (83–88) |
| Lyoluminescence | Excitation induced by dissolution of an irradiated or other energy-donating solid | (89, 90) |
| Sonoluminescence | Excitation of compounds by ultrasonication, either by energy transfer from the intrinsic SL centers of water or by chemical excitation by hydroxyl radicals and atomic hydrogen | (91–110) |

[a]Modified from reference (46)

light by species that can undergo highly energetic electron-transfer reactions; however, luminescence in CL is initiated by the mixing of necessary reagents and often controlled by the careful manipulation of fluid flow. In contrast, luminescence in ECL is initiated and controlled by changing an electrode potential. Figure 13.2 schematically describes the general principles of photoluminescence (PL), CL, and ECL. As an analytical technique, the advantages of CL over PL, and ECL over CL are listed in Table 13.2.

## 13.3 FUNDAMENTAL REACTIONS

### 13.3.1 Ion annihilation ECL

Classical ECL involves the formation of an excited state as a result of an energetic electron transfer between electrochemically generated species, often radical ions, at the surface of

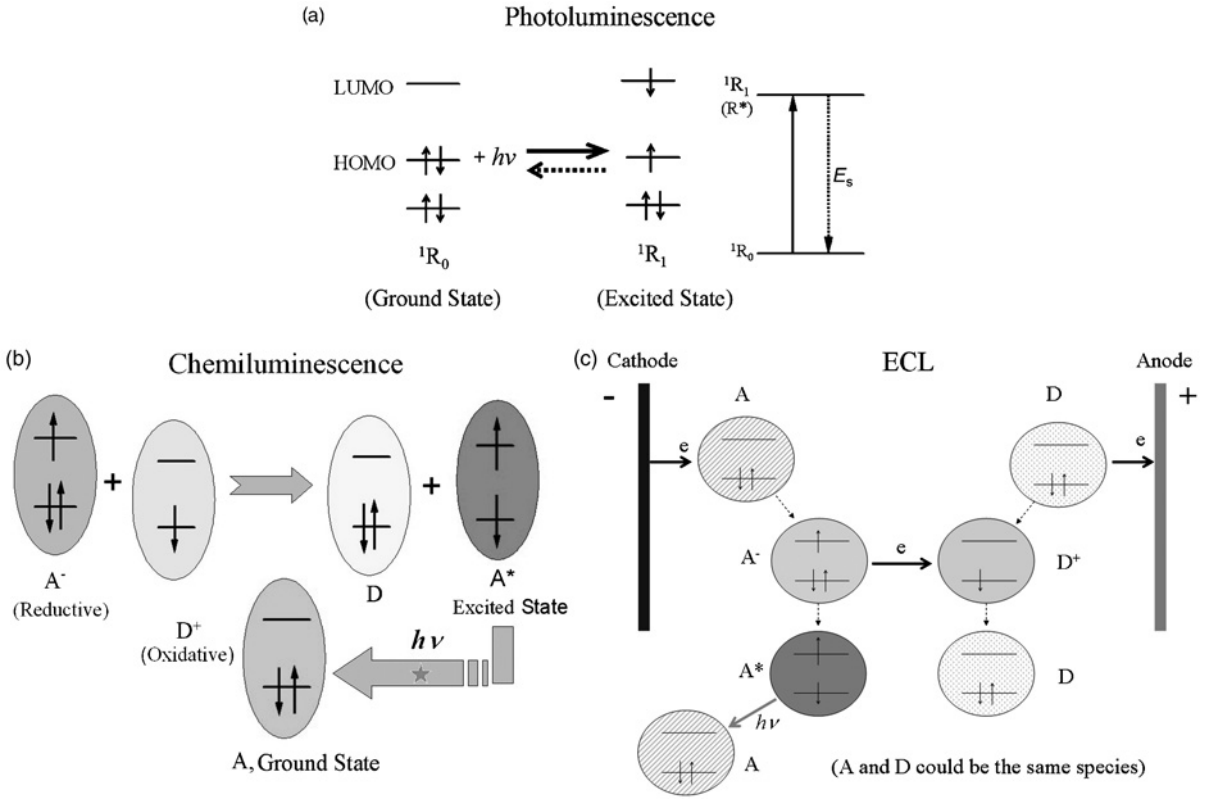


**Figure 13.2** Schematic diagrams showing the general principles of (a) Photoluminescence, (b) Chemiluminescence, (c) ECL. (for colour version: see colour section at the end of the book).

**Table 13.2**

Comparison of photoluminescence (PL), chemiluminescence (CL) and electrochemiluminescence (ECL), in terms of an analytical technique

| Advantages of CL over PL | Advantages of ECL over CL |
|---|---|
| 1. No light source needed<br>2. No scattered light<br>3. No interference from luminescent impurities | 1. ECL reactions are localized spatially and temporally and controllable<br>2. Application is possible through turnover of reactions |

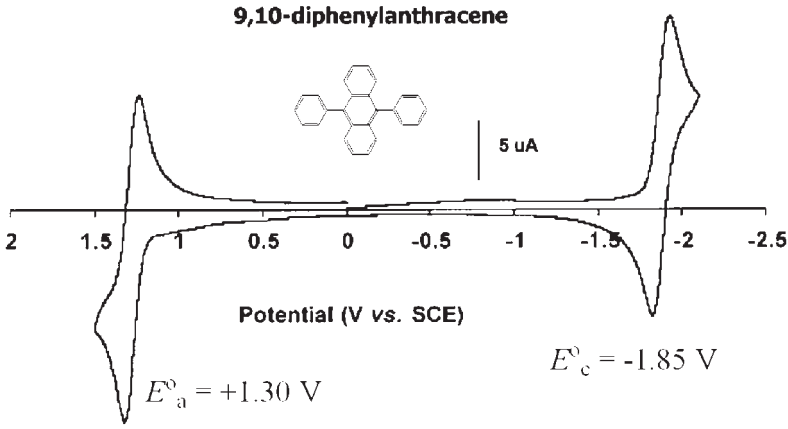


**Figure 13.3** Cyclic voltammogram of 1 mM DPA in MeCN containing 0.1 M TBAP at a 2 mm in diameter Pt disk electrode at a scan rate of 200 mV/s (modified from reference (112)).

an electrode. As shown in Figure 13.2c, species A accepts one electron from the cathode to form $A^{-\bullet}$, and species D loses one electron at the anode to form $D^{+\bullet}$. When $A^{-\bullet}$ and $D^{+\bullet}$ diffuse away from the electrodes and come together, $A^{-\bullet}$ transfers one electron to $D^{+\bullet}$ to produce a neutral species D and the excited state A*. A* immediately emits light ($h\nu$) and returns to its ground state.

Scheme 13.1 summarizes the reaction sequence of the above processes, where A and D could be the same species, e.g., a polycyclic aromatic hydrocarbon (PAH) such as 9,10-diphenylanthracene (DPA, Figure 13.3) (111, 112).

$$A + e \longrightarrow A^{-\bullet} \quad \text{(reduction at electrode)} \tag{13.1}$$

$$D - e \longrightarrow D^{+\bullet} \quad \text{(oxidation at electrode)} \tag{13.2}$$

$$A^{-\bullet} + D^{+\bullet} \longrightarrow A^{*} + D \quad \text{(excited state formation)} \tag{13.3}$$

$$A^{*} \longrightarrow A + h\nu \quad \text{(light emission)} \tag{13.4}$$

**Scheme 13.1**

#### *13.3.1.1 Criteria for efficient ion annihilation occurring*

For a given chemical species, three criteria are generally required for efficient ion annihilation ECL to occur (10): (i) stable radical ions of the precursor molecules in the electrolyte of interest (as seen in the CV response, e.g., DPA in Figure 13.3), (ii) good PL efficiency of a product of the electron-transfer reaction, which often can be evaluated from the fluorescent experiment, and (iii) sufficient energy in the electron-transfer reaction to produce the excited state (see below for details).

#### *13.3.1.2 Energy requirements, S-route, T-route, and ST-route*

The total energy of the ion annihilation reaction (equation (13.3)) is primarily governed by the difference between the thermodynamic potential for oxidation (equation (13.2)) and reduction (equation (13.1)) obtained from the cyclic voltammogram (Figure 13.3) with correction of entropy effects as

$$-\Delta H^0 = \left(E_a^0 - E_c^0\right) - T\Delta S^0 \tag{13.5}$$

The value of $T\Delta S^0$ is usually estimated as 0.10 ($\pm$0.1 eV) (5, 113, 114). Since

$$E^\circ = E_p \pm 1.109\mathrm{RT}/F = E_p \pm 28.5\ \mathrm{mV}\ at\ 298\ \mathrm{K} \tag{13.6}$$

Equation (13.5) is often expressed using CV peak potentials ($E_p$ in volts),

$$-\Delta H^0 = (E_{pa} - E_{pc}) - 0.16 \tag{13.7}$$

If $-\Delta H^0 > E_s$, where $E_s$ (in eV) is the energy gap between the excited singlet state of energy and the ground state of energy (Figure 13.2a), and often determined from the fluorescence spectrum, the ion annihilation reaction can produce an excited singlet state species. Such reactions are sometimes called *energy-sufficient*, and the reaction is said to follow the S-route. A typical example of the energy-sufficient system is the $DPA^{+\bullet}/DPA^{-\bullet}$ system (111, 112).

If $E_s > -\Delta H^0 > E_T$, where $E_T$ is excited triplet state of energy, the annihilation reaction energy can produce the triplet state species $^3A^*$, with excited single production occurring via triplet–triplet annihilation (TTA) (Scheme 13.2). Such reactions are called *energy-deficient,* and the reactions are said to follow the T-route. Typical examples of the energy-deficient system are $TMPD^{+\bullet}/DPA^{-\bullet}$ and $TMPD^{+\bullet}/AN^{-\bullet}$ (TMPD = *N*,*N*,*N*′,*N*′-tetramethyl *p*-phenylenediamine and AN = anthracene) (14, 114). The efficiency of direct emission from $^3A^*$ is usually low in a solution phase because of the long radiative lifetime of $^3A^*$ and its quenching by radical ions or other species, such as molecular oxygen.

$$A^{-\bullet} + D^{+\bullet} \longrightarrow {}^3A^* + D \quad \text{(excited triplet formation)} \tag{13.8}$$

$$^3A^* + {}^3A^* \longrightarrow {}^1A^* + A \quad \text{(triplet-triplet annihilation)} \tag{13.9}$$

$$^1A^* \longrightarrow A + h\nu \quad \text{(light emission)} \tag{13.10}$$

**Scheme 13.2**

If $-\Delta H^0$ is nearly marginal to $E_s$, the T-route can contribute to the formation of $^3A^*$ in addition to the S-route, and the reactions are said to follow the ST-route. A typical system with such a route is the rubrene anion–cation annihilation (115–117).

#### *13.3.1.3 Excimers, exciplexes, and E-route*

In addition to the formation of singlet and triplet excited states, ion annihilation reactions can lead to the direct formation of excimers (excited dimers) and exciplexes (excited complexes). In most cases, the participating molecules must be able to align so that there is significant $\pi$-orbital overlap; thus this occurs mostly among planar PAHs such as pyrene and perylene (118–120). Other reactions such as TTA process can also lead to the formation of excimers and/or exciplexes (121). The reactions associated with the formation of excimers and exciplexes are said to follow the E-route. The relevant reactions are summarized in Scheme 13.3.

$$A^{-\bullet} + A^{+\bullet} \longrightarrow A_2^* \quad \text{(excimer formation)} \tag{13.11}$$

$$A^{-\bullet} + D^{+\bullet} \longrightarrow AD^* \quad \text{(exciplex formation)} \tag{13.12}$$

$$^3A^* + {}^3A^* \longrightarrow {}^1A_2^* \quad \text{(TTA excimer formation)} \tag{13.13}$$

**Scheme 13.3**

Excimer or exciplex emission is generally characterized by broad featureless emission red-shifted from the singlet emission of the molecule. Also, the emission wavelength and intensity change with solvent polarity. Emission from the monomer and the excimer are very often observed in the same spectrum. Although excimers and exciplexes can be formed via photo-excitation as observed in fluorescence spectroscopy, they are most likely to form in ECL due to the close proximity of the radical ions in the contact radical ion pair (122).

### 13.3.2 Coreactant ECL (123)

#### *13.3.2.1 Terms and definitions*

Unlike ion annihilation ECL, in which electrolytic generation of both the oxidized and reduced ECL precursors is required, coreactant ECL is generated with a single potential step or one directional potential scanning at an electrode in a solution containing luminophore species in the presence of a deliberately added reagent (coreactant). Depending on the polarity of the applied potential, both the luminophore and the coreactant species can be first oxidized or reduced at the electrode to form radicals, and intermediates formed from the coreactant then decompose to produce a powerful reducing or oxidizing species that reacts with the oxidized or reduced luminophore to produce the excited states that emit light. Since highly reducing intermediate species are generated after an electrochemical oxidation of a coreactant, or highly oxidizing ones are produced after an electrochemical reduction, the corresponding ECL reactions are often referred to as "*oxidative-reduction*" ECL and "*reductive-oxidation*" ECL, respectively (17, 124). Thus, a coreactant is a species that, upon electrochemical oxidation or reduction, immediately undergoes chemical decomposition to form a strong reducing or oxidizing intermediate that can react with an oxidized or reduced ECL luminophore to generate excited states. Another difference between annihilation and coreactant ECL is that, in annihilation ECL, all starting species can be regenerated after light

emission, while in coreactant ECL, only luminophore species can be regenerated and the coreactant is consumed via the ECE (2) reactions.

#### *13.3.2.2 Advantages of coreactant ECL over ion annihilation ECL*

1. The use of a coreactant can make ECL possible even for some fluorescent compounds that have only a reversible electrochemical reduction or oxidation.
2. Even with solvents for ECL that have a narrow potential window so that only a reduced or oxidized form of a luminophore can be produced, e.g., tris(2,2′-bipyridine) ruthenium(II), $Ru(bpy)_3^{2+}$ (bpy = 2,2′-bipyridine), in aqueous solutions, it is still possible to generate ECL by use of a coreactant.
3. When the annihilation reaction between oxidized and reduced species is not efficient, the use of a coreactant may produce more intense ECL.

#### *13.3.2.3 Criteria for a good coreactant (123)*

The following six criteria are generally required for a good coreactant compound:

1. *Solubility.* The coreactant should be reasonably soluble in the reaction media, because the ECL intensity is generally proportional to the concentration of the coreactants.
2. *Stability.* The intermediate species generated electrochemically and chemically should be sufficiently stable to allow appreciable reaction with the ECL precursor.
3. *Electrochemical properties.* The coreactant should be easily oxidized or reduced with the luminophore species at or near the electrode, and undergo a rapid chemical reaction to form an intermediate that has sufficient reducing or oxidizing energy to react with the oxidized or reduced luminophore to form the excited state.
4. *Kinetics.* The reaction rate between the intermediate and the oxidized, or reduced luminophore species must be rapid (43).
5. *Quenching effect.* The coreactant and its redox products should not be good quenchers of the ECL compound's luminescence (43).
6. *ECL background.* The coreactant itself should not give any ECL signal over the potential range scanned.

#### *13.3.2.4 Typical coreactant ECL systems and their mechanisms*

Although there are a wide variety of molecules that exhibit ECL, the overwhelming majority of publications concerned with coreactant ECL and its analytical applications are based on chemistry involving $Ru(bpy)_3^{2+}$, or closely related analogs as the emitting species (8), because of their excellent chemical, electrochemical, and photochemical properties even in aqueous media and in the presence of oxygen (125). As a result, much of this section concerns $Ru(bpy)_3^{2+}$/coreactant ECL systems.

***(a) Oxalate ($C_2O_4^{2-}$) system***

This was the first account of coreactant ECL system reported in the literature by Bard's group in 1977 (16), and is a classical example of "*oxidative-reduction*" ECL. The ECL mechanism of this system was proposed to be as in Scheme 13.4 (17).

$$Ru(bpy)_3^{2+} - e \longrightarrow Ru(bpy)_3^{3+} \quad (13.14)$$

$$Ru(bpy)_3^{3+} + C_2O_4^{2-} \longrightarrow Ru(bpy)_3^{2+} + C_2O_4^{\bullet-} \quad (13.15)$$

$$C_2O_4^{\bullet-} \longrightarrow CO_2^{\bullet-} + CO_2 \quad (13.16)$$

$$Ru(bpy)_3^{3+} + CO_2^{\bullet-} \longrightarrow Ru(bpy)_3^{2+*} + CO_2 \quad (13.17)$$

$$Ru(bpy)_3^{2+} + CO_2^{\bullet-} \longrightarrow Ru(bpy)_3^{+} + CO_2 \quad (13.18)$$

$$Ru(bpy)_3^{3+} + Ru(bpy)_3^{+} \longrightarrow Ru(bpy)_3^{2+*} + Ru(bpy)_3^{2+} \quad (13.19)$$

$$Ru(bpy)_3^{2+*} \longrightarrow Ru(bpy)_3^{2+} + h\nu \quad (13.20)$$

**Scheme 13.4** (from reference (123)).

Firstly, the $Ru(bpy)_3^{2+}$ is oxidized at the electrode to the $Ru(bpy)_3^{3+}$ cation. This species is then capable of oxidizing the oxalate ($C_2O_4^{2-}$) in the diffusion layer close to the electrode surface to form an oxalate radical anion ($C_2O_4^{\bullet-}$). This breaks down to form a highly reducing radical anion ($CO_2^{\bullet-}$, $E^\circ = -1.9$ V vs. NHE (126)) and carbon dioxide. The reducing intermediate then either reduces the $Ru(bpy)_3^{3+}$ complex back to the parent complex in an excited state, or reduces $Ru(bpy)_3^{2+}$ to form $Ru(bpy)_3^{+}$ that reacts with $Ru(bpy)_3^{3+}$ to generate the excited state $Ru(bpy)_3^{2+*}$, which emits light with $\lambda_{max}$ ~620 nm.

In aqueous solutions, the ECL intensity of the $Ru(bpy)_3^{2+}$/oxalate system has been reported to have a maximum at ~pH 6 (17), and also to be essentially constant from pH 4–8 (19, 127) at macro-electrodes and from pH 5–8 at ultramicroelectrodes (128).

***(b) Peroxydisulfate (persulfate, $S_2O_8^{2-}$) system***

This was the first example of so called "*reductive-oxidation*" coreactant ECL system reported in the literature (124, 129). Because $Ru(bpy)_3^{+}$ is unstable in aqueous solutions and $(NH_4)_2S_2O_8$ has a low solubility in MeCN solutions, the MeCN–$H_2O$ mixed solutions were chosen to produce intense ECL emission (124). Scheme 13.5 summarizes the possible pathways for the production of $Ru(bpy)_3^{2+*}$ when $S_2O_8^{2-}$ is used as the coreactant, in which the strongly oxidizing intermediate $SO_4^{\bullet-}$, generated during reduction of $S_2O_8^{2-}$, has a redox potential of $E^\circ \geq 3.15$ V vs. SCE (130).

$$S_2O_8^{2-} + e \longrightarrow S_2O_8^{\bullet 3-} \quad (13.21)$$

$$Ru(bpy)_3^{2+} + e^- \longrightarrow Ru(bpy)_3^{+} \quad (13.22)$$

$$Ru(bpy)_3^{+} + S_2O_8^{2-} \longrightarrow Ru(bpy)_3^{2+} + S_2O_8^{\bullet 3-} \quad (13.23)$$

$$S_2O_8^{\bullet 3-} \longrightarrow SO_4^{2-} + SO_4^{\bullet-} \quad (13.24)$$

$$Ru(bpy)_3^{+} + SO_4^{\bullet-} \longrightarrow Ru(bpy)_3^{2+*} + SO_4^{2-} \quad (13.25)$$

$$Ru(bpy)_3^{2+} + SO_4^{\bullet-} \longrightarrow Ru(bpy)_3^{3+} + SO_4^{2-} \quad (13.26)$$

$$Ru(bpy)_3^{+} + Ru(bpy)_3^{3+} \longrightarrow Ru(bpy)_3^{2+*} + Ru(bpy)_3^{2+} \quad (13.27)$$

**Scheme 13.5** (from reference (123)).

It is believed that persulfate ion is a coreactant of $Ru(bpy)_3^{2+}$ ECL as well as an effective quencher of the excited state $Ru(bpy)_3^{2+*}$ (124, 131). As a result, the ECL intensity of the $Ru(bpy)_3^{2+}/S_2O_8^{2-}$ system was found to be a function of $S_2O_8^{2-}$ concentration, and for 1 mM $Ru(bpy)_3^{2+}$ solution the maximum ECL intensity was obtained at 15–20 mM $S_2O_8^{2-}$ (124).

***(c) Tri-n-propylamine (TPrA) system***

The majority of ECL applications reported so far involve $Ru(bpy)_3^{2+}$ or its derivatives as an emitter (or label) and TPrA as a coreactant, because the $Ru(bpy)_3^{2+}$/TPrA system exhibits the highest ECL efficiency and this system forms the basis of commercial systems for immunoassay and DNA analysis (132, 133). The ECL mechanism of this reaction is very complicated and has been investigated by many workers (20, 21, 134–138). Generally, the ECL emission of this system as a function of applied potential consists of two waves (Figure 13.4). The first occurs with the direct oxidation of TPrA at the electrode, and this wave is often merged into the foot of the second wave when relatively high concentrations of $Ru(bpy)_3^{2+}$ (~mM) are used. The second wave appears where $Ru(bpy)_3^{2+}$ is oxidized (137, 138). Both waves are associated with the emission from $Ru(bpy)_3^{2+*}$ (138). The relative ECL intensity from the first wave is significant, particularly in dilute $Ru(bpy)_3^{2+}$ solutions (<~μM) containing ~0.1 M TPrA. Thus, the bulk of the ECL signal obtained in this system with low concentrations of analytes, as in immunoassays and DNA probes with $Ru(bpy)_3^{2+}$ as an ECL label, probably originates from the first ECL wave. Scheme 13.6 summarizes the mechanism of the first ECL wave, where cation radical species $TPrA^{\bullet+}$ formed during TPrA oxidation is a sufficiently stable intermediate with a half-life of ~0.2 ms that it can oxidize $Ru(bpy)_3^{+}$ (formed from the reduction of $Ru(bpy)_3^{2+}$ by $TPrA^{\bullet}$ free radical) to give $Ru(bpy)_3^{2+*}$ (137).

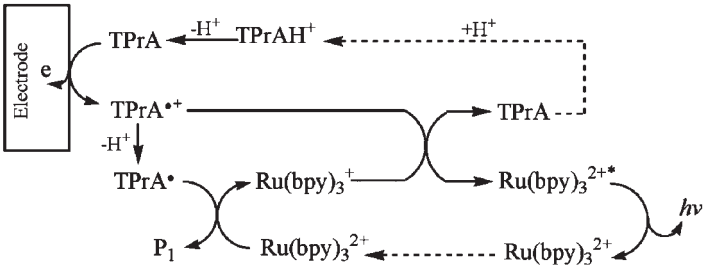


[where $TPrA^{\bullet+} = (CH_3CH_2CH_2)_3N^{\bullet+}$, $TPrAH^+ = Pr_3NH^+$, $TPrA^{\bullet} = Pr_2NC^{\bullet}HCH_2CH_3$
$P_1 = Pr_2N^+C{=}HCH_2CH_3$]

**Scheme 13.6** (from reference (137)).

The mechanism of the second ECL wave follows the classic "*oxidative-reduction*" coreactant mechanism (Section 13.3.2.1), where oxidation of TPrA generates a strongly reducing species $TPrA^{\bullet}$ ($E_{P1/TPrA^{\bullet}} \approx -1.7$ V vs. SCE (112)). This oxidation can be via a "catalytic route" where electrogenerated $Ru(bpy)_3^{3+}$ reacts with TPrA as well as by direct reaction of TPrA at the electrode described by both Scheme 13.7 and Scheme 13.8 (137):

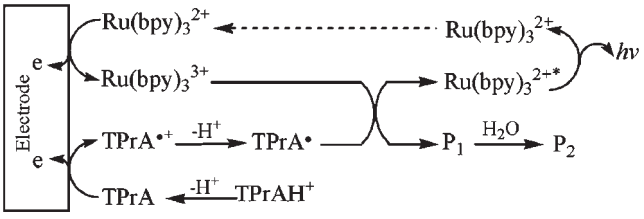


[where $P_2 = Pr_2NH + CH_3CH_2CHO$]

**Scheme 13.7** (from reference (137)).

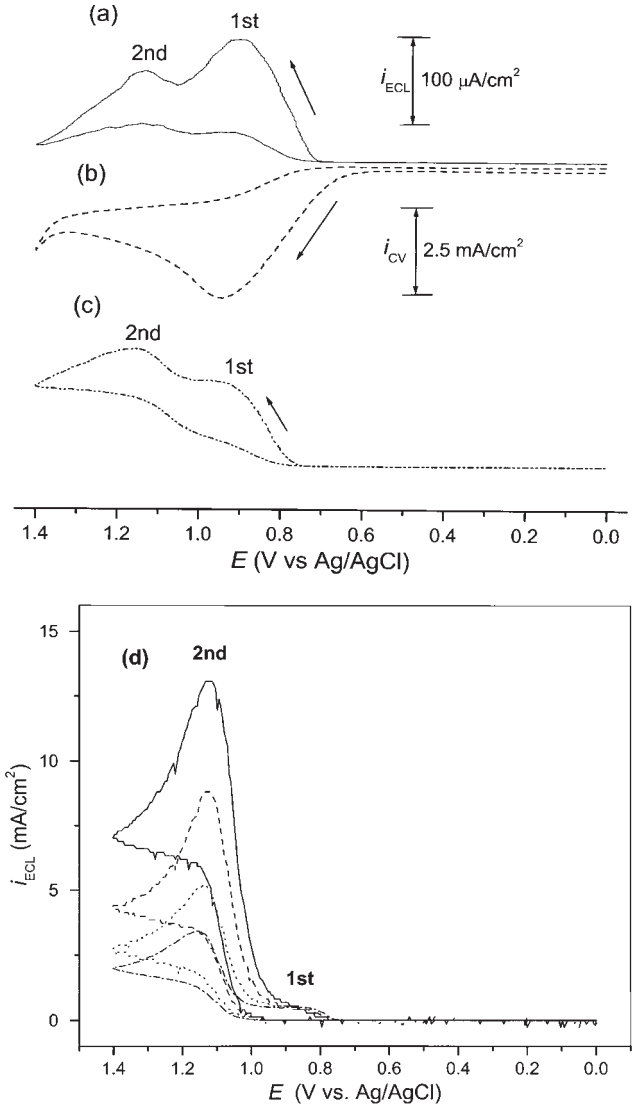


**Figure 13.4** (a) ECL, (b) cyclic voltammogram of 1.0 nM $Ru(bpy)_3^{2+}$ in the presence of 0.10 M TPrA with 0.10 M Tris/0.10 M $LiClO_4$ buffer (pH = 8) at a 3 mm diameter glassy carbon electrode at a scan rate of 50 mV/s. (c) As (a) but with 1.0 μM $Ru(bpy)_3^{2+}$. The ECL intensity scale is given for (c) and should be multiplied by 100 for (a). (d) The first and the second ECL responses in 0.10 M TPrA (0.20 M PBS, pH = 8.5) with different $Ru(bpy)_3^{2+}$ concentrations: 1 mM (solid line), 0.50 mM (dashed line), 0.10 mM (dotted line), and 0.05 mM (dash-dotted line), at a 3 mm diameter glassy carbon electrode at a scan rate of 100 mV/s (from reference (137)).

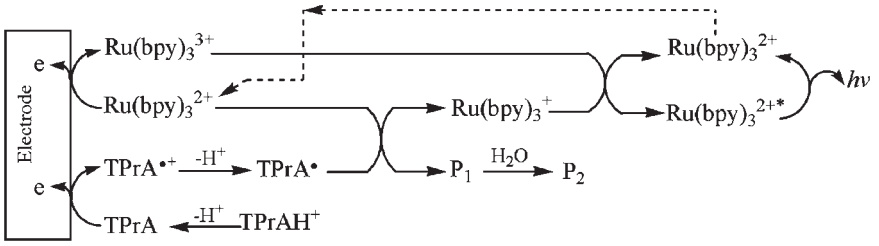


**Scheme 13.8** (from reference (137)).

The "catalytic route" involving homogeneous oxidation of TPrA with $Ru(bpy)_3^{3+}$ is shown in Scheme 13.9 (137). The contribution of this process to the overall ECL intensity, depends upon the $Ru(bpy)_3^{2+}$ concentration, and is small when relatively low concentrations of $Ru(bpy)_3^{2+}$ are used (134).

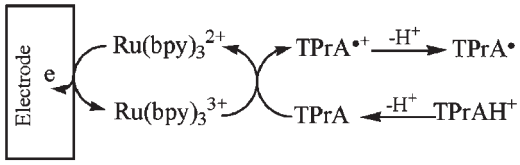


**Scheme 13.9** (from reference (137)).

The excited state of $Ru(bpy)_3^{2+}$ can be produced via three different routes (Scheme 13.10): (i) $Ru(bpy)_3^{+}$ oxidation by $TPrA^{\bullet+}$ cation radicals, (ii) $Ru(bpy)_3^{3+}$ reduction by $TPrA^{\bullet}$ free radicals, and (iii) the $Ru(bpy)_3^{3+}$ and $Ru(bpy)_3^{+}$ annihilation reaction.

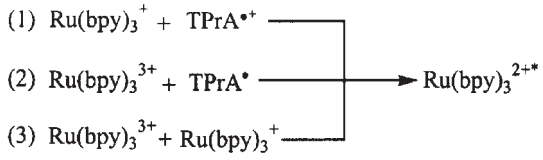


**Scheme 13.10** (from reference (123)).

The nature of a working electrode surface can significantly affect the ECL intensity produced from the $Ru(bpy)_3^{2+}$/TPrA system. Among Au, Pt, and glassy carbon (GC) electrodes, GC exhibits the strongest ECL response. The ECL intensity also depends on the solution pH (20, 44) (Figure 13.5), with dramatic increases at ~pH $>$ 5.5 and a maximum value at pH 7.5. Usually, pHs higher than 9 should not be used, since $Ru(bpy)_3^{3+}$ generated at the electrode could react with hydroxide ions to produce a significant ECL background signal (139).

***(d) Pyruvate/Ce(III) system***

Upon anodic oxidation, ECL can be generated from an acidic solution containing pyruvate, Ce(III), and $Ru(bpy)_3^{2+}$ species (17). The strong oxidant Ce(IV) produced from the oxidation of Ce(III) at the Pt electrode can oxidize pyruvate, resulting in the formation of the strongly reducing intermediate $CH_3CO^{\bullet}$. This species behaves in a similar way to

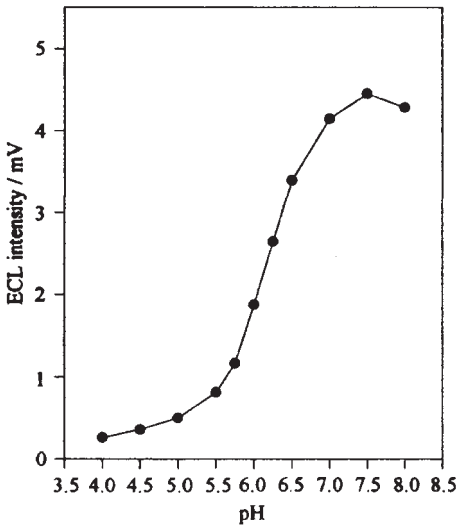


**Figure 13.5** Effect of pH on the ECL intensity from the reaction of $Ru(bpy)_3^{2+}$ with TPrA (from reference (42)).

$CO_2^{\bullet-}$, and participates in electron-transfer reactions with $Ru(bpy)_3^{3+}$ and $Ru(bpy)_3^{2+}$, as shown in Scheme 13.4 for oxalate, to produce ECL. The reaction mechanism of this system is summarized in Scheme 13.11.

$$Ru(bpy)_3^{2+} - e \longrightarrow Ru(bpy)_3^{3+}$$

$$Ce^{3+} - e \longrightarrow Ce^{4+}$$

$$Ce^{4+} + CH_3COCOO^- \longrightarrow Ce^{3+} + CH_3COCOO^{\bullet}$$

$$CH_3COCOO^{\bullet} \longrightarrow CH_3CO^{\bullet} + CO_2$$

$$Ru(bpy)_3^{3+} + CH_3CO^{\bullet} \xrightarrow{H_2O} Ru(bpy)_3^{2+*} + CH_3COOH + H^+$$

$$Ru(bpy)_3^{2+} + CH_3CO^{\bullet} \xrightarrow{H_2O} Ru(bpy)_3^{+} + CH_3COOH + H^+$$

$$Ru(bpy)_3^{3+} + Ru(bpy)_3^{+} \longrightarrow Ru(bpy)_3^{2+*} + Ru(bpy)_3^{2+}$$

$$Ru(bpy)_3^{2+*} \longrightarrow Ru(bpy)_3^{2+} + h\nu$$

**Scheme 13.11** (from reference (123)).

***(e) Hydrazine ($N_2H_4$) system (140–143)***

Scheme 13.12 summarizes the ECL mechanism of $N_2H_4/Ru(bpy)_3^{2+}$ system, in which the reactions between $Ru(bpy)_3^{3+}$ and $N_2H_4$, and between $Ru(bpy)_3^{3+}$ and $N_2H_2$ were believed to be about 1% and about 99% efficient, respectively (140).

$$Ru(bpy)_3^{3+} + N_2H_4 \longrightarrow Ru(bpy)_3^{2+*} + N_2H_3^{\bullet}$$

$$2N_2H_3^{\bullet} \longrightarrow N_2 + NH_3$$

$$Ru(bpy)_3^{3+} + N_2H_3^{\bullet} \longrightarrow N_2H_2 + Ru(bpy)_3^{2+}$$

$$Ru(bpy)_3^{3+} + N_2H_2 \longrightarrow Ru(bpy)_3^{2+*} + N_2$$

$$Ru(bpy)_3^{2+*} \longrightarrow Ru(bpy)_3^{2+} + h\nu$$

**Scheme 13.12** (from reference (123)).

***(f) Benzoyl peroxide (BPO) system***

Benzoyl peroxide (BPO) can be used as a coreactant, because, like persulfate, BPO can produce a reactive oxidizing agent, benzoate radical ($C_6H_5CO_2^{\bullet}$), after it is reduced. The newly formed benzoate radical is energetic enough to react with some cation radicals to form the excited states, since the redox potential value for $C_6H_5CO_2^{\bullet}/C_6H_5CO_2^{-}$ couple ($> +1.5$ V vs. SCE) (144), is quite positive. Akins et al. (145, 146) demonstrated that ECL of various aromatic hydrocarbons, such as 9,10-DPA, rubrene, fluoranthene, and anthracene, can be generated in the presence of BPO, after the electrode was brought to a potential of $-1.90$ V vs. SCE. The ECL mechanism proposed by Akins et al. was considered to be energy-deficient (Scheme 13.13), although the energy-sufficient route may also exist (144).

$$R + e \longrightarrow R^{\bullet-}$$

$$BPO + ne \longrightarrow \text{products}$$

$$R^{\bullet-} + BPO \longrightarrow R + BPO^{\bullet-}$$

$$BPO^{\bullet-} \longrightarrow C_6H_5CO_2^{-} + C_6H_5CO_2^{\bullet}$$

$$R^{\bullet-} + C_6H_5CO_2^{\bullet} \longrightarrow {}^3R^* + C_6H_5CO_2^{-}$$

$${}^3R^* + {}^3R^* \longrightarrow {}^1R^* + R$$

$${}^3R^* + BPO \longrightarrow R^{\bullet+} + BPO^{\bullet-}$$

$${}^3R^* + C_6H_5CO_2^{\bullet} \longrightarrow R^{\bullet+} + C_6H_5CO_2^{-}$$

$$R^{\bullet+} + R^{\bullet-} \longrightarrow {}^1R^* + R$$

$${}^1R^* \longrightarrow R + h\nu$$

(R = aromatic hydrocarbons)

**Scheme 13.13** (from reference (123)).

***(g) Luminol/Hydrogen peroxide system***

The ECL reaction of luminol (5-amino-2,3-dihydro-1,4-phthalazinedione) with hydrogen peroxide in alkaline medium is similar to the CL of luminol triggered by chemical oxidation (34, 147). The general accepted mechanism is shown in Scheme 13.14. In alkaline solution luminol deprotonates to form an anion, which then undergoes electrochemical oxidation to produce a diazaquinone. This species is further oxidized by peroxide or superoxide to give 3-aminophthalate in an excited state that emits light at ~425 nm.

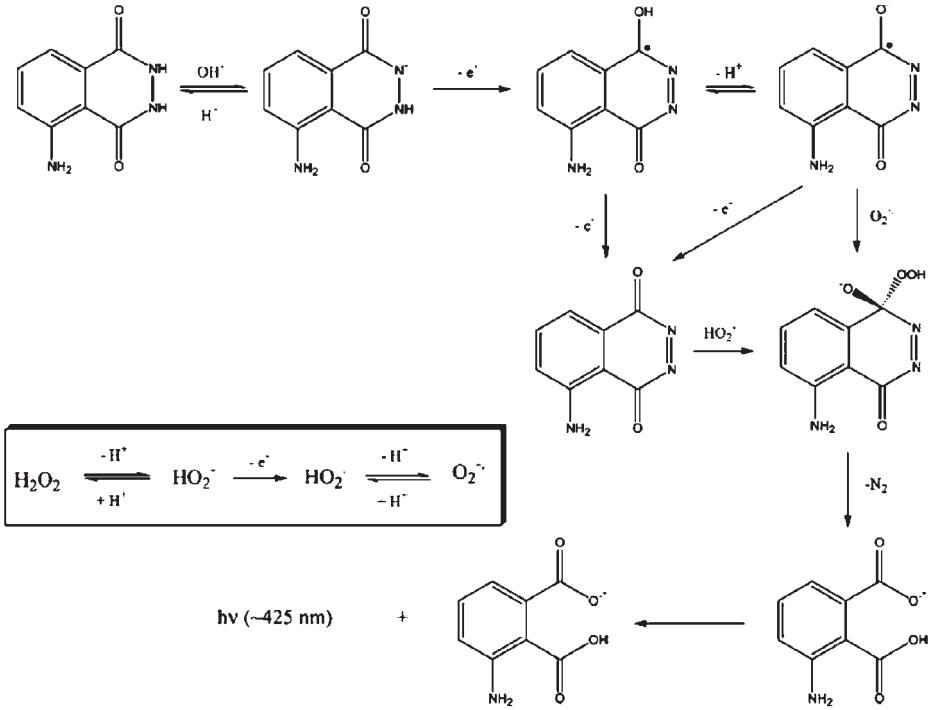


**Scheme 13.14** (from reference (54)).

## 13.4 EXPERIMENTAL SETUP

The basic components of an ECL instrument include an electrical energy supply for the ECL reaction at an electrode within an electrochemical cell and an optical detector for the measurement of either the emitted light intensity or its spectroscopic response. Although certain types of ECL instruments are now commercially available (Section 13.4.3.2), most of the ECL studies reported in the literature were carried out in "home-made" ECL instruments.

### 13.4.1 Electrochemical media

Before the first aqueous ECL was reported in 1981 (17), all ECL studies were almost exclusively carried out in organic media. In these cases, the purity of the solvent/supporting electrolyte is very crucial, because trace amounts of water, and oxygen can significantly affect the ECL production by either disabling the generation of both reductive and oxidative ECL precursor species at the electrode or quenching the newly formed excited state species. As a result, the apparatus is constructed to allow transfer and degassing of solvent on a high-vacuum line or in an inert-atmosphere box (2).

Commonly used electrolytes, such as tetra-*n*-butylammonium perchlorate (TBAP), tetra-*n*-butylammonium fluoborate ($TBABF_4$), tetra-*n*-butylammonium hexafluorophosphate ($TBAPF_6$), tetraethylammonium perchlorate (TEAP), can be purchased from

"Sigma-Aldrich" (www.sigmaaldrich.com) as "electrochemical grade" reagents. They normally can be used as received, but recrystalization is sometimes needed (148). These electrolytes are hydroscopic and must be dried *in vacuo* for 24–48 h at 90–100°C (149). The dried lots should be kept in a desiccator or in a dry box. Solvents are also often required to be dried and purified. Detailed discussions on solvent and electrolyte drying and purification can be found from the literature (150). Although many anhydrous high-purity (spectrophotometric and HPLC grade) solvents are commercially available (e.g., from Sigma-Aldrich, EM, Burdick and Jackson), caution must be taken while handling the solvents. They should be isolated from the atmosphere during storage, and all solutions should be prepared inside an oxygen-free dry box and sealed in an appropriate airtight electrochemical cell for measurements carried out outside the dry box (149).

Oxygen-free solvents can be also obtained by treating them via an "auxiliary vessel" connected to a vacuum line before transferring to electrochemical cells (Figure 13.6) (114). This device is said to be particularly useful for vigorous ECL studies and to offer the best compromise between convenience, flexibility, and effectiveness in handling materials (149).

The simplest way to remove oxygen from the solvent is to bubble the solvent with an inert gas, e.g., high-purity $N_2$ or Ar. Since oxygen has a high solubility in organic solvents with respect to aqueous media, long bubbling time is often required. In order to avoid the

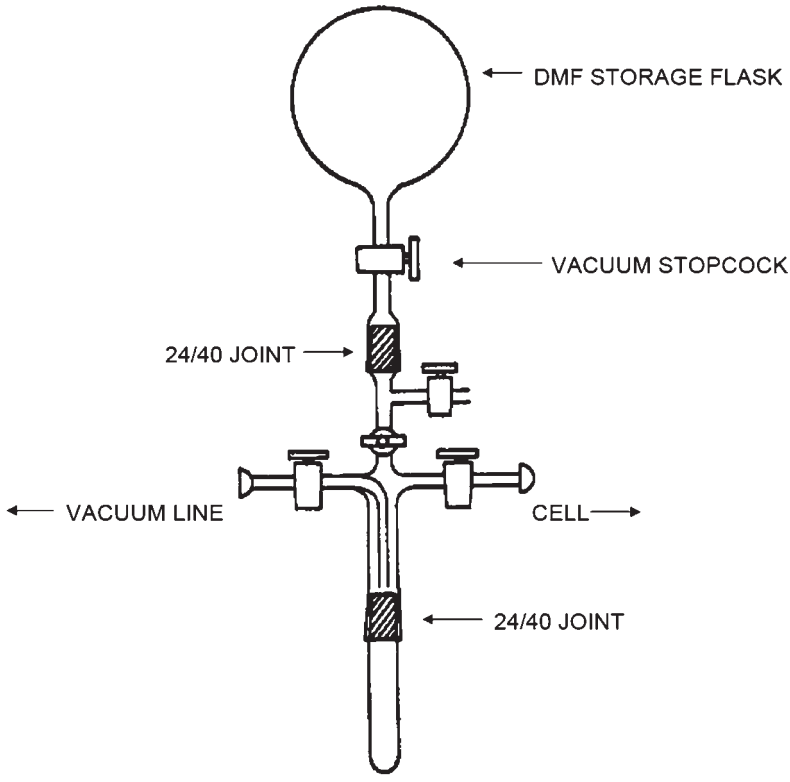


**Figure 13.6** Auxiliary vessel for oxygen-free ECL solution preparation (from reference (114)).

solvent loss and to keep the solution concentration unchanged, a bubbler containing the solvent of interest is frequently needed to be connected between the inlet of inert gas and the solvent cell.

Table 13.3 lists the commonly used solvent-supporting electrolyte systems for ECL study.

### 13.4.2 Cell design and electrodes

Several types of cells with three conventional electrodes have been used for ECL studies. The most commonly used ECL cell for ion annihilation study in Bard's group at the University of Texas at Austin is shown in Figure 13.7a. This type of cell can be easily fabricated from an ACE (www.aceglass.com) internal threaded glass connector

**Table 13.3**

ECL solvent-supporting electrolytes systems (modified from reference (149))

| Solvent | Supporting electrolyte | Potential range (V vs. SCE, at Pt) | Remarks |
|---|---|---|---|
| Acetonitrile | $TBABF_4$, TBAP, TEAP, $TBAPF_6$ | −1.8 to +2.8 | Good stability for both radical anions and cations; potential range strongly depends upon purification |
| Benzonitrile | $TBABF_4$ | −1.8 to +2.5 | Similar to acetonitrile in terms of ion stabilities; commercial spectro-grade solvent can be used without purification |
| *N*,*N*-Dimethylformamide | TBAP | −2.8 to +1.5 | Good stability for radical anions; poor for cations; difficult to purify and tends to decompose or hydrolyze on standing |
| Dimethylsulfoxide | TEAP | −1.8 to +0.9 | Purified by vacuum distillation, collecting the middle 60%; can be stored on molecular serves; limited positive potential range |
| Methylene chloride | TBAP | −1.7 to +1.8 | Excellent stability of cations; limited negative potential range; easily purified; quite resistive |
| Propylene carbonate | TEAP | −2.5 to +2.0 | Purified by reduced pressure distillation at 120–130°C, collect the middle 60% fraction; potential range depends greatly on purity; good stability for radical cation |
| Tetrahydrofuran | TBAP | −3.0 to +1.4 | Excellent stability of anions; easily purified and dried with alkali metals; limited positive potential range; quite resistive |
| Acetonitrile-benzene mixed solvent (1.5:1 to 4:1) | $TBABF_4$, TBAP, $TBAPF_6$ | −2.3 to +2.0 | Better solubility for some aromatic compounds; quite resistive, depending on the ratio of benzene to acetonitrile |

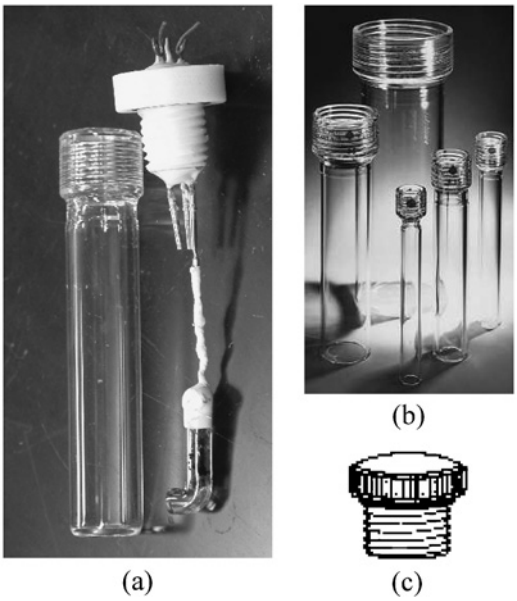


**Figure 13.7** (a) Commonly used cell for annihilation ECL study, (b) which can be fabricated from ACE glass internal threaded connectors, (c) Teflon or PTFE plugs. (for colour version: see colour section at the end of the book).

(Figure 13.7b) by flame sealing of the tube bottom and a suitable-sized Teflon or ACE PTFE plug (Figure 13.7c). Three metal wires for electrode potential connections are pierced through the plug and sealed with an epoxy or "Torr-seal" sealant.

For coreactant ECL studies, e.g., in aqueous $Ru(bpy)_3^{2+}$/TPrA solution, degassing is often unneeded. Thus, Fisherbrand glass tooled-neck vials (www.fishersci.com) are frequently used as ECL cells. When ECL experiments are carried out at a wafer-type electrode, such as indium tin oxide (ITO), Au/Si (151) and highly oriented pyrolytic graphite (HPOG) (152), the effective area of the electrode can be controlled by using a cell similar to that shown in Figure 13.8. The electrode surface exposed to the electrolyte solution containing a coreactant should face the window of the photo-detector.

ECL has been widely used as a detector in FIA, liquid chromatography, and CE (153). Figure 13.9 displays schematic diagrams of a FI-ECL flow-through thin-layer cell (154) and an ECL cell coupled with separation capillary for end-column mode CE detection (155). In addition to millimeter order-sized working electrodes, a microelectrode ($w = 2$ μm, $l = 2.5$ cm) was also constructed by sealing a piece of platinum foil between two microscope slides with epoxy into an ECL flow cell (Figure 13.10) (24). This type of cell has been employed in high-frequency ECL studies. The reduced time scale enables reaction kinetics to be accessed and affords a means for investigating ECL without rigorously purifying solvents or working on a vacuum line or in a dry box (24).

A flow cell system based on ORIGIN technology for ECL assays employing magnetic beads is shown in Figure 13.11 (133).

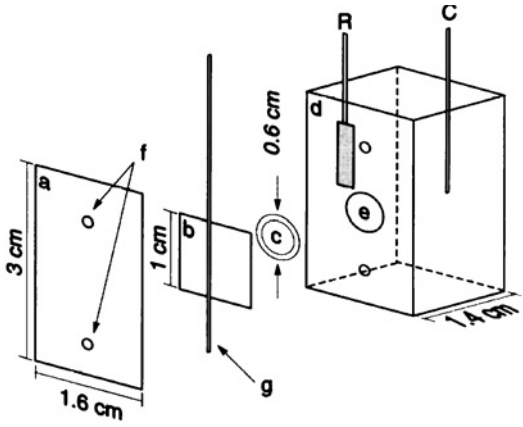


**Figure 13.8** Schematic diagram of the cell used for ECL and electrochemical measurements designed so that the edges of the electrode are not exposed to the solution: (a) Plexiglas sheet; (b) working electrode; (c) O-ring; (d) Plexiglas cell; (e) hole exposing the working electrode to the solution; (f) screw holes; (g) copper wire (from reference (152)).

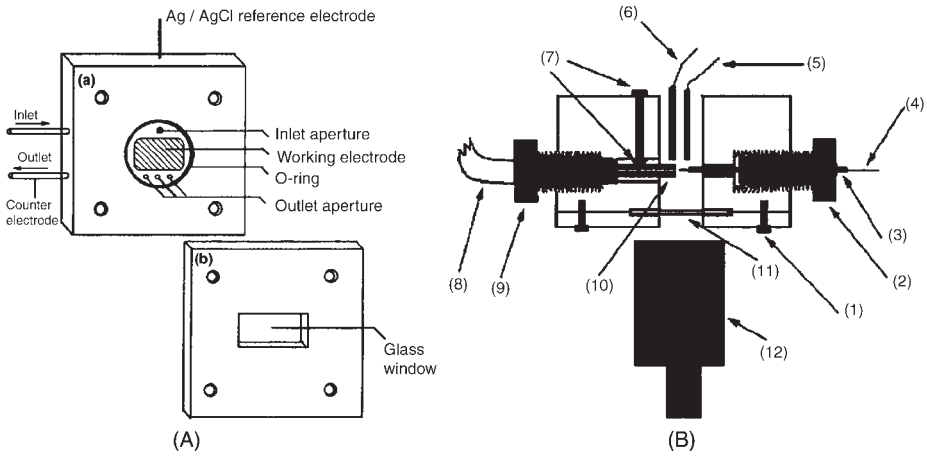


**Figure 13.9** Schematic diagrams of (A) a FI–ECL flow-through thin-layer cell. (a) Cell body; (b) Cell cover window, and (B) an ECL cell coupled with separation capillary for end-column mode. (1) Stainless-steel holding screw; (2) PVC capillary holder; (3) stainless-steel tube; (4) separation capillary; (5) reference electrode; (6) counter electrode; (7) nylon screws for alignment; (8) working electrode cable; (9) PVC electrode holder; (10) working electrode; (11) optical glass window; (12) PMT (from references (154, 155)).

For ECL spectral recording, it is generally required that the working electrode be aligned so that its surface faces the slit of a monochromator. A J-shaped electrode serves such a purpose when an airtight "normal" ECL cell (Figure 13.7a) is used. Alternatively, a "small" ECL cell that fits a spectrometer cuvette holder can be fabricated. As shown in

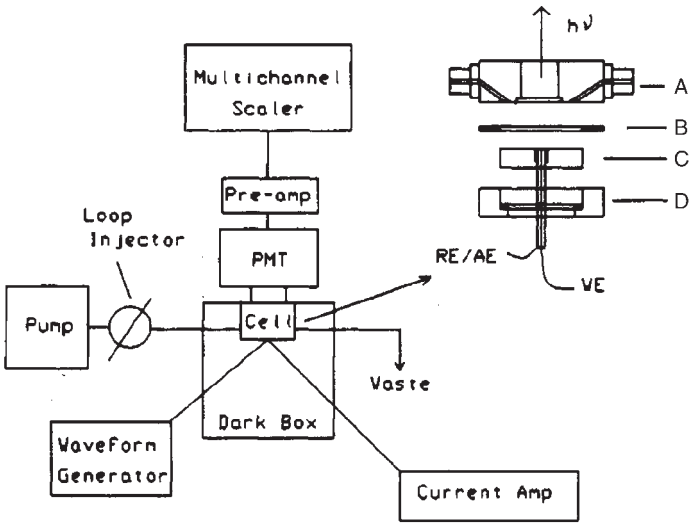


**Figure 13.10** Simplified block diagram of ECL flow cell and equipment: (A) stainless-steel cell body housing an optical window; (B) polyethylene spacer; (C) epoxy-encased microelectrode; (D) stainless-steel electrode retainer (from reference (24)).

Figure 13.12 (156), this special cell features a large-area working electrode made from Pt foil or coil and is capable of being evacuated to less than $10^{-5}$ Torr. The concentric counter electrode is located ~4 cm above the working electrode and is out of the field of view of the photo-detector, so its emission remains undetected. An Ag/AgCl (KCl, sat.) aqueous reference electrode with a non-aqueous salt bridge is fitted into the working/electrode support.

Three types of electrode configurations are commonly used in ECL study: single, dual, and rotating ring disk electrodes (RRDE). In the case of a single electrode, an AC potential, such as multi-step or pulse potential is applied scanning between the redox potential of the particular species desired. Dual electrode configurations, such as shown in Figure 13.2c and a micro-double band electrode (157), use DC potentials for the continuing generation of reductive species at the cathode and oxidative species at the anode. Since the dual electrodes are placed in close proximity (~$<$100 μm apart), annihilation ECL takes place in the region where the newly produced anion and cation species meet because of diffusion and/or electro-hydrodynamic convection. A RRDE can also be regarded as a dual electrode, in which the ring or the disk may be set at a potential to produce the oxidized species and the disk or the ring set to produce a reduced species. The species produced at the disk are swept away and react with the species at the ring. Thus, a ring of light (ECL) is expected to be observed around the internal region of the ring.

The nature of the working electrode, i.e., material and surface properties, can significantly affect the ECL production (158). Most commonly used electrode materials include Pt (159), Au (151), GC (137), HPOG (152), ITO (160), and heavily boron-doped diamond (161, 162). It is generally accepted that a Pt electrode gives the highest ECL intensity for

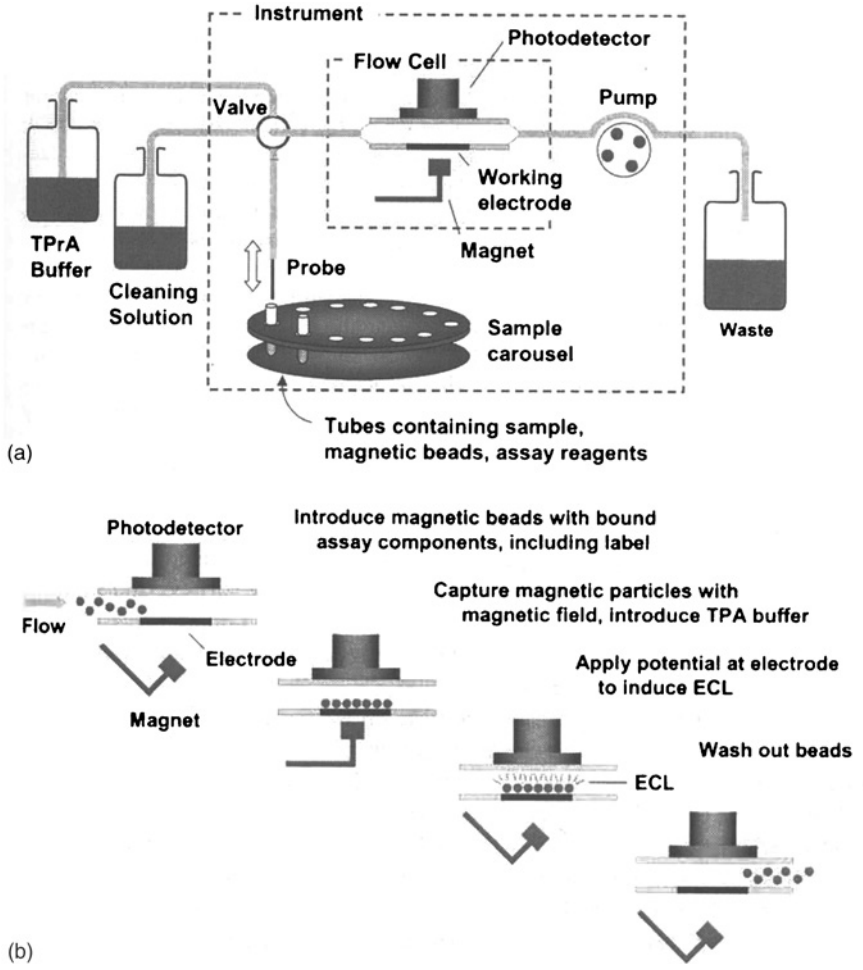


**Figure 13.11** (a) Components of a flow system based on ORIGIN technology, (b) Generic process for measuring magnetic bead-based ECL assays in flow cell (from reference (133)).

organic ECL systems, such as those in MeCN media, while a GC electrode is the best for aqueous ECL generation, such as for aqueous $Ru(bpy)_3^{2+}$/TPrA systems.

### 13.4.3 Light detection and ECL instrumentation

#### *13.4.3.1 Light detection*

In ECL studies, photodiodes, photomultiplier tubes (PMT), and charged coupled device (CCD) cameras are the three most commonly used light detectors. Of them, PMT provide the most sensitive means of detecting light, and are capable of detecting single photons. There are generally two different kinds of light detection modes required in ECL: ECL intensity measurements and ECL spectral recording. The first one is mainly used for

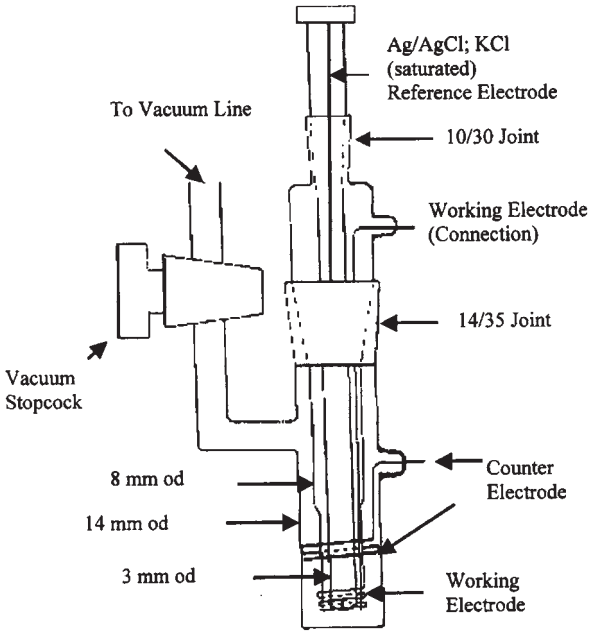


**Figure 13.12** ECL cell designed to fit a spectrometer cuvette holder and to be capable of being evacuated to less than $10^{-5}$ Torr (from references (149, 156)).

quantitative analysis of a given analyte (emitter) or its related species, and the second one is usually used for qualitative analysis. Since ECL signals are often very weak and different emitters have different emitting wavelengths, the selection of ECL light detectors (e.g., types of PMT) and the control of ECL experimental conditions, (e.g., the operating temperature of the detector), are two critical factors that require serious consideration when designing ECL experiments.

Although a wide range of PMT are commercially available, Hamamatsu (www.hamamatsu.com) R4240 and R928 PMT are perhaps the most popular ones used for ECL studies. Hamamatsu R4220 features extremely high cathode sensitivity, high gain, and low dark current. The R928 features extremely high quantum efficiency, high current amplification, good S/N ratio and wide spectral response from UV to near infrared. Table 13.4 lists the specifications of these two types of PMT. Their typical spectral responses are shown in Figure 13.13.

The solid curves of Figures 13.13a and b show the percent cathode radiant sensitivities of the peak sensitivities at each wavelength over the useful spectral range of the devices. Cathode radiant sensitivity is the amount of current leaving the photocathode divided by the incident radiant power at a given wavelength, usually the wavelength of peak response (see Table 13.4). The dashed curves provide the percent quantum efficiencies at each wavelength. Cathode quantum efficiency may be defined as the average number of photoelectrons emitted per incident photons. The cathode quantum efficiency, QE, in percent at any given wavelength can be calculated from the following formula:

$$\mathrm{QE} = S(1239.5/\lambda)(100) \tag{13.28}$$

**Table 13.4**

Hamamatsu R4220 and R928 specifications (from www.hamamatsu.com)

| Parameters | R4220 | R928 |
|---|---|---|
| Spectral response | 185–710 nm | 185–900 nm |
| Wavelength of maximum response | 410 nm | 400 nm |
| Window material | UV glass | UV glass |
| High cathode sensitivity | At 410 nm | At 400 nm |
| Luminous | 100 μA/Im | 250 μA/Im |
| Radiant | 70 mA/W | 74 mA/W |
| High anode sensitivity (at 1000 V) | At 410 nm | At 400 nm |
| Luminous | 1200 A/Im | 2500 A/Im |
| Radiant | $8.4\times10^5$ A/W | $7.4\times10^5$ A/W |
| Gain | $1.2\times10^7$ | $1.0\times10^7$ |
| Low dark current | 0.2 nA | 3 nA |
| Time response | 1.2–22 ns | 1.2–22 ns |
| Anode current sensitivity 1% (voltage hysteresis) | 0.1% (current hysteresis), 1% (voltage hysteresis) | 0.1% (current hysteresis) |

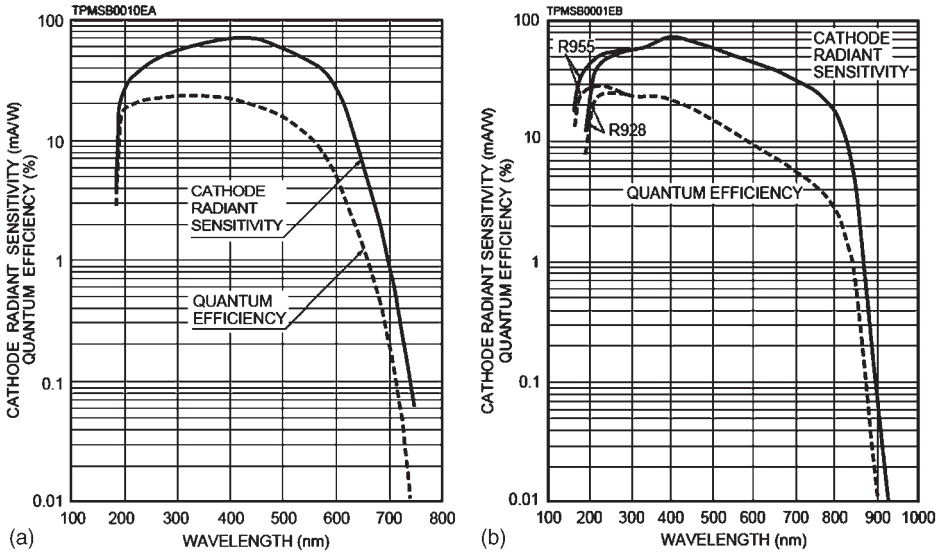


**Figure 13.13** Typical spectral responses of (a) Hamamatsu R4220 and (b) R928 PMT (from www.hamamatsu.com).

where $S$ is the cathode radiant sensitivity at the wavelength $\lambda$ in amperes per watt, and $\lambda$ is the wavelength in nanometers. For example, from Table 13.4, the absolute cathode sensitivities for R4220 and R928 are 0.070 A/W at 410 nm, and 0.074 A/W at 400 nm, respectively. The percent quantum efficiencies of them can be calculated as: QE (R4220, 410 nm) = 0.070(1239.5/410)(100) = 21.2, and QE (R928, 400 nm) = 0.074(1239.5/400)(100) = 22.9, which, as expected, are consistent with the data shown in Figures 13.13a and b, respectively.

The wavelength of peak response and the long-wavelength cutoff are primarily functions of photocathode material. The short-wavelength cutoff is primarily a function of the window material. Each window material has its characteristic cutoff region that varies from about 300 nm for commonly used lime glass to 105 nm for lithium fluoride. For UV glass window used for R4220 and R928, the short-wavelength is around 185 nm (Table 13.4 and Figure 13.13).

Comparing Figure 13.13a with Figure 13.13b, it is clear that R928 PMT covers a much wider spectral range than R4220 does. If a cutoff cathode radiant sensitivity of 10% is chosen, the "effective spectral response range" for R4220 and R928 would be about 190–630 nm and 185–820 nm, respectively. In this respect, R928 PMT is certainly better than R4220 used for the detection of ECL generated from $Ru(bpy)_3^{2+}$ species, since, as shown in Figures 13.20 and 13.22, the $Ru(bpy)_3^{2+}$ ECL spectrum covers a spectral range of about 550 to 800 nm.

Current flows in the anode circuit of a PMT even when the tube is operated in complete darkness. The DC component of this current is called the anode dark current, or simply the dark current. This current and its resulting noise component usually limit the lower level of PMT light detection; as a result, the anode dark current value is nearly always given as part of the data for any tube.

For extremely weak ECL measurements, such as in the ECL spectral recording experiments, the PMT may be cooled down to a certain low temperature so that a much lower dark current with respect to that obtained at room temperature can be achieved. This may be accomplished by using a cooled PMT housing on the basis of thermoelectric, compressor, dry ice, or liquid nitrogen cooler series (www.photocool.com). A typical temperature characteristic of dark current for Hamamatsu R928 is shown in Figure 13.14. The dark current, hence the noise level, is approximately reduced to 1/3 of the previous value for each 10 °C drop in temperature.

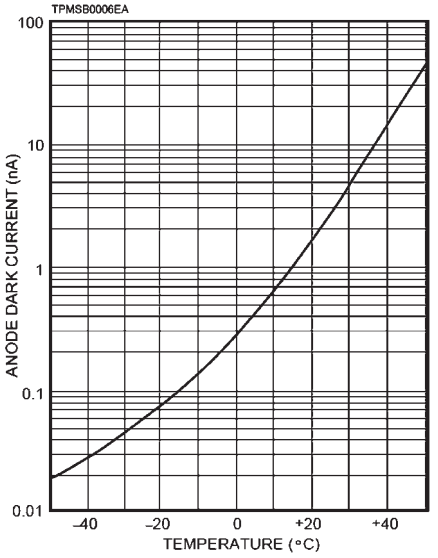


**Figure 13.14** Typical temperature characteristic of dark current for Hamamatsu R928 (at 1000 V after 30 min storage) (from www.hamamatsu.com).

### *13.4.3.2 Commercial ECL instruments*

ECL instrumentation has been commercially available from IGEN International Inc. (now BioVeris) since 1994 on the basis of ORIGEN technology (163). The first commercial ECL instrument was the ORIGEN analyzer (Figure 13.15A), which is adapted to measure ECL labels ($Ru(bpy)_3^{2+}$ or its derivatives) present on the surface of magnetically responsive beads in the presence of TPrA (Figure 13.11). The beads are coated with binding reagents and are used as assay supports in solid-phase binding assays, which are pre-designed so that the amount of label on the beads is correlated with the amount of analyte in a sample. Figure 13.15 shows several examples of commercial flow cell-based ECL instruments (133).

Unlike ECL instruments based on ORIGEN technology, the Sector HTS Imager, and Sector PR Reader instruments (Figures 13.15H and I) use disposable screen-printed carbon ink electrodes within the wells of multiwell plates. Each well contains several binding domains that react with specific targets. ECL is generated using $Ru(bpy)_3^{2+}$ analogs and TPrA or similar coreactants, and the light is collected with either a CCD camera (Sector HTS Imager) or a series of photodiodes (Sector PR Reader) (Figure 13.16) (133).

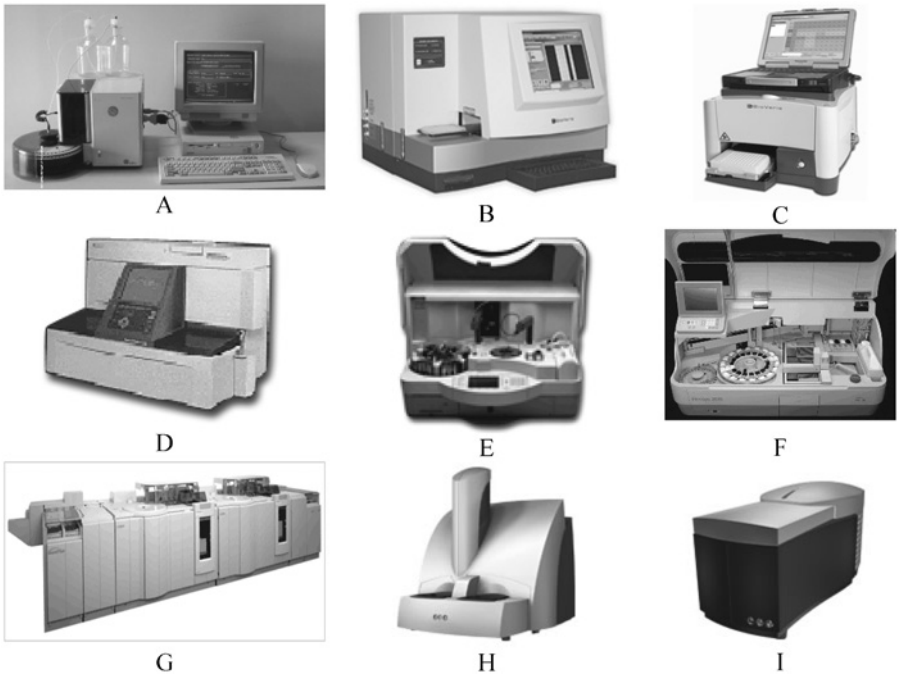


**Figure 13.15** Commercial flow cell-based ECL instrumentation. (A) The ORIGEN 1.5, (B) M series M-384 analyzer by Igen International (now BioVeris, www.bioveris.com), (C) M-1 analyzer by Igen International, (D) PicoLumi by Eisai, Japan, (E) Elecsys 1010, (F) Elecsys 2010, (G) the MODULAR system containing E-170 immunoassay module by Roche Diagnostics (www.roche-diagnostics.com), (H) Sector HTS Imager, and (I) Sector PR Reader by Meso Scale Discovery (meso-scale.com) (modified from reference (133)).

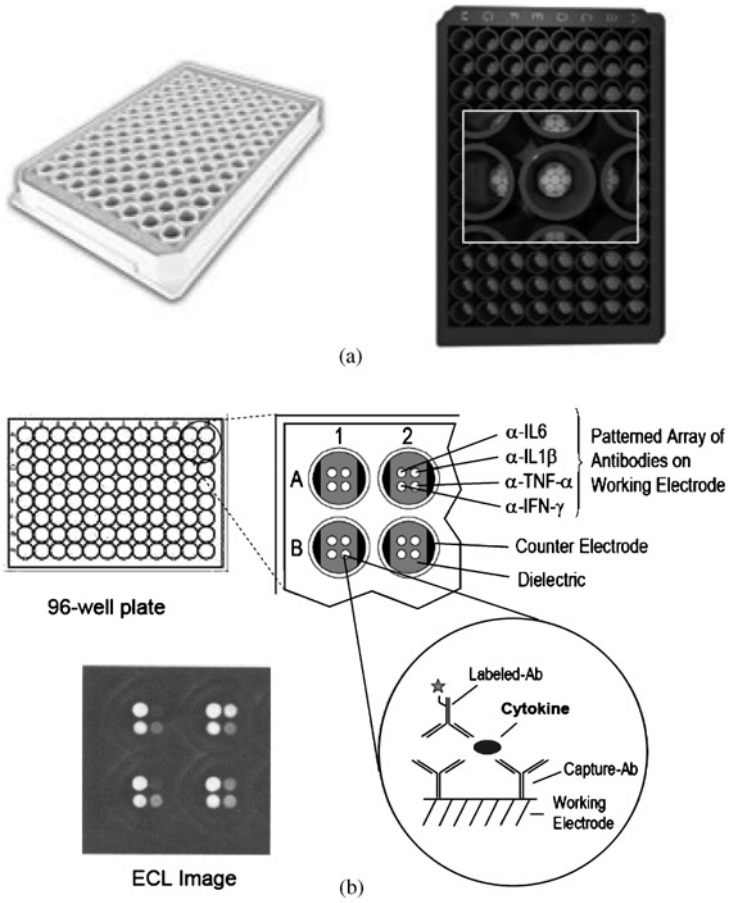


**Figure 13.16** (a) Pictures of Meso Scale Discovery multi-spot plates with seven binding domains in each well of the 96-well plates. (b) Schematic diagram of a multi-spot plate assay for four human cytokines. Each spot within each well of the 96-well plate contains capture antibody specific for one cytokine. Inset shows an image of the ECL emitted from assays in four wells using samples with varying concentrations of cytokines (from reference (133)).

A commercial CE ECL system fabricated in Changchun Institute of Applied Chemistry, Chinese Academy of Science has been recently reported (9).

#### *13.4.3.3 Other ECL setups for emitted light intensity measurements*

The basic components of a home-made ECL instrument for ECL intensity measurement generally consist of a potentiostat, an electrochemical cell, a light detector, and a data acquisition system. Many recently produced computer-based potentiostats, such as CH660A (CH Instruments, Austin, Texas, www.chinstruments.com), Autolab PGSTAT100 (Autolab Electrochemical Instruments, the Netherlands, www.ecochemie.nl), have external signal

recording functions, which can be used to record/collect the ECL signals along with the electrochemical responses obtained at the surface of the working electrode. When an old model or home-made potentiostat combined with a potential function generator is used for the ECL experiment, the LabVIEW software and related hardware (National Instruments, Austin, Texas, www.ni.com) may be used to control the devices, collect all the desired data to a computer, and display them on the screen. In most cases, light detection is made by a bare PMT (e.g., Hamamatsu R4240 or R928) that is applied with a high voltage (~−500 to −1000 V) using a high voltage power supply (e.g., Brandenburg Photomultiplier Power Supply). The light signal (as photocurrent) can be measured with a high sensitive electrometer (e.g., Keithley 6517, 6514 electrometer, Keithley, Cleveland, Ohio, www.keithley.com) and converted to a voltage (normally in the range of ±2 V) that is collected/recorded to the computer. A schematic diagram of an ECL instrumental setup is illustrated in Figure 13.17. The PMT and the electrochemical cell must be placed in a light-tight box to avoid any environmental light interference. Alternatively, ECL light can be measured, converted and then collected to a computer using a PMT module system (www.hamamatsu.com). The PMT module is basically comprised of a PMT to convert light to electrical signals, a high voltage power supply circuit, and voltage divider circuit to distribute the optimum voltage to each dynode, all assembled in a single compact case. Examples of using PMT modules with AD converters and collecting data to a PC are shown in Figure 13.18.

In addition, ECL experiments can also be carried out using a commercial fluorescence spectrometer coupled with an electrochemical instrument with the excitation function of the fluorimeter disabled. For example, one can have the three electrodes fitted into a standard fluorescence cuvette so that the entire cell system fits into the sample compartment of the spectrometer. The electrodes should be arranged so that the working electrode faces the detection window of the emission monochromator. ECL intensity can be measured either at

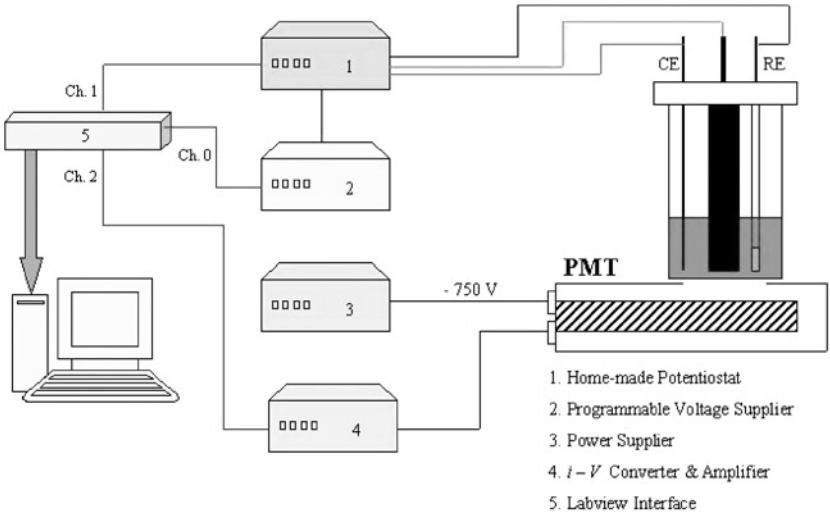


**Figure 13.17** Schematic diagram of an ECL instrumental setup. (for colour version: see colour section at the end of the book).

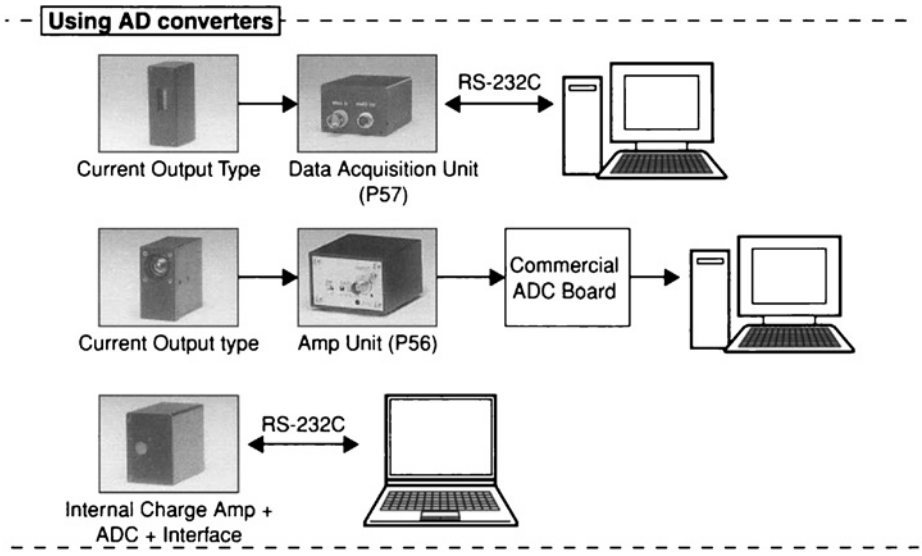


**Figure 13.18** Constitution examples of PMT modules with AD converters (from www.hamamatsu.com).

a specific wavelength or over a range of wavelengths. In the latter case, the overall ECL intensity may be integrated from the ECL spectra. Because of the space limitation of the electrochemical cell and the small slit of the emission monochromator etc., the operation of fluorimeter-based ECL measurements may be not as convenient as the other systems mentioned above, and the ECL signals obtained could also be relatively weak.

#### *13.4.3.4 Instrumentation of ECL spectral recording*

ECL spectra are mainly measured in two ways. The first one is based on a commercial fluorimeter (see Section 13.4.3.3) with a PMT as a light detector. The second way is to use a CCD camera as the light detector. Because the ECL signal is generally very weak, and the acquisition of the signal is often carried out from seconds to minutes, elimination of the background signal (or dark current, Figure 13.14) by cooling down the temperature of the detector is often required. The ECL spectral recording instrument in Bard's Lab at the University of Texas at Austin consists of a potentiostat, a Chemspec 100S spectrometer (American Holographic, Littleton, MA), a Photometrics CH260 CCD camera (Photometrics, Tucson, AZ) cooled to ~−105°C with liquid nitrogen, and a data acquisition system. The spectrometer is calibrated using an Hg (Ar) spectral calibration lamp (e.g., Oriel Instruments, Stratford, CT, www.oriel.com). The whole experimental setup is housed in a dark room, and all lights from, e.g., computer, potentiostat, are all properly covered to avoid any possible interference to the ECL spectra. It is generally believed that the light detecting sensitivity of a CCD camera (even in low temperatures) is much less sensitive than a PMT operated even at room temperature. For example, a 25–30 nA ECL photocurrent was readily measured with a potentiostat/Keithley 6517/Hamamatsu R4220

instrumental setup at room temperature, but the ECL spectrum from the same solution using the exactly same electrochemical parameters was almost impossible to record with the Chemspec 100S spectrometer/Photometrics CH260 CCD camera cooled to −105°C configuration when light integration time was less than 30 min.

## 13.5 TYPES OF EXPERIMENTS

### 13.5.1 Ion annihilation ECL: $Ru(bpy)_3^{2+}$ and derivatives

There have been a number of studies of ECL of $Ru(bpy)_3^{2+}$ in aprotic media (15, 164–168). For example, in MeCN solutions the excited $Ru(bpy)_3^{2+*}$ is produced by ion annihilation reaction (Scheme 13.1) between $Ru(bpy)_3^{+}$ and $Ru(bpy)_3^{3+}$, as outlined in Scheme 13.15.

$$Ru(bpy)_3^{2+} + e^- \rightarrow Ru(bpy)_3^{+}$$
$$Ru(bpy)_3^{2+} \rightarrow Ru(bpy)_3^{3+} + e^-$$
$$Ru(bpy)_3^{+} + Ru(bpy)_3^{3+} \rightarrow Ru(bpy)_3^{2+} + Ru(bpy)_3^{2+*}$$
$$Ru(bpy)_3^{2+*} \rightarrow Ru(bpy)_3^{2+} + h\nu$$

**Scheme 13.15**

As discussed in Section 13.3.1.1, one of the criteria for efficient annihilation ECL generation is that both anion and cation radicals formed from the ECL precursor must be stable in the electrolyte of interest, which can be verified by cyclic voltammetry. Figure 13.19 shows the CV behavior of $Ru(bpy)_3^{2+}$, $Ru(dp\text{-}bpy)_3^{2+}$, and $Ru(dp\text{-}phen)_3^{2+}$ in MeCN containing 0.1 M $TBABF_4$ at a Pt electrode (166). Clearly, these three compounds have very similar electrochemical responses, and their first oxidation and reduction products are all stable. Not surprisingly, the ECL was readily generated by repetitive potential cycling between $E_p^a$ and $E_p^c$ at a suitable frequency of, e.g., 10 Hz (Figure 13.20). It is evident that the emission of the two diphenyl compounds is higher than that of the non-substituted $Ru(bpy)_3^{2+}$. The wavelengths for the emission peaks for all complexes, giving in Table 13.5, are similar, with $Ru(dp\text{-}bpy)_3^{2+}$ shifted to the red compared with the other two.

The relative ECL efficiencies of these compounds can be measured on the basis of the integrated light intensity under the emission curve for a double-pulse experiment (Table 13.5). The ECL efficiencies can be calculated relative to the ECL quantum efficiency of $Ru(bpy)_3^{2+}$, which is ~5% in MeCN (168, 169). The ECL quantum efficiency is defined as the ratio of the number of photons emitted to the number of annihilations between the $3^+$ and the $1^+$ forms of the ruthenium complex. The number of annihilations is somewhat smaller than the number of moles of reactant generated during a pulse, as calculated from the integrated current (170, 171). However, this difference is the same for all three complexes, so that, in estimating the relative efficiencies, the following equation can be employed:

$$\phi_{ECL} = \frac{\int_0^t I\,dt}{\int_0^t i\,dt\,(N_A / F)} \tag{13.29}$$

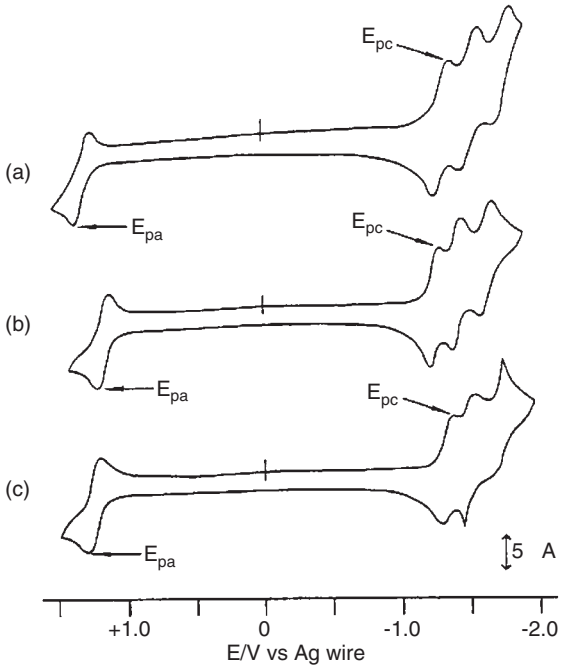


**Figure 13.19** Cyclic voltammograms of (a) 1.0 mM $Ru(bpy)_3^{2+}$, (b) 1.0 mM $Ru(dp\text{-}bpy)_3^{2+}$, and (c) 1.0 mM $Ru(dp\text{-}phen)_3^{2+}$ obtained from MeCN containing 0.1 M $TBABF_4$ at a 0.03 $cm^2$ Pt disk electrode. All the solution preparations and cell preparations were conducted in the glove-box under a helium atmosphere (from reference (166)).

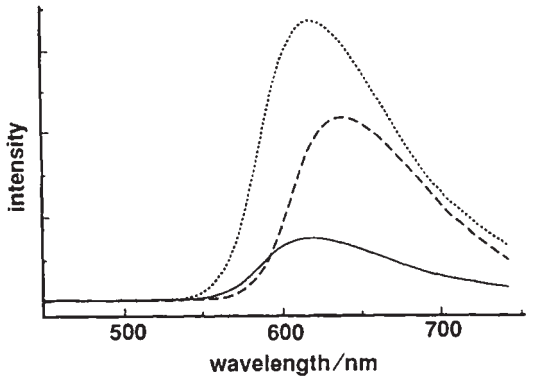


**Figure 13.20** ECL spectra of $Ru(bpy)_3^{2+}$ (——), $Ru(dp\text{-}bpy)_3^{2+}$ (------), and $Ru(dp\text{-}phen)_3^{2+}$ (……). The solutions contained 0.10 M $TBABF_4$ in MeCN. Intensities shown have been normalized to the concentrations of the complexes. Exposure time = 2s (from reference (166)). The experimental setup used was very similar to that described in Section 13.4.3.4 when a cooled CCD camera is used as the light detector.

**Table 13.5**

Emission maximum, integrated intensity, integrated current, ECL and photoluminescence efficiencies in MeCN at 25°C (from reference (166))[a]

| Compounds | $\lambda_{max}$ (nm) | Integrated intensity (arbitrary units) | Integrated current (one cycle)/μC | ECL efficiency $\phi_{ECL}$ | Photoluminescence efficiency $\phi_l$ |
|---|---|---|---|---|---|
| $Ru(bpy)_3^{2+}$ | 616 | 363 (±33) | 17.6 | 0.05[b] | 0.075[b]<br>0.089[c] |
| $Ru(dp\text{-}bpy)_3^{2+}$ | 635 | 761 (±70) | 14.1 | 0.14 | 0.31[c] |
| $Ru(dp\text{-}phen)_3^{2+}$ | 615 | 1723 (±153) | 18.1 | 0.24 | 0.37[d] |

[a]Except for those cited from the references, each of the values in this table is the average of at least five experimental trials.
[b]From reference (168).
[c]In ethanol + methanol (4:1 v/v) solution at 20°C (172).
[d]In ethanol + methanol (4:1 v/v) solution at 20°C (173).

where $I$ is the intensity in photons per second, $i$ is the current in amperes (Coulombs per second), $F$ is Faraday's constant and $N_A$ is Avogadro's constant. Since the same electrode was used for each experiment and concentration of the test solutions were approximately the same, the charge passed for each compound was about the same, as shown in the integrated current values in Table 13.5.

### 13.5.2 Coreactant ECL of $Ru(bpy)_3^{2+}$/TPrA system in aqueous solutions

Since the first report on the CL of $Ru(bpy)_3^{3+}$ with aliphatic amines (21), followed by the ECL study of the $Ru(bpy)_3^{2+}$ with TPrA as a coreactant (20), a wide range of ECL fundamental research and analytical applications involving $Ru(bpy)_3^{2+}$ or its derivatives have been reported (8). The $Ru(bpy)_3^{2+}$ (or its derivatives) with TPrA exhibit the highest ECL efficiency, and the relevant experiments can be carried out in an aqueous solution with a relatively wide range of pH (Figure 13.5) in the presence of oxygen. Consequently, this system is well suitable for ECL demonstrations (174, 175), as well as for ECL instrumental setup examinations.

Typically, 10–100 mM of TPrA in 0.10 M phosphate buffer (PBS) with a pH value of 7–8 can be prepared by dissolving the appropriate amount of phosphate salt and TPrA in water, and adjusting the pH of the TPrA–phosphate mixture with a concentrated $H_3PO_4$, HCl or $HClO_4$ solution while the mixture is stirred magnetically. Initially, the TPrA floats on the top, and a large number of small "oil drops" are distributed in the "solution" mixture after stirring. These "oil drops" should totally disappear (completely dissolved) once the solution pH approaches 7–8. Since the ECL intensity is proportional to the concentration of TPrA, a high concentration of TPrA–PBS buffer solution is always recommended. However, in the pH range of 7–8, 100 mM of TPrA is almost the saturated value. Care must be taken when using an ultrasonic bath to accelerate the TPrA dissolution, because TPrA may partially evaporate during the process. Similarly, the prepared TPrA–PBS solution should be kept in a well-sealed bottle. On the other hand, a mM $Ru(bpy)_3^{2+}$ aqueous

solution can be prepared readily from solid $Ru(bpy)_3Cl_2\ 2H_2O$, and kept in the dark. Only μM levels of $Ru(bpy)_3^{2+}$ in TPrA–PBS solutions are needed for ECL experiments. Instead of phosphate buffer, Tris-$LiClO_4$ can be also used as the buffer electrolyte, and the ECL responses in both buffers are essentially the same (137).

GC, Au, and Pt are all good for ECL studies of the $Ru(bpy)_3^{2+}$/TPrA system, but GC gives the best ECL responses (Figure 13.4). When $Cl^-$ and $ClO_4^-$ containing PBS buffer is used, unusual ECL behavior of $Ru(bpy)_3^{2+}$/TPrA system may be observed at Au electrodes. For example, the second ECL peak could completely disappear. This is probably associated with the generation of gold chloride/perchlorate complexes at the surface of the electrode after a positive potential is applied, although the exact mechanism is still under investigation. Before each experiment, the electrode should be carefully polished with a ~0.3–0.05 μm alumina slurry and rinsed thoroughly with water, because $Ru(bpy)_3^{2+}$ molecules can be very strongly adsorbed onto the electrode surface (and the wall of the electrochemical cell) (152), resulting in the generation of significant amount of ECL background. Either chromic acid or alcoholic KOH cleaning solution can be used to clean $Ru(bpy)_3^{2+}$ contaminated electrodes and glassware.

Several types of reference electrodes can be used in the ECL study: SCE, Ag/AgCl/$Cl^-$ (saturated or 3 M KCl) are two typical examples. Quasi reference electrodes, i.e., Pt wire and Ag wire, are also suitable, but their potentials need to be calibrated immediately after the experiment with an added fully reversible redox reagent, e.g., ferrocene methanol, as an internal potential standard.

Control experiments are always helpful for verifying possible problems from the electrochemical cell and for understanding the ECL mechanism. No ECL should be observed in the absence of either $Ru(bpy)_3^{2+}$ or TPrA. As shown in Figure 13.4, when nM to μM of $Ru(bpy)_3^{2+}$ in 0.10 M Tris/0.10 M $LiClO_4$, pH = 8, were used, two separated ECL waves are observed. The initial ECL signal starts at potentials where the direct oxidation of TPrA at the GC electrode occurs (Figures 13.4a–c), and reaches a first maximum at a potential of about 0.90 V vs. Ag/AgCl, about 50 mV less positive than the peak potential for TPrA oxidation, and well before $Ru(bpy)_3^{2+}$ oxidation. The second ECL signal has a peak potential value of 1.14 V vs. Ag/AgCl, in the potential region of the direct oxidation of $Ru(bpy)_3^{2+}$ at a GC electrode (138). The corresponding TPrA oxidation CV is essentially the same as that in Figure 13.4b. Note that even with a high concentration of $Ru(bpy)_3^{2+}$ (~mM), the ECL signal first appears in a potential range less positive than that for the oxidation of $Ru(bpy)_3^{2+}$. However, the initial ECL signal is relatively small compared to the large one.

Linear relationships were found between the ECL peak intensities and both TPrA and $Ru(bpy)_3^{2+}$ concentrations for the first as well as the second ECL wave in certain concentration ranges (20, 134, 136–138).

ECL spectra of aqueous $Ru(bpy)_3^{2+}$/TPrA system are also easy to record, because of the strong ECL response and the insensitivity of the system to oxygen. Figure 13.21 shows a mercury lamp spectrum measured with the CCD camera-based ECL spectral recording apparatus described in Section 13.4.3.4. For good experimental setup, at least four sharp peaks with the peak wavelengths of 404.86, 435.83, 546.07, and 578.01 nm are expected to be observed. The measured Hg spectrum quality depends on several factors: slit sizes of the monochromator and the lamp, Hg lamp and other optics alignment, exposure time,

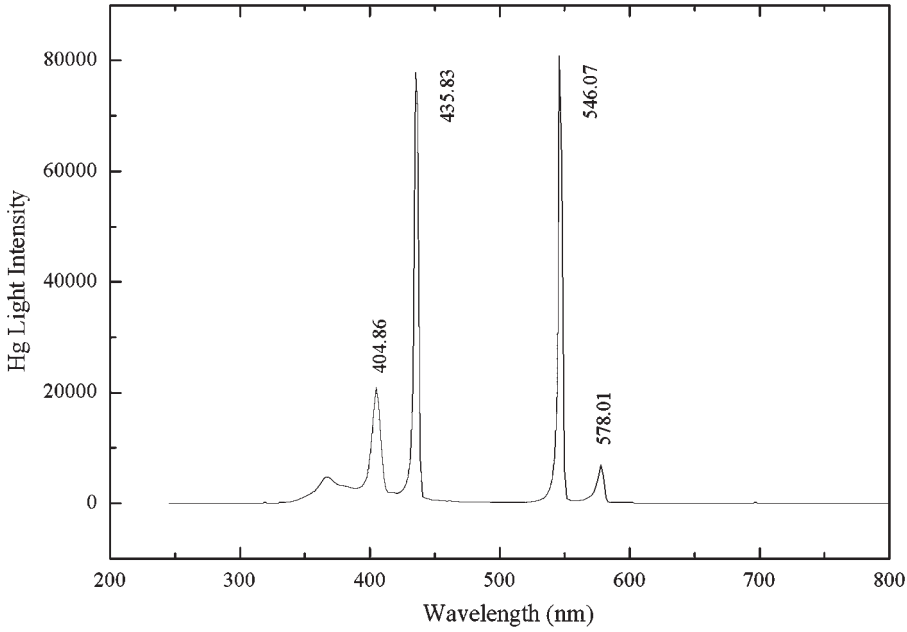


**Figure 13.21** Hg lamp spectrum used to calibrated the CCD-based ECL spectral recording instrument. The operating temperature of the CCD camera was −108°C. Exposure time ~30 ms.

CCD camera cooling temperature, and the CCD camera focus control etc. A typical method for ECL generation and spectrum recording is to use repetitive pulsing potential scanning between the oxidation potential of $Ru(bpy)_3^{2+}$/TPrA (e.g., 1.2 V vs. Ag/AgCl, see Figure 13.4) and 0 V vs. Ag/AgCl at a frequency of ~10 Hz. The wavelength of the measured ECL spectrum is calibrated with a previously measured mercury spectrum (Figure 13.21). An example of $Ru(bpy)_3^{2+}$/TPrA ECL spectrum obtained from a J-shaped Pt electrode (Figure 13.7a) with pulsing potential scanning between 1.2 and 0 V vs. Ag/AgCl is shown in Figure 13.22. As expected, the maximum emissions from the annihilation and coreactant $Ru(bpy)_3^{2+}$ ECL are essentially the same (Figure 13.20/Table 13.5 and Figure 13.22).

## 13.6 APPLICATIONS

A wide range of ECL-based applications have been developed in the last two decades, in which coreactant $Ru(bpy)_3^{2+}$/TPrA system has been overwhelmingly used. This section will list some of the most important/interesting ECL applications in tables, and readers who are interested in particular application aspects are encouraged to consult the relevant references cited (see Tables 13.6–13.13).

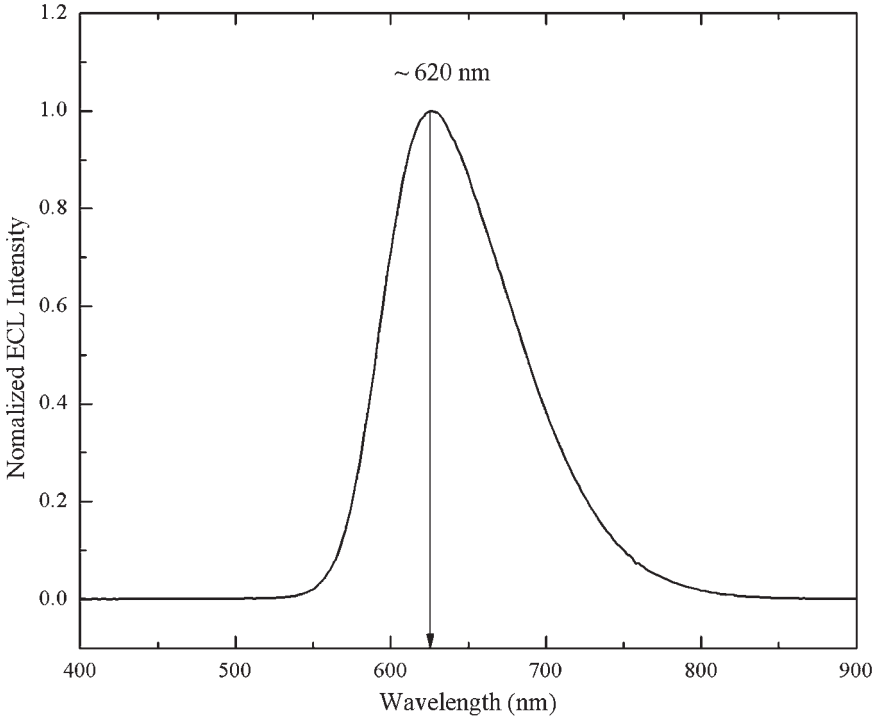


**Figure 13.22** Normalized ECL spectrum obtained from 1 mM $Ru(bpy)_3^{2+}$ − 10 mM TPrA–0.1 M PBS buffer (pH 7.0) solution with a 3 mm in diameter J-shaped Pt electrode. The electrode potential was pulsed between 0 and 1.2 V vs. Ag/AgCl at a frequency of 10 Hz for 30 s. The CCD camera was operated at −108 °C.

### 13.6.1 Applications of $Ru(bpy)_3^{2+}$ ECL: determination of oxalate and organic acids

**Table 13.6**

Applications of $Ru(bpy)_3^{2+}$ ECL for the determination of oxalate and organic acids (adapted from reference (176))

| Analyte | Comments | Matrix | Limit of detection | Reference |
|---|---|---|---|---|
| Oxalate | Batch method, linear range $1.0\times10^{-6}$ to $1.0\times10^{-4}$ M | Synthetic | Not stated | (177) |
| Oxalate | FIA, linear for oxalate up to $10^{-6}$ M, recoveries for oxalate ranged between 97% and 105%, standard derivation 2.3% | Urine | 0.3 pmol | (178) |
| Oxalate | Fibre optic based sensor $Ru(bpy)_3^{2+}$ immobilized on a Nafion modified electrode | Urine, vegetables | $3\times10^{-5}$ M | (179) |

(*Continued*)

**Table 13.6 (Cont.)**

| Analyte | Comments | Matrix | Limit of detection | Reference |
|---|---|---|---|---|
| Oxalate | FIA immobilized $Ru(bpy)_3^{2+}$ in Nafion | Synthetic | $1\times10^{-6}$ M, limited by background | (127) |
| Oxalate | Batch method, fibre optic sensor with (a) $Ru(bpy)_3^{2+}$ immobilized in Nafion and (b) $Ru(bpy)_3^{2+}$ modified in carbon paste electrode | Synthetic | (a) $3\times10^{-5}$ M, (b) $2\times10^{-5}$ M | (180) |
| Oxalate | Sonochemical enhancement of $Ru(bpy)_3^{2+}$ emission | Synthetic | Not determined | (181) |
| Oxalate | LC for determination of oxalate FIA | Urine, plasma | $<1\times10^{-6}$ M | (182) |
| Oxalate | *In situ* and external $Ru(bpy)_3^{3+}$ generation comparison | Synthetic | External generation 1.0 μM, *in situ* solution 0.5 μM, *in situ* immobilized 1.0 μM | (183) |
| Oxalate | Ion-pair LC with $Ru(bpy)_3^{2+}$ included in mobile phase | Urine, blood plasma | $0.1\times10^{-6}$ M | (184) |
| | Batch, fibre optic probe | Synthetic | $0.5\times10^{-6}$ M | (185) |
| Pyruvate | *In situ* oxidation of pyruvate to $CH_3CHO\cdot$ by electrogenerated Ce(IV) | Synthetic | $3.1\times10^{-7}$ M | (186) |
| Ascorbic acid | Ion-pairing LC | Soft drinks, fruit juice | 2 pmol (20 μL injection) | (187) |

## 13.6.2 Applications of $Ru(bpy)_3^{2+}$ ECL: determination of amines

**Table 13.7**

Applications of $Ru(bpy)_3^{2+}$ ECL for the determination of amines (adapted from reference (176))[a]

| Analyte | Comments | Limit of detection | Reference |
|---|---|---|---|
| Cyclic tertiary amines | FIA Solanidine, lincomycin, ergotamine, aconitine | Not stated | (188) |
| Alicyclic amine | FIA, linear ranges estimated at two orders of magnitude | 1-ethylpiperidine 1.8 pmol, 1-methylpyrrolidine 0.7 pmol, *N*-ethylmorphorine 0.8 pmol, sparteine 0.5 pmol, nicotine 0.4 pmol, lincomycin 0.3 pmol, atropine 1.5 pmol, and diphenidol 1.0 pmol | (189) |
| Primary amines | FIA, LC, cyclization to form thiomorpholine with divinylsulfone | 18 alkyl amines evaluated for relative intensities, no detection limits given | (190) |
| Reduced nicotinamide adenine dinucleotide (NADH) and phosphate (NADPH) | FIA, LC, linear range from 0.10 to 40 pmol | NADH 30 fmol NADPH 31 fmol | (191) |

**Table 13.7 (Cont.)**

| Analyte | Comments | Limit of detection | Reference |
|---|---|---|---|
| Alkylamines | FIA, immobilized $Ru(bpy)_3^{2+}$ in Nafion working range TPrA $1\times10^{-6}$ to $1\times10^{-3}$ M, antibiotics evaluated | TPrA $1\times10^{-8}$ M | (127) |
| Reduced nicotinamide adenine dinucleotide | FIA, immobilized $Ru(bpy)_3^{2+}$ in Nafion working range TPrA $1\times10^{-6}$ to $1\times10^{-3}$ M | NADH $1\times10^{-6}$ M | (127) |
| Primary amines | LC, pre-column derivatization with divinylsulfone (cyclo-addition) | Propylamine 30 pmol, 3-aminopentane 1 pmol | (192) |
| Tripropylamine | FIA, log linear calibration over three orders of magnitudes | 140 μg/L (~1 μM) | (193) |
| Tripropylamine, proline | Capillary electrophoresis | TPrA $3.7\times10^{-5}$ M, Proline $1.3\times10^{-5}$ M | (194) |
| Tripropylamine | Sub-μL ECL detector | TPrA $<5\times10^{-13}$ M | (195) |

[a]All matrixes were synthetic.

### 13.6.3 Applications of $Ru(bpy)_3^{2+}$ ECL: determination of amino acids

**Table 13.8**

Applications of $Ru(bpy)_3^{2+}$ ECL for the determination of amino acids (adapted from reference (176))

| Analyte | Comments | Limit of detection | Reference |
|---|---|---|---|
| Tryptophan | FIA | Not stated | (178) |
| Tryptophan, and indole derivatives | FIA | Tryptophan $3\times10^{-11}$ mol | (196) |
| Tryptophan[a] | Ligand exchange chiral LC, calibration for D- and L-tryptophan linear for both enantiomers in the range 2–200 (injected), 96% recovery for spiked samples | Both enantiomers 0.2 pmol | (197) |
| Amino acids, and phenyl thiohydantoin (PTH) derivatized amino acids | FIA, LC, for leucine linear response range 2–3 orders of magnitudes, reproducibility 5% ($n$ = 27) | Proline $5\times10^{-9}$ M, leucine $45\times10^{-9}$ M, aspartic acid $90\times10^{-9}$ M, serine $1.1\times10^{-9}$ M | (198) |
| D- and L-amino acids | Chiral LC, pre-column derivatization | fmol range (10 μL injection) | (199) |
| Dansyl amino acid | FIA, LC, pre-column derivatization with dansyl chloride, working curve (dansyl glutamine) 5–250 mM, RSD (n = 3) 1.5–4.5% | Dansyl chloride 1.0 mM, dansyl alanine 0.1 mM | (200) |

(*Continued*)

**Table 13.8 (Cont.)**

| Analyte | Comments | Limit of detection | Reference |
|---|---|---|---|
| Dansyl amino acids | Ion-pair LC with $Ru(bpy)_3^{2+}$ included in mobile phase | Dansyl glutamine 0.1 μM ($Ru(bpy)_3^{2+}$ in mobile phase), dansylated glutamine 0.2 μM ($Ru(bpy)_3^{3+}$ post-column) | (184) |
| Indoxyl derivatives | LC, detection limits using FIA | Indoxyl sulfate 2.3 pmol, indoxyl phosphate 3.1 pmol, indoxyl acetate 1.7 pmol, indoxyl 1,3-diacetate 0.4 pmol, indoxyl β-D-glucoside 0.0015 pmol, indoxyl β-D-galactoside 0.0015 pmol, indoxyl β-D-glucuronide 0.0023 pmol, tryptophan 0.25 pmol | (201) |
| Proline | FIA, various modes of $Ru(bpy)_3^{3+}$ generation | External generation 0.5 μM, *in situ* solution 0.5 μM, *in situ* immobilized 1.0 μM | (183) |

[a]The matrix was blood plasma.

## 13.6.4 Applications of $Ru(bpy)_3^{2+}$ ECL: determination of pharmaceuticals

**Table 13.9**

Applications of $Ru(bpy)_3^{2+}$ ECL for the determination of pharmaceuticals (adapted from reference (176))

| Analyte | Comments | Matrix | Limit of detection | Reference |
|---|---|---|---|---|
| Oxprenolol | FIA, linear range from 0.0001 to 0.04 mM | Synthetic | 35 nM | (202) |
| Codeine, heroin, detromethorphan | FIA, calibration range range from 0.1 to 1.0 μm | Synthetic | Codeine $15\times10^{-9}$ M, heroin $45\times10^{-9}$ M, detromethorphan $44\times10^{-9}$ M | (203) |
| Amitriptyline | FIA, calibration range from 0 to 40 μM | Synthetic | $3.0\times10^{-7}$ M | (204) |
| Amethocaine (tetracaine), bupivacaine, lignocaine (lindocaine), prilocaine, and procaine | FIA | Lignocaine in local anaesthetic preparation | Bupivacaine and procaine $5\times10^{-8}$ M, lignocaine $7\times10^{-8}$ M | (205) |
| β-Lactam antibiotics and β-lactamases | ORIGEN analyzer | Untreated milk and crude bacterial broth culture | β-Lactamase I from B, *cereus* using penicillin G as a substrate 25 pmol/L | (206) |
| Erythromycin | Microbore LC $Ru(bpy)_3^{2+}$ in mobile phase | Synthetic, blood plasma, urine | In synthetic standard 0.01 μM, in urine 0.05 μM, in blood plasma <0.10 μM, | (207) |

**Table 13.9 (Cont.)**

| Analyte | Comments | Matrix | Limit of detection | Reference |
|---|---|---|---|---|
| $\beta$-Blockers (acebutolol, alprenolol, oxprenolol, propranolol, tomolol, nadolol, labetolol) | Capillary electrophoresis | Synthetic | Oxprenolol 2 μM | (208) |

### 13.6.5 Applications of $Ru(bpy)_3^{2+}$ ECL: determination of $Ru(bpy)_3^{2+}$

**Table 13.10**

Applications of $Ru(bpy)_3^{2+}$ ECL for the determination of $Ru(bpy)_3^{2+}$ (adapted from reference (176))

| Analyte | Comments | Matrix | Limit of detection | Reference |
|---|---|---|---|---|
| $Ru(bpy)_3^{2+}$ | Oxalate and peroxodisulfate coreactants | Synthetic and liver tissue extract | ~$10^{-8}$ M with oxalate, ~$10^{-13}$ M with peroxodisulfate (with deoxygenation) | (19) |
| $Ru(bpy)_3^{2+}$ | Peroxodisulfate coreactants | Synthetic | ~$4.3\times10^{-8}$ M | (209) |
| $Ru(bpy)_3^{2+}$ | TPrA coreactant, ORIGEN analyzer I | Synthetic | 10 pM | (20) |
| $Ru(bpy)_3^{2+}$ | Micro-fabricated ECL cell, TPrA coreactant | Synthetic | ~$10^{-9}$ M | (210) |

### 13.6.6 Applications of $Ru(bpy)_3^{2+}$ ECL in capillary electrophoresis (CE) and micro-total analysis ($\mu$TAS)

**Table 13.11**

Applications of $Ru(bpy)_3^{2+}$ ECL in CE and μTAS (modified, reference (9))

| Analyte | Separation channel (μm) | Matrix | Limit of detection | Electrochemical system | Reference |
|---|---|---|---|---|---|
| Proline, valine, phenylalanine | 75 | Standard soln.[a] | 0.2 μM, 0.7 μM, 0.5 μM | Two-electrode system | (211) |
| Diphen-hydramine | 25 | Rabbit plasma, urine | $2\times10^{-8}$ M | Three-electrode system | (212) |
| Tramadol, lidocaine | 25 | Urine | $6\times10^{-8}$ M, $4.5\times10^{-8}$ M | Three-electrode | (213) |
| Procyclidine | 25 | Urine | $1\times10^{-9}$ M | Three-electrode | (214) |
| Proline, histidine | 50 | Standard soln. | 1 μM | DC battery | (215) |

(*Continued*)

**Table 13.11 (Cont.)**

| Analyte | Separation channel (μm) | Matrix | Limit of detection | Electrochemical system | Reference |
|---|---|---|---|---|---|
| TprA, proline | 21 | Standard soln. | 2−5 μ | DC battery (1.5 V) | (216) |
| TprA, lidocaine | 75 | Urine | $5\times10^{-11}$ M, $2\times10^{-8}$M | Three-electrode | (155) |
| TPrA | 75 | Standard soln. | 1 μM (TPrA) with $Ru(bpy)_3^{2+}$ immobilized | Three-electrode | (217) |
| Proline, oxalic acid | 75 | Degradation soln.of pHPP[b] | 1 mM (Proline), Not given | Three-electrode system | (218) |
| Proline, valine, phenylalanine | 50 | Standard soln. | 1.2, 50, 25 μM | Three-electrode | (219) |
| $Ru(bpy)_3^{2+}$ | 60×20 chip | Standard soln. | $5\times10^{-6}$ M | Voltage required to obtain ECL reaction from the electric field in separation channel | (220) |
| $Ru(phen)_3^{2+}$, proline | 15×48 | Standard soln. | $6\times10^{-6}$M, 1.2 μM | Three-electrode | (221) |

[a]With field decoupler.
[b]pHPP: *p*-hydroxyphenylpyruvic acid.

### 13.6.7 Application of $Ru(bpy)_3^{2+}$ ECL: determination of clinical analytes

**Table 13.12**

Summary of clinical assays using ECL detection (adapted from reference (133))

| Analyte | Application | Detection method | Reference |
|---|---|---|---|
| **I. Assays for ECL labels** | | | |
| *A. Immunoassays* | | | |
| AFP, α-fetoprotein | Tumor, fertility | TPrA, $Ru(bpy)_3^{2+}$ | (222, 223) |
| Anti-Borna disease antibodies | Infectious disease | TPrA, $Ru(bpy)_3^{2+}$ | (224–226) |
| *β*-Amyloid peptide | Alzheimer's disease | TPrA, $Ru(bpy)_3^{2+}$ | (227) |
| CA (cancer antigen) 15-3 | Tumor marker | TPrA, $Ru(bpy)_3^{2+}$ | (223, 228) |
| CA (cancer antigen) 19-9 | Tumor marker | TPrA, $Ru(bpy)_3^{2+}$ | (223) |
| CA (cancer antigen) 72-4 | Tumor marker | TPrA, $Ru(bpy)_3^{2+}$ | (229) |
| CA (cancer antigen) 125 II | Tumor marker | TPrA, $Ru(bpy)_3^{2+}$ | (230, 231) |
| CEA, carcinoembryonic antigen | Tumor marker | TPrA, $Ru(bpy)_3^{2+}$ | (223, 232) |
| *β*-Crosslaps | Bone | TPrA, $Ru(bpy)_3^{2+}$ | (233, 234) |
| C-Telopeptides | Bone | TPrA, $Ru(bpy)_3^{2+}$ | (235) |
| Anti-CMV antibodies | Infectious disease | TPrA, $Ru(bpy)_3^{2+}$ | (236) |
| Cytokeratin 19 | Tumor marker | TPrA, $Ru(bpy)_3^{2+}$ | (237) |
| CKMB, creatine kinase | Cardiac | TPrA, $Ru(bpy)_3^{2+}$ | (232, 238) |
| C-Reactive protein (CRP) | Cardiac | TPrA, $Ru(bpy)_3^{2+}$ | (151, 239) |
| Cytomegalovirus | Infectious disease | TPrA, $Ru(bpy)_3^{2+}$ | (238) |
| Des-γ-carboxy prothrombin | Tumor marker | TPrA, $Ru(bpy)_3^{2+}$ | (240, 241) |

**Table 13.12 (Cont.)**

| Analyte | Application | Detection method | Reference |
|---|---|---|---|
| Estradiol | Reproductive Endocrinology | TPrA, $Ru(bpy)_3^{2+}$ | (242) |
| Ferritin | Anemia | TPrA, $Ru(bpy)_3^{2+}$ | (223) |
| FSH, follitropin | Reproductive Endocrinology | TPrA, $Ru(bpy)_3^{2+}$ | (242) |
| HCG (human chorionic Gonadotropin) | Reproductive Endocrinology | TPrA, $Ru(bpy)_3^{2+}$ | (232, 243) |
| HBsAg, hepatitis B virus surface antigen | Infectious disease | TPrA, $Ru(bpy)_3^{2+}$ | (244–247) |
| HAsAg, hepatitis A virus surface antigen | Infectious disease | TPrA, $Ru(bpy)_3^{2+}$ | (248) |
| HIV-1 p7 antigen | Infectious disease | TPrA, $Ru(bpy)_3^{2+}$ | (249) |
| IgE, immunoglobulin E | Allergy | TPrA, $Ru(bpy)_3^{2+}$ | (250) |
| Insulin | Diabetes mellitus | TPrA, $Ru(bpy)_3^{2+}$ | (251, 252) |
| IL(Interleukin)-18 binding Protein | Sepsis | TPrA, $Ru(bpy)_3^{2+}$ | (253) |
| IL(Interleukin)-2 | Immune system | TPrA, $Ru(bpy)_3^{2+}$ | (254) |
| IL(Interleukin)-4 | Immune system | TPrA, $Ru(bpy)_3^{2+}$ | (254) |
| IL(Interleukin)-6 | Immune system | TPrA, $Ru(bpy)_3^{2+}$ | (223) |
| IL(Interleukin)-8 | Immune system | TPrA, $Ru(bpy)_3^{2+}$ | (223) |
| IL(Interleukin)-10 | Immune system | TPrA, $Ru(bpy)_3^{2+}$ | (254, 255) |
| IL(Interleukin)-10 | Immune system | TPrA, $Ru(bpy)_3^{2+}$ | (253) |
| Interferon-$\gamma$ | Immune system | TPrA, $Ru(bpy)_3^{2+}$ | (254) |
| LH, lutropin | Reproductive Endocrinology | TPrA, $Ru(bpy)_3^{2+}$ | (242) |
| Osteocalcin | Bone | TPrA, $Ru(bpy)_3^{2+}$ | (235) |
| Pancreatic phospholipase A2 | Pancreatic diseases | Terbium chelate | (256) |
| PTH (parathyroid hormone) | Ca metabolism | TPrA, $Ru(bpy)_3^{2+}$ | (257) |
| Prolactin | Reproductive Endocrinology | TPrA, $Ru(bpy)_3^{2+}$ | (242) |
| PSA (prostate specific antigen) | Tumor marker | TPrA, $Ru(bpy)_3^{2+}$ | (232, 258–260) |
| Serum interferon-$\alpha$ | Immune system | TPrA, $Ru(bpy)_3^{2+}$ | (253) |
| T4, thyroxine | Thyroid function | TPrA, $Ru(bpy)_3^{2+}$ | (232, 237, 261, 262) |
| T3, triiodothyronine | Thyroid function | TPrA, $Ru(bpy)_3^{2+}$ | (232, 261, 263) |
| TSH (thyroid stimulating hormone) | Thyroid function | TPrA, $Ru(bpy)_3^{2+}$ | (232, 261, 263) |
| TSH | Thyroid function | Terbium chelate | (264) |
| Testosterone | Reproductive Endocrinology | TPrA, $Ru(bpy)_3^{2+}$ | (242, 263) |
| Troponin | Myocardial Infarction | TPrA, $Ru(bpy)_3^{2+}$ | (232, 238, 257, 265–267) |
| Tumor necrosis factor-a | Immune function | TPrA, $Ru(bpy)_3^{2+}$ | (268) |
| *B. Molecular assays* | | | |
| Apo 8–100 gene mutation | Metabolism | TPrA, $Ru(bpy)_3^{2+}$ | (269) |
| Astrovirus | Infectious disease | TPrA, $Ru(bpy)_3^{2+}$ | (270) |
| Coxsackievirus B3 RNA | Infectious disease | TPrA, $Ru(bpy)_3^{2+}$ | (271) |
| CMV DNA | Infectious disease | TPrA, $Ru(bpy)_3^{2+}$ | (272) |
| Dengue virus RNA | Infectious disease | TPrA, $Ru(bpy)_3^{2+}$ | (273) |
| Enterovirus | Infectious disease | TPrA, $Ru(bpy)_3^{2+}$ | (274) |
| Epstein–Barr virus DNA | Infectious disease | TPrA, $Ru(bpy)_3^{2+}$ | (275) |
| Foot-and-mouth disease | Infectious disease | TPrA, $Ru(bpy)_3^{2+}$ | (276) |
| HIV-1 RNA | Infectious disease | TPrA, $Ru(bpy)_3^{2+}$ | (277, 278) |
| HIV DNA | Infectious disease | TPrA, $Ru(bpy)_3^{2+}$ | (278–281) |

(*Continued*)

**Table 13.12 (Cont.)**

| Analyte | Application | Detection method | Reference |
|---|---|---|---|
| HPIV-1/2/3 | Infectious disease | TPrA, $Ru(bpy)_3^{2+}$ | (282) |
| Influenza virus RNA | Infectious disease | TPrA, $Ru(bpy)_3^{2+}$ | (283–285) |
| mRNA | Tumor marker | TPrA, $Ru(bpy)_3^{2+}$ | (286–289) |
| Prothrombin gene mutation | Venous thromboembolism | TPrA, $Ru(bpy)_3^{2+}$ | (290) |
| St. Louis encephalitis | Infectious disease | TPrA, $Ru(bpy)_3^{2+}$ | (291) |
| Varicella-zoster virus DNA | Infectious disease | TPrA, $Ru(bpy)_3^{2+}$ | (292) |
| West Nile virus RNA | Infectious disease | TPrA, $Ru(bpy)_3^{2+}$ | (293) |
| ΔF508 deletion | Cystic fibrosis | TPrA, $Ru(bpy)_3^{2+}$ | (293) |
| *C. Other* | | | |
| Heavy metals | Toxicology | TPrA, $Ru(bpy)_3^{2+}$ | (294) |
| Potassium | Electrolytes | TPrA, $Ru(bpy)_3^{2+}$ | (294) |
| Sodium | Electrolytes | TPrA, $Ru(bpy)_3^{2+}$ | (295) |
| **II. Assays for coreactants** | | | |
| Carbon dioxide | Blood gases | NADH,$Ru(bpy)_3^{2+}$ | (296) |
| Cholesterol | Lipids | Oxalate, $Ru(bpy)_3^{2+}$ | (296) |
| Ethanol | Toxicology | NADH, $Ru(bpy)_3^{2+}$ | (296, 297) |
| Glucose | Diabetes mellitus | NADH, $Ru(bpy)_3^{2+}$ | (296, 297) |
| Lactate | Exercise | NADH, $Ru(bpy)_3^{2+}$ | (297) |

### 13.6.8 Applications of $Ru(bpy)_3^{2+}$ ECL: analytes associated with food, water, and biological agents

**Table 13.13**

ECL-based assays for food, water, and biological threat agents (adapted from reference (133))

| Analyte | Sample matrix | Assay method[a] | Detection limit | Reference |
|---|---|---|---|---|
| *Cryptosporidium parvum Oocysts* | Water | NASBA RNA amplification, ECL probe detection, NucliSens reader | About five viable oocysts per sample | (298) |
| | Turbid water | IA, ORIGEN analyzer | 50 viable oocysts/mL | (299) |
| | Highly turbid water | LA, ORIGEN analyzer | 1 oocyst/mL | (300) |
| | Karst water | IA, ORIGEN analyzer | 5 oocysts/mL | (301) |
| *Escherichia coli* O157 | Creek water | IA, ORIGEN analyzer | 25 cells/mL, 1–2 viable cells/mL after concentration | (302) |
| | Drinking water | NASBA mRNA amplification, ECL probe detection. NucliSens reader | 40 viable cells/mL | (303) |
| | Feces | PATHIgen IA, ORIGEN analyzer | $1\times10^5$ CFU/g | [b] |
| | Various food matrices | PATHIgen IA, ORIGEN analyzer | 100 cells/sample, more sensitive than culture methods | [b] |

**Table 13.13 (Cont.)**

| Analyte | Sample matrix | Assay method[a] | Detection limit | Reference |
|---|---|---|---|---|
| | Ground beef | IA, Origin analyzer | 100x as sensitive a commercial dipstick | (304) |
| | Ground beef, chicken, fish, milk, juices, serum, water | IA, Origin analyzer | 1000–2000 cells/mL | (305) |
| | Various food and Environmental water matrices | IA, Origin analyzer | Not reported | (306) |
| Campylobacter | Feces | PATHIgen IA, ORIGEN analyzer | $1\times10^4$ CFU/g | [b] |
| | Poultry samples | PATHIgen IA, ORIGEN analyzer | Comparable to culture methods | [b] |
| Salmonella | Feces | PATHIgen IA, ORIGEN analyzer | $5\times10^5$ CFU/g | [b] |
| | Surface swabs | PATHIgen IA, ORIGEN analyzer | 1 CFU/100 $cm^2$ | [b] |
| | Poultry house drag swabs | PATHIgen IA, ORIGEN analyzer | 81% positive predictive value vs. culture | [b] |
| | Various food matrices | PATHIgen IA, ORIGEN analyzer | Equivalent sensitivity to culture methods | [b] |
| | Ground beef, chicken, fish, milk, juices, serum, water | IA, Origin analyzer | 1000-–2000 cells/mL | (305) |
| *Listeria monocyto-genes*, | Environmental surface | PATHIgen IA, ORIGEN analyzer | 1 CFU/100 $cm^2$ | [b] |
| *Staphylococcus aureus*, entero-toxins | Buffer, milk, ground beef, let-tuce, potato salad | PATHIgen IA, ORIGEN analyzer | 10 pg/mL for SEB | [b] |
| | Buffer, various food matrices | IA, ORIGEN analyzer | 5–50 ng/mL (SEA, B, $C_1$, $C_2$, $C_3$, D, E) | [b] |
| | Serum, tissue, buffer, urine | IA, ORIGEN analyzer | 1 pg/mL for SEB | (307) |
| | Buffer | IA, ORIGEN analyzer | ~0.5 pg/mL | (308) |
| *Bacillus anthracis* | Soil | IA, ORIGEN analyzer | $10^5$ spores | (306, 309) |
| | Buffer | LA, ORIGEN analyzer | 100 spores | (310) |
| | Buffer | IA, ORIGEN analyzer | 1000 CFU/mL | (308) |
| | Specific DNA | | Not reported | (151) |
| Botulinus | Buffer | IA, ORIGEN analyzer | ~5 pg/mL | (310) |
| A toxin | Buffer | IA, ORIGEN analyzer | 4 pg/mL | (308) |
| Cholera toxin | Buffer | IA, ORIGEN analyzer | ~0.5 pg/mL | (310) |
| | Buffer | IA, ORIGEN analyzer | 2 pg/mL | (308) |
| Ricin toxin | Buffer | IA, ORIGEN analyzer | ~5 pg/mL | (310) |
| | Buffer | IA, ORIGEN analyzer | 0.5 pg/mL | (308) |

[a]IA = Immunoassay.
[b]Courtesy of Igen International, Inc. (Now BioVeris).

## ACKNOWLEDGMENTS

The support of this work by the University of Southern Mississippi via New Faculty Start-up Funding and the College of Science and Technology Dean's Research Initiative Program is gratefully acknowledged.

## REFERENCES

1. A. D. McNaught, A. Wilkinson, IUPAC, Eds., *IUPAC Compendium of Chemical Terminology*, 2nd ed., Blackwell Science Inc.: Oxford, UK, 1997.
2. A. J. Bard, L. R. Faulkner, *Electrochemical Methods: Fundamentals and Applications*, John Wiley & Sons, Inc.: New York, 2001.
3. D. M. Hercules, *Science (Washington, DC, United States)* **145**, 808 (1964).
4. K. S. V. Santhanam, A. J. Bard, *J. Am. Chem. Soc.* **87**, 139 (1965).
5. R. E. Visco, E. A. Chandross, *J. Am. Chem. Soc.* **86**, 5350 (1964).
6. R. T. Dufford, D. Nightingale, L. W. Gaddum, *J. Am. Chem. Soc.* **49**, 1858 (1927).
7. N. Harvey, *J. Phys. Chem.* **33**, 1456 (1929).
8. A. J. Bard, Ed., *Electrogenerated Chemiluminescence*, Marcel Dekker, Inc.: New York, 2004.
9. X.-B. Yin, S. Dong, E. Wang, *Trends Anal. Chem.* **23**, 432 (2004).
10. A. J. Bard, in *Electrogenerated Chemiluminescence*, A. J. Bard, Ed., Marcel Dekker, Inc.: New York, 2004, Chap. 1.
11. R. A. Maus, *J. Phys. Chem.* **43**, 2654 (1965).
12. S. W. Feldberg, *J. Am. Chem. Soc.* **88**, 390 (1966).
13. S. W. Feldberg, *J. Phys. Chem.* **70**, 3928 (1966).
14. L. R. Faulkner, A. J. Bard, *J. Am. Chem. Soc.* **91**, 209 (1969).
15. N. E. Tokel, A. J. Bard, *J. Am. Chem. Soc.* **94**, 2862 (1972).
16. M.-M. Chang, T. Saji, A. J. Bard, *J. Am. Chem. Soc.* **99**, 5399 (1977).
17. I. Rubinstein, A. J. Bard, *J. Am. Chem. Soc.* **103**, 512 (1981).
18. H. D. Abruna, A. J. Bard, *J. Am. Chem. Soc.* **104**, 2641 (1982).
19. D. Ege, W. G. Becker, A. J. Bard, *Anal. Chem.* **56**, 2413 (1984).
20. J. K. Leland, M. J. Powell, *J. Electrochem. Soc.* **137**, 3127 (1990).
21. J. B. Noffsinger, N. D. Danielson, *Anal. Chem.* **59**, 865 (1987).
22. A. J. Bard, G. M. Whitesides, *US Patent 5, 221, 605*, 1993.
23. G. F. Blackburn, H. P. Shah, J. H. Kenten, J. Leland, R. A. Kamin, J. Link, J. Peterman, M. J. Powell, A. Shah, D. B. Talley, *Clin. Chem. (Washington, DC, United States)* **37**, 1534 (1991).
24. M. M. Collinson, R. M. Wightman, *Anal. Chem.* **65**, 2576 (1993).
25. A.-M. Andersson, R. H. Schmehl, *Mol. Supramol. Photochem.* **7**, 153 (2001).
26. A.-M. Andersson, R. H. Schmehl, *Electron Transfer in Chemistry* **1**, 312 (2001).
27. Anon, *Indian J. Clin. Biochem.* **13**, 129 (1998).
28. N. R. Armstrong, R. M. Wightman, E. M. Gross, *Annu. Rev. Phys. Chem.* **52**, 391 (2001).
29. V. Balzani, A. Juris, *Coord. Chem. Rev.* **211**, 97 (2001).
30. A. J. Bard, F.-R. F. Fan, *Acc. Chem. Res.* **29**, 572 (1996).
31. A. J. Bard, S. M. Park, *Exciplex, Proc. Meet.*, 305 (1975).
32. R. C. Beier, L. H. Stanker, *Recent Res. Dev. Agric. Food Chem.* **4**, 59 (2000).
33. F. Bolletta, S. Bonafede, *Pure Appl. Chem.* **58**, 1229 (1986).
34. K. A. Fahnrich, M. Pravda, G. G. Guilbault, *Talanta* **54**, 531 (2001).
35. L. R. Faulkner, R. S. Glass, *Chem. Biol. Gener. Excited States*, 191 (1982).

36. R. D. Gerardi, N. W. Barnett, S. W. Lewis, *Anal. Chim. Acta* **378**, 1 (1999).
37. J. Gonzalez Velasco, *Electroanalysis* **3**, 261 (1991).
38. J. Gonzalez Velasco, *Bull. Electrochem.* **10**, 29 (1994).
39. G. M. Greenway, *Trends Anal. Chem.* **9**, 200 (1990).
40. A. Kapturkiewicz, *Adv. Electrochem. Sci. Eng.* **5**, 1 (1997).
41. P. T. Kissinger, *J. Pharm. Biomed. Anal.* **14**, 871 (1996).
42. A. W. Knight, *Trends Anal. Chem.* **18**, 47 (1999).
43. A. W. Knight, G. M. Greenway, *Analyst (Cambridge, United Kingdom)* **119**, 879 (1994).
44. A. W. Knight, G. M. Greenway, *Analyst (Cambridge, United Kingdom)* **121**, 101R (1996).
45. A. V. Kukoba, A. I. Bykh, I. B. Svir, *Fresenius J. Anal. Chem.* **368**, 439 (2000).
46. S. Kulmala, J. Suomi, *Anal. Chim. Acta* **500**, 21 (2003).
47. W. Y. Lee, *Mikrochim. Acta* **127**, 19 (1997).
48. U. Mitschke, P. Bauerle, *J. Mater. Chem.* **10**, 1471 (2000).
49. A. Nabi, M. Yaqoob, M. Anwar, *Lab. Rob. Autom.* **11**, 91 (1999).
50. T. A. Nieman, *J. Res. National Bureau of Standards (United States)* **93**, 501 (1988).
51. T. A. Nieman, in *Chemiluminescence and Photochemical Reaction Detection in Chromatography*; J. W. Birks, Ed., VCH: New York, NY, 1989, Ch. 4.
52. S.-M. Park, D. A. Tryk, *Rev. Chem. Intermed.* **4**, 43 (1980).
53. M. M. Richter, *Opt. Biosens.* 173 (2002).
54. M. M. Richter, *Chem. Rev. (Washington, DC, United States)* **104**, 3003 (2004).
55. M. L. Tortorello, D. Stewart, *New Techniques in the Analysis of Foods (Proceedings of an American Chemical Society Symposium on New Techniques in the Analysis of Foods), Las Vegas, NV, Sept. 7–11, 1997*, 91 (1998).
56. J. M. Zaleski, C. Turro, R. D. Mussell, D. G. Nocera, *Coord. Chem. Rev.* **132**, 249 (1994).
57. M. Zhou, J. Heinze, K. Borgwarth, C. P. Grover, *Chem. Phys. Chem.* **4**, 1241 (2003).
58. P. B. Oldham, M. E. McCarroll, L. B. McGown, I. M. Warner, *Anal. Chem.* **72**, 197R (2000).
59. R. A. Agbaria, P. B. Oldham, M. McCarroll, L. B. McGown, I. M. Warner, *Anal. Chem.* **74**, 3952 (2002).
60. A. M. Powe, K. A. Fletcher, N. N. St. Luce, M. Lowry, S. Neal, M. E. McCarroll, P. B. Oldham, L. B. McGown, I. M. Warner, *Anal. Chem.* **76**, 4614 (2004).
61. R. J. Aitken, M. A. Baker, M. O'Bryan, *J. Androl.* **25**, 455 (2004).
62. J. Sherma, *J. AOAC Int.* **87**, 20A (2004).
63. K. Jacobson, P. Eriksson, T. Reitberger, B. Stenberg, *Adv.Polym. Sci.* **169**, 151 (2004).
64. A. Roda, P. Pasini, M. Mirasoli, E. Michelini, M. Guardigli, *Trends Biotechnol.* **22**, 295 (2004).
65. A. M. Jimenez, M. J. Navas, *J. Hazard. Mater.* **106**, 1 (2004).
66. L. J. Kricka, *Anal. Chim. Acta* **500**, 279 (2003).
67. A. Roda, M. Guardigli, E. Michelini, M. Mirasoli, P. Pasini, *Anal. Chem.* **75**, 462A (2003).
68. A. Roda, M. Guardigli, P. Pasini, M. Mirasoli, *Anal. Bioanal. Chem.* **377**, 826 (2003).
69. F. Li, C. Zhang, X. Guo, W. Feng, *Biomed. Chromatogr.* **17**, 96 (2003).
70. J. S. Gaffney, N. A. Marley, *Conference on Atmospheric Chemistry: Urban, Regional, and Global Scale Impacts of Air Pollutants, 4th, Orlando, FL, United States, Jan. 13–17, 2002*, 1 (2002).
71. D. O. Shah, C. D. Chang, J. L. Stewart, *BIOforum Europe* **7**, 44 (2003).
72. N. I. Butkovskaya, D. W. Setser, *Int. Rev. Phys. Chem.* **22**, 1 (2003).
73. W. Qin, *Anal. Lett.* **35**, 2207 (2002).
74. Y.-M. Liu, J.-K. Cheng, *J. Chromatogr. A.* **959**, 1 (2002).
75. R. A. W. Stott, in *Protein Protocols Handbook*; J. M. Walker, Ed., Human Press: Totawa, NJ, 2002, Part 156.
76. A. M. Garcia-Campana, W. R. G. Baeyens, L. Cuadros-Rodriguez, F. A. Barrero, J. M. Bosque-Sendra, L. Gamiz-Gracia, *Curr. Org. Chem.* **6**, 1 (2002).

77. M. Yamaguchi, H. Yoshida, H. Nohta, *J. Chromatogr. A.* **950**, 1 (2002).
78. R. Creton, L. F. Jaffee, *BioTechniques* **31**, 1098 (2001).
79. G. Gubitz, M. G. Schmid, H. Silviaeh, H. Y. Aboul-Enein, *Crit. Rev. Anal. Chem.* **31**, 167 (2001).
80. J. Arnhold, in *Chemiluminescence at the Turn of the Millennium*; S. Albrecht, T. Zimmermann, H. Brandl, Eds., Schweda-Werbedruck GmbH: Dresden, Germany, 2001, pp. 85–94.
81. C. Kuyper, R. Milofsky, *Trends Anal. Chem.* **20**, 232 (2001).
82. L. Rychla, J. Rychly, in *Polymer Analysis and Degradation*; A. Jimenez, G. E. Zaikov, Eds., Nova Science Publishers Inc.: Huntington, NY, 2000, pp. 123–134.
83. K. Papadopoulos, T. Triantis, D. Dimotikali, J. Nikokavouras, *J. Photochem. Photobiol. A: Chem,* **131**, 55 (2000).
84. K. Papadopoulos, J. Lignos, M. Stamatakisy, D. Dimotikali, J. Nikokavouras, *J. Photochem. Photobiol. A: Chem.* **115**, 137 (1998).
85. G. L. Sharipov, R. A. Sadikov, in *Issled. Obl. Khim. Vysokomol. Soedin. Neftekhim*; S. R. Rafikov, Ed., Akad. Nauk SSSR: Ufa, USSR, 1977, pp. 52–53.
86. G. M. Avakyan, T. M. Avakyan, *Biologicheskii Zhurnal Armenii* **8**, 9 (1972).
87. T. M. Avakyan, L. G. Stepanyan, *Biofizika* **17**, 712 (1972).
88. F. Bistolfi, *Panminerva Medica* **42**, 69 (2000).
89. G. T. Reynolds, *J. Lumin.* **54**, 43 (1992).
90. C. D. Kalkar, *Radiat. Phys. Chem.* **34**, 729 (1989).
91. M. Ashok Kumar, F. Grieser, *Chem. Phys. Chem.* **5**, 439 (2004).
92. V. H. Arakeri, *Curr. Sci.* **85**, 911 (2003).
93. T. V. Prevenslik, *Ultrasonics* **41**, 313 (2003).
94. M. P. Brenner, S. Hilgenfeldt, D. Lohse, *Rev. Mod. Phys.* **74**, 425 (2002).
95. M. A. Margulis, I. M. Margulis, *Ultrason. Sonochem.* **9**, 1 (2002).
96. H. Mitome, *Jpn. J. Appl. Phys., Part 1: Regular Papers, Short Notes & Review Papers* **40**, 3484 (2001).
97. D. Hammer, L. Frommhold, *J. Mod. Opt.* **48**, 239 (2001).
98. T. Lepoint, F. Lepoint-Mullie, *Adv. Sonochem.* **5**, 1 (1999).
99. D. Lohse, S. Hilgenfeldt, *Festkoerperprobleme* **38**, 215 (1999).
100. I. V. Ostrovskii, O. A. Korotchenkov, T. Goto, H. G. Grimmeiss, *Phys. Rep.* **311**, 1 (1999).
101. P. T. Greenland, *Contemp. Phys.* **40**, 11 (1999).
102. B. A. DiDonna, T. A. Witten, J. B. Young, *Physica A: Statistical and Theoretical Physics (Amsterdam)* **258**, 263 (1998).
103. S. M. Cordry, L. A. Crum, *Luminescence of Solids*, 343 (1998).
104. S. Putterman, *Phys. World* **11**, 38 (1998).
105. K. S. Suslick, *Proceedings - IEEE Ultrasonics Symposium*, 523 (1997).
106. F. Macintyre, *Ultrason. Sonochem.* **4**, 85 (1997).
107. T. J. Matula, R. A. Roy, *Ultrason. Sonochem.* **4**, 61 (1997).
108. J. D. N. Cheeke, *Can. J. Phys.* **75**, 77 (1997).
109. B. P. Barber, R. A. Hiller, R. Loefstedt, S. J. Putterman, K. R. Weninger, *Phys. Rep.* **281**, 65 (1997).
110. L. A. Crum, *Phys. Today* **47**, 22 (1994).
111. F. E. Beideman, D. M. Hercules, *J. Phys. Chem.* **83**, 2203 (1979).
112. R. Y. Lai, A. J. Bard, *J. Phys. Chem. A.* **107**, 3335 (2003).
113. L. R. Faulkner, A. J. Bard, *Electronal. Chem.* **10**, 1 (1977).
114. L. R. Faulkner, H. Tachikawa, A. J. Bard, *J. Am. Chem. Soc.* **94**, 691 (1972).
115. H. Tachikawa, A. J. Bard, *Chem. Phys. Lett.* **26**, 246 (1974).
116. A. Pighin, B. E. Conway, *J. Electrochem. Soc.* **122**, 619 (1975).
117. N. Periasamy, K. S. V. Santhanam, *Proc. Indian Acad. Sci. Sec. A.* **80**, 194 (1974).

118. B. Fleet, G. F. Kirkbright, C. J. Pickford, *J. Electroanal. Chem. Interfac. Electrochem.* **30**, 115 (1971).
119. A. Weller, K. Zachariasse, *Chem. Phys. Lett.* **10**, 197 (1971).
120. T. C. Werner, J. Chang, D. M. Hercules, *J. Am. Chem. Soc.* **92**, 5560 (1970).
121. J. T. Maloy, A. J. Bard, *J. Am. Chem. Soc.* **93**, 5968 (1971).
122. E. A. Chandross, J. W. Longworth, R. E. Visco, *J. Am. Chem. Soc.* **87**, 3259 (1965).
123. W. Miao, J.-P. Choi, in *Electrogenerated Chemiluminescence*, A. J. Bard, Ed., Marcel Dekker, Inc.: New York, 2004, Chap. 5.
124. H. S. White, A. J. Bard, *J. Am. Chem. Soc.* **104**, 6891 (1982).
125. A. Juris, V. Balzani, F. Barigelletti, S. Campagna, P. Belser, A. Von Zelewsky, *Coord. Chem. Rev.* **84**, 85 (1988).
126. J. Butler, A. Henglein, *Radiat. Phys. Chem.* **15**, 603 (1980).
127. T. M. Downey, T. A. Nieman, *Anal. Chem.* **64**, 261 (1992).
128. F. Kanoufi, A. J. Bard, *J. Phys. Chem. B.* **103**, 10469 (1999).
129. F. Bolletta, M. Ciano, V. Balzani, N. Serpone, *Inorg. Chim. Acta* **62**, 207 (1982).
130. R. Memming, *J. Electrochem. Soc.* **116**, 785 (1969).
131. F. Bolletta, A. Juris, M. Maestri, D. Sandrini, *Inorg. Chim. Acta* **44**, L175 (1980).
132. A. J. Bard, J. D. Debad, J. K. Leland, G. B. Sigal, J. L. Wilbur, J. N. Wohlsatdter, in *Encyclopedia of Analytical Chemistry: Applications, Theory and Instrumentation*; R. A. Meyers, Ed., John Wiley & Sons: New York, 2000, p. 9842.
133. J. D. Debad, E. N. Glezer, J. K. Leland, G. B. Sigal, J. Wohlsadter, in *Electrogenerated Chemiluminescence*; A. J. Bard, Ed., Marcel Dekker, Inc.: New York, 2004, Chap. 8.
134. E. M. Gross, P. Pastore, R. M. Wightman, *J. Phys. Chem. B.* **105**, 8732 (2001).
135. L. He, K. A. Cox, N. D. Danielson, *Anal. Lett.* **23**, 195 (1990).
136. F. Kanoufi, Y. Zu, A. J. Bard, *J. Phys. Chem. B.* **105**, 210 (2001).
137. W. Miao, J.-P. Choi, A. J. Bard, *J. Am. Chem. Soc.* **124**, 14478 (2002).
138. Y. Zu, A. J. Bard, *Anal. Chem.* **72**, 3223 (2000).
139. D. M. Hercules, F. E. Lytle, *J. Am. Chem. Soc.* **88**, 4745 (1966).
140. D. M. Hercules, *Acc. Chem. Res.* **2**, 301 (1969).
141. D. M. Hercules, F. E. Lytle, *Photochem. Photobiol.* **13**, 123 (1971).
142. B. Li, Z. Zhang, X. Zheng, C. Xu, *Chem. Anal. (Warsaw)* **45**, 709 (2000).
143. J. E. Martin, E. J. Hart, A. W. Adamson, H. Gafney, J. Halpern, *J. Am. Chem. Soc.* **94**, 9238 (1972).
144. E. A. Chandross, F. I. Sonntag, *J. Am. Chem. Soc.* **88**, 1089 (1966).
145. D. L. Akins, R. L. Birke, *Chem. Phys. Lett.* **29**, 428 (1974).
146. T. D. Santa Cruz, D. L. Akins, R. L. Birke, *J. Am. Chem. Soc.* **98**, 1677 (1976).
147. A. R. Bowie, M. G. Sanders, P. J. Worsfold, *J. Biolumin. Chemilumin.* **11**, 61 (1996).
148. H. O. House, E. Feng, N. P. Peet, *J. Org. Chem.* **36**, 2371 (1971).
149. F. R. F. Fan, in *Electrogenerated Chemiluminescence*, A. J. Bard, Ed., Marcel Dekker, Inc.: New York, 2004, Chap. 2.
150. A. J. Fry, in *Laboratory Techniques in Electroanalytical Chemistry*, P. T. Kissingerand, W. R. Heineman, Eds., Marcel Dekker, Inc.: New York, 1996, Chap. 15.
151. W. Miao, A. J. Bard, *Anal. Chem.* **75**, 5825 (2003).
152. X.-H. Xu, A. J. Bard, *Langmuir* **10**, 2409 (1994).
153. N. D. Danielson, in *Electrogenerated Chemiluminescence*, A. J. Bard, Ed., Marcel Dekker, Inc.: New York, 2004, Chap. 9.
154. F. Li, H. Cui, X.-Q. Lin, *Anal. Chim. Acta* **471**, 187 (2002).
155. W. Cao, J. Liu, X. Yang, E. Wang, *Electrophoresis* **23**, 3683 (2002).
156. L. R. Faulkner, D. J. Freed, *J. Am. Chem. Soc.* **93**, 2097 (1971).
157. J. E. Bartelt, S. M. Drew, R. M. Wightman, *J. Electrochem. Soc.* **139**, 70 (1992).

158. Y. Zu, A. J. Bard, *Anal. Chem.* **73**, 3960 (2001).
159. W. Miao, A. J. Bard, *Anal. Chem.* **76**, 5379 (2004).
160. X. Zhao, T. You, H. Qiu, J. Yan, X. Yang, E. Wang, *J. Chromatogr. B: Anal. Technol. Biomed. Life Sci.* **810**, 137 (2004).
161. K. Honda, T. Noda, M. Yoshimura, K. Nakagawa, A. Fujishima, *J. Phys. Chem. B.* **108**, 16117 (2004).
162. K. Honda, M. Yoshimura, T. N. Rao, A. Fujishima, *J. Phys. Chem. B.* **107**, 1653 (2003).
163. H. Yang, J. K. Leland, D. Yost, R. J. Massey, *Biotechnology* **12**, 193 (1994).
164. R. S. Glass, L. R. Faulkner, *J. Phys. Chem.* **85**, 1160 (1981).
165. J. D. Luttmer, A. J. Bard, *J. Phys. Chem.* **85**, 1155 (1981).
166. P. McCord, A. J. Bard, *J. Electroanal. Chem. Interfac. Electrochem.* **318**, 91 (1991).
167. N. E. Tokel-Takvoryan, R. E. Hemingway, A. J. Bard, *J. Am. Chem. Soc.* **95**, 6582 (1973).
168. W. L. Wallace, A. J. Bard, *J. Phys. Chem.* **83**, 1350 (1979).
169. K. Itoh, K. Honda, *Chem. Lett.* **1**, 99 (1979).
170. D. Laser, A. J. Bard, *J. Electrochem. Soc.* **122**, 632 (1975).
171. R. Bezman, L. R. Faulkner, *J. Am. Chem. Soc.* **94**, 3699 (1972).
172. M. J. Cook, A. P. Lewis, G. S. G. McAuliffe, V. Skarda, A. J. Thomson, J. L. Glasper, D. J. Robbins, *J. Chem. Soc., Perkin Trans. 2: Phys. Org. Chem.* **8**, 1293 (1984).
173. P. C. Alford, M. J. Cook, A. P. Lewis, G. S. G. McAuliffe, V. Skarda, A. J. Thomson, J. L. Glasper, D. J. Robbins, *J. Chem. Soc., Perkin Trans. 2: Phys. Org. Chem.* **5**, 705 (1985).
174. E. Bolton, M. M. Richter, *J. Chem. Educ.* **78**, 641 (2001).
175. C. Alexander, J. McCall, M. M. Richter, *Chemical Educator (Electronic Publication)* **3**, No pp. given (1998).
176. R. D. Gerardi, N. W. Barnett, A. W. Lewis, *Anal. Chim. Acta* **378**, 1 (1999).
177. I. Rubinstein, C. R. Martin, A. J. Bard, *Anal. Chem.* **55**, 1580 (1983).
178. K. Uchikura, *Bunseki Kagaku* **39**, 323 (1990).
179. N. Egashira, H. Kumasako, K. Ohga, *Anal. Sci.* **6**, 903 (1990).
180. N. Egashira, *Proc. Electrochem. Soc.* **93**, 674 (1993).
181. D. J. Walton, S. S. Phull, D. M. Bates, J. P. Lorimer, T. J. Mason, *Ultrasonics* **30**, 186 (1992).
182. D. R. Skotty, T. A. Nieman, *J. Chromatogr. B.* **665**, 27 (1995).
183. W.-Y. Lee, T. A. Nieman, *Anal. Chem.* **67**, 1789 (1995).
184. D. R. Skotty, W.-Y. Lee, T. A. Nieman, *Anal. Chem.* **68**, 1530 (1996).
185. J. P. Preston, T. A. Nieman, *Anal. Chem.* **68**, 966 (1996).
186. A. W. Knight, G. M. Greenway, *Analyst (Cambridge, United Kingdom)* **120**, 2543 (1995).
187. X. Chen, M. Sato, *Anal. Sci.* **11**, 749 (1995).
188. K. Uchikura, *Chromatography* **11**, 102 (1990).
189. K. Uchikura, M. Kirisawa, *Anal. Sci.* **7**, 803 (1991).
190. K. Uchikura, M. Kirisawa, *Chromatography* **12**, 56 (1991).
191. K. Uchikura, M. Kirisawa, *Chromatography* **13**, 257 (1992).
192. K. Uchikura, M. Kirisawa, A. Sugii, *Anal. Sci.* **9**, 121 (1993).
193. A. W. Knight, G. M. Greenway, E. D. Chesmore, *Anal. Proc.* **32**, 125 (1995).
194. J. A. Dickson, M. M. Ferris, R. E. Milofsky, *J. High Resolut. Chromatogr.* **20**, 643 (1997).
195. A. Arora, A. J. de Mello, A. Manz, *Anal. Commun.* **34**, 393 (1997).
196. K. Uchikura, M. Kirisawa, *Chem. Lett.*, **8**, 1373 (1991).
197. K. Uchikura, M. Kirisawa, *Anal. Sci.* **7**, 971 (1991).
198. W. A. Jackson, D. R. Bobbitt, *Anal. Chim. Acta* **285**, 309 (1994).
199. K. Uchikura, M. Kirisawa, *Chromatography* **15**, 232 (1994).
200. W.-Y. Lee, T. A. Nieman, *J. Chromatogr.* **659**, 111 (1994).
201. K. Uchikura, S. Asami, *Chromatography* **16**, 320 (1995).

202. G. M. Greenway, P. J. Knight, *Anal. Proc.* **32**, 251 (1995).
203. G. M. Greenway, A. W. Knight, P. J. Knight, *Analyst (Cambridge, United Kingdom)* **120**, 2549 (1995).
204. S. J. L. Dolman, G. M. Greenway, *Anal. Commun.* **33**, 139 (1996).
205. A. W. Knight, G. M. Greenway, *Anal. Commun.* **33**, 171 (1996).
206. P. Liang, R. I. Sanchez, M. T. Martin, *Anal. Chem.* **68**, 2426 (1996).
207. J. S. Ridlen, D. R. Skotty, P. T. Kissinger, T. A. Nieman, *J. Chromatogr. B.* **694**, 393 (1997).
208. G. A. Forbes, T. A. Nieman, J. V. Sweedler, *Anal. Chim. Acta* **347**, 289 (1997).
209. L. S. Kuhn, A. Weber, S. G. Weber, *Anal. Chem.* **62**, 1631 (1990).
210. Y. T. Hsueh, R. L. Smith, M. A. Northrup, *Proc. Electrochem. Soc.* **95**, 117 (1995).
211. X. Wang, D. R. Bobbitt, *Anal. Chim. Acta* **383**, 213 (1999).
212. J. F. Liu, W. D. Cao, X. R. Yang, E. K. Wang, *Talanta* **59**, 453 (2003).
213. W. Cao, J. Liu, H. Qiu, X. Yang, E. Wang, *Electroanalysis* **14**, 1571 (2002).
214. X. Sun, J. Liu, W. Cao, X. Yang, E. Wang, Y. S. Fung, *Anal. Chim. Acta* **470**, 137 (2002).
215. M.-T. Chiang, C.-W. Whang, *J. Chromatogr. A.* **934**, 59 (2001).
216. M.-T. Chiang, M. C. Lu, C.-W. Whang, *Electrophoresis* **24**, 3033 (2003).
217. W. Cao, J. Jia, X. Yang, S. Dong, E. Wang, *Electrophoresis* **23**, 3692 (2002).
218. G. N. Chen, Y. W. Chi, X. P. Wu, J. P. Duan, N. B. Li, *Anal. Chem.* **75**, 6602 (2003).
219. X.-J. Huang, S.-L. Wang, Z.-L. Fang, *Anal. Chim. Acta* **456**, 167 (2002).
220. A. Arora, J. C. T. Eijkel, W. E. Morf, A. Manz, *Anal. Chem.* **73**, 3282 (2001).
221. H. Qiu, J. L. Yan, X. H. Sun, J. F. Liu, W. D. Cao, X. R. Yang, E. K. Wang, *Anal. Chem.* **75**, 5435 (2003).
222. Y. Namba, M. Usami, O. Suzuki, *Anal. Sci.* **15**, 1087 (1999).
223. N. Yilmaz, A. B. Erbagci, A. S. Aynacioglu, *Acta. Biochim. Polon.* **48**, 775 (2001).
224. K. Fukuda, K. Takahashi, Y. Iwata, N. Mori, K. Gonda, T. Ogawa, K. Osonoe, M. Sato, S.-I. Ogata, T. Horimoto, T. Sawada, M. Tashiro, K. Yamaguchi, S.-I. Niwa, S. Shigeta, *J. Clin. Microbiol.* **39**, 419 (2001).
225. Y. Horii, N. P. Garcia, D. Noviana, F. Kono, T. Sawada, T. Naraki, K. Yamaguchi, *J. Vet. Med. Sci./The Jpn. Soc. Vet. Sci.* **63**, 921 (2001).
226. K. Yamaguchi, T. Sawada, S. Yamane, S. Haga, K. Ikeda, R. Igata-Yi, K. Yoshiki, M. Matsuoka, H. Okabe, Y. Horii, Y. Nawa, R. W. Waltrip, II, K. M. Carbone, *Ann. Clin. Biochem.* **38**, 348 (2001).
227. O. E. Khorkova, K. Pate, J. Heroux, S. Sahasrabudhe, *J. Neurosci. Methods* **82**, 159 (1998).
228. P. Stieber, R. Molina, D. W. Chan, H. A. Fritsche, R. Beyrau, J. M. G. Bonfrer, X. Filella, T. G. Gornet, T. Hoff, W. Inger, G. J. Van Kamp, D. Nagel, K. Peisker, L. J. Sokoll, F. Troalen, M. Untch, I. Domke, *Clin. Chem. (Washington, DC, United States)* **47**, 2162 (2001).
229. X. Filella, S. Friese, H. J. Roth, S. Nussbaum, B. Wehnl, *Anticancer Res.* **20**, 5229 (2000).
230. W. Hubl, D. W. Chan, H. E. Van Ingen, H. Miyachi, R. Molina, X. Filella, L. Pitzel, A. Ruibal, J. C. Rymer, G. Bagnard, I. Domke, *Anticancer Res.* **19**, 2727 (1999).
231. H. E. Van Ingen, D. W. Chan, W. Hubl, H. Miyachi, R. Molina, L. Pitzel, A. Ruibal, J. C. Rymer, I. Domke, *Clin. Chem. (Washington, DC)* **44**, 2530 (1998).
232. W. Stockmann, W. Bablok, P. Luppa, *Wiener Klinische Wochenschrift* **110**, 10 (1998).
233. T. Seck, I. Diel, H. Bismar, R. Ziegler, J. Pfeilschifter, *Bone (New York, NY, United States)* **30**, 217 (2002).
234. R. Okabe, K. Nakatsuka, M. Inaba, T. Miki, H. Naka, H. Masaki, A. Moriguchi, Y. Nishizawa, *Clin. Chem.* **47**, 1410 (2001).
235. K. Scheunert, S. Albrecht, V. Konnegen, G. Wunderlich, W. Distler, in *Chemiluminescence at the Turn of the Millennium*; S. Albrecht, T. Zimmermannand H. Brandl, Eds., Schweda-Werbedruch GmbH: Dresdin, 2001, p. 347.

236. M. Ohlin, M. Silvestri, V. A. Sundqvist, C. A. Borrebaeck, *Clin. Diagn. Lab. Immunol.* **4**, 107 (1997).
237. M. Sanchez-Carbayo, A. Espasa, V. Chinchilla, E. Herrero, J. Megias, A. Mira, F. Soria, *Clin. Chem. (Washington, DC)* **45**, 1944 (1999).
238. G. Klein, M. Kampmann, H. Baum, T. Rauscher, T. Vukovic, K. Hallermayer, H. Rehner, M. Mueller-Bardorff, H. A. Katus, *Wiener Klinische Wochenschrift* **110**, 40 (1998).
239. W. Miao, A. J. Bard, *Anal. Chem.* **76**, 7109 (2004).
240. A. Shimizu, K. Shiraki, T. Ito, K. Sugimoto, T. Sakai, S. Ohmori, K. Murata, K. Takase, Y. Tameda, T. Nakano, *Int. J. Mol. Med.* **9**, 245 (2002).
241. T. Sassa, T. Kumada, S. Nakano, T. Uematsu, *Eur. J. Gastroenterol. Hepatol.* **11**, 1387 (1999).
242. N. Gassler, T. Peuschel, R. Pankau, *Clin. Lab. (Heidelberg)* **46**, 553 (2000).
243. V. Ehrhardt, G. Assmann, O. Batz, C. Bieglmayer, C. Muller, D. Neumeier, H. J. Roth, A. Veys, J. P. Yvert, *Wiener klinische Wochenschrift* **110 Suppl 3**, 61 (1998).
244. Y. Kobayashi, M. Hayakawa, Y. Fukumura, *Igaku Yakugaku* **42**, 749 (1999).
245. S. Kashiwagi, J. Hayashi, T. Asai, J. Nishimura, N. Arai, M. Kanashima, Y. Asai, *Igaku Yakugaku* **40**, 119 (1998).
246. M. Takahashi, H. Hoshino, Y. Ohuchi, S. Ryan, K. Shimoda, K. Yachuda, J. Tanaka, K. Yoshizawa, K. Hino, S. Iino, *Igaku Yakugaku* **40**, 483 (1998).
247. B. Weber, A. Bayer, P. Kirch, V. Schluter, D. Schlieper, W. Melchior, *J. Clin. Microbiol.* **37**, 2639 (1999).
248. See www.rochediagnostics.com
249. M. P. De Baar, K. H. M. Van der Horn, J. Goudsmit, A. De Ronde, F. De Wolf, *J. Clin. Microbiol.* **37**, 63 (1999).
250. L. Kobrynski, L. Tanimune, N. A. Pawlowski, S. D. Douglas, D. E. Campbell, *Clin. Diagn. Lab. Immunol.* **3**, 42 (1996).
251. A. Liebert, L. Beier, E. Schneider, P. Kirch, *Chemiluminescence at the Turn of the Millennium*, 2001, p. 341.
252. R. Sapin, V. Le Galudec, F. Gasser, M. Pinget, D. Grucker, *Clin. Chem.* **47**, 602 (2001).
253. D. Novick, B. Schwartsburd, R. Pinkus, D. Suissa, I. Belzer, Z. Sthoeger, W. F. Keane, Y. Chvatchko, S. H. Kim, G. Fantuzzi, C. A. Dinarello, M. Rubinstein, *Cytokine* **14**, 334 (2001).
254. S. V. Sennikov, S. V. Krysov, T. V. Injelevskaya, A. N. Silkov, L. V. Grishina, V. A. Kozlov, *J. Immunol. Methods* **275**, 81 (2003).
255. S. J. Swanson, S. J. Jacobs, D. Mytych, C. Shah, S. R. Indelicato, R. W. Bordens, *Developments in Biological Standardization* **97**, 135 (1999).
256. J. Kankare, K. Haapakka, S. Kulmala, V. Nanto, J. Eskola, H. Takalo, *Anal. Chim. Acta* **266**, 205 (1992).
257. D. Hermsen, L. Franzson, J. P. Hoffmann, A. Isaksson, J. M. Kaufman, E. Leary, C. Muller, K. Nakatsuka, Y. Nishizawa, H. Reinauer, W. Riesen, H.-J. Roth, T. Steinmuller, T. Troch, P. Bergmann, *Clin. Lab. (Heidelberg, Germany)* **48**, 131 (2002).
258. X. H. Xu, R. B. Jeffers, J. Gao, B. Logan, *Analyst* **126**, 1285 (2001).
259. A. W. Butch, D. Crary, M. Yee, *Clin. Biochem.* **35**, 143 (2002).
260. A. Haese, T. Dworschack Robert, P. Piccoli Steven, J. Sokoll Lori, W. Partin Alan, W. Chan Daniel, *Clin. Chem.* **48**, 944 (2002).
261. P. B. Luppa, S. Reutemann, U. Huber, R. Hoermann, S. Poertl, S. Kraiss, S. Von Buelow, D. Neumeier, *Clin. Chem. Lab. Med.* **36**, 789 (1998).
262. R. Sapin, J.-L. Schlienger, F. Gasser, E. Noel, B. Lioure, F. Grunenberger, B. Goichot, D. Grucker, *Clin. Chem. (Washington, DC, United States)* **46**, 418 (2000).
263. M. Sanchez-Carbayo, M. Mauri, R. Alfayate, C. Miralles, F. Soria, *Clin. Biochem.* **32**, 395 (1999).

264. S. Kulmala, M. Hakansson, A. M. Spehar, A. Nyman, J. Kankare, K. Loikas, T. Ala-Kleme, J. Eskola, *Anal. Chim. Acta* **458**, 271 (2002).
265. O. Hetland, K. Dickstein, *Clin. Chem.* **44**, 1348 (1998).
266. J. Ishii, T. Ishikawa, J. Yukitake, Y. Nagamura, M. Ito, J. H. Wang, Y. Kato, S. Hiramitsu, S. Inoue, T. Kondo, S. Morimoto, M. Nomura, Y. Watanabe, H. Hishida, *Clin. Chim. Acta, Int. J. Clin. Chem.* **270**, 183 (1998).
267. P. O. Collinson, B. Jorgensen, C. Sylven, M. Haass, F. Chwallek, H. A. Katus, M. Muller-Bardorff, U. Derhaschnig, M. M. Hirschl, R. Zerback, *Clin. Chim. Acta* **307**, 197 (2001).
268. E. Moreau, J. Philippe, S. Couvent, G. Leroux-Roels, *Clin. Chem.* **42**, 1450 (1996).
269. K. R. Klingler, D. Zech, K. Wielckens, *Clin. Lab. (Heidelberg)* **46**, 41 (2000).
270. J. H. Tai, M. S. Ewert, G. Belliot, R. I. Glass, S. S. Monroe, *J. Virol. Methods* **110**, 119 (2003).
271. K. N. Reetoo, S. A. Osman, S. J. Illavia, J. E. Banatvala, P. Muir, *J. Virol. Methods* **82**, 145 (1999).
272. R. Boom, C. Sol, J. Weel, Y. Gerrits, M. de Boer, P. Wertheim-van Dillen, *J. Clin. Microbiol.* **37**, 1489 (1999).
273. S. J. Wu, E. M. Lee, R. Putvatana, R. N. Shurtliff, K. R. Porter, W. Suharyono, D. M. Watts, C. C. King, G. S. Murphy, C. G. Hayes, J. W. Romano, *J. Clin. Microbiol.* **39**, 2794 (2001).
274. J. D. Fox, S. Han, A. Samuelson, Y. Zhang, M. L. Neale, D. Westmoreland, *J. Clin. Virol.* **24**, 117 (2002).
275. S. J. C. Stevens, M. B. H. J. Vervoort, A. J. C. Van den Brule, P. L. Meenhorst, C. J. L. M. Meijer, J. M. Middeldorp, *J. Clin. Microbiol.* **37**, 2852 (1999).
276. R. A. Collins, L.-S. Ko, K. Y. Fung, L.-T. Lau, J. Xing, A. C. H. Yu, *Biochem. Biophys. Res. Commun.* **297**, 267 (2002).
277. B. van Gemen, R. van Beuningen, A. Nabbe, D. van Strijp, S. Jurriaans, P. Lens, T. Kievits, *J. Virol. Methods* **49**, 157 (1994).
278. T. E. Schutzbank, J. Smith, *J. Clin. Microbiol.* **33**, 2036 (1995).
279. J. H. Kenten, S. Gudibande, J. Link, J. J. Willey, B. Curfman, E. O. Major, R. J. Massey, *Clin. Chem. (Washington, DC, United States)* **38**, 873 (1992).
280. H. Yu, J. G. Bruno, T. C. Cheng, J. J. Calomiris, M. T. Goode, D. L. Gatto-Menking, *J. Biolumin. Chemilumin.* **10**, 239 (1995).
281. J. J. Oprandy, K. Amemiya, J. H. Kenten, R. G. Green, E. O. Major, R. Massey, *Technical Advances in AIDS Research in the Human Nervous System (Proceedings of an NIH Symposium on Technical Advances in AIDS Research in the Human Nervous System), Washington, DC, Oct. 4–5, 1993*, 281 (1995).
282. S. Hibbitts, A. Rahman, R. John, D. Westmoreland, J. D. Fox, *J. Virol. Methods* **108**, 145 (2003).
283. R. A. Collins, L.-S. Ko, K.-Y. Fung, K.-Y. Chan, J. Xing, L.-T. Lau, A. C. H. Yu, *Biochem. Biophys. Res. Commun.* **300**, 507 (2003).
284. R. A. Collins, L.-S. Ko, K.-L. So, T. Ellis, L.-T. Lau, A. C. H. Yu, *J. Virol. Methods* **103**, 213 (2002).
285. S. Shan, L.-S. Ko, R. A. Collins, Z. Wu, J. Chen, K.-Y. Chan, J. Xing, L.-T. Lau, A. C.-H. Yu, *Biochem. Biophys. Res. Comm.* **302**, 377 (2003).
286. I. Miyashiro, C. Kuo, K. Huynh, A. Iida, D. Morton, A. Bilchik, A. Giuliano, D. S. B. Hoon, *Clin. Chem. (Washington, DC, United States)* **47**, 505 (2001).
287. C. D. O'Connell, A. Juhasz, C. Kuo, D. J. Reeder, D. S. B. Hoon, *Clin. Chem. (Washington, DC)* **44**, 1161 (1998).
288. B. Taback, A. D. Chan, C. T. Kuo, P. J. Bostick, H.-J. Wang, A. E. Giuliano, D. S. B. Hoon, *Cancer Res.* **61**, 8845 (2001).
289. D. S. B. Hoon, C. T. Kuo, S. Wen, H. Wang, L. Metelitsa, C. P. Reynolds, R. C. Seeger, *Am. J. Pathol.* **159**, 493 (2001).

290. A. Gellings, G. Holzem, K. Wielckens, K. R. Klingler, *Laboratoriumsmedizin* **25**, 26 (2001).
291. R. S. Lanciotti, A. J. Kerst, *J. Clin. Microbiol.* **39**, 4506 (2001).
292. M. D. de Jong, J. F. Weel, T. Schuurman, P. M. Wertheim-van Dillen, R. Boom, *J. Clin. Microbiol.* **38**, 2568 (2000).
293. H. J. Stern, R. D. Carlos, T. E. Schutzbank, *Clin. Biochem.* **28**, 470 (1995).
294. B. D. Muegge, M. M. Richter, *Anal. Chem.* **74**, 547 (2002).
295. R. Y. Lai, M. Chiba, N. Kitamura, A. J. Bard, *Anal. Chem.* **74**, 551 (2002).
296. F. Jameison, R. I. Sanchez, L. Dong, J. K. Leland, D. Yost, M. T. Martin, *Anal. Chem.* **68**, 1298 (1996).
297. A. F. Martin, T. A. Nieman, *Biosens.Bioelectron.* **12**, 479 (1997).
298. A. J. Baeumner, M. C. Humiston, R. A. Montagna, R. A. Durst, *Anal. Chem.* **73**, 1176 (2001).
299. J. L. Call, M. Arrowood, L. T. Xie, K. Hancock, V. C. Tsang, *J. Parasitol.* **87**, 203 (2001).
300. Y. M. Lee, P. W. Johnson, J. L. Call, M. J. Arrowood, B. W. Furness, S. C. Pichette, K. K. Grady, P. Reeh, L. Mitchell, D. Bergmire-Sweat, W. R. Mackenzie, V. C. Tsang, *Am. J. Trop. Med. Hyg.* **65**, 1 (2001).
301. E. Kuczynska, G. Boyer Douglas, R. Shelton Daniel, *J. Microbiol. Methods* **53**, 17 (2003).
302. D. R. Shelton, J. S. Karns, *Appl. Environ. Microbiol.* **67**, 2908 (2001).
303. J. Min, A. J. Baeumner, *Anal. Biochem.* **303**, 186 (2002).
304. C. G. Crawford, C. Wijey, P. Fratamico, S. I. Tu, J. Brewster, *J. Rapid Methods Autom. Microbiol.* **8**, 249 (2000).
305. H. Yu, J. G. Bruno, *Appl. Environ. Microbiol.* **62**, 587 (1996).
306. H. Yu, J. G. Bruno, *Biomed. Prod.* **20**, 20 (1995).
307. T. M. Kijek, C. A. Rossi, D. Moss, R. W. Parker, E. A. Henchal, *J. Immunol. Methods*, **236**, 9 (2000).
308. H. Yu, J. W. Raymonda, T. M. McMahon, A. A. Campagnari, *Biosens. Bioelectron.* **14**, 829 (2000).
309. J. G. Bruno, H. Yu, *Appl. Environ. Microbiol.* **62**, 3474 (1996).
310. D. L. Gatto-Menking, H. Yu, J. G. Bruno, M. T. Goode, M. Miller, A. W. Zulich, *Biosens. Bioelectron.* **10**, 501 (1995).

# – 14 –

# Spectroelectrochemistry

**Tia E. Keyes and Robert J. Forster**

National Centre for Sensor Research, School of Chemical Sciences,
Dublin City University, Dublin 9, Ireland

## 14.1 INTRODUCTION

Electrochemistry can provide both thermodynamic and kinetic information on a range of chemical processes driven by electron transfer. However, electrochemistry can rarely unequivocally identify electroactive species; the molecular identity of a new electrogenerated material is typically inferred from the measured physical properties of a known standard system. In addition, electrochemistry provides only limited and indirect information on structural changes accompanying redox events.

In the past two decades, spectroelectrochemical techniques (i.e., tandem spectroscopic and electrochemical methods) have been exploited across diverse applications ranging from inorganic and organic chemistry to biochemistry. Spectroscopically acquired molecular information under potential control, including vibrational frequencies, molar absorptivities, luminescence intensities, and electronic or magnetic resonance frequencies, are now routinely available. Such combinations of electrochemical and spectroscopic techniques have contributed to the elucidation of electron transfer reaction mechanisms and to the understanding of fundamental molecular states at interfaces. For example, spectroelectrochemistry can yield clues to the mechanism of photoinduced electron transfer processes by providing static products which mirror those that are produced only fleetingly in transient spectroscopy (1).

There is extensive literature on applications of spectroelectrochemistry and the myriad of cell designs and techniques which have been applied. We focus here on the most common optical techniques that are performed *in situ* and those which can be undertaken under ambient conditions. By focusing in this way on optical methodologies we exclude a range of important non-optical techniques such as mass spectrometry, EPR, and NMR and those which require specialized conditions such as ultra high vacuum including X-ray and photoelectron methods. Details of these experiments and methods can be found in the literature (2). This chapter gives insight into experimental considerations for qualitative and quantitative spectroelectrochemical measurements and outlines common applications. We


**Handbook of Electrochemistry**
**Edited by C.G. Zoski**

focus on the use of spectroelectrochemistry in elucidating mechanisms and intermediates in electrode reactions rather than in elucidation of interfacial structure.

Conventional spectroelectrochemistry involves bulk electrolysis of an analyte in a low volume cell combined with simultaneous or subsequent *in situ* spectroscopic investigation. The key point is that investigations are *in situ* with spectroscopic studies undertaken within an electrochemical cell that is under potential control. Spectroelectrochemical experiments are frequently qualitative and are used to structurally characterize an intermediate redox state. Quantitative measurements can be experimentally challenging because they require rigorous geometric arrangement of the cell to avoid problems such as iR drop and low current densities as a consequence of the relative size of the working electrode and its orientation with respect to the other electrodes.

The spectroelectrochemical cell design is critically dependent on the spectroscopic technique being used. Parameters such as cell orientation with respect to optical source and detector and electrode transparency are dictated by how the optical changes are interrogated (i.e., whether through light transmission as in electronic spectroscopy or light scattering as in Raman spectroscopy). Most cells follow the conventional three-electrode configuration: with reference and auxiliary electrodes and a working electrode on which the optical path is generally trained. Another common feature of spectroelectrochemical methods is the requirement for small reagent volumes in order to minimize the time required for the cell to reach equilibrium at a given applied potential. Small solution volumes can also minimize background interference from solvent and electrolyte. Thin layer cells are consequently common in spectroelectrochemistry and these are described below. We begin by examining how light interacts with a solid electrode material.

## 14.2 LIGHT TRANSMISSION AND REFLECTION AT AN ELECTRODE SURFACE

Light striking a dielectric interface can undergo a number of processes, the most important of which are reflection, absorption, and scattering. In a spectroscopic experiment, the intensity of light incident on a surface, $I_0$, is compared to that which has been transmitted through the medium, $T = I_0/I$, scattered from the medium $S = I_s/I_0$ or reflected from the medium, where $R = I_r/I$. A material's optical parameters (i.e., reflectivity, transmissivity, and absorbtivity) are described by the Fresnel equations which define these properties in terms of the materials refractive index, $n'$, where $n' = n_r + ik_i$ or complex dielectric constant $\varepsilon' = \varepsilon_r + ik_i$. These two parameters are interrelated since $n' = \sqrt{\varepsilon'}$. Fresnel also describes the incident angle dependent intensity reflection coefficients and transmission coefficients for the electric field vectors of light which are perpendicularly (s) and parallel (p) polarized relative to the plane of incidence (when light is incident, but not normal on a surface) (3). In other words, the intensities of the s and p-polarized components of reflected light varies and depends on the angle of the incident beam. The dominant processes in light interaction at an interface are reflection, transmission, and elastic scattering of light. Inelastic scattering, as in the case of Raman scattering, is a much weaker phenomenon. Figure 14.1 shows common optical geometries for transmission and reflectance measurements used in optical spectroelectrochemistry. Optical transmission

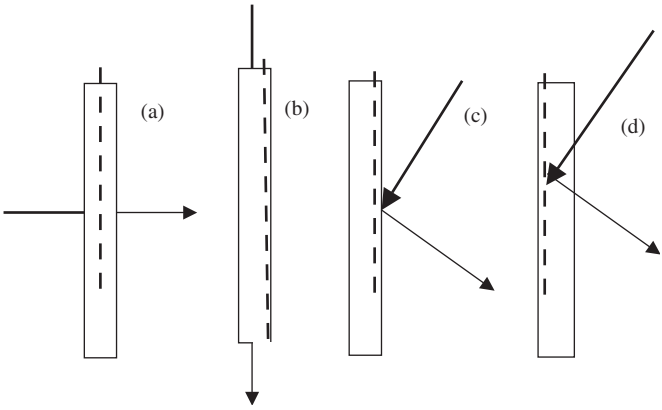


**Figure 14.1** Common optical configurations for spectroelectrochemical cells showing path of incident light (thick line) and detected light (thin line) in (a) transmission mode normal to the electrode and (b) transmission mode parallel to the electrode, internal (c) and external (d) reflectance modes. The dashed line represents the electrode solution interface.

experiments are the most common optical arrangement. They are based on the measurement of the wavelength-dependent decrease in the intensity of incident light, $I_0$, following its passage through an absorbing medium. In a conventional absorbance experiment, the optical arrangement minimizes the contribution of scatter and reflection from the sample so that the main contribution to the decrease in $I_0$ arises from absorption; therefore absorbance $A = -\log(I/I_0)$ or $-\log(T)$.

In absorbance or transmission measurements in spectroelectrochemistry, scattering and reflection must also be minimized to provide an optimum signal-to-noise ratio. Since the working electrode generally presents a reflective surface, minimizing scatter and reflection can prove challenging and lead to distortions of the optical signal in an absorbance experiment. The use of optically transparent electrodes (OTEs) in which the incident light is perpendicular or normal to the electrode surfaces significantly reduces such interferences. An alternative transmission arrangement directs the optical path parallel to the electrode (Figure 14.1b).

In a reflectance experiment, incident light reflected from a sample at a surface $R_2$ is measured and compared to light reflected from a bare surface, $R_1$. The differential reflectance, $\Delta R/R_1$, where $\Delta R$ is $R_2 - R_1$, is the difference in reflectance between a clean surface and that on which the analyte is placed. In a spectroelectrochemical experiment, it may indicate the difference in reflectance in the absence and presence of applied potential. Since this is a differential value, it is frequently very small and therefore it is important to limit background contributions to the signal.

## 14.3 ELECTRONIC SPECTROSCOPY

Electronic spectroelectrochemistry is the most commonly reported form of spectroelectrochemistry due to its ease of use, low cost, and its value in obtaining both quantitative and qualitative information on electrochemical processes. Electronic spectroscopy addresses

the transitions that occur between electronic states within a target analyte. Such transitions generally occur in the ultra-violet or visible region (190–700 nm of the electromagnetic (EM) spectrum) or less frequently in the near infrared (NIR), ~700–3000 nm. Electrochemistry directly addresses the valence electrons of a given species through oxidation or reduction and changes in these electronic states are naturally reflected in the associated electronic spectroscopy. Therefore, UV-vis-NIR or electronic spectroelectrochemistry is valuable for elucidating the nature of electronic changes induced by a redox process. UV-vis spectrometers conventionally operate in a transmission mode, where absorbance is expressed in terms of percentage transmittance where $A = \log(100/\%T) = 2.000 - \log(\%T)$ is the measured absorbance. Absorbance is directly related to an absorbing species concentration according to the Beer–Lambert Law, $A = \varepsilon cL$, where $L$ is the path length through the sample, $c$ is the concentration of the absorbing species, and $\varepsilon$ is the molar absorptivity or extinction coefficient.

### 14.3.1 Transmittance spectroscopy and optically transparent cell materials

Transmission electronic spectroscopy, the most facile and readily available spectroscopic technique for investigating electrochemical reactions, became possible due to the availability of OTEs. The underlying principle is that the working electrode, usually solid, is optically transparent. This means that it transmits more than 50% of incident light within the wavelength region of interest.

Prerequisites of working electrode materials for OTEs include optical transparency, amenable potential windows, and stability towards electrolyte and solvent. There are broadly two types of OTE materials in common use:

#### *14.3.1.1 Thin conducting film electrodes*

Thin metal films include vapor deposited or sputtered Au, Ag, or Pt on transparent substrates such as glass, quartz, or plastic. On quartz, an optical window ranging from 220 nm through the visible and NIR spectral regions is possible, whereas glass or plastic substrates are useful only in the visible and to a variable extent, in the NIR region. The deposition of metal films of Pt and Au typically requires an undercoating of transition metal (ca. 5 nm), such as W or Ti to improve adhesion and to stabilize the conducting metal film. Another useful approach in stabilizing such thin metal films on glass or quartz is to silylate the substrate with mercaptotrimethoxysilane. The thiol group binds the metal and stabilizes the metal film. This is particularly important in the case of gold which is vulnerable to damage from friction and produces very robust transparent electrode materials (4). The metal film must be sufficiently thin (i.e., less than ~200 nm thick) to maintain optical transparency. A drawback then is that the metal film can be poorly conducting.

Thin films of transparent metal oxide semiconductor (e.g., indium tin oxide and fluorine doped tin oxide) deposited on a transparent medium are finding increasing application because thick films can be used due to the optical transparency of metal oxides in the visible region of the spectrum and there are fewer problems with resistance than for thin metal films. The drawback to these materials is that they do not transmit ultra violet

wavelengths and are thus limited to optical studies in the visible and NIR spectral regions. High levels of dopant can also reduce their optical transmittance.

Diamond electrodes are finding increasing application in transmission spectroelectrochemical methods (5). Optically transparent diamond electrodes are fabricated in a number of ways. Chemical vapor deposited diamond (CVD) is the most common form. Polycrystalline diamond can be grown on metal substrates and then separated for use as an optical window (6). Thin film diamond can be deposited on optically transparent substrates (7, 8). Conducting diamond film has been used as a transparent electrode for attenuated total reflectance infrared (ATR-IR) spectroscopy (9). High purity diamond has an excellent optical transparency, transmitting from ~225 nm (where it has a bandgap absorption) to the far IR (typically >50% transparency). However, diamond is a poor conductor and requires doping (e.g., with boron) to produce a useful electrode material. Unfortunately, the optical properties are degraded by doping and the available wavelength range and transparency are considerably reduced. Even so, diamond possesses a wide potential window, is resistant to fouling, and can tolerate extreme solvent conditions.

#### *14.3.1.2 Minigrid electrodes*

Semi-transparent materials in the form of minigrids or meshes of conducting materials have found extensive application in UV-vis and UV-vis-NIR spectroelectrochemistry. These are metals which are primarily commercially available as meshes (e.g., gold, platinum, or platinum–rhodium alloy) but porous reticulated vitreous carbon and other less common metals and alloys such as Hg coated gold have also been used (10, 11). The optical transparency of the minigrid depends on the dimensions of the crossbars and the pitch of the mesh but overall the transparency is 50% or greater. The very large surface areas and conductivity of these materials means exhaustive electrolysis can be achieved very quickly. The dimensions of the micromesh, pore size, and wire thickness is important in determining the diffusion behavior at a mesh electrode. A simulation of cyclic voltammetry at a minigrid Pt electrode was recently reported; useful limits were given for electrode dimensions within which thin layer behavior is maintained (12).

The auxiliary and reference electrodes in electronic and other spectroelectrochemical experiments are similar to those used in conventional electrochemical cells. They must be small enough to fit into the cell without complicating its construction. Common auxiliary electrodes are small platinum wires, paddles, or coils. Reference electrodes (see Chapter 4) are frequently $Ag/Ag^+$ or AgCl because these can be miniaturized. In non-quantitative applications, silver wire coated with AgCl or a simple silver wire as a pseudo reference (quasi-reference electrode, QRE) can be used. However, commercially available aqueous and non-aqueous $Ag/Ag^+$ in which the electrode is separated from the analyte solution via a frit are preferable because they are more stable. The majority of electronic spectroelectrochemical experiments are conducted using OTEs in either thin layer (finite) or semi-infinite diffusion regimes.

### 14.3.2 Thin layer spectroelectrochemistry

A challenge in using bulk electrolysis to generate redox states for *in situ* spectroscopic investigations is to minimize the time for exhaustive electrolysis. The most common

approach uses large working electrode area-to-solution volume ratios to create efficient convective mass transfer. An extensive range of optically transparent thin layer electrode (OTTLE) spectroelectrochemical designs have been used for transmission experiments in electronic spectroelectrochemistry (13–16). Some simple OTTLE designs for electronic spectroscopy for static and flow cells are shown in Figure 14.2.

In the simplest approach, a short path length quartz cuvette is constructed either with a reservoir at the top or side arms into which the counter and reference electrodes can be placed.

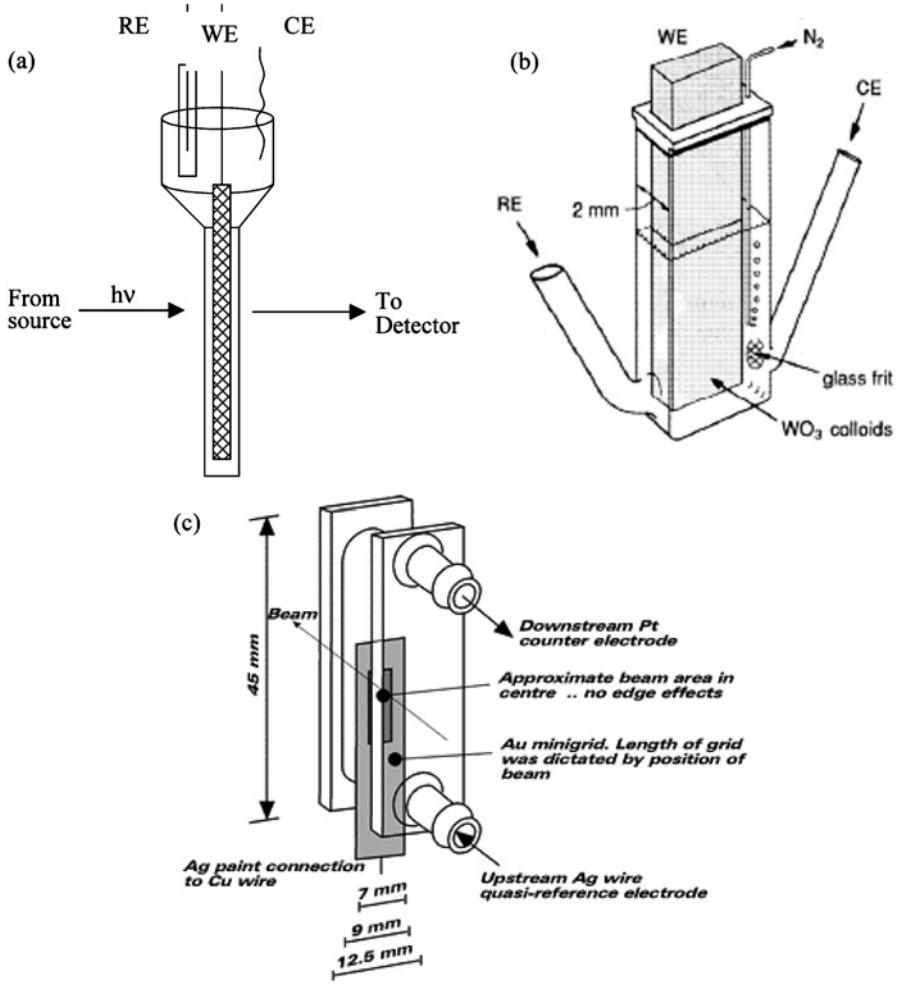


**Figure 14.2** OTTLE cells for UV-vis-NIR spectroscopy (a) employing a metal mesh electrode and conventional thin layer cuvette with reservoir for counter and reference electrodes, (b) a thin layer cuvette with side arms for counter and reference electrodes, reproduced with permission of American Chemical Society, (c) a thin layer flow cell. Reprinted with permission from reference (16). Copyright 1989 and 1993, American Chemical Society.

A common arrangement for thin layer geometry is to sandwich the solution between glass and an ITO electrode using a Teflon or Kapton spacer; such cells are now commercially available. For a thin layer arrangement, the cell width through which the excitation beam is directed ranges between 50 and 250 μm and the electrolysis rate is controlled by finite diffusion.

At short electrolysis times when mass transport occurs via linear diffusion, the approximate time, $t$, required to fully electrolyze the cell is given by

$$t = \delta^2 / \pi D \tag{14.1}$$

where $\delta$ is the thin layer thickness and $D$ is the diffusion coefficient of the analyte. Taking a typical diffusion coefficient of $1 \times 10^{-5}$ cm$^2$ sec$^{-1}$, equation (14.1) predicts that a 25 μm path length of a typical spectroelectrochemical cell (17) can be exhaustively electrolyzed in ~200 msec. This relatively rapid electrolysis time can provide the opportunity for the collection of dynamic information. In a system with slow heterogeneous electron transfer, this time can be significantly extended.

The cuvette is usually constructed so that it sits within a conventional spectrometer cell holder or it can be used with a fiber optic spectrometer. The reference and counter electrodes should be sufficiently small to fit into the reservoir or can be soldered to the nonconducting window of the cell. Elimination of oxygen is most frequently achieved by bubbling an inert gas such as argon or nitrogen through the solution prior to electrolysis and maintaining a blanket of inert gas over the solution during electrolysis.

Experimental set-ups have also included the use of milled polyethylene or Teflon stands into which optical windows are incorporated. These are designed to replace the sample holder in conventional spectrometers and may incorporate temperature control through the flow of cooled $N_2$. Modern spectrometers have a range of options for cell holders including temperature control. For applications employing thin layer cells with the optical path normal to the electrode, cells such as those shown in Figure 14.2 work well. Because the cell is so narrow in the thin layer arrangement, there is no bulk solution within the optical path and all of the material in this cell geometry lies within the diffusion layer; electrolysis is very rapid, typically occurring within a few tens of milliseconds. This arrangement is used to provide spectral information on an electrochemical system when the reagents have achieved equilibrium at an applied potential. In flow cells based on the OTTLE cell design, the channel electrode geometry consists of a gold minigrid electrode mounted within a thin layer silica cell as shown in Figure 14.2c with a reference electrode positioned upstream and a counter electrode downstream (16). Solution flows into the cell from a reservoir, is electrolyzed, and the spectrum collected. The low cell volume permits exhaustive electrolysis, eliminating contribution from the parent species.

Poor geometric arrangement of auxiliary and reference electrodes relative to the working electrode results in significant and spatially varying iR drop across the surface of the working electrode. This ohmic polarization is a serious problem in conventional bulk electrolysis, and can be difficult to overcome in the OTTLE arrangement (18). It is not important as long as quantitative time-dependent data are not required, the volume of the cell and concentration of the analyte is sufficiently small so that extensive convective mass transfer is not required and sufficient time is allowed for exhaustive electrolysis during each spectroelectrochemical potential step, as given by equation (14.1). For quantitative

measurements, poor geometric arrangement is alleviated by using a sandwich arrangement in which Pt foils, for example, are positioned at either side of the working electrode to regulate current flow and an internal reference point is set to alleviate poor potential control (19). In qualitative studies, bulk electrolysis is used as a means of electrolyzing the sample exhaustively at one or more discrete potentials. There is usually no requirement for kinetic control at the working electrode and a slow response at the counter-electrode, due to its small relative area, is not as critical a consideration as it is for conventional electrode measurements.

Qualitative electronic spectroelectrochemistry using thin layer cells has found broad application across organic and inorganic chemistry. In such an experiment, a complete UV-vis-NIR spectrum is recorded at a fixed potential. The voltammetry of the species in question is obtained first, followed by the spectroscopic signature of the chemical species formed in each redox step using spectroelectrochemistry. Analysis of such voltammograms can provide clues to the nature of intermediate redox states and lead to quantitative information gathered from the resulting spectroscopy on molecular parameters such as electron delocalization in a new species. Investigation of the extent of electronic communication in multinuclear metal complexes has been studied using spectroelectrochemistry in this way and provides information about mixed valence complexes which are frequently inaccessible synthetically. Figure 14.3a illustrates the spectroelectrochemical response of a 2,3,5,6-tetrakis(2-pyridyl)-pyrazine (tppz)-bridged diruthenium complex $[\{(L)ClRuII\}_2(\mu\text{-tppz})](ClO_4)_2$, where L = 2,2-dipyridylamine, Figure 14.1b (20). Voltammetry demonstrates that the two metal oxidations in this symmetric complex are separated by 380 mV. Such large peak-to-peak separations exceed what would be expected from electrostatic and statistical effects of oxidizing only one side of the complex on the remaining reduced metal center and is generally indicative of metal–metal communication.

Spectroelectrochemistry provides a convenient avenue to assess whether this conclusion is correct by allowing the isolation and spectroscopic study of the mixed valence state. Oxidation of the first metal center results in the formation of the mixed valence Ru(II)Ru(III) ion reflected in the grow-in of a new optical transition centered at 1700 nm ($\varepsilon$ = 2250 $dm^3\ mol^{-1}\ cm^{-1}$) and identified as an intervalence charge transfer transition (IVCT). The optical characteristics of such transitions can be analyzed according to the Hush theory (21) and used to estimate the extent of electronic coupling between two metals across the intervening bridge. The full width at half maximum (FWHM) ($v_{1/2}$) of the

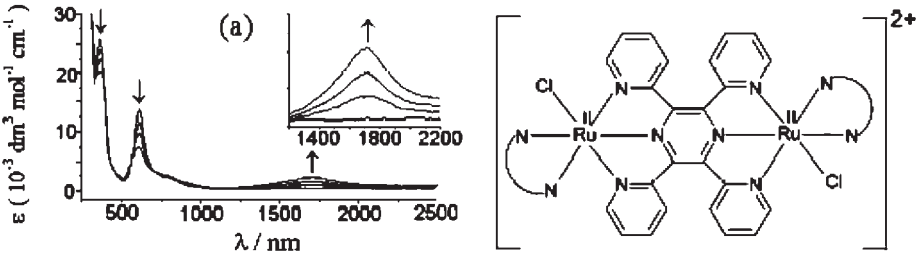


**Figure 14.3** UV-vis-NIR spectroelectrochemistry of a mixed valence metal complex, reproduced from reference (20) with permission from The Royal Society of Chemistry.

IVCT band reflects the extent of electronic delocalization between the metal centers and this was measured to be 1390 $cm^{-1}$. For a compound in which the electron on the reduced metal is localized on that metal, known as a class II system, $v_{1/2}$ can be theoretically predicted from the Hush theory and this was estimated to be 3680 $cm^{-1}$ for this complex. The considerably narrower experimental IVCT observed reflects significant delocalization of electron density across the metal centers which is further reflected in the coupling constant, $H_{AB}$, which was estimated be 2940 $cm^{-1}$. On the basis of spectroelectrochemistry, this complex is assigned as a class III or delocalized species in which the mixed valence state is more accurately described as Ru(2.5)-Ru(2.5).

Electronic spectroelectrochemistry can provide insight into the nature of electrochemical intermediates in redox active materials where the identity of each redox step is ambiguous. For example, in metal complexes containing redox active ligands, it may be difficult to distinguish between the metal and ligand-based redox processes by electrochemistry alone.

Figure 14.4 shows the electronic spectroelectrochemistry of a dinuclear ruthenium complex bridged via a hydroquinone linker (22).

Voltammetry of this complex showed three reversible oxidation waves at 0.13, 0.54, and 1.32 V vs. SCE. On the basis of electrochemistry alone, it was difficult to assign the redox responses as being metal or hydroquinone bridge based. UV-vis-NIR spectroelectrochemistry shown in Figure 14.4 confirmed that the first two oxidation steps were hydroquinone bridge based. The metal to ligand charge transfer (MLCT) persisted through the first two oxidation steps and new NIR transitions associated with semiquinone to metal charge transfer and quinone to metal charge transfer were observed. As for the dinuclear complexes described above, the bandwidth of these new transitions revealed different extents of delocalization of electron density across the molecule for each oxidation state.

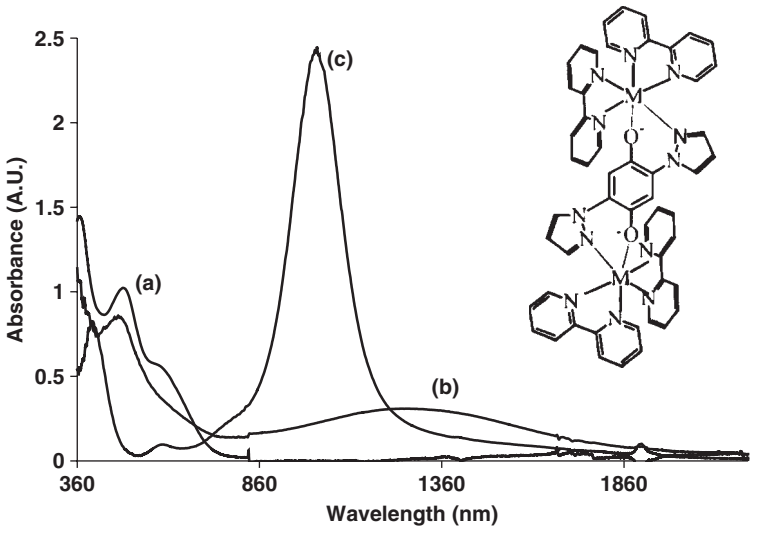


**Figure 14.4** Electronic spectroelectrochemistry of $[Ru(bpy)_2)_2(Pqyr)]^{4+}$ (inset) (a) at open circuit potential and on application of (b) 0.3 V and (c) 0.8 V versus SCE.

Spectroelectrochemistry reveals that the semiquinone state is highly localized whereas there is considerable mixing of quinone and metal states. Such information is impossible to extract from electrochemical measurements alone.

One of the most useful quantitative experiments in thin layer spectroelectrochemistry is the Nernst plot which leads to accurate values for the formal redox potential $E^{\circ\prime}$ and the number of electrons, $n$, transferred during an electrochemical reaction. For reversible electrochemistry, the following reaction

$$O + ne^- \rightleftharpoons R$$

exhibits Nernstian behavior. In a thin layer cell, electrolysis equilibrium is achieved rapidly thus ensuring that the concentrations of oxidized and reduced species in solution and at the interface are the same. Then

$$E_{applied} = E^{\circ\prime} + \frac{RT}{nF} \ln \frac{[O]}{[R]} \tag{14.2}$$

In a Nernst plot, a series of potentials encompassing the peak potentials of the redox process under interrogation are applied sequentially and spectra collected when the system has reached equilibrium at each potential. The resulting ratios of the oxidized and reduced form of the reagent are calculated for each potential using the Beer–Lambert law

$$\frac{[O]}{[R]} = \frac{(A_i - A_R)/\Delta\varepsilon.L}{(A_O - A_i)/\Delta\varepsilon.L} = \frac{A_i - A_R}{A_O - A_i} \tag{14.3}$$

where $A_O$ and $A_R$ are the absorbances of the fully oxidized and reduced forms of the analyte and $A_i$ is the absorbance at intermediate applied potentials. $\Delta\varepsilon$ is the difference in extinction coefficient between O and R at the monitoring wavelength and $L$ is the path length. Substituting equation (14.3) into the Nernst equation (14.2), leads to equation (14.4)

$$E_{applied} = E^{\circ\prime} + \frac{RT}{nF} \ln \frac{A_i - A_R}{A_O - A_i} \tag{14.4}$$

Plots of $E_{applied}$ versus $\ln(A_i - A_R)/(A_O - A_i)$ are linear for reversible systems; $E^{\circ\prime}$ is determined from the intercept and $n$ from the slope. Because the spectra are measured under equilibrium conditions, iR drop is unimportant to the measurement. This description of $E^{\circ\prime}$ determination assumes that the two redox forms of the analyte have discrete absorbance spectra which do not overlap. It is also possible to assess $E^{\circ\prime}$ for more complex systems in which spectra are not well resolved through deconvolution of the contributions to the composite spectra. Spectropotentiostatic measurements of this type have been applied to multiredox steps in supramolecular systems containing several of the same chromophore units undergoing sequential redox steps. Distributions of redox species can be estimated using iterative algorithms based on the Nernst equation to obtain $E^{\circ\prime}$ values for each step (23).

Chronoabsorptometry has been used extensively in protein electrochemistry to obtain kinetic information on heterogeneous electron transfer rates for forward and reverse reactions. Heterogeneous electron transfer in such systems is often kinetically slow due to

inaccessibility of the redox center which can be embedded deeply within a protein structure. The small volumes used in thin layer cells makes them amenable to biological studies where only limited amounts of reagent are available. Chronoabsorptometry has provided insight into structure–function relationships in complex biological systems which would not have been possible through electrochemistry alone. Single potential step chronoabsorptometry, asymmetric double potential step chronoabsorptometry, and cyclic potential scan chronoabsorptometry are used in assessing kinetic parameters for heterogeneous electron transfers in complex and sometimes irreversible systems (24).

Indirect electrochemical methods are used to investigate a site which may be embedded in a macromolecular structure, making direct heterogeneous electron transfer at the electrode impossible. Smaller redox active species, electron transfer mediators, are then employed which diffuse to the redox active site in the biomolecule, undergo a homogenous electron transfer, and then diffuse to the electrodes to undergo oxidation or reduction. These mediators are ideally spectroscopically silent in the region of interest and possess suitable thermodynamic characteristics to undergo facile electron transfer with the redox active site, without participating in any interfering interactions with the target molecule (25). This method has found use in protein electrochemistry. Figure 14.5 illustrates an example of a Nernst plot taken from absorbance data for the mediated spectroelectrochemistry of recombinant ferric soybean leghemoglobin (26) a (rLb), an oxygen binding heme protein, in its free form and when bound to nicotinate (rLb-N). The objective of the study was to examine the influence of alterations in axial ligand structure on the redox properties of the heme. Replacement of the water in (rLb) with nicotinamide, resulted in a cathodic shift of 95 mV in the heme reduction potential.

Detailed spectroelectrochemical studies on myoglobin and hemoglobin were undertaken using the same potentiospectrometric methodology but with $Ru(NH_3)_6Cl_2$ as the electron transfer mediator (27). The Nernst plots for these metalloproteins were shown to be sensitive indicators of alterations to the heme environment where sensitivity to aerobic and anaerobic conditions has provided important insights into heme binding of $O_2$ (28).

### 14.3.3 Spectroelectrochemistry: semi-infinite linear diffusion

Exhaustive electrolysis can be achieved within a short period of time in spectroelectrochemistry under semi-infinite diffusion conditions, even in the absence of convective mass transport. In these cells, the solution layer is thicker than that in the OTTLE cell and on application of potential the diffusion layer does not extend over the entire optical path.

For quantitative spectroelectrochemistry, chronocoulometric experiments are performed in semi-infinite diffusion spectroelectrochemical cells such as that shown in Figure 14.6 (29). An adjustable cell capable of both finite and semi-infinite diffusion conditions has also been reported which permits both thin layer and semi-infinite diffusion conditions to be selected (30). Typically, transparent film electrodes such as ITO are employed as the working electrode to avoid complicated diffusion parameters associated with a minigrid. Application of a potential step leads to a time-dependent response which is reflected in absorption changes. Assuming that the detector is set to monitor absorbance at a region where only the product, $P$, of the electrolysis absorbs, the absorbance change d$A$ across a

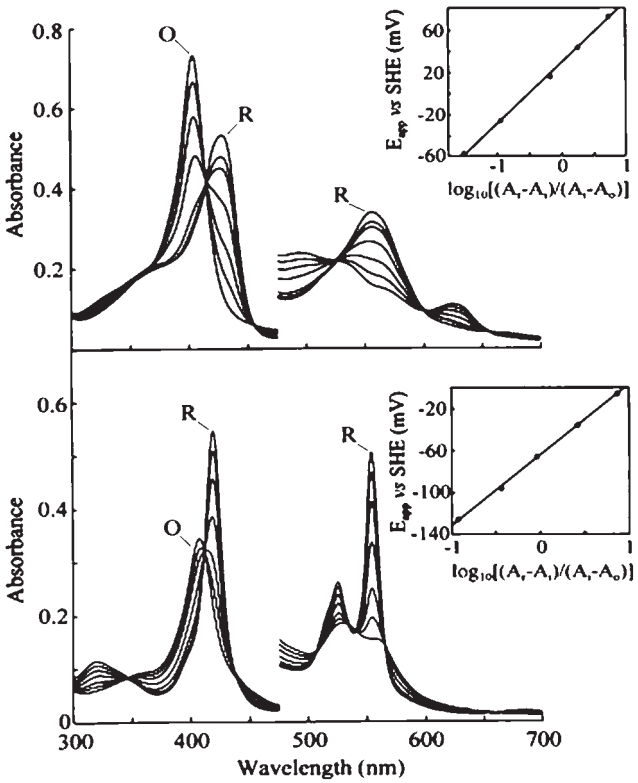


**Figure 14.5** Thin layer spectroelectrochemical data for rLb (top) and rLb–N (bottom) at various applied potentials, $E_{app}$ (mV vs. SHE). Fully oxidized (O) and fully reduced (R) spectra for each derivative are indicated. The insets show fits of the absorbance data at 403.5 nm (for rLb) and 419.5 (for rLb-N) to the Nernst equation. Absorbance values in the visible region (475–700 nm) have been multiplied by a factor of five. Conditions: sodium phosphate, pH 5.40, 25.0 °C, μ = 0.10 M for rLb; sodium phosphate, pH 5.42, 10 mM nicotinic acid, 25.0 °C, μ = 0.10 M for rLb-N. Reproduced from reference (26) with permission of Blackwell Publishing.

cross sectional area of thickness d$x$ which is uniformly irradiated is d$A = \varepsilon_P c(x,t)\mathrm{d}x$, where $c_P$ is the concentration of P and $\varepsilon_p$ its extinction coefficient, the integrated total absorbance $A$ is

$$A = \varepsilon_P \int_0^\infty c_P(x,t)\mathrm{d}x \tag{14.5}$$

Assuming the product $P$ is stable, this integral represents the total concentration of $P$ per unit area, which is equal to $Q/nFA$. $Q$, the charge passed during the electrolysis, is described by the integrated Cottrell or Anson equation. Therefore

$$A = \frac{2\varepsilon_P C_0^* D_0^{1/2} t^{1/2}}{\pi^{1/2}} \tag{14.6}$$

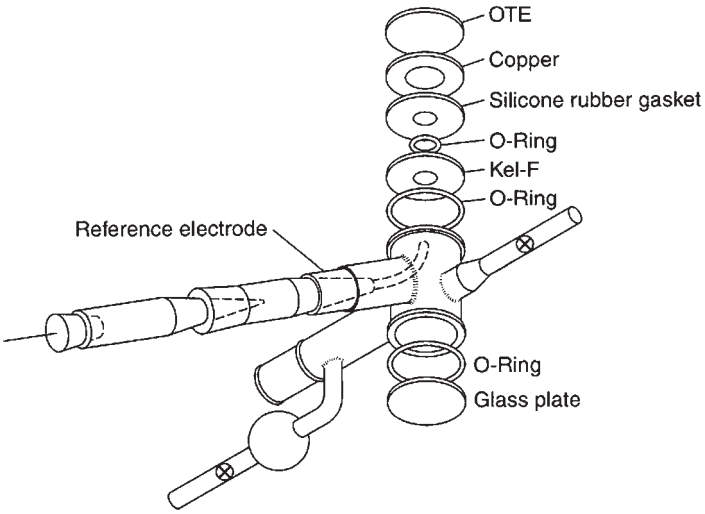


**Figure 14.6** Sandwich cell for semi-infinite diffusional spectroelectrochemistry. Reproduced from reference (29) with permission of Blackwell Publishing.

where $C_0^*$ is the bulk concentration of the precursor species and $D_0$ is the diffusion coefficient of this reagent. Plots of absorbance versus $t^{1/2}$ should be linear and once the extinction coefficient is known, can be used to determine $D_0$. In practice, this means that in transmittance mode, with the incident light normal to the electrode surface, the absorbance contains contributions from reagent within and outside of the diffusion layer.

Spectroelectrochemical cells employing OTTLE and semi-infinite diffusion dimensions work well as long as the material under investigation and its redox product have sufficient absorption cross sections to give reasonable a signal-to-noise ratio. The ideal absorbance working range is 0.3–1 AU because this range is least susceptible to interference from stray light and other noise.

### 14.3.4 Long optical pathway thin layer cells (LOPTLC)

For materials with low molar absorptivities, the use of thin layer cells is not practical because the concentrations required to achieve measurable absorption spectra using the thin cell regime may be prohibitive. Long optical path thin layer cells (LOPTLC) are useful in these circumstances (31, 32). In such a cell, the optical path runs parallel to the working electrode as demonstrated in Figure 14.1b. The advantages of this method are that the electrode, which is not in the optical path, can be opaque and lower concentrations of reagents can be used because of the increased sensitivity arising from the long optical path. Disadvantages include the electrolysis time which is often compromised in such cells. Additionally, because the incident light is not directed through the electrode, equations (14.5) and (14.3) no longer apply, so such cells are not suitable for dynamic studies. As described, the absorbance spectrum reflects the integral of the absorption of all species along the light

path. As the light is directed through a path in front of the working electrode and assuming the cell is symmetric along its length, this arrangement monitors the same set distance from the electrode, usually in the diffuse layer. This means that if the electrochemical reaction is anything other than a purely diffusive process, the parallel cell arrangement can lead to different spectral information than observed for the conventional optical path. This is particularly true for semi-infinite diffusion regimes where the absorbance spectrum from the conventional arrangement will simultaneously contain contributions from bulk, diffuse layer, and interface.

For example, a bidirectional thin layer cell was used to compare visible spectral data simultaneously collected for incident light normal to and parallel with the working electrode (Figure 14.7) (33) for a spectroelectrochemical study of the electropolymerization of 4,4′-bis(methylthio)-2,2′-bithiophene in acetonitrile. Significant spectral discrepancies were observed between the two optical arrangements as shown in Figure 14.7(ii). This was

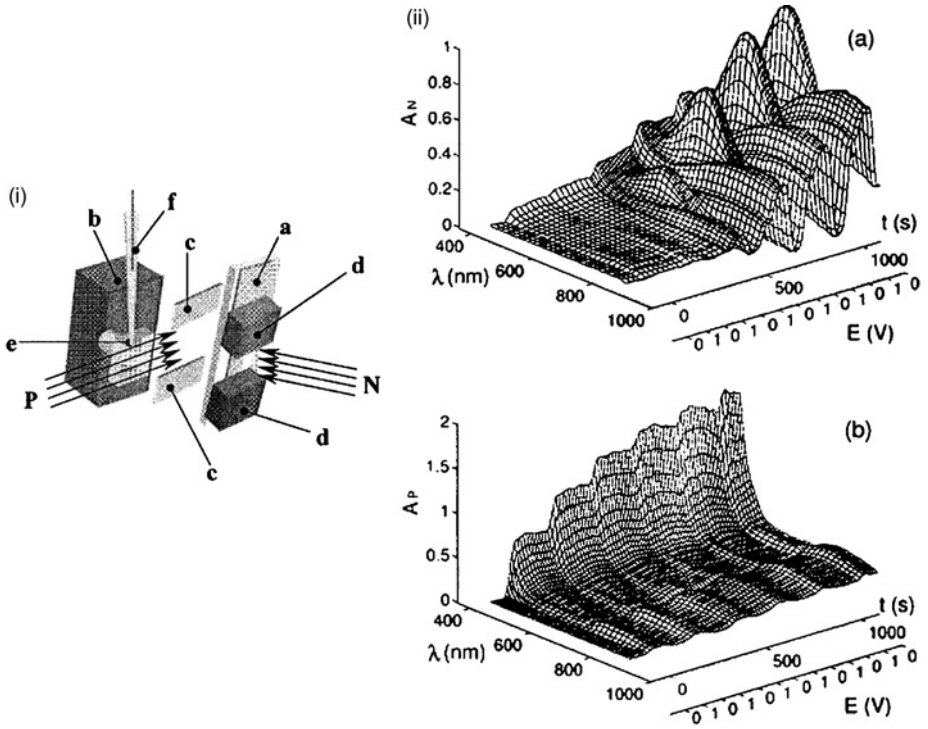


**Figure 14.7** (i) Schematic diagrams (3D, front and side views) of a bidirectional thin layer spectroelectrochemical cell. (a) Gold-sputtered working electrode; (b) epoxy resin piece; (c) spacers; (d) epoxy resin brackets; (e) circular window, diameter 3 mm; (f) reference electrode; (g) counter electrode. (N) Normal and (P) parallel-beam incident light paths. (ii) 3D plot of absorbance, potential time and wavelength obtained during electropolymerization of 0.005 mol $L^{-1}$ of 4-4′-bis(methylthio)-2,2′-bithiophene in acetonitrile with $TBAPF_6$ 0.1 M as the supporting electrolyte. Display of six scans at $v = 0.01$ V $sec^{-1}$; $\omega = 220$ μm; and $l = 3$ mm. (a) Normal-beam signal, (b) parallel-beam signal. Reprinted with permission from reference (33). Copyright 2001, American Chemical Society.

attributed to a complex electrochemical process that involved interfacial adsorption of the polymer in addition to diffusion-controlled electrolysis. A spectral response which included both the adsorption and diffusive processes was obtained in the normal optical arrangement, whereas the spectra from a parallel beam arrangement contained contributions from the diffuse species only. This example serves to highlight that caution must be exercised in the interpretation of data from parallel beam arrangements in complex electrochemical processes.

### 14.3.5 Reflectance spectroscopy

The majority of electronic spectroelectrochemical studies are based on transmission experiments interrogating solution phase analytes. Reflectance spectroscopy is particularly important in studies of thin films, solid deposits, or self-assembled mono- and multilayers at reflecting surfaces. The two most commonly applied techniques of reflectance spectroscopy are external reflectance and attenuated total reflectance (ATR).

#### *14.3.5.1 External reflectance spectroscopy*

In external differential reflectance spectroscopy, light incident on an opaque, reflective interface may be partially reflected and partly absorbed. The reflected light is detected and this contains the intensity of the incident beam minus components of the light absorbed by material at the interface. In UV-vis reflectance spectroscopy, the intensity of the reflected light is divided by the intensity of the incident beam according to equation (14.6). The reflectance is typically normalized at each potential against a blank electrode or thin layer at the electrode containing only electrolyte and this normalized differential reflectance, $\Delta R/R$, is plotted against wavelength. Both specular and diffuse reflectance occur concurrently and both have been used in UV-vis reflectance spectroelectrochemistry. Specular reflectance requires mirror like surfaces and the reflectance is dependent on the angle of the incident light; this phenomena is well understood and described by the Fresnel equations. Specularly reflected light is polarized and highly anisotropic (i.e., specularly reflected light is emitted only over a limited range of angles with respect to the incident beam). Variable angle specular reflectance spectroscopy provides useful information about film homogeneity and thickness (2). Diffuse reflectance occurs principally from rough or granular surfaces and is isotropic. Specular and diffuse reflectance are experimentally distinguished through control of the angle of detection (or incident beam). The majority of reflectance reports for electronic spectroelectrochemistry study specular reflectance using highly polished metal electrodes as the interface. Highly polished carbon is also used.

Reflectance accessories are available on modern UV-vis spectrometers and many are available which allow for variation of the incident angle for separation of specular reflectance and diffuse reflectance. Reflectance UV-vis has found application in spectroelectrochemistry of thin films, polymer modified electrodes, and surface adsorbates such as self-assembled mono- and multilayers. A number of cell designs have been applied and these are generally designed to fit into commercial reflectance attachments. A thin film reflectance cell is shown in Figure 14.8 (34). The electrode was fabricated by anodization of a thin layer

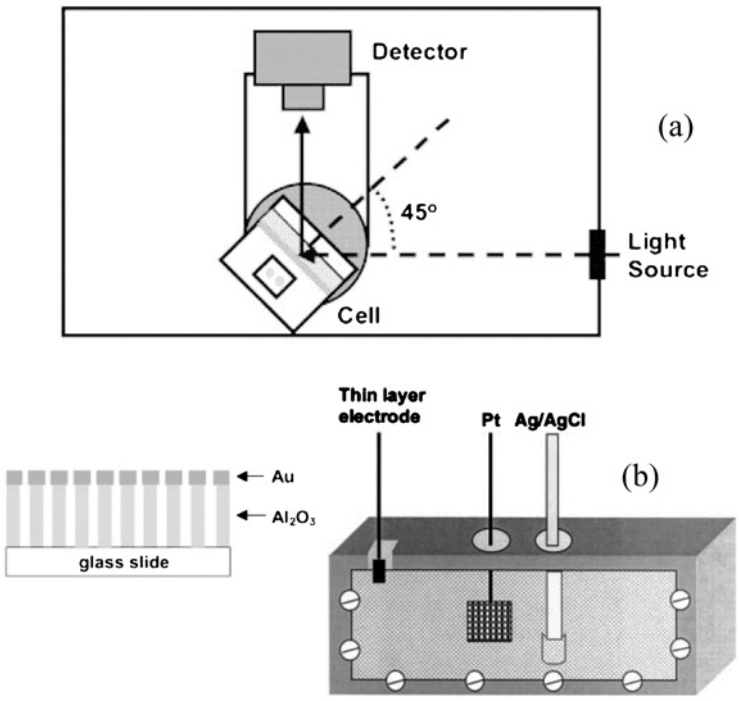


**Figure 14.8** Schematic of spectroelectrochemical experiment (a) and employing a thin layer optically reflective thin layer cell. (b) Side profile of the optically reflective thin layer electrode. Reproduced from reference (34) with permission from Wiley.

of aluminum sputtered onto a plain glass microscope slide to create a 750 nm thick transparent porous alumina film. A thin film of gold was then sputtered on top of the alumina film. The reflective gold layer retained the pores of sub-optical wavelength dimensions and filled with analyte solution; despite this, the surface remained specularly reflective. This cell was used in a study which combined specular reflectance spectroscopy and chronoamperometry to determine the onset of water reduction from shifts in the interference fringes of the specularly reflected light from the electrode surface.

A thin layer cell for specular reflectance measurements with temperature control is shown in Figure 14.9 (35, 36), where the cell is surrounded by a hollow brass heat exchanger. The temperature of the cell was controlled using an external heating:cooling circulator which pumped low viscosity silicone oil through the hollow brass heat exchanger surrounding a three-electrode cell. Polished Pt or Au foil soldered on a brass post served as the working electrode and a circular 0.5 mm Ag wire, placed 0.5 mm outside the perimeter of the working electrode, was used as pseudo-reference electrode. A platinum wire held beyond the perimeter of the working electrode was used as the auxiliary electrode. This cell was designed for use in a commercial reflectance attachment for both electronic and IR instruments.

External reflectance spectroscopy has been used in the study of proton coupled electron transfers at a dinuclear ruthenium complex $[(phen)_2Ru(tatpp)Ru\text{-}(phen)_2]^{4+}$ (Figure 14.10) (37).

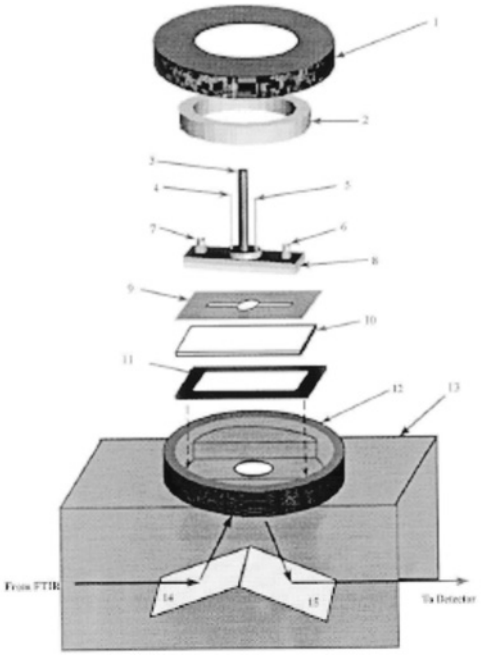

**Figure 14.9** Thin layer cell for temperature controlled specular reflectance spectroelectrochemistry. (1) Tightening brass cap (threaded inside). (2) Teflon or brass washer required to tighten the cell. (3) Working electrode (a brass rod with platinum foil soldered to the base. (4) Auxiliary electrode: platinum wire with the tip made flush to the Teflon base of the cell. (5) Pseudo-reference electrode: silver wire, also made flush to the Teflon. (6, 7) Luer lock type injection ports. (8) Cell body, top part aluminum, lower part Teflon. (9) Teflon spacer which determines the path length of the cell. (10) Calcium fluoride window. (11) Rubber gasket. (12) Hollow brass cell body. (13) Two mirror reflectance accessory (Nicolet FT-30). (14, 15) Mirrors. Reproduced from reference (35) with permission from Elsevier.

Both difference and differential reflectance spectroelectrochemistry were used in this study. In the difference mode, the reflectance (R) data were acquired during square-wave modulation with the potential limits of the square-function selected to encompass the redox wave being probed. Conventional $\Delta R/R$ versus wavelength spectra result. Differential reflectance–potential profiles show the spectral changes that occur for an electrochemical species as a function of a small amplitude potential perturbation. The monitoring wavelength, which is associated with an absorbance of the target analyte, is held constant. Lock-in detection of the changes in the reflected intensity of this wavelength off the working electrode surface as a function of AC potential (11 Hz) modulation was monitored, after demodulation, as a function of the DC electrode potential. The optical signal generated by such AC modulation is expressed as

$$\frac{1}{R}\frac{\delta R}{\delta E} = -\frac{1}{R}\frac{\delta A}{\delta c_{\text{int}}}\left|\frac{\delta c_{\text{int}}}{\delta E} + \frac{1}{R}\frac{\delta R}{\delta q}\frac{\delta q}{\delta E}\right|_{AuER} \tag{14.7}$$

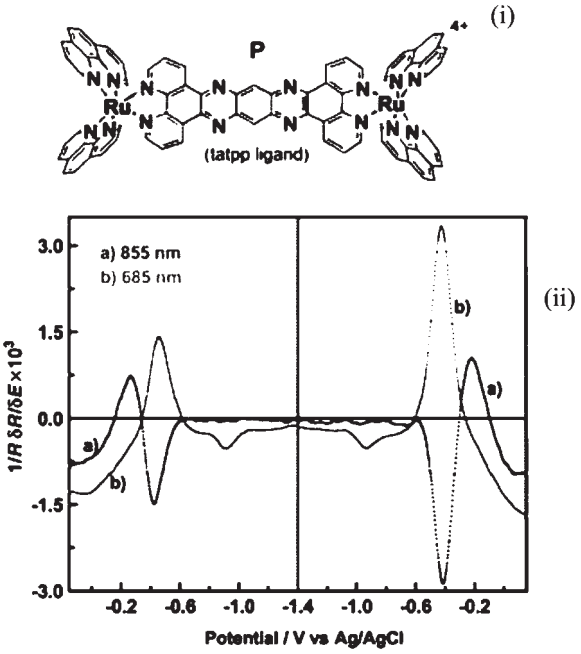


**Figure 14.10** (i) Structure of $[(phen)_2Ru(tatpp)Ru\text{-}(phen)_2]^{4+}$ and (ii) in-phase differential reflectance versus potential curves for $3.5 \times 10^{-5}$ M P at pH 11 during a cyclic linear potential scan at 2 $mVs^{-1}$ on a polycrystalline gold disk electrode. Two wavelengths were used to monitor the singly and doubly reduced products from P: (a) 855 nm and (b) 685 nm. The switch potential, −1.35 V, was used to separate the plot in two halves. Reproduced from reference (37) with permission from Wiley.

where $E$ is the electrode potential, $A$ is the optical absorbance, $R$ the reflectance, and $\delta c_{int}$ is the modulation of the interfacial concentration. An example of an optical response using this method is shown in Figure 14.10 for the study of $[(phen)_2Ru(tatpp)Ru\text{-}(phen)_2]^{4+}$. These electroreflectance studies were used to characterize the interfacial reaction occurring with AC voltammetry and led to the identification of the redox products and their pH dependence to generate a scheme of squares for the protonation states of the various redox states of $[(phen)_2Ru(tatpp)Ru\text{-}(phen)_2]^{4+}$.

The increasing availability of fiber optic probes and microscope objectives on conventional spectroscopic instrumentation have improved the sensitivity and versatility of reflectance spectroelectrochemical measurements. These features have reduced the need for special spectroelectrochemical cells to fit into reflectance accessories and in the case of fiber optic instruments, can reduce the costs of spectroelectrochemical measurements considerably.

Fiber optic spectrometers with reflectance probes build an additional degree of flexibility into reflectance spectroelectrochemical measurements. Fiber optic reflectance probes are typically made of multiple fiber optics which direct the light from the source to the sample surrounding one or more fiber optics which collect the reflected light and direct it to the detector. These fibers are usually combined within a single cable which is bifurcated

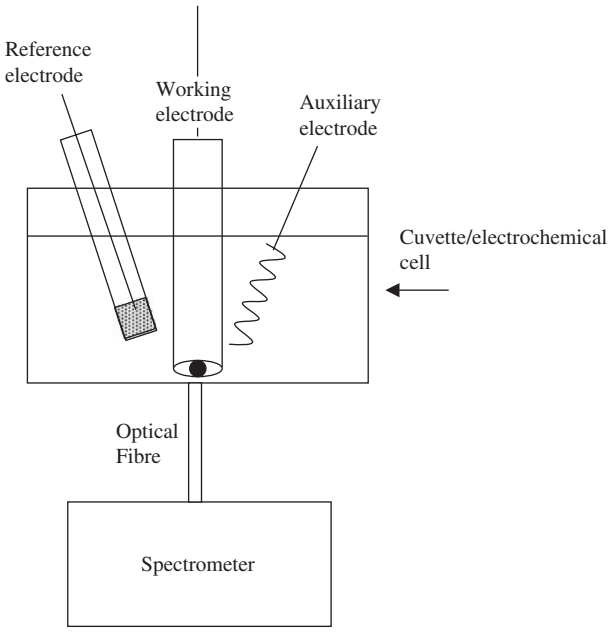


**Figure 14.11** Fiber optic spectroelectrochemical arrangement for electronic spectroscopy. A conventional electrochemical cell is combined with a fiber optic spectrometer in which the optical fiber is directed in front of the working electrode at the bottom of the cell.

at one end to connect the respective detector and illumination fibers separately to the light source and detector. A reflectance spectroelectrochemical configuration with a fiber optic probe is shown in Figure 14.11. This configuration is simple and highly versatile for both semi-infinite and thin layer configurations (30). A highly polished working electrode is placed very close to the optical window to generate thin film conditions. The fiber optic probe is oriented directly in front of the electrode where it directs the monitoring light normal to the electrode and collects the reflected light at the same angle for specular reflectance.

The growing use of microscopy in spectroscopic methods has had a significant impact on both the versatility of reflectance spectroscopy and sensitivity as a result of the increased capacity to focus onto the electrode solution interface. An example of a spectroelectrochemical cell for diffuse reflectance spectroscopy in which an optical microscope fiber is optically coupled to a spectrometer is shown in Figure 14.12. The optical geometry imposed by the use of the microscope means that the angle between the incident and detected beams is zero and this, combined with the use of crossed polarizers, eliminates specular reflectance making it possible to use the Kubelka–Munk function for quantifying optical measurements. This arrangement was used in the study of electrochromic responses of solid silver octacyanomolybdate (IV/V) deposited on a graphite electrode in contact with a silver nitrate solution (38). In this arrangement, a microscope objective was used to focus the incident beam onto the electrode. Because the film was

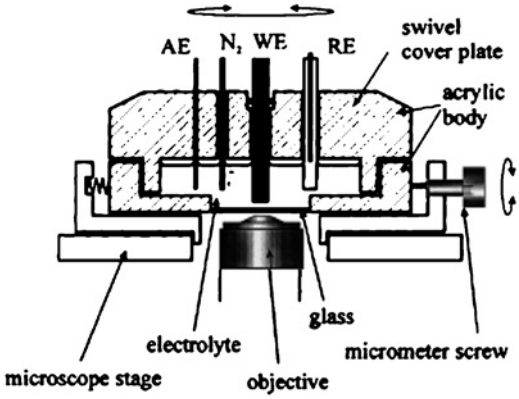


**Figure 14.12** Spectroelectrochemical cell for UV-vis reflectance studies using a microscope. Reproduced from reference (38) with kind permission of Springer Science and Business Media.

immobilized on the electrode, small volumes were not necessary in contrast to the OTTLE experiment.

#### *14.3.5.2 Internal reflectance spectroscopy*

The drawback in conventional absorbance and reflectance measurements is that their sensitivity relies strongly on the extinction coefficient of the analyte. If this is low then only thick films or highly concentrated solutions can be detected at an electrode surface using these methods. For increased sensitivity at a surface layer, external reflectance and UV-vis ATR spectroelectrochemistry can be used. This latter method, for thin films at least, can provide spectra which are very similar to transmission spectra. In ATR, a beam of light incident on a surface is bent normal from the surface as it passes from a higher to lower refractive index material; the beam is said to undergo internal reflection. A high refractive index crystal and a high angle of incidence must be used. Germanium is a commonly used ATR material. In ATR, the total reflection of a light beam at a transparent electrode/solution interface is obtained when the incident light is directed through the electrode toward the solution at an incident angle that exceeds the critical angle $\theta_c$ according to

$$\theta_c = \arcsin\left(\frac{n_1}{n_2}\right) \tag{14.8}$$

where $n_1$ and $n_2$ are refractive indices of the transmitting and incident media respectively. This propagates an evanescent wave perpendicular to the internally reflected beam through the electrolyte with a penetration depth $d$:

$$d = \frac{\lambda}{4\pi(n_1^2 \sin^2\theta - n_1^2)^{1/2}} \tag{14.9}$$

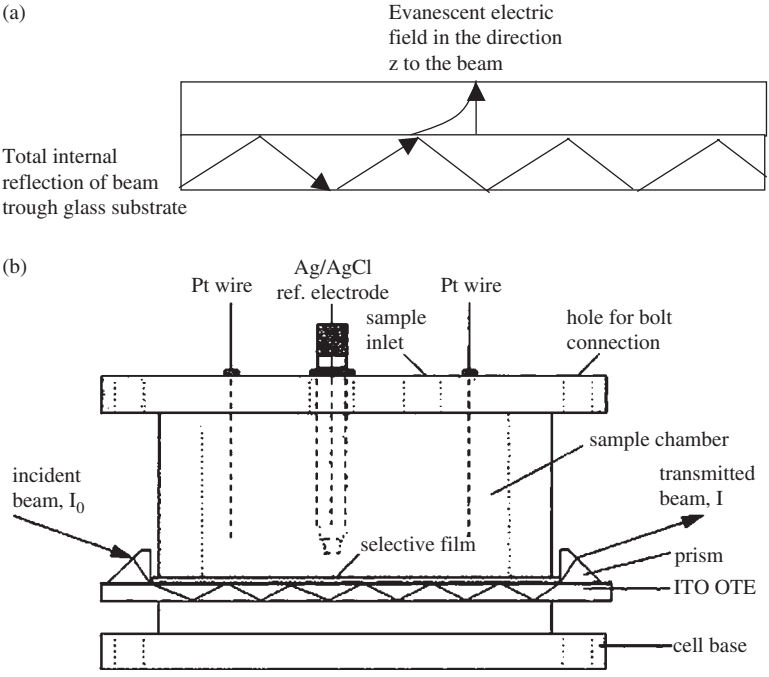


**Figure 14.13** (a) Schematic showing light incident on a substrate undergoing total internal reflection and the evanescent field of the totally reflected light which propagates through the adjacent media. (b) A spectroelectrochemical cell for attenuated total reflectance spectroelectrochemical cell. Reprinted with permission from reference (39). Copyright 1997, American Chemical Society.

where $\theta$ is angle of incidence within the substrate, Figure 14.13a. This method offers significant sensitivity in the interfacial region where the evanescent field propagates, particularly for cells with multiple reflectances. The penetration depth of the evanescent wave depends on the excitation wavelength but is typically of the order of 500–1000 Å this means that it is strictly limited to interrogation of the interfacial region.

Figure 14.13b shows a spectroelectrochemical cell for ATR which illustrates the concept (39). The spectroelectrochemical cell was an optically transparent electrode made of ITO deposited on glass. The incident light was coupled into the ITO glass slide of the spectroelectrochemical cell with a coupling prism and a high viscosity refractive index standard fluid spanned the prism–ITO glass gap. The light propagated by internal reflection through the slide was collected into a prism at the detector end of the slide and directed by fiber optic into the detector. This arrangement was investigated as a charge selective sensor by immobilizing a thin film of a silica sol-gel poly(dimethyldiallylammonium chloride) composite over the ATR element.

A consideration in spectroelectrochemical cell design in ATR is that the working electrode must be transparent. Typically metal or metal oxide deposited thin films on the germanium reflection element and are used as the working electrode. As described in Section 14.3.1,

poor conductance can present a problem for thin film electrodes. Nonetheless, this method can provide significant sensitivity and selectivity for optical changes localized at the electrode solution interface and has found application in studies of conducting polymer films and self-assembled monolayers (40, 41). In a related approach, spectroelectrochemical responses in less than 1% of an equivalent monolayer at adsorbed films of Prussian blue on an ITO electroactive integrated optical waveguide (EA-IOW) (42) have been reported. An advantage of this method lies in its immunity to perturbation of the surrounding solution due to the low penetration depth of the radiation into the solution phase making it amenable to spectroelectrochemical measurements in moving media (43). Internal reflection methods have been exploited extensively in IR studies, as discussed in Section 14.6.1, where solvent interference is particularly important.

## 14.4 LUMINESCENCE SPECTROELECTROCHEMISTRY

### 14.4.1 Steady-state luminescence spectroelectrochemistry

Luminescence spectroscopy (fluorescence or phosphorescence) is one of the relatively under explored areas of spectroelectrochemistry. This is surprising given the high sensitivity and selectivity of this technique, but may be due to the experimental difficulties in achieving 90° orientation between excitation and detector. Reports employing this spectroelectrochemical method have been increasing.

In a conventional luminescence experiment, the detector and excitation source must be maintained at a 90° angle to one another in order to limit the amount of excitation light reaching the detector. To achieve this requirement, a square clear sided cuvette is needed as shown in Figure 14.14a. The use of such a square cuvette as a cell for spectroelectrochemistry is not easily adaptable to the thin layer or semi-diffusion cell arrangements conventionally used in UV-vis spectroscopy. Two approaches have been taken to circumvent this problem. First, a thin layer cell comparable to that used in an OTTLE experiment, where the cell is positioned at a 45° angle relative to the excitation source and detector, can be used as shown in Figure 14.14b.

Such an arrangement is analogous to the OTTLE experiment described for electronic spectroscopy. The working electrode is frequently a wire mesh such as gold, platinum, or a

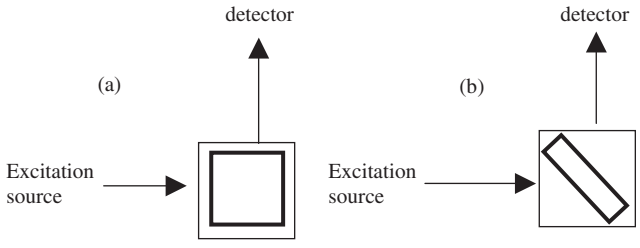


**Figure 14.14** Orientation of cuvette in (a) conventional luminescence spectrometer. (b) Spectroelectrochemical experiment employing a thin cell.

rhodium–platinum alloy. This and the 45° angle of the cuvette, particularly if orientation of the cuvette is not exact, can lead to significant spectral scattering of the excitation source resulting in serious interference from stray light in the resulting emission spectroscopy. In addition, small alterations to the angle of the cuvette can lead to lack of reproducibility in the luminescence signal between experiments. This can be overcome by careful placement of the cell in the spectrofluorimeter. A simple solution is to use a PTFE insert in the instrument cuvette holder which is milled to hold the spectroelectrochemical cell securely and reproducibly at a 45° angle. This is a simple method which works well.

There are a number of options for using a fluorescence cell in the conventional 90° orientation. One 90° cell incorporated a chair shaped gold coated Teflon electrode milled to fit into a conventional fluorescence cuvette. The large Teflon insert provided was also milled to support the reference and auxillary electrodes at the bottom of the cell. The size of the insert significantly reduced the volume of the cell permitting use of 90° excitation and detection (44). Another 90° oriented cell is shown in Figure 14.15 (45) where a quartz

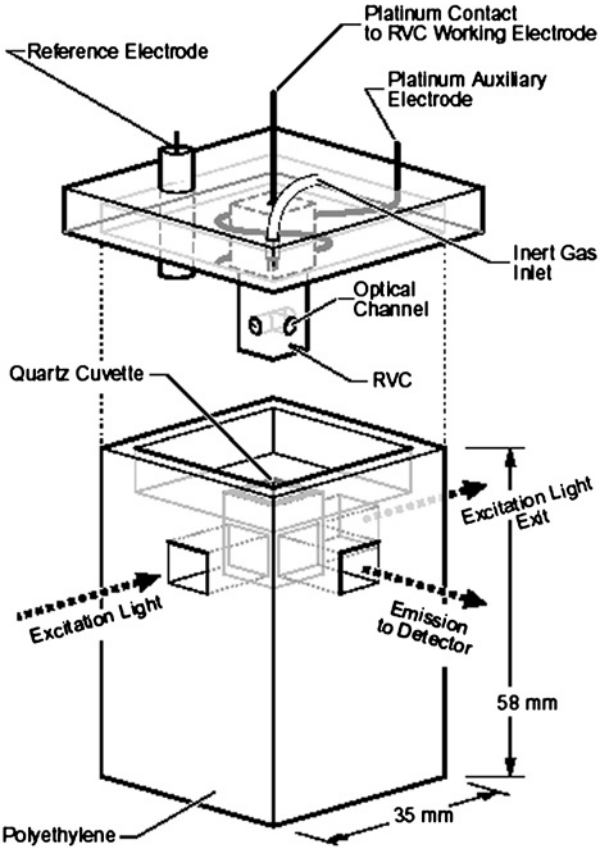


**Figure 14.15** Low volume spectroelectrochemical cell for luminescence, reprinted from reference (45b) with kind permission of Prof. J. R. Kirchhoff and Bioanalytical Services Incorporated.

optical cell is housed in the lower part of a milled PTFE block which fits snuggly into the spectrometer cell holder like a conventional cell.

The upper part of the arrangement houses the auxiliary and reference electrodes. The shaped optical channels were drilled into the lower portion of the cell configuration to permit a 90° angle between excitation and emission pathways and a long optical path for better sensitivity. A reticulated carbon electrode was used as the working electrode. This use of a non-metal electrode may be advantageous in avoiding luminescence quenching which can occur at a metal surface. The large volume of this cell led to exhaustive electrolysis times of up to 25 min depending on the arrangement used.

Nernst plots analogous to those in UV-vis spectroelectrochemistry are achievable using luminescence spectroelectrochemistry in which the concentrations of oxidized and reduced species are obtained by using the luminescence quantum yields of the analyte according to

$$\frac{[\mathrm{Ox}]}{[\mathrm{Re\,d}]} = \frac{(I_{\mathrm{red}} - I)/\phi L}{(I - I_{\mathrm{ox}})/\phi L} = \frac{I_{\mathrm{red}} - I}{I - I_{\mathrm{ox}}} \tag{14.10}$$

$$E_{\mathrm{applied}} = E^{\circ\prime} + \frac{RT}{nF} \ln\left(\frac{I_{\mathrm{red}} - I}{I - I_{\mathrm{ox}}}\right) \tag{14.11}$$

where $I_{\mathrm{red}}$, $I_{\mathrm{ox}}$, and $I$ are the luminescence intensities of the analyte at potentials where it is fully reduced, fully oxidized, and at intermediate potentials respectively. $\phi$ is the luminescence quantum yield and $L$ is the path length. Substitution of equation (14.10) to the Nernst equation leads to equation (14.11) indicating that a plot of $E_{\mathrm{applied}}$ versus $\ln(I_{\mathrm{red}} - I)/(I - I_{\mathrm{ox}})$ will yield $E^{\circ\prime}$ from the intercept and $n$ from the slope. Such a Nernst plot was constructed for rhodamine 6G at a 4,4-bipyridine modified gold electrode using a 90° thin layer cell. Good agreement was found between the spectroelectrochemically derived value for the formal potential of the rhodamine 6G (−0.787 V) and that obtained from cyclic voltammetry (−0.791 V) (46).

In the simplest spectroscopic description of the Nernst equation, the two redox states should not emit in the same spectral region. Since it is unusual for a single species to emit in two different oxidation states, this requirement is usually fulfilled in emission measurements and is a distinct advantage over absorbance measurements. In many instances, however, the oxidized or reduced form of the analyte can quench the luminescent precursor leading to lower intensity values. This can lead to serious errors in the apparent concentrations of the oxidized and reduced species and therefore the values derived from the Nernst plots.

The strength of spectroelectrochemistry lies in its ability to achieve states which are frequently inaccessible synthetically. An example of such a species is $[\mathrm{Re(dmpe)_3}]^+$, where dmpe is 1,2-bis(dimethylphosphino) ethane (47). This $d^6$ Re(I) complex is colorless and non-luminescent. As Figure 14.16 shows, oxidation resulted in the formation of the $d^5$ Re(II) complex which exhibited an absorbance at 530 nm and an intense emission at 593 nm; the luminescence quantum yield exceeded that of the well-known $[\mathrm{Ru(bpy)_3}]^{2+}$ complex.

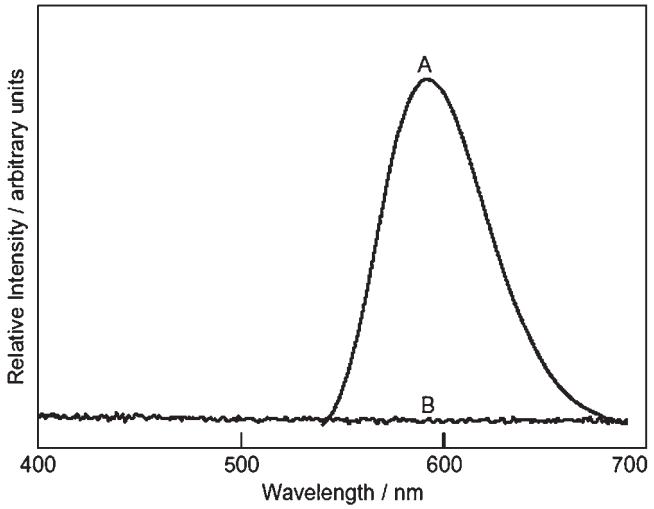


**Figure 14.16** Uncorrected emission spectra of 0.14 mM. (A) $[Re(dmpe)_3]^{2+}$, $\lambda_{ex}$ = 530 nm; and (B) $[Re(dmpe)_3]^{+}$, $\lambda_{ex}$ = 220 nm in acetonitrile with 0.1 M $(n\text{-}Bu)_4NPF_6$ in the luminescence spectroelectrochemical cell. Reprinted with permission from reference (47). Copyright 1994, American Chemical Society.

### 14.4.2 Time-resolved luminescence spectroelectrochemistry

Time-resolved luminescence spectroelectrochemistry (TRLS) is less common than but complementary to luminescence spectroelectrochemistry. TRLS can be used to monitor the lifetime of a luminescent species, provided it is sufficiently long-lived. TRLS may be useful in studying the photophysics of an electroactive species to understand its temporal behavior under application of potential and can be used to provide a unique perspective on the electrochemical interface.

The two most common methods for studying luminescent lifetimes are time correlated single photon counting and flash photolysis. Single photon counting has not been used with spectroelectrochemical studies due to instrumental difficulties associated with the need for complete light tightness. Laser flash photolysis methods have been used in spectroelectrochemical studies (48, 49). A typical instrumental set-up for nanosecond TRLS is shown in Figure 14.17.

A pulsed light source (e.g., a neodymium YAG laser) is set up at a right angle to the detector which may be a fast photodiode or more complex detection device such as an intensified charge coupled device (iCCD) or diode array. The iCCD or diode array offers significant advantages because it allows a complete emission spectrum (spectral range for a typical iCCD of about 250 nm) to be obtained within times as short as 10 nsec, but also permits collection of a steady-state spectrum. This means that both static and dynamic fluorescence studies can be carried out simultaneously using a single instrument. The gate width (i.e., the exposure time of the iCCD) for time-resolved measurements, controlled using a delay generator, is never more than 5% of the excited state lifetime. The step size

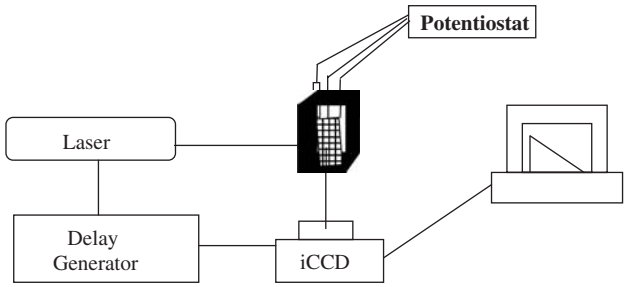


**Figure 14.17** Schematic of instrumental layout for nanosecond flash photolysis for collection of luminescence lifetime.

(i.e., the time between the acquisition of discrete spectra) is typically between 2 and 5% of the excited state half-life. For steady-state spectra, the gate width is set to at least six times the lifetime and no temporal steps are required.

An example which highlights both the steady-state and time-resolved aspects of luminescence spectroelectrochemistry is shown in Figure 14.18. This study reported a dinuclear ruthenium (II) complex bridged by dianionic bridge shown in the inset of the figure (49).

In this system the metals are bound through N,N coordination to the pyridine and triazole and O,N coordination to the triazole and phenolate. In its native state the dinuclear compound is weakly emissive with a lifetime of 50 nsec. The mixed valence complex was prepared *in situ* electrochemically through oxidation of the O,N bound metal. Electronic spectroelectrochemistry suggested the metals were weakly coupled. Oxidation of the first metal lead to strong luminescence from the complex which was reflected in its increased lifetime of 130 nsec. This luminescence is reversibly switched on at 0.3 V and reversibly switched off by application of 1.3 or 0 V. This study was carried out using a thin layer OTTLE cell which was held using an insert at a 45° angle to the detector and light source. Time-resolved spectroscopy was carried out using the methodology described in Figure 14.17. The use of an intensified iCCD meant that both the full luminescence spectrum and the lifetime of the complex could be determined with one instrument operated in different time domains (50).

## 14.5 VIBRATIONAL SPECTROELECTROCHEMISTRY

Vibrational spectroelectrochemistry has now almost superseded UV-vis spectroelectrochemistry as the most commonly reported method. Because vibrational spectroscopy can give structural information, it has found extensive application in the study of the double layer, redox products in solution, and surface adsorbed species. The two most prevalent vibrational spectroscopies applied to spectroelectrochemistry are Infrared and Raman. Though the underlying mechanism and theory of each technique is fundamentally different, both methods give detailed vibrational information which may be used in spectroelectrochemistry to determine and monitor structural changes accompanying electrochemical

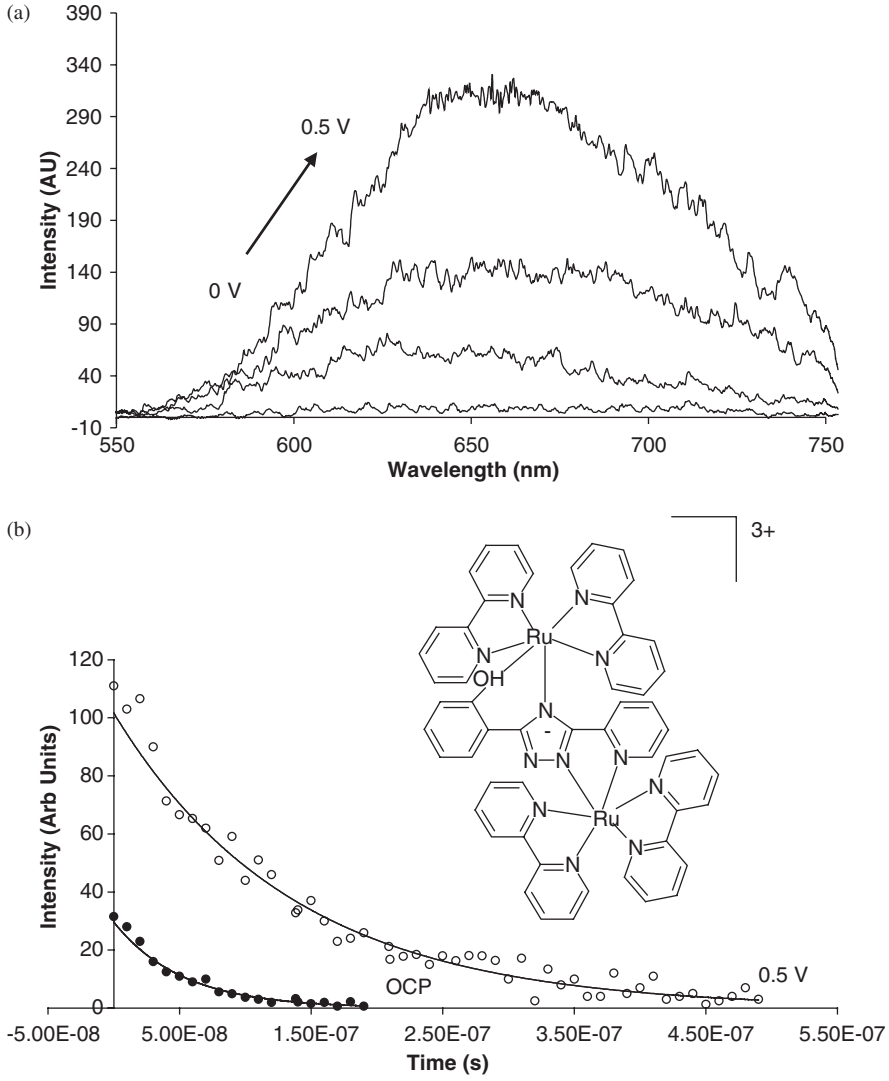


**Figure 14.18** (a) Luminescence spectroelectrochemistry and (b) time resolved luminescence spectroelectrochemistry of mixed valence state of dinuclear ruthenium complex, shown in inset. Experiments were conducted in dry acetonitrile containing 0.1 M TEABF4 as supporting electrolyte. Emission spectra were collected using iCCD with gate width at 500 nsec. Luminescent decays, collected using iCCD with gate width at 20 nsec. Reproduced from reference (49) with permission from the Royal Society of Chemistry.

processes. In electronic spectroscopy, the majority of spectroelectrochemical experiments are conducted in the transmission mode; for infrared spectroelectrochemistry, the reflectance mode is mainly used. Since Raman is a scattering technique, it is fundamentally suited to interfacial measurement.

### 14.5.1 IR spectroelectrochemistry

The infrared (IR) region of the EM spectrum lies between 50 and $10^4$ $cm^{-1}$. Absorption of IR light by a molecule occurs when the electric field of an incident photon is resonant with the frequency of a vibrational mode. In order to be excited in this way (i.e., IR active) the vibration must elicit a change in the permanent electric dipole in the molecule. Modern IR spectrometers are Fourier transform IR (FTIR) instruments in which an interferometer interrogates the IR transmission of a sample at all wavelengths simultaneously. The operation of the FTIR technique is described extensively elsewhere (51). In short, an interferometer is composed of a beamsplitter and two flat mirrors, one fixed and one movable. The beamsplitter splits the incident analyzing laser source into two optical beams. One beam reflects off the fixed mirror while the second beam reflects off the movable mirror which moves within a path of millimeters from the beamsplitter. The two reflected beams are recombined when they meet at the beamsplitter as an interference pattern or interferrogram. This interference pattern arises as a consequence of the displacement of the moving mirror. The interferrogram is then directed through the sample compartment where, if a sample is present, components of the interferrogram are transmitted or absorbed by the sample. The interferrogram that reaches the detector is then transformed to spectral information using the FT. An advantage of the FT method applied to spectroelectrochemistry is its speed, which permits rapid spectral collection particularly in difference experiments where, for example, the applied potential is modulated. IR spectroscopy, like electronic spectroscopy, is commonly conducted in the transmission mode. Due to large solvent background, particularly in aqueous environments as a consequence of the large permanent dipole of water, the use of transmission in IR spectroelectrochemistry is relatively uncommon, although there are a number of reports on transmission cells (52–54). Reflectance methods are more commonly used for spectroelectrochemistry, the most common of which are ATR, external reflectance, and infrared reflection absorption spectroscopy (IRRAS). In general, the IR signal in spectroelectrochemistry is collected and distinguished from the signal in the absence of applied potential by using a difference method or a modulation method. IR spectroelectrochemistry is an extensive area; a number of reviews are available (55–57).

#### *14.5.1.1 Internal reflectance*

In internal reflection spectroelectrochemistry, the working electrode is a reflective metal surface which behaves like a mirror directing the specularly reflected incident light through the solution to the detector. Because the path length must be very small, the surface of the working electrode should be as flat as possible to minimize solvent contribution. A metal electrode polished to a mirror finish is usually used. A common IR spectroelectrochemical cell is shown in Figure 14.19 (58). The cell construction is syringe-like. A mirror-like working electrode, frequently a 5–10 mm diameter gold or platinum disk, is adhered to the end of a plunger. Gold is most commonly used because it has excellent IR reflectance; however, it has a limited potential window. Electrical connection is made at the back of the working electrode and the wires run through the hollow plunger body. A luggin reference electrode and auxiliary are placed within a few millimeters of the

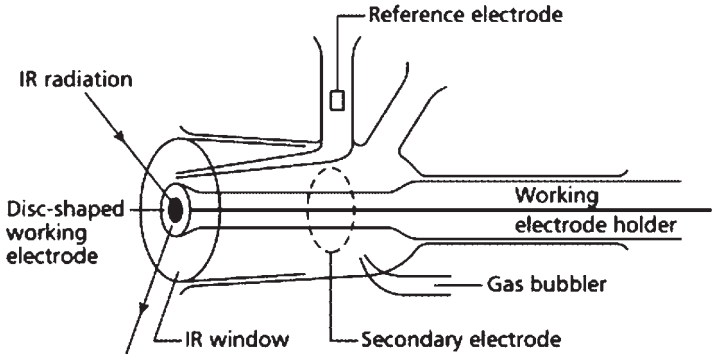


**Figure 14.19** IR spectroelectrochemical cell for external reflectance. Reproduced from reference (58) with permission from Elsevier.

working electrode. The bottom of the cell is a flat window of appropriate optical material. The plunger is forced close to the window to form a thin layer of electrolyte between the working electrode and the window. In this configuration, incident light is directed through the optical window onto the thin film of solution compressed between the optical window and working electrode. The light is then reflected from this surface towards the detector. The material used for the optical window is critical because it must simultaneously transmit IR light and be stable toward the solvent system used (which is frequently aqueous). Silicon, calcium fluoride, zinc sulfide, and zinc selenide are commonly used materials for the optical window in the IR spectroelectrochemical cell.

In aqueous systems the electrode may be sealed onto the glass plunger using epoxy resin. Because most epoxy resins are unsuitable for organic solvents, the metal is usually sealed directly to the glass. The solvent and electrolyte are typically present in large excess over the analyte and will frequently have a significant IR absorbance. Correction for this background IR contribution is best achieved by modulation of the applied potential, polarization of the incident light, or by using a difference method. SNIFTIRS (subtractively normalised interfacial Fourier transform infrared spectroscopy) is a difference technique developed for spectroelectrochemistry. SNIFTIRS involves collection of a successive series of interferrograms (59) at two potential limits, $E_1$ and $E_2$, where $E_1$ is a reference potential typically corresponding to a potential at which no faradaic process occurs and $E_2$ corresponds to the potential at which the analyte redox step occurs. The step between $E_1$ and $E_2$ is cycled until an acceptable signal-to-noise ratio is obtained. If $R_1$ and $R_2$ are the reflectances measured at $E_1$ and $E_2$ respectively, the change of reflectivity $\Delta R/R$ is given as $(R_2 - R_1)/R_1 = R_2/R_1 - 1$. This method has been developed for a commercial FTIR spectrometer (60). The SNIFTIRS method has been used for the *in situ* detection of electrogenerated intermediates in the double layer or species adsorbed at the electrode surface. For example, the SNIFTIRS of self-assembled monolayers of short chain alkyl thiols terminated with ferrocene (Fc) at Au(111) surfaces has been reported. Figure 14.20 shows representative SNIFTIRS spectra for these monolayers (61). Using p-polarized light and exploiting the surface selection rule described below, orientational changes in the ferrocene moieties could be detected on oxidation of the ferrocene groups in the monolayers. This

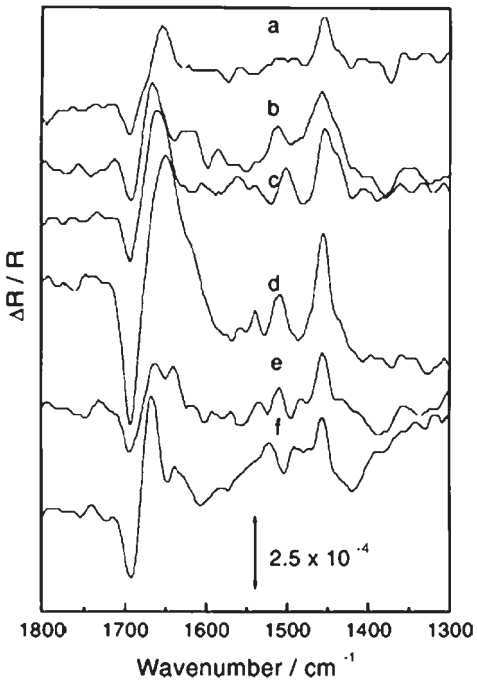


**Figure 14.20** SNIFTIRS spectra in the region 1300–1800 $cm^{-1}$ for a single crystal gold(111) disc electrode modified with $FcC_3$ (a), $FcC_4$ (b), $FcC_5$ (c), $FcC_6$ (d), $FcC_8$ (e), and $FcC_{10}$ (f), obtained at 650 mV using p-polarized radiation. The reference spectrum for each monolayer was obtained at 200 mV. Reproduced from reference (61) with permission from Elsevier.

was attributed to rotation of the ferrocene groups towards a position where the plane of the cyclopentadienyl rings moves to a position normal to the surface of the electrode (61).

Infrared reflection absorption spectroscopy (IRRAS) has also been applied to electrochemical measurements. This method is interesting because of the additional selection rules it confers to the method which can be exploited for detailed structural assignment. IRRAS involves the rapid and continuous modulation of the polarization of the infrared light between s and p polarization states using a photoelastic modulator. The potential at the electrode is fixed at a chosen voltage during this process. For incident s-polarized light (perpendicular to the plane of reflection), the reflected beam is out-of-phase with the incident beam and they destructively interfere to produce a node in the electric field at the surface. This means there is no electric field at the surface to interact with the molecular dipole of the adsorbate. For p-polarized light (parallel to the plane of reflection) the two fields are in phase. This means that s-polarized radiation interacts only with species in solution, while p-polarized radiation interacts with both surface and solution species. Subtracting the s- and p-polarized spectra produces a spectrum which only shows bands associated with species in the interfacial region and eliminates any contribution from solvent or electrolyte. In addition, because the exciting radiation at the surface is p-polarized, only those modes with a dipole moment perpendicular to the metal surface can interact

with the electric field of IR radiation. This is known as the metal surface selection rule for IR spectroscopy, Figure 14.21.

Figure 14.22 shows a IRRAS spectroelectrochemical *in situ* study of *trans*-$[NBu_4][RuX_4(CNXyl)_2]$ (X = Cl or Br, Xyl = 2,6-dimethylphenyl) (62). These materials undergo temperature dependent electrochemically induced isomerization reactions involving reductive elimination of a halide ion. In Figure 14.22a, the potential of the working electrode was stepped to 0.50 V and single scan IR spectra were collected following the step at 2-min intervals. Reduction of *trans*-[RuCl4(CNXyl)2] is indicated by increasing negative absorbance at 2154 $cm^{-1}$. In Figure 14.22b, re-oxidation is achieved at $E_{app}$ = 0.50 V where the band at 2076 $cm^{-1}$ collapses and another grows at 2176 $cm^{-1}$.

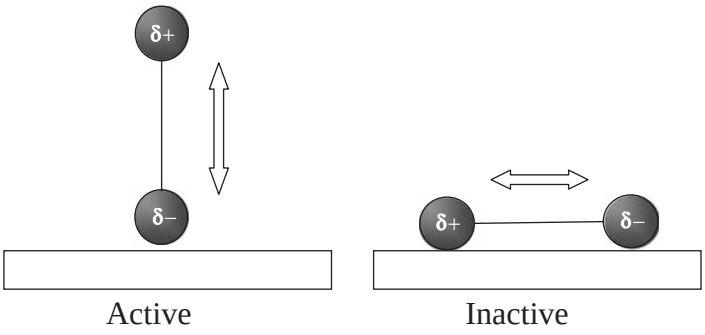


**Figure 14.21** Schematic illustrating surface metal selection rule for IR spectroscopy. Only vibrational modes with a dipole moment component perpendicular to the metal surface can interact with the electric field of IR radiation (i.e., the stretching mode on the left is IR active whereas that on the right is not).

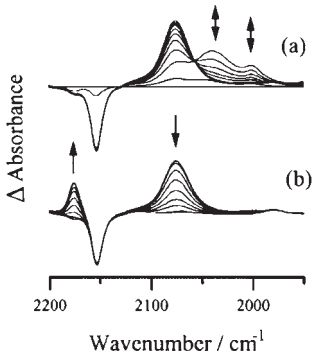


**Figure 14.22** Changes in the IR difference absorption spectra accompanying (a) reduction of *trans*-$[NBu_4][RuCl_4(CNXyl)_2]$ in an IRRAS cell at 293 K at −0.5 V. The horizontal line at zero absorbance corresponds to the initial spectrum (i.e., that of *trans*-$[RuCl_4(CNXyl)_2]^-$) prior to electrolysis, ratioed against itself. (b) Reoxidation of *trans*-$[NBu_4][RuCl_4(CNXyl)_2]$ at +0.5 V. Reproduced from reference (62) by permission of The Royal Society of Chemistry.

### *14.5.1.2 External reflectance*

Electronic reflectance spectroscopy and attenuated total internal reflection (ATR) cells provide significant improvement in discrimination of background and interfacial signals because ATR minimizes penetration of the monitoring beam into the solvent. The mechanism of ATR is described in Section 14.3.2. The cell design for external reflectance IR methods is similar to those described for electronic spectroscopy. The total internal reflection component, which doubles as a working electrode, must be made of high refractive index material which is also IR transparent. A prism or parallel plate made from semiconductor material can be used as the ATR element as can silicon or germanium because they have good IR transparency. The ATR element may be coated with a thin layer of gold (for IR transparency). A balance must be achieved between the conductivity of the film and its optical transparency because the IR beam must penetrate the metallic layer to reach the sample. Alternatively, at moderate doping levels semiconductors such as silicon and germanium can be used as both ATR element and electrode, although, doping reduces the transparency of the material (57).

Figure 14.23 shows an example of an ATR a cell for FTIR spectroscopy (63). A thin layer of gold (10–15 nm) on a right-handed silicon prism serves as the working electrode. The prism was clamped to the electrochemical cell which was rotated so that the position of the electrochemical cell permitted an angle of incidence of the infrared beam of 45°. The detector, which was liquid nitrogen-cooled mercury cadmium telluride, was oriented so that the angle between the incident and reflected beams was 90°. The cell was used to study step-scan double-modulation (phase and electrochemical potential) ATR FT-IR spectrometry experiments using the ferricyanide redox couple to explore digital signal processing as an alternative to two lock-in amplification for demodulation of optical at two modulation frequencies.

The main advantages of ATR for IR arise from the fact that the IR EM field decays exponentially from the ATR surface into solution. This means that only a very thin film material in direct contact with the electrode is interrogated. This leads to limited solvent

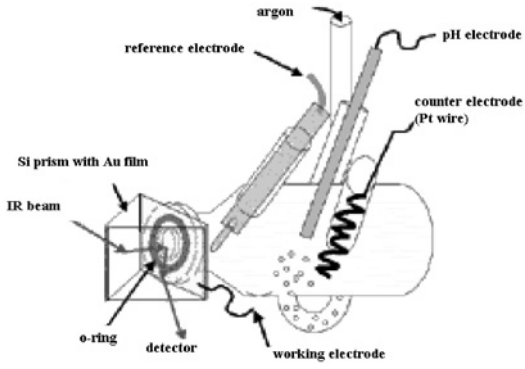


**Figure 14.23** Schematic of IR ATR spectroelectrochemical cell. Reproduced from reference (63) with permission from Elsevier.

contribution to the signal and also as multiple reflections occur, the sensitivity to interfacial species is increased.

A number of practical limitations for IR attenuated ATR have been highlighted. Theoretical and experimental refraction have been found to differ substantially and these differences have been attributed to the difference in optical properties of the thin metal layers and the bulk, due to either non-ideal geometric arrangement of the atoms or through compositional changes caused by inter-diffusion of the phases in the process of film formation (64).

### 14.5.2 Raman spectroelectrochemistry

In Raman spectroscopy the inelastic scattering of light incident on an analyte is investigated. Light is inelastically scattered when there is an exchange of energy between an incoming photon and the analyte molecule. This leads to the emission of a second photon with a different frequency, $v$ to the incident photon, $v_0$. Therefore, Raman is fundamentally a two photon process. The frequency of the Raman scattered photon may be greater than that of the incident photon (i.e., $v_0 + v$) known as anti-Stokes Raman scatter, or less than that of the incident phonton, $v_0 - v$, known as Stokes Raman scatter. In each instance the $\Delta v$ corresponds to vibrational quanta. The Raman effect is fundamentally weak with between only 1 in $10^8$ and $10^{11}$ molecules in a sample scattering inelastically. Figure 14.24 illustrates the mechanism of Raman scattering which originates from electronic excitation into a "virtual" state.

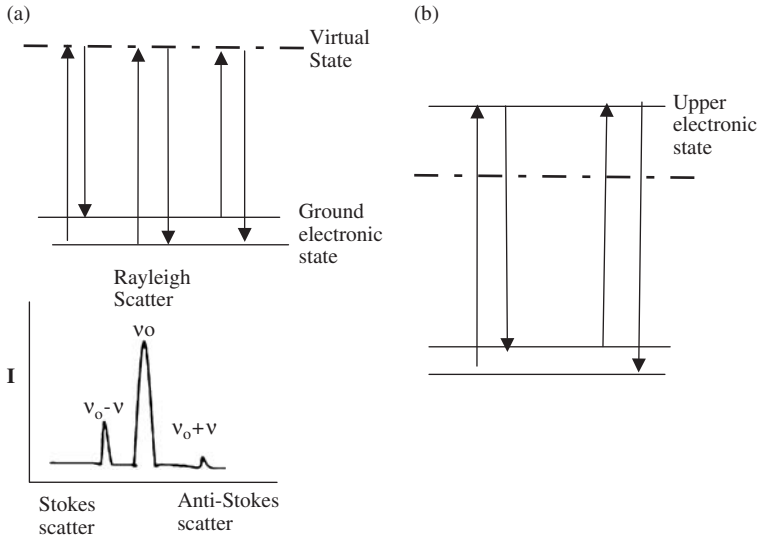


**Figure 14.24** Schematic illustration of the concept of Raman excitation. (a) Conventional Raman spectroscopy: excitation to a virtual state leads to reemission of a photon of the same frequency as the excitation source, Rayleigh scattering, or inelastic scattering where the reemitted photon has greater (Anti-Stokes) or less energy (Stokes) than the incident photon. (b) Resonance Raman conditions: the frequency of the incident photon matches or is close to the energy of an optical absorbance, resulting in scatter which originates from an excited electronic state.

The most probable Raman process is Stokes scatter because this originates from a ground vibrational level $v = 0$, the most likely state to be populated at room temperature. After excitation to a virtual level, the scattered photon is released and the molecule returns to a higher vibrational level, $v = 1$. Therefore, $\Delta v = v_0 - v =$ corresponds to a vibrational quantum. Anti-Stokes is the weaker process because it involves excitation from the higher ground state vibrational level which is usually poorly populated at room temperature. Thus Raman spectroscopy is usually conducted on Stokes radiation. Similar to IR spectroscopy, vibrational information is gleaned from the Raman experiment although the selection rules for each process are quite different. The selection rule for Raman spectroscopy states that for a given molecular vibrational mode to be Raman active it must cause a change in a component of the molecular polarizability. This is substantially different from the selection rule for IR spectroscopy. Thus for highly symmetric molecules, a vibration which is IR active is frequently excluded from being Raman active. For example, molecules with large permanent dipoles (such as water) that are strongly IR active tend to be difficult to polarize and therefore have weak Raman signals. This offers a substantial advantage of Raman over IR spectroscopy for electrochemical studies because it is possible to study reactions *in situ* in aqueous or polar media without the significant background interference which makes IR so difficult. Additionally, since excitation is usually conducted in the visible region in Raman, there is no requirement for special IR transmissible optical windows such as the alkali salt windows required in IR. However, because of inherent signal weakness, Raman spectroscopy requires the use of high power monochromatic light sources and sensitive detection. With the increasing availability of affordable laser sources and sensitive detection by CCDs, the popularity of this technique has soared.

Raman spectroelectrochemistry has been reviewed in detail (65, 66). The type of cell used for spectroelectrochemistry depends to some extent on the optical layout of the Raman experiment. The main optical layouts in conventional Raman spectroscopy are front incident and collection mode, 180° backscattering, and ATR mode. For most solution phase applications of Raman spectroelectrochemistry, a three-electrode cell for bulk electrolysis is used and a number of such cells have been described (67). The conventional OTTLE cell described for electronic spectroscopy can be used in Raman spectroelectrochemistry. However, this cell can suffer from solvent interference in non-aqueous media. Thin layer cells like those described for IR are also frequently used (66).

An interesting approach uses the immersion cell shown in Figure 14.25 which has been used to study self-assembled monolayers and interfacial structure using Raman spectroscopy (68, 69). In this approach a slowly rotating electrode is in partial contact with a droplet of analyte solution. The laser samples a portion of the electrode that has been rotated through and out of this solution drop, and which retains a thin film of the solution on the order of tens of angstroms thickness on its surface. The interfacial solvent species in this layer retains any preferred orientation that occurred *in situ*. Electrical contact is maintained with the working electrode through the droplet. This approach minimizes the amount of bulk solvent sampled leading to reduced background interference. Because the electrode is turned during the Raman study, local heating due to the incident laser is minimized.

A more recent advance in Raman spectroscopy which has increased its versatility is Raman confocal microscopy. In confocal microscopy, out-of-focus information, which contributes to the overall image in conventional microscopy, is eliminated by means of a

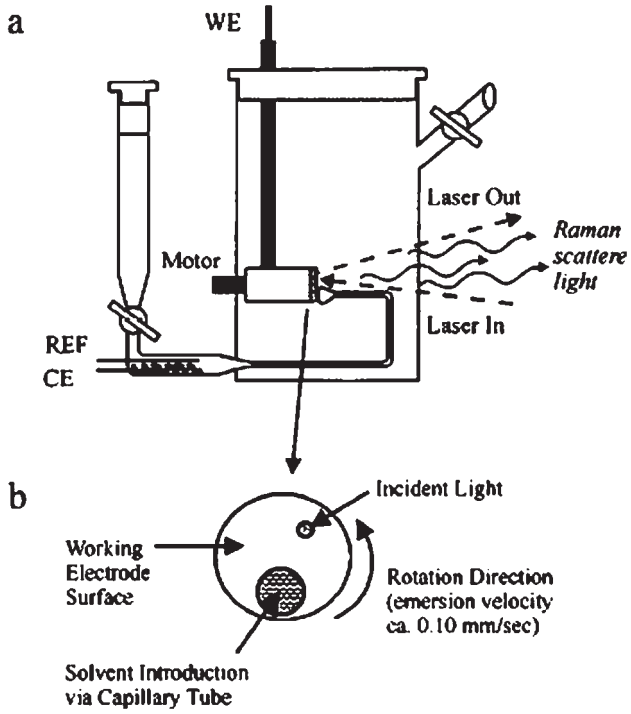


**Figure 14.25** (a) Schematic of Raman spectroelectrochemical emersion cell. Reference electrode (Ag wire), (CE) counter electrode (Pt wire), (WE) working electrode (Ag disk); (b) front view of working electrode surface. Reprinted with permission from reference (69). Copyright 1997, American Chemical Society.

confocal "pinhole" aperture which lies in front of the image plane, Figure 14.26. This acts as a spatial filter permitting only the in-focus portion of the light to be imaged. In Raman spectroscopy this permits discrimination of Raman scatter from outside the plane of focus of the laser thus limiting the portion of the sample interrogated to a tiny volume and allowing depth profiling with a resolution of 1–2 μm.

The spatial resolution in a confocal Raman microscope is typically sub-micron. Confocal microscopy improves the axial and lateral resolution of Raman spectroscopy permitting Raman imaging and has improved fluorescence rejection, which can hinder conventional Raman experiments. This tiny sample volume allows the same kind of selectivity as does using a thin layer method in spectroelectrochemistry. The fine depth control and very narrow sample volume means that background contributions from solvent/electrolyte and background fluorescence interferences can be eliminated. A rotating disk electrode for Raman electrode spectroelectrochemistry has also been described for fast bulk electrolysis at a large area Pt electrode which achieved bulk electrolysis of a 5 mL solution in less than 6 min (70). The spectroelectrochemical set-up using this method provides the ability to interrogate very limited volumes, thus reducing background interference.

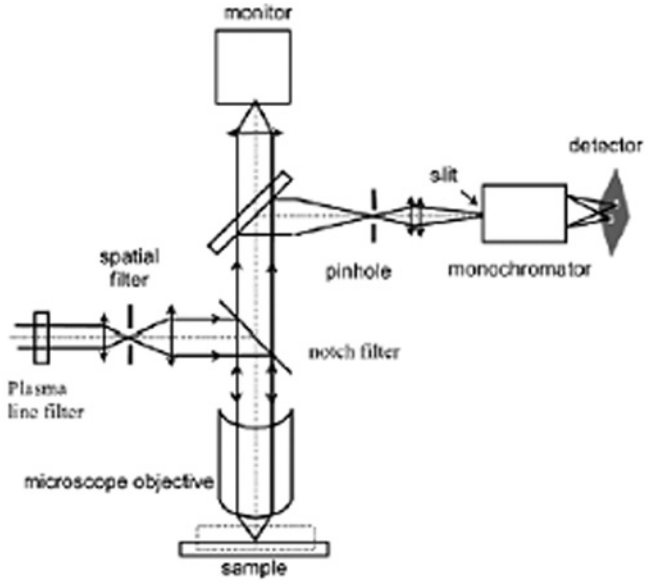


**Figure 14.26** Instrumental set-up for confocal Raman microscopy. Reproduced from reference (66) with permission from Wiley-VCH.

Raman spectroelectrochemistry can provide detailed information about structural changes which accompany an electrochemically induced process in solution. In addition, confocal methods are increasingly being used on surfaces, interfaces, and in thin solid films. Because confocal microscopy is a scattering rather than a transmission technique, it can be used for electrochemical studies at solid electrodes and is a valuable means of probing the electrode/solution interface. An L bend microscope objective can be used with the cell shown in Figure 14.27. In this arrangement the working electrode is inserted into the side of a conventional cuvette. Typically a methacrylate cuvette into which a hole has been bored is used for visible excitation. The cell is sealed against leakage with a rubber o-ring or wax. A thin layer of solution is then compressed between the cuvette window and the electrode. For monolayers or thin films, the compression of the electrode to the window is not required. The auxiliary and reference electrodes and the solution may be degassed and a blanket of inert gas may be maintained over the top of the cell during spectral acquisition.

The precise focusing of the confocal method can be used to obtain good signal intensities from Raman of thin films deposited onto electrode surfaces and this limits spectral contributions from background solvent or electrolyte or the cell material. This cell has been used with confocal Raman microscopy for studying the spectroelectrochemistry of thin solid films and self-assembled monolayers (71, 72). For example, Figure 14.28 shows the Raman spectroelectrochemistry for solid crystalline films of hydroquinone 3,5-bis (2-pyridyl)-1,2,4-triazole co-crystal adhered to a glassy carbon working electrode using the cell shown in Figure 14.27. Reversible oxidation of the hydroquinone moiety could be mapped through Raman spectroscopy.

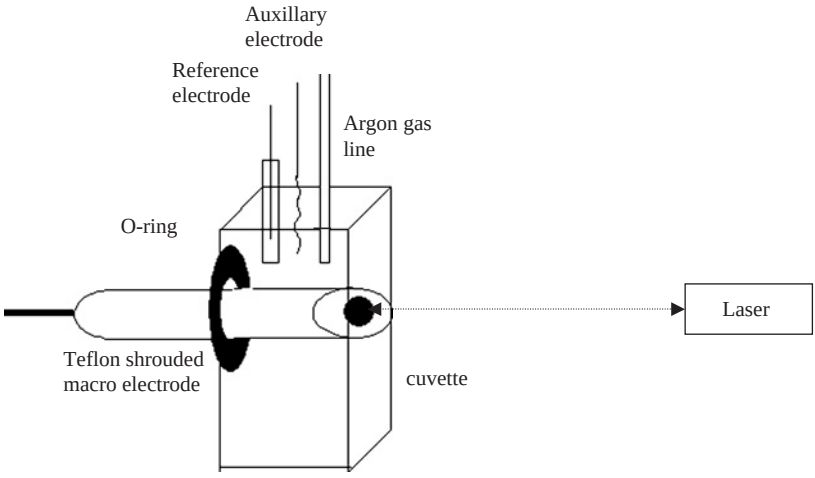


**Figure 14.27** Spectroelectrochemical cell for Raman. (a) Simple thin layer set-up for Raman spectroelectrochemistry for use with solid films or monolayers and suitable for use with backscattering and microscope geometries.

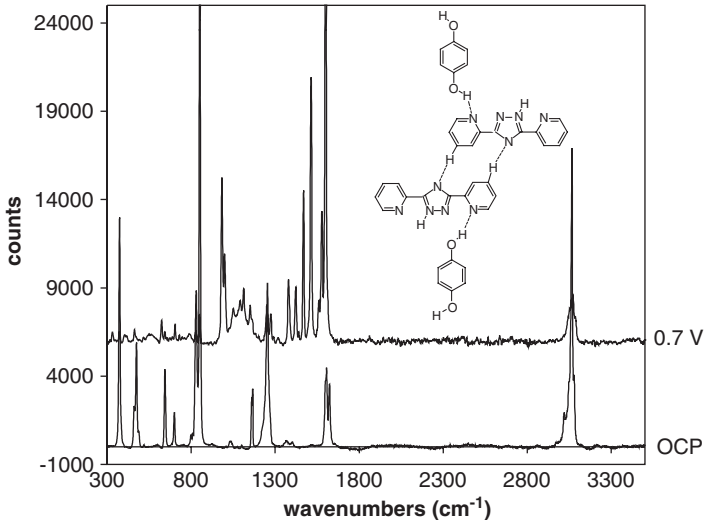


**Figure 14.28** Confocal Raman spectroelectrochemistry of a thin surface layer of solid films of HQBpt (inset) on a glassy carbon electrode (A) at open circuit potential, (B) at +0.700 V. The supporting electrolyte was aqueous 0.1 M $LiClO_4$. Reprinted with permission from reference (71). Copyright 2001, American Chemical Society.

The overriding drawback of Raman spectroscopy is that Raman scatter is fundamentally a weak phenomenon. Resonance Raman spectroscopy and surface enhanced Raman spectroscopy (SERS) are two methods which can be exploited in a spectroelectrochemical experiment to enhance the signal and increase the selectivity of the signal.

#### *14.5.2.1 Resonance Raman spectroscopy*

In resonance Raman spectroscopy (73), the Franck Condon modes of a chromophore can be resonantly enhanced by up to seven orders of magnitude by using excitation wavelengths that are coincident with the absorbances under interrogation. The theory behind this condition is complex (74) and beyond the scope of this chapter. Employing the resonance condition in spectroelectrochemistry provides a unique and powerful opportunity to unequivocally identify new optical transitions resulting from electrode reactions.

In terms of experimental set-up, the methods described for conventional Raman spectroscopy apply. Typically a number of laser excitation wavelengths are required to elucidate overlying transitions. Figure 14.29 illustrates the utility of this technique for $[M(bpy)_2(box)]^+$, where bpy is 2,2-bipyridyl, box is 2-(2-hydroxyphenyl)benzoxazole, and M is either Ru or Os which are coordinated through a N of the benzoxazole and through the phenolate O. For these metal complexes, the assignment of the oxidation steps was unclear, but electrochemical and UV spectroelectrochemical behavior suggested that the first oxidation was metal based. Resonance Raman of the native complex suggested the highest energy occupied molecular orbital, HOMO, lay on the phenolate suggesting that this should be site of the most cathodic oxidation (75). The inset of Figure 14.29 shows the electronic spectroelectrochemistry observed for the first oxidation step of the ruthenium complex which resulted in loss of the visible MLCT transition with the development of a new optical transition in the NIR.

Resonance Raman spectroelectrochemistry was carried out on $[Ru(bpy)_2(box)]^+$ and the osmium analogue in which the bipyridyl units were perdeuteriated $[Os(d_8\text{-}bpy)_2(box)]^+$ by holding the cell potential beyond the first oxidation step for each sample. The resonance Raman spectra of $[Ru(bpy)_2(box)]^{2+}$ and $[Os(bpy)_2(box)]^{2+}$ are in essence analogous. This implies that the bipyridyl unit does not participate in the new optical transition in the oxidized complex and therefore confirmed that for both M(bpy) containing complexes the NIR band is a phenolate ($\pi$) to M(III) (d$\pi$) ligand to metal charge transfer LMCT transition. This example also serves to illustrate how a simple synthetic modification such as deuteriation can yield detailed information on electron transfer processes. If the bipyridyl unit were involved in the optical transition, shifts of between 30 and 60 $cm^{-1}$ would have been observed between the deuteriated and non-deuteriated spectra.

#### *14.5.2.2 Surface enhanced Raman spectroscopy*

Surface enhanced Raman spectroscopy (SERS) is becoming an increasingly popular technique for probing interfacial structure in electrochemical reactions. It has been exploited to study adsorbate structure and orientation changes on application of potential and to interrogate the interfacial distribution of solvent and ions. The mechanism of SERS has been described in detail (76, 77) and is only broadly outlined here. The intensity of a Raman signal is proportional to the square of the magnitude of any incident EM field. SERS exploits this sensitivity by using the enhanced EM field at a roughened metal surface to achieve significantly enhanced Raman scattering of the vibrational modes of adsorbates. Up to $10^{14}$ signal enhancements have been reported for silver in conditions where "hot particles" of magnitude of ~100 nm appear (78). The origin of this enhancement is still debated, but is believed to draw on two contributions: EM and chemical enhancements.

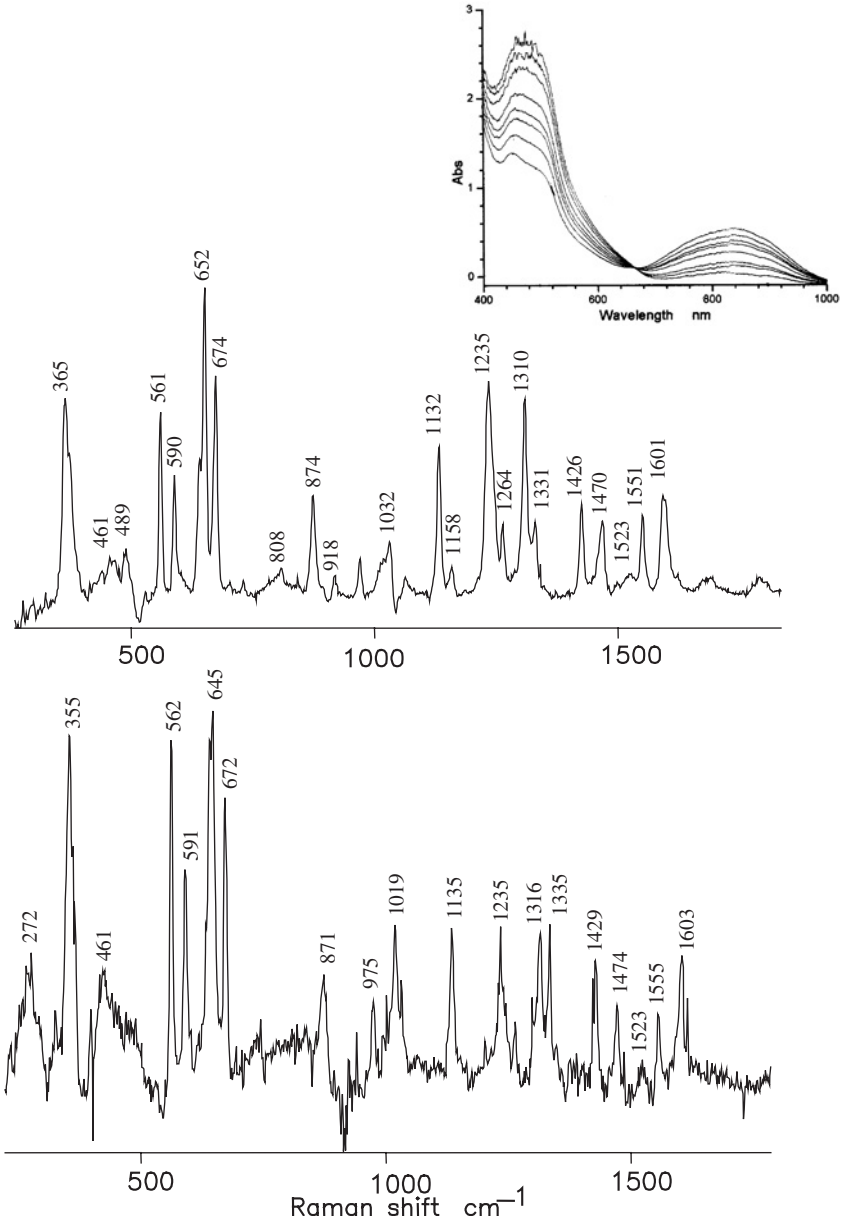


**Figure 14.29** Controlled potential spectroscopy of (a) $[Ru(bpy)_2(box)]^+$ electronic spectroscopy, (b) $[Ru(bpy)_2(box)]^+$ resonance Raman spectroscopy in dichloromethane, excited at 785 nm, (c) resonance Raman of $[Os(d_8\text{-}bpy)_2(box)]^+$ in dichloromethane, excited at 785 nm, the applied potential in each instance was 0.5 V versus Ag/AgCl and the electrolyte was 0.1 M $TeaBF_4$. Reproduced from reference (75) by permission of The Royal Society of Chemistry.

The former is best understood and arises when the incident photon excites plasmons at the metal surface thus augmenting, through energy transfer from the plasmons, the electric field experienced by the analyte molecules. The chemical enhancement mechanism remains controversial. It is thought that as a consequence of the perturbation of the adsorbate states on substrate binding that excited states induced at the metal undergo a charge transfer to the adsorbate enhancing the Raman scatter.

SERS enhancement is largely limited to the coinage and alkali metals: Ag, Au, Cu, Na, Li, K. In principle all metals should be capable of enhancement and Pd and Pt, Rh, and Ru will produce enhancements with UV excitation (79). The difficulty lies in the availability of accessible laser lines. UV lasers are expensive and their associated optic constraints make instrumentation expensive. Herein lies the main limitation for the use of SERS in spectroelectrochemistry. The best SERS enhancements reported are for Ag and Au, but these metals, particularly Ag, have very limited working potential windows. This has been overcome by depositing overlayers of platinum group metals such as Pt on a SERS active substrate such as silver or gold, using a range of methods including constant current deposition (80) and electrochemical replacement of an underpotential-deposited copper or lead monolayer with a Pt-group metal cation (81, 82). This method works with relatively little loss of enhancement because the EM field enhancement mechanism operates over several nanometers. The requirement for roughened surfaces for optimal SERS enhancement is well established (83). Surface roughness should be on the order of between 10 and 200 nm and the surface morphology is critical in dictating the quality of SERS achieved. Theory dictates that the highest SERS enhancements of electric field will be achieved where the surface roughness has the highest curvature (84). A range of methods have been explored for development of SERS substrates including electrochemical, chemical, and laser-induced roughening of metal surfaces, immobilization of metal particles onto an etched or modified substrate, vapor deposition, metal nanoparticle assembly via lithography (85), colloidal metal nanoparticles, and electrodeposition over polystyrene nanospheres which can be used to create highly reproducible surface structures (86). All of these methods leave the metal surface with small metal particles or aggregates of particles that behave as rough surface features. Electrochemical roughening is a useful method of surface roughening (87). Typical roughening procedures involve sequential oxidative and reductive cycles (ORC). For gold or silver this is achieved in $Cl^-$ electrolyte (88, 89). Figure 14.30 shows the effect of electrochemical surface roughening of gold.

In general, this method produces stable surface morphologies that give good levels of signal enhancement which depend inherently on the number of oxidation reduction cycles conducted. Figure 14.31 illustrates the impact of increasing ORC on surface roughness, R, for a gold electrode (90). In this study, the SERS intensity of a pyrazine adsorbate ring-breathing mode (ca. 1016 $cm^{-1}$) was used as a measure of the impact of surface morphology on SERS signal enhancement. The intensity of this mode reached a maximum between 20 and 30 ORCs. AFM studies indicated that roughness features with an average size of approximately 100 nm corresponded to this strongest SERS signal.

SERS has found application across a broad range of electrochemical investigations, including studies of morphological changes associated with redox states (91). It has been used to dynamically determine molecular orientation, and to characterize the structure of

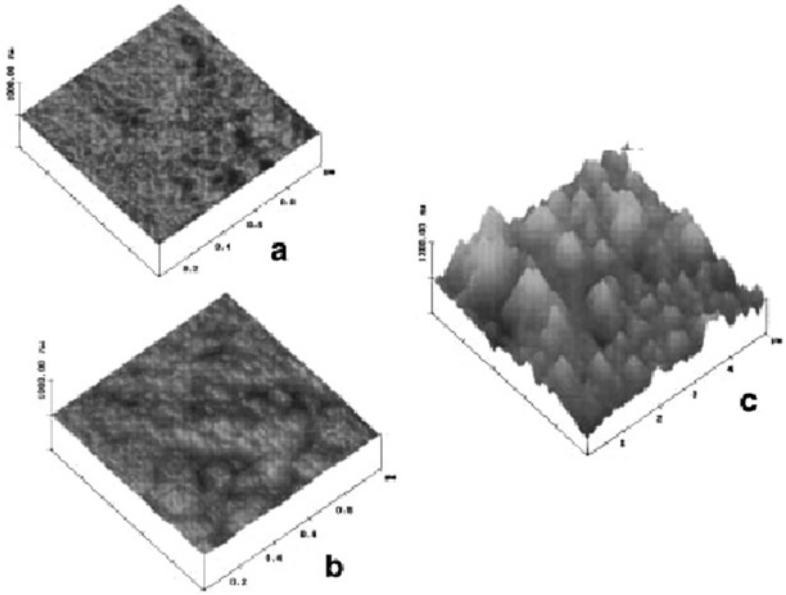


**Figure 14.30** Contact mode AFM images of roughened gold electrodes following oxidation reduction cycling (ORC) in 0.1 M KCl (a) *R* 0.7 (five ORCs); (b) *R* 3.1 (20 ORCs); (c) *R* 10.5 (60 ORCs). Reprinted with permission from reference (90). Copyright 1998, American Chemical Society.

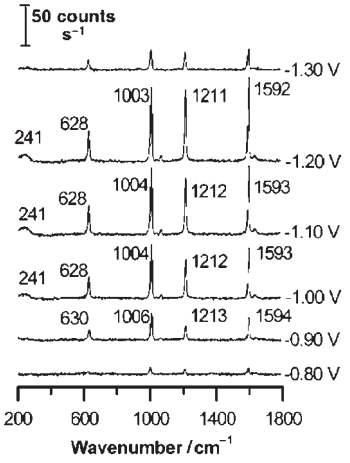


**Figure 14.31** The potential-dependent SERS spectra of adsorbed pyridine from a cobalt electrode in $10^{-2}$ M pyridine/0.1 M $NaClO_4$. The electrode was roughened electrochemically. The laser excitation line was 632.8 nm. Reproduced from reference (86) with permission from the Royal Society of Chemistry.

adsorbate and how this influences heterogeneous electron transfer (92). Studies focusing on the potential dependence of SERS spectra for water and hydroxyl ions on silver have demonstrated the feasibility of probing solvent molecules within the inner layer of the interface, as well as those associated with the solvation shells of adsorbed cations (93, 94). The comparative power of IRRAS and Raman methods in probing the interfacial layer have been discussed and the power of SERS in probing this environment arises from: (a) much less restrictive selection rules than IRRAS which is subject to the surface selection rule that dictates that only adsorbed species with dipole moments perpendicular to the surface are IR active; (b) greater sensitivity due to EM and chemical enhancement; (c) wider optical ranges (95). Although IRRAS methods can also benefit from surface plasmon enhancement (96), the effect is considerably weaker than for SERS. The surface selection rules for IR spectroscopy are not necessarily a disadvantage because they can yield clues to orientation of adsorbates on surfaces. Although both SERS and IRRAS have their merits, combination of both techniques to study a single surface can lead to unprecedented structural insights.

## 14.6 OUTLOOK

Spectroelectrochemistry continues to provide unique insights into interfacial reaction and redox processes. Electrochemical methods continue to find partners across a diverse range of spectroscopic methods, both optical and non-optical. As spectroscopic methods continue to develop and improvements in light focusing and collection optics improve, increasing use of imaging is likely. The increasing use of microscopes as optical elements in spectroelectrochemistry leads to the possibility of imaging, which will compliment and may be used in tandem with existing electrochemical methods. For example, epifluorescence imaging of potential-dependent adsorption and desorption at an electrode interface has been described (97) and wavelength-dispersive multispectral imaging of ion-selective membranes have been reported (98). Imaging of spectroelectrochemical and interfacial processes will inevitably extend to IR and Raman methods as well. In particular, the use of confocal optics is likely to find increasing use in spectroelectrochemical studies, particularly in interfacial studies as a result of the ability of this arrangement to selectively interrogate very small sample volumes. Z-piezo control on many confocal microscopes will allow depth resolved studies into the diffusion layer and beyond. Combination of less common spectroscopic methods such as circular dichroism have been applied to spectroelectrochemical methods and this is likely to increase, particularly in studies of biological materials where conformational changes in response to an electric field or potential responses can be monitored.

Scanning near field optical microscopy (SNOM), developed in the 1990s, combines the advantages of conventional scanning probe methods for topological information and the advantages of optical imaging for structural information, and permits the optical imaging of materials and structures beyond the optical diffraction limit. This method utilizes a scanning probe reminiscent of that used in other scanning probe methods; the critical difference is that the micromachined probe tip acts as a nanoscale light source. The tiny distances between probe and sample are in the near field, which means that the optical resolution of the image is not restricted as conventional far-field imaging is by the diffraction limit.

SNOM can be applied in a range of modes including transmission, reflectance, and emission. Such techniques are likely to be coupled to electrochemical studies in the future. The spatial resolution of such imaging makes the possibility of interrogating potential control of single molecules a reality.

## REFERENCES


1. E. Wolcan, M. R. Feliz, G. T. Ruiz, M. P. Juliarena, R. O. Lezna, *J. Electroanal. Chem*. **101**, 533 (2002).
2. R. J. Gale, Ed., *Spectroelectrochemistry, Theory and Practise*, Plenum Press: New York, 1988.
3. G. R. Fowler, *Introduction to Modern Optics*, Dover: New York, 1989.
4. C. A. Goss, D. H. Charych, M. Majda, *Anal. Chem*. **63**, 85 (1991).
5. (a) J. Stotter, J. Zak, Z. Behier, Y. Show, G. M. Swain, *Anal. Chem.* **74**, 5924 (2002). (b) M. Hupert, A. Muck, R. Wang, J. Stotter, Z. Cvackova, S. Haymond, Y. Show, G. M. Swain, *Diamond Relat. Mat*. **12**, 1940 (2003).
6. J. K. Zak, J. E. Butler, G. M. Swain, *Anal. Chem.* **73**, 908 (2001).
7. J. Stotter, S. Haymond, J. K. Zak, Y. Show, Z. Cvackova, G. M. Swain, *Interface* **12**, 33 (2003).
8. J. Stotter, J. Zak, Z. Behler, Y. Show, G. M. Swain, *Anal. Chem.* **74**, 5924 (2002).
9. H. B. Martin, P. W. Morrison, *Electrochem. Solid State Lett.* **4**, E17 (2001).
10. P. A. Flowers, M. A. Maynor, D. E. Owens, *Anal. Chem.* **74**, 720 (2002).
11. M. L. Meyer, T. P. DeAngelis, W. R. Heineman, *Anal. Chem.* **49**, 602 (1977).
12. Y. Zhy, G. Cheng, S. Dong, *Electroanalysis* **12**, 10736 (1999).
13. D. A. Scherson, S. Sarangapani, F. L. Urback, *Anal. Chem.* **57**(7), 1501 (1985).
14. D. Collison, F. E. Mabbs, E. J. L. McInnes, K. J. Taylor, A. J. Welch, L. J. Yellowlees, J. *Chem. Soc., Dalton Trans.* **3**, 329 (1996).
15. X. Q. Lin, K. M. Kadish, *Anal. Chem.* **57**(7), 1498 (1985).
16. (a) M. B. G. Pilkington, B. A. Coles, R. G. Compton, *Anal. Chem.* **61**, 1787 (1989). (b) I. Bedja, S. Hotchandani, P. V. Kamat, *J. Phys. Chem*. **97**, 11064, (1993).
17. A. T. Hubbard, F. C. Anson, *Electroanal. Chem.* **4**, 129 (1970).
18. T. Chen, S. J. Dong, Y. W. Xie, *J. Electroanal. Chem.* **379**, 239 (1994).
19. R. G. Compton, J. Winkler, D. J. Riley, S. D. Bearpark, *J. Phys. Chem.* **98**, 6818 (1994).
20. N. Chanda, B. Sarkar, J. Fiedler, W. Kaim, G. K. Lahiri, *Dalton Trans.* **18**, 3550 (2003).
21. (a) N. S. Hush, *Prog. Inorg. Chem.* **8**, 391 (1967). (b) M. B. Robin, P. Day, *Adv. Inorg. Radiochem.* **10**, 247 (1967).
22. T. E. Keyes, R. J. Forster, P. M. Jayaweera, C. G. Coates, J. J. McGarvey, J. G. Vos, *Inorg. Chem.* **37**, 5925 (1998).
23. H. E. Toma, K. Araki, *Curr. Org. Chem.* **6**, 21 (2002).
24. S. Dong, J. Niu, T. Cotton, *Methods Enzymol.* **246**, 701 (1995).
25. M. L. Fultz, R. Durst, *Anal. Chim. Acta* **140**, 1 (1982).
26. N. Patel, D. K. Jones, E. L. Raven, *Eur. J. Biochem*. **267**, 2581 (2000).
27. C. Taboy, C. Bonaventure, A. Crumbliss, *Methods Enzymol.* **353**, 187 (2002).
28. C. Taboy, K. M. Faulkner, D. Kraiter, C. Bonaventure, A. Crumbliss, *J. Biol Chem.* **275**, 39048 (2000).
29. N. Winograd, T. Kuwana, *Electroanal. Chem.* **7**, 1 (1974).
30. J. Salbeck, *J. Electroanal. Chem.* **340**, 169 (1992).
31. M. Shi, X. Gao, *Electroanalysis* **2**, 471 (1990).
32. N. J. Simmons, M. D. Porter, *Anal. Chem.* **69**, 2866 (1997).

33. J. López-Palacios, A. Colina, A. Heras, V. Ruiz, L. Fuente, *Anal. Chem.* **73**, 2883 (2001).
34. P. G. Miney, M. V. Schiza, M. L. Myrick, *Electroanalysis* **16**, 113 (2004).
35. I. S. Zavarine, C. P. Kubiak, *J. Electroanal. Chem.* **495**, 106 (2001).
36. M. G. Hill, J. P. Bullock, T. Wilson, P. Bacon, C. P. Blaine, K. Mann, *Inorg. Chim. Acta* **226**, 61 (1994).
37. N. R. de Tacconi, R. O. Lezna, R. Konduri, F. Ongeri, K. Rajeshwar, F. M. MacDonnell, *Chem. Eur. J.* **11**, 4327 (2005).
38. U. Schröder, F Scholz, *J. Solid State Electrochem.* **1**, 62 (2001).
39. Y Shi, A. F. Slaterbeck, C. J. Seliskar, W. R. Heineman, *Anal. Chem.* **69**, 3679 (1997).
40. J. Tarabek, P. Rapta, M. Kalbac, L. Dunsch, *Anal. Chem.* **76**, 19, 5918 (2004).
41. I. T. Bae, M. Sandifer, Y. W. Lee, D. A. Tryk, C. N. Sukenik, D. A. Scherson, *Anal. Chem.* **67**, 24, 4508 (1995).
42. D. R. Dunphy, S. B. Mendes, S. S. Saavedra, N. R. Armstrong, *Anal. Chem.* **69**, 3086 (1997).
43. S. Simison, A. Pellicano, D. J. Schiffrin, *J. Chem. Soc., Faraday Trans.* **94**, 3439 (1998).
44. M. J. Simone, W. R. Heineman, G. P. Kreishman, *Anal. Chem.* **54**, 2382 (1982).
45. (a) Y. F. Lee, J. R. Kirchoff, *Anal. Chem.* **65**(23), 3430 (1993). (b) J. R. Kirchoff, *Curr. Sep.* **16**, 1 (1997).
46. J.-S. Yu, T.-Y. Zhou, *J. Electroanal. Chem.* **504**, 89 (2001).
47. Y. F. Lee, J. R. Kirchhoff, *J. Am. Chem. Soc.* **116**, 3599 (1994).
48. Z. Ding, R. G. Wellington, P. F. Brevet, H. H. Girault, *J. Phys. Chem.* **100**, 10658 (1996).
49. T. E. Keyes, B. Everard, C. Brady, J. G. Vos, *Dalton Trans.* **15**, 2341 (2004).
50. R. J. Forster, T. E. Keyes, *J. Phys. Chem.* **102**, 10004 (1998).
51. J. M. Hollas, *Modern Spectroscopy*, Wiley: Chichester, UK, 1996.
52. K. M. Kadish, X. H. Mu, X. Q. Lin, *Electroanalysis* **1**, 35 (1989).
53. M. Krejcik, M. Danek, F. Hartl, *J. Electroanal. Chem. Interfacial Electrochem.* **317**, 179 (1991).
54. F. Hartl, H. Luyten, H. A. Nieuwenhuis, G. Schoemaker, *Appl. Spectrosc.* **48**, 1522 (1994).
55. T. Iwasita, F. C. Nart, *Prog. Surf. Sci.* **55**, 271 (1997).
56. K. Ashley, S. Pons, *Chem. Rev.* **88**, 673 (1988).
57. J.-N. Chazalviel, B. H. Erne, F. Maroun, F. Ozanam, *J. Electroanal. Chem.* **502,** 180 (2001).
58. A. Bewick, K. Kunimatsu, S. Pons, J. W. Russell, *J. Electroanal. Chem.* **160**, 47 (1984). (b) S. Pons, *J. Electroanal. Chem.* **150**, 495 (1983).
59. C. Korzeniewski, S. Pons, *J. Vac. Sci. Tech. B* **3,** 1421, (1985).
60. J. D Mozo, M. Dominguez, E. Roldan, J. M. Rodrigues Mellado, *Electroanalysis* **12**, 767 (2000).
61. A. S. Viana, A. H. Jones, L. M. Abrantes, M. Kalaji, *J. Electroanal. Chem.* **500**, 290 (2001).
62. J. P. al Dulaimi, A. M. Bond, R. J. H. Clark, N. C. Harden, D. G. Humphrey, *J. Chem. Soc., Dalton Trans.* **12**, 2541 (2002).
63. D. A. Brevnon, E. Hutter, J. H. Fendler, *Appl. Spectrosc.* **2**, 58 (2004).
64. B. W. Johnson, J. Bauhofer, K. Doblhofer, B. Pettinger, *Electrochim. Acta* **37**(12), 2321 (1992).
65. W. Plieth, G. S. Wilson, G. C. de la Fe, *Pure Appl. Chem.* **70**, 1395 (1998).
66. Z. Q. Tian, B. Ren, "Raman Spectroscopy of Electrode Surfaces", in *Encyclopedia of Electrochemistry, Instrumentation and Electroanalytical*, A. J. Bard, M. Stratmann, P. R. Unwin, Eds., Wiley-VCH: Weinheim, 2003, Vol. 3, pp. 572–659.
67. (a) I. C. G. Thanos, *J. Electroanal. Chem.* **200**, 23 (1986). (b) A. J. McQuillan, P. J Hendra, M. Fleischmann *J. Electroanal. Chem.* **65**, 933 (1975).
68. M. H. Schoenfisch, J. E. Pemberton, *Langmuir* **15**, 509 (1999).
69. J. E. Pemberton, A. Shen, *Phys. Chem. Chem. Phys*. **1**, 5671 (1999).
70. Q. Hu, A. S. Hinman, *Anal. Chem.* **72**, 3233 (2000).
71. T. E. Keyes, R. J. Forster, A. M. Bond, W. Miaou, *J. Am. Chem. Soc.* **123**, 2877 (2001).
72. R. J. Forster, T. E. Keyes, A. M. Bond, *J. Phys. Chem. B* **104**, 27, 6389 (2000).

73. We refer here to vibronic resonance Raman spectroscopy.
74. D. A. Long, *The Raman Effect*, Wiley: Chichester, UK, 2002.
75. T. E. Keyes, D. Leane, R. J. Forster, C. G. Coates, J. J. McGarvey, J. G. Vos, *Inorg. Chem.* **41**, 5721 (2002).
76. Z.-Q. Tian, B. Ren, D.-Y. Wu, *J. Phys. Chem. B* **106**, 37 (2002).
77. A. Campion, P. Kambhampati, *Chem. Soc. Rev.* **27**, 241 (1998).
78. (a) D. J. Maxwell, S. R. Emory, S. M. Nie, *Chem. Mater.* **13**(3), 1082 (2001). (b) S. Nie, S. R. Emory, *Science* **275**, 1102 (1997).
79. (a) Z. Q. Tian, B. Ren, D. Y. Wu, *J. Phys. Chem. B* **106**, 9463 (2002).
80. S. Zou, M. J. Weaver, *Anal. Chem.* **70**, 2387 (1988).
81. M. F. Mrozek, Y. Xie, M. J Weaver, *Anal. Chem.* **73**, 5953 (2001).
82. M. F. Mrozek, S. A. Wasileski, M. J. Weaver, *J. Am. Chem. Soc.* **123**, 12817 (2001).
83. T. R. Jensen, M. D. Malinsky, C. L. Haynes, R. P. Van Duyne, *J. Phys. Chem. B* **104**, 10549 (2000).
84. M. Moskovits, *Rev. Mod. Phys.* **57**, 783 (1985).
85. L. A. Dick, A. D. McFarland, C. L Haynes, *J. Phys. Chem. B* **106**, 853 (2002).
86. K. Kneipp, H. Kneipp, I. Itzkan, R. R. Dasar, M. S. Feld, *Chem. Rev.* **99**, 2957 (1999).
87. D. Y. Wu, Y. Xie, B. Ren, J. W. Yan, B. W. Mao, Z. Q. Tian, *Phys. Chem. Commun.* **18**, 1 (2001).
88. P. Gao, D. Gosztola, L-W. H. Leung, M. J. Weaver, *J. Electroanal. Chem.* **233**, 211 (1987).
89. S. Byahu, T. E. Furtak, *Langmuir* **7**, 508 (1991).
90. A. G. Brolo, D. E. Irish, G. Szymanski, J. Lipkowski, *Langmuir* **14**, 517 (1998).
91. Y.-Y. Song, Z.-D. Gao, J. J. Kelly, X.-H. Xia, *Electrochem. Solid State Lett.* **8**, 10, C148 (2005).
92. L. A. Dick, A. J. Haes, R. P. Van Duyne, *J. Phys. Chem B* **104**, 11752 (2000).
93. Z. Q Tian, B. Ren, *Ann. Rev. Phys. Chem.* **55**, 197 (2004).
94. Y. X. Chen, S. Z. Zou, K. Q. Huang, Z. Q. Tian, *J. Raman Spectrosc.* **29**, 749 (1998).
95. M. J. Weaver, *Top. Catal.* **8**, 65 (1999).
96. R. Kellner, B. Mizaikoff, M. Jakusch, H. D. Wanzenbock, N. Weissenbacher, *Appl. Spectrosc.* **5**, 495 (1997).
97. J. Shepherd, Y. Yang, D. Bizzotto, *J. Electroanal. Chem*. **524**, 54 (2002).
98. R. E. Gyurcsányi, E. Lindner, *Anal. Chem.* **77**, 2132 (2005).

This page intentionally left blank

# Part Four

## APPLICATIONS

This page intentionally left blank

# – 15 –

# Determination of Electrode Kinetics

**Michael V. Mirkin**

Department of Chemistry and Biochemistry,
Queens College—CUNY, Flushing, NY 11367, USA

## 15.1 INTRODUCTION TO KINETIC MEASUREMENTS

This chapter is concerned with measurements of kinetic parameters of heterogeneous electron transfer (ET) processes (i.e., standard heterogeneous rate constant $k^\circ$ and transfer coefficient $\alpha$) and homogeneous rate constants of coupled chemical reactions. A typical electrochemical process comprises at least three consecutive steps: diffusion of the reactant to the electrode surface, heterogeneous ET, and diffusion of the product into the bulk solution. The overall kinetics of such a multi-step process is determined by its slow step whose rate can be measured experimentally. The principles of such measurements can be seen from the simplified equivalence circuit of an electrochemical cell (Figure 15.1).

According to Figure 15.1, electrons can be transferred across the electrode/solution interface via two parallel pathways, i.e., the faradaic process, which is represented by the charge transfer resistance and diffusion (Warburg) impedance connected in series, and the charging/discharging of the electrical double layer. In both cases, the current flows through solution, which is represented by the ohmic resistance $R_s$. The second pathway is important only if the electrode potential (or surface area) is changed rapidly, as in chronoamperometry, fast-scan voltammetry, or polarography. In this case, the kinetic parameters can be determined only after separating faradaic current from the double layer charging current. Under steady-state conditions, the charging current is negligibly small and the range of accessible kinetic parameters is determined by the values of $R_{ct}$, $Z_w$, and $R_s$. Clearly, the charge transfer resistance can be measured accurately only if it is much larger than the solution resistance. The $R_{ct}$ value is inversely proportional to the standard rate constant of the charge transfer (CT) reaction, $k^\circ$. Therefore, the magnitude of solution resistance is less important when relatively slow kinetics (i.e., $k^\circ \ll 0.1$ cm/sec) is measured. In contrast, fast electrode kinetics (e.g., $k^\circ > 0.1$ cm/sec) can be studied if the ohmic potential drop is either very small (e.g., at ultramicroelectrodes (UMEs) under steady-state conditions) or fully compensated.

Another requirement for successful measurement of heterogeneous kinetics is that $R_{ct}$ must be at least comparable to $Z_w$, i.e., the overall process must not be diffusion controlled.


**Handbook of Electrochemistry**
**Edited by C.G. Zoski**

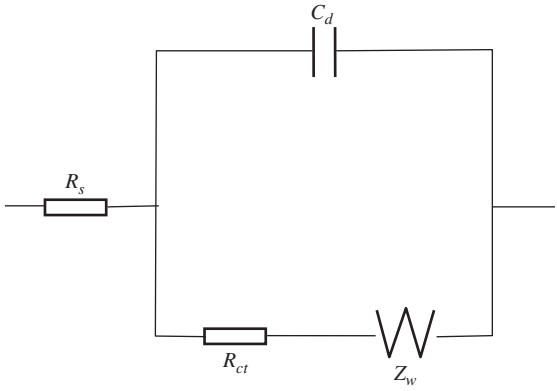


**Figure 15.1** Equivalent circuit model of a simple electrochemical process. $R_s$ is the solution resistance, $R_{ct}$ is the charge transfer resistance, $Z_w$ is the Warburg impedance, and $C_d$ is the double layer capacitance.

When the ET rate is much slower than that of the mass transfer, the process is practically irreversible, and the determination of the kinetic parameters is relatively straightforward (see Section 2.1.1 in reference (1) for the discussion of electrochemical reversibility). In contrast, when the mass transfer and ET rates are comparable, the process is quasi-reversible and the kinetic analysis is more complicated.

The mass transfer rate can be expressed in terms of the mass transfer coefficient $m$. For uniformly accessible electrodes, the mass transfer coefficient can be defined as

$$m = i_l/(nFAc^\circ) \tag{15.1}$$

where $i_l$ is the characteristic mass transfer current for a specific electrochemical method, e.g., diffusion limiting current in polarography or peak current in linear sweep voltammetry (2), $n$ is the number of transferred charges, $F$ is the Faraday constant, $A$ is the electrode surface area, and $c^\circ$ is the bulk concentration of the reactant.

There are many ways to increase the mass transfer rate, e.g., by employing fast convection in hydrodynamic techniques or by applying high-frequency perturbation in impedance measurements. In this chapter, we will focus on two approaches: steady-state techniques and transient methods. In the former case, the high mass transfer rate is achieved by decreasing a suitable geometric parameter, e.g., the UME radius or the thickness of a thin-layer cell. However, to investigate fast heterogeneous reactions ($k^\circ \geq 1$ cm/sec) under steady-state conditions one has to fabricate submicrometer-sized devices, which is not straightforward. In contrast, transient measurements are based on quick perturbation of electrochemical equilibrium and monitoring of the response on a sufficiently short experimental time scale. In this way, high mass transfer rates can be obtained with macroscopic electrodes or micrometer-sized UMEs. Unfortunately, the problems caused by resistive potential drop in solution and charging current, which are more significant at shorter times, often hamper the applications of transient techniques to fast kinetic measurements.

The kinetic parameters of a coupled homogeneous chemical reaction can be determined electrochemically as long as they affect the magnitude of the measured signal. Because of the large variety of possible multi-step processes, it is not easy to define the limits of measurable

homogeneous rate constants (they are typically described by kinetic zone diagrams applicable to specific mechanisms; see Chapter 12 in reference (1)). Generally, the time window of the electrochemical experiment should match the time scale of the homogeneous reaction. Thus, the need for a high mass transfer rate and the problems caused by uncompensated solution resistance and double layer charging current discussed above are equally important for studies of fast coupled chemical reactions.

In this chapter, we focus on extraction of kinetic parameters from experimental dependences generated by several widely used electrochemical methods. It is presumed that the reader is familiar with the fundamentals of those methods as well as with the basics of electrode kinetics discussed in the previous chapters of this handbook and in standard electrochemistry texts (1, 3).

## 15.2 HETEROGENEOUS ELECTRON TRANSFER: TRANSIENT METHODS

### 15.2.1 Linear sweep and cyclic voltammetry

The mass transfer coefficient in linear sweep voltammetry and cyclic voltammetry is directly proportional to the square root of the potential scan rate $v^{1/2}$. Accordingly, the apparent reversibility of an ET reaction under voltammetric conditions is determined by the value of the dimensionless parameter $\Lambda = k^{\circ}\sqrt{RT/FDv}$ (4), and the kinetic zones can be specified as follows:

Reversible: $\Lambda > 15$
Quasireversible: $15 \geq \Lambda \geq 10^{-2(1+\alpha)}$
Irreversible: $\Lambda < 10^{-2(1+\alpha)}$

Assuming common parameter values ($T$ = 298 K, $D = 10^{-5}$ cm$^2$/sec, and $\alpha = 0.5$), the quasi-reversibility limits can be defined in terms of $k^{\circ}$ and $v$: $0.3v^{1/2} \geq k^{\circ} \geq 2 \times 10^{-5}v^{1/2}$, where the unit of $k^{\circ}$ cm/sec and of $v$ is in V/sec. In theory, by increasing $v$, one can render a completely reversible (Nernstian) electrode reaction quasi-reversible and even irreversible (i.e., totally controlled by ET kinetics) in order to determine its kinetic parameters. Practically, this approach is limited by the simultaneous increases in the double layer charging current and resistive potential drop in solution.

It is relatively easy to extract the kinetic parameters of a one-step irreversible ET reaction from a linear sweep voltammogram obtained at a large, e.g., mm-sized electrode (see Chapter 6 for discussion of the differences between macro- and microelectrode behaviors). The transfer coefficient $\alpha$ can be found from the slope of the linear dependence of the peak current vs. square root of the potential scan rate ($i_p$ vs. $v^{1/2}$):

$$i_p = 2.99 \times 10^5 \alpha^{1/2} Ac\ D^{1/2} v^{1/2} \tag{15.2}$$

The same parameter can also be found from the difference between the peak potential $E_p$ and the half-peak potential:

$$\alpha = \frac{47.7\ \text{mV}}{|E_p - E_{p/2}|} (\text{at } 25\ ^{\circ}\text{C}) \tag{15.3}$$

where $E_{p/2}$ is the potential where the current equals one half of the peak value. The standard rate constant of a one-electron reduction reaction can be found from equation (15.4):

$$E_p = E^{\circ\prime} - \frac{RT}{\alpha F}\left[0.78 - \ln\frac{D_O^{1/2}}{k^\circ} + 0.5\ln\frac{\alpha F v}{RT}\right] \tag{15.4}$$

where $E^{o\prime}$ is the formal potential and $D_O$ is the diffusion coefficient of oxidized species.

The task to measure quasi-reversible kinetic parameters is more common than the analysis of completely irreversible voltammograms. The method developed by Nicholson (5) for extraction of standard rate constants from quasi-reversible cyclic voltammograms (CVs) has been most frequently used (and misused) during the last four decades. The method of Nicholson became so popular because of its extreme simplicity. The only required experimental parameter is the difference of two peak potentials, $\Delta E_p = |E_{pa} - E_{pc}|$, where $E_{pa}$ and $E_{pc}$ are the potentials of the anodic and cathodic peaks, respectively. Nicholson showed that $\Delta E_p$ is a function of the single dimensionless kinetic parameter,

$$\psi = \frac{(D_O / D_R)^{\alpha/2} k^\circ}{(\pi D_O v F / RT)^{1/2}} \tag{15.5}$$

After measuring the $\Delta E_p$ value, one can use Table 15.1 to find the corresponding value of $\psi$ (5). When the transfer coefficient is within the range $0.3 < \alpha < 0.7$, which is most common for simple ET reactions, the $\Delta E_p$ value is essentially independent of $\alpha$. Moreover, the diffusion coefficients of oxidized and reduced species are typically similar. Therefore $(D_O / D_R)^{\alpha/2} \cong 1$, and the $k^\circ$ value can be easily calculated from equation (15.5).

Although Nicholson's method has been used extensively to determine the rate constants of quasi-reversible ET reactions, it must be employed judiciously to avoid getting totally

**Table 15.1**

Variation of $\Delta E_p$ with $\psi$ at 25 °C

| $\Psi$ | $\Delta E_p$ (mV) |
|---|---|
| 20 | 61 |
| 7 | 63 |
| 6 | 64 |
| 5 | 65 |
| 4 | 66 |
| 3 | 68 |
| 2 | 72 |
| 1 | 84 |
| 0.75 | 92 |
| 0.5 | 105 |
| 0.35 | 121 |
| 0.25 | 141 |
| 0.10 | 212 |

misleading results. The most common source of error is the uncompensated ohmic potential drop, which may increase the peak separation and produce severe underestimation of the rate constant. Also a $\Delta E_p$ value can be extracted from any cyclic voltammogram including a distorted curve whose shape significantly deviates from the theory. Such deviations may be caused by a number of factors including adsorption, charging current, etc. Therefore, it may be safer to fit the entire voltammogram to the theory (e.g., by using DigiSim program discussed in Section 15.4.3) than to use the values of two peak potentials. Alternatively, the results of Nicholson's analysis can be validated by calculating theoretical curves using the determined parameter values and comparing them to experimental voltammograms obtained at different scan rates.

In addition to analysis of CVs obtained at macroscopic planar electrodes, the approaches discussed above are applicable to fast-scan voltammetry at UMEs. The faradaic response of an UME is essentially equivalent to that of a "large" planar electrode if $v \gg RTD/nFa^2$ (for discussion, see reference (1, p. 232)), where $a$ is the radius of a UME. At high sweep rates, a very high mass transfer rate can be obtained, and the problems associated with the resistive potential drop and charging current are less severe for UMEs than for macroelectrodes. By carefully choosing the experimental conditions to keep both factors under control, and using background subtraction, one can obtain ultrafast CVs—e.g., up to 1 MV/sec (6)—in a good agreement with the theory and use them to determine fast heterogeneous rate constants (Figure 15.2).

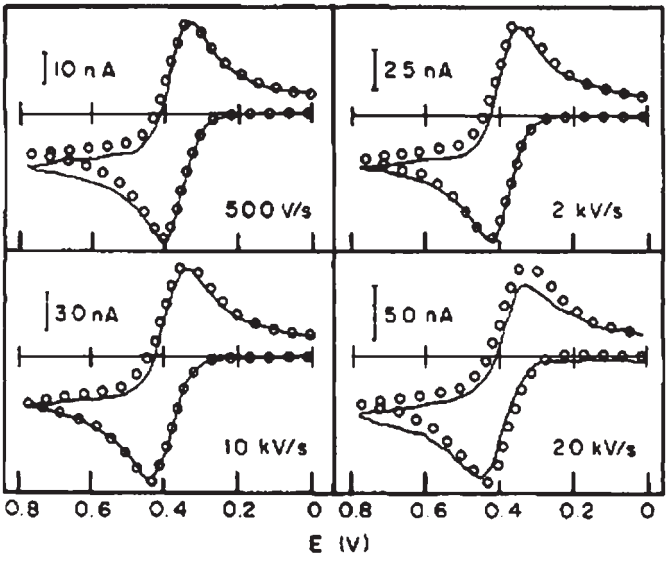


**Figure 15.2** Voltammograms with background current subtracted for the oxidation of 2 mM ferrocene in acetonitrile containing 0.6 M tetraethylammonium perchlorate obtained at a 5-μm-radius gold disk electrode. Solid lines: experimental data. Open circles: simulated data for $k^\circ$ = 3.1 cm/sec and $\alpha$ = 0.5. Reprinted with permission from reference (7). Copyright 1988 American Chemical Society.

### 15.2.2 Sampled-current voltammetry

A large number of potential-relaxation and current-relaxation techniques have been developed in 1950s–1980s for fast kinetic measurements (8). The later advances in UMEs resulted in a less frequent use of relaxation techniques in kinetic experiments. Because of the space limitations, only one large-perturbation method (sampled-current voltammetry) and one small-perturbation technique (alternating current voltammetry) will be considered.

In sampled-current voltammetry, a sigmoidal current vs. potential curve is obtained by applying several potential steps (from the rest potential to the desired value) to the working electrode and recoding current at the same sampling time ($t = \tau$) after the beginning of each step. The mass transfer coefficient in this method is inversely proportional to $\tau^{1/2}$, so that the given electrode process can be fully reversible at a long sampling time, quasi-reversible at shorter $\tau$, and irreversible at very short sampling times. As discussed above, the practical limit for $\tau$ is determined by the resistive and capacitive effects, which impair short-time measurements at macroelectrodes.

Equation (15.6) describes the shape of a sampled-current voltammogram for a general case of a quasi-reversible ET reaction:

$$\frac{i}{i_d} = \frac{F_1(\lambda)}{1+\xi\theta_1} \tag{15.6}$$

where $i_d$ is the Cottrell current, $\xi = \sqrt{D_O/D_R}$, $\theta_1 = \exp[RT/F(E-E^{\circ\prime})]$, $F_1(\lambda) = \pi^{1/2}\lambda\exp(\lambda^2)\mathrm{erfc}(\lambda)$,

$$\lambda = \frac{k_f\tau^{1/2}(1+\xi\theta_1)}{D_O^{1/2}} \tag{15.7}$$

and $k_f = k^\circ \exp[-\alpha nF(E-E^{\circ\prime})/RT]$ for a reduction reaction following Butler–Volmer kinetics.

The kinetic zones in sampled-current voltammetry are determined by the value of the kinetic parameter $\lambda^\circ = k^\circ\tau^{1/2}(1+\xi)/D_O^{1/2}$, and the quasi-reversibility region can be expressed as $10^{-2\alpha} \le \lambda^\circ \le 2$ (for details, see reference (1, p. 196)).

The most general way to determine kinetic parameters from sampled-current voltammetry is to fit an experimental $i/i_d$ vs. $E$ dependence to the theory [equation (15.6)] using $k^\circ$, $\alpha$, and $E^{\circ\prime}$ as adjustable parameters. This can be done using a number of commercially available programs, e.g., TableCurve 2D.

Alternatively, one can determine $k_f$ point-by-point by calculating $F_1(\lambda)$ from the experimental $i/i_d$ values using equation (15.6), and then finding $\lambda$ either numerically or from the table of $F_1$ function. Once $\lambda$ is determined, one can use equation (15.7) to calculate $k_f$ for a given $E$, provided that both $D_O$ and $E^{\circ\prime}$ values are known. $\alpha$ and $k^\circ$ can be found from the slope and the intercept of the linear $\ln k_f$ vs. $E$ plot, respectively.

In the case of a totally irreversible voltammogram, equation (15.6) is simplified to yield

$$\frac{i}{i_d} = F_1(\lambda) \tag{15.8}$$

where $\lambda = k_f \tau^{1/2} / D_O^{1/2}$. Although the kinetic parameters can be found either by curve fitting or calculated point-by-point using equation (15.8), simpler analytical expressions can be used in this case. $k^\circ$ and $\alpha$ can be found from the intercept and the slope of the $E_{1/2}$ vs. $\ln(\tau^{1/2})$ dependence, respectively:

$$E_{1/2} = E^{\circ\prime} + \frac{RT}{\alpha F} \ln\left(\frac{2.31 k^\circ \tau^{1/2}}{D_O^{1/2}}\right) \tag{15.9}$$

Alternatively, from the difference of two quartile potentials $|E_{3/4} - E_{1/4}|$, where $E_{1/4}$ and $E_{3/4}$ are the potential values at which $i = \frac{1}{4} i_d$ and $i = \frac{3}{4} i_d$, respectively, one can find $\alpha$ using Tomeš criterion:

$$|E_{3/4} - E_{1/4}| = 45.0 \text{ mV}/\alpha \tag{15.10}$$

When $\alpha$ is determined, equation (15.9) can be used to calculate $k^\circ$.

### 15.2.3 Ac voltammetry

Ac voltammetry is one of the techniques based on the analysis of faradaic impedance. A low-amplitude sinusoidal voltage ($E_{ac}$) is applied to the working electrode, which is also biased at some dc potential ($E_{dc}$) with respect to the reference electrode. Because of the difference in the time scale, the ac component of the total current can be readily separated from the dc component. The kinetic parameters can be extracted either from the amplitude of ac current, which is measured as a function of $E_{dc}$, or from the phase angle between the ac current and ac voltage, $\phi$.

There are several modifications of this technique. In ac polarography, which employs a dropping mercury working electrode, $E_{dc}$ is changed step-wise (one step per drop lifetime) and the diffusion layer is completely renewed after every drop fall. In linear sweep ac voltammetry, the working electrode is stationary, and $E_{dc}$ is a linear function of time. However, when the sweep rate is slow, the polarographic and voltammetric responses are quite similar, and we will neglect the difference between those two modifications. For more details, one should consult Chapter 10 in reference (1) and the review articles cited therein.

The equivalent circuit corresponding to an uncomplicated electrochemical reaction (i.e., a one-step CT process) is shown in Figure 15.1. An important advantage of ac voltammetry is that it allows relatively easy evaluation of the solution resistance ($R_s$) and double layer capacitance ($C_d$). These elements can be separated from the $Z_w$ and $R_{ct}$ components, which together make faradaic impedance. Without simplifying assumptions, the analysis of faradaic impedance even for a simple ET reaction is rather complicated (9). The commonly used assumptions are that the dc and ac components of the total current can be uncoupled, and the dc response is Nernstian because of the long dc time scale. The latter assumption is reasonable because ac voltammetry is typically used to measure fast electrode kinetics. The ac response of the same electrochemical process may be quasi-reversible on the much shorter ac time scale. Quasi-reversible ac voltammograms are bell-shaped,

and at the high-frequency limit both the peak potential and the peak current become independent of ac frequency, according to equations (15.11a) and (15.11b):

$$E_p = E_{1/2} + \frac{RT}{F}\ln\frac{1-\alpha}{\alpha} \tag{15.11a}$$

$$I_p = \frac{F^2 A k^\circ c^\circ \Delta E \xi^\alpha}{RT}(1-\alpha)^{(1-\alpha)}\alpha^\alpha \tag{15.11b}$$

Although it is possible to determine $\alpha$ from the peak potential [equation (15.11a)] and then use its value to find $k^\circ$ from equation (15.11b), it is more common to extract the kinetic parameters from the phase angle $\phi$. The dependence of cot$\phi$ on the ac frequency ($\omega$) and dc potential is given by equation (15.12), which is valid for both quasi-reversible and irreversible ET kinetics:

$$\cot\phi = 1 + \frac{(2D_R\xi^\beta\omega)^{1/2}}{k^\circ}\frac{1}{e^{(1-\alpha)F(E_{dc}-E_{1/2})/RT}[1+e^{-F(E_{dc}-E_{1/2})/RT}]} \tag{15.12}$$

Kinetic parameters can be determined by fitting experimental cot$\phi$ vs. ($E_{dc} - E_{1/2}$) dependences obtained at different ac frequencies to equation (15.12) (10).

At $E_{dc} = E_{1/2}$, equation (15.12) is simplified to yield

$$\cot\phi = 1 + \frac{(0.5D_R\xi^\beta\omega)^{1/2}}{k^\circ} \tag{15.13}$$

Assuming $D_o \cong D_R$, one can find the standard rate constant from the slope of the linear cot$\phi$ vs. $\omega^{1/2}$ plot (Figure 15.3).

More recently, ac voltammetry was carried out at μm-sized UMEs to further diminish the effect of the resistive potential drop in studies of fast ET reactions (11). These experiments yielded kinetic parameters for several rapid electrode processes in agreement with the results obtained by steady-state techniques.

## 15.3 HETEROGENEOUS ELECTRON TRANSFER: STEADY-STATE METHODS

### 15.3.1 Steady-state voltammetry

There are several ways of obtaining a time-independent (steady-state or pseudo-steady-state) voltammogram. For example, in classical polarography, the current is time dependent, but by measuring it at a same fixed moment during the lifetime of each drop one can obtain a pseudo-steady-state current-potential curve, i.e., a polarogram. True steady-state voltammograms are obtained at a rotating disk electrode, as well as with thin-layer electrochemical cells, and at various UMEs, e.g., microdisks, rings, and spherical caps (12). Steady-state voltammetry is one of the best techniques for studying fast electrochemical kinetics. Its important advantages over the transient methods include the absence of the limitations caused by the charging current (and also ohmic potential drop in the case of UME

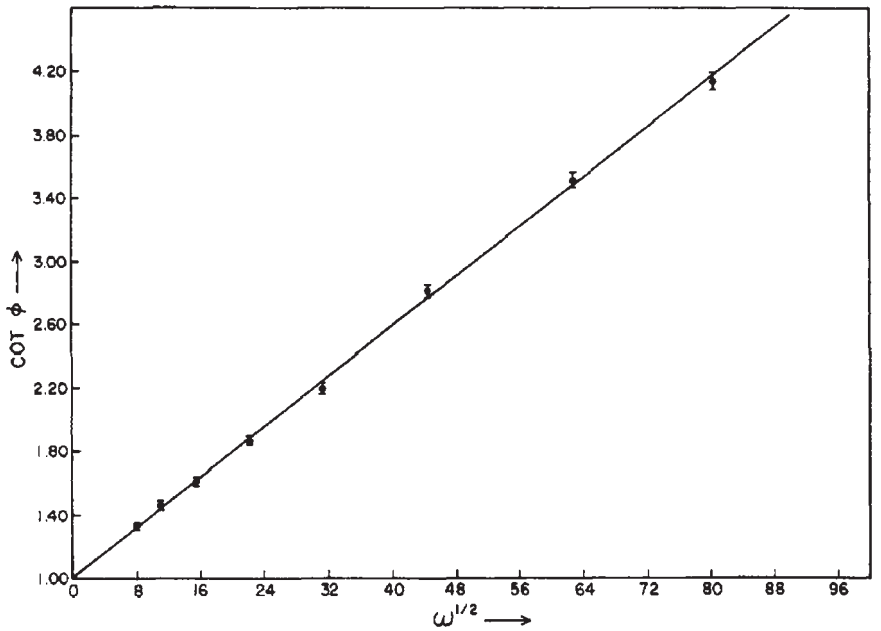


**Figure 15.3** Frequency dependence of phase angle with 3.36 mM $TiCl_4$ in 0.2 M $H_2C_2O_4$. $\Delta E = 5.00$ mV, $E_{dc} = -0.290$ V vs. SCE, $T = 25$ °C. Reprinted with permission from reference (10). Copyright 1963 American Chemical Society.

experiments), insensitivity to low levels of reactant adsorption, relative simplicity of data acquisition, high accuracy, and reproducibility of the results.

Unlike transient methods, the theory for steady-state techniques is relatively simple. Equation (15.14) describes the shape of a steady-state voltammogram at any uniformly accessible working electrode (i.e., when the surface concentrations and diffusion fluxes of redox species are uniform over the entire electrode surface):

$$\frac{i}{i_d} = \frac{1}{\theta + 1/\kappa} \tag{15.14}$$

where $\theta = 1 + \exp[nF(E - E^{\circ\prime})/RT]m_O/m_R$, $\kappa = k^{\circ}\exp[-\alpha nF(E - E^{\circ\prime})/RT]/m_O$. The mass transfer coefficients of oxidized and reduced species, $m_O$ and $m_R$, can be calculated from equation (15.1).

No general analytical expression similar to equation (15.14) is available for a steady-state current vs. potential curve at an electrode whose surface is not uniformly accessible. An exception is a microdisk electrode for which an analytical approximation (15.15) provides an accurate description of a quasireversible steady-state voltammogram (13)

$$\frac{\theta i}{i_d} = \left[1 + \frac{\pi}{\kappa'\theta}\frac{2\kappa'\theta + 3\pi}{4\kappa'\theta + 3\pi^2}\right]^{-1} \tag{15.15}$$

where $\kappa' = (\pi ak^{\circ}/4D_{\mathrm{O}})\exp[-\alpha nF(E-E^{\circ\prime})/RT]$ and $a$ is the disk radius.

If the process is totally irreversible, equation (15.14) is simplified as follows:

$$\frac{i}{i_{\mathrm{d}}} = \frac{1}{1+1/\kappa} \tag{15.16}$$

The kinetic analysis in this case is rather straightforward. The transfer coefficient can be determined directly from the difference of two quartile potentials

$$\alpha = 56.4 \text{ mV}/|E_{3/4} - E_{1/4}| \tag{15.17}$$

Next, one can use equation (15.16) to obtain $\kappa$ for a specific potential value and calculate $k^{\circ} = \kappa m_{\mathrm{O}} \exp[\alpha nF(E-E^{\circ\prime})/RT]$. To use this approach one needs the formal potential value $E^{\circ\prime}$, which may not be readily available for a totally irreversible reaction.

For quasi-reversible processes, both kinetic parameters, $k^{\circ}$ and $\alpha$, and also the formal potential can be determined from the differences of quartile potentials, $\Delta E_{1/4} = |E_{1/2} - E_{1/4}|$ and $\Delta E_{3/4} = |E_{3/4} - E_{1/2}|$ (14). To obtain the parameter values, one has to carefully measure the diffusion limiting current and find the quartile potential values (for reliable determination of a fast rate constant, the uncertainty in both $\Delta E_{3/4}$ and $\Delta E_{1/4}$ values should be $\leq$0.5 mV). Two extensive tables are available in reference (14) for uniformly accessible electrodes and for the microdisk geometry. The $k^{\circ}$, $\alpha$, and $E^{\circ\prime}$ values can be found in the table cell corresponding to the experimentally determined $\Delta E_{1/4}$ and $\Delta E_{3/4}$. This method provides two useful diagnostic criteria: (i) the inequality $|\Delta E_{3/4}| > |\Delta E_{1/4}|$ holds true for any undistorted quasi-reversible voltammogram; and (ii) reliable values of kinetics parameters can only be obtained if $\Delta E_{1/4} \geq 30.5$ mV and $\Delta E_{3/4} \geq 31$ mV (otherwise the voltammogram is essentially Nernstian). For a microdisk electrode, the upper limit for the measurable rate constant can be estimated as $k^{\circ} \lesssim 5D/a$. Taking $D = 10^{-5}$ cm/sec, this limit is ~0.5 cm/sec for a 1-μm-radius UME.

The advantages and disadvantages of the three-point method are similar to those of the Nicholson's method discussed above. The analysis is very fast and simple, and requires no calculations. On the other hand, from the $\Delta E_{1/4}$ and $\Delta E_{3/4}$ values alone one cannot detect imperfections in the shape of the voltammogram caused by uncompensated resistance, electrode surface fouling, and other experimental problems. An alternative approach is to fit the entire experimental voltammogram to either equation (15.14) or equation (15.15) using a suitable curve-fitting computer program.

### 15.3.2 Scanning electrochemical microscopy (SECM)

Scanning electrochemical microscopy (SECM) (see Chapter 12) combines useful features of UMEs and thin-layer cells. The mass transfer rate in SECM is a function of the tip-substrate distance $d$. For an UME far from a substrate, the mass transfer coefficient, $m \sim D/a$, while for the tip near a conductive substrate ($d < a$), $m \sim D/d$. By decreasing the tip-substrate distance, the mass transport rate can be increased sufficiently for quantitative characterization of the ET kinetics, preserving the advantages of steady-state methods, i.e., the absence of problems associated with ohmic drop, adsorption, and charging current. For example, with

$D = 10^{-5}$ cm$^2$/sec, $d = 0.1$ $\mu$m corresponds to $m = 1$ cm/sec. This gives the upper limit for the determinable rate constant of about 10 cm/sec.

SECM theory has been developed for extraction of kinetic parameters of heterogeneous ET reactions occurring at both tip and substrate electrodes. If the mediator regeneration at the substrate is diffusion-controlled, the finite kinetics at the tip can be extracted from steady-state tip voltammograms (15). Conversely, when the tip process is diffusion-controlled, the finite kinetics at the substrate can be extracted from the tip current vs. distance curves (16). For the former situation, two approximate equations have been proposed for calculating the tip current at any potential and separation distance values (15). However, more recent simulations (17) showed that both equations in reference (15) are not very accurate and may yield underestimated $k^\circ$ values. Equation (15.18) is a significantly better approximation:

$$I_T(E,L) = \frac{0.78377}{L(\theta + 1/\kappa)} + \frac{0.68 + 0.3315\exp(-1.0672/L)}{\theta\left[1 + \frac{\pi}{\kappa\theta}\frac{2\kappa\theta + 3\pi}{4\kappa\theta + 3\pi^2}\right]} \tag{15.18}$$

where $\kappa = \pi k^\circ a \exp[-\alpha nF(E - E^{\circ\prime})/RT]/(4D_O I_T^c)$ and $\theta = 1 + \exp[nF(E - E^{\circ\prime})/RT]D_O/D_R$, $E$ is the tip potential, $L = d/a$ is the normalized tip/substrate separation distance, and $I_T^c$ is the normalized tip current for the same $L$ and a diffusion-controlled positive feedback at a conductive substrate

$$I_T^c = 0.68 + 0.78377/L + 0.3315\exp(-1.0672/L) \tag{15.19}$$

At a constant $L$, equation (15.18) describes a quasi-reversible steady-state voltammogram of a reduction reaction at the tip. Kinetic parameters can be determined either by fitting steady-state voltammograms to this equation or by using the three-point method (14) and assuming uniform accessibility of the tip surface, as discussed in the previous section. In this way, the kinetics of the fast oxidation of ferrocene at a Pt tip electrode was measured (15). The reproducible standard rate constant value (3.7 $\pm$ 0.6 cm/sec) was obtained at different tip/substrate distances (Figure 15.4). Thus, one can check the validity of the experimental results and the reliability of the kinetic analysis.

While the mass transfer rate in Figure 15.4 increased with a decrease in the tip-substrate separation, the heterogeneous rate constant and transfer coefficient remained constant within the range of experimental error.

The rate constant of an irreversible heterogeneous reaction occurring at the substrate ($k_f$) can be extracted by fitting an experimental current-distance curve to equation (15.20) (16):

$$I_T(L) = I_S(1 - I_T^{ins}/I_T^c) + I_T^{ins} \tag{15.20a}$$

$$I_S = 0.78377/L(1 + 1/\Lambda) + [0.68 + 0.3315\exp(-1.0672/L)]/[1 + F(L,\Lambda)] \tag{15.20b}$$

where $I_T^c$ and $I_T^{ins}$ are given by equations (15.19) and (15.21), respectively; $I_S$ is the normalized kinetically controlled substrate current; $\Lambda = k_f d/D$, and $F(L,\Lambda) = (11/\Lambda + 7.3)/110 - 40L)$

$$I_T^{ins} = 1/(0.15 + 1.5385/L + 0.58\exp(-1.14/L) + 0.0908\exp[(L - 6.3)/(1.017L)]) \tag{15.21}$$

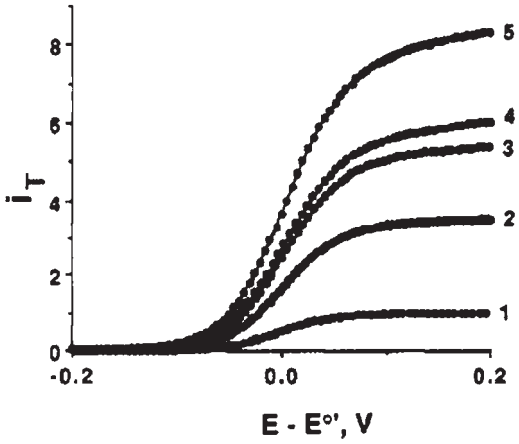


**Figure 15.4** Tip steady-state voltammograms for the oxidation of 5.8 mM ferrocene in 0.52 M $TBABF_4$ in acetonitrile at a 1.08-μm-radius Pt tip. Solid lines calculated from equation (15.25) in reference (15). Tip/substrate normalized separation decreases are $L = \infty$ (1), 0.27 (2), 0.17 (3), 0.14 (4), and 0.10 (5). Reprinted with permission from reference (15). Copyright 1988 American Chemical Society.

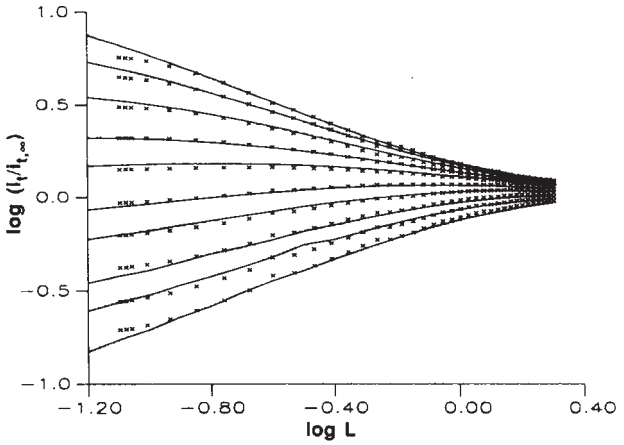


**Figure 15.5** SECM current vs. distance curves for the Fe(III)/Fe(II) system (symbols) and the best theoretical fits to the data (solid curves). The tip (5.5-$\mu$m-radius carbon fiber electrode) was held at a potential of −0.6 V, while the GC substrate electrode was held at various potentials, 300–750 mV, positive of the formal potential (50 mV increments). Reprinted with permission from reference (18). Copyright 1992 American Chemical Society.

Figure 15.5 shows a family of the SECM approach curves obtained at different substrate potentials. $Fe^{3+}$ was reduced at a carbon fiber tip, and the product of this reaction ($Fe^{2+}$) was reoxidized at a glassy-carbon substrate. The rate of the irreversible oxidation of $Fe^{2+}$ increased with increasing substrate potential (from the bottom to the top curve).

A heterogeneous rate constant value corresponding to the specific substrate potential was extracted by fitting each current-distance curve to the theory.

The radius of the portion of the substrate surface participating in the SECM feedback loop can be evaluated as $r \cong a + 1.5d$ (18). Thus at small tip-substrate separations (e.g., $L \leq 2$), a large substrate behaves as a virtual UME of a size comparable with that of the tip electrode. The SECM allows probing local kinetics at a small portion of the macroscopic substrate with all of the advantages of microelectrode measurements.

One should keep in mind that equations (15.19)–(15.21) are valid for RG = 10. Deviations of the experimental approach curves from theory can be expected when a tip with a very small RG (e.g., $< 3$) is used and the kinetics is relatively slow (i.e., $k_f \lesssim D/d$ ).

## 15.4 PROCESSES WITH COUPLED HOMOGENEOUS REACTIONS

### 15.4.1 Linear sweep and cyclic voltammetry

Since the 1960s, cyclic voltammetry has been the most widely used technique for studies of electrode processes with coupled chemical reactions. The theory was developed for numerous mechanisms involving different combinations of reversible, quasi-reversible, and irreversible heterogeneous ET and homogeneous steps. Because of space limitations, we will only consider two well-studied examples—$C_rE_r$ (i.e., first-order reversible reaction preceding reversible ET) and $E_rC_i$ (i.e., reversible ET followed by a first-order irreversible reaction)—to illustrate general principles of the coupled kinetics measurement. A detailed discussion of other mechanisms can be found in Chapter 12 of reference (1) and references cited therein, including a seminal publication by Nicholson and Shain (19).

The kinetic analysis of a complicated electrochemical process involves two crucial steps: the validation of the proposed mechanism and the extraction of the kinetic parameter values from experimental data. In cyclic voltammetry, the variable factor, which determines the mass transfer rate, is the potential sweep rate $v$. Therefore, the kinetic analysis relies on investigation of the dependences of some characteristic features of experimental voltammograms (e.g., peak potentials and currents) on $v$. Because of the large number of factors affecting the overall process rate (concentrations, diffusion coefficients, rate constants, etc.), such an analysis may be overwhelming unless those factors are combined to form a few dimensionless kinetic parameters. The set of such parameters is specific for every mechanism. Also, the expression of the potential and current as normalized (dimensionless) quantities allows one to generalize the theory in the form of dimensionless working curves valid for different values of kinetic, thermodynamic, and mass transport parameters.

In the $C_rE_r$ process, an electroinactive species X is converted into the oxidized species O via reversible chemical reaction (15.22a) preceding reversible ET (15.22b):

$$\mathrm{X} \underset{k_b}{\overset{k_f}{\rightleftharpoons}} \mathrm{O} \tag{15.22a}$$

$$\mathrm{O} + ne^- \rightleftharpoons \mathrm{R} \tag{15.22b}$$

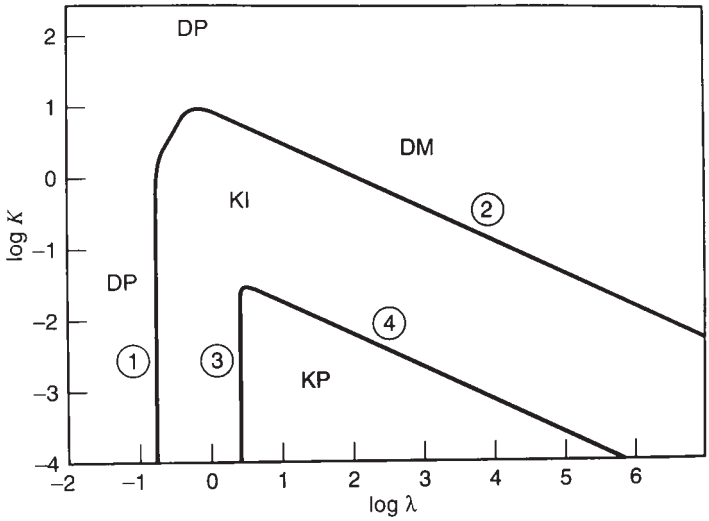


**Figure 15.6** Zone diagram for $C_rE_r$ process. The zones are DP, pure diffusion; KI, intermediate kinetics; KP, pure kinetics; and DM, diffusion modified by equilibrium constant of preceding reaction. Adapted with permission from reference (20). Copyright 1963 Pergamon Press.

The appropriate dimensionless kinetic parameters are $K = k_f/k_b$ and $\lambda = (RT/nF)[(k_f + k_b)/v]$. Using these parameters, the voltammetric behavior of a $C_rE_r$ process can be summarized in a zone diagram (Figure 15.6).

The small $\log\lambda$ (i.e., large $v$) values in Figure 15.6 correspond to the pure diffusion regime (DP). In this zone, reaction (15.22a) is slow on a short experimental time scale and does not significantly affect the concentrations of the redox species in the electrode proximity. The chemical kinetics is too slow to be measured. At higher $\lambda$ values (smaller $v$), the process shifts to the intermediate kinetic zone (KI), where the response is under mixed diffusion/kinetic control. By further decreasing the sweep rate, one can reach the pure kinetic zone (KP). Finally, if the sweep rate is slow and the equilibrium constant, $K$ is sufficiently large (zone DM), reaction (15.22a) comes to equilibrium. The process behavior is diffusion-controlled, but the current magnitude depends on the $K$ value.

These features can also be seen in a family of working curves calculated for $K = 10^{-4}$ (Figure 15.7) (20). When $\lambda \lesssim 0.1$, the process is diffusion-controlled, i.e., $E_p$ is independent of the sweep rate, and $i_p \sim v^{1/2}$. $0.1 \lesssim \lambda \lesssim 1$ corresponds to the KI zone, where the voltammograms gradually change from peak-shaped to sigmoidal. Sigmoidal (S-shaped) curves obtained for $1 \lesssim \lambda \lesssim 100$ represent the KP zone. The current is independent of $v$, and at extreme potentials it reaches the plateau value

$$i_L = nFAD^{1/2}c^{\circ}K(k_f + k_b)^{1/2} \tag{15.23a}$$

The "half-plateau" potential of such a voltammogram (i.e., the potential at which $i = 0.5i_L$) is

$$E_{p/2} = E^{\circ\prime} - \frac{RT}{2nF}(\ln\lambda + 0.554) \tag{15.23b}$$

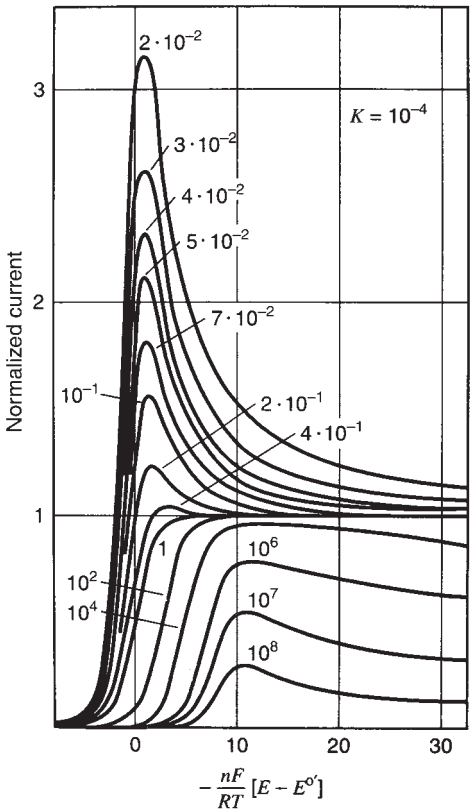


**Figure 15.7** Dimensionless linear sweep voltammograms of $C_rE_r$ process calculated for different values of $\lambda$ shown on each curve and $K = 10^{-4}$. Adapted with permission from reference (20). Copyright 1963 Pergamon Press.

At $\lambda \gtrsim 1000$, the mixed diffusion/kinetic control becomes apparent again (KI zone), and finally, the DM zone is reached at very low scan rates ($\lambda \gtrsim 10^6$).

The kinetic analysis of a $C_rE_r$ process requires a series of experimental voltammograms obtained at various scan rates. The changes in the voltammogram shape with $v$ similar to those shown in Figure 15.6 would be indicative of the $C_rE_r$ mechanism. The next step is to fit the experimental voltammograms to theoretical curves that can be produced by digital simulation (see Section 15.4.3) or generated from the current function tabulated in reference (19), and to extract the rate constant values. The $k_f$ and $k_b$ values are constant and independent of $v$ thus confirming the validity of the proposed mechanism.

The $k_f$ and $k_b$ values can also be determined from a sigmoidal voltammogram obtained under complete kinetic control. Using equation (15.23b), one can obtain $\lambda$ from the $E_{p/2}$ of such a curve and use it to calculate the sum of two rate constants, $k_f + k_b$. Then, equation (15.23a) can be used to find $K$ from the plateau current. With both $\lambda$ and $K$ known, the calculation of $k_f$ and $k_b$ is straightforward.

The kinetic behavior of a $E_rC_i$ process

$$O + ne^- \rightleftharpoons R \tag{15.24a}$$

$$R \xrightarrow{k} X \tag{15.24b}$$

is determined by the single dimensionless kinetic parameter, $\lambda = (RT/nF)(k/v)$, and the corresponding zones are

KP (pure kinetic control): $\lambda > 5$
KI (intermediate kinetic zone): $5 \geq \lambda \geq 0.1$
DP (pure diffusion control): $\lambda < 0.1$

A dramatic effect of $v$ on the voltammogram shape can be seen in Figure 15.8.

In the DP zone (e.g., at $\lambda = 0.01$), the following reaction is too slow to be detected, and the corresponding voltammogram is essentially indistinguishable from CVs of a simple, diffusion-controlled ET. At a lower $v$ (e.g., $\lambda = 0.1$; KI zone), reaction (15.24b) becomes sufficiently fast to compete with diffusion. A significant fraction of species R is converted to electroinactive X before being reoxidized at the electrode surface during the potential sweep in the reverse (anodic) direction. Hence, the decreased height of the reverse peak. The disappearance of the reverse peak at slower $v$ ($\lambda = 10$ or 500; KP zone) is typical of an irreversible chemical reaction following the ET step.

The value of $\lambda$, and subsequently the rate constant of reaction (15.24b), can be obtained by measuring the difference between the peak potential and $E_{1/2}$. The following equation shows that in the KP region this quantity is a linear function of ln $v$:

$$E_p - E_{1/2} = \frac{RT}{2nF}(\ln\lambda - 1.56) \tag{15.25}$$

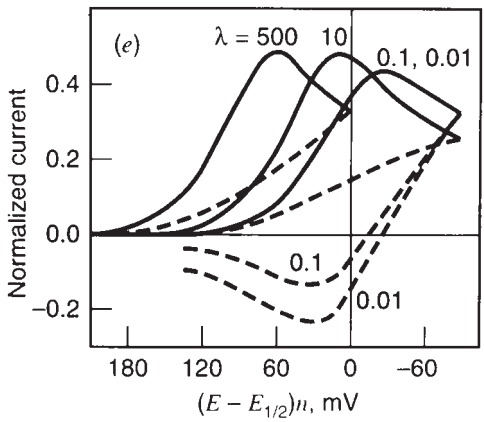


**Figure 15.8** Dimensionless cyclic voltammograms of $E_rC_i$ process calculated for different values of $\lambda$ shown on each curve. Reprinted with permission from reference (19). Copyright 1964 American Chemical Society.

Alternatively, $\lambda$ can be found from the ratio of the reverse and forward voltammetric peaks ($i_{pa}/i_{pc}$) using a working curve presented in reference (19).

### 15.4.2 Scanning electrochemical microscopy (SECM)

Unlike heterogeneous kinetics measurements, which typically employ the feedback mode of the SECM operation (see Chapter 12), homogeneous rate constants are often determined using the tip generation/substrate collection (TG/SC) mode. A TG/SC experiment includes simultaneous measurements of both tip and substrate currents ($i_T$ and $i_S$). For a one-step heterogeneous ET at steady-state, these quantities are almost identical, if $L$ is not very large (the collection efficiency, $i_S/i_T$, is more than 0.99 at $L \leq 2$). Under these conditions, the tip-generated species predominantly diffuse to the large substrate, rather than escape from the tip-substrate gap. For a process with a coupled chemical reaction, there are large differences between $i_S$ and $i_T$, and both quantities provide important kinetic information.

Under TG/SC conditions, the homogeneous chemical reaction competes with diffusion in the tip/substrate gap. For example, consider an ET process followed by an irreversible homogeneous reaction of any order

$$O + 1e^- \rightarrow R \text{ (tip electrode)} \tag{15.26a}$$

$$R + \ldots \rightarrow \text{ electroinactive products (tip-substrate gap)} \tag{15.26b}$$

$$R - 1e^- \rightarrow O \text{ (substrate electrode)} \tag{15.26c}$$

If both heterogeneous processes at the tip and substrate are rapid (at extreme potentials of both electrodes), the overall process rate is controlled either by diffusion in the gap or by the rate of homogeneous chemical reaction (15.26b). If that reaction is slow, the process is diffusion-controlled, the $i_T$ vs. $d$ curves follow the positive feedback theory, and $i_S/i_T \rightarrow 1$ at short separation distances. If reaction (15.26b) is very fast, most species R get converted to electroinactive products before reaching the substrate. Hence, the very low substrate current, and $i_S/i_T \rightarrow 0$. Between these two extreme cases, the kinetics of reaction (15.26b) can be determined by measuring the collection efficiency as a function of $L$. A family of theoretical working curves showing the collection efficiency as a function of the dimensionless rate constant ($K$) is shown in Figure 15.9. As one can expect, $i_S/i_T$ increases with decreasing $L$ and $K$.

The TG/SC theory was developed for several mechanisms; $E_rC_{2i}$ (ET followed by second-order irreversible dimerization of the product) (21), $E_rC_i$ (22), and more complicated ECE/DISP mechanisms involving two ET steps (23). In all cases, the kinetics have to be found by fitting the experimental approach curves to theoretical curves generated by numerically solving two-dimensional diffusion equations. These procedures are rather complicated, and here we consider only the determination of $E_rC_i$ and $E_rC_{2i}$ rate constants based on analytical approximations (24). A comprehensive discussion of the SECM studies of coupled chemical reactions is available (25).

For each mechanism, $i_S/i_T$ is determined by the single dimensionless parameter $\kappa$. In case of the $E_rC_i$ mechanism, $\kappa = k_c d^2/D$; and for $E_rC_{2i}$, $\kappa = c^\circ k d^3/aD$. Two analytical approximations can be used to relate $\kappa$ to collection efficiency (24)

$$\kappa = 5.608 + 9.347\exp(-7.527x) - 7.616\exp(-0.307/x) \quad (E_rC_i) \tag{15.27a}$$

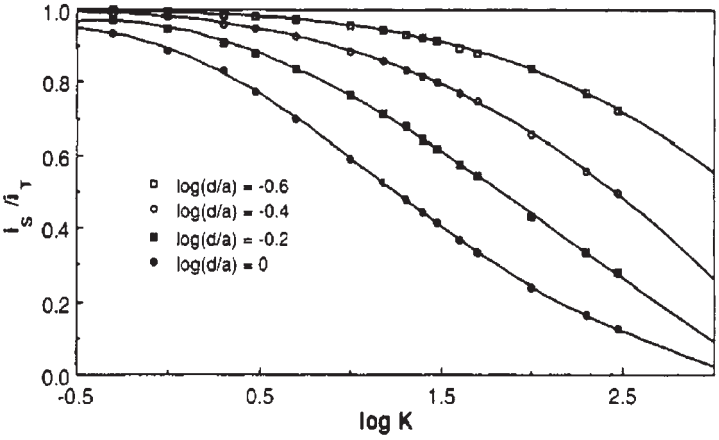


**Figure 15.9** Simulated SECM collection efficiency ($i_S/i_T$) vs. $K$ dependences for the $E_rC_{2i}$ mechanism. The tip/substrate separation distances corresponding to each curve are shown. $K = ka^2c^*/D$. Reprinted with permission from reference (21). Copyright 1992 American Chemical Society.

and

$$\kappa = 104.87 - 9.948x - 185.89/x^{1/2} + 90.199/x + 0.389/x^2 \quad (E_rC_{2i}) \tag{15.27b}$$

where $x = i_S/i_T$. The collection efficiency values most suitable for determination of $k$ are those between about 0.2 and 0.8.

To find the collection efficiency experimentally, one has to measure both $i_S$ and $i_T$ values as functions of $d$. This is possible if the substrate current is produced only by oxidation/reduction of species generated at the tip (i.e., $i_S = 0$ at large $d$). If the substrate current cannot be measured accurately, the collection efficiency can be calculated from the experimental tip current vs. distance curve using equation (15.28):

$$i_S/i_T = (1 - I_T^{ins}/I_T)/[1 - f(L)] \tag{15.28}$$

which can be derived from equation (15.20a); $f(L) = I_T^{ins}/I_T^c$.

Most other electrochemical techniques employed for homogeneous kinetics studies are also based on the generation/collection scheme. Among them is the rotating ring-disk method (the employed probe comprises concentrical disk generator and ring collector electrodes), which has been very popular before the introduction of UMEs (26). A more recent and powerful approach employing arrays of parallel microband electrodes has been reviewed in reference (27).

### 15.4.3 Simulations and curve fitting

The theory for most systems involving coupled chemical reactions is rather complicated. Analytical approximations are available only for a limited number of relatively simple processes. "Semi-analytical" solutions based on infinite series, integral equations, tabulated

functions, etc., are available for some systems (see reference (19) for several useful examples of such solutions). In general—especially for multi-dimensional UME diffusion problems—numerical solution of partial differential equations is required to generate theoretical curves; this complicates the extraction of the kinetic parameters from experimental data.

Since Feldberg's pioneering publication (28), many approaches to numerically solving electrochemical diffusion problems—"digital simulation"—have been developed to treat various mechanisms and electrode geometries. A more recent trend has been from developing new algorithms to using commercially available simulation packages. Typical advantages of the commercial packages are computational efficiency, versatility, and ease of use. For example, modifying the system geometry or changing the reaction sequence typically takes only a few minutes using commercial software, while a similar task may not be straightforward for a home-written simulation program.

In macroelectrode electrochemistry, where the diffusion problem is typically one-dimensional (either linear, spherical, or cylindrical), a powerful DigiSim program (Bioanalytical Systems, West Lafayette, IN) allows one to treat various mechanisms without doing any calculus or computer programming (29). The program is designed mainly for CV simulations, but potentiostatic transients can also be obtained. To generate a theoretical curve using DigiSim, one only needs to type in chemical equations of the related electrochemical/homogeneous reactions and the values of rate constants, diffusion, coefficients, and other parameters. The simulation results include concentration profiles of all species involved at any time moment, and current vs. time dependences. The effects of the double layer charging and the resistive potential drop in solution can be included. A typical example of data simulated using DigiSim for the $E_qC_r$ mechanism is shown in Figure 15.10. The possibilities to consider simultaneously concentration profiles and CVs and to see curves corresponding to different parameter values in the same graph facilitate the mechanistic analysis.

Another important feature of DigiSim is automated curve fitting. An experimental voltammogram can be imported and fitted to the theory generated for the chosen mechanism and geometry. Figure 15.11 shows the fit between the experimental and theoretical CVs obtained for the square scheme, which involves two ET steps coupled with two homogeneous reactions.

To fit the data, one inputs the values of all known parameters (e.g., formal potentials, concentrations, diffusion coefficients) and uses the unknown quantities as adjustable parameters. For a relatively simple mechanism (e.g., one-step ET or EC), the number of fitting parameters is small, and DigiSim can easily find the best fit and determine the unique values of adjustable parameters. However, for a relatively complicated mechanism like the one pictured in Figure 15.11A, the number of fitting parameters is large (e.g., six rate constants, two transfer coefficients), and it may not be possible for DigiSim to find the unique best fit. Moreover, the shape of the theoretical voltammogram may be determined largely by the values of a few kinetic parameters with a weak dependence on the rest of them. If this is the case, the determined values of such parameters are highly uncertain. To ensure that the results are meaningful, one has to fit a number of experimental CVs obtained for a wide range of sweep rates.

Several commercially available simulation packages can be used to simulate two-dimensional or three-dimensional UME and SECM problems, from relatively simple and

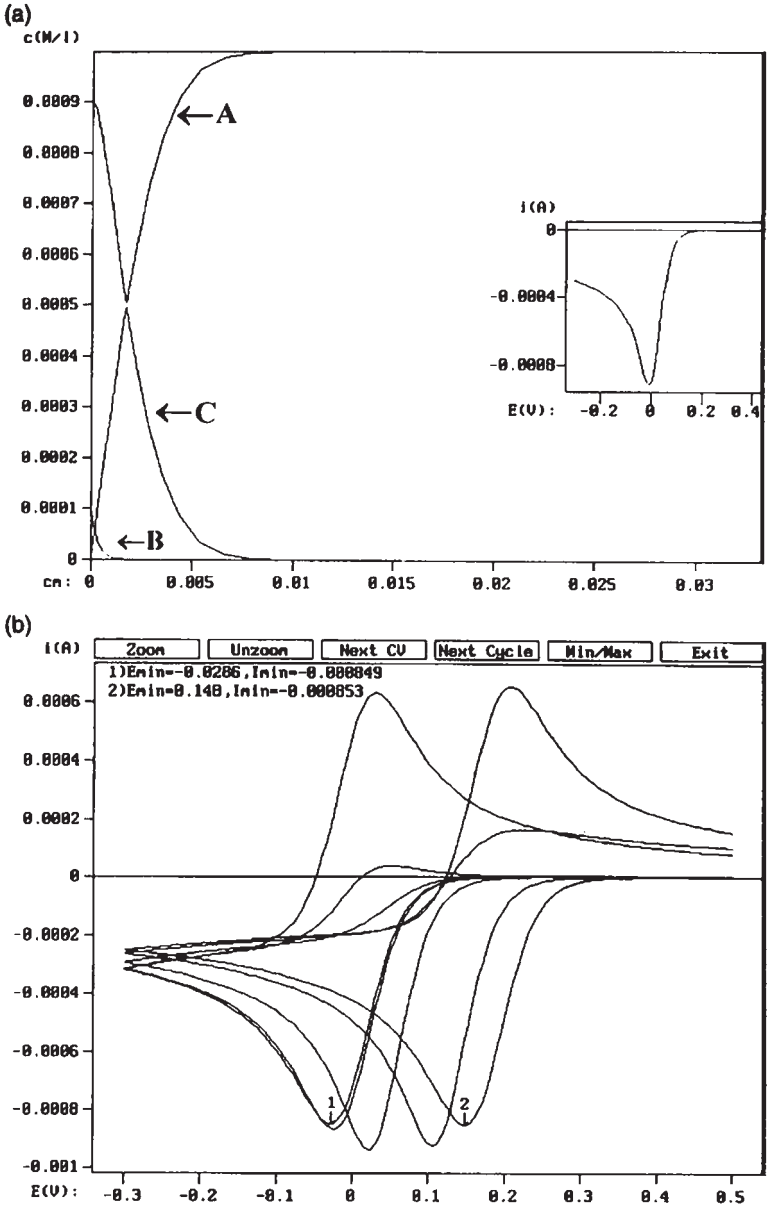


**Figure 15.10** (a) Concentration profiles and (b) cyclic voltammograms at a large planar electrode simulated for the $E_qC_r$ mechanism $[A + 1e^- \rightleftharpoons B,\ B \underset{k_b}{\overset{k_f}{\rightleftharpoons}} C]$. $A$ = 1 cm$^2$. $E^\circ$ = 0 V, $K$ = 1000 (equilibrium constant), $D_A = D_B = D_C = 10^{-5}$ cm$^2$/sec, $v$ = 1 V/sec, $c_A^\circ$ =1 mM, $c_B^\circ = c_C^\circ = 0$. (a) $k^\circ$ = 1 cm/sec, $k_f$ = 100 sec$^{-1}$, $E = -0.3$ V. (b) $k^\circ = 10^4$ cm/sec; $k_f$ = 0, 10, 1000, $10^6$, and $10^{10}$ sec$^{-1}$. Arrow 1 marks the reduction peak of the CV with $k_f = 0$; arrow 2 marks the reduction peak of the CV with $k_f = 10^{10}$ sec$^{-1}$. Reprinted with permission from reference (29). Copyright 1994 American Chemical Society.

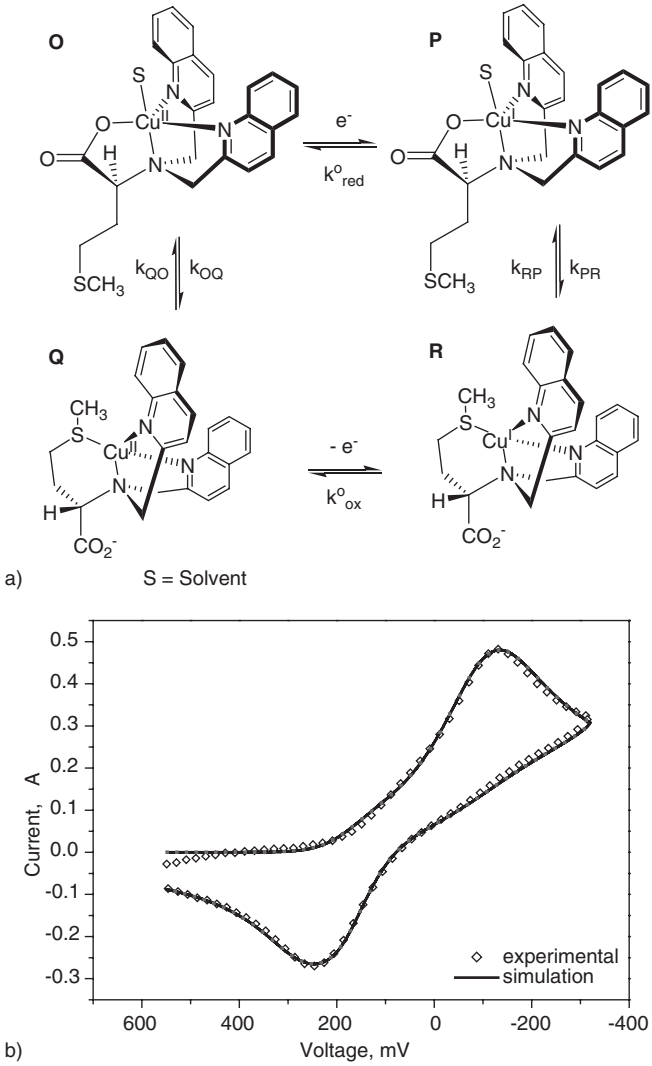


**Figure 15.11** (A) Square mechanism: electron-induced ligand reorganization results in an inversion of the chromophore orientation ($k_{red,\ ox}$ = rate of electron transfer, $k_{PR,\ OQ}$ = forward rate of reaction, $k_{RP,\ QO}$ = reverse rate of reaction); and (B) corresponding experimental voltammogram and the best theoretical fit obtained by DigiSim at $v$ = 60 mV/sec. Reprinted with permission from reference (30). Copyright 2005 American Chemical Society.

inexpensive FlexPDE software package (PDE Solutions Inc., Antioch, CA) to more complicated and versatile FEMLAB (COMSOL, Inc., Burlington, MA) to very complicated, powerful and expensive Flux Expert (Simulog, Guyancourt, France). Unlike DigiSim, all these packages are general solvers of partial differential equations rather than electrochemical simulators. Thus, they are suitable for modeling a broad range of physico-chemical

problems involving mass transfer, fluid dynamics, electrostatics, etc. However, unlike DigiSim, the user has to write pertinent differential equations and specify the geometry of his problem. Simulating more complicated systems (e.g., coupled two-phase systems or three-dimensional geometries) may be challenging.

## REFERENCES


1. A. J. Bard, L. R. Faulkner, *Electrochemical Methods: Fundamentals and Applications*, 2nd ed., John Wiley & Sons: New York, 2001.
2. Z. Galus, *Fundamentals of Electrochemical Analysis*, 2nd ed., Harwood & PWN: New York, 1994.
3. H. H. Girault, *Analytical and Physical Electrochemistry*, Marcel Dekker: New York, 2004.
4. H. Matsuda, Y. Ayabe, *Z. Electrochem.* **59**, 494 (1955).
5. R. S. Nicholson, *Anal. Chem.* **37**, 1351 (1965).
6. R. M. Wightman, D. O. Wipf, *Acc. Chem. Res.* **23**, 64 (1990).
7. D. O. Wipf, E. W. Kristensen, M. R. Deakin, R. M. Wightman, *Anal. Chem.* **60**, 306 (1988).
8. A. M. Bond, *Modern Polarographic Methods in Analytical Chemistry*, Marcel Dekker: New York, 1980.
9. H. Matsuda, *Z. Electrochem.* **62**, 977 (1958).
10. D. E. Smith, *Anal. Chem.* **35**, 610 (1963).
11. K. Winkler, A. Baranski, *J. Electroanal. Chem.* **346**, 197 (1993).
12. A. M. Bond, K. B. Oldham, C. G. Zoski, *Anal. Chim. Acta* **216**, 177 (1989).
13. K. B. Oldham, C. G. Zoski, *J. Electroanal. Chem.* **256**, 11 (1988).
14. M. V. Mirkin, A. J. Bard, *Anal. Chem.* **64**, 2293 (1992).
15. M. V. Mirkin, T. C. Richards, A. J. Bard, *J. Phys. Chem.* **97**, 7672 (1993).
16. C. Wei, A. J. Bard, M. V. Mirkin, *J. Phys. Chem.* **99**, 16033 (1995).
17. P. Sun, M. V. Mirkin, *Anal. Chem.* in press (2006).
18. A. J. Bard, M. V. Mirkin, P. R. Unwin, D. O. Wipf, *J. Phys. Chem.* **96**, 1861 (1992).
19. R. S. Nicholson, I. Shain, *Anal. Chem.* **36**, 706 (1964).
20. J.-M. Savéant, E. Vianello, *Electrochim. Acta* **8**, 905 (1963).
21. F. M. Zhou, P. R. Unwin, A. J. Bard, *J. Phys. Chem.* **96**, 4917 (1992).
22. P. R. Unwin, A. J. Bard, *J. Phys. Chem.* **95**, 7814 (1991).
23. C. Demaille, P. R. Unwin, A. J. Bard, *J. Phys. Chem.* **100**, 14137 (1996).
24. D. A. Treichel, M. V. Mirkin, A. J. Bard, *J. Phys. Chem.* **98**, 5751 (1994).
25. P. R. Unwin, in *Scanning Electrochemical Microscopy*, A. J. Bard, M. V. Mirkin, Eds., Marcel Dekker: New York, 2001, p. 241.
26. W. J. Albery, M. L. Hitchman, *Ring-Disk Electrode*, Oxford University: Oxford, 1971.
27. C. Amatore, in *Physical Electrochemistry: Principles, Methods, and Applications*, I. Rubinstein, Ed., Marcel Dekker: New York, 1995, p. 131.
28. S. W. Feldberg, in *Electroanalytical Chemistry*, A. J. Bard, Ed., Marcel Dekker: New York, 1969, Vol. 3, p. 228.
29. M. Rudolph, D. P. Reddy, S. W. Feldberg, *Anal. Chem.* **66**, 589A (1994).
30. H. S. Barcena, B. Liu, M. V. Mirkin, J. W. Canary, *Inorg. Chem.* **44**, 7652 (2005).

# – 16 –

# Metal Deposition

## 16.1 ELECTRODEPOSITION OF NANOSTRUCTURES AND MICROSTRUCTURES ON HIGHLY ORIENTED PYROLYTIC GRAPHITE (HOPG)

*Reginald M. Penner*

University of California, Irvine, CA, USA

### 16.1.1 Introduction and perspective

In spite of the exquisite control of reaction rate and duration afforded by electrochemical methods, electrodeposition has hardly been used for preparing nanomaterials. An exception to this generalization is the synthesis of nanoparticles and nanorods using the template synthesis method pioneered by Martin (1–6), Moskovits and co-workers (7–9), and Searson and co-workers (10–16). Template synthesis (Scheme 16.1.1) involves the electrodeposition of materials into the pores of ultrafiltration membranes (e.g., Nuclepore® and Anopore™) that have uniform, cylindrical, or prismatic pores of a particular size.

Dissolution of the membrane material exposes arrays of cylinders that are attached at one end to a conductive electrode. Template synthesis can be used to prepare size-monodisperse particles or cylindrical wires that are up to 50 μm in length and 15 nm to 5.0 μm in diameter. Template synthesis is the most popular method for preparing nanostructures of various materials using electrodeposition. Its primary disadvantage is that commercial templates are usually less than 50 μm in thickness and this places an upper limit on the length of the nanowires that can be obtained.

We have sought to develop a "templateless" scheme for preparing nanoparticles and nanowires using electrodeposition (17, 18). The methods we have developed are based on electrodeposition onto highly oriented pyrolytic graphite electrodes (HOPG), as shown in Scheme 16.1.2. HOPG basal plane surfaces are coordinately saturated and have a low surface free energy (19). On such low-energy surfaces, simple energetic arguments (20) can be used to show that deposition processes will prefer a Volmer–Weber (or VW) (21) mechanism. VW growth involves the prompt appearance of three-dimensional islands on the


**Handbook of Electrochemistry**
**Edited by C.G. Zoski**

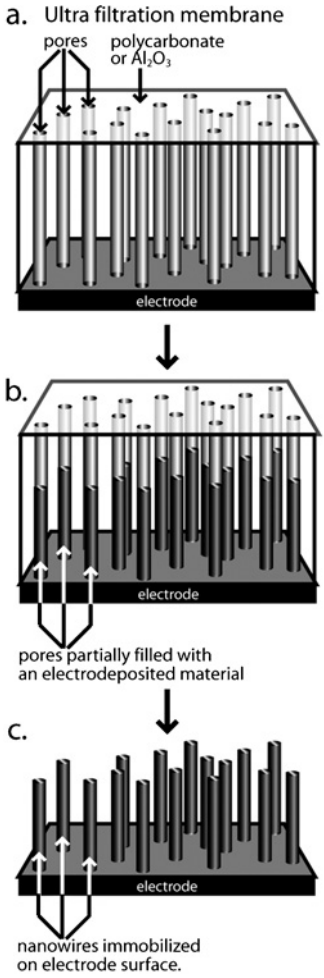


**Scheme 16.1.1** Template (e.g., Anopore™ and Nuclepore®) synthesis of nanowires using electrodeposition.

graphite surface. VW growth can be contrasted with Frank–Van der Merwe (FV) growth which involves the atomic layer-by-layer deposition of a material. Intermediate between these two extremes is Stanski–Krastanov (SK) growth in which a deposition process occurs initially via a layer-by-layer process but which transitions to three-dimensional growth after several layers are deposited (20). Often at noble metal electrodes (e.g., gold and platinum), the electrodeposition of a less noble metal is preceded by the electrodeposition of one or more "underpotentially" deposited (or UPD) metal monolayers just as in the SK growth mechanism. These UPD monolayers do not form on the HOPG basal plane. This "non-wetting" behavior is observed because the system (defined in an electrodeposition experiment as the solution + the deposited material + HOPG) can minimize its energy by minimizing the area of the interface between the deposited material and the HOPG surface (20).

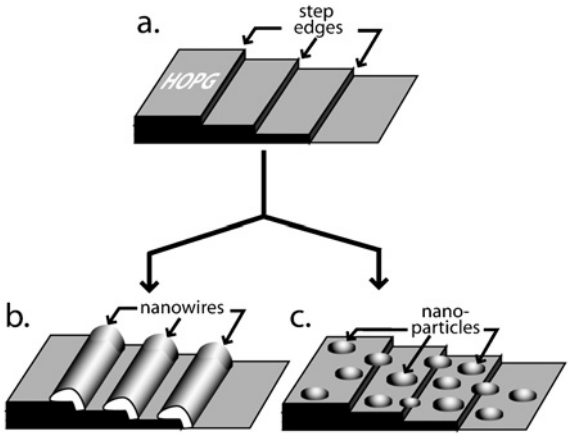


**Scheme 16.1.2** Two schemes for generating nanowires (b) or nanoparticles (c) on an HOPG electrode (a).

Our unconventional approach presents two main synthetic challenges: the first is to identify the factors affecting the shape of electrodeposited islands and to manipulate these to favor the production of billions of nanostructures that are identical in shape (e.g., hemispherical islands vs. nanowires, as shown in Schemes 16.1.2b and c). The second challenge is to understand the mechanism by which nanostructures "coarsen", or become increasingly heterogeneous in size during growth, so that dimensionally uniform nanostructures can be synthesized. In order for this strategy to be generally useful, these two problems must be addressed for a variety of electrodeposited materials. In this section, progress toward this objective is summarized.

### 16.1.2 HOPG: seeing electrodeposited metal nano- and microparticles

Some of the first *in situ* STM images of electrodes published by Sonnenfeld and Schardt in 1986 (22) showed silver electrodeposits on HOPG. The conclusion of that paper, reinforced by subsequent work (23–25), was that the electrodeposition of silver proceeded by a Volmer–Weber mechanism characterized by prompt 3D growth of silver islands. It was also concluded (23, 24) that the nucleation of silver islands occurred at defects present on the HOPG surface. This was an entirely reasonable conclusion that was supported by the *in situ* STM data.

Our efforts in this area were initiated in 1995 with investigations of the electrodeposition of silver (26, 27) and, soon thereafter, platinum (28) nanoparticles on HOPG surfaces. The primary characterization tool employed in these experiments was *ex situ* non-contact atomic force microscopy (NC-AFM). In the silver work, HOPG electrode surfaces were examined by NC-AFM after the application of large amplitude potentiostatic pulses with amplitudes of $-100$ to $-500$ mV (vs. $Ag/Ag^+$) and durations of 10–50 msec in dilute silver-plating solutions. These images looked dramatically different from the

STM images acquired previously. Specifically, they showed the presence of silver nanoclusters that were just 30–50 Å in diameter. These nanoclusters are present at a much higher density—$10^9$–$10^{10}$ $cm^{-2}$—than the silver nanostructures seen by *in situ* STM in previous studies. The NC-AFM images for platinum, shown in Figure 16.1.1, were very similar.

Since coulometry showed that much less than one atomic layer of silver or platinum was present on these surfaces, these NC-AFM images were consistent with a Volmer–Weber mechanism of deposition, but they contradicted the prior STM work because they showed that the nucleation of these metals occurred readily on defect-free terraces. Why were these nanoparticles not observed in the earlier STM experiments?

Our explanation for these conflicting results is that metal nanoclusters that nucleate on defect-free regions of the HOPG surface interact weakly with the surface and are easily dislodged and removed from terraces by the action of the scanning STM tip. Metal particles that nucleate at steps and other defects are more strongly attached to the surface and many of these are not scraped off the surface during STM imaging. Thus, the STM images show only those particles that interact strongly enough with defects to resist the lateral forces applied to them by the STM tip during imaging. It is likely, but unproven, that *in situ* STM imaging (carried out in electrolyte solutions) is more perturbing than *ex situ* STM in air or vacuum because the solvent provides for efficient viscous coupling of tip motion to electrodeposited structures present on the surface. The tapping action of the NC-AFM tip, in contrast, is apparently much less perturbing with the result that metal particles located on terraces are accurately rendered without being displaced.

These experiments proved the value of NC-AFM for characterizing electrodeposits on HOPG and other surfaces. Beyond this, the NC-AFM data demonstrated that a high density of size-similar ($RSD_{height}$ of $\approx 30\%$ (26, 28)) metal nanoparticles could be prepared by electrodeposition at large overpotentials ($>100$ mV) on HOPG surfaces and that the particle diameter could be controlled by adjusting either the pulse amplitude or its duration. One puzzling observation was related to the size dispersion of these metal nanoparticles. The standard deviation of the particle diameter increased with the mean diameter of the particles. Typical particle height histograms for platinum nanoparticles, for example, are shown in Figure 16.1.2.

Subsequent work carried out over the next 2 years (18, 29–32) revealed the origin of this "coarsening" and also led to techniques for minimizing it, as discussed in the next section.

### 16.1.3 Brownian Dynamics simulations: understanding particle size distribution broadening

The observation of size heterogeneity for electrodeposited micro- or nanostructures is often attributed to "progressive nucleation", a scenario in which individual particles begin growing at different times, and therefore grow for a range of different durations. Colloid chemists have understood for a long time that "instantaneous nucleation" (33)—in which the initiation of nanoparticle growth is separated in time from the subsequent growth of these particles—is essential for the synthesis of size-monodisperse colloid particles (34).

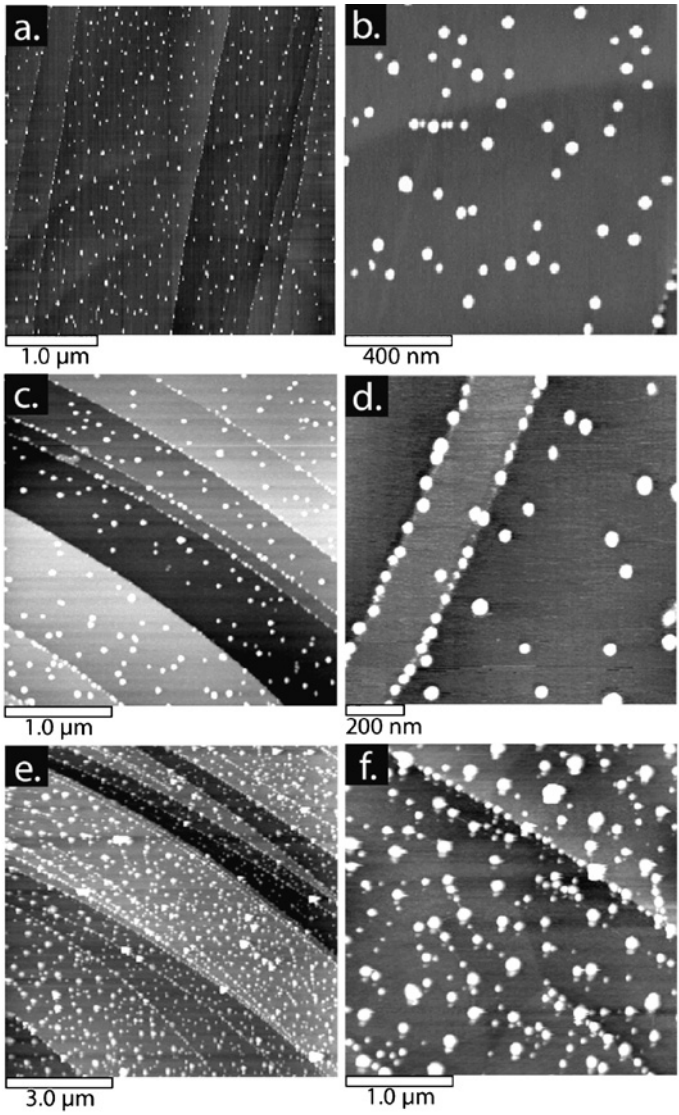


**Figure 16.1.1** NC-AFM images of an HOPG surface after the application of potentiostatic plating pulses with a voltage of −600 mV vs. mercurous sulfate reference electrode. (a and b) Pulse duration = 10 msec and deposition charge = 4.84 μC $cm^{-2}$. The mean particle height on this surface was 25 ± 9 Å. (c and d) Pulse duration = 50 msec platinum pulse and deposition charge = 37.6 μC $cm^{-2}$. The mean particle height on this surface was 52 ± 9 Å. (e and f) Pulse duration = 100 msec platinum pulse and deposition charge = 77.1 μC $cm^{-2}$. The mean particle height on this surface was 72 ± 27 Å. In both (e) and (f), a "double tip" imaging artifact, manifest as a smaller "particle" observed below each larger one, is present. Reference (28). Reprinted with permission of the American Chemical Society.

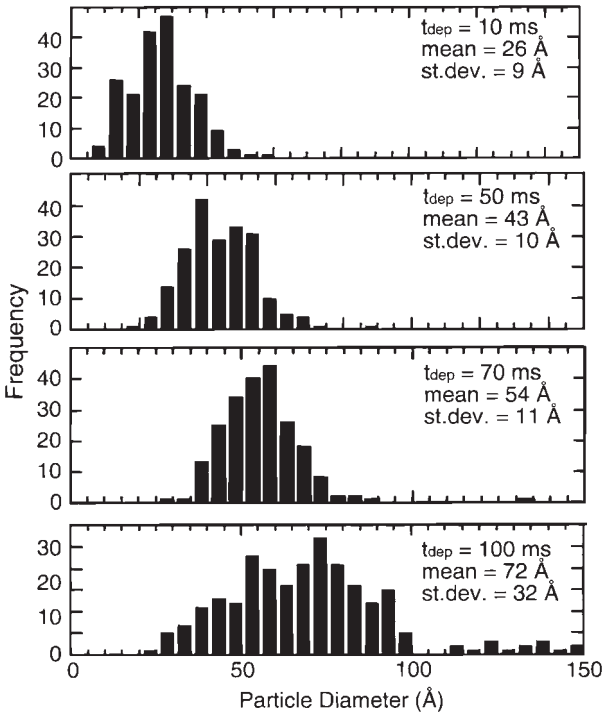


**Figure 16.1.2** Histograms of particle heights for platinum nanoparticles prepared by potentiostatic pulse on HOPG surfaces. Heights were measured from NC-AFM images. Data for four different surfaces prepared using the conditions specified on the diagram. Reprinted with permission of the American Chemical Society.

Instantaneous nucleation is a necessary but insufficient condition for preparing dimensionally uniform nanoparticles on an electrode surface. The reason, shown schematically in Figure 16.1.3 (29, 31), is that the growth rates of individual particles can be inversely related to their proximity to other particles on the electrode surface.

If a particular particle is located in proximity to other growing particles (within 10 particle radii, $r_o$), it can be deprived of reactant relative to particles that are located in relative isolation on the surface. This means that even when nanoparticles nucleate instantaneously, a distribution of growth rates can exist for individual particles on the surface. This deleterious phenomena, which we have termed "interparticle diffusional coupling" or IDC, does not occur for the growth of colloid particle suspensions because particles are constantly moving during growth and they typically do not persist in proximity to other particles.

Brownian Dynamics computer simulations (30, 32) facilitate the study of IDC by eliminating other possible mechanisms of particle coarsening. Since IDC occurs when the depletion layers for adjacent particle overlap, a simple strategy for minimizing IDC is to shrink the radii of these depletion layers. Experimentally, this is accomplished by reducing the particle growth rate, as shown schematically in Figure 16.1.3 (middle and bottom). The

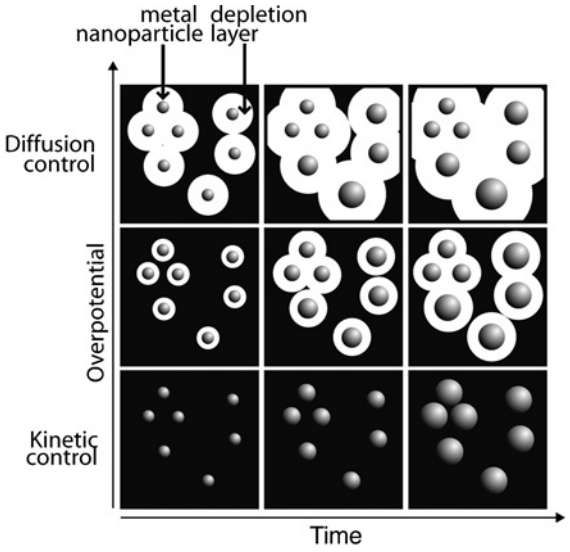


**Figure 16.1.3** Schematic diagram depicting the effect of interparticle diffusion coupling (or IDC) on particle size dispersion at three deposition rates: diffusion control (top), activation control (bottom), and an intermediate reaction rate (middle). Reprinted with permission of the American Chemical Society.

results of computer experiments in which the effect of growth rate on the development of particle size heterogeneity can be seen are shown in Figure 16.1.4.

In a Brownian Dynamics simulation, the growth of individual particles is explicitly modeled using a simulation "box" like that shown in Figure 16.1.4a (30). In the experiments documented in Figure 16.1.4, 200 particles were first grown rapidly for a short interval so that a significant size distribution developed. This distribution, characterized by a standard deviation of the particle radius, $\sigma_r = 0.095$ nm, was then grown in a range of overpotentials between $-1$ mV (very slow) and $-200$ mV (fast; nearly diffusion controlled). $\sigma_r$ is plotted vs. the mean particle radius, $\langle r \rangle$, at each of these overpotentials in Figure 16.1.4b. Over the entire range of overpotentials explored here, $\sigma_r$ increased linearly as a function of $\langle r \rangle$, and the slope $d\sigma_r/dr$ was higher at $\eta_{dep} = -200$ mV by a factor of 8 as compared with $\eta_{dep} = -1$ mV (Figure 16.1.4c) (30). A more detailed analysis of these simulation data (described in reference (30)) revealed that the mechanism of particle coarsening seen in Figure 16.1.4b is IDC, and that the reduction of the growth rate effectively decouples nearby particles and permits them to grow more nearly at the same rate.

### 16.1.4 "Slow-growth" electrodeposition: dimensionally uniform metal nano- and microparticles

In metal particle growth experiments, the "slow growth" strategy shown to be effective in Brownian Dynamics simulations can be implemented using a two-step procedure (18, 29, 31).

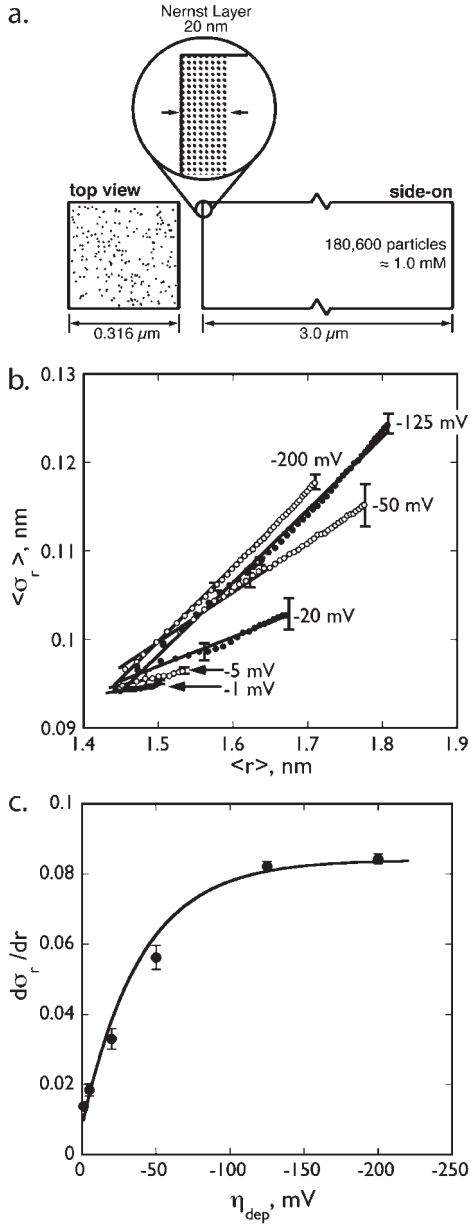


**Figure 16.1.4** (a) A simulation box for the simulation by Brownian Dynamics of the growth of 200 silver nanoparticles. (b) The standard deviation of the particle radius, $s_r$, vs. the mean radius, $\langle r \rangle$, for simulations at six deposition overpotentials, $h_{dep}$, as indicated. Solid lines are the results of linear least-squares analysis for each $h_{dep}$. The error bars in this plot represent $\pm 1$ sec for the $s_r$ obtained from three or four replicate simulations conducted at each $h_{dep}$. (c) Plot of the coarsening rate, d$s$/d$r$, obtained from the straight lines plotted in (b). The error bars in this plot represent $\pm 1$ sec for d$s_r$/d$r$ obtained from three or four replicate simulations conducted at each $h_{dep}$. Reprinted with permission of the American Chemical Society.

Preparation of our electrode surface involves cleaving a crystal of ZYA-grade HOPG (source: GE Advanced Ceramics, Inc.) using adhesive tape to expose a clean, basal plane surface. This crystal is then placed in Teflon® electrode holder that masks the edges of the crystal, and exposes a small (3–5 $mm^2$) circular area to an aqueous metal-plating solution having $[M^{n+}] \approx$ 1–5 mM. This solution also contains an electrochemically inert supporting electrolyte, such as NaF, and other additives, specified in Table 16.1.1, are also sometimes included. Metal nanoparticles are nucleated by applying a very negative voltage pulse with $\eta_{dep}$ of up to –1.0 V and a duration of 5–50 msec. This nucleation pulse produces a one-dimensional ensemble of metal nanoparticles, or "seeds", arrayed along each step edge on the HOPG surface. These seeds are then grown (without further nucleation) at an overpotential in the range from −5 to −75 mV. Typical results for the growth of silver particles prepared using $\eta_{dep} = -70$ mV are shown in Figure 16.1.5.

Particle size histograms for such particles (Figure 16.1.5a) show a relative standard deviation ($RSD_{dia}$) of 6–33%. Silver particles with a mean diameter of 2.0 μm, prepared by

**Table 16.1.1**

Metal nanoparticle/nanowire growth solutions and potentials[a]

| Material | Plating solution(s)/comments[b] | Growth potential[c] | References |
|---|---|---|---|
| Silver | 1–5 mM $Ag^+$ in 0.10–0.30 M NaF (pH ≈ 5), $NaCH_3COO$ (pH ≈ 6.5), $NaNO_3$ (pH = 1–2), and/or $Na_2SO_4$ (pH = 1–2)<br>Silver nanoparticles have also been obtained from acetontrile solutions containing: 1 mM $AgClO_4$ and 0.1 M $LiClO_4$<br>Nanowire growth (in aqueous solutions only) is promoted by the addition of saccharine (1 mM).<br>Of the metals listed here, silver presents the most difficulties for synthesizing nanowires | −180 to −60 mV vs. $Ag^0/Ag^+$ | (18, 29, 31, 37, 40) |
| Platinum | Aqueous 1–5 mM $PtCl_6^{2-}$ in 0.10–0.30 M HCl | 150 to −30 mV vs. MSE | (18, 29) |
| Nickel | 1–10 mM $Ni(NO_3)_2$ or $NiSO_4$ 0.1–0.2 M NaCl, 0.2 M $NH_4Cl$, pH = 7.5–8.5, or $Na_2SO_4$ | −900 mV vs. SCE | (18, 29, 37) |
| Gold | 1–5 mM $AuCl_3$, 0.1 M NaCl<br>Nanowire growth is promoted by the addition of saccharine (1 mM) | 560–600 mV vs. SCE | (18, 29, 37) |
| Copper | 1 mM $CuSO_4$, 0.1 M $K_2SO_4$ or $Na_2SO_4$ | −5 to 20 mV vs. $Cu^0/Cu^{2+}$ | (18, 29, 37) |
| Palladium | 2 mM $Pd^{2+}$, 0.1 M HCl or 0.1 M $HclO_4$ | 300–450 mV vs. SCE | (17, 36, 41) |
| Cadmium | 10 mM $CdF_2$, 0.1 M NaF (particles)<br>5 mM $CdCl_2$, 6 mM $Na_2EDTA$, 0.5 M NaCl, 0.5 M $NH_4Cl$ buffered at pH = 8.5 using $NH_3$ $H_2O$ (nanowires) | −770 mV (particles)<br>−1150 mV (nanowires) vs. SCE | (29, 42) |

[a]The selection between nanoparticles and nanowires is decided by the electrode preparation procedure and the nucleation conditions as described in the text. All experiments involved "slow growth" of particles or nanowires.

[b]All solutions aqueous, and prepared with nanopure water ($\rho > 18$ M cm).

[c]MSE: saturated mercurous sulfate reference electrode; SCE: saturated calomel reference electrode.

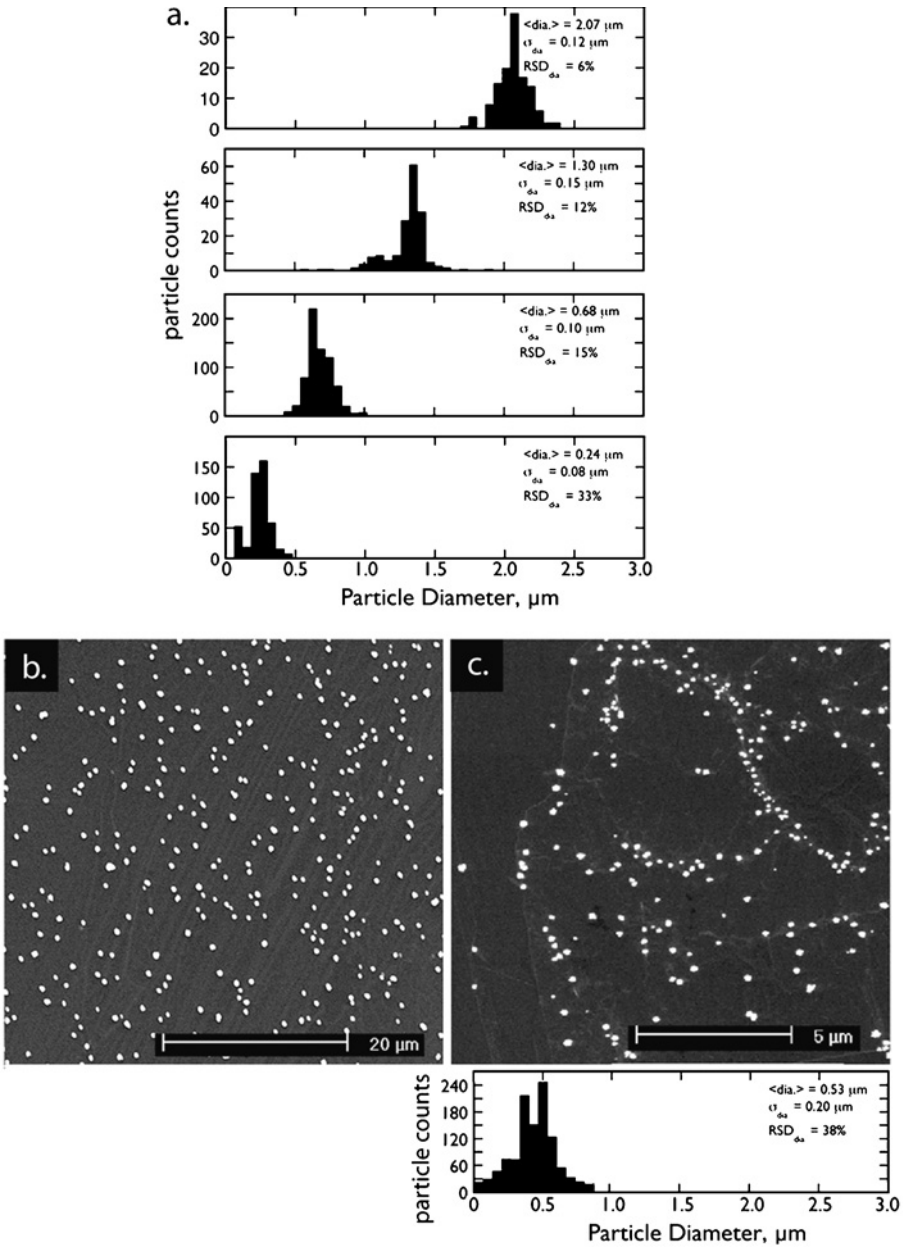


**Figure 16.1.5** (a) Particle size histograms for silver particles prepared using $\eta_{dep}$ of $-70$ mV and deposition durations of: 500 msec (bottom), 5.0 sec, 30 sec, and 120 sec (top). (b) An SEM image of silver particles prepared by "slow growth" using $\eta_{dep} = -70$ mV and a growth duration of 120 sec. (c) An SEM image of silver particles prepared by growth at diffusion control ($\eta_{dep} = -500$ mV) and a growth duration of 150 msec. The histogram corresponding to the sample shown below this image is plotted below it. Reprinted with permission of the American Chemical Society.

growth at $\eta_{dep} = -70$ mV for 120 sec, are shown in the SEM image of Figure 16.1.5b. By comparison, growth at $\eta_{dep} = -500$ mV for 150 msec produces particles like that shown in Figure 16.1.5c. Two important differences can be discerned: first, the nucleation pulse employed in a slow growth experiment produces a high, and uniform, density of particles on the graphite surface. A careful examination of this image reveals that particles in densely nucleated regions of the surface are noticeably smaller than those nucleated in sparse regions of the surface. This inverse correlation between the number density of particles and the particle diameter is clear evidence for IDC. The $RSD_{dia}$ for this surface (38%) was approximately twice as large as for silver particles of the same diameter prepared by slow growth ($RSD_{dia} \approx 16\%$). One should not be convinced of the generality of the slow growth approach based on the data shown in Figure 16.1.5 because silver is a special case, exhibiting excellent reversibility and the fastest heterogeneous electron transfer kinetics of any metal (35).

We have studied a range of different metals and metal oxides with widely varying degrees of electrochemical reversibility and electrodeposition kinetics. In contrast to silver, many important noble metals and metal oxides electrodeposit irreversibly. In Figure 16.1.6a, for example, irreversible cyclic voltammograms acquired in plating solutions for $MoO_2$ (a metallic oxide of molybdenum) and platinum are compared with the reversible CVs seen for silver.

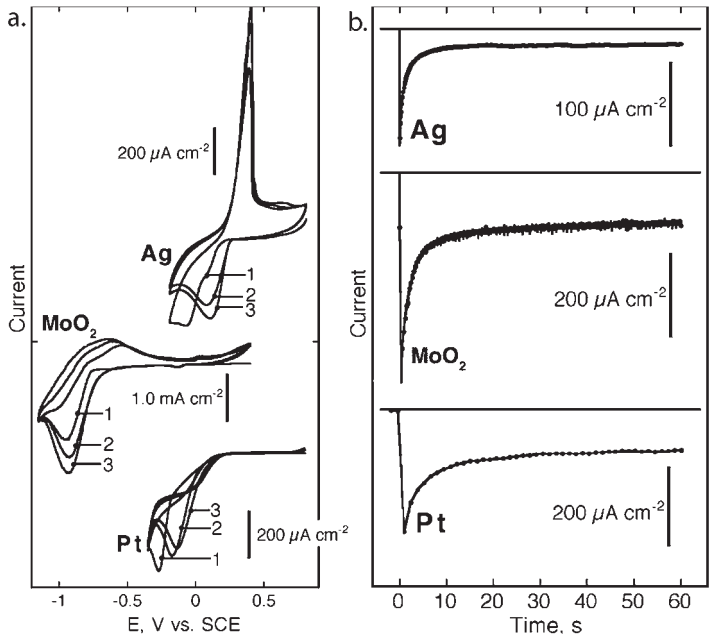


**Figure 16.1.6** (a) Cyclic voltammograms for an HOPG electrode immersed in plating solutions containing $Ag^+$ (20 mV $sec^{-1}$ in 1 mM $AgClO_4$, 0.1 M $LiClO_4$, acetonitrile), $MoO_4^{2-}$ (20 mV $sec^{-1}$ in 1.0 mM $MoO_4^{2-}$, 1.0 M NaCl, 1.0 M $NH_4Cl$, pH = 7.5–8.5), and $PtCl_6^{2-}$ (30 mV $sec^{-1}$ in 1 mM $PtCl_6^{2-}$, 0.1 M HCl). (b) Current–time transients for the electrodeposition of silver, molybdenum dioxide, and platinum using the deposition solutions indicated in (a). Reprinted with permission of Elsevier.

For all three systems, the growth phase of a particle slow growth experiment is characterized by a constant current, as shown in Figure 16.1.6b. In addition to $MoO_2$ and platinum, we also prepared nano- and micro-particles of copper, nickel, cadmium, and gold. Representative SEMs of particles prepared by slow growth are shown in Figure 16.1.7.

The particles in these images range from 100 nm in diameter (Cd) to more than 2 μm (Cu), but for all of these metals, particles ranging in size from 50 nm to 2 μm with a comparable degree of size monodispersity have been obtained. These data support the conclusion that

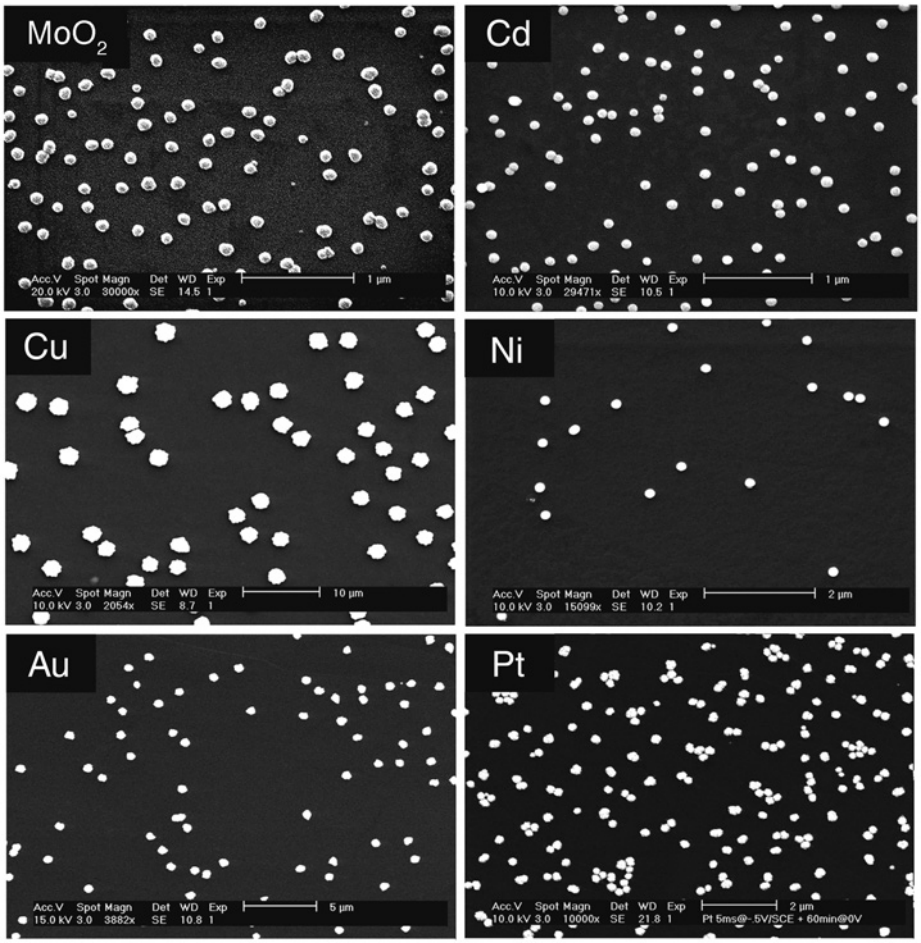


**Figure 16.1.7** Scanning electron micrographs of metal particles prepared using the slow growth method. The composition of the plating solutions employed for the electrodeposition of these metal particles is listed in Table 16.1.1. The deposition current density observed in each experiment was as follows: ($MoO_2$) 180–140 μA $cm^{-2}$, (Cd) 40–60 μA $cm^{-2}$, (Cu) 40–60 μA $cm^{-2}$, (Ni) 240–260 μA $cm^{-2}$, (Au) 30–40 μA $cm^{-2}$, and (Pt) 5–100 μA $cm^{-2}$. Reprinted with permission of the American Chemical Society and Elsevier.

the slow growth method for obtaining particles size selectively is a general one for a variety of metals and at least one metal oxide (i.e., $MoO_2$).

### 16.1.5 Electrodeposition of metal nanowires

A variant of the slow growth method for obtaining dimensionally uniform metal nanoparticles can be used to prepare metal nanowires, as shown in Scheme 16.1.2b (17, 18, 36–39). Nanowires are obtained instead of nanoparticles when the nucleation of the electrodeposited material occurs preferentially at the step edges present on the HOPG surface. Nucleation at step edges is enhanced by oxidizing them immediately prior to the application of the nucleation pulse. This oxidation can conveniently be carried out electrochemically in the metal-plating solution at a potential of $\approx$0.8 V vs. SCE for 5 sec, typically. On such pre-oxidized surfaces, the nucleation pulse that is normally applied in a slow growth experiment produces a high density of metal nuclei—usually in excess of 10 $\mu m^{-1}$—on step edges. Initially, these nanoparticles have a diameter of 1 nm or so. This means that the nucleation pulse produces a disconnected 1D array of metal nanoparticles at step edges—not a continuous nanowire. Nanowires are obtained during the subsequent growth phase as these nuclei coalesce into an electrically continuous wire that has a minimum diameter usually in the 30–70 nm range.

The behavior of copper is typical of that for many other metals including gold, platinum, palladium, nickel, and cadmium (37). Shown in Figure 16.1.8 is the pulse program employed for nanowires growth and the cyclic voltammogram for an aqueous copper-plating solution containing 2.0 mM $CuSO_4$ $5H_2O$ and 0.1 M $Na_2SO_4$.

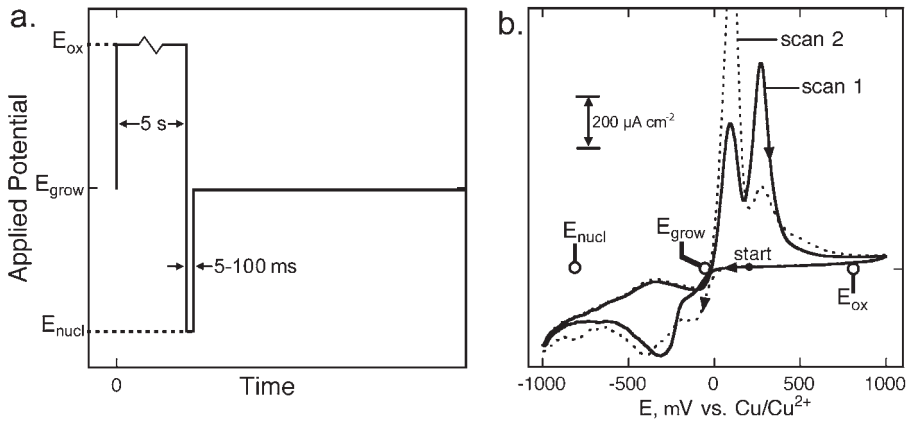


**Figure 16.1.8** (a) Triple voltage pulse used to prepare metal nanowires in this study. (b) Cyclic voltammograms of a copper-plating solution at an HOPG electrode showing the values for $E_{ox}$, $E_{nucl}$, and $E_{grow}$ typically used for the preparation of copper nanowires. The solution was aqueous 2.0 mM $CuSO_4$ $5H_2O$, 0.1 M $Na_2SO_4$. Two oxidation waves seen at +100 $mV_{SCE}$ and +350 $mV_{SCE}$ are assigned to copper stripping (+100 $mV_{SCE}$) and oxidation of $Cu^0$ to CuO (+350 $mV_{SCE}$). Reprinted with permission of the American Chemical Society.

Nanowire growth was accomplished by pre-oxidizing the HOPG surface at +0.80 V vs. SCE, applying a nucleation pulse of −0.8 V × 5 msec, and then growing at −5 mV vs. SCE for between 100 sec and 40 min. As shown in the scanning electron micrographs of Figure 16.1.9, the nanowires obtained range in diameter from 70 nm to more than 300 nm.

These polycrystalline nanowires possess a unique morphology, consisting of single crystalline metal grains arranged in series along the step edge, that is a direct consequence of the growth mechanism.

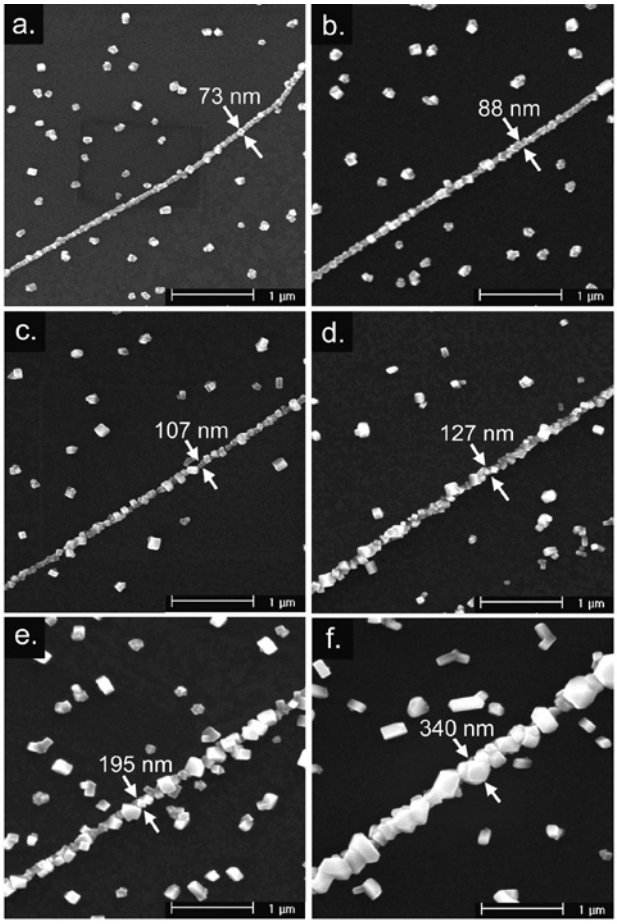


**Figure 16.1.9** Scanning electron micrographs of copper nanowires. These nanowires were electrodeposited from the solution indicated in Table 16.1.1, using $E_{nucl} = -800\ mV_{SCE}$ and $E_{grow} = -5\ mV_{SCE}$. The growth times employed in each experiment were: (a) 120 sec, (b) 180 sec, (c) 300 sec, (d) 600 sec, (e) 900 sec, and (f) 2700 sec. Reprinted with permission of the American Chemical Society.

As in the slow growth experiments described earlier involving particles, nanowire growth is characterized by a constant deposition current. The transport of metal ions under these conditions occurs under conditions of mixed diffusion and convection control and a simple growth law can be derived (18):

$$r(t) = \sqrt{\frac{2i_{\text{dep}}t_{\text{dep}}V_{\text{m}}}{\pi nFl}} \tag{16.1.1}$$

In this equation, $t_{\text{dep}}$ is the total deposition duration, $V_{\text{m}}$ is the molar volume of the electrodeposited metal, and $l$ is the total length of metal nanowires on the graphite surface. Equation (16.1.1) assumes a hemicylindrical nanowire geometry. As shown in Figure 16.1.10, the radii of the electrodeposited copper nanowires, measured from SEM data like that of Figure 16.1.1, increased in proportion to $t^{1/2}$ as predicted by equation (16.1.1). A similar relationship is obtained for other metals, including gold, silver, and nickel, as shown in Figure 16.1.10.

We have termed this method of nanowire growth Electrochemical Step Edge Decoration or ESED. In recent work, we have demonstrated that ESED can be applied to materials other than metals. Specifically, ESED seems to provide a general method for synthesizing nanowires composed of a variety of technologically interesting compounds including $\beta$-$MnO_2$ (43) (a lithium ion intercalation compound), $MoS_2$ (44) (an indirect-gap semiconductor), CdS (44) (a direct-gap semiconductor), and $Bi_2Te_3$ (45)

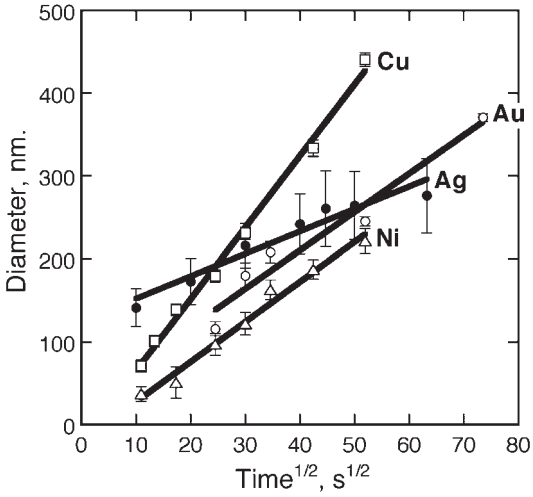


**Figure 16.1.10** Nanowire diameter vs. (deposition time)$^{1/2}$ for the growth of nanowires composed of four metals as indicated. Each series of experiments for a particular metal were performed using a single graphite crystal in order to limit the variation in the step edge density from experiment to experiment (see equation (16.1.1)). This crystal was cleaved before each experiment to expose a fresh, clean graphite surface. Error bars for each data point are twice the standard deviation for the mean particle diameter as measured from SEM images. Reprinted with permission of the American Chemical Society.

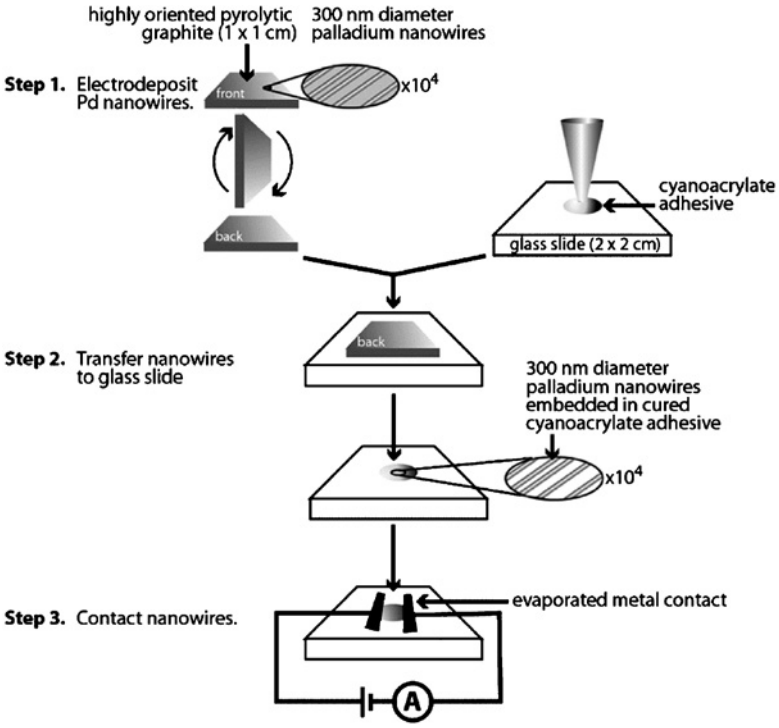


**Figure 16.1.11** Schematic diagram of the method for transferring nanowires (palladium in this case) from an HOPG surface on which they are synthesized onto a second surface for characterization and/or device fabrication. Reprinted with permission of the American Chemical Society.

(a thermoelectric material). Relative to competing methods, such as template synthesis (Scheme 16.1.1), ESED has two important advantages. First, much longer nanowires with lengths of a millimeter or more can be prepared. Second, these nanowires can be transferred from the HOPG surface onto the surface of an insulator. This is accomplished by embedding the nanowires in a film of adhesive (usually a cyanoacrylate) dispersed on another surface composed of glass, semiconductor, polymer, etc., as shown schematically in Figure 16.1.11.

After the adhesive hardens, the graphite surface can be separated from the insulator surface and the nanowires are presented at the surface of the adhesive layer. This ability to transfer nanowires onto various surfaces simplifies the characterization of the nanowires by TEM, and it facilitates the fabrication of devices such as chemical sensors.

## REFERENCES

1. C. A. Foss, M. J. Tierney, C. R. Martin, *J. Phys. Chem.* **96**, 9001 (1992).
2. C. J. Brumlik, C. R. Martin, *J. Am. Chem. Soc.* **113**, 3174 (1991).

3. C. J. Brumlik, V. P. Menon, C. R. Martin, *J. Mater. Res.* **9**, 1174 (1994).
4. C. R. Martin, *Science* **266**, 1961 (1994).
5. C. R. Martin, *Adv. Mater.* **3**, 457 (1991).
6. C. A. Foss, G. L. Hornyak, J. A. Stockert, C. R. Martin, *J. Phys. Chem.* **98**, 2963 (1994).
7. D. N. Davydov, J. Haruyama, D. Routkevitch, B. W. Statt, D. Ellis, M. Moskovits, J. M. Xu, *Phys. Rev. B* **57**, 13550 (1998).
8. C. K. Preston, M. Moskovits, *J. Phys. Chem.* **97**, 8495 (1993).
9. D. Routkevitch, T. Bigioni, M. Moskovits, J. M. Xu, *J. Phys. Chem.* **100**, 14037 (1996).
10. P. C. Searson, R. C. Cammarata, C. L. Chien, *J. Electron. Mater.* **24**, 955 (1995).
11. T. M. Whitney, J. S. Jiang, P. C. Searson, C. L. Chien, *Science* **261**, 1316 (1993).
12. K. Liu, K. Nagodawithana, P. C. Searson, C. L. Chien, *Phys. Rev. B* **51**, 7381 (1995).
13. K. Liu, C. L. Chien, P. C. Searson, Y. Z. Kui, *Appl. Phys. Lett.* **73**, 1436 (1998).
14. K. Liu, C. L. Chien, P. C. Searson, *Phys. Rev. B* **58**, R14681 (1998).
15. K. Liu, C. L. Chien, P. C. Searson, Y. Z. Kui, *IEEE Trans. Magn.* **34**, 1093 (1998).
16. G. Oskam, J. G. Long, A. Natarajan, P. C. Searson, *J. Phys. E Appl. Phys.* **31**, 1927 (1998).
17. E. C. Walter, M. P. Zach, F. Favier, B. J. Murray, K. Inazu, J. C. Hemminger, R. M. Penner, *Chemphyschem* **4**, 131 (2003).
18. R. M. Penner, *J. Phys. Chem. B* **106**, 3339 (2002).
19. I. Morcos, *J. Chem. Phys.* **57**, 1801 (1972).
20. A. Zangwill, *Physics at Surfaces*, Cambridge University Press: Cambridge, 1988.
21. M. Volmer, A. Weber, *Z. Phys. Chem.* **119**, 277 (1926).
22. R. Sonnenfeld, B. C. Schardt, *Appl. Phys. Lett.* **49**, 1172 (1986).
23. L. Vazquez, A. H. Creus, P. Carro, P. Ocon, P. Herrasti, C. Palacio, J. M. Vara, R. C. Salvarezza, A. J. Arvia, *J. Phys. Chem.* **96**, 10454 (1992).
24. R. T. Pötzschke, C. A. Gervasi, S. Vinzelberg, G. Staikov, W. J. Lorenz, *Electrochim. Acta* **40**, 1469 (1995).
25. K. Itaya, E. Tomita, *Surf. Sci.* **201**, L507 (1988).
26. J. V. Zoval, R. M. Stiger, P. R. Biernacki, R. M. Penner, *J. Phys. Chem.* **100**, 837 (1996).
27. J. V. Zoval, P. Biernacki, R. M. Penner, *Anal. Chem.* **68**, 1585 (1996).
28. J. V. Zoval, J. Lee, S. Gorer, R. M. Penner, *J. Phys. Chem.* **102**, 1166 (1998).
29. H. Liu, F. Favier, K. Ng, M. P. Zach, R. M. Penner, *Electrochim. Acta* **47**, 671 (2001).
30. R. M. Penner, *J. Phys. Chem. B* **105**, 8672 (2001).
31. H. Liu, R. M. Penner, *J. Phys. Chem. B* **104**, 9131 (2000).
32. J. L. Fransaer, R. M. Penner, *J. Phys. Chem. B* **103**, 7643 (1999).
33. Nucleation is termed "instantaneous" when the interval over which nucleation occurs is much smaller than the total duration of growth.
34. V. K. LaMer, R. H. Dinegar, *J. Am. Chem. Soc.* **72**, 4847 (1950).
35. J. D. Porter, T. O. Robinson, *J. Phys. Chem.* **97**, 6696 (1993).
36. E. C. Walter, F. Favier, R. M. Penner, *Anal. Chem.* **74**, 1546 (2002).
37. E. C. Walter, B. J. Murray, F. Favier, G. Kaltenpoth, M. Grunze, R. M. Penner, *J. Phys. Chem. B* **106**, 11407 (2002).
38. M. P. Zach, K. Inazu, K. H. Ng, J. C. Hemminger, R. M. Penner, *Chem. Mater.* **14**, 3206 (2002).
39. M. P. Zach, K. H. Ng, R. M. Penner, *Science* **290**, 2120 (2000).
40. B. J. Murray, E. C. Walter, R. M. Penner, *Nano Lett.* **4**, 665 (2004).
41. F. Favier, E. C. Walter, M. P. Zach, T. Benter, R. M. Penner, *Science* **293**, 2227 (2001).
42. Q. Li, R. M. Penner, *Nano Lett.* **5**, 1720 (2005).
43. Q. G. Li, J. B. Olson, R. M. Penner, *Chem. Mater.* **16**, 3402 (2004).
44. Q. Li, J. T. Newberg, E. C. Walter, J. C. Hemminger, R. M. Penner, *Nano Lett.* **4**, 277 (2004).
45. E. J. Menke, Q. Li, R. M. Penner, *Nano Lett.* **4**, 2009 (2004).

## 16.2 TEMPLATE DEPOSITION OF METALS

*Paolo Ugo and Ligia Maria Moretto*

Department of Physical Chemistry, University of Venice,
Santa Marta 2137, 30123 Venice, Italy

### 16.2.1 Introduction

Template synthesis is a relatively simple and easy procedure which has made the fabrication of rather sophisticated nanomaterials accessible to almost any laboratory. Template synthesis requires access to instrumentation capable of metal sputtering and electrochemical deposition. The characterization of the fabricated nanostructures can be done using instrumental techniques including spectrophotometry, voltammetry, optical microscopy, atomic force microscopy, and electronic microscopies (scanning electron microscopy (SEM) and transmission electron microscopy (TEM)).

The method is based on the simple but effective idea that the pores of a host material can be used as a template to direct the growth of new materials. Historically, template synthesis was introduced by Possin (1) and refined by Williams and Giordano (2) who prepared different metallic nanowires with widths as small as 10 nm within the pores of etched nuclear damaged tracks in mica. It was further developed by Martin's group (3–5) and followed by others (6) with the number of examples and applications (7) continually increasing. The nanoporous membranes usually employed as templates are alumina or track-etched polymeric membranes which are widely used as ultrafiltration membranes. Recently, metal nanostructures have also been obtained using the pores created by self-assembly in block copolymer structures under the influence of electric fields and high temperatures (8, 9).

The first part of this section focuses on the main characteristics and fabrication techniques used for obtaining templating membranes and depositing metal nanostructures by suitable electroless and electrochemical procedures. Methods such as sol–gel (10–12) or chemical vapor deposition (10, 13), which have been used primarily for the template deposition of carbon, oxides, or semiconducting-based materials, will not be considered here in detail. The second part of the section focuses on the electrochemical properties of the fabricated nanomaterials with emphasis on the characteristics and applications of nanoelectrode ensembles (NEEs).

### 16.2.2 Templating membranes

#### *16.2.2.1 Alumina membranes*

Aluminum oxide films with regular pore distribution can be formed by electrooxidation of high-purity aluminum substrates in acidic electrolytes (14, 15). The structure of the oxide film consists of a uniform array of parallel alumina cells packed hexagonally, each containing a nearly cylindrical pore. The uniform diameter of the pores is a consequence of the

equilibrium between the growth rate of the alumina and its dissolution in the acidic electrolyte. The hexagonal self-order of the pores can be explained by the repulsive forces due to the volume expansion associated with the anodization process (14). By appropriate selection of the process conditions, films with pore diameters between $<10$ nm up to 2 μm, pore density between $10^8$ and $10^{11}$ pores $cm^{-2}$, and film thickness up to 200 μm can be prepared (16).

The electrolysis of aluminum is carried out in a two-electrode cell. The anode is usually a high-purity (99.9% or even 99.99%) aluminum sheet. The metal surface must be carefully cleaned via chemical or electrochemical polishing (17). After degreasing in 1:2:1 ethanol–dichloromethane–acetone solution (17), the aluminum surface is cleaned by immersion in NaOH (1 M (18) or 0.05 M (17)), followed by rinsing in distilled water, and then electropolished using one of the following typical experimental conditions:

- ***Potentiostatic control:*** Applied potential 20–21 V for 2–5 min in 61% perchloric acid–95% ethanol (19/81, v/v) at 2 °C (18, 19).
- ***Galvanostatic control:*** Current density of 75 mA $cm^{-2}$ (or 125 mA $cm^{-2}$ (20)) in a 2:3 (v/v) phosphoric/sulfuric acid solution in 1% glycerol at 70–80 °C (17).

According to Hornyak *et al.* (17), the electropolished aluminum is rinsed immediately in distilled water (often with the aid of a strong stream of distilled water to remove the tenacious gelatinous oxide layer), immersed in concentrated nitric acid for 10 min, rinsed and left to dry in air. Well-polished aluminum should present a shiny/mirror-like surface; accurate polishing is crucial for obtaining high-quality aluminum oxide membranes.

The pre-treated aluminum is then anodized potentiostatically or galvanostatically in a thermostatically controlled bath (14, 16, 21). Potentials from 10 to 160 V and current densities from 10 to 30 mA $cm^{-2}$ are usually applied; however, for high pore spacing, voltages as high as 700 V have been used (22). The electrolyte is typically 15% sulfuric acid (10 °C), 4% phosphoric acid (24 °C), 2% oxalic acid (24 °C), or 3% chromic acid (38 °C) (14); the temperature ranges from 38 to 0 °C and even lower (18, 23).

The cathode used for the anodization of aluminum consists of a large plate of aluminum, lead, platinum, or stainless steel.

As shown in Table 16.2.1, the pore diameter is proportional to the DC potential or the current density used. The thickness of the porous aluminum oxide increases linearly with

**Table 16.2.1**

Conditions used for the electrochemical preparation of nanoporous alumina membranes

| Applied potential (V) | Pore diameter (nm) | Pore density ($\times 10^9$ $cm^{-2}$) |
|---|---|---|
| 30 | 52[a] | 30[d] |
| 20 | 32[b] | 56[d] |
| 15 | 22[b] | 83[d] |
| 10 | 16[c] | |

[a]In 4% oxalic acid, reference (17).
[b]In 10% sulfuric acid, reference (17).
[c]In 15% sulfuric acid, reference (17).
[d]From reference (14).

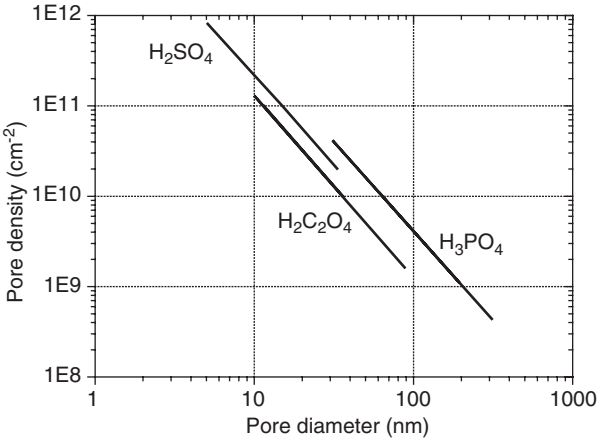


**Figure 16.2.1** Pore density vs. pore diameter in alumina nanoporous membranes prepared in the three electrolytes indicated. Reproduced with permission from http://www.synkera.com/. (for colour version: see colour section at the end of the book).

the anodization time at a given voltage and temperature and can be adjusted from 0.1 to 10 μm. The pore spacing varies with the applied potential and the electrolyte pH; the effect of the applied voltage on pore density for films formed in 15% sulfuric acid at 10 °C is presented in the last column of Table 16.2.1.

As shown in Figure 16.2.1, there is a bi-logarithmic linear relationship between the pore density and the pore diameter.

The growth of the oxide layer is such that it advances into the aluminum phase with simultaneous formation and dissolution of the oxide to form the pores. During the pore formation, the aluminum anode material is never directly exposed to the solution since it is always coated by a relatively thin (10–100 nm) non-porous insulating oxide layer called the "barrier layer" (see Figure 16.2.2A). Various procedures can be used to separate the unoxidized aluminum from the porous oxide layer (14, 24). The most widely used is the so-called voltage reduction sequence (VRS) developed by Furneaux *et al.* (22). VRS entails the stepwise reduction of the potential so that a progressive reduction of the pore diameter is produced at the bottom of the pore (see Figure 16.2.2).

After formation of this highly porous layer, the electrode is immersed into an acidic detachment solution, typically 25% sulfuric acid or phosphoric acid, which causes the rapid dissolution of the interfacial oxide. This process is faster in the areas indented by the smaller and smaller branched pores. Under such conditions, the acid can readily access the Al electrode so that $H_2$ gas is evolved; when the $H_2$ bubbles coalesce, the process is completed. The Al electrode is then rinsed by immersion in water and dried in air. The porous alumina membrane is finally collected by sliding an index card between the alumina layer and the Al electrode. The two faces of the detached alumina membrane are not equivalent; the face that was detached from the Al electrode surface contains remnants of the interfacial oxide layer. However, these remnants can be

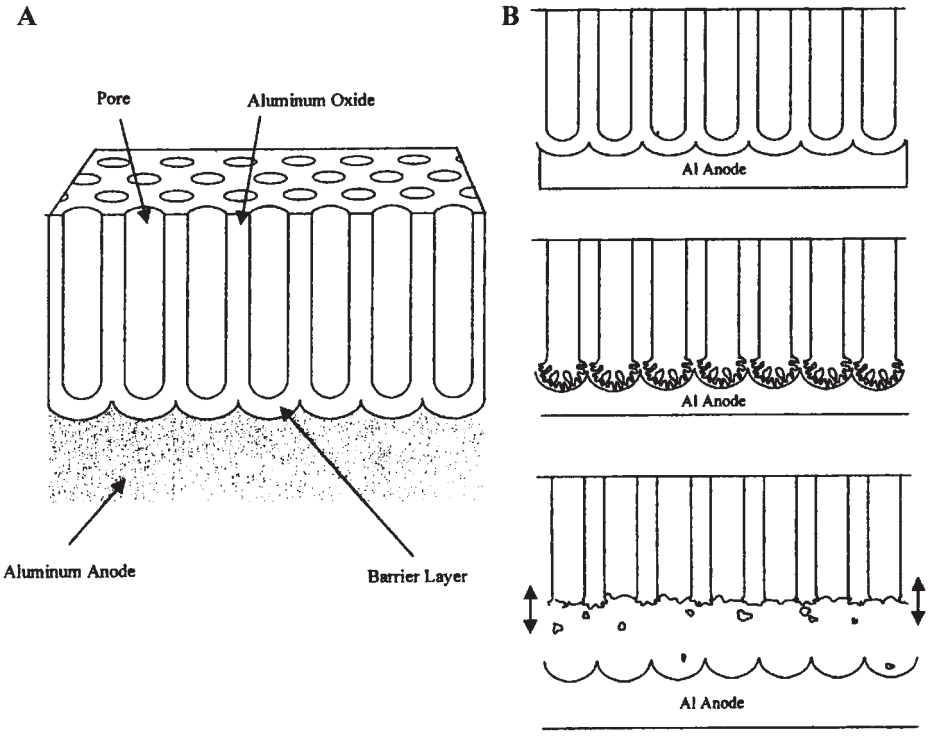


**Figure 16.2.2** (A) Schematic drawing of the porous anodic aluminum oxide layer that is formed during aluminum anodization. (B) Steps involved in the detachment of the aluminum oxide layer from bulk aluminum by using the voltage reduction sequence. Top: growth of the primary pores; middle: voltage reduction and infiltration of barrier layer by branched pore network; bottom: dissolution of branched network region of the porous film and separation from aluminum anode. Reproduced with permission from reference (25).

removed by floating the membrane on the surface of a 0.2 M KOH solution in ethylene glycol. Such a procedure tends to make both faces of the membrane essentially equivalent (17). Another procedure to separate the porous film from the Al electrode is by immersing the anodized foil in a saturated aqueous $HgCl_2$ solution. This results in the amalgamation of aluminum along the $Al_2O_3$/Al interface and delamination of the oxide layer. The remaining part of the insulating barrier layer is then etched away with 0.025 M NaOH solution (26).

Note that both of these approaches induce isotropic chemical etching with concomitant enlargement of pore size. Very recently, Mallouk and coworkers (20) proposed a new method to penetrate and detach the barrier layer by applying a reverse bias voltage ($-3.5$ to $-5$V) immediately after the completion of the anodization; both anodization and reverse bias are carried out in the same 3% $H_2SO_4$ solution. When $H_2$ bubbles are observed, the bias voltage is reduced until no more bubbles are detected; the process takes a few minutes. It was postulated (20) that the application of a reverse bias voltage in acidic

solution results in an increase of the local $H^+$ concentration, thus promoting the dissolution of the oxide barrier layer by the following reaction:

$$Al_2O_3(s) + 6H^+(aq) \rightarrow 2Al^{3+}(aq) + 3H_2O(l)$$

The reverse bias method was applied successfully to both bulk aluminum and thin aluminum layers deposited on $Ti/Si_xO/Si$ wafers (20).

Recently, Mozalev *et al.* (27) detached the alumina film from the residual aluminum foil by dipping in an $HCl-CuCl_2$ solution, until the aluminum metal was completely dissolved. The pores of the alumina film were protected with gelatine gel and the oxide barrier layer was finally dissolved with 5% NaOH from the bottom side of the film. This method allows the complete removal of the barrier layer without introducing discontinuities in the pore network across the membrane.

Freestanding alumina microporous membranes are commercially available, for example, from Anopore™ or Synkera Technologies Inc. The rather limited number of pore sizes available limits a wider use of the commercial alumina membranes as templates so that many research groups still prefer to prepare their own membranes.

#### *16.2.2.2 Track-etched polymer membranes*

Nanoporous polymeric membranes can be prepared by the track-etch method. This method involves tracking a film of solid material (polymer) with a beam of high-energy particles to create damage tracks in the film. Such tracks are then etched into monodisperse pores by exposure to an alkaline etching solution. The time the material is exposed to the tracking particles determines the number of tracks (and thus pores), while the etching time (as well as the composition of the etching solution) determines the size of the pores (28, 29).

Polymeric materials used for the production of track-etched membranes include poly(ethylene terephthalate) (PET), polycarbonate (PC), polyimide (Kapton), polypropylene, polyvinylidene fluoride, and CR-39 (allyl diglycol carbonate) (29). The most widely used are PET, PC, and Kapton.

PET presents a high etch ratio that allows the production of membranes with a wide range of pore diameters. The membranes are relatively hydrophilic, rather stable to acids and organic solvents, and biologically inert. However, PET-tracked membranes require UV irradiation before etching. The membrane is exposed to UV light with maximum intensity at 320 nm for approximately 30 min. The UV treatment leads to saturation of the damage in the tracks so that further storage of the samples in air or illumination with visible light does not change the etching behavior (30).

PC is the material used for preparing the majority of commercially available track-etched membranes. It is characterized by high sensitivity to tracking and it does not require UV sensitization. However, PC is soluble in organic solvents and has low wettability in aqueous solutions. Its hydrophilicity can be increased by impregnation with polyvinylpyrrolidone (29).

Kapton foils are also used to produce nanoporous track-etched membranes (31, 32). Track-etched membranes are commercially available as filtration membranes with pore

diameters ranging from as small as 10 nm to as large as 10 μm and pore densities between $10^7$ and $10^9$ pores $cm^{-2}$. Track but not etched nanoporous membranes are also commercially available, for example, from Osmonics (50 tracks $cm^{-2}$) or from Whatman ($10^7$ tracks $cm^{-2}$).

***(a) Tracking***

There are two basic methods of producing latent tracks in the polymer foils to be transformed into porous membranes. The first method is based on the irradiation with fragments from the fission of heavy nuclei such as californium, bismuth, or uranium (33) of energy 11.4 MeV per nucleon (30, 34). Typical energy losses of the fission fragments are about 10 keV $nm^{-1}$. The fission fragments coming from a thin layer target have an almost isotropic angle distribution. To create an array of latent tracks penetrating the foil, a collimator is normally used. The advantages of this tracking method are: (a) good time stability of the particle flux and (b) relatively low cost. The limitations of the method are: (a) contamination of the tracked foil with radioactive products ("cooling" of the irradiated material is needed, which usually takes few months); (b) limited thickness of the membrane to be tracked; (c) limited possibilities of controlling the angle distribution of the tracks; (d) fragments of different masses and energies produce tracks with different etching properties (29).

The second method is based on the use of ion beams in accelerators (29). The intensity of the ion beam should be at least $10^{11}$ $sec^{-1}$. To irradiate large areas, a scanning beam is normally used. The advantages of the ion beam accelerator tracking method are: (a) no radioactive contamination of the material when the ion energy is below the Coulomb barrier; (b) identity of the bombarding particles gives tracks with the same etching properties; (c) large range of high-energy particles makes possible the tracking of thicker membranes; (d) better conditions for producing high-density ($>10^9$ $cm^{-2}$) track arrays; (d) particles heavier than fission fragments can be used ($^{238}U$, for example); (e) it is easier to control the impact angle and produce arrays of parallel tracks or create some particular angular distributions for getting rid of merging pores (29).

Very recent advances have shown that it is possible to control the number and the geometric distribution of tracks with an ion beam (35). The sample is covered by a metallic mask with a hole of small diameter (0.1 mm) so that the ions can penetrate the film only within a small area. By registering the ions passing through the film and shutting down and moving the membrane after one single ion has passed through (31, 34), it is possible to obtain single pore membranes or membranes with geometrically patterned arrays of tracks (and pores). The limitations of the ion beam accelerator method are: (a) relative instability of the particle flux and (b) higher cost than irradiation.

In the past decade, a decrease in the popularity of reactor-based irradiation facilities and an increase in the use of accelerated ion beams were observed (29). With the use of ion beams from accelerators, it is easier to control the impact angle for getting rid of merging pores of the kind shown in Figure 16.2.3A (29).

***(b) Chemical etching***

Chemical etching is the process of pore formation during which the damaged zone of a latent track is removed and transformed into a hollow channel (pore) (29, 33). The most

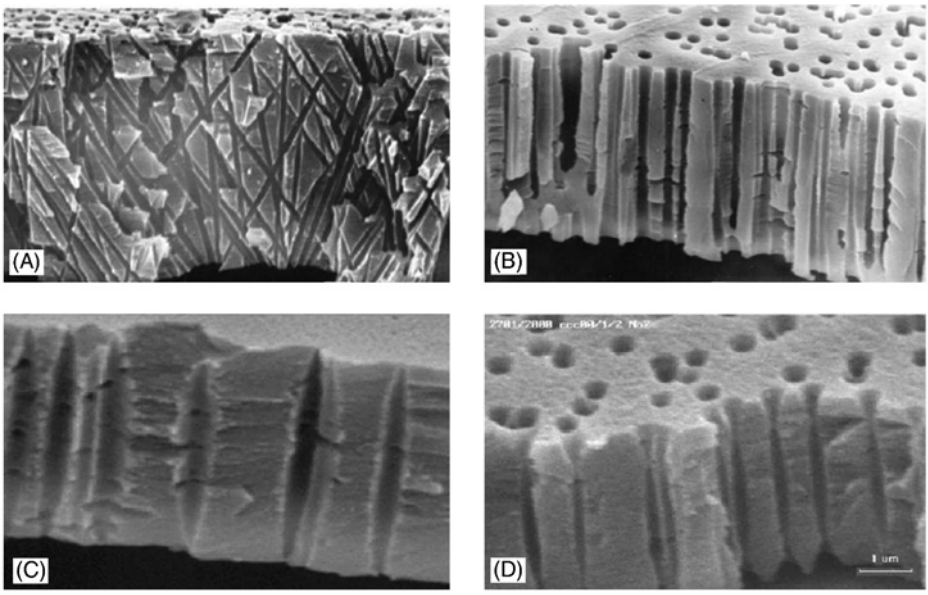


**Figure 16.2.3** Porous structures produced in thin polymeric films using various methods of irradiation and chemical treatment: (A) cross-section of a polycarbonate membrane with cylindrical nonparallel pore channels; (B) polypropylene with slightly conical (tapered toward the center) parallel pores; (C) poly(ethylene terephthalate) with cigar-like pores; (D) poly(ethylene terephthalate) with "bow-tie" pores. Reprinted with permission from reference (29).

widely used etching agents are alkali solutions (KOH or NaOH) although the etching of polyimide (Kapton) requires an oxidizing agent such as NaClO (31, 32). The simplest description of the kinetics of the etching process is based on two parameters: the bulk etch rate ($V_B$) and the track-etch rate ($V_T$). While $V_B$ depends on the material, the etchant composition, and the temperature, $V_T$ depends on additional parameters such as sensitivity of the material, irradiation, post-irradiation conditions, and etching conditions (29). Etching with KOH or NaOH on both sides of the tracked membrane generates pores with a symmetric shape that are typically cylindrical or cigar-like (see Figure 16.2.3).

The formation of cigar-like-shaped pores has been explained by two hypotheses (36): (a) further exposure by electrons generated in the secondary electron cascade caused by the impact of the high-energy particle and (b) an acceleration of the etching rate caused by the etching products, which are more concentrated inside the pores. It was shown that perfectly cylindrical pores could be obtained if a special PC film ($PC^+$) is used instead of standard PC films (36).

It was recently shown that strict control of the etching conditions allows one to control the shape of the pores, obtaining, for example, funnel-like or conically shaped pores (30). Conical pores can be obtained by asymmetric etching with oxygen plasma of initially cylindrical pores (37), or by performing an asymmetric chemical etching, so that $V_B > V_T$, with the ratio changing throughout the thickness of the membrane. Asymmetric etching of

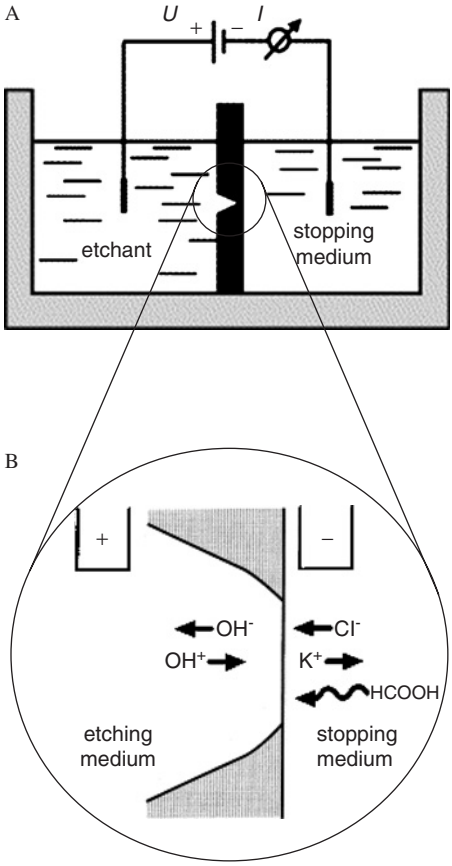


**Figure 16.2.4** (A) Scheme of the experimental set-up with the etching cell for asymmetric pore etching. (B) Direction of electromigration and diffusion during break-through under stopping electric field conditions (30). (→) Migration and (~>) diffusion direction. Adapted with permission from references (30, 34).

tracked membranes was first described three decades ago (38). It is based on the treatment of an ion-irradiated sample with an etchant on one side, while the opposite face is in contact with a stopping medium that neutralizes the etchant as soon as it perforates the sample. This method was modified recently by applying an additional electric field (34). The application of the electric field allows one to detect the instant of pore break-through and, additionally, to protect the etched cone pore from further chemical attack. The scheme of the apparatus used for the asymmetric etching is shown in Figure 16.2.4A.

For asymmetric etching of PC or PET, one side of the membrane is put in contact with an alkaline etching solution, usually 9 M NaOH or KOH, and the other side is in contact with the stopping medium, typically a weak acid solution such as 1 M HCOOH in 1 M KCl (30). For asymmetric etching of polyimide (Kapton), the etching solution is NaClO

(with 13% active chlorine) while the stopping medium is a suitable reducing agent such as 1 M KI (39). A potential of some tens of volts is applied across the membrane by two Pt electrodes. As shown in Figure 16.2.4A, a positive potential is applied to the electrode in the etching solution, while the electrode in the stopping solution is at a negative potential. As shown in Figure 16.2.4B, if a positive potential is applied from the alkali (etchant) side during the break-through, the $OH^-$ anions are pulled out of the pore which accelerates the stopping process. It was demonstrated (30) that electrostopping at voltages around 1 V is more efficient in producing conical pores than chemical stopping alone.

The application of a potential across the membrane is stopped as soon as a monitoring ammeter records an increase in the current that passes through the membrane up to reaching a pre-set value, typically 1 mA (40). The membrane is then immediately immersed (both sides) in the stopping medium, thus blocking the asymmetric etching. At the end of the process, conical nanopores of controlled shape are obtained (37, 40). It was also shown that the addition of alcohols (such as methanol, ethanol, or propanol) to the etch solution allows further control of the etching rate (24) and the $V_B/V_T$ ratio (40, 41).

#### *16.2.2.3 Comparison between alumina and track-etched polymer nanoporous membranes*

Track-etched membranes are flexible with a smooth surface while alumina films are brittle and rather rough. Another difference is the pore density which is typically $10^9$ pores $cm^{-2}$ for track-etched membranes compared to $10^{11}$ pores $cm^{-2}$ for alumina membranes (42). Alumina membranes are therefore interesting as templates for producing high-density nanomaterials. Track-etched membranes are more suitable for obtaining low-density nanomaterials, for example, in the fabrication of NEEs where low nanoelectrode densities are often desired. As shown in Figure 16.2.3, a problem with track-etched membranes is the fact that the pores are not always parallel to each other. Their shape is not always cylindrical and pore positions are randomly distributed unless special procedures are applied (43). For alumina membranes, depending on the method used to separate the membrane from the aluminum, the pores on the side of the barrier layer can be branched into smaller pores (see Figure 2 in reference (44)).

### 16.2.3 Template deposition of metals

#### *16.2.3.1 Electrochemical deposition*

Electrochemical deposition of metals in the pores of templating membranes requires that one side of the membrane be in direct contact with a metallic layer. This can be produced by plasma or vacuum deposition of a metal layer on one side of the membrane (25) and requires that the membrane film be robust enough to tolerate this kind of manipulation. The thickness of the conductive layer is typically 100–1000 nm (45–47). The metal which produces the conductive layer can be the same or different from the one that will provide the final template structure. In electrochemical template deposition, the coated film is placed in an electrochemical cell where the template membrane acts as the cathode and a counter electrode is the anode. The deposition can be carried out under galvanostatic or

potentiostatic conditions. In the case of track-etched PC, it was recently shown that the addition of 1–2% gelatin to the plating solution improves the wettability of the nanoporous membrane, thus improving the reproducibility of the electrodeposition step (45, 48–50).

Final products of the electrochemical deposition are solid nanoparticles, typically nanowires and not hollow structures (e.g., nanotubes or nanocapsules). The electrochemical process is based on the progressive growth and filling of the pores starting from the bottom metallic layer and proceeding progressively toward the open end of the templating pore.

Figure 16.2.5B summarizes the steps for electrochemical growth of continuous metal wires for use as micro- or nanoelectrodes, for example. To form smaller template nanoparticles or nanowire segments, procedure 1–2–5–6 is used. For this latter case, sputtering and

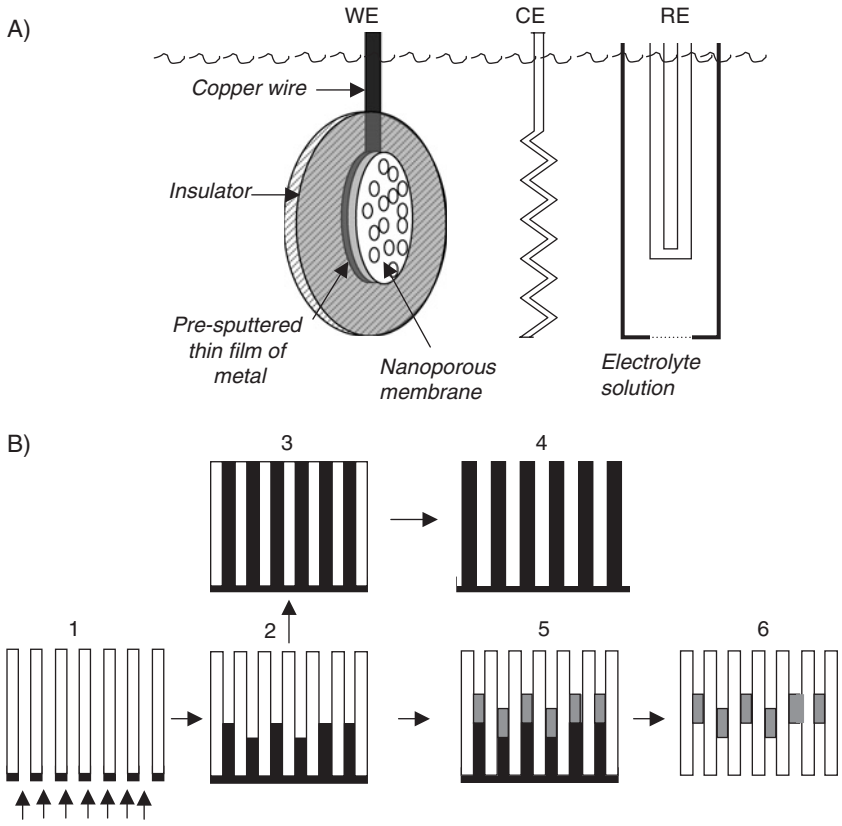


**Figure 16.2.5** Electrochemical template deposition of metals: (A) scheme of the electrochemical cell and (B) sequence of the growth of the template for the preparation of single metal continuous nanowires (sequences 1–4) or segmented nanoparticles (sequences 1, 2, 5, and 6). Detailed steps: (1) metal sputtering to provide a conductive layer for the subsequent electrodeposition; (2) electrodeposition of the same metal to form the fibers; (3) growth of the fibers; (4) etching of the template; (5) electrodeposition of another metal; (6) composite structure after the etching of the foundation metal. Part (B) redrawn with permission from reference (25).

the first growth of nanowires are performed with an etchable metal such as silver which acts as a foundation for the deposition of the metal of interest to be deposited in a desired amount in a second step as shown in Figure 16.2.5B-5 (15). The silver foundation is then etched away with nitric acid leaving the nanoparticles or nanowire segments composed of the second metal (gold, for example) in the pores of the template (Figure 16.2.5B-6). A similar procedure is also used for fabricating multilayered nanowires composed of cylindrical segments of different metals such as Ni/Cu (51), Co/Cu (52), or Au/Sn (50). Table 16.2.2 summarizes examples of template electrochemical deposition of nanowires, nanoparticles, or nanowire segments.

#### *16.2.3.2 Electroless deposition of metals*

Electroless metal deposition involves the use of chemical reducing agents to plate a metal from a solution onto a surface (68). The key requirement for this process is to arrange the chemistry so that the kinetics of homogeneous electron transfer from the reducing agent to the metal ion is very slow. A catalyst that accelerates the rate of metal ion reduction is then applied to the surface to be coated. In this way, the metal ion is reduced at the surface incorporating the catalyst so that only this surface is coated with the desired metal. The thickness of the metal film deposited can be controlled by changing the plating time (7).

The principles of electroless deposition in templates are exemplified for Au deposition developed in Martin's laboratory for the template fabrication of NEEs, nanotubes, and other shaped gold nanomaterials (5, 7). The electroless plating of gold (5) consists of three steps: (i) "sensitization" with $Sn^{2+}$; (ii) reduction of $Ag^{+}$ to produce discrete Ag metal nanoparticles; (iii) galvanic displacement of Ag particles by reduction of gold followed by auto-catalytic reduction of more Au.

Detailed conditions for Au electroless deposition include (5, 69):

(i) After wetting for 2 h in methanol, the PC membrane is sensitized with $Sn^{2+}$ by immersion into a solution 0.026 M in $SnCl_2$ and 0.07 M in trifluoroacetic acid in 50:50 methanol/water as the solvent for 45 min.

(ii) After rinsing with methanol for 5 min, the sensitized membrane is immersed for 10 min in 50 mL of 0.029 M $Ag[(NH_3)_2]NO_3$. This solution is prepared by a dropwise addition of concentrated $NH_4OH$ from a burette (1 mL or less will be needed) to a 0.029 M $AgNO_3$ aqueous solution. With a careful, dropwise addition, a brown precipitate will appear and then disappear with further addition of $NH_4OH$. At the first disappearance of the brown precipitate, the $Ag[(NH_3)_2]NO_3$ solution is ready.

(iii) The membrane is then immersed into an Au plating bath (volume ~ 20 mL) composed of $7.9 \times 10^{-3}$ M $Na_3Au(SO_3)_2$, 0.127 M $Na_2SO_3$, and approximately 0.6 M formaldehyde (1 mL of formaldehyde 37% solution in water is added); the pH of the plating bath is around 11–11.5 for nanowires, which is lowered to 8 for nanotubes (see below). Note that the Au electroless bath component is typically obtained by 1:40 dilution of commercial plating baths, such as Oromerse SO Part B (Technic Inc.) which contains 0.4 troy ounces of gold in 200 mL (1 troy ounce = 31.1035 g of gold), that is, 0.316 M in $Na_3Au(SO_3)_2$ (5).

(iv) After 15 h of electroless deposition, an additional 0.2 mL of formaldeheyde is added.

**Table 16.2.2**

Conditions and materials used for the electrochemical template deposition of metals

| Metal deposited | Templating membrane | Electrodeposition conditions | Nanomaterial obtained | Note | References |
|---|---|---|---|---|---|
| Au | Mica (track-etched) | Commercial Au electroplating solution, pH = 6, $T$ = 60 °C, potential step up to a constant current value, or Au–Ag alloys electroplating solution, pH = 8–9 | Wires ($\phi$ = 8 nm for commercial bath and 20 nm for Au–Ag alloy bath) | | (2) |
| Au | Alumina | Commercial electroless bath (Orotemp 24, Technic Inc.), galvanostatic (0.8–1.2 mA/cm$^2$), two-compartment cell | Wires (microhole array); $\phi$ ~ 200 nm | | (53) |
| Au | Alumina | 0.32 M Au(I) cyanide, 0.26 M citric acid, 0.65 M KOH, pH = 5–6, potentiostatic | Nanorods, $\phi$ = 12–22 nm, length = 39–729 nm | | (54) |
| Au | Alumina | 12 g/L $HAuCl_4$, 160 g/L $Na_2SO_3$, 5 g/L EDTA, 30 g/L $K_2HPO_4$, 0.5 g/L $CoSO_4$, pH = 9.0, potentiostatic, 0.8 V | Wires ($\phi$ = 45 nm) | | (55) |
| Au | Polycarbonate | 0.32 M gold(I)cyanide + 0.26 M citric acid, 0.65 M KOH, pH = 5–6, potentiostatic: −1.0 V vs. SCE | Wires | Wire diameter even three times the nominal diameter of the membrane | (47) |
| Au | Alumina | Commercial Au electrodeposition bath (Orotemp Technic Inc.); deposition at −2.5 V | Au nanowires ($\phi < 10$ nm) | Electrodeposition takes advantage of penetration of aluminum oxide barrier layer by reverse bias voltage | (20) |
| Au, Ag, Cu, Ni, Co, Rh | Polycarbonate | Electrodeposition from suitable baths added with 1–2% gelatin to improve polycarbonate wettability | Au, Ag, Cu single-crystalline nanowires; Ni, Co, Rh polycrystalline nanowires | | (45) |
| Co | Crystalline bisphenol-A polycarbonate | $CoSO_4$ bath, three-electrode cell, room temperature | Wires, $\phi$ = 70 and 10 nm | Wires "toothpick" shape | (56) |

(*Continued*)

**Table 16.2.2 (Cont.)**

| Metal deposited | Templating membrane | Electrodeposition conditions | Nanomaterial obtained | Note | References |
|---|---|---|---|---|---|
| Co | Alumina | 40 g/L $CoSO_4 \cdot H_2O$, 40 g/L $H_3BO_3$, 20g/L ammonium citrate, pH = 3.5, $T$ = 50 °C, current density: 0.3–0.8 mA/cm$^2$, two-electrode cell | Wires, $\phi$ ~ 100 nm | | (57) |
| Co | Polycarbonate | 400 g/L $CoSO_4 \cdot 7H_2O$ + 40 g/L $H_3BO_3$, potentiostatic: −1.1 V vs. Saturated Calomel Electrode | Wires, $\phi$ ~ 10–200 nm | Wire diameter even three times the nominal pore diameter | (47) |
| Co | Polycarbonate | 0.1 M $H_3BO_3$ + 5 × $10^{-2}$ M $CoSO_4$, potentiostatic, applying a sequence of pulses (−1.3 and −0.8 V), three-electrode cell | Cigar-shaped monocrystalline wires ($\phi \approx$ 60 nm) | | (58) |
| Co | Polycarbonate | 0.1 M $H_3BO_3$ + 0.1 M $CoSO_4$, potentiostatic, applying a sequence of pulses (−1.5 and −0.8 V), three-electrode cell | Wires or nanotubes | The nanotubes are obtained changing the pulse cycles | (59) |
| Co | Polycarbonate | 20 g/L $H_3BO_3$ + 252 g/L $CoSO_4 \cdot 7H_2O$ + 7 g/L NaCl, pH = 3.6, potentiostatic | Arrays of nanowires | | (60) |
| Cu | Polycarbonate | 0.6 M $CuSO_4$ + $H_2SO_4$ (pH = 2), potentiostatic, −0.4 V vs. Cu ref. | Wires | "Foundation" film of Pt–Pd | (61) |
| Cu | Polycarbonate | 125 g/L $CuSO_4 \cdot 5H_2O$ + $H_2SO_4$ up to pH = 1.0, potentiostatic: −0.2 V vs. SCE | Wires | Wire diameter even three times the nominal pore diameter | (47) |
| Fe | Polycarbonate | 0.1 M $H_3BO_3$ + 5 × $10^{-2}$ M $FeSO_4$, potentiostatic, applying a sequence of pulses (−1.3 and −0.8 V), three-electrode cell | Cigar-shaped monocrystalline wires or tubes ($\phi \approx$ 60 nm) | Short deposition time produced mainly nanotubes | (58) |
| Fe | Polycarbonate | 0.1 M $H_3BO_3$ + 0.1 M $FeSO_4$, potentiostatic, applying a sequence of pulses (−1.3 V/0.1 sec, cell off/2 sec), three-electrode cell | Nanotubes | | (59) |
| Ni | Alumina | 270 g/L $NiSO_4 \cdot 7H_2O$, 40 g/L $NiCl_2 \cdot H_2O$, 40 g/L $H_3BO_3$, pH = 3.6, $T$ = 50 °C, current density: 0.3–0.8 mA/cm$^2$ | Wires, $\phi$ ~ 100 nm | | (57) |

| | | | | | |
|---|---|---|---|---|---|
| Ni | Alumina | 300 g/L $NiSO_4 \cdot 6H_2O$, 45 g/L $NiCl_2 \cdot 6H_2O$, 45 g/L $H_3BO_3$, pH = 4.5, $T$ = 35 °C, constant current pulses | Wires, magnetic material | | (62) |
| Ni | Polycarbonate | 515 g/L $Ni(H_2NSO_3)_2 \cdot 4H_2O$ + 20 g/L $NiCl_2 \cdot 6H_2O$ + 20 g/L $H_3BO_3$, pH = 3.4, potentiostatic: −1.2 V vs. SCE | Wires | Wire diameter even three times the nominal pore diameter | (47) |
| Pd | Alumina | $1 \times 10^{-3}$ M $(NH_4)_2PdCl_4$ + 50 mM LiCl + 50 mM $LiSO_4$, four-electrode mode | Nanoparticles ($\phi \approx$ 3–5 nm) | Deposition at the polarized interface between aqueous solution and 1,2-dichloroethane | (63, 64) |
| Pt | Alumina | $1 \times 10^{-3}$ M ammonium tetrachloroplatinate + 50 mM LiCl + 50 mM $LiSO_4$, four-electrode mode | Nanoparticles ($\phi \approx$ 3–5 nm) | Deposition at the polarized interface between aqueous solution and 1,2-dichloroethane | (63, 64) |
| Sn | Polycarbonate | 0.1 M $Sn_2SO_4$ + 2% gelatin, pH = 1 with $H_2SO_4$, $E_{applied} = -80$ mV | Single crystal nanowires | Super conducting material with nanoscopic effects on electric transport properties | (48) |
| Sn | Alumina | 7 g/L $SnCl_2 \cdot 2H_2O$ + 25 g/L $Na_3C_6H_5O_7 \cdot 2H_2O$, potentiostatic, −0.8 V (vs. Ag/AgCl saturated), Sn wires annealed in the air give $SnO_2$ wires | Sn and $SnO_2$ nanowires array | | (65) |
| Au/Sn | Polycarbonate | Sequential electrodeposition of Au and Sn using conditions as in references (20, 45) for Au and reference (48) for Sn | Striped Au/Sn/Au nanowires | | (50) |
| $Bi_2Te_3$ | Alumina | $HTeO_2$ + 25 mM, $Bi(NO_3)_3 \cdot 5H_2O$ 33 mM, galvanostatic deposition, 3.5 mA/cm$^2$ | Nanowires | | (66) |
| $Bi_2Te_3$ | Alumina | 1 M $HNO_3$ + elemental Bi and Te, three-electrode cell, potentiostatic ($E < -0.45$ V vs. $Hg/Hg_2SO_4$) | Wires | | (67) |

(*Continued*)

**Table 16.2.2 (Cont.)**

| Metal deposited | Templating membrane | Electrodeposition conditions | Nanomaterial obtained | Note | References |
|---|---|---|---|---|---|
| Co/Cu | Polycarbonate | Sulfate bath: $10^{-3}$ M Cu, 0.5 M Co, potentiostatic pulsed (−0.2 and −0.9 V) | Co/Cu multilayered wires | Giant magnetoresistance | (52) |
| Ni/Cu | Polycarbonate | 2 M Nickel sulfamate, 0.02 M copper sulfate, 0.5 M boric acid, room temperature, pH = 3.5–4.0; potentiostatic pulsed; for Cu: −0.80 V; for Ni: −1.90 V vs. SCE | Multilayered wires ($\phi$ = 60–80 nm, 5 μm length) | | (51) |
| NiFe | Alumina | 6 g/L $FeSO_4(7H_2O$, 218 g/L $NiSO_4(7H_2O$, 40 g/L $H_3BO_3$, pH = 3.6, current density: 0.3–0.8 mA/cm$^2$, two-electrode cell | Magnetic nanowires | | (57) |

(v) Deposition is carried out for 9 h more to give a total of 24 h of electroless deposition.
(vi) The membrane is removed from the plating solution, rinsed with water, and immersed for approximately 6 h in 10% $HNO_3$ to eliminate traces of tin or silver.
(vii) The membrane is then rinsed with water and dried in air.

Note that if the plating procedure is stopped after a relatively short time, Au nanotubes are formed within the pores (70–73). To fill the pores completely and obtain nanowires, the electroless plating process must proceed for about 24 h as described above (5). In order to slow the kinetics of the deposition, the process is performed between 0 and 5 °C.

In contrast to electrochemical template deposition, in the electroless method, the growth of the metal layer starts from the sensitized/activated sites located on the pore walls and progresses from the pore walls toward the center of the pore. This is the reason why stopping the deposition at short times results in hollow metal nanomaterials such as nanotubes (70). In fabricating Au nanotubes, it is also important to control the size of the gold particles that are deposited on the pore walls. This is achieved by controlling the pH of the deposition bath at a value around 10, for example, by adding carbonate buffer (73). After completion of the deposition, it is possible to separate the nanowires or nanotubes from the template membrane (see Section 16.2.3.3) or to keep them in the template. By keeping metal nanotubes in the membrane, it is possible to obtain separation membranes with metallized pores (71, 72) which can be further functionalized chemically by resorting to thiol chemistry (73), for example. In contrast, NEEs can be fabricated from the continuous metal nanowires which are kept inside the template membrane.

Examples of nanomaterials obtained by template electroless deposition of metals are listed in Table 16.2.3.

A new method for the chemical deposition of carbon/gold composite nanotubes in alumina templates has been proposed recently (79). It is based on the impregnation of the template pores with diluted hydrogen tetrachloroaurate ($HAuCl_4$)/acetone solutions and subsequent thermolysis. Gold(III) is reduced, whereas the solvent acetone is oxidized. The results are nanotubes whose walls consist of gold nanocrystals supported by amorphous carbon. The authors report that when the template pores have a diameter smaller than 180 nm, single crystal gold nanowires are obtained.

An elegant way to obtain nanotubes made of preformed metal nanoparticles (named nanoparticle nanotubes (NPNT)) has been reported recently by Rubinstein and coworkers (80). Their method is based on the assembly of gold or silver nanoparticles on the pore walls of a silane-treated alumina template. Following a published procedure (81), the silyl groups of 3-aminopropyl trimethoxysilane react with the hydroxyl groups on the alumina surface (80), thus leaving the amine groups available for binding the metal nanoparticles. The particles self-assemble and coalesce at room temperature within the pores to form the NPNTs.

#### *16.2.3.3 Separation from the template*

When the goal of the deposition is to obtain freestanding nanostructures in the form of nanowires, nanotubes, or nanocones, then the nanomaterial must be separated from the templating membrane. Track-etched membranes can be dissolved by using suitable organic solvents such as $CH_2Cl_2$ for PC (3, 47) or 1,1,1,3,3,3-hexafluoro-2-propanol (HFIP) for

**Table 16.2.3**

Examples of conditions and materials used for the electroless template deposition of metals

| Metal deposited | Templating membrane | Electroless conditions | Nanomaterial obtained | References |
|---|---|---|---|---|
| Au | Polycarbonate | Sensitization: 0.026 M $SnCl_2$ + 0.07 M trifluoroacetic acid, 50/50 methanol/water; activation: 0.029 M $AgNO_3$; Au deposition: $7.79 \times 10^{-3}$ M $Na_3Au(SO_3)_2$ + 0.127 M $Na_2SO_3$ + 0.625 M formaldehyde; temperature ~ 0 °C | Wires | (5) |
| Au | Polycarbonate | The same as reference (5), but with a different deposition time and at pH = 10 controlled with 0.025 M $NaHCO_3/H_2SO_4$ | Nanotubes | (73) |
| Au | Home-etched polycarbonate (37) or poly(ethylene terephthalate) (40) with conical pores | Same as above and in reference (73) | Nanocones | (37, 40) |
| Ag | Polycarbonate | 1st step: 0.026 M $SnCl_2$ + 0.07 M trifluoroacetic acid; 2nd step: 2.3 g $AgNO_3$ + 1.9 mL $NH_4OH$ + 22.7 mL $H_2O$; 3rd step: 7.95 g $KNaC_4O_6H_4$ + 0.57 g $MgSO_4$ + 18.2 mL $H_2O$, temperature = 35 °C | Nanotubes | (74) |
| Cu | Polycarbonate | Pre-activation: $SnCl_2$ 10g/L + 10 mL/L HCl; activation: $PdCl_2$ 0.1 g/L + 10 mL HCl; deposition: $CuSO_4$ $5H_2O$ 10 g/L + NaOH 12 g/L (pH = 12.1) + tartaric acid 18 g/L (complexing agent) + formaldehyde 10 mL/L (reducing agent) | Tubes: cylindrical, cigar-shaped, conical; $\phi_{external}$ = 300–2000 nm; $\phi_{internal}$ = function of deposition time | (75) |
| Pd | Polycarbonate, alumina | Ammonium tetrachloropalladate + decamethylferrocene in 1,2-dichloroethane | Nanoparticles | (76) |
| Ni–P | Polycarbonate | Sensitization: 0.026 M $SnCl_2$ + 0.07 M trifluoroacetic acid, methanol/water solution; activation: 0.25 g/L $PdCl_2$ + 1.0 g/L HCl; Ni plating: $NaH_2PO_2 \cdot H_2O$ 20 g/L, $NiSO_4 \cdot 6H_2O$ 40 g/L, $NaC_6H_5O_7 \cdot 2H_2O$ 100 g/L, $NH_4Cl$ 50 g/L; $NH_4OH$ (pH adjustment) | Ni–P tubules electrode array; internal diameter ≅ 180 nm; wall thickness ≅ 20 nm; length 2 μm | (77) |
| Co–Fe–P | Alumina | Sensitization: $SnCl_2$ 10 g/L; activation: $PdCl_2$ 1 g/L; plating: $CoSO_4 \cdot 7H_2O$ 20 g/L + $FeSO_4 \cdot 7H_2O$ 5 g/L + $NaH_2PO_2 \cdot H_2O$ 25 g/L + $KNa(C_4H_4O_6) \cdot 4H_2O$ (Rochelle salt) 60 g/L at 80–85 °C | Nanowire arrays | (78) |

PET (40). Polymers can also be etched by treatment with oxygen plasma (82). Dissolution of alumina templates is easily achieved by immersion in strong alkali such as 5 M KOH or NaOH (20).

### 16.2.4 Morphological and optical properties

#### *16.2.4.1 SEM–TEM studies*

Scanning or transmission electron microscopy (SEM or TEM, respectively) are typically used for performing morphological characterization of nanomaterials obtained by template synthesis. The resolution of the images is improved if the nanomaterial is separated from the host membrane.

As an example, Figure 16.2.6 shows SEM and TEM images of nanostrucutures produced in PC templates. Figure 16.2.6A images 30 nm nanofibers of an NEE still in the

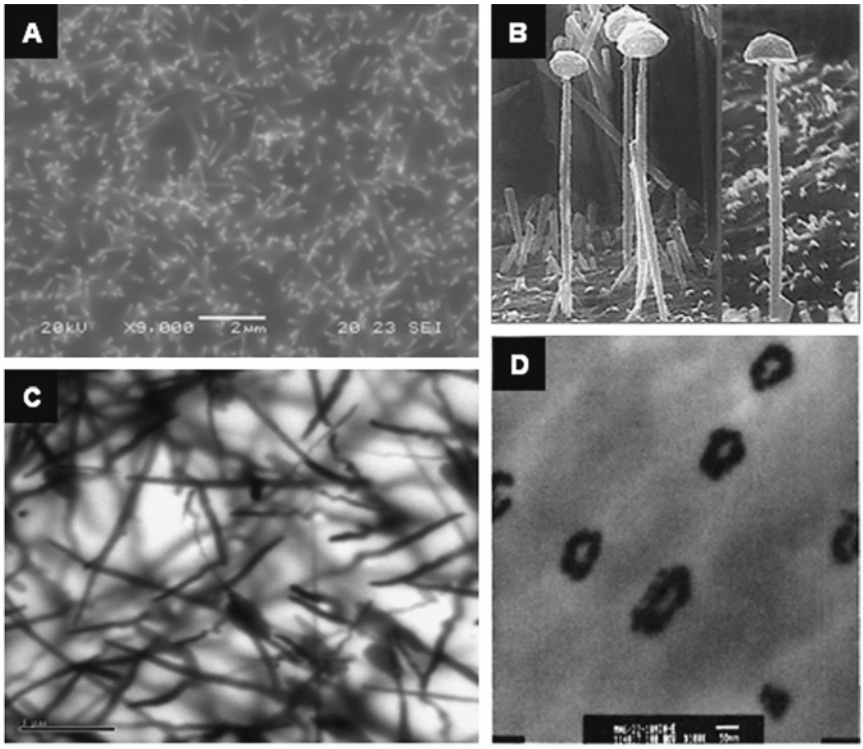


**Figure 16.2.6** (A) SEM image of the surface of an Au-NEE, in PC template, pore diameter 30 nm; (B) SEM image of Ni wires, template pore diameter 80 nm, after dissolution of the PC membrane; (C) TEM image of an Au-NEE, template pore diameter 30 nm with the nanofibers still embedded in the polycarbonate; (D) TEM image of a microtomed section of a PC membrane after deposition of Au tubes within the pores of the membrane. Reprinted with permission from reference (83) for (A) and (C), reference (47) for (B), and reference (5) for (D).

polymer membrane. The surface gold layers present on both sides of the membrane at the end of the deposition step have been removed before the SEM analysis. This image clearly shows the surface of the nanodisks emerging from the PC template. The fading lines behind the nanodisks are the traces of the nanofibers that grew inside the membrane. The observation of such traces is related to the partial transparency of the PC template to the electron beam. The nanofibers are not aligned parallel, but have a considerable angular distribution as a consequence of the angles of the original trajectories of the tracks used to sensitize the membrane before etching of the pores in the membrane production (47). Figure 16.2.6B shows that more detailed images are obtained after the removal of the guest membrane by dissolution with $CH_2Cl_2$; in this case, the nickel nanowires have a curious mushroom shape (47). Figure 16.2.6C shows that information about the inner structure of the nanofibers inside PC templates can be obtained by TEM without removal of the guest membrane thanks to the transparency of the PC to electron beams (83). However, some distortion and artifacts cause apparent whirling and bending of the fibers and are attributed to possible interactions between the e-beam and the polymer. High-resolution TEM images of nanowires isolated from template membranes (51, 63) also permit the study of the structure and crystallinity of the nanofibers. Finally, Figure 16.2.6.D demonstrates that microtomy can also be used to characterize templated nanostrucutures, in this case, gold nanotubes of 30 nm diameter in PC (5).

#### *16.2.4.2 Optical properties*

Nanometals have interesting optical properties, whether they are inside the host template or liberated from it. For example, suspensions of nanoscopic Au particles can be pink, purple, or blue, depending on the diameter of the particles. These colors arise from the plasmon resonance absorption of the nanometal particle (25). Membranes containing Au nanowires also show this plasmon resonance band, and as a result, such membranes can show a wide variety of colors (42). This absorption in the visible region, typically between 400 and 800 nm for 10–30 nm diameter particles, provides an interesting optical approach to characterizing Au nanowires (5).

One attractive feature of host templates such as porous anodic alumina is the parallel alignment of the pores. This feature permits the straightforward interpretation of the plasmon resonance spectra of non-spherical metal particles that are prepared within such pores. Figure 16.2.7A shows the plasmon resonance spectra of a series of gold nanorod/porous alumina composite films measured with light incident normal to the film surface (23, 84).

Since the rods are also aligned perpendicular to the film surfaces, the electric field of the light is incident only along the diameter (or short axis) of the rods. Thus, only one plasmon resonance band appears in each spectrum (the transverse resonance). An increase in the aspect ratio (length/diameter) of the particles causes a blue shift in the maximum of the plasmon resonance absorption (17). The change in the incidence angle ($\theta$) modifies the spectrum (see Figure 16.2.7B): as $\theta$ increases, a second spectral band grows in corresponding to the long-axis resonance. Converse to the transverse resonance case, the wavelength maximum of the longitudinal resonance increases with increasing particle aspect ratio (23, 85).

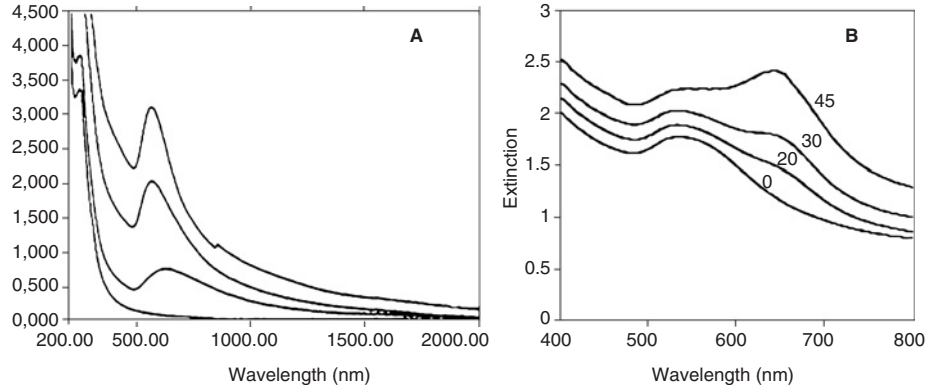


**Figure 16.2.7** UV–vis spectra of oriented Au nanoparticle composites. (A) Normal incidence spectra of 60 nm diameter Au rods in alumina membrane; particle aspect ratios: (1) blank; (2) 1; (3) 3.38; (4) 5.28. (B) Polarization spectra of Au nanorods (diameter = 30 ± 4 nm; length = 54 ± 4 nm) in host alumina membrane at different incident angles $\theta$, indicated in the graph and measured in degrees relative to membrane normal surface. Adapted with permission from references (23, 84).

The spectra resulting from the aqueous dispersion of the nanorods removed from the host template show two plasmon resonance bands: a strong one at long wavelengths due to the long-axis resonance and a weaker one at shorter wavelengths that originates from the transverse resonance (85).

All of these optical features are useful in characterizing the shape and spatial distribution of the nanostructures.

### 16.2.5 Electrochemistry with template nanomaterials: nanoelectrode ensembles

Nanoelectrode ensembles (NEEs) (see also Chapter 10 of this handbook) are nanotech-based electroanalytical tools which find application in a variety of fields ranging from electroanalysis to sensors (86) and electronics (7). They are fabricated by growing metal nanowires in the pores of a template, typically a PC nanoporous membrane. The density of the pores in the template determines the number of Au-disk nanoelectrode elements per $cm^2$ of NEE surface and, correspondingly, the average distance between the nanoelectrode elements. Such electrode systems proved to be valuable tools for trace determinations and kinetics studies by simply using cyclic voltammetry (CV) (5, 69, 86, 97).

The NEE fabrication procedure used in our laboratory is described below and is based on that reported in reference (5) apart from minor modifications such as positioning of the copper tape (see below and reference (83)). A scheme of an NEE is presented in Figure 16.2.8; specific details on the construction can be found in the original papers (5, 83) as well as in recent reviews (7, 86, 87). The starting material is a piece of golden PC membrane with

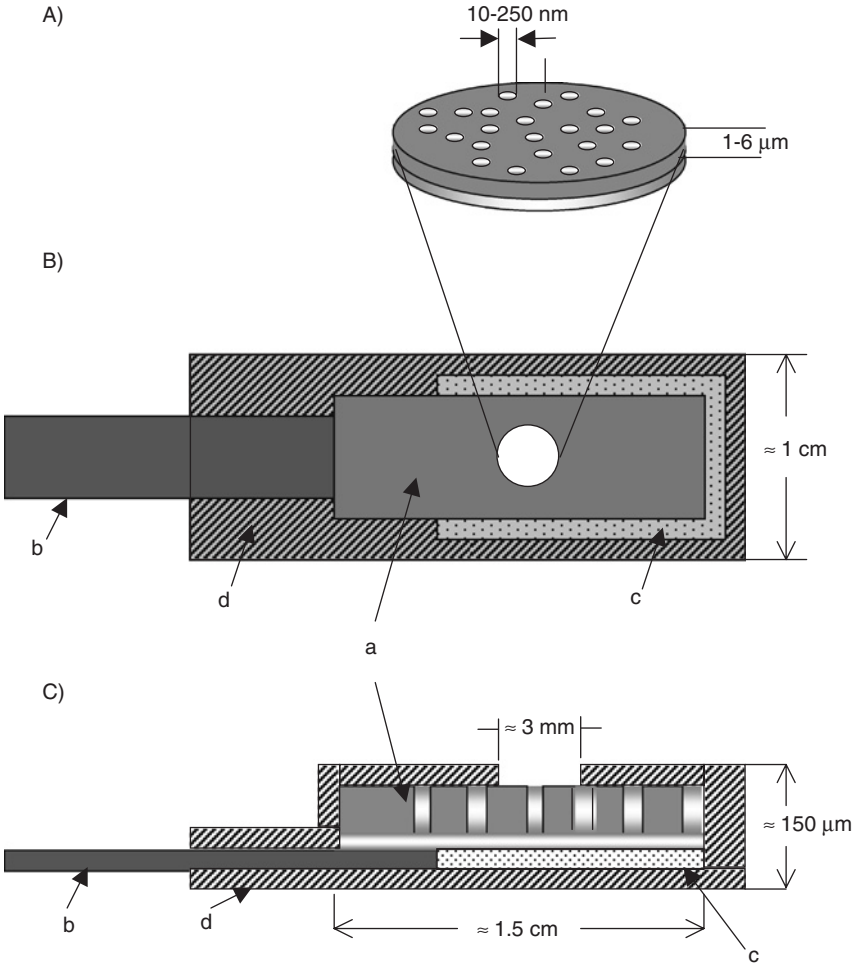


**Figure 16.2.8** Scheme of an Au-NEE prepared using a track-etched polycarbonate membrane as template (A). Particular of the section of the active area; (B) top view; (C) section of the all NEE ready for use as working electrode. (a) Track-etched golden membrane; (b) copper adhesive tape with conductive glue to connect to instrumentation; (c) aluminum adhesive foil with non-conductive glue; (d) insulating tape. *Note*: Some dimensions are only indicative and not in scale.

gold within the pores and on both faces of the membrane; this membrane, named Au/Au-PC/Au, is the final product of the Au electroless deposition process. In particular, a 5 × 6 mm piece of the Au/Au-PC/Au membrane is first affixed to a 6 × 15 mm piece of adhesive aluminum foil tape. The Au/Au-PC/Au membrane is placed on the Al foil tape such that the Au film covering the rough face of the membrane is down (i.e., against the adhesive). A rectangular strip (6 × 40 mm) of copper foil with a conductive adhesive is affixed to the lower Au-coated surface of the Au/Au-PC/Au membrane between the Au on the rough face

of the membrane and the Al foil. The copper foil is positioned such that it covers only about 1 mm of the 6 mm length of the Au/Au-PC/Au membrane. This copper foil tape acts as a current collector and working electrode lead for the NEE. The upper Au surface layer from the portion of the Au/Au-PC/Au membrane not covered by the Cu foil tape is then removed by simply applying and then removing a strip of Scotch tape. Removal of the Au surface layer exposes the disk-shaped ends of the Au wires within the pores of the membrane. These nanodisks will become the active electrode elements. At this point, the NEE assembly is heat-treated at 150 °C for 15 min. This procedure produces a water-tight seal between the Au nanowires and the pore walls. Finally, strips of strapping tape are applied to the lower and upper surfaces of the assembly to insulate the Al and Cu foil tapes. A hole (diameter of 3 mm) is punched into the upper piece of tape prior to the placement on the assembly. This hole defines the geometric area ($A_{geom}$) of the NEE. All the nanoelectrodes in the NEE are connected to each other, so that they all experience the same applied potential.

Track-etched polymer membranes are preferred for NEE fabrication over alumina membranes because track-etched membranes are not brittle and they have smaller pore densities. From an electroanalytical viewpoint, the latter is an important feature since it reduces the interactions between individual nanoelectrode elements (see below).

#### *16.2.5.1 Current signals of nanoelectrode ensembles*

From a voltammetric viewpoint, an NEE is a large assembly of very small ultramicrolectrodes confined in a rather small space. As shown in Figure 16.2.9, NEEs can exhibit three distinct voltammetric response regimes depending on the scan rate or distance between the nanoelectrode elements (88, 89; see also Chapter 10 of this handbook)—(A) *Total Overlap Regime*: when radial diffusion boundary layers overlap totally (slow scan rates and/or small distance between nanoelectrodes); (B) *Pure Radial*: when the nanoelectrodes behave independently (higher scan rates, larger distances between nanoelectrodes; (C) *Linear*: when the nanoelectrodes behave as isolated planar electrodes (very high scan rates).

The transition from the Total Overlap to the Pure Radial Regime has been demonstrated experimentally as a function of the template pore density (88). For electroanalytical applications, the most advantageous regimes are the Total Overlap and the Pure Radial Regimes because they give high faradaic-to-capacitive current ratios (90). The diffusion regime usually observed at NEEs fabricated from commercial track-etched membranes is the Total Overlap Regime (5).

Relevant geometric parameters that define the behavior of NEEs include:

(i) ***Total geometric area*** **($A_{geom}$):** Overall area (nanodisks plus bare membrane area) of the ensemble exposed to the sample solution; typical values for this parameter range from 0.008 to 0.580 $cm^2$ (91). $A_{geom}$ is determined by the dimension of the hole punched into the insulator (see Figure 16.2.8).

(ii) ***Active area*** **($A_{act}$):** Area of the metal nanoelectrode elements alone. It can be calculated by the pore density ($p$), the average radius of the pores ($r$), and the geometric area, according to the following equation:

$$A_{act} = \pi r^2 p A_{geom} \tag{16.2.1}$$

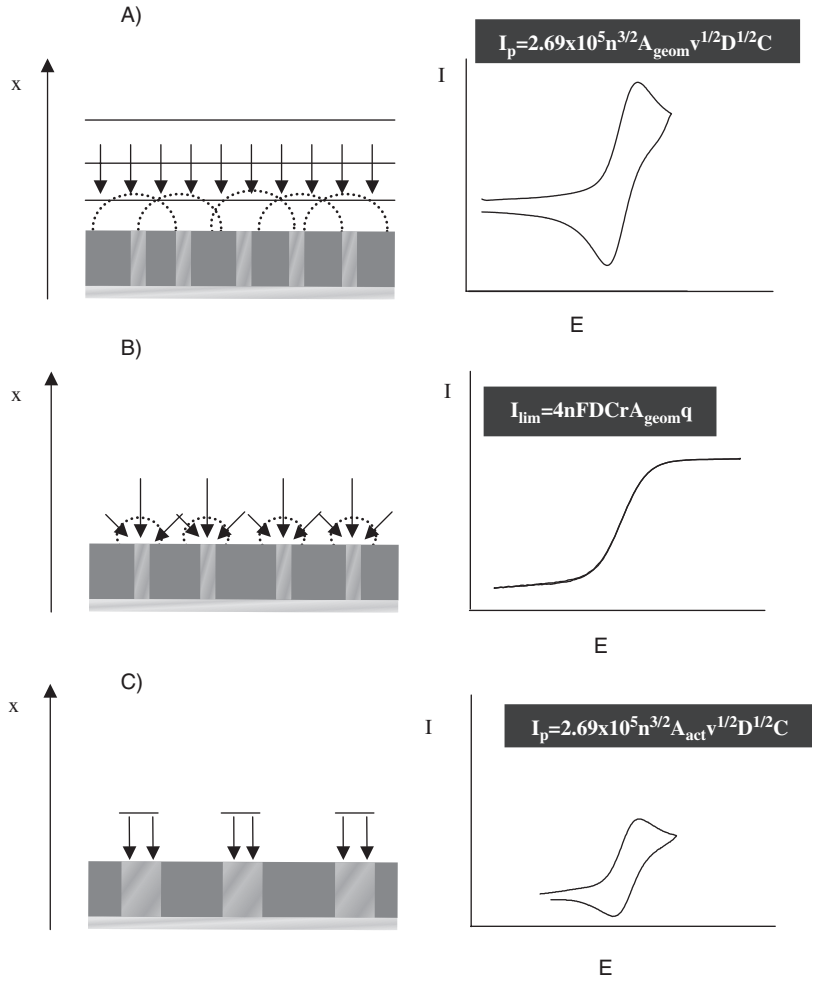


**Figure 16.2.9** Schematic drawing of the different diffusional regimes at NEE: (A) Total Overlap; (B) Pure Radial; (C) Linear active. The scan rate or the distance between the nanodisk elements increases from (A) to (C). Relevant equations for peak currents (A and C) and plateau current (B) refer to reversible redox systems. $A_{act}$ is the active area (nanodisk surface), $A_{geom}$ is the total geometric area of the ensemble (nanodisks and insulator), $q$ is the nanodisk density (disk $cm^{-2}$), and all other symbols have their usual meaning. Reprinted with permission from reference (86). (for colour version: see colour section at the end of the book).

(iii) ***Fractional electrode area*** **($f$):** It is defined as the ratio between active and geometric areas:

$$f = \frac{A_{act}}{A_{geom}} \tag{16.2.2}$$

By substitution of equation (16.2.1), it can be easily calculated also as:

$$f = \pi r^2 p \tag{16.2.3}$$

The faradaic peak current at an NEE operating in the Total Overlap Regime for a reversible redox system obeys the Randles–Sevcik equation (5):

$$i_p = 2.69 \times 10^5 n^{3/2} A_{geom} D^{1/2} C^* v^{1/2} \tag{16.2.4}$$

where $i_p$ is the peak current (A), $A_{geom}$ is the geometric area of the ensemble ($cm^2$), $D$ is the diffusion coefficient ($cm^2\ sec^{-1}$), $C^*$ is the redox species bulk concentration (mol $cm^{-3}$), and $v$ is the scan rate (V $sec^{-1}$).

At the same NEE, the double-layer charging current ($i_C$) is proportional to the area of the electrode elements (active area, $A_{act}$) (92, 93):

$$i_C = vC_{dl}A_{act} \tag{16.2.5}$$

where $C_{dl}$ is the double-layer capacitance of the metal nanodisks of the NEE. Typical $i_C$ values will be in the range of 1 and 2 nA (based on a $C_{dl}$ value between 20 and 40 μF $cm^{-2}$ (93), a gold NEE with $A_{geom} = 0.079 cm^2$, pore density $= 6 \times 10^8$ pore $cm^{-2}$, average pore radius $= 1.5 \times 10^{-6}$ cm, and scan rate ($v$) $= 0.1$ V $sec^{-1}$).

Faradaic-to-capacitive current ratios at an NEE and a conventional electrode with the same geometric area are related by equation (16.2.6) (86):

$$\left(\frac{i_F}{i_C}\right)_{NEE} = \left(\frac{i_F}{i_C}\right)_{conv} \left(\frac{A_{geom}}{A_{act}}\right) = \left(\frac{i_F}{i_C}\right)_{conv} \left(\frac{1}{f}\right) \tag{16.2.6}$$

This ratio is larger at the NEE than that at the conventional electrode by a factor that is the reciprocal of the fractional electrode area $f$. Since typical $f$ values for NEEs are between $10^{-3}$ and $10^{-2}$, $i_F/i_C$ ratios at NEEs can be 2–3 orders of magnitude higher than the ratios at conventional electrodes of the same geometric area. Thus, detection limits at NEEs are 2–3 orders of magnitude lower than that at regular electrodes (5, 68, 69).

From a practical viewpoint, the values given for the faradaic peak currents and for the double-layer charging currents calculated by equations (16.2.4) and (16.2.5) can be used to discriminate between "good" and "bad" NEEs. In our laboratory, from a commercial PC nanoporous membrane of 47 mm diameter, we prepare a rather large number (typically around 30) of NEEs, which are then selected on the basis of the agreement between theoretical and experimental $i_F$ and $i_C$ values. The latter can be obtained from the cyclic voltammogram recorded in supporting electrolyte alone (5; 92, p. 18) and the former by recording the CV in solution containing a known concentration of a reversible redox probe of known diffusion coefficient. From the CVs with and without the redox probe we select as "good NEEs" those that are characterized by $i_{F(exp)} = i_{F(theor)}(1 \pm 0.2)$ and $i_{C(exp)} = i_{C(theor)}(1 \pm 0.5)$, where $i_{F(exp)}$ and $i_{C(exp)}$ are the faradaic and double-layer charging currents measured experimentally, and $i_{F(theor)}$ and $i_{C(theor)}$ are values calculated by equations (16.2.4) and (16.2.5). Figure 16.2.10 reports typical experimental CVs (dotted and dashed lines) recorded at "good" (part A) and "bad" NEEs (part B). The comparison with the simulated CV curves (full lines in the same figure) allows one to immediately distinguish good ensembles from bad ones. Note that the two experimental curves in part B show the features typical for two kinds of defects which can be produced during the NEEs preparation.

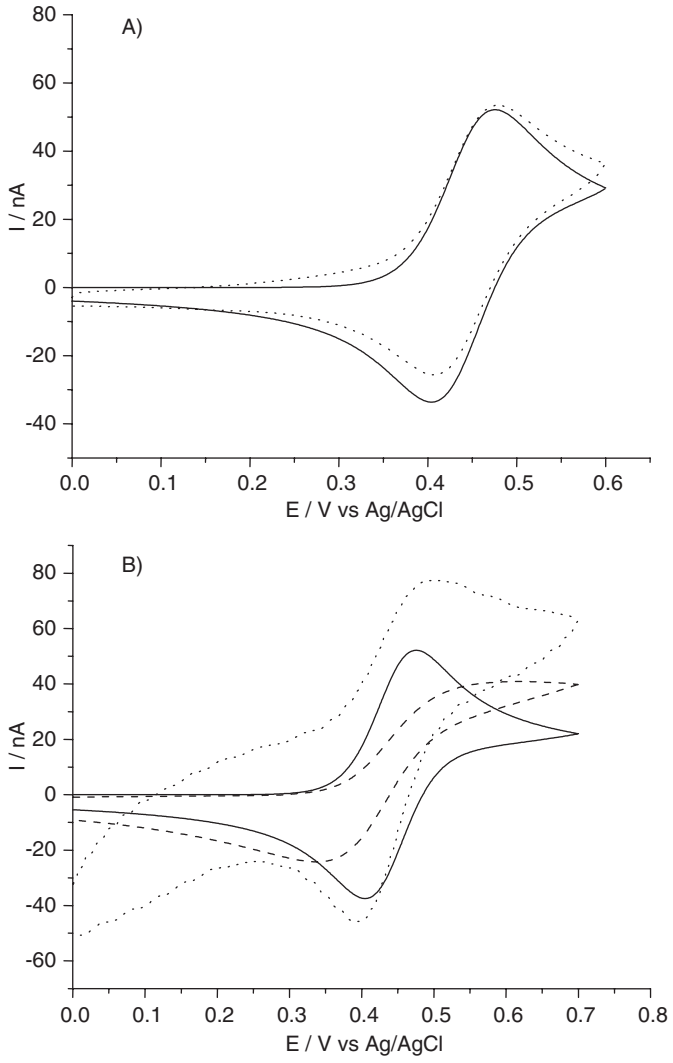


**Figure 16.2.10** Comparison between digital simulations (—) and experimental CVs; the experimental curves refer to (A) (···) a "good" NEE; (B) (··· and - - -) a "bad" NEE. Experimental conditions: $10^{-2}$ M $NaNO_3$, $6 \times 10^{-6}$ M (ferrocenylmethyl)-trimethylammonium hexafluorophosphate, $A_{geom} = 0.07$ cm$^2$, scan rate 50 mV sec$^{-1}$. Additional parameters used for the digital simulation (run with CH Instruments software): $E^\circ = 0.44$ V, $k^\circ = 0.007$ (which is really $k^\circ_{app}$, see equation (16.2.8)), and $D = 4 \times 10^{-6}$ cm$^2$ sec$^{-1}$ (94).

The dotted-line voltammogram indicates that this NEE is affected by a large capacitive current, which was probably produced by poor sealing between the nanowires and the surrounding PC insulator and/or by heavy scratches or abrasions of the PC membrane caused by improper handling of the NEE. The dashed-line voltammogram shows a radial diffusive contribution to the overall signal and a current smaller than the theoretical one. This

suggests larger distances between and a smaller number of nanoelectrode elements with respect to expected values, possibly due to not all of the pores being filled by gold in the final NEE. The number of NEEs that satisfy the above criteria ranges typically from 25 to 40% in a batch of NEEs obtained from one PC membrane.

#### *16.2.5.2 Electron transfer kinetics*

A distinctive feature of NEEs is that electron transfer kinetics appear slower than those at conventional electrodes (5). In fact, NEEs behave as electrodes with a partially blocked surface (PBE). According to the model elaborated by Amatore *et al.* (95), the current response at a PBE is identical to that at a bare electrode of the same overall geometric area but with a smaller apparent standard rate constant for the electron transfer which decreases as the coverage with the blocking agent increases. Such an apparent rate constant ($k^{\circ}_{app}$) is related to the true standard charge transfer rate constant ($k^{\circ}$) and the fraction of blocked surface ($\vartheta$) by the following relationship (95):

$$k^{\circ}_{app} = k^{\circ}(1-\vartheta) \tag{16.2.7}$$

Considering that $\vartheta = (A_{geo} - A_{active})/A_{geo}$, then equation (16.2.7) can be easily converted into:

$$k^{\circ}_{app} = k^{\circ} f \tag{16.2.8}$$

where $f$ is the fractional electrode area, defined by equation (16.2.2).

In CV at a conventional electrode, the reversibility depends on both $k^{\circ}$ and the scan rate, while at an NEE, it depends on $k^{\circ}_{app}$ and the scan rate (5). At a conventional electrode, a redox system gives a reversible voltammetric pattern when $v^{1/2} \leq (k^{\circ}/0.3)$ (see p. 239 in reference (92)). At NEEs, equation (16.2.8) suggests that, for a certain redox couple, the scan rate that defines the transition between reversible and quasi-reversible behavior will be placed at a lower value than that at conventional electrodes. Note that such a boundary scan rate will decrease with decreasing $f$.

From a mechanistic viewpoint, this behavior means that with NEEs characterized by small $f$ values (for example, very small diameter nanodisks and/or very small pore densities), it is experimentally easier to measure large $k^{\circ}$ values (5, 69, 94). Values of $k^{\circ}_{app}$ are measured typically by CV operating within a scan rate range where the redox system behaves quasi-reversibly (92, 93). By the analysis of the $\Delta E_p$ dependence on the scan rate (93) and by using suitable working curves (96), $k^{o}$ values are readily obtained. At NEEs, quasi-reversible behavior is observed at scan rates 2–3 orders of magnitude lower than those at conventional electrodes (depending on $f$). What is measured experimentally under such conditions is really the smaller $k^{\circ}_{app}$ value, which is converted into the larger $k^{\circ}$ by equation (16.2.8) (69, 94).

#### *16.2.5.3 Electroanalysis with NEEs*

The potential window accessible at gold disk NEEs (Au-NEEs) has been studied in detail (5, 69). It was shown that the limit at negative potentials is determined by the hydrogen evolution reaction and depends on the solution pH (69). The limit at positive potentials is

given by the formation of gold oxide. NEEs are typically used at low analyte concentrations (typically from $10^{-5}$ to lower than $10^{-9}$ M) (5, 69) so that faradaic peak current signals can be on the order of a few nA down to a few pA. Therefore, relatively high electronic amplification of the current signal is required. By operating with suitable amplification levels at pH around 7 and micromolar (or lower) analyte concentrations, the potential window accessible at Au-NEEs is limited approximately to the range between $-0.750$ and $+0.800$ V vs. Ag/AgCl. Such limits can change with the nature of the metal of which the nanoelectrode is made, but no precise information is available up to now for materials different from gold.

The ability of NEEs to furnish well-resolved cyclic voltammograms has allowed researchers to develop sensitive methods for trace determination of redox species characterized by relatively fast electron transfer kinetics and an electroactivity range within the above-mentioned potential window. As explained in Section 16.2.5.2, the high sensitivity of NEEs to electron transfer kinetics causes the observation of a perfectly reversible electrochemical behavior only to very fast redox couples, while for "sluggish" redox couples, quite flattened voltammetric patterns are recorded. In addition to the application for trace electroanalysis at well-known reversible redox probes such as ferrocene derivatives or ruthenium complexes (5, 97), Figure 16.2.11 shows that NEEs can be used for CV at micromolar concentration levels of more complex redox systems such as organic mediators like phenothiazines (azure B in Figure 16.2.11B), methylviologen (69) (not shown), or the heme-protein cytochrome *c* (see Figure 16.2.11A). Note that for these redox systems, $k^\circ$ values are $8 \times 10^{-3}$ cm sec$^{-1}$ for azure B (69) and $>0.1$ cm sec$^{-1}$ for cytochrome *c* (98).

The cytochrome *c* case is noteworthy because at NEEs, well-resolved CVs are obtained in diluted solutions of the protein both with and without promoters such as 4,4′-bipyridyl typically used for promoting cytochrome *c* electrochemistry (99–101). These promoters are generally required to avoid adsorption/denaturation (83, 102, 103) of cytochrome *c* on the Au surface. However, such an adsorption is concentration dependent so that lowering the cytochrome *c* solution concentration below the adsorption limit (possible at NEEs thanks to their lower detection limit) can overcome adsorption-related problems. A similar situation has been reported for the adsorption of some organic dyes such as the phenothiazines (69).

Recently, it was shown that by etching only a layer of the templating membrane, it is possible to fabricate ensembles of 3D nanowires instead of 2D nanodisks (82, 104). The partial etching can be performed by either oxygen plasma (82) or partial dissolution of the PC using a mixture of ethanol and dichloromethane (105). The use of nanowire ensembles together with suitable redox indicators (104, 106, 107) has been demonstrated to be useful for improving the sensitivity for the electrochemical detection of DNA duplexes. This example illustrates how NEEs can be used advantageously for advanced bio-electroanalytical sensing.

### 16.2.6 Conclusions and prospects

The use of nanoporous membranes as templates constitutes an attractive and practical methodology for the fabrication of nanomaterials characterized by high aspect ratios, ranging from relatively simple nanomaterials made of just one component, such as metal nanowires

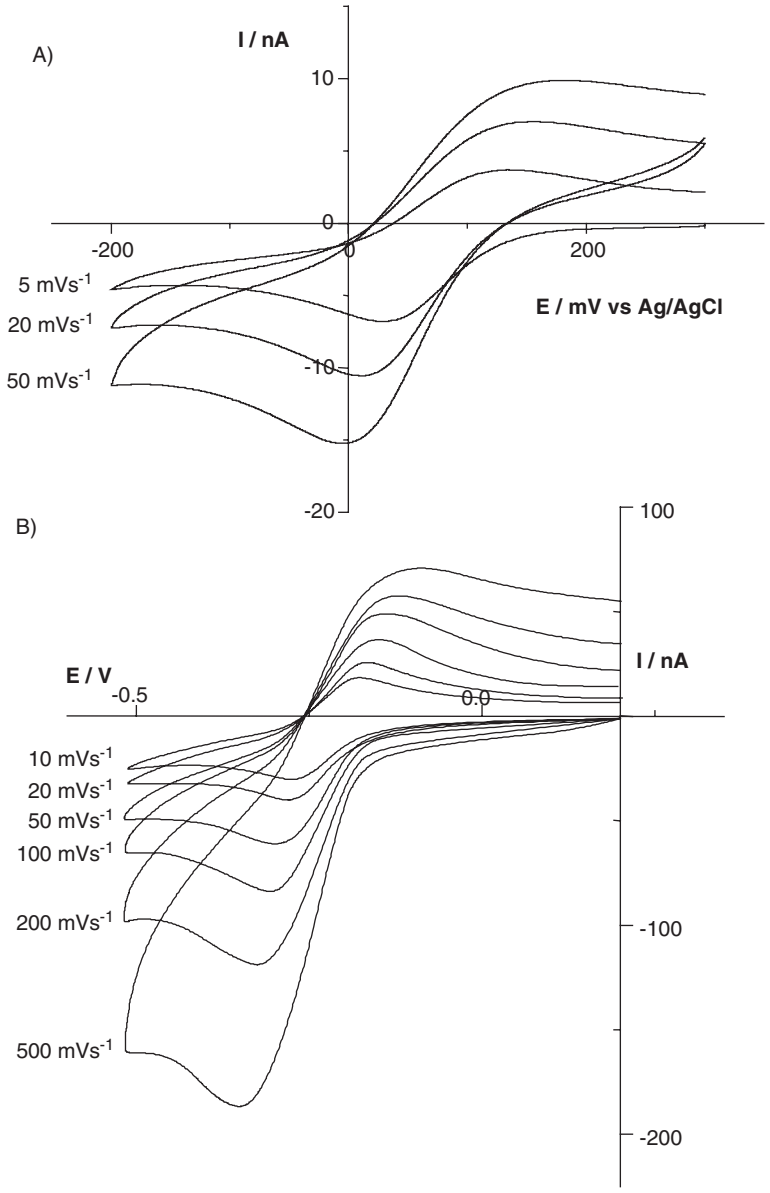


**Figure 16.2.11** CVs recorded at Au-NEEs in: (A) $5 \times 10^{-6}$ M cytochrome *c* and (B) $5 \times 10^{-6}$ M azure B; scan rates as indicated in the figure; supporting electrolyte in both cases: $10^{-2}$ M phosphate buffer at pH = 7.4; nominal diameter of the Au nanodisks = 30 nm; disks' density = $6 \times 10^{8}$ disks $cm^{-2}$. Reprinted with permission from reference (83) for (A) and reference (69) for (B).

and nanotubes, to more complex structures such as nanotubes of nanoparticles, nanotubes in nanotubes, or segmented nanowires.

The description presented here focused mainly on metal-based nanomaterials. However, the same principles can find application and extension to the preparation of nanostructures made of organic polymers, oxides, and salts.

It is reasonable to think that such a membrane-based approach to the synthesis of nanomaterials will find wider application due to the fact that it allows easy fabrication and rapid screening of the properties of new and unusual nanomaterials.

Template synthesis has made accessible to almost any electrochemical laboratory the fabrication of electrode systems with critical dimensions in the nanometer domain. Future research efforts will likely be devoted to fundamental studies aimed at better understanding the effects related to decreasing the size of electrodes to dimensions comparable or smaller than the dimensions of the double- and diffusion layers. From a practical and application perspective, the next frontier will focus on the development of methods and materials that allow one to better control the size, spatial distribution, and addressability of the single nanoelectrode elements in rather complex arrays or ensembles.

## REFERENCES

1. G. E. Possin, *Rev. Sci. Instrum.* **41**, 772 (1970).
2. W. D. Williams, N. Giordano, *Rev. Sci. Instrum.* **55**, 410 (1984).
3. R. M. Penner, C. R. Martin, *Anal. Chem.* **59**, 2625 (1987).
4. J. F. Cheng, C. R. Martin, *Anal. Chem.* **60**, 2163 (1988).
5. V. P. Menon, C. R. Martin, *Anal. Chem.* **67**, 1920 (1995).
6. K. Uosaki, K. Okazaki, H. Kita, H. Takahashi, *Anal. Chem.* **62**, 652 (1990).
7. C. R. Martin, D. T. Mitchell, in *Electroanalytical Chemistry, A Series of Advances*, A. J. Bard, I. Rubinstein, Eds., Marcel Dekker: New York, 1999, Vol. 21, p. 1.
8. T. Thurn-Albrecht, J. Schotter, G. A. Kästle, N. Emley, T. Shibauchi, L. Krusin-Elbaum, K. Guarini, C. T. Black, M. T. Tuominen, T. P. Russel, *Science* **290**, 2126 (2000).
9. E. Jeoung, T. H. Galow, J. Schotter, M. Bal, A. Ursache, M. T. Tuominen, C. M. Stafford, T. P. Russel, V. M. Rotello, *Langmuir* **17**, 6396 (2001).
10. B. B. Lakshmi, C. J. Patrissi, C. R. Martin, *Chem. Mater.* **9**, 2544 (1997).
11. C. J. Patrissi, C. R. Martin, *J. Electrochem. Soc.* **146**, 3176 (1999).
12. N. Li, C. R. Martin, B. Scrosati, *J. Power Sources* **97–98**, 240 (2001).
13. G. Che, K. B. Jirage, E. R. Fisher, C. R. Martin, H. Yoneyama, *J. Electrochem. Soc.* **144**, 4296 (1997).
14. J. W. Diggle, T. C. Downie, C. W. Goulding, *Chem. Rev.* **69**, 365 (1969).
15. A. Despic, V. P. Parkhutik, in *Modern Aspects of Electrochemistry*, J. O. Bockris, R. E. White, B. E. Conway, Eds., Plenum Press: New York, 1989, Vol. 20, p. 401.
16. A. T. Shawaqfeh, R. E. Baltus, *J. Membr. Sci.* **157**, 147 (1999).
17. G. L. Hornyak, C. J. Patrissi, C. R. Martin, *J. Phys. Chem. B* **101**, 1548 (1997).
18. P. Bocchetta, C. Sunseri, A. Bottino, G. Capannelli, G. Chiavarotti, S. Piazza, F. D. Quarto, *J. Appl. Electrochem.* **32**, 977 (2002).
19. Y. Piao, H. Lim, J. Y. Chang, W.-Y. Lee, H. Kim, *Electrochim. Acta* **50**, 2997 (2005).
20. M. Tian, S. Xu, J. Wang, N. Kumar, E. Wertz, Q. Li, P. M. Campbell, M. H. W. Chan, T. E. Mallouk, *Nano Lett*. **5**, 697 (2005).

21. G. Patermarakis, *J. Electroanal. Chem.* **404**, 69 (1996).
22. R. C. Furneaux, W. R. Rigby, A. P. Davidsons, *Porous Films and Methods Forming Them*, USA, Patent number 4,687,551 (1987).
23. J. C. A. Foss, G. L. Hornyak, J. A. Stockert, C. R. Martin, *J. Phys. Chem.* **98**, 2963 (1994).
24. Z. Zhang, D. Gekhtman, M. S. Dresselhaus, J. Y. Ying, *Chem. Mater.* **11**, 1659 (1999).
25. C. A. Foss, Jr., in *Metal Nanoparticles, Synthesis, Characterization and Applications*, D. L. Feldheim, J. C. A. Foss, Eds., Marcel Dekker: New York, 2002, p. 119.
26. T. Parpaleis, J. M. Laval, M. Majda, C. Bourdillon, *Anal. Chem.* **64**, 641 (1992).
27. A. Mozalev, S. Magaino, H. Imai, *Electrochim. Acta* **46**, 2825 (2001).
28. C. C. Harrell, S. B. Lee, C. R. Martin, *Anal. Chem.* **75**, 6861 (2003).
29. P. Apel, *Radiat. Meas.* **34**, 559 (2001).
30. P. Y. Apel, Y. E. Korchev, Z. Siwy, R. Spohr, M. Yoshida, *Nucl. Instrum. Methods Phys. Res. B* **184**, 337 (2001).
31. C. Trautman, W. Bruchle, R. Spohr, J. Vetter, N. Angert, *Nucl. Instrum. Methods Phys. Res. Sect. B* **111**, 70 (1996).
32. L. Klintberg, M. Lindberg, G. Thornell, *Nucl. Instrum. Methods Phys. Res. Sect. B* **184**, 536 (2001).
33. R. L. Fleisher, P. B. Price, R. M. Walker, *Nuclear Tracks in Solids: Principle and Applications*, University of California Press: Berkley, CA, 1975.
34. Z. Siwy, P. Apel, D. Baur, D. D. Dobrev, Y. E. Korchev, R. Neumann, R. Spohr, C. Trautmann, K.-O. Voss, *Surf. Sci.* **532**, 1061 (2003).
35. R. Spohr, *Methods and Device to Generate a Predetermined Number of Ion Tracks*, Germany, Patent number DE 2951376C2 (1983).
36. E. Ferain, R. Legras, *Nucl. Instrum. Methods B* **174**, 116–122 (2001).
37. N. Li, S. Yu, C. C. Harrell, C. R. Martin, *Anal. Chem.* **76**, 2025 (2004).
38. C. P. Bean, W. De Sorbo, US Patent 3,770,532-19731 106 (9 February 1968).
39. Z. Siwy, D. Dobrev, R. Neumann, C. Trautmann, K. Voss, German and US patent, registration on 26.02.2002, no. 102 08 023.2, Verfahren zur Herstellung von Nanostrukturen in Membranen und Asymmetrische Membran, *Appl. Phys. A* **76**, 781 (2003).
40. P. Scopece, L. A. Baker, P. Ugo, C. R. Martin, *Nanotechnology* **17**, 3951 (2006).
41. V. A. Oleinikof, Y. V. Tolmachyova, V. V. Berezkin, A. I. Vilensky, B. V. Mchedlishvili, *Radiat. Meas.* **25**, 713 (1995).
42. C. R. Martin, *Science* **266**, 1961 (1994).
43. L. D.-D. Pra, E. Ferain, R. Legras, S. Demoustier-Champagne, *Nucl. Instrum. Methods Phys. Res. B* **196**, 81 (2002).
44. P. Ugo, L. M. Moretto, G. A. Mazzocchin, P. Guerriero, C. R. Martin, *Electroanalysis* **10**, 1168 (1998).
45. M. Tian, J. Wang, J. Kurtz, T. E. Mallouk, M. H. W. Chan, *Nano Lett.* **3**, 919 (2003).
46. W. Kautek, S. Reetz, S. Pentzien, *Electrochim. Acta* **40**, 1461 (1995).
47. C. Schönenberger, B. M. I. v. d. Zande, L. G. J. Fokkink, M. Henny, C. Schmid, M. Krüger, A. Bachtold, R. Huber, H. Birk, U. Staufer, *J. Phys. Chem. B* **101**, 5497 (1997).
48. M. L. Tian, J. Wang, J. Snyder, J. Kurtz, Y. Liu, P. Schiffer, T. E. Mallouk, M. H. W. Chan, *Appl. Phys. Lett*. **83**, 1620 (2003).
49. J. Wang, M. Tian, T. E. Mallouk, M. H. W. Chan, *J. Phys. Chem. B* **108**, 841 (2004).
50. J. G. Wang, M. L. Tian, T. E. Mallouk, M. H. W. Chan, *Nano Lett*. **4**, 1313 (2004).
51. L. Wang, K. Yu-Zhang, A. Metrot, P. Bonhomme, M. Troyon, K. Ounadjela, A. Fert, *Thin Solid Films* **288**, 86 (1996).
52. L. Piraux, J. M. George, J. F. Despres, C. Leroy, E. Ferain, R. Legras, *Appl. Phys. Lett.* **65**, 2484 (1994).

53. C. J. Brumlik, C. R. Martin, K. Tokuda, *Anal. Chem.* **64**, 1201 (1992).
54. B. M. I. v. d. Zande, M. R. Böhmer, L. G. J. Fokkink, C. Schönenbergher, *Langmuir* **16**, 451 (2000).
55. X. Y. Zhang, L. D. Zhang, Y. Lei, L. X. Zhao, Y. Q. Mao, *J. Mater. Chem.* **11**, 1732 (2001).
56. L. Piraux, S. Dubois, S. D. Champagne, *Nucl. Instrum. Methods Phys. Res. B* **131**, 357 (1997).
57. H. Chiriac, A. E. Moga, M. Urse, T.-A. Óvári, *Sens. Actuators A* **106**, 348 (2003).
58. J. Verbeeck, O. I. Lebedev, G. Van Tendeloo, L. Cagnon, C. Bougerol, G. Tourillon, *J. Electrochem. Soc.* **150**, E468 (2003).
59. G. Tourillon, L. Pontonnier, J. P. Levy, V. Langlais, *Electrochem. Solid State Lett.* **3**, 20 (2000).
60. T. M. Whitney, J. S. Jiang, P. C. Searson, C. L. Chien, *Science* **261**, 1316 (1993).
61. Y. Konishi, M. Motoyama, H. Matsushima, Y. Fukunata, R. Ishii, Y. Ito, *J. Electroanal. Chem.* **559**, 149 (2003).
62. K. R. Pirota, D. Navas, M. Hernández-Vélez, K. Nielsch, M. Vásquez, *J. Alloys Compd.* **369**, 18 (2004).
63. M. Platt, R. A. W. Dryfe, E. P. L. Roberts, *Electrochim. Acta* **49**, 3937 (2004).
64. M. Platt, R. A. W. Dryfe, E. P. L. Roberts, *Electrochim. Acta* **48**, 3037 (2003).
65. M. Zheng, G. Li, X. Zhang, S. Huang, Y. Lei, L. Zhang, *Chem. Mater.* **13**, 3859 (2001).
66. S. A. Sapp, B. Lakshmi, C. R. Martin, *Adv. Mater.* **11**, 402 (1999).
67. A. L. Prieto, M. S. Sander, M. S. M. González, R. Gronsky, T. Sands, A. M. Stacy, *J. Am. Chem. Soc.* **123**, 7160 (2001).
68. M. Paunovic, M. Schlesinger, *Fundamentals of Electrochemical Deposition*, Electrochemical Society Series, Wiley-Interscience: New York, 1998.
69. B. Brunetti, P. Ugo, L. M. Moretto, C. R. Martin, *J. Electroanal. Chem.* **491**, 166 (2000).
70. M. Wirtz, C. R. Martin, *Adv. Mater.* **15**, 455 (2003).
71. K. B. Jirage, J. C. Hulteen, C. R. Martin, *Science* **278**, 655 (1997).
72. J. C. Hulteen, K. B. Jirage, C. R. Martin, *J. Am. Chem. Soc.* **120**, 6603 (1998).
73. K. B. Jirage, J. C. Hulteen, C. R. Martin, *Anal. Chem.* **71**, 4913 (1999).
74. S. Demoustier-Champagne, M. Delvaux, *Mater. Sci. Eng. C* **15**, 269 (2001).
75. B. Bercu, I. Enculescu, R. Spohr, *Nucl. Instrum. Methods B* **225**, 497 (2004).
76. R. A. W. Dryfe, A. O. Simm, B. Kralj, *J. Am. Chem. Soc.* **125**, 13014 (2003).
77. Y.-L. Tai, H. Teng, *Chem. Mater.* **16**, 338 (2004).
78. X. Y. Yuan, G. S. Wu, T. Xie, Y. Geng, Y. Lin, G. W. Meng, L. D. Zhang, *Solid State Sci.* **6**, 735 (2004).
79. P. Göring, E.Pippel, H. Hofmeister, R. B. Wehrspohn, M. Steinhart, U. Gösele, *Nano Lett*. **4**, 1121 (2004).
80. M. Lahav, T. Sehayek, A. Vaskevich, I. Rubinstein, *Angew. Chem. Int. Ed.* **42**, 5576 (2003)
81. C. A. Goss, D. H. Charych, M. Majda, *Anal. Chem*. **63**, 85 (1991).
82. S. Yu, N. Li, J. Wharton, C. R. Martin, *Nano Lett*. **3**, 815 (2003).
83. P. Ugo, N. Pepe, L. M. Moretto, M. Battagliarin, *J. Electroanal. Chem.* **560**, 51 (2003).
84. M. L. Sandrock, C. D. Pibel, F. M. Geiger, C. A. Foss, Jr., *J. Phys. Chem. B* **103**, 2668 (1999).
85. N. A. F. Al-Rawashdeh, M. L. Sandrock, C. J. Seugling, C. A. Foss, Jr., *J. Phys. Chem. B* **102**, 361 (1998).
86. (a) P. Ugo, L. M. Moretto, F. Vezzà, *Chemphyschem* **3**, 917 (2002). (b) P. Ugo, L. M. Moretto, F. Vezzà, in *Sensors Update*, H. Baltes, G. K. Fedder, J. G. Korvink, Eds., Wiley-VCH: Weinheim, 2003, Vol. 12, p. 121.
87. P. Ugo, in *Encyclopedia of Sensors*, C. A. Grimes, E. C. Dickey, M. V. Pishko, Eds., American Scientific Publishers: Stevenson Ranch, USA, 2006, Vol. 8, p. 67.
88. J. C. Hulteen, V. P. Menon, C. R. Martin, *J. Chem. Soc. Faraday Trans.* **92**, 4029 (1996).
89. I. F. Cheng, L. D. Whiteley, C. R. Martin, *Anal. Chem.* **61**, 762 (1989).

90. C. Amatore, in *Physical Electrochemistry*, I. Rubinstein, Ed., Marcel Dekker: New York, 1995, p. 131.
91. L. M. Moretto, N. Pepe, P. Ugo, *Talanta* **62**, 1055 (2004).
92. A. J. Bard, L. Faulkner, *Electrochemical Methods*, Wiley: New York, 2000.
93. R. Greef, R. Peat, L. M. Peter, D. Pletcher, J. Robinson, *Instrumental Methods in Electrochemistry*, Ellis Horwood Ltd.: Chichester, UK, 1985.
94. E. Sabatani, J. Rubinstein, *J. Phys. Chem. B* **91**, 6663 (1987).
95. C. Amatore, J. M. Saveant, D. Tessier, *J. Electroanal. Chem.* **147**, 39 (1983).
96. R. S. Nicholson, *Anal. Chem*. **37**, 1351 (1965).
97. P. Ugo, L. M. Moretto, S. Bellomi, V. P. Menon, C. R. Martin, *Anal. Chem.* **68**, 4160 (1996).
98. H. A. O. Hill, Y. Nakagawa, F. Marken, R. G. Comptom, *J. Phys. Chem*. **100**, 17395 (1996).
99. M. J. Eddowes, H. A. O. Hill, *J. Chem. Soc. Chem. Commun*. 771 (1977).
100. P. M. Allen, H. A. O. Hill, N. J. Walton, *J. Electroanal. Chem.* **178**, 69 (1984).
101. M. J. Eddowes, H. A. O. Hill, *J. Am. Chem. Soc*. **101**, 4461 (1979).
102. T. Sagara, H. Murakami, S. Igarashi, H. Sato, K. Niki, *Langmuir* **7**, 3190 (1991).
103. T. Sagara, K. Niwa, A. Sone, C. Innen, K. Niki, *Langmuir* **6**, 254 (1990).
104. R. Gasparac, B. J. Taft, M. A. Lapierre-Devlin, A. D. Lazareck, J. M. Xu, S. O. Kelly, *J. Am. Chem. Soc.* **126**, 12270 (2004).
105. K. Krishnamoorthy, C. G. Zoski, *Anal. Chem*. **77**, 5068 (2005).
106. E. Finot, E. Bourillot, R. Meunier-Prest, Y. Lacroute, G. Legay, M. Cherkaoui-Malki, N. Latruffe, O. Siri, P. Braunstein, A. Dereux, *Ultramicroscopy* **97**, 441 (2003).
107. J. Li, H. T. Ng, A. Cassell, W. Fan, H. Chen, Q. Ye, J. Koehne, J. Han, M. Meyyappan, *Nano Lett.* **3**, 597 (2003).

## 16.3 SINGLE PARTICLE DEPOSITION ON NANOMETER ELECTRODES

*Anthony Kucernak*

Department of Chemistry, Imperial College London, London SW7 2AZ, UK

### 16.3.1 Introduction

This section describes the electrochemical deposition of single particles onto electrodes of nanometer dimensions. Methods for producing sharp tips from a range of materials have been discussed in previous sections of this work and by Melmed (1), and more recently with specific reference to electrochemical systems (2–4). Arrigan has given a review of some of the applications to which such insulated electrodes have been put (5). This section will consider both the *deposition* of material on nanometer-sized electrodes and the uses of such composite systems. The use of these nanoelectrodes in studying biological systems and enzymes will not be covered. There are a number of methods which in principle allow the formation of a nanoelectrode-film/particle composite (Figure 16.3.1):

(a) direct physical contact of electrode to particle;
(b) electrochemical deposition of particle or film;
(c) electrophoretic deposition of particles.

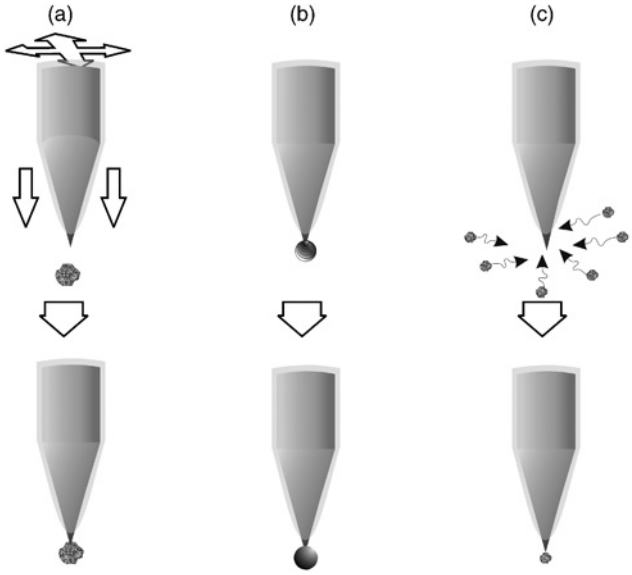


**Figure 16.3.1** Three different approaches which can be used to create a nanoelectrode/single particle composite electrode: (a) "spearing" of a particle; (b) single particle nucleation and growth; (c) electrophoretic deposition.

All of these approaches have been applied to electrodes with dimensions on the micron scale. For instance, physical contact between microelectrodes and individual particles of materials has been used to study materials used in lithium-based (6, 7) and nickel-based batteries (8–10); microelectrodes have been extensively used to study single nucleation and growth on a range of substrates (11–13); and electroactive particles have been electrophoretically deposited onto microelectrodes (14, 15). Increasingly, such approaches are also being used to make composite electrodes utilizing substrates with radii $<1$ μm.

### 16.3.2 Electrode selection

The choice of electrode material, its morphology, and the method of insulation depends critically on the desired use of the electrode system, and is somewhat limited in choice due to the small number of systems which have been studied. Currently available nanometer-sized electrodes are either conical in shape and composed of Pt (2, 3, 16, 17), Ag (18), W (19), or carbon (20, 21) or disk-like and composed of Pt, Ag (22, 23), or Au (24) or even liquid—that is, the junction formed at the interface between two immiscible electrolytes (25).

In order to reduce the magnitude of background currents, it is important to insulate all of the electrodes apart from the working tip. Electrode insulation may be glass—formed by translating the tip at 0.1 mm $s^{-1}$ through a molten glass bead held in a Pt heating

coil (2, 3) or by heating and pulling a glass capillary using a laser-based micropipettete puller so that both the electrode material and the glass sheath are greatly reduced in diameter (22, 23). It may be a polyimide—produced by heating the electrode body while the electrode is immersed in dimethyl acetamide containing 1,2,4,5-benzenetetracarboxylic anhydride and 4,4′-diaminodiphenyl (26); or it may be a ptfe-like substance—produced by either dipping in a ptfe-like precursor (Cytop, Asahi Glass Co. Ltd.) (27–31) or photopolymerization of a ptfe-like precursor material (32). Commonly because of the ease of insulation, it is an electrophoretic paint (16, 17, 20, 21, 33).

Direct physical contact with a particle is made difficult in the nanoscopic regime because of the difficulty in imaging the particle system. For electrodes and particles in the micron-size domain, it is possible to use optical microscopes to see the particles and, using micromanipulators, move the electrode so that it is in contact with the particle (8–10, 34, 35). Using optical microscopy to guide the making of contact between particles and electrodes with radii $<1$ μm may be difficult unless the particle is $>1$ μm in size, although having a conical-shaped electrode may be beneficial to allow 'spearing' of the particle (19). Conically shaped and suitably insulated electrodes of suitable materials are increasingly being used as probes in AFM, STM, and SECM. Utilizing these techniques, a suitable particle can be imaged and then the tip can be used to make contact with that particle in order to perform electrical experiments on it.

Deposition of particles through electrochemical deposition requires a suitable substrate and electrochemical system which shows a suitable nucleation density. Although many studies of single-particle nucleation and growth have been undertaken on microelectrodes, many of those studies have been on systems which are not of major commercial relevance, presumably because the nucleation density of commercially relevant electrochemical systems (e.g., Au on Ni) is too high to afford single nucleation and growth, even on microelectrodes. The use of nanoelectrodes of suitable materials will allow a significant growth of understanding of nucleation and growth of a diverse number of systems. A special case of single nucleation and growth is the production of potentiometric electrodes in which the electrode material is typically one which can be easily anodized to produce the requisite electrochemical couple—thus, an Ag electrode can be anodized in 0.1 M KCl (18) or 0.01 M KI + 0.1 M $KNO_3$ (22) to make Ag/AgCl or Ag/AgI nanoreference electrodes; a W electrode can be anodized in 2.0 M $H_2SO_4$ to produce a surface $WO_3$ layer in order to produce a pH-sensitive electrode (36).

In the following sections, the discussion focuses on electrochemical deposition of particles, as this is the most developed method for producing single particle on electrode composites.

### 16.3.3 Electrodeposition of particles: electrokinetic vs. diffusion control

Early work on single particle nucleation and growth involved the use of either Pt or carbon microelectrodes on which was deposited a material which had a suitably low nucleation density, for instance, Ag, Hg, or Cu (11–13). Later work expanded this to look at other systems such as $PbO_2$ on carbon (37), or $PbSO_4$ on Pb (34). Working with single particles allows analysis of the electrokinetics of deposition without the complication due to overlap of growing particles or their diffusion spheres.

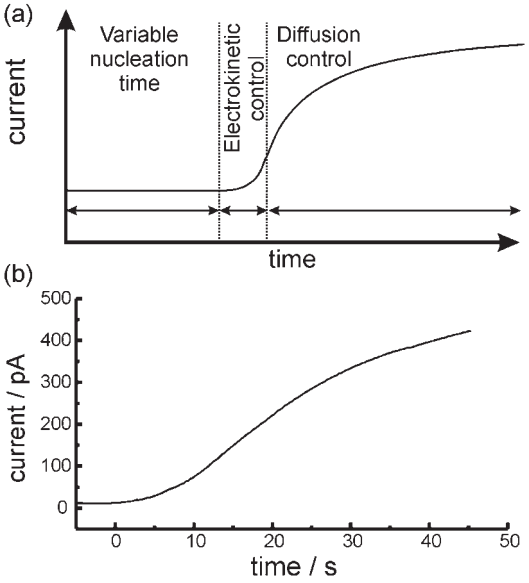


**Figure 16.3.2** Different stages of nucleation and growth of single electrodeposited particles: (a) cartoon showing the different phases of particle growth and (b) current–time transient for the electrodeposition of a single Pt nuclei on a carbon electrode of radius 5 nm from a solution composed of 0.1 M $H_2SO_4$ + 0.001 M $H_2PtCl_6$ at a potential of 0.27 V (vs. SCE).

The growth of a single particle during single nucleation and growth is commonly preceded by an induction period (Figure 16.3.2).

This induction period is described as being due to the required formation of a nucleus of critical size. The formation of new nuclei is a result of aggregation of small atom clusters due to surface diffusion along the electrode surface (38). The small clusters may also dissolve into the solution. A stable growing center can only be formed when a cluster contains enough atoms and exceeds a critical size. The size of that stable nucleus is around 1 nm diameter, corresponding to about 30–40 atoms (38). Once such a stable nucleus is formed, spontaneous growth can then easily proceed. Measurement of the stochastic nature of induction times during single nucleation/growth has already been performed on microelectrodes (12, 37), although such measurement on nm-sized electrodes is complicated by the difficulty in producing large number of electrodes with exactly the same geometry required for such studies.

After the induction period, growth of the particle may be measured by following the current transient. Typically, analyses of current transients during the single nucleation and growth of a particle have been performed either at low overpotentials so that growth is assumed under electrokinetic control (34)

$$i(t) = FHK^3 n V_M^2 t^2 \tag{16.3.1}$$

or at larger overpotentials where it is assumed that the growth is under diffusion control (39)

$$i(t) = \frac{1}{2} FHn(2DC^*)^{3/2} V_M^{1/2} t^{1/2} \tag{16.3.2}$$

where $H$ is a geometric factor related to the shape of the growing particle ($H = 4\pi$ for hemispherical particles); $K$ (mol cm$^{-2}$ s$^{-1}$) is the rate of the electrocrystallization process; $n$ is the number of electrons involved in the deposition process; $V_M$ is the molar volume of the material being deposited; and $D$ and $C^*$ are the diffusion coefficient and concentration of the precursor in the surrounding solution.

However, the situation is somewhat more complicated when considering deposition on nanometer-sized electrodes. Because of the small surface area of the substrate electrodes, the growth transients can be followed from a very early stage, as shown in Figure 16.3.2. The growing particles will act as microelectrodes in their own right, and for such microelectrodes, the mass transport coefficient for species $i$ is

$$m_i = \frac{D_i}{r} \tag{16.3.3}$$

where $r$ is the radius of the growing particle. Table 16.3.1 plots the mass transport coefficient and the equivalent rotation rates required to produce those same mass transport coefficients in a rotating disk experiment for a range of different particle sizes. It is clear that for particles with radii $\leq 1$ μm, the mass transport coefficients are larger than the kinetic rate constants which might be expected for metal reductions (for comparison, the hexacyanoferrate redox couple, $Fe(CN)_6^{3-/4-}$, has a kinetic rate constant of 0.14–0.18 cm s$^{-1}$ in KCl solution (27)). This suggests that for small particles, it is very difficult to have the particles grow under pure diffusion control, and that virtually all particles initially grow under electrokinetic control.

This is illustrated in Figure 16.3.2, where it can be seen that at short times, the current grows quadratically with time—only at longer times does the current start showing a $t^{1/2}$ dependence as would be expected for diffusion-controlled growth.

**Table 16.3.1**

Comparison of mass transport coefficient for particles of different sizes

| $r$ (nm) | $m$ (cm s$^{-1}$) | $w$ (rpm) |
|---|---|---|
| 1 | 100 | $2.48\times10^{11}$ |
| 10 | 10 | $2.48\times10^{9}$ |
| 100 | 1 | $2.48\times10^{7}$ |
| 1000 | 0.1 | $2.48\times10^{5}$ |
| 10,000 | 0.01 | 2480 |

*Note:* Also shown are the disk rotation rates required to produce the same mass transport coefficient in a rotating disk experiment. Calculations assume $D = 1.00 \times 10^{-5}$ cm$^2$ s$^{-1}$ and $v = 0.01$ cm$^2$ s$^{-1}$.

A more complete analysis of single particle and growth suggests that under combined electrokinetic and diffusion control, and taking into account the concentration overpotential due to depletion of reactant at the surface, the radius and current associated with the growth of a particle as a function of time should follow (40)

$$r(t) = \frac{\sqrt{A^2 + 8ABV_M t} - A}{2C} \tag{16.3.4}$$

$$i(t) = \frac{ABFHn\left(\sqrt{A^2 + 8ABV_M t} - A\right)^2}{2C^3\sqrt{A^2 + 8ABV_M t}}$$

$$A = c_\infty DFn$$

$$B = \frac{j_0^2}{Fn}\left(\exp\left(\frac{2\alpha nF\eta}{RT}\right) - \exp\left(\frac{(2\alpha - 1)nF\eta}{RT}\right)\right) \tag{16.3.5}$$

$$C = j_0 \exp\left(\frac{\alpha nF\eta}{RT}\right)$$

The latter equation predicts a crossover from approximate $t^2$ dependence to $t^{1/2}$ dependence, and can be used for extracting various parameters from the current transients. A current transient simulated using this equation is shown in Figure 16.3.3.

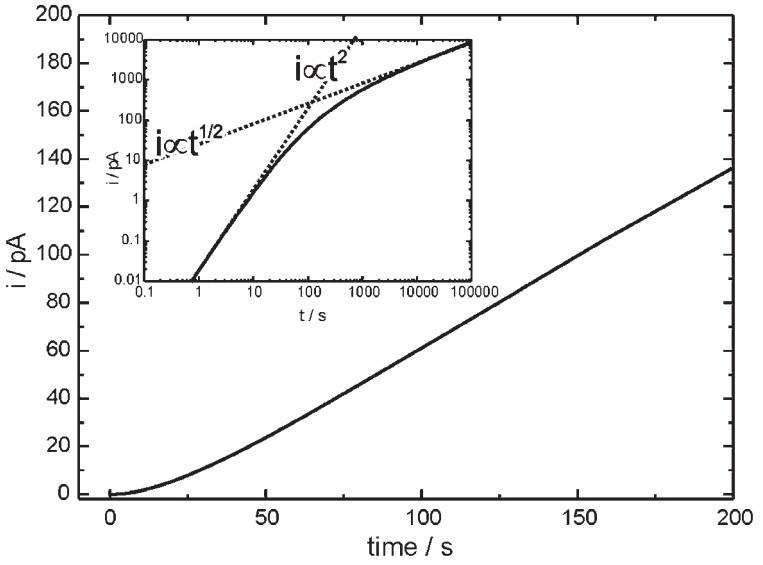


**Figure 16.3.3** Simulated current transient using equation (16.3.5) for the growth of single particle. Inset: double-log axis plot of the same transient showing limiting electrokinetic ($i \propto t^2$) and diffusion ($i \propto t^{1/2}$) control. $n = 1$; $DC^* = 5 \times 10^{-12}$ mol cm$^{-1}$ s$^{-1}$; $j_0 = 1 \times 10^{-5}$ A cm$^{-2}$; $T = 298$ K; $\eta = 0.2$ V.

### 16.3.4 Nucleation exclusion zones: modeling particle growth

Standard electrochemical theory has been applied to the growth of single particles on microelectrodes, for instance, looking at the stochastic nature of induction times during single nucleation/growth (12, 37). Some modification from standard electrochemical theory is typically required for these very small electrodes because of geometric effects, violation of electroneutrality (41), and even changes to the double-layer structure at interfaces with high curvature (20). For instance, when dealing with the cone-shaped electrodes mentioned above, standard approaches are based on disk or hemispherical electrodes. Mirkin *et al.* have performed some work on establishing what differences are expected from this change of geometry, although this work is predominantly targeted at SECM work (42).

The production of single nuclei is somewhat helped by the formation of 'nucleation exclusion zones' around the growing particles (43–45). In the area surrounding a growing particle, there will be a reduction in the concentration of precursor, and this will reduce the probability of nucleating a new particle. Milchev *et al.* have derived an equation for the stationary nucleation rate around a growing stable cluster (46, 47).

This approach then allows a useful set of conditions under which single particle nucleation and growth are favored (40). The distance from a growing particle within which the nucleation rate decreases by an amount $J_{\text{rel}}$ of the value on the unperturbed surface is

$$\rho(t) = \frac{\left(\sqrt{A^2 + 8ABV_{\text{M}}t} - A\right)^3}{16Dc_\infty V_{\text{M}} C^3 t(1 - J_{\text{rel}}^{1/1+n_k})} \tag{16.3.6}$$

where $A$, $B$, and $C$ are defined above, and $n_k$ is the number of atoms above which a nucleus becomes stable, and is expected to be about 30–40 atoms (38). We can put this in a dimensionless form by dividing by the radius of the electrode

$$\frac{\rho(t)}{r(t)} = \frac{\left(\sqrt{A^2 + 8ABV_{\text{M}}t} - A\right)^2}{8Dc_\infty V_{\text{M}} C^2 t(1 - J_{\text{rel}}^{1/1+n_k})} \tag{16.3.7}$$

Figure 16.3.4 shows a set of plots displaying the radius of a growing particle as a function of time and overpotential, and the corresponding size of the nucleation exclusion zone as a ratio to the actual size of the particle. When the growth of the particle is under electrokinetic control, the nucleation exclusion zone is always within a few radii of the growing particle. This means that under electrokinetic control, it is quite possible that other particles can nucleate and grow at other points on the electrode, unless the area of the electrode is very small. In contrast, when the particle is growing under diffusion control, the nucleation exclusion zone can extend some distance from the growing particle.

In the limit when $8BV_{\text{m}}t \gg A$ (i.e., long time, large $j_0$, and small $c_\infty D$), equation (16.3.7) simplifies to

$$\frac{\rho(t)}{r(t)} = \frac{1 - \exp(-nF\eta / RT)}{1 - J_{\text{rel}}^{1/1+n_k}} \tag{16.3.8}$$

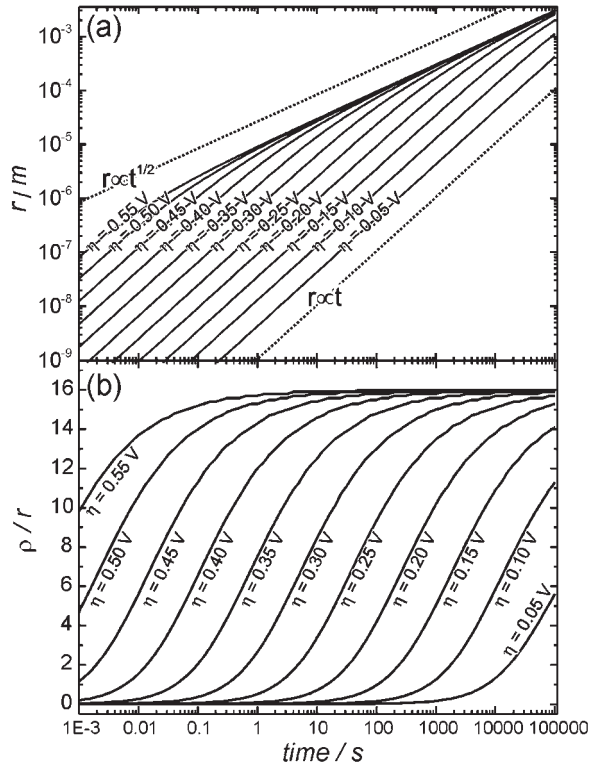


**Figure 16.3.4** Variation of the size of a growing particle as a function of applied overpotential and time calculated using equation (16.3.4) (a). Lines corresponding to the limiting cases of diffusion limiting growth ($r \propto t^{1/2}$) and electrokinetic growth ($r \propto t$) are also shown. (b) Variation of the size of the nucleation exclusion zone nucleation for the cases mentioned in (a) calculated using equation (16.3.7). The size of the nucleation exclusion zone is shown as a ratio to the radius of the particle. $n = 1$; $DC^* = 5 \times 10^{-12}$ mol cm$^{-1}$ s$^{-1}$; $j_0 = 1 \times 10^{-5}$A cm$^{-2}$; $T = 298$ K; $J_{rel} = 0.1$; $n_k = 35$.

For most applicable overpotentials, the numerator becomes 1 and the nucleation exclusion zone extends a distance $(1-J_{rel}^{1/1+n_k})^{-1}$ particle radii from the growing particle—that is, the size of the nucleation exclusion zone is sensitively dependent upon the size of the critical nucleus. For realistic values of $J_{rel}$ (0.1—corresponding to a reduction of nucleation probability by a factor of 10) and $n_k$ (35), this corresponds to a value of $\rho(t)/r(t)$ of 16—that is, the nucleation probability is reduced by at least a factor of 10 within a 16 radii distance from the growing particle when that particle is growing under diffusion control.

These results suggest important criteria for maximizing the likelihood for producing single particles—growth of particles should be on small electrodes (maybe no more than ~10× the radius of the intended particle), and at high overpotentials and low concentrations. Where these conditions cannot be met, the electrode size must be decreased so that it is similar in size to the particle which is being created.

### 16.3.5 Examples of systems

Guo *et al.* have examined the growth of silver particles at the water/dichloroethane interface formed at the end of a ~0.5 μm radius pipette, and interpreted the current transients in terms of diffusion-limited growth of multiple non-interacting particles (25). Chen and Kucernak have followed the single nucleation and growth of Pt particles on carbon electrodes with radii from several hundred nm down to <5 nm. Single nucleation and growth under conditions of high overpotential are seen with electrodes up to a few hundred nm in radii, whereas under less extreme conditions, where electrokinetic control would be expected, single nucleation and growth are only reproducibly seen when the electrode radius <5 nm (40). The resulting Pt/carbon composite electrodes have been used to study the hydrogen oxidation reaction (48) and the oxygen reduction reaction (49).

Electrodeposition of silver particles on single wall nanotubes (SWNT) has been used as an aid to visualization of the SWNTs, although the deposition transients have not been analyzed (50, 51).

Finally, one interesting approach to depositing small nm-sized clusters on suitable substrates has been developed in which the first step is the deposition of metal onto an SECM tip prior to transfer to a surface. The approach utilizes the local creation of a concentration cell during the local dissolution of metal from the tip to nucleate and grow a particle on the adjacent surface. The approach has been utilized for the growth of Ag on C (52), Co growth on Au, and Pb on Si (53, 54).

## REFERENCES


1. A. J. Melmed, *J. Vac. Sci. Technol. B* **9**, 601 (1991).
2. R. M. Penner, M. J. Heben, N. S. Lewis, *Anal. Chem.* **61**, 1630 (1989).
3. R. M. Penner, M. J. Heben, T. L. Longin, N. S. Lewis, *Science* **250**, 1118 (1990).
4. C. J. Slevin, N. J. Gray, J. V. Macpherson, M. A. Webb, P. R. Unwin, *Electrochem. Commun.* **1**, 282 (1999).
5. D. W. M. Arrigan, *Analyst* **129**, 1157 (2004).
6. M. Nishizawa, H. Koshika, I. Uchida, *J. Phys. Chem. B* **103**, 192 (1999).
7. M. Nishizawa, H. Koshika, R. Hashitani, T. Itoh, T. Abe, I. Uchida, *J. Phys. Chem. B* **103**, 4933 (1999).
8. H. S. Kim, T. Itoh, M. Nishizawa, M. Mohamedi, M. Umeda, I. Uchida, *Int. J. Hydrogen Energy* **27**, 295 (2002).
9. A. Palencsar, D. A. Scherson, *Electrochem. Solid State Lett.* **6**, E1 (2003).
10. A. Palencsar, D. A. Scherson, *Electrochem. Solid State Lett.* **8**, A328 (2005).
11. G. Hills, A. K. Pour, B. Scharifker, *Electrochim. Acta* **28**, 891–898 (1983).
12. B. Scharifker, G. Hills, *J. Electroanal. Chem.* **130**, 81 (1981).
13. G. Gunawardena, G. Hills, B. Scharifker, *J. Electroanal. Chem.* **130**, 99 (1981).
14. D. J. Caruana, A. Heller, *J. Am. Chem. Soc.* **121**, 769 (1999).
15. T. de Lumley-Woodyear, D. J. Caruana, C. N. Campbell, A. Heller, *Anal. Chem.* **71**, 394 (1999).
16. J. L. Conyers, H. S. White, *Anal. Chem.* **72**, 4441 (2000).
17. J. J. Watkins, J. Y. Chen, H. S. White, H. D. Abruna, E. Maisonhaute, C. Amatore, *Anal. Chem.* **75**, 3962 (2003).
18. N. J. Gray, P. R. Unwin, *Analyst* **125**, 889 (2000).

19. Q. F. Shi, L. J. Rendek, W. B. Cai, D. A. Scherson, *Electrochem. Solid State Lett.* **6**, E35 (2003).
20. S. Chen, A. Kucernak, *J. Phys. Chem. B* **106**, 9396 (2002).
21. S. L. Chen, A. Kucernak, *Electrochem. Commun.* **4**, 80 (2002).
22. Y. H. Shao, M. V. Mirkin, G. Fish, S. Kokotov, D. Palanker, A. Lewis, *Anal. Chem.* **69**, 1627 (1997).
23. B. B. Katemann, T. Schuhmann, *Electroanalysis* **14**, 22 (2002).
24. D. H. Woo, H. Kang, S. M. Park, *Anal. Chem.* **75**, 6732 (2003).
25. J. D. Guo, T. Tokimoto, R. Othman, P. R. Unwin, *Electrochem. Commun.* **5**, 1005 (2003).
26. P. Sun, Z. Q. Zhang, J. D. Guo, Y. H. Shao, *Anal. Chem.* **73**, 5346 (2001).
27. K. Dokko, M. Umeda, T. Itoh, I. Uchida, *Electrochem. Commun.* **2**, 717 (2000).
28. K. Dokko, S. Horikoshi, T. Itoh, M. Nishizawa, M. Mohamedi, I. Uchida, *J. Power Sources* **90**, 109 (2000).
29. K. Dokko, M. Nishizawa, S. Horikoshi, T. Itoh, M. Mohamedi, I. Uchida, *Electrochem. Solid State Lett.* **3**, 125 (2000).
30. K. Dokko, M. Mohamedi, Y. Fujita, T. Itoh, M. Nishizawa, M. Umeda, I. Uchida, *J. Electrochem. Soc.* **148**, A422 (2001).
31. K. Dokko, Q. F. Shi, I. C. Stefan, D. A. Scherson, *J. Phys. Chem. B* **107**, 12549 (2003).
32. B. Liu, J. P. Rolland, J. M. DeSimone, A. J. Bard, *Anal. Chem.* **77**, 3013 (2005).
33. J. Abbou, C. Demaille, M. Druet, J. Moiroux, *Anal. Chem.* **74**, 6355 (2002).
34. L. J. Li, M. Fleischmann, L. M. Peter, *Electrochim. Acta* **34**, 459 (1989).
35. M. Mohamedi, T. Sato, T. Itoh, M. Umeda, I. Uchida, *J. Electrochem. Soc.* **149**, A983 (2002).
36. K. Yamamoto, G. Y. Shi, T. S. Zhou, F. Xu, M. Zhu, M. Liu, T. Kato, J. Y. Jin, L. T. Jin, *Anal. Chim. Acta* **480**, 109 (2003).
37. M. Fleischmann, L. J. Li, L. M. Peter, *Electrochim. Acta* **34**, 475 (1989).
38. F. Gloaguen, J. M. Leger, C. Lamy, A. Marmann, U. Stimming, R. Vogel, *Electrochim. Acta* **44,** 1805 (1999).
39. G. J. Hills, D. J. Schiffrin, J. Thompson, *Electrochim. Acta* **19**, 657 (1974).
40. S. Chen, A. Kucernak, *J. Phys. Chem. B* **107**, 8392 (2003).
41. C. P. Smith, H. S. White, *Anal. Chem.* **65**, 3343 (1993).
42. M. V. Mirkin, F. R. F. Fan, A. J. Bard, *J. Electroanal. Chem.* **328**, 47 (1992).
43. B. R. Scharifker, J. Mostany, A. Serruya, *Electrochim. Acta* **37**, 2503 (1992).
44. I. Markov, A. Boynov, S. Toschev, *Electrochim. Acta* **18**, 377 (1973).
45. A. Milchev, E. Vassileva, V. Kertov, *J. Electroanal. Chem.* **107**, 323 (1980).
46. W. S. Kruijt, M. Sluytersrehbach, J. H. Sluyters, A. Milchev, *J. Electroanal. Chem.* **371**, 13 (1994).
47. A. Milchev, W. S. Kruijt, M. Sluytersrehbach, J. H. Sluyters, *J. Electroanal. Chem.* **362**, 21 (1993).
48. S. L. Chen, A. Kucernak, *J. Phys. Chem. B* **108**, 13984 (2004).
49. S. L. Chen, A. Kucernak, *J. Phys. Chem. B* **108**, 3262 (2004).
50. D. P. Burt, N. R. Wilson, J. M. R. Weaver, P. S. Dobson, J. V. Macpherson, *Nano Lett.* **5**, 639 (2005).
51. B. M. Quinn, C. Dekker, S. G. Lemay, *J. Am. Chem. Soc.* **127**, 6146 (2005).
52. W. Li, G. S. Hsiao, D. Harris, R. M. Nyffenegger, J. A. Virtanen, R. M. Penner, *J. Phys. Chem.* **100**, 20103 (1996).
53. W. Schindler, D. Hofmann, J. Kirschner, *J. Electrochem. Soc.* **148**, C124 (2001).
54. W. Schindler, P. Hugelmann, A. Hugelmann, F. Kartner, *J. Electroanal. Chem.* **522**, 49 (2002).

# – 17 –

# Electrochemistry in Small Places and at Novel Interfaces

## 17.1 ELECTROCHEMISTRY IN AND AT SINGLE BIOLOGICAL CELLS

*Nathan J. Wittenberg and Andrew G. Ewing*

Pennsylvania State University, Department of Chemistry,
University Park, PA 16802

### 17.1.1 Electrochemistry at the cell membrane–solution interface

In nature, secretory cells are thought to release chemical messengers to the extracellular space through a process called exocytosis. Many different electrochemically detectable substances are released from a variety of cell types by this process. Chemical release by exocytosis is a complex process that involves the fusion of a membrane bound vesicle filled with a chemical messenger with the plasma membrane (Figure 17.1.1A).

The initiation of this process is triggered by a cascade of biochemical processes, which are being studied extensively by numerous research groups (1–4). Depolarization of the plasma membrane and a rise in intracellular calcium levels are hallmarks of the initiation of the exocytotic process.

Electrochemical detection of exocytosis from single, isolated cells is typically carried out in amperometric or voltammetric mode (see Chapter 11). This is accomplished by placing a carbon fiber microelectrode (UME, see Chapter 6) at the surface of a cell by micromanipulation and holding it at a constant potential for amperometric experiments, or rapidly sweeping the potential for voltammetric experiments. Amperometric experiments require the electrode be held at high enough potentials to oxidize released molecules in a diffusion-limited fashion. In the amperometric mode, the resulting current vs. time trace exhibits a characteristic current transient corresponding to the release and subsequent oxidation of the contents of a single vesicle (Figure 17.1.1B). By integrating the current transient it is possible via Faraday's Law to determine the number of neurotransmitter molecules released in each event ($N = Q/nF$ where $N$ is the number of moles detected, $Q$ is


**Handbook of Electrochemistry**
**Edited by C.G. Zoski**

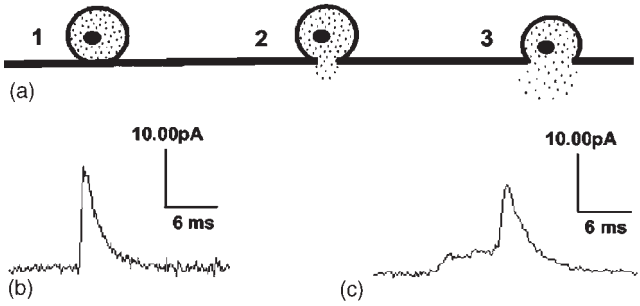


**Figure 17.1.1** (A) A schematic representation of a neurotransmitter filled vesicle fusing with the plasma membrane and releasing its contents to the extracellular space. (B) An amperometric spike recorded from a PC12 cell undergoing exocytosis. (C) An amperometric spike displaying a "foot" corresponding to leakage of neurotransmitter through the fusion pore. Reproduced with permission from reference (36).

the charge integrated under the current transient, $n$ is the number of electrons transferred in the oxidation reaction, and $F$ is the Faraday constant). Using background subtracted fast scan cyclic voltammetry it is possible to determine the neurotransmitter identity and concentration at the electrode surface as a function of time (5, 6). Exocytosis and its electrochemical detection has been thoroughly reviewed (7–10).

In addition to exocytosis of neurotransmitters, other chemical processes can be monitored electrochemically, including insulin release from pancreatic cells (11–14), monitoring of cellular respiration (15, 16), drug efflux from cells (17), and determination of cholesterol content in the plasma membrane of a single cell (18), among others. Recently scanning electrochemical microscopy (SECM, see Chapter 12) (19, 20) has been employed to probe cellular activity with respect to electroactive molecules at the plasma membrane–solution interface (21–24). In the following sections we review significant advances in electrochemical monitoring of exocytosis and other processes at the cell membrane/solution interface.

#### *17.1.1.1 Detection of biogenic amine release*

A number of chemical messengers released by neurons, neuroendocrine, and immune response cells are electrochemically active. These include dopamine, epinephrine, norepinephrine, and serotonin, all of which can be oxidized at moderate potentials. Development of electrochemical methods for detection of neurotransmitters began with the work of Adams (25) and has progressed to the point where it is now possible to detect the release of neurotransmitters from a single vesicle, as demonstrated by Wightman and coworkers (26, 27). In those experiments a carbon fiber UME 5 μm in diameter was placed adjacent to a bovine adrenal chromaffin cell isolated in a culture dish and the cell was stimulated to release neurotransmitters either by chemical or mechanical means. Individual current transients corresponding to the release of roughly 5 attomoles of catecholamine were resolved on the millisecond timescale. The results from those experiments were highly significant because they were the first demonstration that current transients recorded from stimulated cells correspond to the release of the oxidizable content from a single vesicle.

The bovine adrenal chromaffin cells used by Wightman et al. typically release roughly 5 attomoles of detectable epinephrine and norepinephrine. Efforts have been made to detect smaller numbers of molecules released via exocytosis to the point where it has been reported that the release of 4700 and 6000 molecules can be detected per event from release of a small portion of transmitter in a vesicle (28, 29).

The first demonstration of zeptomole detection was shown by Chen et al. (30) for amperometric detection of dopamine during exocytosis at PC12 cells. The average single PC12 vesicle from this study contained 190 zeptomole of catecholamine. Using previous electron microscopy data (31) that estimated the average vesicular radius to be 74 nm, the concentration of catecholamine in a single vesicle was estimated to be 0.11 M. Chen *et al*. reported a limit of detection of 31 zeptomole with the amperometric technique, which is within the range needed to detect exocytosis at mammalian neurons. Mammalian neurons contain between 1.8 and 96.4 zeptomole of catecholamine in a synaptic vesicle (32).

Among the smallest amounts of detected release reported was from the Retzius cell of the leech *Hirudo medicinalis* which synthesizes, stores, and releases serotonin. Bruns and Jahn detected release from two populations of vesicles (large and small) from this cell type, with the current transients from the small population averaging 3.0 fC in area and 595 μsec wide, while the larger vesicles had an average area of 47.4 fC and width of 3.66 msec (28). Earlier reports by Chow *et al*. and Alvarez de Toledo *et al*. were among the first to describe electrochemical detection of discrete stages of exocytosis, specifically the release of chemical messenger through the fusion pore in the adrenal chromaffin and mast cells (33, 34). The fusion pore forms shortly after the vesicle fuses with the plasma membrane and soluble messenger is free to diffuse through the pore, resulting in a small current rise (termed a "foot") before the main current spike that results from completed exocytosis. A current spike exhibiting a foot is shown in Figure 17.1.1C. Chow *et al*. reported an average foot duration of 8.26 msec, an average foot area of 34 fC, and an average foot amplitude of 7.17 pA. Since the discovery of this prespike feature, many groups have tried to elucidate the physiological significance of neurotransmitter release through the fusion pore (35, 36). One prominent example is the electrochemical detection of rapid opening and closing of the fusion pore known as flicker (29). A rapid succession of transient dopamine release from ventral midbrain neurons was detected amperometrically giving rise to the idea that dopaminergic neurons regulate the amount of dopamine released by controlling the flicker rate as well and the number of flickers per event.

Both the Wightman and Ewing groups have exploited the minute dimensions of microelectrodes (UME, see Chapter 6) to explore zones of exocytotic release on chromaffin and differentiated PC12 cells. Zerby and Ewing used 5 μm diameter carbon fiber UME to probe local zones of dopamine exocytosis at PC12 cells that were induced to sprout varicose neurites via exposure to neuronal growth factor (NGF) (37). These experiments showed that quantal size from differentiated PC12 cell varicosities is not significantly different from undifferentiated PC12 cell quantal size, and exocytotic events were absent from the cell body of the NGF treated cells. For detection of localized exocytosis at bovine adrenal chromaffin cells Schroeder *et al*. used a carbon fiber UME that was flame etched to 1-μm diameter for greater spatial resolution (38). The smaller electrode dimension allowed two electrodes to be placed directly on the cell and simultaneous recordings to be carried out. These experiments showed that distinct zones of exocytosis exist and are

spatially persistent on the minute time scale. Also, there are zones where no release occurs and these do not change position on the scale of minutes.

Certain cell types, in particular chromaffin and mast cells, are known to synthesize and release more than one messenger molecule. Chromaffin cells synthesize, store, and release epinephrine and norepinephrine, while mast cells synthesize and release serotonin and histamine. In an attempt to determine if corelease of these molecules takes place in chromaffin cells, Pihel *et al*. used fast scan cyclic voltammetry with a scan rate of 800 V/sec repeated every 16.7 msec at a 5-μm diameter carbon fiber UME (6). Expanded potential scan limits were employed to distinguish epinephrine from norepinephrine, because a second oxidation wave is present at large positive potentials for the oxidation of epinephrine *o*-quinone, an amine, to the imine form of the molecule. The second oxidation wave made it possible to determine whether an individual release event was attributable to epinephrine or norepinephrine. The results from this study suggest that the majority of chromaffin cells release either norepinephrine or epinephrine. However, 17% of the cells observed released both epinephrine and norepinephrine, and each secretory vesicle contained either epinephrine or norepinephrine, but in general not both.

Mast cells are immune response cells that are found distributed throughout the body. Mast cells synthesize, store, and release both histamine, a neurohormone, and serotonin, a common neurotransmitter. In mast cells, histamine is found in much greater abundance than serotonin. By some reports there is an average of 140–240 fmol of histamine and 2–24 fmol of serotonin per cell (39, 40). Previous data have suggested that histamine and serotonin are coreleased from single vesicles in mast cells; however, the evidence for this was indirect. Using electrochemically pretreated carbon fiber electrodes and a high positive potential scan limit, two oxidative waves for histamine were observed, as well as an oxidation wave for serotonin (5). This allowed the simultaneous detection of the two analytes, leading to the conclusion that both histamine and serotonin are released from the same vesicles in mast cells.

#### *17.1.1.2 Electrochemical detection of insulin release*

Insulin is another biochemically relevant molecule that can be detected electrochemically at the cell surface. It is released by exocytosis from pancreatic β cells. Insulin, however, is not detected at an untreated carbon fiber electrode, so a chemically modified electrode is used to catalyze the oxidation of the disulfide bonds that are present in the insulin molecule. Initially Kennedy and coworkers used an electrochemically deposited composite thin film of ruthenium oxide and cyanoruthenate (41, 42). The film was deposited by placing a clean carbon fiber electrode in a solution of KCl, $RuCl_3$, and $K_4Ru(CN)_6$ at pH 2. Then the electrode potential was cycled between +0.47 and +1.07 V (vs. SSCE) at 50 mV/sec for 25 min. This approach proved useful as amperometric detection of single events was possible from both human and rat pancreatic β cells (12, 43). However, the ruthenium oxide/cyanoruthenate modified electrode was not stable over long periods of time under physiological conditions. Therefore an alternative ruthenium oxide catalytic film was developed resulting in an insulin sensitive electrode that was stable over many hours (44). Using amperometry and these two types of chemically modified electrodes, Kennedy's group has determined that serotonin loaded into β cell vesicles is coreleased with insulin (14). In addition, Kennedy and

coworkers demonstrated that the insulin receptor can function with positive feedback, stimulating β cells to secrete insulin in response to an insulin stimulus (13).

#### *17.1.1.3 Combined electrochemical/electrophysiological measurements: patch amperometry*

Although electrochemical methods alone are powerful tools for the detection and analysis of single exocytotic events, they can be combined with electrophysiological methods such as patch clamp, for example, to provide more detailed information about the events. This technique is known as patch amperometry. Patch amperometry is typically accomplished by inserting a carbon fiber, which functions as the electrochemical sensor, into a glass patch clamp pipette and performing cell attached voltage clamp experiments simultaneously with electrochemical experiments. This is shown in Figure 17.1.2A.

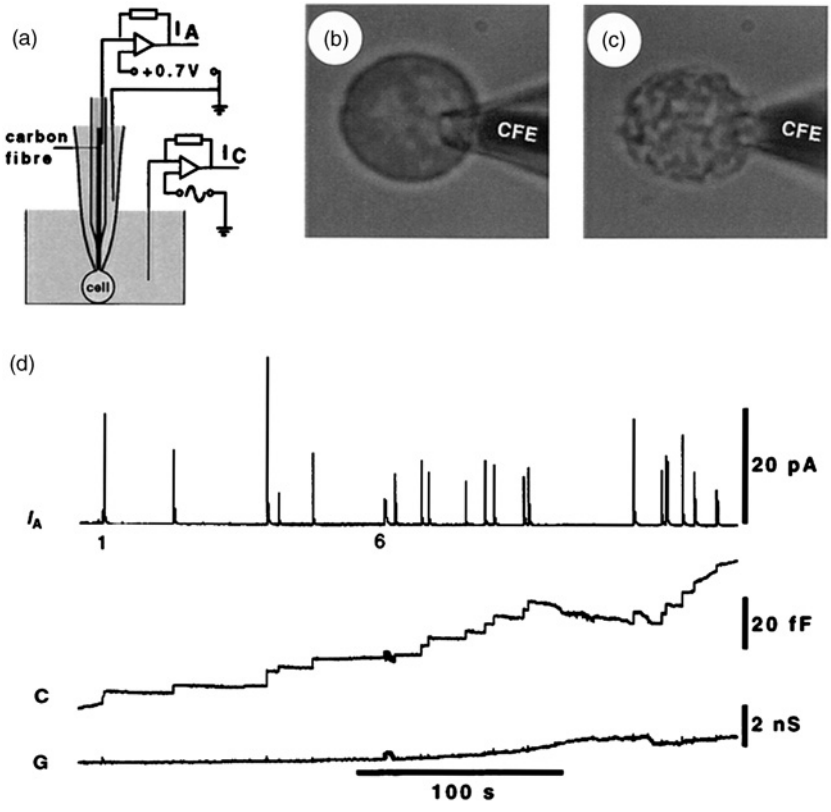


**Figure 17.1.2** (A) Arrangement of a CFE inside a patch pipette. $I_A$, Amperometric current; $I_C$, sine wave current used to measure capacitance changes. (B), (C) Chromaffin cell with attached patch pipette containing CFE at the beginning (B) and end (C) of the experiment. (D) Recording from this cell shows amperometric transients (top), associated capacitance steps (middle), and conductance trace (bottom). Reproduced with permission from reference (45).

This configuration allows simultaneous monitoring of membrane capacitance as well as detection of the opening of individual fusion pores and the monitoring of catecholamine release kinetics from the same vesicle (45). Membrane capacitance is directly proportional to membrane area; therefore discrete jumps in capacitance signify fusion of individual vesicles with the plasma membrane and allow estimation of the size of the fusing vesicles (Figure 17.1.2D). These experiments were used with currently accepted models of the structure of the fusion pore to estimate the diameter of the pore preceding full release in chromaffin cells to be less than 3 nm. Additionally, this technique was used to determine that release of transmitter through the pore in adrenal cells is much faster than release through the pore of mast cells. In other studies on mast cells, Tabares *et al*. demonstrated that the size of the initial fusion pore does not determine the rate of neurotransmitter efflux during the early or late stages of full exocytotic release (46). This technique has also been used to elucidate the coregulation of vesicle membrane area and the amount of neurotransmitter contained in vesicles in response to pharmacological treatment (47). Patch amperometric experiments have reinforced the conclusion put forth by Colliver *et al*. that neurotransmitter concentration in vesicles remains constant when vesicles are induced to grow or shrink by drug treatment (48). While the cell attached configuration is the most prevalent configuration, patch amperometry has also been applied to excised membrane patches, thereby allowing control over the environment on both sides of the plasma membrane (49).

#### *17.1.1.4 Electrochemical determination of cholesterol in the plasma membrane*

Devadoss *et al*. (18) have developed a cholesterol oxidase modified electrode that has been used to detect cholesterol in the plasma membranes of *Xenopus* oocytes. A platinum electrode modified with a lipid bilayer containing cholesterol oxidase (50) is operated in the amperometric mode and placed adjacent to an oocyte (Figure 17.1.3A–B).

As the electrode moves closer to the cell surface, the amperometric current rises (Figure 17.1.3C). When the electrode is placed in contact with the cell surface, cholesterol is extracted from the membrane and moves across the thin membrane layer and partitions into the electrode-supported enzyme-modified lipid bilayer. Subsequent enzyme catalyzed oxidation of cholesterol by molecular oxygen produces hydrogen peroxide which is oxidized at the platinum electrode and detected. This is an efficient and simple method to determine cholesterol levels in the plasma membrane of cells which should find applicability in determining the role cholesterol plays in the organization of cellular membranes (51).

#### *17.1.1.5 Scanning electrochemical microscopy (SECM) at single cells*

Scanning electrochemical microscopy (SECM, see Chapter 12) is another microelectrode technique that has been used at the cellular surface. Briefly, with SECM a microelectrode (UME, see Chapter 6) functions as a scanning probe that detects local electrochemical activity. When the UME is rastered over a sample, electrochemical data is recorded at multiple positions and an image is constructed based on the local electrochemical properties of the area of interest. SECM has been thoroughly reviewed (19, 20, 52, Chapter 12 of this

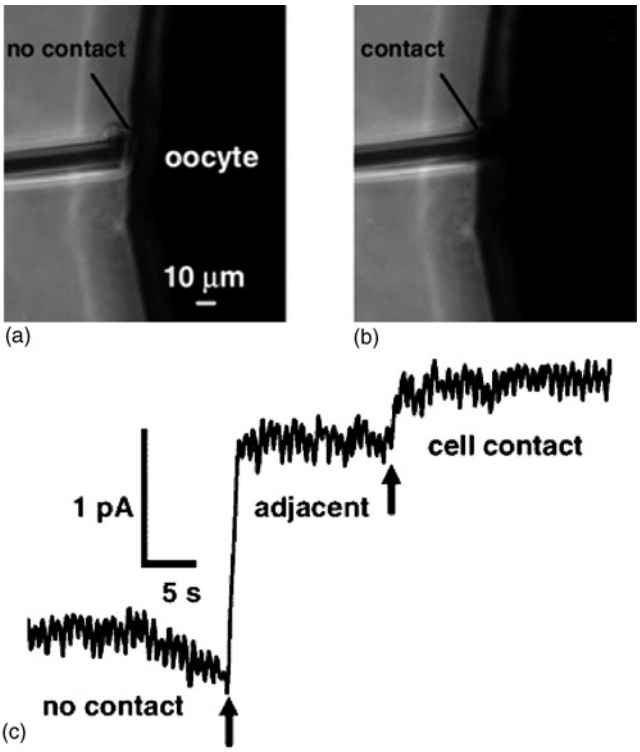


**Figure 17.1.3** Photographs and amperometric detection of cholesterol in the plasma membrane of a *Xenopus* oocyte. Photographs showing the electrode (A) positioned about 5 μm from the plasma membrane and (B) contacting the plasma membrane. (C) Amperometric data for detection of cellular cholesterol at a microelectrode (11.5-μm diameter) modified with a lipid bilayer membrane containing cholesterol oxidase. No contact (Figure 17.1.3A): baseline data; no cholesterol detection. Adjacent: data for positioning the electrode within about 1 μm of (or partially touching) the plasma membrane. Cell contact: data for contacting the oocyte plasma membrane. Arrows indicate the approximate times of changing the electrode position. The buffer was 0.1 M sodium phosphate, pH 6.5. The electrode potential was 800 mV vs. NHE. Reproduced with permission from reference (18).

handbook). A cellular property than can be assessed by SECM is membrane permeability. In one such permeability study, algal protoplasts were incubated in solutions of redox active molecules and redox current was monitored as a function of the distance between the microelectrode and the cell (53). These types of curves are known as approach curves. Molecules resulting in lower current at close approach were determined to have lower permeability with respect to the cellular membrane because the membrane hindered diffusion of the molecules to the microelectrode surface. Cellular redox activity can also be probed with the scanning electrochemical microscope, as demonstrated by Liu and coworkers (54). This study focused on measuring the rate and assessing the pathway of transmembrane charge transfer. Additionally, an electrochemical image of cellular redox activity showed that the periphery of cells had the highest redox activity while the area occupied

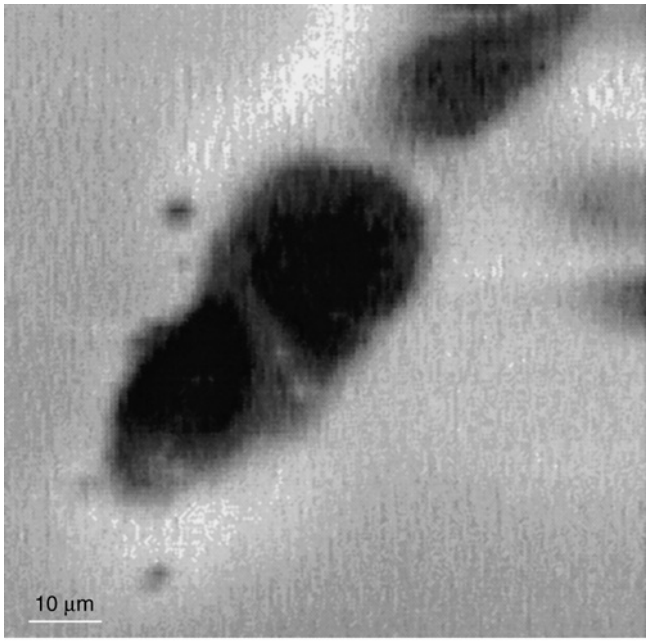


**Figure 17.1.4** Normal human breast (MCF-10A) cells imaged by the SECM with a 1-μm-radius Pt tip and 40 μM 1,2-naphthoquinone as mediator. Reproduced with permission from reference (54).

by the nucleus had the lowest activity, due to the impermeability of the nuclear membrane to the redox mediator (Figure 17.1.4).

In a subsequent study, Liu *et al*. used SECM to image the local pH around groups of cells, noting that surrounding pH differs for cells in different metastatic stages (55). Liebetrau and coworkers used negative feedback SECM to image differentiation of PC12 exposed to nerve growth factor, which initiates cellular neurite outgrowth (56). With this technique it was possible to image neurites 1–2 μm in width and observe cellular surface morphology not apparent with a light microscope. In a follow-up study Kurulugama *et al*. used constant-height mode SECM to monitor topographical changes and faradaic current simultaneously (55). This allowed imaging of cellular morphology (seen as an impedance change) concurrent with amperometric monitoring of neurotransmitter release. This approach to imaging and amperometry has the potential to determine spatiotemporal dynamics of exocytosis *in vitro*. SECM has been employed in numerous other investigations of cellular surfaces and function including studies of redox activity and respiration of bacteria (16, 58), respiration activity of single bovine embryos (15, 59), and the permeability of bovine cartilage to various molecules (60, 61).

### 17.1.2 Electrochemistry at lipid bilayer membranes

Processes occurring at the cellular surface are of great interest to biologists and biophysicists. However, the plasma membrane surface of a cell is quite complex because the

membrane is not a homogeneous structure. It is a bilayer structure formed by a wide variety of lipids, is imbedded with proteins, decorated by carbohydrates, and supported by cytoskeletal elements. Numerous processes crucial to cellular survival occur at the plasma membrane including exocytosis and endocytosis as well as ionic transport via ion channels. Many of these processes are the result of a number of proteins acting in concert with the lipid bilayer in a complex symbiotic relationship. A model system was developed by Bangham in the 1960s in an effort to exclude influences from proteins and focus on the role of lipid bilayer properties in cellular membrane processes (62). Planar lipid bilayers were the first manifestation of a system to model the cellular surface and the unmodified varieties of these membranes have similar resistance and capacitance values to cell membranes (63, 64). The composition of bilayer lipid membranes can be altered to make them more conductive. This is accomplished by insertion of lipophilic molecules into the membrane that form channels or increase the permeability to certain ions (64). By doping lipid bilayers with lipophilic electron donors (e.g., ferrocene or tetrathiafulvalene) or acceptors (e.g., 7,7,8,8-tetracyanoquinodimethane) membranes can function as working electrodes (65, 66). Membrane modified electrodes (67, 68) have been suggested as a platform for biosensor development and have proved useful in development of enzyme electrodes.

Since lipid bilayer membranes have physical and electrical properties quite similar to those of cellular membranes, they are useful for constructing simple models of cells. The most efficient cellular model is the liposome, which is a spherical lipid bilayer. Liposomes can range in diameter from a few nanometers to hundreds of micrometers (depending on preparation method) and have found application in fields varying from drug delivery (69–73) to cosmetics (74, 75). Recently technology has been developed by Orwar and coworkers that allows transformation of single liposomes into networks of multiple liposomes with lipid membrane nanotube connections (76–78). Networks of this sort have been suggested as a new generation of microfluidics. However, it is the ability to manipulate liposomes into biologically relevant geometries that is of interest to the biological electrochemist. To mimic exocytosis, the process of cellular chemical secretion, a network of two liposomes can be constructed (79). This model system can be used to study the dependency of electrochemical response on electrode size and can be used to model neurotransmitter efflux from synapses *in vivo* (80).

#### *17.1.2.1 Electrochemistry at a liposome-based artificial cell*

Exocytosis is a complex process that involves protein–protein and protein–lipid interactions, membrane fusion, and release of neurotransmitter. A model system that mimics this process in a protein free fashion is advantageous to study the role of the lipid bilayer in exocytosis. A totally lipidic system is useful to study the effects of altered membrane physical properties, typically accomplished by altering the components that form the membrane. Thus an "artificial cell" composed of two liposomes with a lipid membrane nanotube connection and one inside the other (Figure 17.1.5) was developed (79).

The liposome inside a liposome configuration is analogous to a vesicle inside a secretory cell during the last stages of the release process. Microelectroporation (77) assisted insertion and careful micromanipulation of a micropipette is required for formation of the artificial cell. Briefly, a micropipette filled with the redox molecule of choice (typically catechol) is positioned next to a surface immobilized giant unilamellar vesicle (GUV) with

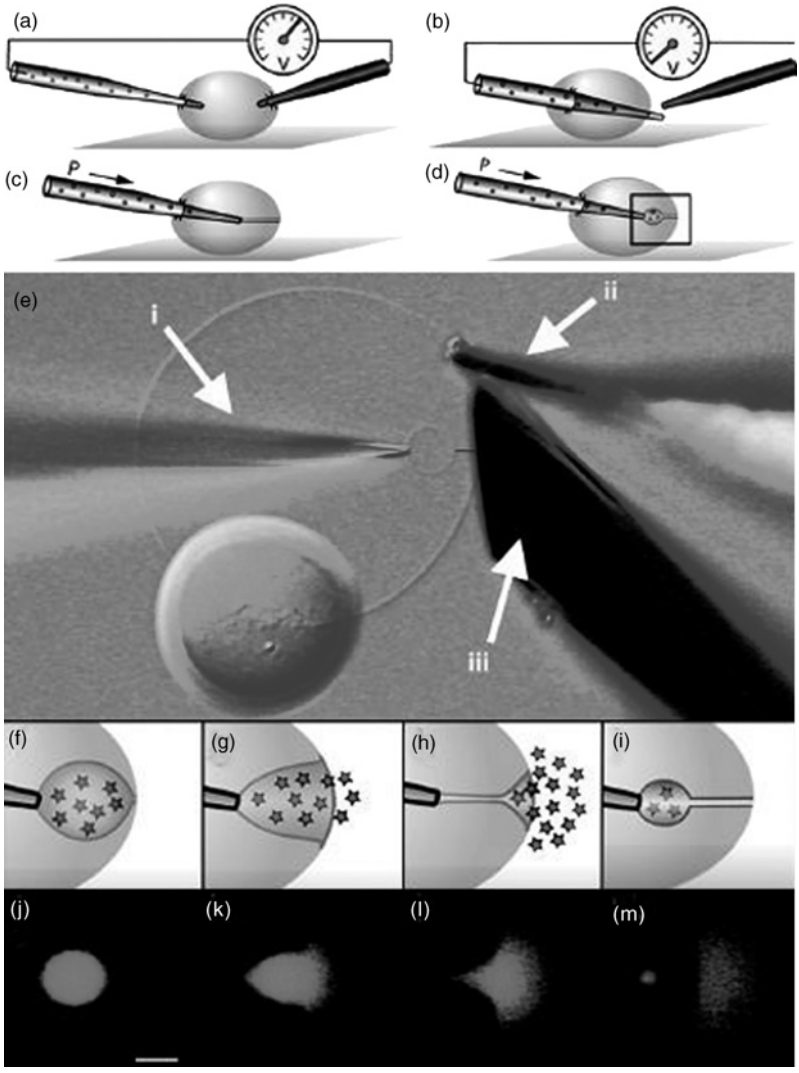


**Figure 17.1.5** Formation and release of vesicles in an artificial cell. (A–D) Schematics of a microinjection pipette electroinserted into the interior of a unilamellar liposome and then through the opposing wall, pulled back in to the interior, followed by spontaneous formation of a lipid nanotube and formation of a vesicle from flow out of the tip of the micropipette. (E) Nomarski image of a unilamellar liposome, with a multilamellar liposome attached as a reservoir of lipid, microinjection pipette (i), electrode for electroinsertion (ii), and 30-μm diameter amperometric electrode beveled to a 45° angle (iii). A small red line depicts the location of the lipid nanotube, which is difficult to observe in the computer image with a 20× objective, illustrating a vesicle with connecting nanotube inside a liposome. (F–I) Fluid injection at a constant flow rate results in growth of the newly formed vesicle with a simultaneous shortening of the nanotube until the final stage of exocytosis takes place spontaneously and a new vesicle is formed with the attached nanotube. (J–M) Fluorescence microscopy images of fluorescein-filled vesicles showing formation and final stage of exocytosis matching the events in F–I. (Scale bar represents 10 μm.) Reproduced with permission from reference (79). (for colour version: see colour section at the end of the book).

an attached multilamellar vesicle. At the opposite side of the vesicle is the electroporation counter electrode. When a voltage pulse is applied across the GUV, the membrane is transiently destabilized, allowing insertion of the micropipette. The micropipette is then translated across the interior of the GUV and a voltage is applied again, allowing the micropipette to exit the distal side of the GUV. The micropipette is rapidly withdrawn into the interior with part of the membrane adhered to the tip. This forms a nanotube and when solution flows from the micropipette a small vesicle begins to form. When the vesicle has grown to the size where it nearly contacts the larger exterior vesicle, the geometry is exactly like that of a cell undergoing exocytosis. There is a small vesicle fused to a larger vesicle with an aqueous pore connecting the vesicular contents with the extracellular space. At this point in the artificial cell, the interior vesicle empties its content to the surrounding solution in a process that resembles exocytosis. The nanotube remains adhered to the pipette tip, however, allowing successive release events without pipette reinsertion. The size of the fusing vesicle can be adjusted by varying the distance from the pipette tip to the large vesicle membrane, and release from vesicles ranging from 4 μm in diameter to larger than 30 μm has been measured.

Monitoring the material released is accomplished by amperometrically detecting the redox molecule contained in the smaller interior vesicle as it is released. Typically a carbon fiber electrode measuring 33 μm in diameter is employed for amperometric detection. The resulting current transient appears qualitatively similar to those recorded at living secretory cells, such as mast cells, chromaffin cells, and PC12 cells (Figure 17.1.6A–B).

The difference in time scale, amplitude, and area of the artificial cell current spike is due to the fact that the vesicle is larger and contains more electroactive molecules than those in living cells. However, release from the smallest vesicles measured (approximately 4 μm diameter) is similar in time to events measured from the large vesicles of the beige mouse mast cell which average 700 nm in diameter (81). In Figure 17.1.6C, the relationship between vesicle radius and full width at half maximum (half-width) is shown for experiments with artificial cells. The fit is nearly perfectly cubic, meaning that release kinetics scale linearly with vesicle volume.

An interesting feature of this system is the transport or leakage of catechol through the nanotube prior to full release. This can be thought of as analogous to neurotransmitter leakage through the fusion pore formed before full release in living cells (33, 34). Transpore catechol transport is apparent on the amperometric traces as a prespike rise in current, which in live cells is termed a “foot” (Figure 17.1.7A–B).

This transport was characterized at artificial cells as a function of vesicle size and as a function of the pressure applied to the micropipette used to inflate the vesicles (Figure 17.1.7C–E). The pressure applied to the inflation micropipette correlates with the flow rate of catechol solution from the micropipette. The duration of the foot is strongly dependent on vesicle size for larger vesicles (size of vesicle just before release), and is also dependent on the flow rate. However, the number of molecules detected during the foot portion of the event (foot area) is not dependent on solution flow rate. The ratio of area to the duration of the foot is dependent on both vesicle size and flow rate. These electrochemical data coupled with models of membrane and fluid dynamics lead to cogent explanation of leakage through the membrane nanotube (Figure 17.1.7F). As the vesicle is inflated, additional membrane required to accommodate the growing volume is drawn along the nanotube thus

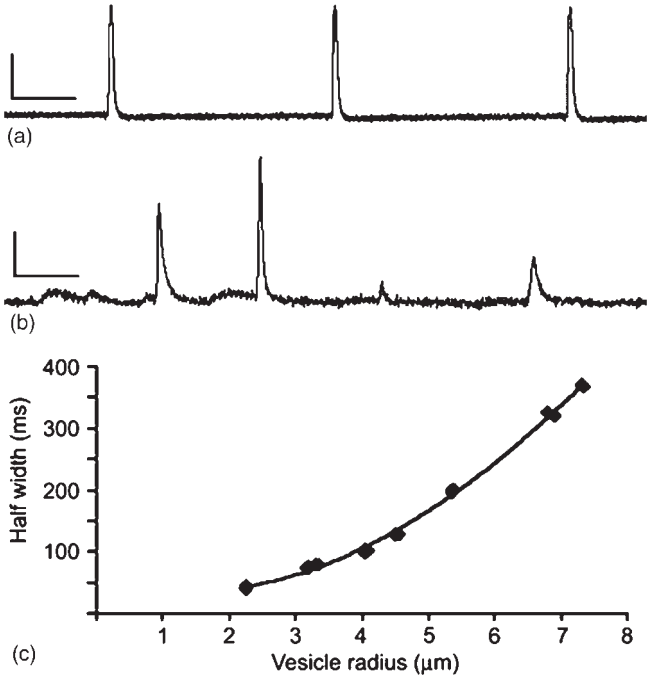


**Figure 17.1.6** Amperometric monitoring of repeated exocytosis events at artificial cells and cells. (A) Amperometric detection of continuous exocytosis of three vesicles from an artificial cell (scale bars are 40 pA and 3000 msec). (B) Amperometric detection of dopamine exocytosis from a PC12 cell (scale bars are 10 pA and 40 msec). (C) Plot of half-width vs. vesicle radius for vesicles fusing from an artificial cell where the vesicle radius has been the only parameter varied in the experiment. Reproduced with permission from (79).

inducing shear flow of the solution inside the nanotube. Opposing shear flow is Poiseuille flow resulting from the pressure difference across the nanotube. As the interior vesicle is inflated, its volume grows at a constant rate, whereas the rate of surface area growth slows as the vesicle grows larger. Thus, shear flow has a high velocity when the vesicle is small and slows as the surface area to volume ratio decreases. Additionally, as the vesicle grows the nanotube connecting it to the larger vesicle shrinks, Poiseuille flow velocity increases as the nanotube shortens, and outward flow begins to dominate. When Poiseuille flow overcomes shear flow, catechol solution is transported out of the nanotube and is amperometrically detected as a prespike foot.

In this sense, transport through the nanotube is analogous to leakage through an elongated fusion pore in living cells. Intravesicular pressure and membrane transfer through the fusion pore have been suggested previously as significant driving forces for exocytosis (82–85). Finally, the most significant finding from this work is that membrane mechanics alone seem to be sufficient to drive exocytosis-like behavior at biological time scales without protein intervention.

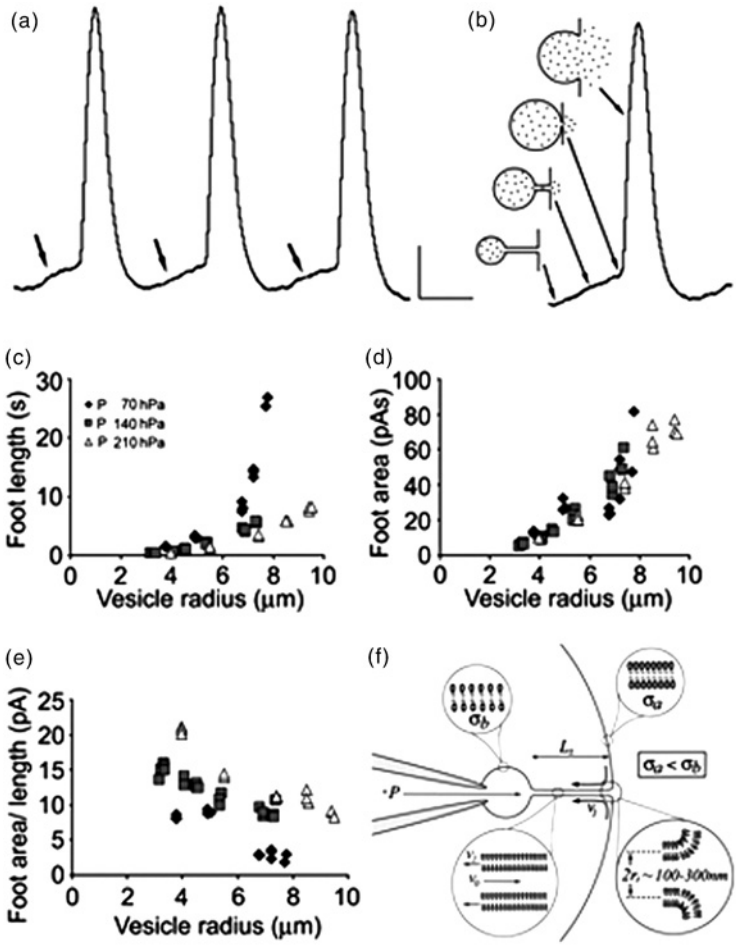


**Figure 17.1.7** Amperometric monitoring of release via an artificial fusion pore. (A) Amperometric detection of release from a 5-μm radius vesicle showing prespike feet (arrows), indicating catechol transport through the lipid nanotube or fusion pore. (Scale bar is 80 pA and 500 msec.) (B) Time correlation of vesicle growth, transport of transmitter through the lipid nanotube, and the final stage of exocytosis with amperometric detection. (C–E) Plots of foot length (C), foot area (D), and the ratio of foot area over foot length (E) observed with amperometry for vesicles fusing with an artificial cell at three different pressures used to inflate the vesicles. (F) Schematic model of the factors affecting flow in the vesicle and nanotube of the artificial cell. Reproduced with permission from reference (79).

### *17.1.2.2 Modeling a synapse with the liposome-based artificial cell*

In a separate set of experiments, the artificial cell model was used to develop models of coulometric efficiency as a function of electrode size and to determine the size of the space between the electrode and the membrane (80). In this case, coulometric efficiency is defined as the ratio of the total number of molecules detected from a vesicle to the total

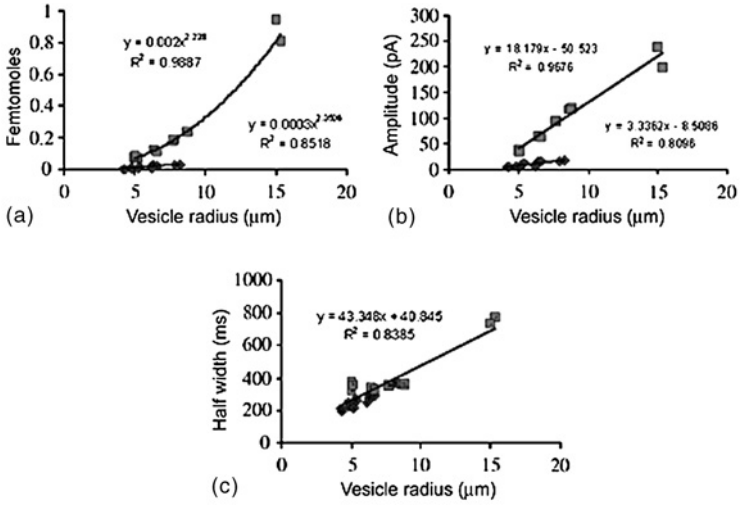


**Figure 17.1.8** Amperometric data for fusion of vesicles of varying size at beveled 5- (♦) and 33-μm (■) electrodes: (A) the amount of catechol observed at each electrode, (B) the amplitude of each current transient, and (C) the half-width of each transient vs. the radius of vesicles undergoing exocytosis. Each data set has been curve fit to observe the trend in the data as indicated. Reproduced with permission from reference (80). (for colour version: see colour section at the end of the book).

number of molecules released by the vesicle. These studies employed two different size electrodes (5 and 33 μm diameter) to detect release and compared the electrochemical responses as a function of electrode and vesicle size. When a vesicle is released from the artificial cell, its size relative to the detection electrode is a strong determinant of the amount of vesicular content detected as well as the spike amplitude (Figure 17.1.8A–B). However, the measured kinetics of release is not affected by the size of the electrode used for detection (Figure 17.1.8C).

To model coulometric efficiency and determine the size of the electrode membrane gap, a simple geometric representation of the system was devised (Figure 17.1.9). The space between the electrode and the membrane was modeled as a cylinder and the ratio of the vesicle volume to cylinder volume determines the coulometric efficiency. If the vesicular volume is smaller than the cylinder volume, 100% oxidation is expected.

For a 33-μm electrode, the best fit of the data is obtained when the height of the cylinder is 300 nm suggesting that even when the electrode is in direct contact with the membrane there is a small volume of solution trapped between the electrode and the membrane. Moreover, even for somewhat smaller vesicles a significant portion of the released molecules escape undetected. This is probably caused by solution flow out of the membrane–electrode gap due to volume limitation and not diffusion (i.e., the volume of the gap cannot accommodate the total volume of liquid released from the vesicle).

The first model presented in this work was quite simplistic and did not take into account the distinct stages of release that are characteristic of the artificial cell model. Therefore a second model was proposed with distinct stages of release and each stage was represented as having a distinct geometric shape (Figure 17.1.10).

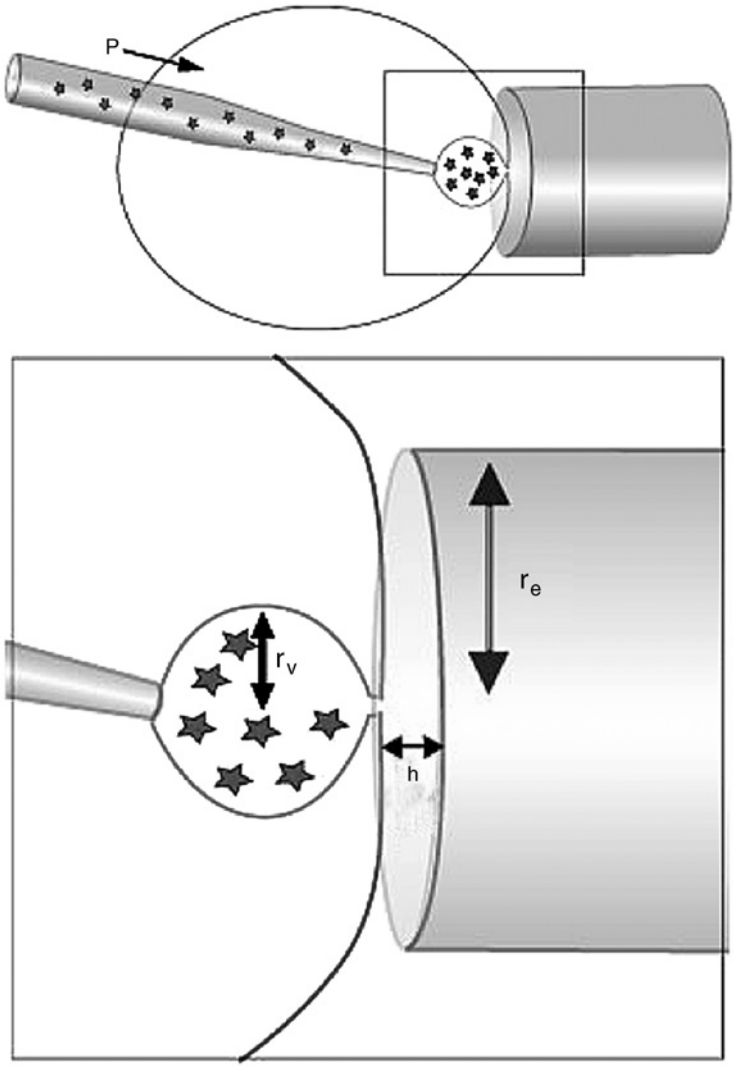


**Figure 17.1.9** Simple model of coulometric efficiency for artificial exocytosis. This first-stage model assumes that the efficiency of oxidation for material released is simply the ratio of the membrane–electrode space (calculated as $\pi r_e^2 h$) over the volume of the vesicle ($4\ \pi r_v^3/3$). This assumes that all the catechol that is present in the membrane–electrode space after exocytosis will be oxidized, but also that only catechol in the solution that fits in this volume will be oxidized. Reproduced with permission from reference (80). (for colour version: see colour section at the end of the book).

In the first stage of release the nanotube begins to dilate and at this stage some vesicular material escapes the vesicle as revealed by fluorescence imaging of release events (Figure 17.1.10B). The next stage is characterized by a membrane structure that is between a spherical vesicle and a frustum (Figure 17.1.10C). The final stage is after full release

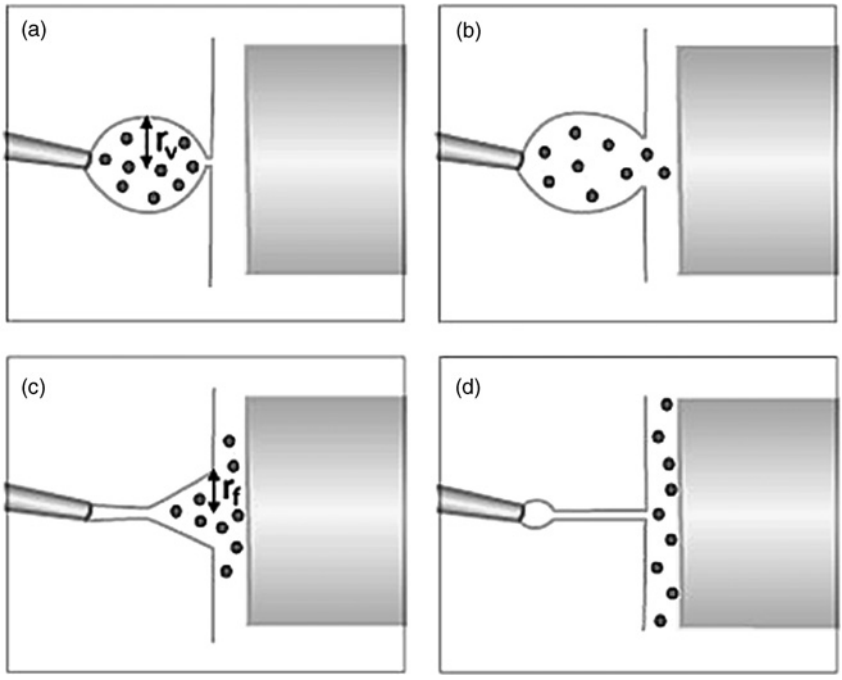


**Figure 17.1.10** A more complete model of the release process during exocytosis based on the fluorescence observations. This model assumes that as the vesicle opens, it has a transitory period where mass transport of catechol to the electrode is via diffusion from a frustum with opening $r_f$ defined the value of $r_v$. Catechol diffusing to the electrode is oxidized. After exocytosis is complete, the membrane–electrode space is filled with solution from the inside of the vesicle and catechol present continues to be oxidized as in the thin-layer representation of Figure 17.1.9. Reproduced with permission from reference (80). (for colour version: see colour section at the end of the book).

when the small vesicle has become fully incorporated into the larger liposome membrane and the nanotube remains attached to the pipette tip (Figure 17.1.10D). During the time the vesicle is in the frustum state (calculated as twice the spike half-width for each vesicle) the charge passed is estimated from the integrated Cottrell equation

$$Q_{\text{frustum}} = \frac{2nFAD^{1/2}C^{*}t^{1/2}}{\pi^{1/2}} \tag{17.1.1}$$

where $n$ is the number of electrons transferred in the electrochemical reaction, $F$ is Faraday's constant, $A$ is the effective electrode area which is taken to be the area defined by the opening of the frustum or the electrode area, which ever is smaller, $D$ is the diffusion coefficient ($6 \times 10^{-6}$ cm$^2$/sec), $C^*$ is the concentration of catechol in the vesicle, and $t$ is the time the frustum is open, taken to be twice the peak half-width. During the next stage, after full exocytosis, the charge passed by oxidation of catechol in the electrode–membrane space is given by the equation

$$Q_{\text{space}} = nFC'\pi r_e^2 h \tag{17.1.2}$$

where $r_e$ is the average radius of the beveled electrode and $h$ is the distance between the membrane and the electrode. $C'$ is the concentration of the remaining unoxidized catechol in the membrane–electrode space and is calculated by subtracting the number of moles oxidized during the previous (frustum) stage by the equation

$$C' = \frac{\left[C^*(V_v + V_{flow})\right] - 2AD^{1/2}C^* t^{1/2} / \pi^{1/2}}{V_v + V_{flow}} \tag{17.1.3}$$

where $V_v$ is the volume of the vesicle and $V_{flow}$ is the volume of flow out of the pipette during the release event. Flow during the event is calculated by dividing the vesicle volume by the time between events to get a volume flow rate in $cm^3$/sec then multiplying by twice the event half-width. Combining Faraday's Law ($N = Q/nF$) and the integrated Cottrell equation, $Q = 2nFAD^{1/2}C^*t^{1/2}/\pi^{1/2}$ the number of moles oxidized during the frustum stage is given by $N = 2AD^{1/2}C^*t^{1/2}/\pi^{1/2}$.

Oxidation of all the catechol in the vesicle prior to release results in the following coulometric charge

$$Q_{max} = nFC^*(V_v + V_{flow}) \tag{17.1.4}$$

Thus the predicted coulometric efficiency is the ratio of the sum of the charge from the two stages of opening over $Q_{max}$. The resulting equation that predicts percent coulometric efficiency is given as

$$\%\ \text{Coulometric Efficiency} = 0.38[(0.25Q_{frustum} + Q_{space})/Q_{max}] \times 100 \tag{17.1.5}$$

Only 25% of the Cottrell equation is used in the final expression to correct for the diminished diffusion in the narrowing frustum. This model correctly predicts the shape of the percent coulometric efficiency vs. vesicle radius; however, the predicted magnitude is 2.6 times larger than that observed. To correct this a factor of 0.38 has been applied to the theoretical prediction. Experimental data, predicted coulometric efficiency, and the best fit of the experimental data is shown in Figure 17.1.11.

The discrepancy in magnitude leading to the 0.38 correction term may arise from numerous factors. One possible explanation is that the detection electrode may not always be centered over the release site, resulting in a greater than expected escape of undetected catechol. Also, solution flow due to the distention of the vesicle membrane may lead to loss of material and the reduced oxidation efficiency. The calculation for charge passed during the frustum stage assumes mass transport by diffusion only, but it seems that the changing membrane geometry may lead to solution flow causing molecules to escape the membrane–electrode gap without being oxidized. In cell-to-cell communication, it is assumed that diffusion is the predominant mass transport process, but this model shows that convective flow is likely to play an important role in mass transport over short distances.

Applying this model to exocytosis in biological systems permits the prediction of coulometric efficiency for any size electrode if the vesicle size is known. Two cell types commonly used in exocytosis experiments, adrenal chromaffin and PC12 cells, have average vesicle radii of 99 and 125 nm, respectively (33, 48). The model set forth here predicts

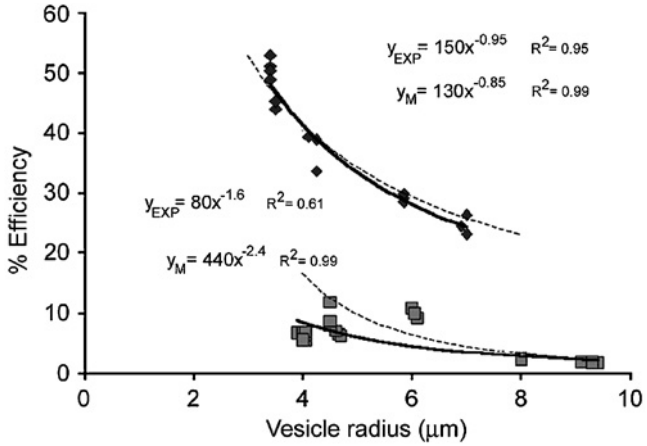


**Figure 17.1.11** Coulometric efficiencies for a data set obtained with a beveled 33-μm electrode (♦) compared to data obtained with a 5-μm electrode (■) for release of catechol measured from a range of vesicle sizes. This is compared to the theoretical coulometric efficiencies for these electrode dimensions calculated with the conditions outlined in Figure 17.1.5 and with the model discussed in the text (dashed lines). These are compared to each set of experimental data, which are shown with best-fit equations (thick lines). The equations for all lines, and their correlation coefficients, are given with the symbols $y_{exp}$ for experimental data sets and $y_m$ for the modeled efficiencies with that for the 5-μm electrode to the left and that for the 33-μm electrode to the right. Reproduced with permission from reference (80). (for colour version: see colour section at the end of the book).

100% coulometric efficiency for amperometric experiments employing 5 μm electrodes at adrenal chromaffin and PC12 cells. In contrast, for cell types that release larger vesicles, such as the beige mouse mast cells, the model predicts less than 100% coulometric efficiency. In fact, for beige mouse mast cells (average vesicle radius is 1.35 μm) coulometric efficiency at a 5 μm electrode is predicted to be 47% and for the largest mast cell vesicles (vesicle radii as large as 2 μm) coulometric efficiency drops to 25%. The model predicts that even 33 μm electrodes will not quantitatively oxidize all material released from beige mouse mast cell vesicles. Most cellular experiments performed to date use a 5 or 10 μm electrode for detection. Therefore it is doubtful, based on this model, that measurements made on cells releasing large vesicles are quantifiable with the assumption of 100% coulometric efficiency.

The data gathered with the artificial cell system shows that under certain conditions much of the released catechol will escape the membrane–electrode space undetected. Also the model suggests that in addition to diffusion, solution flow is a significant mode of mass transport of neurotransmitter in synapses. This system can be used to model what happens in a synapse *in vivo*. The membrane–electrode space can be considered analogous to the synaptic cleft and the detection electrode can be thought of as the post-synaptic membrane which has receptors that "capture" the released neurotransmitter. If a synapse is considered to be a 20-nm gap between cells and the average diameter of the post-synaptic surface is 100 nm, then 70% of the volume of a 100-nm diameter vesicle will be pumped directly to the extrasynaptic space during release. This agrees with recent *in vivo* work that suggests

that at dopamine and serotonin synapses much of the neurotransmitter escapes the synapse following exocytotic release (86, 87). There are still many experimental models to examine before a thorough understanding of exocytosis is achieved. However, the models presented here provide a means to simplify the experiments and to examine the effect of membrane mechanics and structure on exocytotic release measured with amperometry.

### 17.1.3 Electrochemistry in small drops and vials

Many of the intriguing problems yet to be solved in biology and medicine require the chemical analysis of minute amounts of material in constricted geometries. The study of photosynthesis, cellular metabolism, and neurotransmission, to name a few, all require chemical analyses in tiny volumes. Electrochemical methods employing microelectrodes are perfectly suited to analyze small volumes, provided the analytes of interest are electrochemically active, which is the case with many neurochemical analytes. Neurotransmitters such as dopamine, serotonin, epinephrine, and norepinephrine are easily oxidized at moderate potentials. The study of these molecules *in vivo* and *in vitro* may lead to breakthroughs in the treatment of neurological disorders such as Parkinson's disease and Alzheimer' disease, as well as depression and anxiety related disorders. Detection and analysis of these molecules, however, is not always easily accomplished due to a wide variety of interferences and due to the volume-limited nature of the measurement, which may have confounding effects on the electrochemical response. For these reasons many groups have devised model systems employing small volume droplets and vials, some even in the picoliter regime, to investigate electrochemical responses in confined geometries. In this section we review the techniques and results for detection of small amounts of analytes in small drops and vials, as well as some biological applications of these techniques.

#### *17.1.3.1 Fabrication of microvials*

Exploration of electrochemical behavior in small volume containers requires fabrication methods capable of defining micrometer size structures from a suitable substrate. Initially, Bowyer et al. (88) sandwiched silver and platinum foil between layers of Tefzel film and glass to form an electrochemical cell with auxillary, reference and working band electrodes, the smallest of which measured 4 μm thick. This electrochemical cell was used to investigate the differential pulse, normal pulse, and cyclic voltammetric behavior of ferrocence in aqueous solutions with volumes ranging from 2 mL to 50 nL.

More recently, however, photolithography has been employed to define and fabricate vials with a capacity as small as 1 picoliter (89, 90). Small vials, described by Clark *et al*. have been fabricated using silicon template photolithographically, then transferring the template pattern into polystyrene using a hot press method. This results in arrays of transparent microvials. An alternative approach to producing transparent sample vials has been taken by Bratten and coworkers whereby a polyimide chamber is photolithographically defined on a transparent glass slide (91–93). These structures differed from those of Clark and Ewing in that the reference, auxiliary, and working electrodes were formed by *in situ* gold deposition on the bottom surface of the container.

A third method of vial fabrication uses a combination of screen printing and laser ablation (94, 95). Briefly, carbon ink was screen printed through a patterned stencil onto a ceramic substrate. An insulating dielectric ink was screen printed on top of the carbon layer and a Ag/AgCl ink was printed on top of the dielectric ink. A final layer of dielectric ink was printed on the outermost layer. The carbon and Ag/AgCl layers eventually form, after laser ablation, the working and reference electrodes of the device. Formation of the vials was accomplished by Kr-F excimer laser ablation at 248 nm and resulted in vial with a volume of 7.2 nL. Figure 17.1.12 shows scanning electron micrographs of the three types of vials described above.

There are two prominent electrochemical detection schemes when working in small volume vials. The simplest method is to use micromanipulators to position the working and reference electrodes into the vial. This is the approach taken by Clark and Ewing, as well as some groups conducting biological electrochemical experiments in microvials, which will be discussed later in this section. Secondly, electrodes can be formed *in situ* in the chambers by traditional microfabrication and photolithography techniques (91–93, 96) or by a combination of screen printing and laser ablation (94–95). The drawback to some of these fabrication methods is that the materials that form the sides and bottom of the vials are not always the same. This could lead to differential adsorption of analytes and erroneous voltammograms.

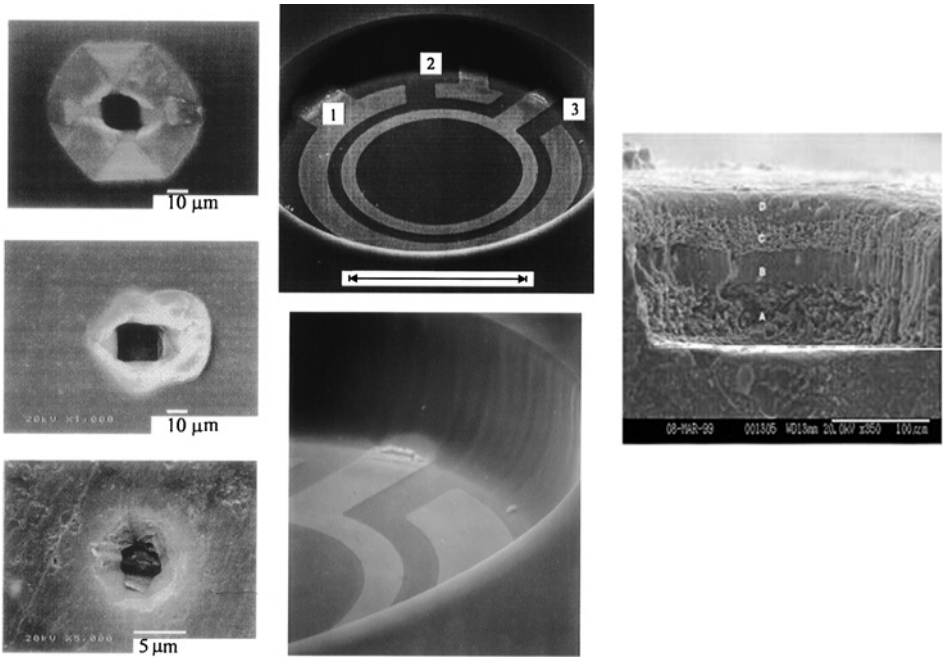


**Figure 17.1.12** Scanning electron micrographs of three types of microvials. The leftmost images are polystyrene microvials fabricated with a hot press method. The center images are vials photolithographically defined polyimide wells. The rightmost image is a vial prepared by ink jet printing followed by laser ablation. Reproduced with permission from references (89, 91, 94).

### *17.1.3.2 Microscopic droplets*

Performing electrochemistry in small volumes does not require that the sample container be defined by solid boundaries. By directly depositing a droplet on a substrate (or electrode), the need for access to photolithographic equipment is circumvented. Gratzl and coworkers have directly deposited microscale droplets on a flat polystyrene substrate resulting in sample volumes as small as 75 pL (97, 98). These experiments required that both the working and reference electrode be positioned in the sample by micromanipulation. The reference electrode used in these experiments was a Ag/AgCl reference inserted in a modified diffusional microburet (DMB). A DMB is essentially a glass micropipette that has a diffusion membrane in the tip allowing diffusional delivery of reagents contained within the pipette.

A second method of droplet formation involves modifying the surface of the working electrode with a small droplet of the solution to be examined. This method has the advantage that the droplet does not have to contain any deliberately added supporting electrolyte as the droplet-coated electrode is inserted in an immiscible conductive solution to perform the analysis. The electrochemistry of electrode immobilized droplets has been thoroughly reviewed by Banks *et al*. (99).

Whether investigating redox reactions in small drops or microvials, one of the main considerations is sample handling since evaporation can significantly change analyte concentration as well as solution pH and viscosity. Evaporation is proportional to surface area to volume ratio of the sample solution, which is quite large for small samples. Thus, total evaporation can occur in seconds for picoliter aqueous samples. Evaporation can be minimized by coating the sample with a membrane lid (100), saturating the experimental headspace with water (88), or covering the sample with a saturated hydrophobic liquid such as heptane (101) or glycerol (89).

### *17.1.3.3 Electrochemical response in small volume samples*

The examination of the voltammetric response at carbon fiber UMEs as a function of microvial volume was undertaken by Clark *et al*. (89). The experimental volume was varied from about 4 nL to as little as 1 pL. For a 5 μm diameter electrode, the volammograms of ferrocenecarboxylic acid did not vary as a function of sample volume. The shape of the voltammograms was sigmoidal which is expected for disk microelectrodes scanned at slow rates (1–1000 mV/sec) under steady-state conditions (102). The half wave potential measured in the microvials was identical to that of ferrocenecarboxylic acid in bulk solution and the current value also matched the expected value. In addition, Clark *et al*. performed voltammetry with a 1 μm diameter flame etched carbon fiber electrode in a 1 pL vial; however, no deviation from bulk solution behavior was apparent.

More detailed analyses of microdisk electrode behavior has been provided by both Clark and Ewing (90) as well as Kashyap and Gratzl (101). The work by Clark *et al*. was done in picoliter vials while the work by Kashyap *et al*. was carried out in picoliter droplets, and in these experiments the researchers investigated the sample volume, voltammetric scan rate, and analyte concentration dependence of the electrochemical response. Clark and Ewing showed that the voltammetric response as a function of scan rate displayed some interesting characteristics (Figure 17.1.13).

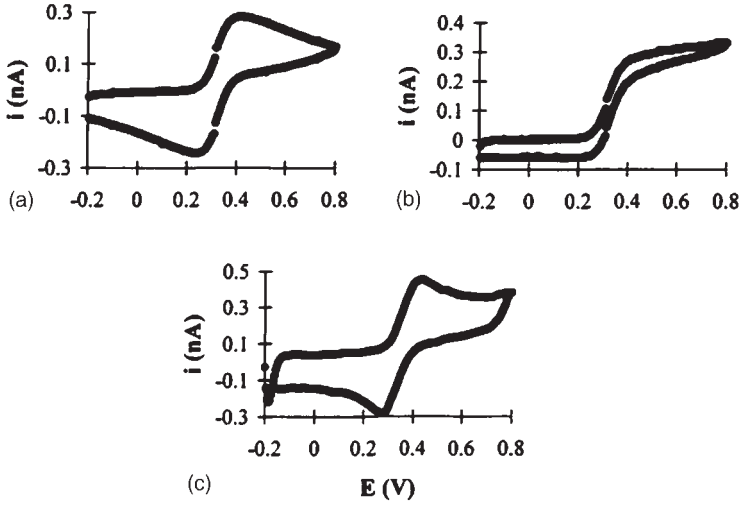


**Figure 17.1.13** Cyclic voltammograms of 1.0 mM ferrocenecarboxylic acid in a 16-pL vial. The scan rates are (A) 0.1, (B) 1.0, and (C) 10 V/sec. Carbon fiber working electrodes are 5 μm in diameter. Reproduced with permission from reference (90).

At the highest scan rate (10 V/sec, Figure 17.1.13C) the voltammetric peak shape was not significantly different from that observed in bulk solution. At an intermediate scan rate (Figure 17.1.13B) the voltammogram was sigmoidal, similar to bulk solution voltammograms at the same scan rate with microelectrodes. However, a significant deviation from bulk solution behavior is apparent when a voltage is scanned slowly (0.1 V/sec, Figure 17.1.13A) in a 16-pL vial. Unlike in bulk solution where voltammograms obtained at slow scan rate with microelectrodes are sigmoidal, voltammograms obtained at slow scan rate in picoliter vials are peak shaped and display a large current increase on the reverse (reduction) wave. In general, the data for fast and intermediate scan rates follow microelectrode theory, and the data for slow scan rates can be described as quasi-thin layer behavior.

Peak shaped voltammograms at slow scan rates only appeared in smaller vials (16 pL or less) and can be explained by comparison of diffusion in bulk solution vs. diffusion in microvials. In microvials the diffusion profile to the electrode is altered due to the vial boundaries. Thus, depletion of electroactive molecules near small electrodes can be achieved in the smallest vials. In bulk solution the amount of molecules reduced at a microelectrode is negligible compared to the bulk analyte concentration. But, in a 16-pL vial the data show that 21% of the total analyte in solution is oxidized by a 5-μm electrode scanned at 0.1 V/sec. These data suggest that bulk electrolysis in microvials can be easily implemented to determine the total amount of analyte present in a vial.

Experiments in microvials also reveal an increase in current on the reverse wave for slow scan rates. After ruling out any effect from interactions between the analytes and the microvial surface, a diffusion-based explanation was formulated. By determining the concentration dependence of the ratio of reduction currents in microvials and bulk solution

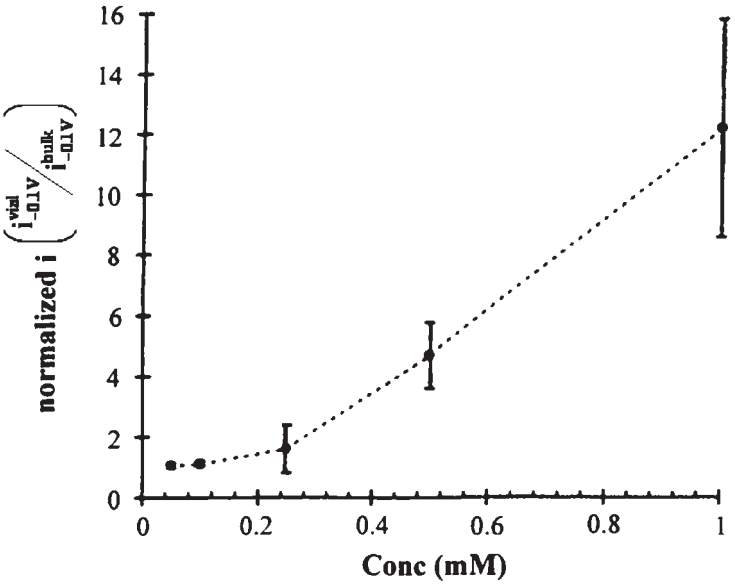


**Figure 17.1.14** Normalized reduction current as a function of concentration. Concentration range is from 0.05 to 1.0 mM. Scan rate is 0.2 V/sec, and the vial size is 7 pL. Error bars indicate the mean ± standard deviation. Reproduced with permission from reference (90).

($i_{vial}/i_{bulk}$) (Figure 17.1.14) in a 16-pL microvial it was determined that diffusion of the oxidized species away from the electrode is restricted.

Unlike experiments in bulk solution where the oxidation product at a UME diffuses away prior to the reverse scan, in a microvial, the oxidation product is restricted by the vial boundaries and forms a depletion layer that can be re-reduced. The increase in the ratio $i_{vial}/i_{bulk}$ with higher concentration occurs because more oxidized molecules are produced in the vicinity of the electrode at higher concentrations and are available for reduction on the reverse scan. Reducing the size of the microvials has a related effect on the ratio $i_{vial}/i_{bulk}$. When the vial size is decreased, diffusion of oxidized species is further restricted thus maintaining a more concentrated depletion layer near the electrode resulting in increased $i_{vial}/i_{bulk}$. These experiments demonstrate that the characteristics of the diffusion/depletion layer, which is dependent on the ratio of the sizes of the sample microvial and the electrode, is the largest determining factor on the voltammetric response.

#### *17.1.3.4 Biological applications of electrochemistry in microvials*

Microvials are attractive environments for single cell experiments due to their limited volumes and the possibility to create integrated devices with electrodes fabricated by photolithographic techniques inside the vials. Such studies include the monitoring of purine release during cardiac cell ischemia (93), monitoring metabolic flux due to stress response (103), and monitoring dopamine transport into cells (104). Microvials with spatially distinct electrodes have been fabricated by Dias *et al.* and have been used to determine the

spatial distribution of exocytosis events on the surface of adrenal chromaffin cells (96). In a study by Troyer and Wightman, HEK-293 cells transfected to express the dopamine transporter were placed in vials ranging from 100 to 200 pL (104). Dopamine was then injected into the vials and the rate of clearance of dopamine by the cell was monitored with fast scan rate cyclic voltammetry. Monitoring dopamine concentration change with time allows the calculation of the kinetics of the dopamine transporter, specifically the initial transport rate, $V_{max}$. Using the single cell microvial approach, $V_{max}$ was determined to be 55 ± 17 amol/sec-cell. In populations of cells, $V_{max}$ was determined to 18.9 ± 1.4 amol/sec-cell by rotating disk electrode voltammetry (105) (see Chapter 11). The discrepancy in $V_{max}$ measured by competing techniques may be due to the difference in the cell volume/solution ratio. In microvial experiments, this ratio is larger indicating that there is less extracellular volume per cell and thus fewer dopamine molecules are transported into the cell. Fewer transported molecules generally prevents the cytosolic concentration from reaching a high enough concentration for reverse transport to occur. However, in some cells in microvial experiments, reverse transport did occur as determined by a nonzero dopamine concentration plateau. Cells exhibiting this behavior were not taken into account in the calculation of $V_{max}$ because the calculated $V_{max}$ from these experiments appeared lower.

### 17.1.4 Intracellular electrochemistry

Extracellular measurements are powerful tools for elucidating mechanisms of cellular secretion. However, to gain information on cellular synthesis and storage of various molecules, measurements in the cell cytoplasm are necessary. Microseparation techniques, such as capillary electrophoresis, with electrochemical detection schemes are useful in measuring and identifying neurotransmitters from whole cells as well as from samples of cell cytoplasm (106, 107). Voltammetric methods have also been used to monitor neurotransmitters inside single cells. Invertebrate cells are typically chosen for intracellular studies because they are generally much larger than their mammalian counterparts, allowing the use of larger electrodes and detection of larger amounts of analyte.

#### *17.1.4.1 Intracellular voltammetry*

Early studies by Meulemans *et al*. used differential pulse voltammetry (see Chapter 11) to measure the concentration of electroactive drugs in the cytoplasm of cholinergic neurons of *Aplysia californica* and to determine rates of cellular uptake and clearance (108). Another report by Meulemans *et al*. described a needle tipped glass insulated platinum electrode for detection of intracellular serotonin in metacerebral neurons from *Aplysia* (109). Again differential pulse voltammetry was used to measure intracellular concentration of serotonin after cell stimulation, after injection of serotonin into the cell, and after extracellular treatment with tryptophan, a serotonin precursor. Serotonin concentration in resting untreated cells was determined to be 0.94 ± 0.61 mM. Chen *et al*. have also used platinum electrodes with multiple pulse voltammetry to measure dopamine levels in the giant dopamine neuron of *Planorbis corneus* (110).

Monitoring neurotransmitters as well as oxygen in cytoplasm can be accomplished using carbon ring and platinized carbon ring microelectrodes (111–113). In the giant dopamine neuron of *Planorbis*, baseline dopamine concentration was below the limit of detection. However, after membrane permeabilization, the total dopamine content of the cell was determined. The ratio of the total dopamine content to the detection limit lead the authors to conclude that roughly 98% of cellular dopamine is bound and not available for detection in the cytoplasm (114). Intracellular oxygen levels are proportional to glucose metabolism and have been determined with platinized carbon ring electrodes (113). The platinization of the electrode is important since oxygen is not detected at a bare carbon ring electrode. Inside the giant dopamine neuron of *Planorbis* the measured oxygen concentration was found to be $0.032 \pm 0.004$ mM. Oxygen transport into the cell has also been evaluated with this experimental setup by bathing the neuron sequentially in oxygen free, air saturated, and oxygen saturated solutions. As expected, intracellular oxygen was lowest when the cell was surrounded by oxygen free solution and highest when bathed in oxygen saturated solution. After only a few minutes following a pulse of exposure to these solutions, oxygen levels returned to baseline levels presumably due to oxygen consumption for cellular respiration and metabolism.

In addition to neurotransmitters and oxygen, intracellular glucose has also been measured. The detection scheme for glucose relies on an enzyme modified platinized carbon ring microelectrode that is 2 μm in diameter (115, 116). In the presence of glucose and oxygen, glucose oxidase will oxidize glucose resulting in gluconolactone and hydrogen peroxide which is oxidized at the platinized electrode. These ultra small enzyme electrodes displayed a response time to the presence of glucose as low as 270 msec and the characteristic response time of an electrode was linearly proportional to the electrode diameter. Other groups have used different enzymes and coupling chemistries to make *in vivo* measurements with microelectrodes (117–119).

#### *17.1.4.2 Intracellular patch electrochemistry*

As with extracellular measurements, intracellular measurements can be made by combining electrophysiological and electrochemical techniques (120). For intracellular measurements, the initial patch electrochemical setup is in the cell attached configuration. However, after some time additional suction is applied to the patch pipette, the membrane is ruptured and the whole cell configuration is attained (Figure 17.1.15). Disruption of the membrane allows oxidizable intracellular content to diffuse to the UME where it is detected in either the amperometric or voltammetric mode.

In the amperometric mode all easily oxidized molecules (including catechols) are detected whereas in the voltammetric mode catecholamines can be preferentially measured. Because membrane capacitance is recorded simultaneously, it is possible to determine if exocytosis is taking place and how it affects cytosolic catecholamine concentration in real time. Figure 17.1.16 shows representative voltammetric data for intracellular patch electrochemistry.

Effects of drug treatment on cytosolic levels of catecholamines and total oxidizable species were also investigated. Reserpine, an inhibitor of the vesicular monoamine transporter (this transporter loads vesicles with catecholamines), had no effect on the amount

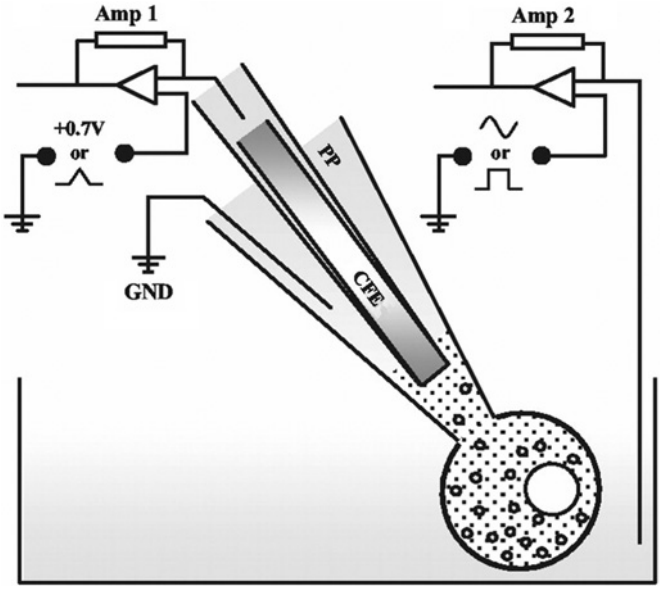


**Figure 17.1.15** Schematic diagram of the intracellular patch electrochemistry setup. Amp 1, Amp 2, Amplifiers; GND, electric ground; CFE, carbon fiber electrode; PP, patch pipette. Reproduced with permission from reference (120).

of catecholamines but increased total oxidizable species by four or five times. A transient five-fold increase in cytosolic catecholamines and slow increase in total oxidizable species was observed when cells were treated with amphetamine.

### 17.1.5 Conclusions

Significant advances in biological analysis with electrochemical methods have been made. At the cellular surface, amperometry and voltammetry are effective in measuring chemical secretion with detection of fewer than 5000 molecules possible. Inroads into electrochemical analysis of the lipid composition are possible with enzyme modified electrodes. Scanning probe methodologies are emerging for topographic and metabolic imaging of live cells, and combined electrophysiological and electrochemical measurements are shedding new light on the biochemistry and biophysics of exocytosis. Liposome-based systems mimic exocytosis without protein intervention and have been useful in elucidating the role membrane properties play in exocytosis. They can also be used to model mass transport of neurotransmitter molecules in synapses. Electrochemical analyses in small droplets and microvials are effective methods for determining electrochemical responses in volume-limited samples. Microvials have also been used as cellular chambers for analysis of chemical secretion and transport. Advances in intracellular electrochemistry have lead to greater understanding of cellular metabolism of drugs and cellular neurotransmitter synthesis and

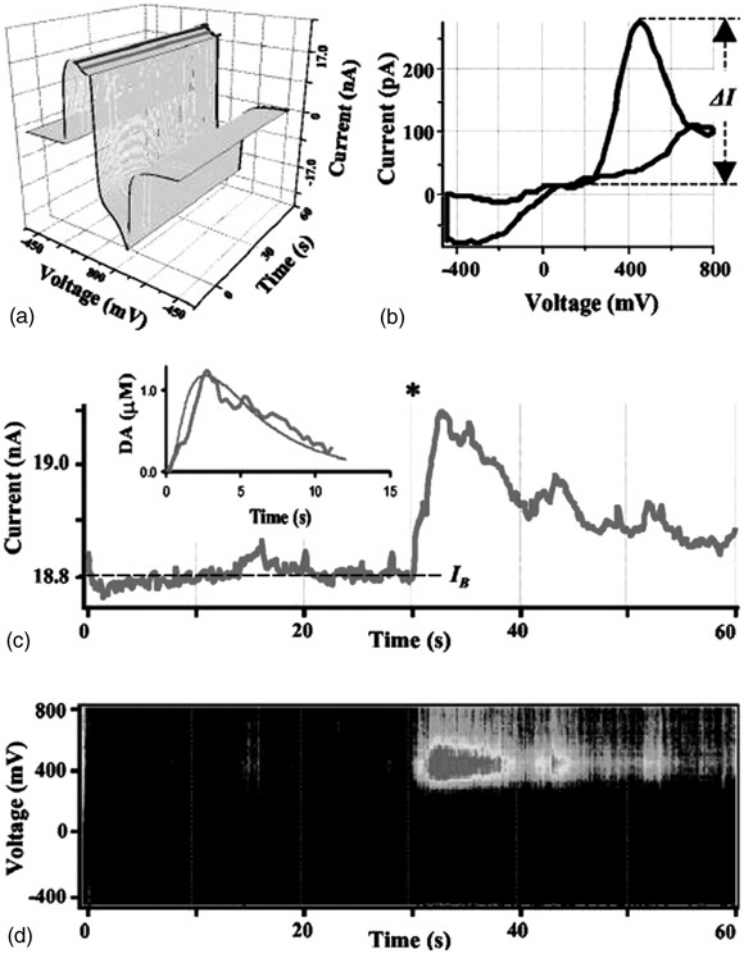


**Figure 17.1.16** Analysis of cyclic voltammetry recordings from a single rat chromaffin cell. (A) A representative recording shown as a three-dimensional matrix of data. Red and blue lines represent samplings of the current at 400 and 0 mV, respectively. (B) Voltammogram of catecholamines released during the same recording. A subtraction was made between 10 consecutive averaged I–V profiles at 10 sec from those at 33 sec. Dashed line indicates ΔI, the height of DA oxidation peak. (C) Current sampled at 400-mV oxidation potential. The asterisk indicates a time when the patch was disrupted by suction and a whole-cell configuration was attained. The inset shows a random walk fit (green) of the sampled current trace (red) using 15 MΩ access resistance, 8 μm cell radius, 60 μm distance between the CFE and the pipette tip, and 6.7 μM cytosolic catecholamine concentration. (D) Pseudo-three-dimensional representation of approximate voltammograms of intracellular metabolites encountering the CFE during the recording, in which the intensity of color ("Planet Earth" color table) indicates the current at a given voltage and time. Reproduced with permission from reference (120). (for colour version: see colour section at the end of the book).

storage. Intracellular patch amperometry may prove valuable in elucidating the coupling of the neurotransmitter synthesis, storage, and release processes.

## REFERENCES


1. J. Monck, J. Fernandez, *Neuron* **12**, 707 (1994).
2. R. Jahn, T. Lang, T. C. Sudhof, *Cell* **112**, 519 (2003).
3. R. Jahn, T. C. Sudhof, *Annu. Rev. Biochem.* **68**, 863 (1999).
4. R. Jahn, T. C. Sudhof, *Annu. Rev. Neurosci.* **17**, 219 (1994).
5. K. Pihel, S. Hsieh, J. W. Jorgenson, R. M. Wightman, *Anal. Chem.* **67**, 4514 (1995).
6. K. Pihel, T. Schroeder, R.M Wightman, *Anal. Chem.* **66**, 4532 (1994).
7. R. A. Clark, A. G. Ewing, *Mol. Neurobiol.* **15**, 1 (1997).
8. E. R. Travis, R. M. Wightman, *Annu. Rev. Biophys. Biomol. Struct.* **27**, 77 (1998).
9. D. M. Cannon, Jr., N. Winograd, A. G. Ewing, *Annu. Rev. Biophys. Biomol. Struct.* **29**, 239 (2000).
10. G. Chen, A. G. Ewing, *Crit. Rev. Neurobiol.* **11**, 59 (1997).
11. J. M. Finnegan, K. Pihel, P. S. Cahill, L. Huang, S. E. Zerby, A. G. Ewing, R. T. Kennedy, R. M. Wightman, *J. Neurochem.* **66**, 1914 (1996).
12. L. Huang, H. Shen, M. A. Atkinson, R. T. Kennedy, *Proc. Natl. Acad. Sci. U.S.A.* **92**, 9608 (1995).
13. C. A. Aspinwall, J. R. Lakey, R. T. Kennedy, *J. Biol. Chem.* **274**, 6360 (1999).
14. C. A. Aspinwall, L. Huang, J. R. Lakey, R. T. Kennedy, *Anal. Chem.* **71**, 5551 (1999).
15. H. Shiku, T. Shiraishi, S. Aoyagi, Y. Utsumi, M. Matsudaira, H. Abe, H. Hoshi, S. Kasai, H. Ohya, T. Matsue, *Anal. Chim. Acta*, **522**, 51 (2004).
16. T. Kaya, D. Numai, K. Nagamine, S. Aoyagi, H. Shiku, T. Matsue, *Analyst* **129**, 529 (2004).
17. H. Lu, M. Gratzl, *Anal. Chem.* **71**, 2821 (1999).
18. A. Devadoss, J. D. Burgess, *J. Am. Chem. Soc.* **126**, 10214 (2004).
19. A. J. Bard, G. Denuault, C. Lee, D. Mandler, D. O. Wipf, *Acc. Chem. Res.* **23**, 357 (1990).
20. M. V. Mirkin, B. Horrocks, *Anal. Chim. Acta*, **406**, 119 (2000).
21. M. V. Mirkin, B. Liu, S. A. Rotenberg, *Methods Enzymol.* **352**, 112 (2002).
22. T. Yasukawa, T. Kaya, T. Matsue, *Electroanalysis* **12**, 653 (2000).
23. J. Mauzeroll, A. J. Bard, *Proc. Natl. Acad. Sci. U.S.A.* **101**, 7862 (2004).
24. J. Mauzeroll, A. J. Bard, O. Owhadian, T. J. Monks, *Proc. Natl. Acad. Sci. U.S.A.* **101**, 17582 (2004).
25. R. N. Adams, *Anal. Chem.* **48**, 1126A (1976).
26. D. J. Leszczyszyn, J. A. Jankowski, O. H. Viveros, E. J. Diliberto, Jr., J. A. Near, R. M. Wightman, *J. Biol. Chem.* **265**, 14736 (1990).
27. R. M. Wightman, J. A. Jankowski, R. T. Kennedy, K. T. Kawagoe, T. J. Schroeder, D. J. Leszczyszyn, J. A. Near, E. J. Diliberto, Jr., O. H. Viveros, *Proc. Natl. Acad. Sci. U.S.A.* **88**, 10754 (1991).
28. D. Bruns, R. Jahn, *Nature* **377**, 62 (1995).
29. R. G. Staal, E. V. Mosharov, D. Sulzer, *Nat. Neurosci.* **7**, 341 (2004).
30. T. K. Chen, G. Luo, A. G. Ewing, *Anal. Chem.* **66**, 3031 (1994).
31. D. Schubert, M. LaCorbiere, F. G. Klier, J. H. Steinbach, *Brain Res.* **190**, 67 (1980).
32. A. Dahlstrom, J. Haggendal, T. Hokfelt, *Acta Physiol. Scand.* **67**, 289 (1966).
33. R. H. Chow, L. von Ruden, E. Neher, *Nature* **356**, 60 (1992).
34. G. Alvarez de Toledo, R. Fernandez-Chacon, J. M. Fernandez, *Nature* **363**, 554 (1993).
35. S. Choi, J. Klingauf, R. W. Tsien, *Philos. Trans. R. Soc. Lond. B Biol. Sci.* **358**, 695 (2003).

36. L. A. Sombers, H. J. Hanchar, T. L. Colliver,N. Wittenberg, A-S. Cans, S. Arbault, C. Amatore, A. G. Ewing, *J. Neurosci.* **24**, 303 (2004).
37. S. E. Zerby, A. G. Ewing, *Brain Res.* **712**, 1 (1996).
38. T. J. Schroeder, J. A. Jankowski, J. Senyshyn, R. W. Holz, R. M. Wightman, *J. Biol. Chem.* **269**, 17215 (1994).
39. U. Wingren, A. Wasteson, L. Enerback, *Int. Arch. Allergy Appl. Immunol.* **70**, 193 (1983).
40. W. M. Prucell, D. L. Cohen, T. H. Hanahoe, *Int. Arch. Allergy Appl. Immunol.* **90**, 382 (1989).
41. J. Cox, T. Gray, *Anal. Chem.* **61**, 2462 (1989).
42. J. Cox, T. Gray, *Electroanalysis* **2**, 107 (1990).
43. R. T. Kennedy, L. Huang, M. A. Atkinson, P. Dush, *Anal. Chem.* **65**, 1882 (1993).
44. W. Gorski, C.A. Aspinwall, J. R. Lakey, R. T. Kennedy, *J. Electroanal. Chem.* **425**, 191 (1997).
45. A. Albillos, G. Dernick, H. Horstmann, W. Almers, G. Alvarez de Toledo, M. Lindau, *Nature* **389**, 509 (1997).
46. L. Tabares, M. Lindau, G. Alvarez de Toledo, *Biochem. Soc. Trans.* **31**, 837 (2003).
47. L. W. Gong, I. Hafez, G. Alvarez de Toledo, M. Lindau, *J. Neurosci.* **23**, 7917 (2003).
48. T. L. Colliver, S. J. Pyott, M. Achalabun, A. G. Ewing, *J. Neurosci.* **20**, 5276 (2000).
49. G. Dernick, G. Alvarez de Toledo, M. Lindau, *Nat. Cell Biol.* **5**, 358 (2003).
50. A. Devadoss, J. D. Burgess, *Langmuir* **18,** 9617 (2002).
51. K. Simons, E. Ikonen, *Science* **290**, 1721 (2000).
52. A. J. Bard, M. V. Mirkin, Eds., *Scanning Electrochemical Microscopy*, Marcel Dekker: New York, NY, 2001.
53. T. Yasukawa, I. Uchida, T. Matsue, *Biochim. Biophys. Acta* **1369**, 152 (1998).
54. B. Liu, S. A. Rotenberg, M. V. Mirkin, *Proc. Natl. Acad. Sci. U.S.A.* **97**, 9855 (2000).
55. B. Liu, W. Cheng, S. A. Rotenberg, M. V. Mirkin, *J. Electroanal. Chem.* **500**, 590 (2001).
56. J. M. Liebetrau, H. M. Miller, J. E. Baur, S. A. Takacs, V. Anupunpisit, P. A. Garris, D. O. Wipf, *Anal. Chem.* **75**, 563 (2003).
57. R. T. Kurulugama, D. O. Wipf, S. A. Takacs, S. Pongmayteegul, P. A. Garris, J. E. Baur, *Anal. Chem.* **77**, 1111 (2005).
58. C. Cai, B. Liu, M. V. Mirkin, H. A. Frank, J. F. Rusling, *Anal. Chem.* **74**, 114 (2002).
59. H. Shiku, T. Shiraishi, H. Ohya, T. Matsue, H. Abe, H. Hoshi, M. Kobayashi, *Anal. Chem.* **73**, 3751 (2001).
60. M. Gonsalves, A. L. Barker, J. V. Macpherson, P. R. Unwin, D. O'Hare, C. P. Winlove, *Biophys. J.* **78**, 1578 (2000).
61. M. Gonsalves, J. V. Macpherson, D. O'Hare, C. P. Winlove, P. R. Unwin, *Biochim. Biophys. Acta*, **1524**, 66 (2000).
62. A. D. Bangham, *Chem. Phys. Lipids* **64**, 275 (1993).
63. M. Montal, P. Mueller, *Proc. Natl. Acad. Sci. U.S.A.* **69**, 3561 (1972).
64. R. B. Gennis, *Biomembranes: Molecular Structure and Function*, Springer-Verlag: New York, NY, 1989.
65. H. Tien, *J. Phys. Chem.* **88**, 3172 (1984).
66. H. Tien, *Bioelectrochem. Bioenerg.* **13**, 299 (1984).
67. P. Krysinki, H. Tien, A. Ottova, *Biotechnol. Prog.* **15**, 974 (1999).
68. H. Tien, S. Wurster, A. Ottova, *Bioelectrochem. Bioenerg.* **42**, 77 (1997).
69. O. Medina, Y. Zhu, K. Keiremo, *Curr. Pharm. Des.* **10**, 2981 (2004).
70. R. Mainardes, L. Silva, *Curr. Drug Targets* **5**, 449 (2004).
71. D. Meisner, M. Mezei, *Adv. Drug Deliv. Rev.* **16**, 75 (1995).
72. A. Chonn, P. Cullis, *Curr. Opin. Biotechnol.* **6**, 698 (1995).
73. N. Maurer, D. Fenske, P. Cullis, *Expert Opin. Biol. Ther.* **1**, 923 (2001).
74. D. Lasic, *Trends Biotechnol.* **16**, 307 (1998).

75. P. Aikens, S. Friberg, *Curr. Opin. Colloid Interface Sci.* **1**, 672 (1996).
76. A. Karlsson, R. Karlsson, M. Karlsson, A. S. Cans, A. Stromberg, F. Ryttsen, O. Orwar, *Nature* **409**, 150 (2001).
77. M. Karlsson, K. Nolkrantz, M. Davidson, A. Stromberg, F. Ryttsen, B. Akerman, O. Orwar, *Anal. Chem.* **72**, 5857 (2000).
78. M. Karlsson, K. Sott, A. S. Cans, A. Karlsson, R. Karlsson, O. Orwar, *Langmuir* **17**, 6754 (2001).
79. A. S. Cans, N. Wittenberg, R. Karlsson, L. Sombers, M. Karlsson, O. Orwar, A. G. Ewing, *Proc. Natl. Acad. Sci. U.S.A.* **100**, 400 (2003).
80. A. S. Cans, N. Wittenberg, D. Eves, R. Karlsson, A. Karlsson, O. Orwar, A. G. Ewing, *Anal. Chem.* **75**, 4168 (2003).
81. L. J. Breckenridge, W. Almers, *Proc. Natl. Acad. Sci. U.S.A.* **84**, 1945 (1987).
82. C. Amatore, Y. Bouret, E. R. Travis, R. M. Wightman, *Biochimie* **82**, 481 (2000).
83. C. Amatore, Y. Bouret, E. R. Travis, R. M. Wightman, *Angew. Chem. Int. Ed.* **39**, 1952 (2000).
84. J. R. Monck, G. Alvarez de Toledo, J. M. Fernandez, *Proc. Natl. Acad. Sci. U.S.A.* **87**, 7804 (1990).
85. Y. A. Chizmadzhev, D. A. Kumenko, P. I. Kuzmin, L. V. Chernomordik, J. Zimmerberg, F. S. Cohen, *Biophys. J.* **76**, 2951 (1999).
86. M. A. Bunin, R. M. Wightman, *J. Neurosci.* **18**, 4854 (1998).
87. M. A. Bunin, R. M. Wightman, *Trends Neurosci.* **22**, 377 (1999).
88. W. Bowyer, M. Clark, J. Ingram, *Anal. Chem.* **64**, 459 (1992).
89. R.A Clark, P.B Heitpas, A. G. Ewing, *Anal. Chem.* **69**, 259 (1997).
90. R.A Clark, A. G. Ewing, *Anal. Chem.* **70**, 1119 (1998).
91. C. D. T. Bratten, P. H. Cobbold, J. M. Cooper, *Anal. Chem.* **69**, 253 (1997).
92. C. D. T. Bratten, P. H. Cobbold, J. M. Cooper, *Chem. Commun.* **4**, 471 (1998).
93. C. D. T. Bratten, P. H. Cobbold, J. M. Cooper, *Anal. Chem.* **70**, 1164 (1998).
94. J. C. Ball, D. L. Scott, J. K. Lumpp, S. Daunert, J. Wang, L. G. Bachas, *Anal. Chem.* **72**, 497 (2000).
95. J. C. Ball, J.K, Lumpp, S. Daunert, L. G. Bachas, *Electroanalysis*, **12**, 685 (2000).
96. A. F. Dias, G. Dernick, V. Valero, M. G. Yong, C. D. James, H. G. Craighead, M. Lindau, *Nanotechnology* **13**, 285 (2002).
97. M. Gratzl, C. Yi, *Anal. Chem.* **65**, 2085 (1993).
98. C. Yi, M. Gratzl, *Anal. Chem.* **66**, 1976 (1994).
99. C. E. Banks, T. J. Davies, R. G. Evans G. Hignett, A. J. Wain, N. S. Lawrence, J. D. Wadhawan, F. Marken, R. G. Compton, *Phys. Chem. Chem. Phys.* **5**, 4053 (2003).
100. M. Jansson, A. Emmer, J. Roeraade, U. Lindberg, B. Hok, *J. Chromatogr.* **626**, 310 (1992).
101. R. Kashyap, M. Gratzl, *Anal. Chem.* **70**, 1468 (1998).
102. R. M. Wightman, D. O. Wipf in *Electroanalytical Chemistry*, A. J. Bard, Ed., Marcel Dekker: New York, NY, Vol. 15, 1998.
103. T. Yasukawa, A. Glidle, J. M. Cooper, T. Matsue, *Anal. Chem.* **74**, 5001 (2002).
104. K. P. Troyer, R. M. Wightman, *Anal. Chem.* **74**, 5370 (2002).
105. C. Earles, J. O. Shenk, *Synapse*, **33**, 230 (1999).
106. T. M. Olefirowicz, A. G. Ewing, *J. Neurosci. Methods* **34**, 11 (1990).
107. T. M. Olefirowicz, A. G. Ewing, *Anal. Chem.* **62**, 1872 (1990).
108. A. Meulemans, B. Poulain, G. Baux, L. Tauc, D. Henzel, *Anal. Chem.* **58**, 2088 (1986).
109. A. Meulemans, B. Poulain, G. Baux, L. Tauc, *Brain Res.* **414**, 158 (1987).
110. T. K. Chen, Y. Y. Lau, D. K. Y. Wong, A. G. Ewing, *Anal. Chem.* **64**, 1264 (1992).
111. Y. Y. Lau, J. B. Chien, D. K. Y. Wong, A. G. Ewing, *Electroanalysis* **3**, 87 (1991).
112. Y. Y. Lau, D. K. Y. Wong, A. G. Ewing, *Microchem. J.* **47**, 308 (1993).
113. Y. Y. Lau, T. Abe, A. G. Ewing, *Anal. Chem.* **64**, 1702 (1992).

114. J. B. Chien, R. A. Wallingford, A. G. Ewing, *J. Neurochem.* **54**, 633 (1990).
115. T. Abe, Y. Y. Lau, A. G. Ewing, *J. Am. Chem. Soc.* **113**, 7421 (1991).
116. T. Abe, Y. Y. Lau, A. G. Ewing, *Anal. Chem.* **64**, 2160 (1992).
117. P. Pantano, W. G. Kuhr, *Anal. Chem.* **65**, 623 (1993).
118. P. Pantano, T. H. Morton, W. G. Kuhr, *J. Am. Chem. Soc.* **113**, 1832 (1991).
119. P. Pantano, W. G. Kuhr, *Electroanalysis* **7**, 405 (1995).
120. E. V. Mosharov, L. W. Gong, B. Khanna, D. Sulzer, M. Lindau, *J. Neurosci.* **23**, 5835 (2003).

## 17.2 SINGLE MOLECULE ELECTROCHEMISTRY

*Fu-Ren F. Fan*

The University of Texas at Austin, Texas, USA

### 17.2.1 Introduction

The detection of single molecules, their characterization, and their chemical and physical manipulation are within current scientific capability and are of significant interest. A number of electrochemical techniques have been used in recent years to detect single molecules or ions and to study single electron-transfer events. We focus here on a few topics involving these processes. These include trapping an electroactive molecule in solution between a small ultramicroelectrode (UME, see Chapter 6) tip and a conductive substrate in a scanning electrochemical microscope (SECM, see Chapter 12). In this arrangement, the tip current represents repeated collisions and electron transfer of the molecule with the tip. An alternative approach is to use electrogenerated chemiluminescence (ECL, see Chapter 13) in which the product of the electron transfer of the electroactive molecules reacts to form an excited state that emits a photon, which can be detected with a time-resolved single photon counter. The third approach is to utilize very small UME or nanoparticles to study quantized double layer charging associated with single electron-transfer events. The final approach we illustrate is the deposition of molecules, particularly polymers or macromolecules of biological interest, on a mica surface and subsequent imaging of the surface topology with a highly sensitive SECM or scanning tunneling microscope (STM). This technique requires the use of a high relative humidity (RH) to form a thin film of water on the mica surface that allows electrochemical reactions to take place and produce a faradaic current (~1 pA).

### 17.2.2 Special topics

#### *17.2.2.1 Scanning electrochemical microscopy (SECM) and single molecule electrochemistry*

***(a) Operational principles***

Trapping of a molecule in solution and detection of the electrolysis current are carried out with SECM (1). The principle and various techniques of SECM have been described in

Chapter 12 of this handbook. We describe here only very briefly how this technique can be used to study the electrochemistry of a single molecule and its underlying operational principle. Detailed discussions on earlier SECM works can be found in reference (1) and the literature cited therein.

SECM is based on observing the electrolysis current of an electroactive species, A, at a very small (nm–μm) electrode (an UME or SECM tip, see Chapter 6) to form a product, $A^+$, as shown in the following oxidation reaction

$$A \rightarrow A^+ + e \tag{17.2.1}$$

in which e is the electron charge. The current that flows represents the flux A to the electrode as it diffuses to the tip. The presence of a surface near the tip can affect the tip current, $i_T$, in two ways. When the tip is close to the surface, diffusion is blocked; this causes a decrease in the current. If, however, the product of the tip reaction $A^+$ can be reduced back to A at the surface, then an additional flux of A to the tip occurs (termed positive feedback), and the tip current is increased compared to the tip current when it is far away from the surface, $i^0_{T,\infty}$. If the tip is a conductive disk in an insulating plane, the tip radius $a$ can be found from the following equation (2)

$$i^0_{T,\infty} = 4nFDC^* a \tag{17.2.2}$$

where $D$ is the diffusion coefficient of $A$, $C^*$ is its concentration, and $F$ is Faraday's constant.

Current instrumentation does not allow measurement of the charge or current from single electron-transfer events at an electrode. To detect a single molecule electrochemically, one must provide some amplification process. In the SECM experiment, illustrated schematically in Figure 17.2.1, this amplification is provided by the positive feedback process, i.e., the repeated conversion of A to B at the tip and B to A at the substrate as the molecule, in the oxidized or reduced state, shuttles back and forth between the tip and substrate. Since the transport between the tip and the substrate is by diffusion, the transit time, $\tau$, between the two electrodes separated by a distance $d$ is about $d^2/2D$, in which $D$ is the diffusion coefficient of A. If $d = 10$ nm and $D = 10^{-5}$ cm$^2$/sec, then $\tau = 5 \times 10^{-8}$ sec or the molecule cycles $10^7$ times per second. If each cycle results in the exchange of one electron ($1.6 \times 10^{-19}$C), then an average current of about 1.6 pA will flow. Thus, positive feedback provides a 10-million-fold amplification that results in a readily measurable current. It is necessary to trap the molecule within the small pocket of solution in the gap between the tip and substrate for a sufficient time to make the measurement possible, which is governed by the time constant of the picoammeter.

***(b) Tip fabrication and experimental methods***

The single-molecule trapping experiments require a tip with a diameter on the order of 10–20 nm and the particular geometry that results from the procedures used in the tip preparation. The ultramicrotips used in this experiment were prepared by insulating an electrochemically sharpened Pt–Ir (80:20) wire (0.250-mm diameter) by passing it through molten Apiezon wax or polyethylene based on the procedure used by Nagahara *et al*. (3). The insulated tip was then mounted on the SECM in a cell containing a redox electrolyte

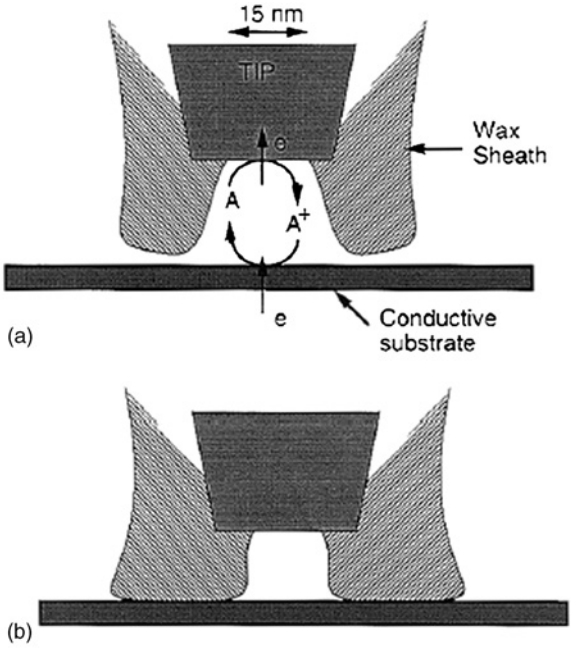


**Figure 17.2.1** (A) Idealized diagram of the trapping of molecule A that is oxidized at the tip electrode. The product $A^+$ is reduced at the substrate. (B) Schematic diagram of the effect of compressing wax tip coating against substrate. Adapted with permission from reference (8).

(e.g., 2 mM [(trimethylammonio)methyl]ferrocene ($Cp_2FeTMA^+$) in 1.0 M $NaNO_3$). The success of the tip insulation was checked by cyclic voltammetry in this solution. For a well-insulated tip, $i_T$, during an initial scan, was less than 50 fA. The very end of the tip was then exposed in the SECM by the following procedure. The potentials of the tip and a conductive substrate (e.g., indium tin oxide (ITO)) were biased at suitable values (e.g., 0.60 V vs. SCE for the tip and −0.20 V for the substrate) with the SECM operated in the constant-current mode (e.g., with a reference current of 10 pA). As the well-insulated tip approached the surface of the substrate, the onset of an enhanced current flow caused the z-piezo to retract the tip. This process produced a hole in the tip insulation at the point of closest approach of tip to substrate, while leaving most of the tip still insulated. The exposed area of the tip was estimated from the steady-state tip current with the tip far away from the substrate (equation 17.2.2). The basic instrument used in this experiment is a custom-built scanning probe microscope (SPM) (4) capable of both STM and SECM measurements with a current sensitivity of 50 fA for SECM experiments. The electrochemical cell contained a Pt counter electrode and an SCE as the reference electrode.

***(c) Experimental results and data analyses***

***SECM approach tip current vs. distance curve.*** The SMD experiment, as stated above, requires a tip of small diameter that is slightly recessed within the soft insulating sheath.

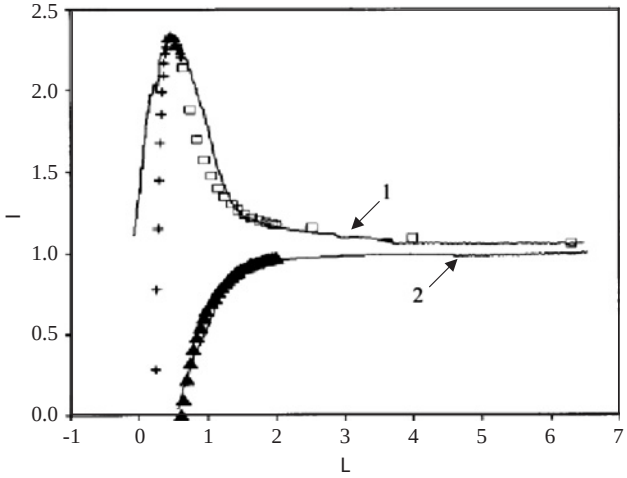


**Figure 17.2.2** Dependence of tip current (normalized to $i_{T,\infty}$) on relative tip displacement (normalized to tip radius) over a conductive n-$TiO_2$ substrate ($E_S = -0.7$ V vs. SCE), curve 1, and an insulating n-$TiO_2$ substrate ($E_S = 0.0$ V vs. SCE), curve 2, in a solution containing 2 mM $Cp_2FeTMA^+$ and 1.0 M $NaNO_3$. The tip was biased at 0.60 V vs. SCE. The tip moved to the substrate surface at a rate of 38 Å/sec. Solid curves are experimental data and symbols are theory. Squares: Simulated data for conducting substrate; pluses: calculated data based on equation 17.2.4; triangles: simulated data for insulating substrate. Fitting parameters: $a = 45$ nm, $a_0 = 67$ nm, $l = 28$ nm, and $D = 5.0 \times 10^{-6}$ $cm^2$/sec. Experimental $i_{T,\infty}$ is equal to 9.0 pA. Adapted with permission from reference (8).

While it is not possible to remove the tip after preparation from the SECM cell and examine it by electron microscopy, information about the exposed area of the tip and the shapes of the tip and insulating sheaths can be obtained indirectly from SECM approach curves where $i_T$ is measured as a function of tip–substrate spacing, $d$, as the tip is moved toward the substrate. Tips with correct configuration show approach curves similar to those shown in Figure 17.2.2. These curves were obtained with a solution containing 2 mM $Cp_2FeTMA^+$ and 1.0 M $NaNO_3$, with the tip biased at 0.6 V vs. SCE (where $Cp_2FeTMA^+$ oxidation is diffusion-controlled). In the experiment shown in curve 1, the n-$TiO_2$ substrate (a semiconductor) was biased at $-0.7$ V vs. SCE (a potential well negative of its flat-band potential, $V_{fb} \sim -0.25$ V vs. SCE), so that $Cp_2FeTMA^{2+}$ generated at the tip was rapidly reduced back to $Cp_2FeTMA^+$ at the n-$TiO_2$ surface, since it is operated in the accumulation region and acts as a conductor. A similar approach curve was also observed for the same solution and ITO substrate (5). When the n-$TiO_2$ substrate is biased at a potential positive of $V_{fb}$ (e.g., 0 V vs. SCE), the n-$TiO_2$ surface becomes insulating (it is now operated in the depletion region). The negative feedback approach curve is shown in curve 2. Hence, experiments can be carried out with the same tip and solution without making any changes, while the conductance of an n-$TiO_2$ substrate is controlled by adjusting bias potential.

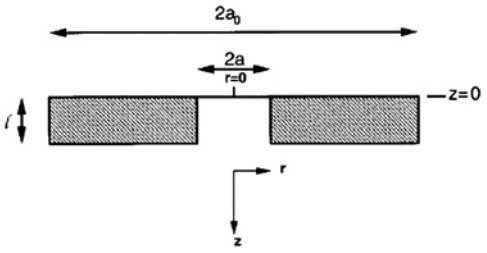


**Scheme 1**

Different from an inlaid microdisk electrode with $i^0_{T,\infty}$ expressed in equation 17.2.2, a recessed disk-shaped electrode with the geometry shown in Scheme 1, $i_{T,\infty}$ is given by an approximate equation

$$i_{T,\infty} = \left[\frac{\pi a}{(4l + \pi a)}\right] i^0_{T,\infty} \tag{17.2.3}$$

in which $l$ is the recessed depth of the disk electrode. $i_{T,\infty}$ can also be obtained by digital simulation as a function of $L = l/a$ (as tabulated in Table 1 of reference (8)). For the normalized tip current ($I_T = i_{T,\infty} / i^0_{T,\infty}$), the difference between the value calculated by the approximate analytical equation (equation 17.2.3) and the simulated value is less than 3.4%, when $l > 0.2a$.

The shape of the approach curve also depends on the tip shape. For a coplanar disk, the tip current, $i_{T,}$ increases monotonically with decreasing $d$ for a conductive substrate and diffusion-controlled reactions at tip and substrate (6). For a recessed disk, the SECM positive feedback process starts to become significant when the tip approaches a conductive n-$TiO_2$ substrate (biased at $-0.7$ V vs. SCE) to within a few tip diameters (curve 1 of Figure 17.2.2). The agreement between experimental and simulated data (for $l = 0.62a$, $a = 45$ nm) is reasonably good up to a distance $d \sim l$, at which point the insulating sheath starts to compress against the substrate. Different from an inlaid disk electrode, with a recessed disk, $i_T$ increases to reach a maximum and then decreases as the tip comes even closer before showing a large increase (not shown in curve 1 of Figure 17.2.2) presumably because of the occurrence of electron tunneling between tip and substrate. Although this current decrease might be attributed to heterogeneous kinetic effects on the electron-transfer reactions (7), this behavior was observed at even more extreme tip or substrate potentials for various substrates and other redox couples. We thus believe that this region of current behavior is associated with the deformation of the soft insulating sheath as it is press against the substrate at very small distance as shown in Figure 17.2.1B.

Consider an idealized thin-layer cell as shown in Scheme 2, where we assume that the insulating wax flows inward and outward by equal amounts as it is compressed against the substrate, the steady-state current of the thin-layer cell confined by the disk, substrate, and insulating sheath is given by the following equation (8),

$$I_{TLC} = \left\{\frac{\pi[2la^2 - \Delta l(a_0^2 + a^2)]}{[8a(l - \Delta l)^2]}\right\} i^0_{T,\infty} \tag{17.2.4}$$

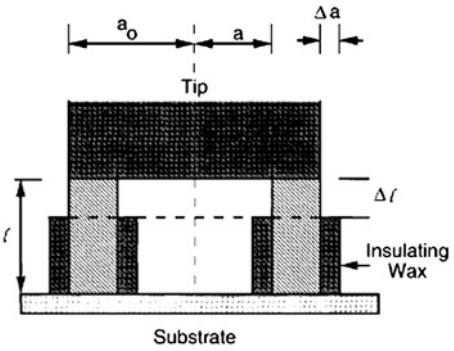


**Scheme 2**

where $a$ is the initial disk radius, $a_0$ is the initial outer radius of the insulating sheath before the compression occurs, and $\Delta l$ is the change of the recessed depth of the disk electrode during compression. As implied in equation 17.2.4, if $a_0 < \sqrt{3}a$, the tip current will increase to reach a maximum at $\Delta l$ equal to $l(3a^2 - a_0^2)/(a_0^2 + a^2)$ and then decrease as the tip approaches even closer to the surface of the substrate; otherwise, it will reach the maximum at $\Delta l = 0$. As shown in curve 1 of Figure 17.2.2, there is some discrepancy between the experimental curve and the theoretically calculated data based on equation 17.2.4, perhaps because $\Delta l$ is not exactly equal to the nominal tip displacement due to the finite compressibility of the insulting wax and deviations from the assumed idealized model. With a diffusion coefficient of $Cp_2FeTMA^+$ of $5 \times 10^{-6}$ cm$^2$/sec, the theoretical fit of the experimental approach curve yields $a = 45$ nm, $a_0 = 67$ nm, and $l = 28$ nm.

When the n-$TiO_2$ substrate is in its insulating state (e.g., biased at 0 V vs. SCE), the approach curve is that shown in curve 2 of Figure 17.2.2. Here the approach behavior of a recessed tip is similar to that of a usual inlaid disk electrode and decreases monotonically with decreasing distance.

***Fluctuation of the tip current at small distances.*** Figure 17.2.3A shows an experiment with a water soluble ferrocene derivative, $Cp_2FeTMA^+$, as the species oxidized at the tip to produce the ferrocenium form that is then reduced at the conductive ITO substrate (5). In this experiment, the tip (radius ~10 nm) was brought to a position where the approach curve was near its minimum current value, estimated as about 10 nm. At the concentration (~2 mM) of electro active species employed, the resultant volume under the tip would contain, on the average, one molecule of $Cp_2FeTMA^+$. When the current at the tip is recorded with time, one finds fluctuations of the current (on top of the noise signal on the order of 0.2 pA), which were interpreted to indicate the presence of zero, one, or two molecules. This finding is clarified by examining the data by autocorrelation and probability density function (PDF) analyses (Figure 17.2.3B and C) as discussed below. The time correlation function (TCF) (or autocorrelation function) analysis indicated multiple fluctuation processes with the frequencies on the order of a few tenths of a Hertz. The PDF contains several bell-shaped peaks. The most probable tip currents at the given cell parameters and concentrations are spaced 0.5 ($\pm$0.1 pA) apart. These fluctuation amplitudes of the tip current–time series correspond quite well with the contribution to the current expected for

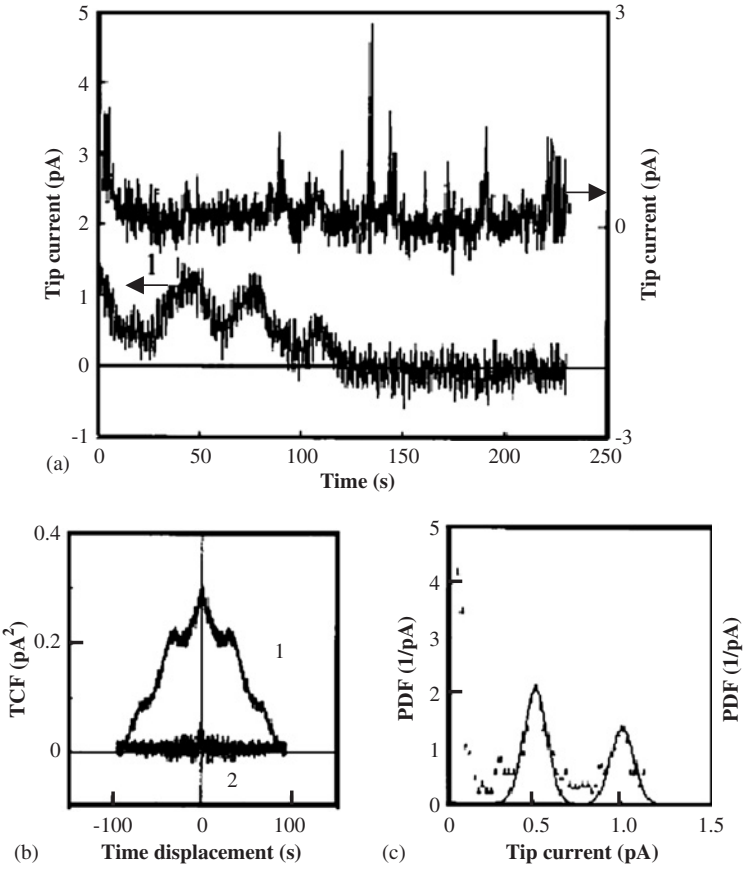


**Figure 17.2.3** (A) Curve 1: Tip current with time for a solution of 2 mM $Cp_2FeTMA^+$ and 2.0 M $NaNO_3$ with a Pt–Ir tip at 0.55 V vs. SCE and an ITO substrate at −0.3 V; $d$ ~ 10 nm. Curve 2: Time series of the tip current for $d$ within the tunneling range in a solution containing only 2.0 M $NaNO_3$; tip radius ~7 nm. Data sampling rate was 0.4 sec per point. (B) Corresponding time correlation function. (C) Probability density function of time series 1 in (A). Adapted with permission from reference (8).

a single molecule in a thin-layer cell of that geometry. Control experiments with the tip at longer and closer distances to the ITO and with two different species that oxidize at two different potentials are consistent with this interpretation (5).

We compare the fluctuation behavior of the $i_T$ on both conductive and insulating substrates by using an n-$TiO_2$ electrode as the substrate. As found in the previous studies, the fluctuation intensity in $i_T$ was strongly dependent on the distance and the conductance states of the substrate. To ensure that we were measuring two different fluctuation behaviors at the same distance, we used the same substrate, n-$TiO_2$, held at a fixed distance and changed in conductance simply by varying its bias potential. When the tip was far away from the substrate surface (e.g., $d/a > 2$), as expected, only a very small fluctuation in $i_T$ was observed when the substrate was either conductive (biased at −0.7 V vs. SCE) or

insulating (biased at 0.0 V vs. SCE) (see Figure 17.2.4A). When the tip approached the recessed depth of the disk electrode (i.e., $d < 1$), considerable fluctuation in $i_T$ was observed when the substrate was conductive, while $i_T$ was essentially zero and its fluctuation was negligibly small when the substrate was insulating (see Figure 17.2.4B). This suggests that the positive feedback of the SECM is responsible for the high amplification of the $i_T$ When the tip was moved even closer to the surface of the substrate, $i_T$ decreased because of the decrease of the active area of the electrode (as discussed in the previous section), but the relative fluctuation of $i_T$ intensified (see Figure 17.2.4C).

In spite of the lack of sufficient knowledge of the basic mechanisms of the fluctuation phenomena, a limited description of the general shape of the current fluctuation is of interest. Assuming that the redox molecule diffuses inside the TLC with a constant diffusion coefficient, there are at least two possibilities which might cause $i_T$ to change with time: (1) changes in $d$ and the electrode area, for example, because of temperature fluctuations and (2) fluctuations in the number of molecules inside the TLC, $N$. The probability of large step or quantized change in $d$ without changing $N$ is small. A continuous change in $d$ without changing $N$ cannot cause a stepwise fluctuation in $i_T$, either; however, it might account for a slow drift of the TLC current. We cannot rule out the possibility that the electric field in the gap may affect the observed behavior, especially at very small supporting electrolyte concentration, which will be discussed later. In the work described here, however, a high concentration of supporting electrolyte was employed.

***Data analyses.*** Exact mathematical descriptions of the data shown in Figures 17.2.3A and 17.2.4C are difficult in the absence of a better understanding of the processes causing the large current fluctuations and of the microscopically detailed cell geometry. However, one can analyze the results by taking the data to be non-deterministic or random. In cases where no explicit mathematical equations can be written for the microscopic pictures of the time histories produced by a random phenomenon, statistical procedures are usually used to define the descriptive properties of the data (9, 10). Three of the basic statistical properties for describing random data, i.e., TCF, spectral density function (SDF), and PDF, for the time series in Figure 17.2.4C are shown in Figure 17.2.5. Those for the time series in Figure 17.2.3A are shown in Figure 17.2.3B and C (see the discussion below). The TCF is a measure of time-related properties in the data that are separated by fixed time delays and is defined as

$$\mathrm{TCF}\ (\tau) = \lim_{T\to\infty} \frac{1}{T} \int_0^T x(t)x(t+\tau)dt \tag{17.2.5}$$

in which $\tau$ is the time delay and $T$ is the available record length or some desired portion of the record length. The SDF of $x(t)$ is related to TCF through Fourier transformation and is given by

$$\mathrm{SDF}\ (f) = 4\int_0^\infty \mathrm{TCF}(\tau)\cos(2\pi f\tau)d\tau \tag{17.2.6}$$

in which $f$ is the frequency. Both TCF and SDF provide information on the rate of fluctuation in a time history record.

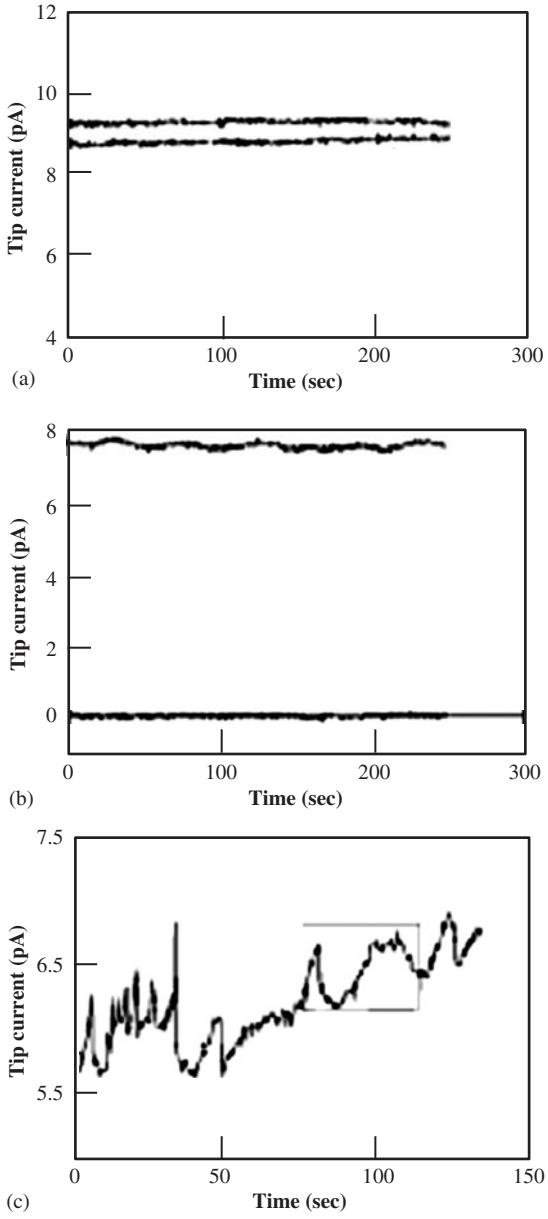


**Figure 17.2.4** Time evolution of the tip current observed at a tip potential $E_T = 0.6$ V and a n-$TiO_2$ substrate potential $E_S = -0.7$ V (curve 1) or 0.0 V (curve 2) vs. SCE for various distances in a solution containing 2 mM $Cp_2FeTMA^+$ and 1.0 M $NaNO_3$. The data sampling rate was 0.4 sec per point. (A) With tip far away from the substrate; (B) $d \sim 13$ nm, which gave an average steady-state current of ~7.6 pA when $E_S = -0.7$ V vs. SCE; (C) $d \sim 11$ nm, which gave an average steady-state tip current of ~6.1 pA. Adapted with permission from reference (8).

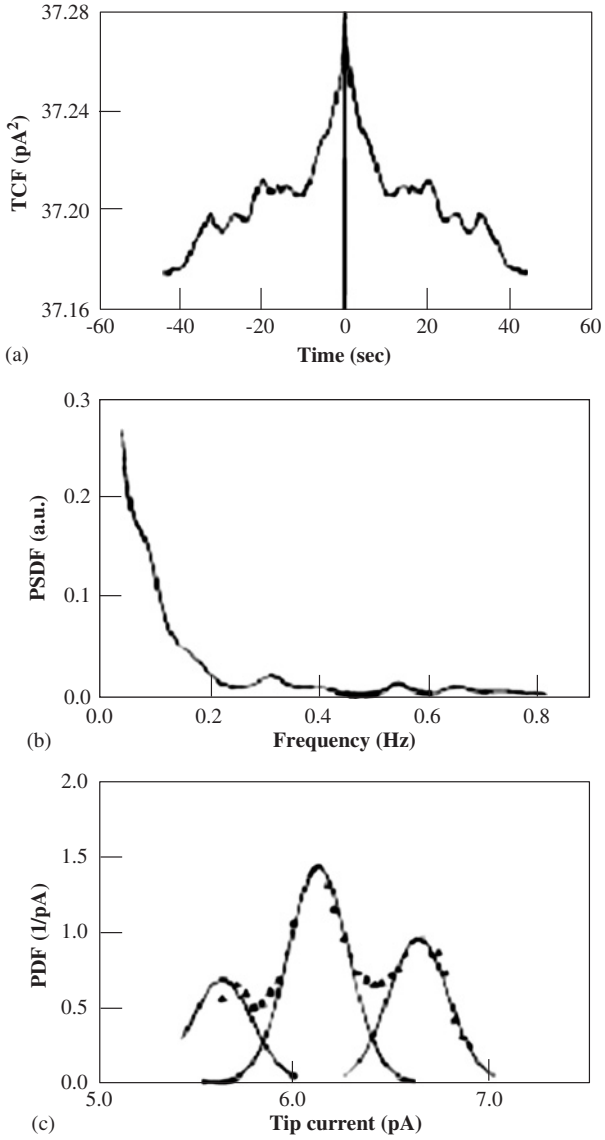


**Figure 17.2.5** (A) Time correlation function, (B) power spectral density function, and (C) probability density function of the time series in Figure 17.2.4C. Adapted with permission from reference (8).

As shown in Figure 17.2.5A, the coherence of the data is high, and TCF indicates that several fluctuation processes occur at frequencies on the order of a few tenths of Hertz. Parallel to the TCF, the SDF of the time series is fairly broad and contains several peaks at frequencies on the order of fractions of Hertz (Figure 17.2.5B). From the autocorrelation of the time series at zero and infinite time displacement, a mean square $i_T$ of 37.3

$(pA)^2$ and a mean $i_T$ of 6.1 pA can be obtained, respectively. A mean tip current of 6.1 pA is consistent with the estimate from Figure 17.2.4B, which shows that $i_T$ fluctuates around 6 pA with fluctuating amplitude of about 0.5 pA. A more accurate analysis is based on the PDF, which describes the probability that the data will assume a value within some defined range at any instant of time. In equation form, it is defined as follows:

$$\mathrm{PDF} = \lim_{\Delta x \to \infty} \frac{\mathrm{Prob}[x < x(t) < x + \Delta x]}{\Delta x} = \lim_{\Delta x \to 0} \left[ \lim_{T \to \infty} \frac{Tx}{T} \right] \tag{17.2.7}$$

in which $\mathrm{Prob}[x < x(t) < x + \Delta x]$ is the probability that $x(t)$ assumes a value within the range between $x$ and $(x + \Delta x)$, and $Tx$ is the total amount of time that $x(t)$ falls inside the range $(x, x + \Delta x)$ during an observation time $T$. As shown in Figure 17.2.5C, the PDF of the time series of Figure 17.2.4C contains several Gaussian peaks. The most probable tip currents are spaced 0.5 pA apart, with a standard deviation of ~0.1 pA.

Some statistical methods have also been applied to analyze the $i_T$ time series observed on a different conductive ITO substrate (as shown in Figure 17.2.3A). This series was obtained using a tip with a much smaller radius ($a \sim 7$ nm) than that used in Figure 17.2.4 so that the average $i_T$ was much smaller than that shown in Figure 17.2.4C for comparable tip–substrate spacing and the same concentration of electroactive species; however, similar fluctuation amplitude in $i_T$ was observed in both cases. The TCF of the series (see Figure 17.2.3B) also shows that multiple fluctuation processes with fluctuating frequencies in the range of fractions of hertz are involved. The probability density plot shown in Figure 17.2.3C again is characterized by a stepwise transition character of the fluctuation of $i_T$. Thus, the fluctuation pattern of $i_T$ is apparently not strongly dependent on the substrate as long as the heterogeneous electron-transfer kinetics on the substrate is fast.

It is interesting to notice that the current fluctuations mapped as the PDF will be related to the probability of the number of molecules in the tip–substrate gap as a function of solution composition. At a solution concentration of 2 mM for a solution volume of $10^{-18}$ $cm^3$, for example, the actual occupancy is one molecule. However, the actual occupancy, because of fluctuation, is governed by the Poisson distribution (10),

$$\mathrm{P_b(m)} = (\mathrm{b^m/m!})\exp(-\mathrm{b}) \tag{17.2.8}$$

in which $P_b(\mathrm{m})$ is the probability of m molecules occupying the solution volume when the average occupancy is $b$. Thus, for $b = 1$, $P_b(0) = 0.368$, $P_b(1) = 0.368$, and $P_b(2) = 0.184$. The distribution shown in Figure 17.2.3C approaches this, favoring slightly less than an average of one molecule per gap volume.

#### *17.2.2.2 Electrogenerated chemiluminescence (ECL) on microelectrodes; single electron-transfer events*

##### *(a) Introduction and principles*

Electron-transfer theories (11) predict that the highly exothermic production of the ground states proceeds in the inverted region. This allows the formation of the excited state to be kinetically competitive with other non-radiative pathways which are predicted to occur near the diffusion-controlled limit. Time-resolved fluorescence quenching has commonly

been used to measure the rates to form the separated radical ions and ground state donor and acceptor molecules in the photoinduced electron-transfer reactions (12). The back electron-transfer rate to reform the emitting excited state, however, is not readily accessible from such experiments. This value can be obtained from ECL (13) providing the ECL efficiency and total rate of ion annihilation ($k_{annih}$) are known. The principle and various techniques of ECL are described in Chapter 13 of this handbook, and detailed discussions can be found in reference (13) and the literature cited therein.

***(b) Experimental methods***

As carried out in Collinson's experiments discussed below, high-speed electrochemical and photon-detection techniques were used to monitor the real time rate of ECL generation of several compounds, e.g., 9, 10-diphenylanthracene, DPA. In these experiments, a microelectrode in a flow cell is continuously stepped between the oxidation and reduction potentials of DPA to alternatively generate the radical ions. The cation and anion radicals react in a thin plane at a point where the inward and outward fluxes meet and subsequently produce light. The ECL intensity was monitored with a Hamamatsu 4632 PMT. A high-voltage power supply (Bertan Series 230) applied −800 V to the PMT. The PMT signal was amplified by a fast preamplifier (EG&G Ortec VT120A, 150 MHz bandpass, 200 gain) and the output was directed to the discriminator of a multichannel scaler (EG&G Ortec T-914). The discriminator level was set at −600 mV. A Wavetek Model 143 function generator applied a symmetric square wave to a silver counter electrode and triggered the multichannel scaler. The microelectrode was connected to a current amplifier. Particularly worth stressing is that these short-time steps (or high square-wave frequencies) are not suitable for larger electrodes because the current during the step is dominated by double-layer charging and the electrode potential does not follow the applied potential step waveform.

***(c) Results and data analyses***

In order to ensure that the electrode potentials are chosen so that the cation and anion radicals are produced at a diffusion-controlled rate at all frequencies, following frequency selection of the square wave, the cathodic and anodic potentials were adjusted so that they roughly correspond to those of the redox potentials for the generation of the cation and anion radicals (14). Figure 17.2.6 shows two cycles of the potential waveform applied to a gold disk (radius = 5 μm) and the resulting luminescence from a 0.6 mM DPA solution. Two pulses of light are observed from each cycle. When the potential is stepped positive, the cation radical reacts with the anion radical formed on the previous step in a reaction zone lying near the electrode surface. The light increases sharply as the diffusion layers meet and then decays as the reactants are depleted. If the cation and anion radicals are stable during the time scale of the experiment, equal-size light pulses should be obtained on the forward and reverse steps. Increasing the frequency of the applied square wave usually results in more equivalent luminescent curves. As shown in Figure 17.2.6, at ~1 kHz, a slightly smaller pulse of light is observed when the electrode is stepped from a negative to a positive potential, indicating that the DPA anion is less stable than the cation on this time scale. At ~20 kHz, both the cation and anion radical are stable as evident from the equivalent light pulses.

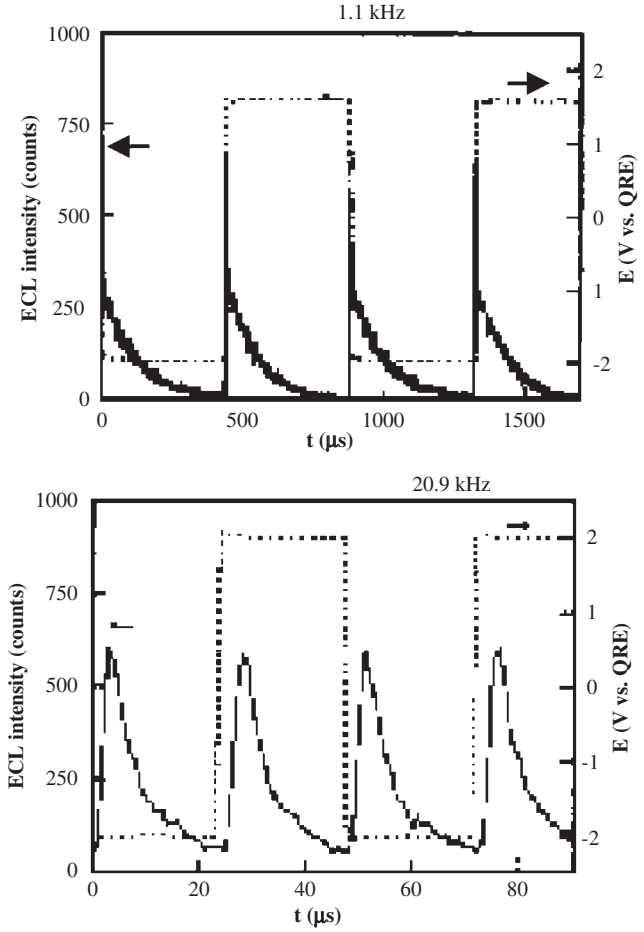


**Figure 17.2.6** Potential waveform with the corresponding ECL curves from 0.6 mM DPA at a gold disk (radius = 5 μm) in acetonitrile containing 0.2 M $TBAPF_6$ at two different frequencies. The ordinate represents the number of counts collected during 1-μsec time bins. The luminescence curves were summed 100 times. Adapted with permission from reference (14a).

When the dimensionless kinetic parameter, $\lambda_k = k_{annih} t_f C^*$, approaches infinity, the reaction layer is an infinitely thin parallel plane which moves nearly linearly away from the electrode surface with time. This plane of light broadens and becomes Gaussian-like as $\lambda_k$ decreases. When $\lambda_k$ drops below 1000, i.e., when $t_f$ and $C^*$ are significantly reduced, the transfer from diffusion to kinetic control begins and distinct changes in the width and the shift in the peak maximum of the ECL-time curves become apparent. The $k_{annih}$ can be theoretically evaluated from the characteristic shapes of ECL-time curves in dilute solutions and at reduced step times (cf. Chapter 3 of reference (13) for detailed theoretical discussion on ECL). For illustration, we show only some comparisons of the simulated curves

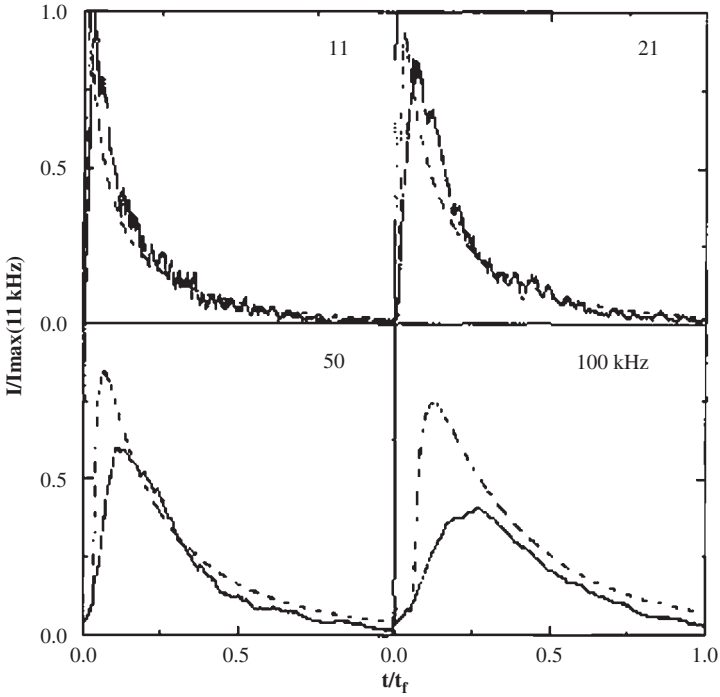


**Figure 17.2.7** Normalized ECL from 0.38 mM DPA in acetonitrile containing 0.1 M $TBAPF_6$ at a Pt disk (radius = 1 μm) (solid lines) and corresponding simulated curves (dashed lines) as a function of frequency of potential pulse. Simulations for $k_{annih} = 2 \times 10^{10}$/M/s and double-layer charging time constant, $RC_d$, of 0.10 μsec. Adapted with permission from reference (14b).

to the experimental data with a $k_{annih}$ of $2 \times 10^{10}$/M/sec in Figure 17.2.7 (14). Roughly agreeing with experimental observations, the simulation predicts certain features in the data such as the delay time in the initial ECL and the diminished amplitude and increased breath of the ECL curve with decreasing step time. The delay time is due to the electrochemical time constant (the product of the double-layer capacitance and the uncompensated solution resistance) whereas the diminished amplitude and increased breadth are due to the finite ECL kinetics. The simulation, however, does not predict the slow rise in emission or the substantially lower amplitude evident in Figure 17.2.7 as the step time is decreased from 48 to 5 μsec. Similar results were obtained with Au or Pt disk electrodes (radius = 3–10 μm), with different solvents, and with half the electrolyte concentration.

However, the shape of the ECL curve is dependent on the concentration of DPA. At higher concentration, e.g., 5.8 mM, distinct oscillation in the ECL intensity can be observed on the decaying emission. These features have been attributed to the direct interaction of the emission with the metal electrode due to the close proximity of the light-emitting species to the metal electrode surface (15). These effects were least apparent with carbon-fiber microelectrodes due to their low reflectivity and density of states. In this case,

diffusion-controlled $k_{annih}$ of $2 \times 10^{10}$/M/sec was measured for DPA in acetonitrile and $4 \times 10^{9}$/M/sec for DPA in propylene carbonate, a more viscous solvent.

In a later experiment (16), the DPA concentration was decreased to 15 μM and the temporal resolution to the nanosecond regime. In this case, an unsymmetrical waveform (a 500 μsec anodic pulse followed by a 50 μsec cathodic pulse) was used. The emission occurred predominantly during the shorter cathodic pulse (Figure 17.2.8) as the electrogenerated radical anion diffused into the sea of DPA radical cations generated in the anodic pulse. When the photons were counted over 1 sec intervals, no evidence for individual reaction events was observed. The ensemble average of the counts detected during 1000 cathodic voltage pulses also masked individual reaction events but revealed that the luminescence approached steady-state (Figure 17.2.8D). When events during a single cathodic pulse were viewed with greater temporal resolution (i.e., bin size of 5 nsec), photons

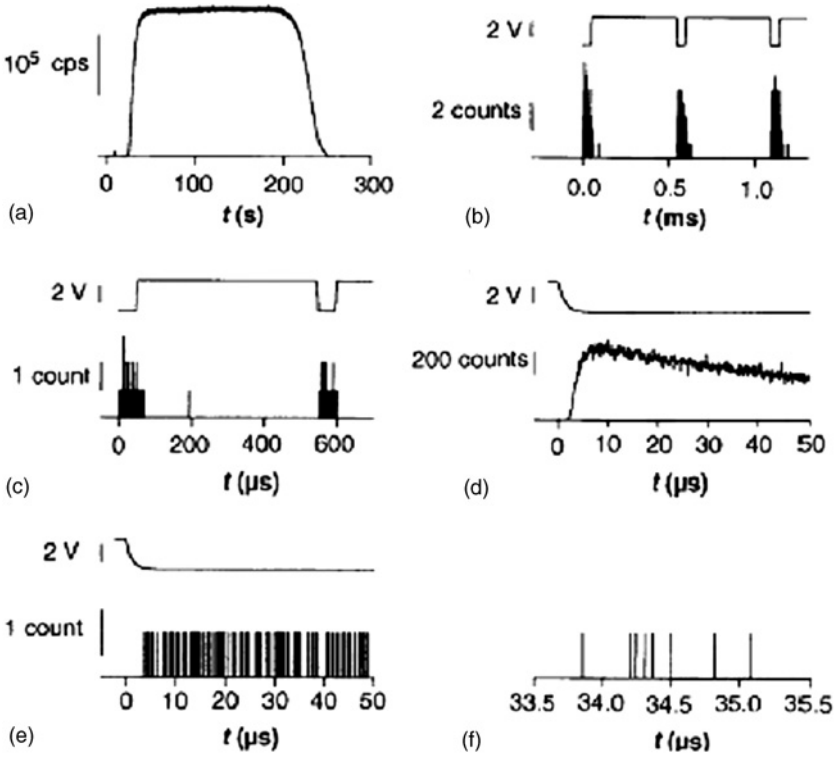


**Figure 17.2.8** Temporal resolution of single reaction events. (A) Chemiluminescence from a bolus of 15 μM DPA in acetonitrile containing 0.1 M $TBAPF_6$. The electrode was a gold disk (radius = 5.4 μm) pulsed from 1.7 to −2.1 V at 550-μsec intervals. Data collected during the time interval between 50 and 200 sec have been expanded through a successive decrease in the bin size from 1 sec (A) to 1 μsec (B), 100 nsec (C and D), and 5 nsec (E and F). The double-layer capacitance (14 pF) and the solution resistance (75 kΩ) were used to calculate the rise time of the voltage pulses shown in (D) and (E). The curve shown in (D) is an ensemble average of events measured during 1000 cathodic pulses. Adapted with permission from reference (16).

resulting from individual reactions were revealed (Figure 17.2.8E and F). Virtually no background photons were detected so the corrections were unnecessary. Thus, the individual photon counts shown in Figure 17.2.8E and F, resulted from single chemical reactions between individual DPA radical ions in solution.

The stochastic nature of these events was characterized in two ways. First, a histogram of the time between individual photons was constructed (Figure 17.2.9A). Such a histogram for random events should be an exponential whose frequency, *f*, gives the mean rate of the events (10). The value of *f* from the exponential was in excellent agreement with the mean rate of photon arrival obtained by ensemble averaging data from repetitive cathodic pulses. Second, the data followed a Poisson distribution. The measured value of *f* should be a function of the generation rate and diffusion of the radical ions, the rate and efficiency of the light-producing chemical reaction, as well as the photon collection efficiency. At concentrations greater than 20 μM, *f*, normalized by concentration and electrode area, was essentially constant (inset, Figure 17.2.9B). The ratio of the mean photon rate (accounting for the detection efficiency) and the mean rate of generation of radical anions during each cathodic pulse directly yields the probability of a reaction generating a photon, i.e., the ECL quantum yield, $\Phi_{ecl}$. At the high concentrations, this ratio yields a value of $\Phi_{ecl}$ of 6%, in good agreement reported values for DPA in acetonitrile. At lower concentrations, the normalized value of *f* decreases (inset, Figure 17.2.9B).

#### *17.2.2.3 Coulomb staircase (CS) in electrochemistry*

##### *(a) Electrode potential and double-layer structure effects on voltammetric behavior of nanoelectrodes*

All of the experiments described in Section 17.2.2.1 were carried out with a high concentration of supporting electrolyte so that electric field effects on the movement of the electroactive molecules were negligible. However, at low electrolyte concentrations, electric migration effects, in addition to diffusion, should be important; i.e., when the electroactive molecules make a significant contribution to the ionic strength, their movement to maintain electroneutrality (and double-layer charge equilibrium) contributes to their flux and hence to the current (17). We have performed several sets of SECM experiments to address this problem (18). The first involves oxidative voltammetric measurements on a positively-charged species ($Cp_2FeTMA^+$) at various gap separations *d*. The second experiment compared the limiting tip current for the oxidation of a positively-charged species ($Cp_2FeTMA^+$), a singly negatively-charged species ($Cp_2FeCOO^-$), and a doubly negatively-charged species ($Fe(CpCOO^-)_2$). This experiment was carried out by biasing the tip potential ($E_T$) at a constant value, e.g., 0.6 V vs. a platinum quasireference electrode (PtQRE), to obtain a limiting anodic $i_T$. $i_T$ was then monitored while the substrate potential ($E_S$) was scanned.

As shown in Figure 17.2.10, when the tip ($a \sim 18$ nm) was fairly far away from the ITO substrate, a steady-state plateau-shaped cyclic voltammogram (CV) was obtained for the oxidation of $Cp_2FeTMA^+$ in an aqueous solution containing no supporting electrolyte. When the tip was brought to a distance within the range where $i_T$ started to decrease significantly with decreasing *d*, a steady-state, somewhat peak-shaped voltammogram was obtained (curve 2). The dramatic decrease in $i_T$ with decreasing distance,

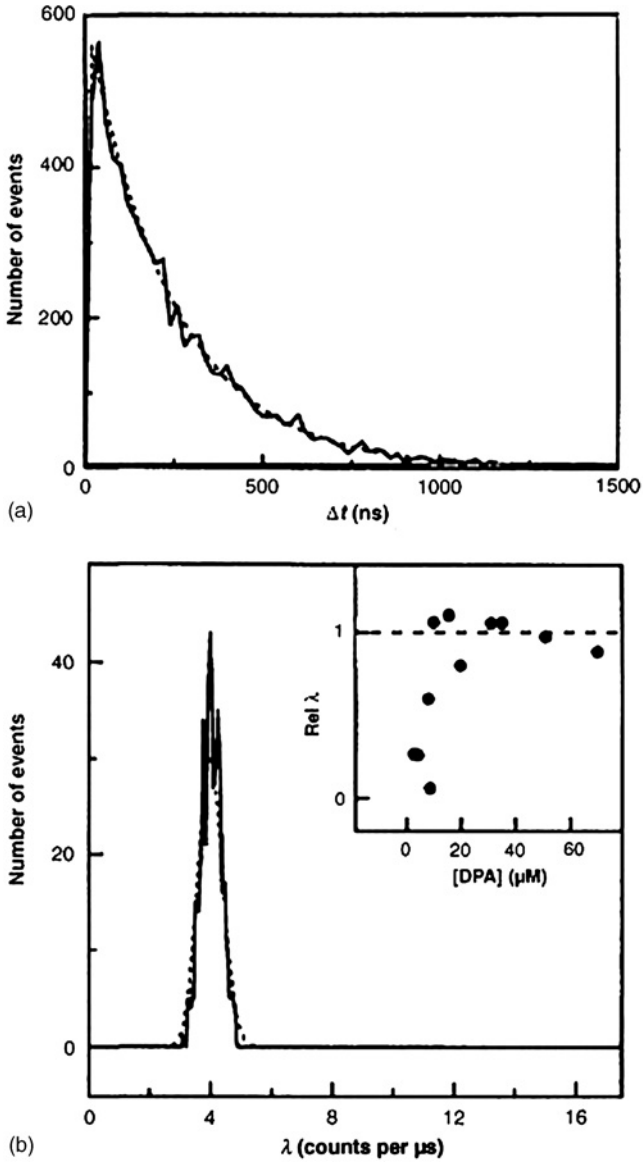


**Figure 17.2.9** ECL time series in acetonitrile solution containing 31 μM DPA. (A) Histogram (7000 interevent times and a bin size of 20 nsec) of interarrival times and (B) histogram (375 voltage pulses and a bin size of 0.8 counts per microsecond). The counts used were from the last 25 μsec of the voltage pulse where the emission rate is pseudo-steady state. Dashed line: (A) exponential fit to data with rate of 205 counts per 50 μsec and (B) Poisson fit to data with rate of 200 counts per 50 μsec. Other conditions are same as in Figure 17.2.8. Insert: Plot of relative f values (f normalized by DPA concentration and electrode area and given as a ratio of the highest value) obtained from Poisson distribution. Data were obtained with electrodes of radii of 5.4 or 2.5 μm. Adapted with permission from reference (16).

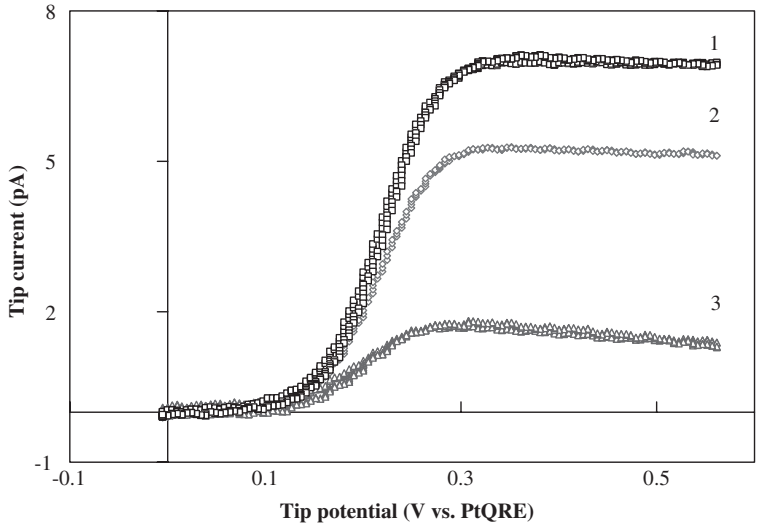


**Figure 17.2.10** SECM tip cyclic voltammograms of 2 mM $Cp_2FeTMA^+$ in an aqueous solution containing no supporting electrolyte at a Pt tip ($a \sim 18$ nm) at three different gap separations. Curve 1: Tip held far away from the substrate (ITO) surface. Curve 2: Tip at a distance within the range where the tip current started to decrease with decreasing distance. Curve 3: Tip closer to the surface as compared with curve 2. Tip potential scan rate 5 mV/sec for all cases. $E_S = -0.3$ V vs. PtQRE. (for colour version: see colour section at the end of the book).

as discussed previously, is mainly due to diffusion to the tip being hindered by the insulating sheath and by the decrease in the effective tip radius as the tip is pushed against the ITO substrate. The peaking became more evident as the tip was brought even closer to the surface (curve 3). No evident peaking under such conditions was observed in the presence of 1.0 M $NaNO_3$.

The results of the second experiment are shown in Figure 17.2.11A. When the tip was far away from the ITO surface, $i_T$, as expected, was essentially independent of $E_S$ in the potential range studied. However, at small $d$, a significant increase in the limiting $i_T$ with $Cp_2FeTMA^+$ (or decrease with $Cp_2FeCOO^-$ and $Fe(CpCOO^-)_2$) was observed when $E_S$ was scanned toward more negative potentials. The higher the charge of the species, the more significant was the effect (compare green-triangle curve (curve 3) with blue-circle curve (curve 4)). The overall qualitative behavior of the experimental tip current as a function of $E_S$ is consistent with that predicted by a simplified model (19), based on the consideration of both the effect of charge on mass transfer coefficient (2) and the effect of space charge associated with excess or deficiency of the electroactive species in the gap region (Figure 17.2.11B).

***(b) CS at nanoelectrodes***

***Operational principles and experimental methods.*** It is of interest to consider whether the effect of a single electron-transfer event might ultimately be detected at electrodes or interfaces. The problem is to detect the difference a single electron makes in the measured signal

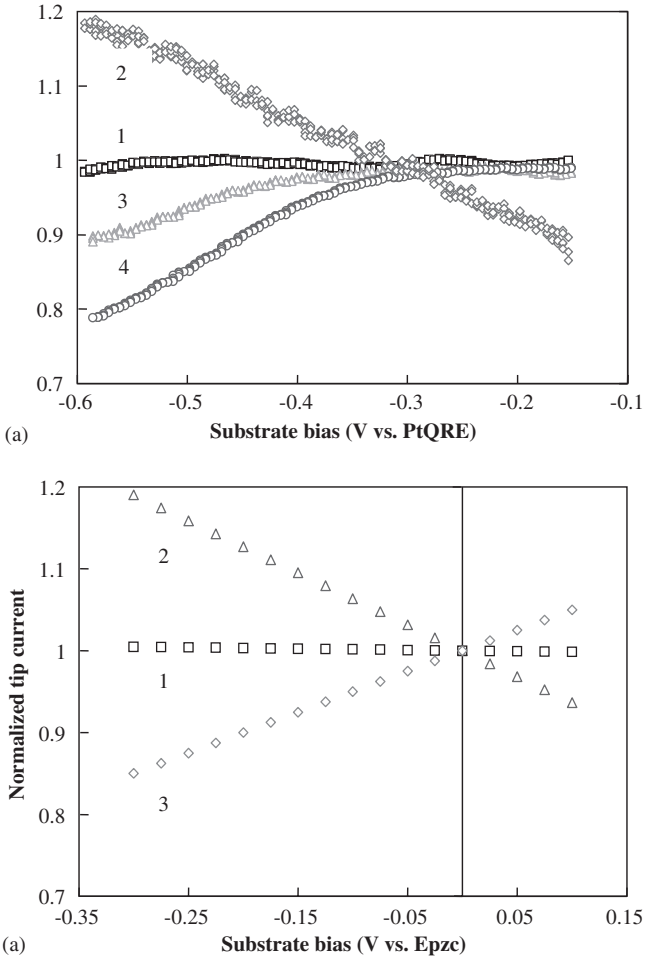


**Figure 17.2.11** (A) Tip limiting current at $E_T = 0.6$ V vs. PtQRE as a function of the substrate potential, $E_S$, for different charged species. Curve 1: 2 mM $C_pFeC_pCOO^-$ in 1.0 M $NaNO_3$. Curve 2: 2 mM $Cp_2FeTMA^+$, no supporting electrolyte. Curve 3: 2 mM $C_pFeC_pCOO^-$, no supporting electrolyte. Curve 4: 2 mM $Fe(C_pCOO^-)_2$, no supporting electrolyte. All limiting currents are normalized with respect to the limiting tip current of curve 1 at $E_S = -0.3$ V vs. PtQRE. Substrate potential scan rate: 5 mV/sec. (B) Normalized theoretical tip current as a function of $E_S$, with respect to the tip current at $E_S = E_{pzc}$ (the potential of zero charge) of ITO. Curve 1: 1 mM $Cp_2FeTMA^+$ in 1.0 M $NaNO_3$. Curve 2: 1 mM $Cp_2FeTMA^+$ only. Curve 3: 1 mM $C_pFeC_pCOO^-$ only. (for colour version: see colour section at the end of the book).

above noise level. Such single electron events are seen at two tunnel junctions formed by very small metal or semiconductor structures (quantum dots) at low temperatures in so called "Coulomb blockade" (CB) or "Coulomb staircase" (CS) experiments (20, 21). When an external voltage scan is applied to this two-junction system, an *i–V* characteristic

showing discrete steps is obtained. The semiclassical model of the CS takes account only of coulombic interactions and yields a peak spacing (or step width) of

$$\Delta V_{p-p} = \frac{e}{C} \tag{17.2.9}$$

in which $C$ is the capacitance of the junction having higher electron-transfer rate (20, 21).

In an analogous electrochemical experiment, consider the double-layer capacitance, $C_d$, of an electrode with an area of 1000 nm$^2$. If the differential capacitance per unit area near the (electrode/solution) interface is the same as that (~10 μF/cm$^2$) for a typical larger electrode, then its capacitance would be ~$10^{-16}$ farad. The change of a charge corresponding to one electron would produce a voltage change ($e/C_d$) of ~1.6 mV. If a suitable high input impedance device is available, such a charge step would be measurable. One can achieve such a structure in an electrochemical system by using a nanometer-scale electrode (nanode) immersed in a solution containing a redox couple. A schematic representation of two (electrode/solution) interfaces coupled in series through a solution for measurements is shown in Figure 17.2.12 (22). A voltage is applied to the (cell/electrometer) system and the current flowing through the interface system is monitored in a voltage measurement mode with an electrometer, as shown in Figure 17.2.12A. Current was found from the potential drop across the nominally 200-Tohm internal resistance at the most sensitive voltage setting. The leads were connected in the guard mode with the inner shield connected to the ungrounded electrode lead. The cell was placed inside a grounded Faraday cage. All current or voltage measurements were carried out at room temperature (25.0 ± 0.5°C) in a deaerated solution with an electrometer (Keithley). The Ir–Pt nanodes used in this experiment were prepared and characterized by the procedures described in Section 17.2.2.1.2. As shown in Figure 17.2.12B, each interface is characterized by a double-layer capacitance ($C_d$) and charge-transfer resistance ($R_f$) and thus mimics a tunnel junction which is connected in series to the electrometer. The redox molecules in the solution serve as donors and acceptors for electron transfer and also as charge carriers for ionic conduction between two interfaces.

Another approach to the single electron charging phenomenon is through a coulostatic-type experiment based on a single nanode as shown in Figure 17.2.12C. In this experiment, the

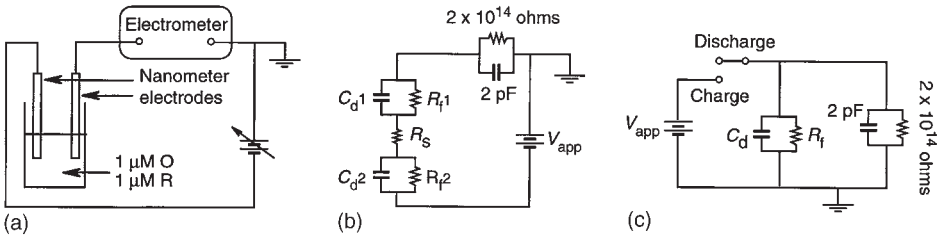


**Figure 17.2.12** (A) Experimental setup for the current or voltage measurements. (B) Schematic representation of two (electrode/solution) interfaces coupled in series through the solution. $C_d$, double-layer capacitance; $R_f$, faradaic impedance of each interface; $R_s$, solution resistance; $V_{app}$, voltage source. The electrometer has an input impedance of ~$2 \times 10^{14}$ Ω and a shunt capacitance of 2 pF. (C) Schematic representation of the experimental setup for the coulostatic experiment. Adapted from reference (22).

other electrode was a saturated calomel electrode (SCE) or a large Pt quasireference electrode (PtQRE, area ~ 0.2 $cm^2$). The two electrodes were immersed in a cell containing the $Fe(CN)_6^{4-}/Fe(CN)_6^{3-}$ couple. The potential of the nanode was displaced by ~85 mV from the equilibrium potential when this voltage was applied for 30–60 sec between the two electrodes. After the applied voltage was switched off, the cell voltage, measured with a high input impedance electrometer, relaxed back to the equilibrium value. Because the input impedance of the electrometer is not higher than the faradic impedance of the (nanode/solution) interface, the discharge of the cell voltage is convoluted by the input *RC* of the electrometer.

***Results and discussion.*** In Figure 17.2.13, we show experimental data for a two-interface system consisting of two electrodes with radii of 2.5 and 3.2 nm about 2.5 cm apart in a solution containing 1 μM each of $Cp_2FeTMA^+$, $Cp_2FeTMA^{2+}$, $NH_4^+$, and $SO_4^{2-}$, and 2 μM $PF_6^-$. The $i-V$ characteristic in the low-bias region (Figure 17.2.13A) exhibits a staircase shape, and the differential conductance (d*i*/d*V*) (Figure 17.2.13B) consists of a series of peaks. The peak spacing, corresponding to the step width of the CS, is 65 (±6) mV. The step heights of the staircase show some variation but were typically ~60 attoamperes (aA or $10^{-18}$ A). The general shape of the staircase was reproducible, although sharp change in the current at some voltage locations sometimes occurred. The step width was independent of data sampling rate, voltage scan rate (<20 mV/sec), and the concentration of the redox couple as long as it was low. The data in Figure 17.2.13 give a calculated $C_d$ of ~$2.5 \times 10^{-18}$ farad, which is close to the expected $C_d$ of an electrode of radius 2.8 nm, if we assume a double-layer capacitance of ~10 μF/$cm^2$. At a higher bias voltage (>0.3 V), the current attains a diffusion-limited plateau of ~530 aA (Figure 17.2.13C). This corresponds to only about 3300 collisions per second of electroactive molecule ($Cp_2FeTMA^+$) with the electrode. A current staircase is observed in the low-bias region where the electron transfer is kinetically controlled. Similar $i-V$ curves were also observed at similar experimental conditions by Watkins and White (23).

A staircase $i-V$ curve is also observed for another redox couple with the same pair of electrodes in a solution containing 10 μM $K_4Fe(CN)_6$ and 10 μM $K_3Fe(CN)_6$. The estimated step height for this $Fe(CN)_6^{4-}/Fe(CN)_6^{3-}$ solution is <7 aA, even though the concentration of the electroactive species is 10 times that of the ferrocene couple. The estimated staircase width is 0.07 ± 0.01 V, which is near the value seen with the ferrocene couple. This result is consistent with the predictions of the semiclassical CS model and the much slower heterogeneous electron-transfer kinetics. On the basis of the semiclassical model of the CS, the step height ($\Delta i_{cs}$) is, to the first approximation, inversely proportional to the charge-transfer resistance, $R_f$, at the interface. $R_f$ controls the charge-transfer kinetics of the electrochemical system, and $\Delta i_{cs}$ is given by (21, 22)

$$\Delta i_{cs} = \frac{e}{[R_f(C_d 1 + C_d 2)]} \tag{17.2.10}$$

$R_f$ at low overpotential is given by

$$R_f = \left(\frac{RT}{F}\right)\left[\frac{1}{(nFAk_s C^*)}\right] \tag{17.2.11}$$

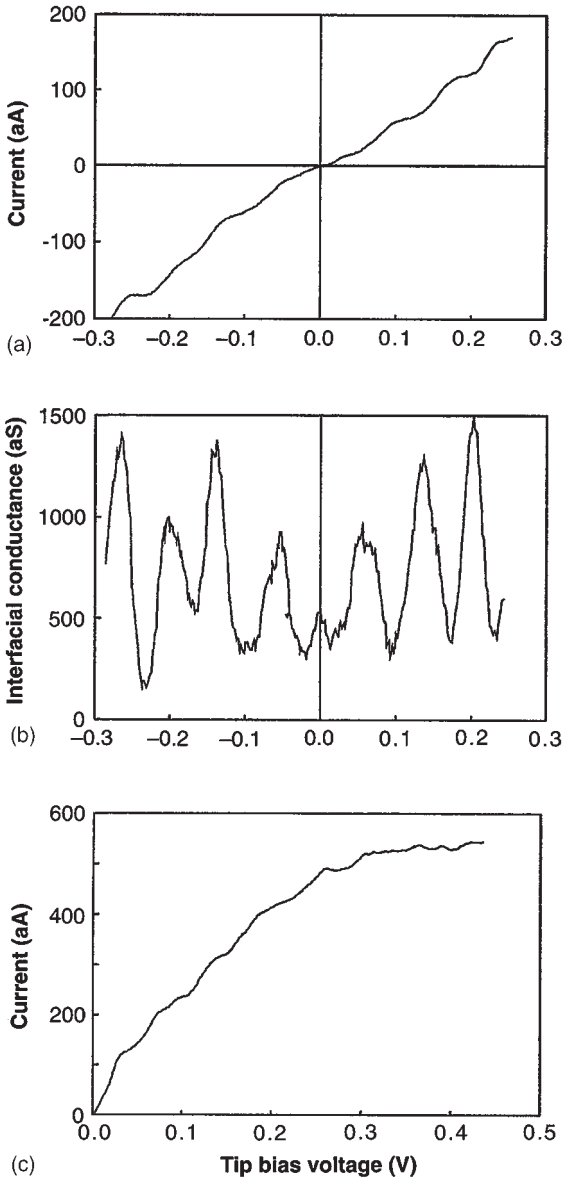


**Figure 17.2.13** (A) Experimental $i-V$ characteristic of a two-interface system consisting of a pair of electrodes with radii of 2.5 and 3.2 nm immersed in a deaerated solution containing 1 μM each of $Cp_2FeTMA^+$, $Cp_2FeTMA^{2+}$, $NH_4^+$, and $SO_4^{2-}$, and 2 μM $PF_6^-$. (B) The corresponding differential conductance ($di/dV$) $-$ $V$ plot. (C) $i-V$ curve taken to more positive potentials. Adapted from reference (22).

in which $R$ is the gas constant, $T$ is the absolute temperature, $k_s$ is the heterogeneous electron-transfer rate constant, and $A$ is the electrode area. Thus, the step height depends on $A$, $k_s$, $C^*$, and $C_d$, whereas the step width depends mainly on $C_d$ as given by equation (17.2.9). The results shown here suggest that $k_s$ for the $Fe(CN)_6^{4-}/Fe(CN)_6^{3-}$ couple is at least two orders of magnitude smaller than that for the $Cp_2FeTMA^+/Cp_2FeTMA^{2+}$ couple, which has a $k_s = 2.5$ cm/sec as calculated from $\Delta i_{cs} = 60$ aA, $C_d1 + C_d2 = 4.4 \times 10^{-18}$ farad, $C^* = 1$ μM, and $A = 2.0 \times 10^{-13}$cm$^2$. We should point out that the $i-V$ curve at low bias (e.g., <0.3 V) for a pair of large Pt microdisk electrodes with radii of 5 and 12.5 μm in the same solutions is smooth and linear, since the coulomb energy of one electron for electrodes of this size is very small (<50 nV). At higher bias voltage, the current is expected to reach a diffusion-limited plateau.

Figure 17.2.14 shows the results of the coulostatic-type experiment. Curve a of Figure 17.2.14A shows the observed uncorrected cell voltage ($V_u$) as a function of discharge time for an electrode (effective radius ~7 nm). A distorted staircase can be seen over an envelope of a smooth discharge background. Curve b shows the smooth discharge curve for a larger disk microelectrode (radius, 1 μm). This discharge curve is nearly coincident with the background discharge curve ($V_m$) associated with the shunt capacitance of the electrometer alone. $V_{corr}$ ($V_u$ after correction for $V_m$ based on the relation $V_{corr} = 2V_u - V_m$) is shown in Figure 17.2.14B. As shown in this figure, when the discharge time is longer than 200 sec, successive stepwise discharge steps become apparent and clearly resolved. The step height was ~9 mV. The step near the starting portion of the discharge curve (between 100 and 200 sec) may be a two-electron step that is not well resolved. These data suggest that the temporal relation of the voltage of the electrochemical system, $V_{corr}$, can be represented as

$$V_{corr} = n(t)\left(\frac{e}{C_d}\right) + \text{terms independent of } n(t) \tag{17.2.12}$$

in which $n(t)$ is a step function, representing the discrete number of electron gained by the electrode during the discharge process.

***(c) CS on nanoparticles***

The quantization of double-layer capacitance charging has also been observed on monolayer-protected cluster (MPC) in solutions and is one of the most interesting solution electrochemical properties of alkanethiolate MPCs (24). The capacitance is associated with the double layer formed around an MPC dissolved in an electrolyte solution, upon electronic charging of the core (Figure 17.2.15a). Because of the small capacitance of an MPC, charging of the tiny capacitor by single electrons occurs in potential intervals (as given by equation (17.2.9)) that exceed $k_BT$, in which $k_B$ is the Boltzmann constant. These potential intervals are readily observable in voltammetry (Figure 17.2.15b) of MPC solutions. The discretized (one electron) double layer charging steps are smeared out when the MPC core sizes are not mono-disperse or are too large (25). MPC quantized double layer charging is formally analogous to classical CS experiments on single MPCs, but the equivalent circuits are different (26, 27). The spacing of the current peaks on the potential axis in Figure 17.2.15b reflects the underlying nature of the MPC core charging process (24).

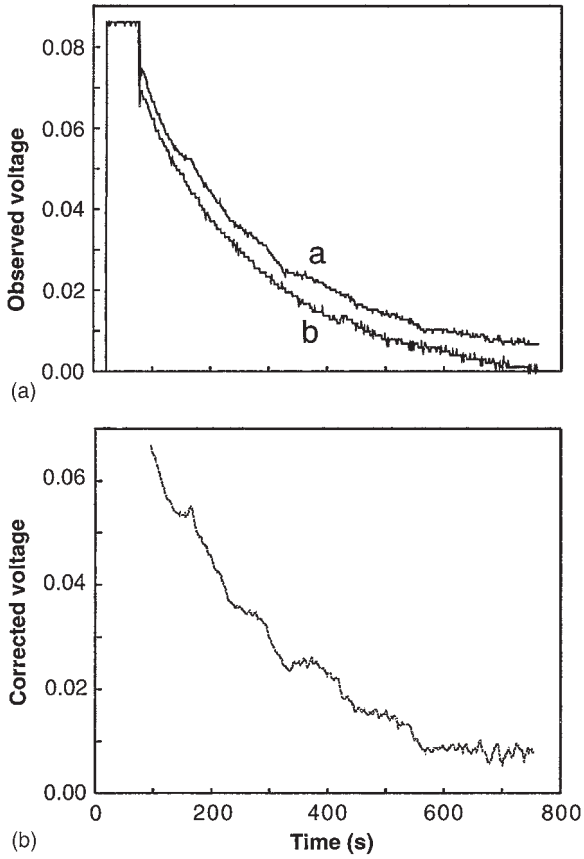


**Figure 17.2.14** (A) Curve a: Discharge curve ($V_u$) of an electrode (radius, 7 nm) in a deaerated solution containing 2 μM each of $K_4Fe(CN)_6$ and $K_3Fe(CN)_6$ after biasing at 85 mV vs. the equilibrium cell voltage, $V_0$, for 60 sec. Curve b: The corresponding curve for a microdisk electrode (radius, 1 μm) (shifted down by 4.8 mV for clarity). (B) Corrected discharge curve ($V_{corr}$) based on the relation $V_{corr} = 2V_u - V_m$. $V_m$ is the background discharge curve of the shunt capacitance of the electrometer. Adapted from reference (22).

An even peak spacing signifies a metal-like core whose charging is controlled by electrostatic principles. The evolution of molecule-like properties when the MPC core is very small is seen as a wide spacing between the two current peaks adjacent to the MPC potential-of-zero charge ($E_{pzc}$, ca. −0.2 V vs. Ag/AgCl). It is important to understand that one-electron double layer charging peaks in MPC solutions are formally analogous to those produced by traditional redox reactions (e.g., oxidation of ferrocene). The double layer charging of MPCs is kinetically fast (demonstrably controlled by mass transport (25, 26)), so that the profile of working electrode current vs. average potential of MPC cores in the adjacent solution is determined by traditional combinations of the Nernst equation

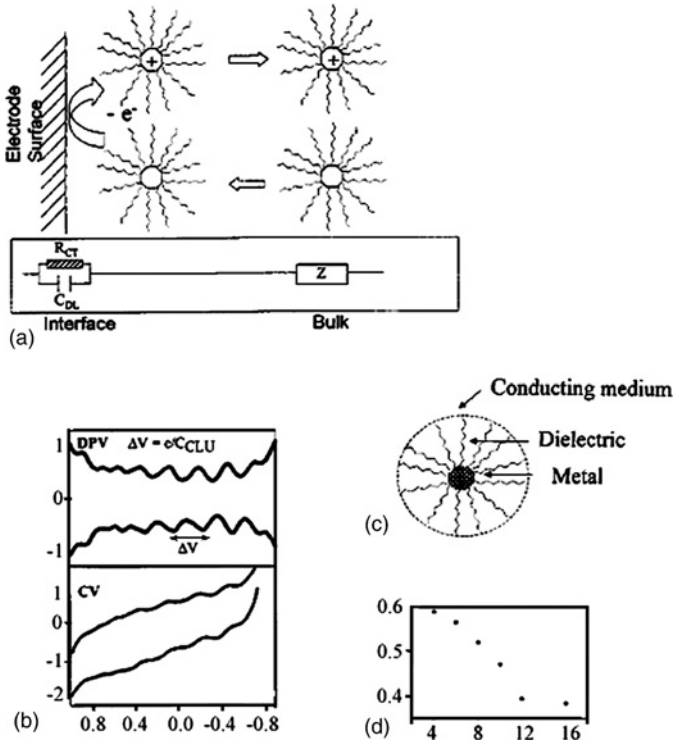


**Figure 17.2.15** (a) Cartoon of quantized double layer charging of neutral MPCs (with PZC core potential) diffusing from bulk solution to an electrode/solution interface with a potential $E_{pzc} \pm e/C_d$; all MPC cores are charged to that potential by $\pm$ a single electron. The MPCs then diffuse back into the solution. Box: Equivalent circuit, which determines current flow, in which $R_{CT}$ and $C_d$ are interfacial charge-transfer resistance (between electrode and MPC) and electrode double-layer capacitance, respectively, and $Z$ is MPC diffusional Warburg impedance. (b) Cyclic voltammogram (bottom) and differential pulse voltammogram (top) of hexanethiolate Au MPC, in $CH_2Cl_2$ at a 1.6 mm diameter Au working electrode. (c) Cartoon of the concentric sphere capacitor model used in describing MPC capacitance. (d) Average MPC capacitance vs. chain length. Adapted with permission from reference (24).

with mass transport relationships. Each core charging step has a "formal potential", which is referenced to the $E_{pzc}$, is (25)

$$E^0_{z,z-1} = E_{pzc} + (z - 1/2)(e/C_d) \tag{17.2.13}$$

where $E^0_{z,z-1}$, the formal potential of the $z/(z-1)$ charge state "couple", corresponds to the differential pulse voltammetry (DPV) peak currents (Figure 17.2.15b) and $C_d$ is the double-layer capacitance of the MPCs. $z$ is signed such that $z > 0$ and $z < 0$ correspond to core "oxidation" and "reduction", respectively. Insofar as $C_d$ is potential independent, which seems to be so for potentials not far removed from $E_{pzc}$, this relation predicts a linear plot of $E^0_{z,z-1}$ vs. charge state, with $C_d$ determined from its slope. Recent studies (28, 29) of the monolayer chain length dependence of $C_d$ show that it varies with the

dielectric thickness in remarkable agreement with a simple concentric sphere capacitor model (Figure 17.2.15c and d). The simple model predicts no dependence in $C_d$ on solvent or electrolyte changes.

It is interesting to point out that the charges stored on MPC cores can be used for chemical reactions. One can electrolytically store charge on MPCs in solutions (30); these solutions can be dried and reconstituted with minimal loss of the MPC core charge upon re-dissolution. Charges can also be stored on MPCs using chemical reactions. Charged MPCs can be used as quantitative redox reagents. For example, without a drying step, the titration of an ethyl ferrocene solution with oxidatively charged MPCs has been demonstrated. Charged MPCs can also undergo electron-transfer reactions with themselves, as shown by observing equilibrium potentials in solution mixtures of differently charged MPCs.

#### *17.2.2.4 Electrochemistry in humid environments*

Most SECM measurements are carried out with the sample under a thick liquid layer with a tip that must be sheathed in an insulator in order to achieve high resolution. SECM measurements can also be carried out within a thin layer of water that forms on the surface of a sample in air. In this case very high resolution can be attained using tips without insulation (e.g., the usual uninsulated W or Pt–Ir tips) because the tip area is defined by the small part of the tip that touches the liquid layer (31, 32). Studies of mica surfaces, polymer films, and some biological samples as described below are possible by this technique. With this mode, it is also possible to fabricate small metal structures in polymer films as demonstrated previously (33). High-resolution electrochemical deposition of silver nanostructures on mica surfaces in humid air was also achieved (32).

##### *(a) Gas/liquid/solid interface*

Theory (34) predicts that high-resolution imaging surface topologies of non-conducting bulk materials, especially biological specimens by scanning tunneling microscopy (STM) is possible. The realizability of this technique relies mainly upon surface condensation of water molecules on the specimens and substrate (35), with the measured current carried by ions rather than tunneling electrons. As a tip is brought into contact with the water layer (Figure 17.2.16) with an appropriate bias voltage between tip and substrate and with a sufficient concentration of ions, a measurable current proportional to the contact area should occur. Before the contact breaks, there is a column of water, called a bridge (34), at the tip/water layer/water vapor interface. When the constant current mode is used, the feedback mechanism will keep the tip-surface distance, $d$, and thus the contact area constant, provided the thickness of the water film is approximately uniform. Therefore, the altitude of the tip provides information about the surface topology of the specimen. According to theoretical calculation, the resolution is on the order of nanometers, strongly dependent on the humidity and temperature, and independent of specimen thickness. At nanometer resolution, this mode of operation will be useful in imaging surface structures of biological macromolecules and polymer thin films, as will be discussed below.

We should note that a previous report (36) also described “gas phase electrochemistry” in a thin film of liquid on an insulator surface, in agreement with the mechanism we describe here.

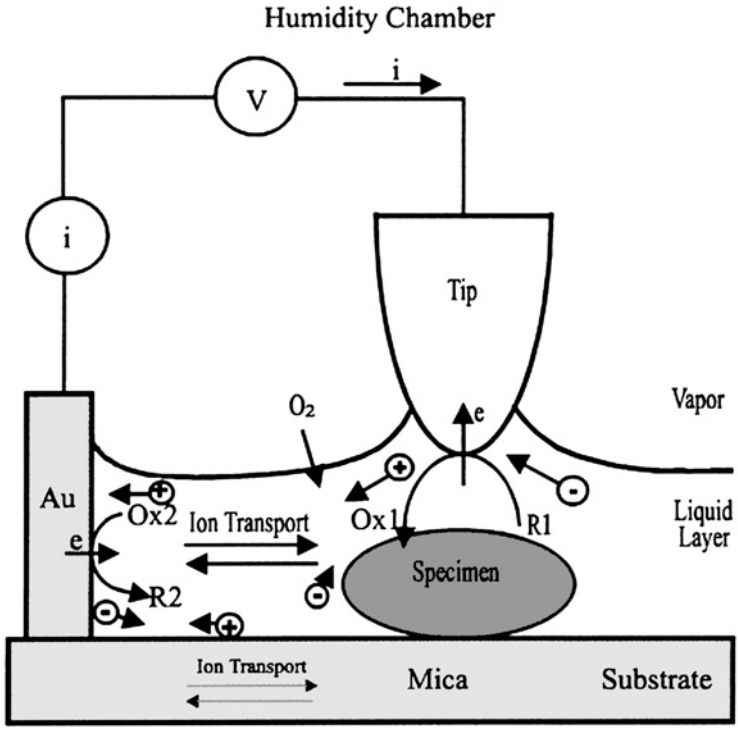


**Figure 17.2.16** Schematic diagram for the SECM chamber with controlled humidity, and the electrochemical processes that control the current. The tip was located laterally ca. 1 – 2 mm away from Au counter electrode. For illustration purposes, the thickness of the liquid layer is exaggerated to accommodate equations for various electrochemical processes. *V*: Voltage bias between the tip and Au contact; *i*: current flow through the tip. R and Ox represent the reduced and oxidized forms of an electroactive species. ⊕ and ⊖ represent cations and anions in the liquid layer and in the mica sheet. Adapted from reference (38).

### *(b) Surface conductance of mica: effect of relative humidity and ion concentration*

To obtain information about the surface conductance of a mica substrate, after treatment with a buffer solution that can serve as a source of ions in the condensed liquid layer as a function of RH, the following experiment was carried out. Two 50 nm thick layers of Au separated by ca. 1 mm were deposited on 1 × 0.8 cm pieces of mica. One small drop (~10 μL) of a buffer solution was spread over the gap to cover an area of ca. 0.3 × 0.8 cm. After partially dried in the ambient for ca. 10 min, the treated (or untreated) mica substrate was then allowed to equilibrate with the atmosphere within the humidity chamber for at least 1 h before the voltammetric experiments were carried out. Figure 17.2.17 shows a series of semilog plots of current–voltage curves for a bare mica substrate at different RH. The measured current was very small (ca. 20 fA at 2 V bias) in a desiccated (anhydrous $MgClO_4$ as the desiccant, RH $<$ 10%) chamber, while it increased at least five orders of magnitude to ca. 6.9 nA at 93% RH.

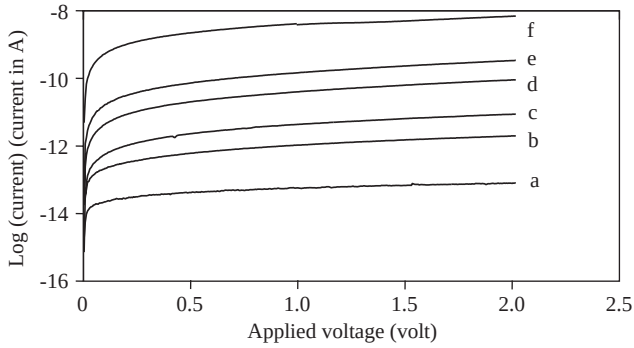


**Figure 17.2.17** A series of semilogarithmic plots of $i-V$ curves for a bare mica substrate at different relative humidity, RH: 33% (a); 58% (b); 65% (c); 74% (d); 81% (e); and 93% (f). Adapted from reference (38).

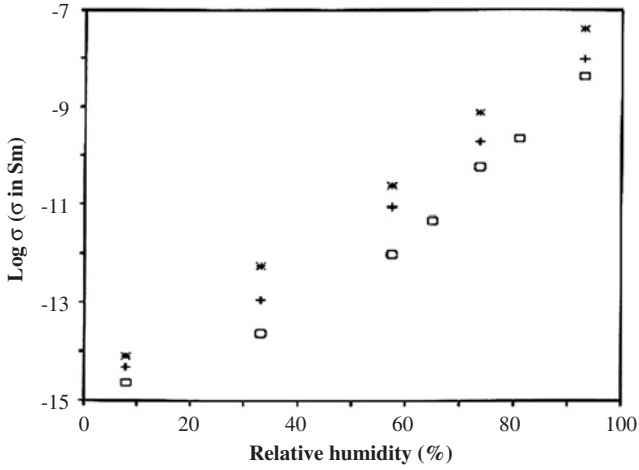


**Figure 17.2.18** Conductance values at various RH for the same sheet before (rectangles) and after (asterisks) the treatment with TE or phosphate (pluses) buffer. The conductance was measured as the slope of the $i-V$ curve in the bias range of 1.5 – 2.0 V. Adapted from reference (38).

Figure 17.2.18 summarizes the conductance values (measured as the slope of the current–voltage curve in the bias range of 1.5–2.0 V) at various RH for the same mica sheet before and after the treatment of Tris/EDTA (TE) buffer [10 mM Tris·HCl (pH 7.6)/1 mM EDTA] or phosphate buffer solution. As shown, the absolute conductance values of the bare mica surface increased slowly at low RH and more rapidly at high RH. Similar behavior was reported previously (35) for the adsorption isotherm measured by ellipsometry, suggesting that the observed conductance is closely related to the amount of water adsorbed on the mica surface. The adsorption isotherm indicates initial weak interaction between water molecule and the mica surface followed by growth of layers of water. The

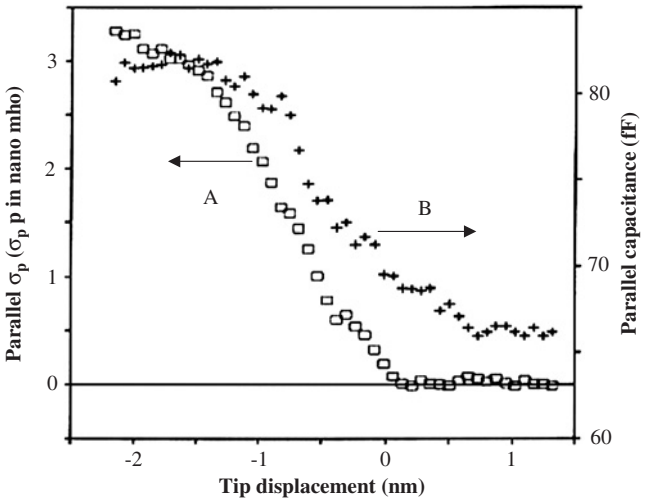


**Figure 17.2.19** Typical parallel conductance (A) and parallel capacitance (B) vs. tip displacement curves for a blunt W tip at 100% at 25°C for a mica substrate treated with TE buffer solution. Tip bias was 3 V with respect to the Au counter electrode. The tip approached the substrate surface at 3 nm/sec. Adapted from reference (38).

average thickness of the water layer on a bare mica surface is ca. 0.4 nm at 70% RH. It is interesting to notice that although the surface conductance of the mica substrate was substantially enhanced (one to two orders of magnitude) by the treatment with TE or phosphate buffer solution, similar behavior was observed for the RH dependence of the conductance. The enhanced conductance could be attributed to the increased ion concentration in the thin electrolyte film on the mica substrate, which in turn can affect the thickness and structure of the water layer that forms on it. The conductance on untreated mica can probably be attributed to the presence of a small amount of ionic species that exist or desorb from the mica or are included in the liquid layer from the air.

In SECM experiments, when a W or Pt–Ir tip (biased at +3 V) approached the sample at a scan speed of 3 nm/sec, the current remained at zero until it contacted the liquid layer where it increased sharply, showing several orders of magnitude increase over a distance of a few nanometers. Accompanying this sharp increase in the tip current when it contacted the liquid layer, both parallel tip conductance and parallel tip capacitance also increased very rapidly (see Figure 17.2.19). This is characteristic of the occurrence of an electrochemical process and provides the necessary feedback mechanism to control the tip position for high-resolution imaging. As reported previously, this arrangement can be used for imaging (31, 37, 38) and fabrication (33, 39).

***(c) Voltammetric behavior***

Information about the mechanism of current flow was obtained from current–voltage ($i-V$) curves under different conditions (31). In these experiments, a rather blunt tip (radius of curvature ~10 μm) was brought into contact with the sample and the piezo-feedback was

switched off to avoid changes in the tip–substrate gap during the potential scan. $i-V$ curves for a Nafion film with a Pt–Ir tip show some hysteria in the range of $+1$ and $-1$ V where pA currents flow. Outside this range the curves become linear and are largely independent of scan direction (31). The shape of the curves is consistent with an electrochemical reaction, presumably mainly water electrolysis, at the tip and Au contact. Above this region the current is limited by the resistance of the thin film (~$7.5 \times 10^{11}$ Ω). $i-V$ curves with a blunt Pt–Ir tip on a mica substrate treated with TE buffer solution are more complex and depend on scan history (31). Thus for scans from 0 V to negative tip potential, the $i-V$ relation is fairly linear with the current increasing slightly on each scan. An initial scan of the tip towards positive potentials following these scans is also almost linear. However, on successive positive tip potential scans, a definite peak appears; the current decreases and the peak shifts to less positive potentials on each scan (31). The voltammetric scan is restored if the tip is biased to negative potentials for about 2 min, suggesting that a species, probably $H_2$, builds up around the tip at negative bias that is depleted during successive anodic tip scans. After a series of scans of the tip to positive potentials, an initial cathodic tip scan shows decreased current, but gradually attains the linear behavior shown in successive cathodic scans (31). For purposes of imaging with a Pt–Ir tip, the current is fairly stable for negative tip bias values; with positive tip bias, oscillations frequently occurred.

As expected for an electrochemical process, the $i-V$ curves also depend upon the tip material. For a blunt W tip on mica treated with TE buffer solution (Figure 17.2.20B), the current is stable and increases almost linearly for positive tip bias, but tends to saturate and shows considerable hysteria on scan reversal in the negative tip bias region. Thus with a W tip, imaging at positive bias is appropriate. The observed electrochemical behavior also depends on the pretreatment of the insulating substrate like mica. For example, the voltammetric behavior is very different when the mica is simply immersed in water (even for a

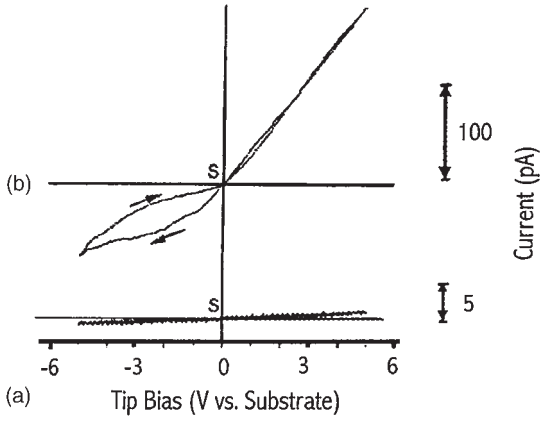


**Figure 17.2.20** Typical voltammetric curves in the humidity chamber at 100% RH, 25°C over a bare mica substrate (A) or a mica substrate treated with TE buffer solution (B). Radius of curvature of the W tip is ~10 μm. In all cases, the voltage was scanned from 0 V (the starting point S) in either direction and then returned to 0 V; the scan rate was 0.2 V/sec. Adapted from reference (38).

few hours) rather than treated with TE buffer solution. Here $i-V$ curves at 100% RH at a W tip (Figure 17.2.20A) shows only very small currents across a region of $\pm 5$ V. For a Ir–Pt tip, the current at 100% RH is at least one order of magnitude smaller for a water-treated sample as compared to one treated with TE buffer solution. The current under these conditions, however, was steady and showed little hysteria (38). At low RH (e.g., 33%), no appreciable current ($<0.1$ pA) was observed in the region of $\pm 5$ V. Thus pretreatment of the insulating substrate to provide ions in the water layer and thus increase its conductivity appears to be useful. Following treatment with TE buffer solution it appears that sufficient ions remain adsorbed on the mica surface, even after washing, to yield some conductance in the water film that forms on exposure to humid air.

The electrochemical signal observed here could arise from both capacitive charging and faradaic processes. However, charging processes are transient and cannot sustain a true steady direct current. Because the observed $i-V$ curves are perturbed by resistive drops in the solution, one cannot identify with certainty the nature of the faradaic processes at the tip and Au contact. At Pt–Ir, candidate reactions are oxidation of water to $O_2$ or $Cl^-$ to $Cl_2$ when TE buffer solution is used, reduction of water or protons to $H_2$, reduction of dissolved $O_2$ or reduction of $Cl_2$ generated in the oxidation process, and processes involving adsorbed species, e.g., oxidation of EDTA or adventitious impurities. At W, in addition to these processes, oxidation of the W to form the oxide and transiently, reduction of native or electrochemically-generated oxide, are possible. The large and stable currents with a W tip at positive tip bias compared to Pt–Ir (see also the following discussion) suggest that the W oxidation reaction occurs at the tip. Note that the faradaic processes also generate ions that can contribute to the solution conductivity. Ions in the water layer also play an important role in establishing the double layers at both electrodes and providing charge compensation for electrogenerated species. They may also affect the hydrophilicity of the substrate surface and the thickness and structure of the water layer that forms on it.

***(d) Imaging of polymers or biological macromolecules***

As stated above, on the specimen and the mica substrate, there is normally a thin film of water (a few nanometers or less) at moderate RH. As the tip, biased at a certain voltage, is brought into contact with the film containing a sufficient concentration of ions, a measurable current occurs. When the constant-current mode is used, the feedback mechanism will allow the tip to move up and down to maintain contact in the thin electrolyte layer. The altitude of the tip provides some information about the surface topology of the specimen as shown in the following examples.

***Mica surfaces and Nafion thin films.*** Figure 17.2.21A shows the image of the mica surface obtained in the constant-current mode at a reference tip current of 0.3 pA. The step running diagonally from the lower left corner represents a cleavage plane for a single mica layer, ca. 1 nm high, and the small pieces seen on the lower plane probably represent salt residue or debris left after cleavage. A thin film (~200 nm) of Nafion could also be imaged by this technique. The film was prepared on the mica substrate by spin-coating at 3000 rpm with a photoresist spinner (Headway Research, Garland, TX) from an isopropanol–ethanol (4:1 by volume) solution containing 5% Nafion. The image of this film (Figure 17.2.21B) shows smaller circular domain structures, 1–2 nm diameter, consisting of

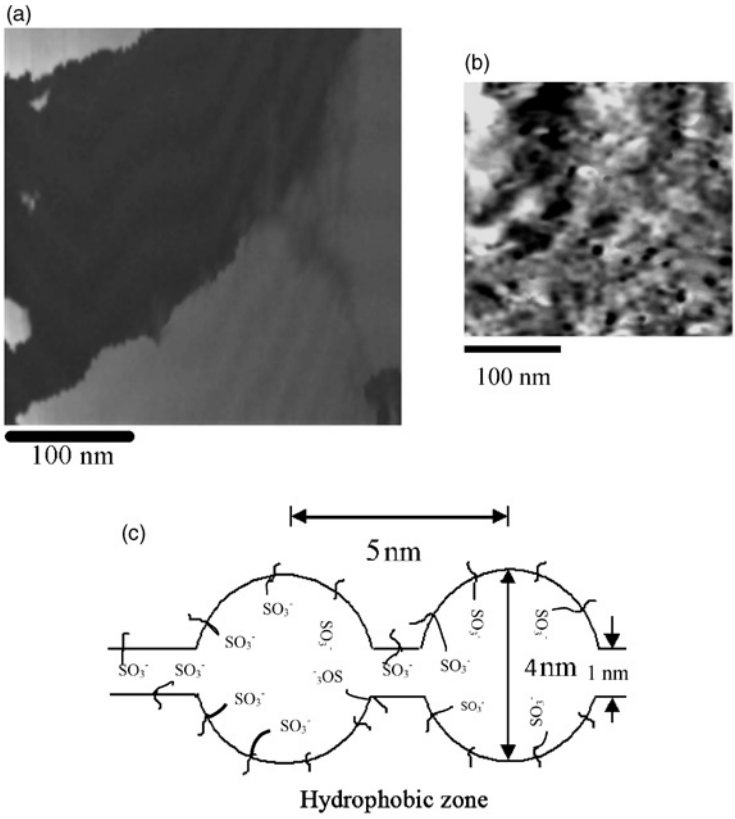


**Figure 17.2.21** (A) Image of a mica surface treated with TE buffer solution taken in humid air (80% RH at 25°C) with a sharp W tip at a reference current of 0.3 pA and a tip bias of 3 V. The tip raster rate was 0.25 Hz. The total z-range is 3 nm. (B) Image of a Nafion film on mica taken in humid air (100% RH at 25°C) with a sharp Pt–Ir tip at a reference current of 3 pA and a tip bias of 3 V with respect to the Au counter electrode. The tip raster rate was 0.25 Hz. The image is inverted to enhance the visual effect of the domain structure; the dark region has a higher transient current than the lighter region and is corresponding to the hydrophilic domain. (C) Gierke's cluster model for Nafion membrane. Adapted from reference (31).

a more conductive central zone surrounded by a less conductive region. These structures correspond to those proposed in Gierke's cluster model (Figure 17.2.21C) for a Nafion membrane (40) in which a central hydrophilic domain consisting of backbone ions and water is surrounded by a Teflon-like hydrophobic zone. This image demonstrates that SECM can distinguish between zones of different ionic conductivity in a sample. It also suggests that such an imaging mode does not pose serious limitation on the specimen thickness as long as the surface water film provides a closed circuit for ion conduction.

***DNA.*** As first reported by Guckenberger *et al*. (37), images of DNA on mica could also be obtained in this configuration. DNA on mica was prepared as follows: A small drop

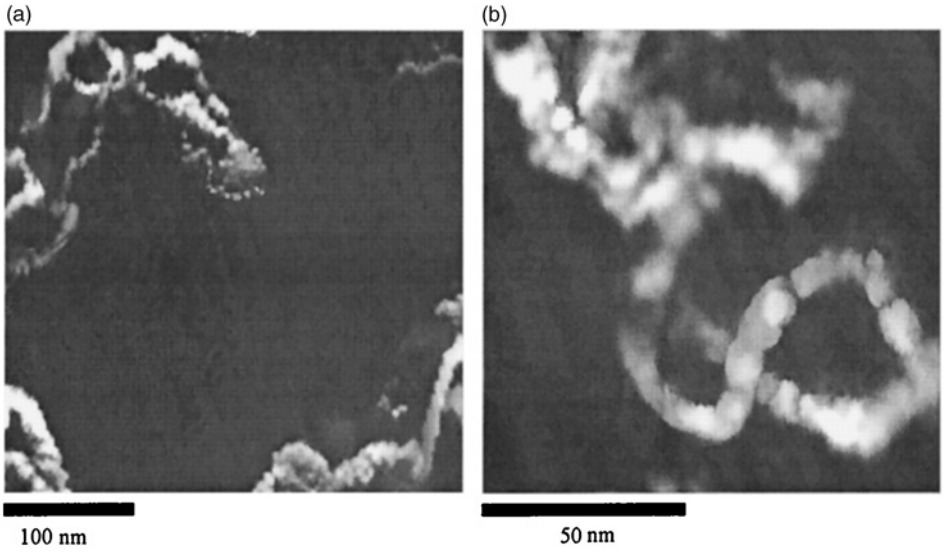


**Figure 17.2.22** (A) Constant-current image of fragments of DNA specimen in humid air (80% RH at 25°C). The DNA specimen was deposited on a TE buffer-treated mica substrate. Image was taken with a sharp W tip at a reference current of 0.3 pA and a tip bias of 3 V. The tip raster rate was 0.25 Hz. (B) A high-resolution image of a DNA molecule obtained by scanning over a smaller area. Adapted from reference (38).

(10 μL) of the DNA specimen (2.96 kbp, 21.75 μg/mL) in TE buffer solution was placed on mica to cover ca. 1 $cm^2$ and left to adsorb for ca. 5 min. The sample was then dipped (1 sec) in water, dried for 5 min in air, and dipped again for 1 sec in water. Excess water on the surface was carefully removed with filter paper and the sample was mounted on the SECM/STM and allowed to equilibrate with the atmosphere within the box before the imaging was carried out. Figure 17.2.22A shows corresponding images of several supercoiled DNA molecules on mica. In general, imaging is more stable at positive tip bias if a W tip is used. There is a tendency to lose the image after repeated scans at the same area, presumably due to the depletion of electroactive species at or near the tip and the non-negligible tip–sample interaction. Interestingly, the magnitude of the signal can be partially recovered if there is a short period of waiting time between different frames of imaging. The signal can also be recovered by imaging different areas of the sample. As shown in Figure 17.2.22B, the lateral resolution obtained (4–8 nm) is considerably larger than the expected diameter of DNA (~2.5 nm). Information in the *z*-axis is limited, due to the lack of a quantitative relation between the charge-transfer rate and the tip–sample distance for this system.

***Proteins.*** In addition to DNA, it is also possible to image antibody (e.g., a mouse monoclonal IgG), enzyme (e.g., glucose oxidase, GOD), and haemocyanin (e.g., keyhole limpet haemocyanin, KLH) molecules by the same technique (38). All of these protein molecules

have characteristic three-dimensional structures and the majority of their surfaces are hydrophilic; thus one can test the applicability of this technique for imaging. A small drop of 10 μL protein solution to cover ca. 1 $cm^2$ of the mica surface was used for the experiment. A stock solution of GOD (22.5 μg/mL) was prepared from a buffer solution containing 24 μM $KH_2PO4$, 170 μM NaCl, and 10 μM $NaN_3$. It is important to use low concentrations of protein to minimize aggregate formation. However, for imaging purposes, the protein concentration should be high enough to have a proper coverage of protein molecules on the mica surface. The images were recorded using a W tip. The reference current was 1 pA at a tip bias of 1.5 V (vs. the Au contact).

Figure 17.2.23 shows the image of a group of GOD (MW = 160,000 Da, from *A. niger*) molecules on a mica surface at 81% RH. Most of the molecules show a dimeric structure corresponding to the folded form of the two identical polypeptide chains of the GOD molecules. The monomeric unit is apparently a compact spheroid with approximate dimensions of 8 × 4 nm. The top-view images of some of the molecules are observed as near circles with diameters of ca. 7 nm, which might represent the third dimension of the spheroidal monomeric unit. Contact between two monomeric units forming the dimer is confined to a long, narrow stretch. The overall dimensions of the GOD molecules are thus approximately 8 × 7 × 8 nm, which are significantly larger than those (6.0 × 5.2 × 7.7 nm) determined from X-ray crystallographic data on the partially deglycosylated enzyme (41).

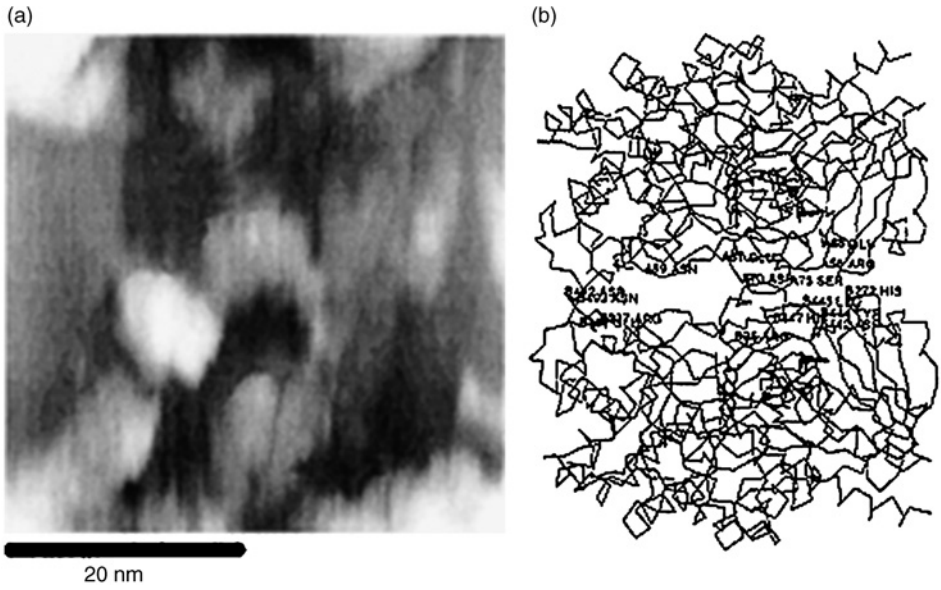


**Figure 17.2.23** (A) Constant-current image showing several glucose oxidase molecules on mica substrates treated with phosphate buffer. The images were recorded with a W tip in humid air (80% RH at 25°C). The reference current was 1 pA at a tip bias of 1.5 V. (B) $C^{\alpha}$ tracing of the dimmer structure of a glucose oxidase molecule. Contacts between molecules forming the dimmer are confined to a long, narrow stretch. Adapted from reference (38).

The significant increases in size of the DNA and small protein molecules determined by this technique as compared with other techniques are most likely due to the presence of water and salt around the molecules, and the convolution of the non-negligible tip size. They could also be caused by the deformation of the molecules by the tip during imaging, as frequently encountered in SPM images for biological samples (42). It is conceivable that when the dimensions of the specimen are large compared with the tip curvature, the relative deviation due to tip geometry is small. It is also possible to de-convolute the images if one knows the exact tip dimensions and the detailed mechanisms of imaging. One can also minimize the size deviation by optimizing the RH and the salt concentration. In spite of this discrepancy, the overall shapes of the DNA and protein molecules are well reproduced in this experiment and are similar to those determined from other more established techniques. They further indicate that the use of a mica surface, which is atomically flat and can easily be chemically modified, is a suitable substrate for studying protein samples as suggested previously.

### 17.2.3 Conclusions

These studies have shown that single molecules can be trapped and detected electrochemically at electrodes and single reaction events of reactants generated at electrodes can be observed. These have involved soluble species and UMEs or nanoparticles. It should also be possible to observe single molecules adsorbed on a surface, e.g., self-assembled monolayers (SAMs), if a suitable amplification process can be developed. Such studies would be of use in determining free energies and reaction kinetics with tiny samples. They would also represent the ultimate sensitivity for electroanalytical detection.

Moreover, as with other SMD techniques, there is the expectation that will allow one to uncover phenomena and properties of materials, that are not apparent when one observes processes involving a large number of molecules, as are typical in conventional electrochemical experiments. For example, one can adsorb DNA on a suitably structured surface and detect DNA by itself or after intercalation with other agents. In principle, given sufficient stability of (DNA/intercalate) system, single molecule DNA detection would be possible.

## REFERENCES

1. *Scanning Electrochemical Microscopy*, A. J. Bard, M. V. Mirkin, Eds., Marcel Dekker: New York, 2001.
2. A. J. Bard, L. R. Faulkner, *Electrochemical Methods, Fundamentals and Applications*, John Wiley & Sons, Inc.: New York, 2001, p. 174.
3. L. A. Nagahara, T. Thundat, S. M. Lindsay, *Rev. Sci. Instrum.* **60**, 3128 (1989).
4. F.-R. F. Fan, A. J. Bard, *J. Electrochem. Soc.* **136,** 3216 (1989).
5. F.-R. F. Fan, A. J. Bard, *Science* **267**, 871 (1995).
6. A. J. Bard, F.-R. F. Fan, M. V. Mirkin, in *Electroanalytical Chemistry*, A. J. Bard, Ed., Marcel Dekker: New York, 1994, Vol. 18, pp. 243–373.

7. M. V. Mirkin, A. J. Bard, *J. Electroanal. Chem.* **323**, 1 (1992).
8. F.-R. F. Fan, J. Kwak, A. J. Bard, *J. Am. Chem. Soc.* **118**, 9669 (1996).
9. J. S. Bendat, A. G. Piersol, *Random Data Analysis and Measurement Procedures*, 2nd ed., John Wiley and Sons: New York, 1986.
10. N. G. Van Kampen, *Stochastic Processes in Physics and Chemistry*, North Holland: Amsterdam, 1992.
11. R. A. Marcus, *J. Chem. Phys.* **43**, 2654 (1965).
12. See, for example, G. J. Kavarnos, "*Fundamental Concepts of Photoinduced Electron Transfer*," in *Topics in Current Chemistry*, J. Marray, Ed., Springer-Verlag: New York, 1990, Vol. 156, pp. 21–58.
13. *Electrogenerated Chemiluminescence,* A. J. Bard, Ed., Marcel Dekker: New York, 2004.
14. (a) M. M. Collinson, R. M. Wightman, *Anal. Chem.* **65**, 2576 (1993). (b) M. M. Collinson, R. M. Wightman, P. Pastore, *J. Phys. Chem.* **98**, 11942 (1994).
15. M. M. Collinson, P. Pastore, K. M. Maness, R. M. Wightman, *J. Am. Chem. Soc.* **116,** 4095 (1994).
16. M. M. Collinson, R. M. Wightman, *Science* **268**,1883 (1995).
17. C. P. Smith, H. S. White, *Anal. Chem.* **65**, 3343 (1993).
18. A. J. Bard, F.-R. F. Fan, *Acc. Chem. Res.* **29**, 572 (1996).
19. F.-R. F. Fan, A. J. Bard (unpublished results).
20. M. Amman, R. Wilkins, E. Ben-Jacob, P. D. Maker, R. C. Jaklevic, *Phys. Rev. B* **43**, 1146 (1991).
21. A. E. Hanna, M. Tinkham, *Phys. Rev. B* **44**, 5919 (1991).
22. F.-R. F. Fan, A. J. Bard, *Science* **277**, 1791 (1997).
23. J. Watkins, H. S. White (private communication).
24. A. C. Templeton, W. P. Wuelfing, R. W. Murray, *Acc. Chem. Res.* **33**, 27 (2000).
25. S. Chen, R. W. Murray, S. W. Feldberg, *J. Phys. Chem. B* **102**, 9898 (1998).
26. S. Chen, R. S. Ingram, M. J. Hostetler, J. J. Pietron, R. W. Murray, T. G. Schaaff, J. T. Khoury, M. M. Alvarez, R. L. Whetten, *Science* **280**, 2098 (1998).
27. R. S. Ingram, M. J. Hostetler, R. W. Murray, T. G. Schaaff, J. T. Khoury, R. L. Whetten, T. P. Bigioni, D. K. Guthrie, P. N. First, *J. Am. Chem. Soc.* **119**, 9279 (1997).
28. J. F. Hicks, A. C. Templeton, S. Chen, K. M. Sheran, R. Jasti, R. W. Murray, J. Debord, T. G. Schaaff, R. L. Whetten, *Anal. Chem.* **71**, 3703 (1999).
29. J. F. Hicks, D. T. Miles, R. W. Murray, *J. Am. Chem. Soc.* **124**, 13322 (2002).
30. J. J. Pietron, J. F. Hicks, R. W. Murray, *J. Am. Chem. Soc.* **121**, 5565 (1999).
31. F.-R. F. Fan, A. J. Bard, *Science* **270**, 1849 (1995).
32. F. Forouzan, A. J. Bard, *J. Phys. Chem. B* **101**, 10876 (1997).
33. D. H. Craston, C. W. Lin, A. J. Bard, *J. Electrochem. Soc.* **135**, 785 (1988).
34. J.-Y. Yuan, Z. Shao, C. Gao, *Phys. Rev. Lett.* **67**, 863 (1991).
35. D. Beaglehole, E. Z. Radlinska, B. W. Ninham, H. K. Christenson, *Phys. Rev. Lett.* **66**, 2084 (1991).
36. Y. Fang, J. Leddy, *J. Electroanal. Chem.* **384**, 5 (1995).
37. R. Guckenberger, M. Heim, G. Ceve, H. Knapp, W. Wiegräbe, A. Hillebrand, *Science* **266**, 1538 (1994).
38. F.-R. F. Fan, A. J. Bard, *Proc. Nat. Acad. Sci. U.S.A.* **96**, 14222 (1999).
39. R. L. McCarley, S. A. Hendricks, A. J. Bard, *J. Phys. Chem.* **96**, 10089 (1992).
40. W. Y. Hsu, T. D. Gierke, *J. Membr. Sci.* **13**, 307 (1983).
41. H. J. Hecht, H. M. Kalisz, J. Hendle, R. D. Schmid, D. Schomburg, *J. Mol. Biol.* **229**, 153 (1993).
42. H. Hansma, J. Hoh, *Annu. Rev. Biophys. Biochem. Struct.* **23**, 115 (1994).

# 17.3 ELECTROCHEMISTRY AT LIQUID/LIQUID INTERFACES

*Yuanhua Shao*

College of Chemistry and Molecular Engineering, Peking University, Beijing 100871, China

## 17.3.1 Introduction

Charge (electron and ion) transfer at a liquid/liquid (L/L) interface, or at an oil/water (O/W) interface, or at an interface between two immiscible electrolyte solutions (ITIES) is one of the most fundamental physicochemical processes. The study of such soft molecular interfaces by various electrochemical techniques is referred to as electrochemistry at liquid/liquid interfaces. This field has developed quickly over the past 30 years (1–10) due to applications in areas including exploration of mechanisms of phase transfer catalysis, extraction processes and chemical sensing, investigation of solar energy conversion systems, drug release and delivery, and in mimicking the function of biological membranes.

The first work in this field can be traced back to the beginning of last century when Nernst and Riesenfield carried out experiments at a water/phenol interface in the presence of colored inorganic electrolytes [$KI_3$, $K_2CrO_4$, $Fe(SCN)_3$, etc.]. They were mainly interested in developing suitable methods to evaluate transport numbers in non-aqueous solvents (11). After Cremer (12) pointed out in 1906 the analogy between water/oil/water concentration cells and biological membranes studied by Ostwald (13), interest in this field spread to physiologists and the liquid/liquid interface became a model for the investigation of bioelectrical potentials and currents. In 1939, Verwey and Niessen (14) published the first theoretical paper regarding the electrical double layer and potential distribution at a liquid/liquid interface. In the mid-1950s, Guastalla *et al*. (15) investigated the effect of passing current across the water/ nitrobenzene (NB) interface and also began to study electrosorption (which was later found by Blank (16) to be based on a depletion–accumulation effect of surface active electrolytes).

The progress however was rather slow in the first half of the century. This was mainly due to a lack of knowledge of the interfacial structure and associated potential distribution across the interface, and secondly to the inherent difficulty in gathering reliable data due to the presence of *iR* drop caused by the use of an organic solvent. There are two landmarks in the establishment of modern electrochemistry at liquid/liquid interfaces. One is around the end of the 1960s, after recognition that the liquid/liquid interface could be polarized just like the metallic electrode/electrolyte interface. For example, Gavach *et al*. (17–20) first employed modern electrochemical techniques such as chronopotentiometry to investigate ion transfer across liquid/liquid interfaces and used the Modified Verwey–Nissen (MVN) model to rationalize the experimental data (18, 19). The second is around the late 1970s when Samec *et al*. (21, 22) in Prague employed a four-electrode potentiostat with *iR* drop compensation to record the cyclic voltammograms of charge transfer across the liquid/liquid interfaces. Meanwhile, Koryta *et al*. (23–27) established the theoretical background for a series of

electrochemical cells and pioneered the study of facilitated ion transfer by ionophores. The research groups who have shown interest in this field are spread all over the world (28–32).

## 17.3.2 Fundamentals

### *17.3.2.1 Thermodynamics of a liquid/liquid interface (33)*

When two electrically conducting phases such as *w (water)* and *o (organic)* are in contact, the partition of the charge carriers (electron and ion) between the two adjoining phases occurs due to the difference in energy of the carriers in both phases. Thus, an interfacial region is built up. Within the interfacial region, the electrical field strength differs from zero and a Galvani potential difference, $\Delta_o^w\phi = \phi^w - \phi^\circ$, is established across the interface. In the case of a metallic electrode/electrolyte interface, the region of excess charge at the interface consists of electrons (or holes) on the metallic side and of ions on the electrolyte side. In the case of a liquid/liquid interface, both charge regions are formed by ions: anions on one side and cations on the other. As a whole, in any case, the interfacial region should be electrically neutral (see Figure 17.3.1).

In general at liquid/liquid interfaces, there are two types of charge partition (3):

(A) The transfer of an ion $M^z$ with the charge number z from phase w to phase o and the reverse:

$$M^z(w) \rightleftarrows M^z(o) \qquad (17.3.2.1)$$

(B) The electron transfer between a redox couple $O_1/R_1$ in phase w and a redox couple $O_2/R_2$ in phase o, can be represented as:

$$O_1(w) + R_2(o) \rightleftarrows R_1(w) + O_2(o) \qquad (17.3.2.2)$$

Each of these two heterogeneous charge transfer reactions may be coupled to a series of homogeneous chemical reactions inside phase w or o or to heterogeneous reactions occurring at the interfacial region (e.g., ion-pair formation and adsorption), so that the interfacial charge transfer may be very complicated. As an example, the transfer of an ion $M^+$ facilitated by complex formation with a ligand (ionophore) L at a liquid/liquid interface may be written as:

$$M^+(w) + L(o) \rightleftarrows ML^+(o) \qquad (17.3.2.3)$$

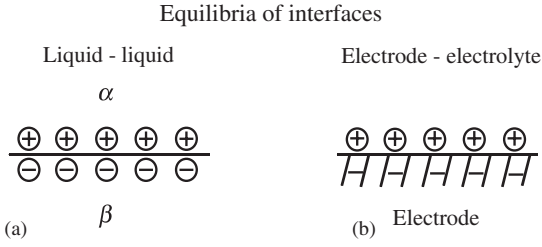


**Figure 17.3.1** The equilibria of the interfaces. (a) Liquid/liquid interface; (b) Electrode/electrolyte interface. (Reprinted with permission from (25). Copyright 1979 Elsevier Science).

The conditions for equilibrium of ion ($M^z$) at a liquid/liquid interface are such that their electrochemical potentials are equal

$$\overline{\mu}_M^w = \overline{\mu}_M^o \tag{17.3.2.4}$$

with

$$\overline{\mu}_M^w = \mu_M^{0,w} + RT \ln \alpha_M^w + zF\phi^w \tag{17.3.2.5}$$

and

$$\overline{\mu}_M^o = \mu_M^{0,o} + RT \ln \alpha_M^o + zF\phi^o \tag{17.3.2.6}$$

where $\mu_M^0$, $\alpha_M$ and $\phi$ are standard chemical potentials, activities of $M^z$ and inner potentials in water (w) and organic (o) phases, respectively.

The equilibrium potential difference $\Delta_o^w\phi$ is obtained by combination of the above equations, and is as follows:

$$\begin{aligned}\Delta_o^w\phi &= \phi^w - \phi^o \\ &= (\mu_M^{0,o} - \mu_M^{0,w})/zF + (RT/zF)\ln(\alpha_M^o/\alpha_M^w) \\ &= \Delta_o^w\phi_M^0 + (RT/zF)\ln(\alpha_M^o/\alpha_M^w)\end{aligned} \tag{17.3.2.7}$$

Equation (17.3.2.7) is analogous to the Nernst equation for electrode potential, and $\Delta_o^w\phi_M^0$ is called the standard transfer potential.

The standard Galvani potential difference between the two phases can be further written as:

$$\Delta_o^w\phi_M^0 = -(\mu_M^{0,w} - \mu_M^{0,o})/zF = \Delta G_{tr}^{0,w\to o}/zF \tag{17.3.2.8}$$

where $\Delta G_{tr}^{0,w\to o}$ is the standard single ion Gibbs energy of transfer from water to oil. However, this quantity, in contrast to the electrolytes as a whole, is not amenable to direct measurement. For quantitative determination, extra-thermodynamic assumptions must be made. So far, as pointed out by Girault and Schiffrin (34) there are at least six categories of assumptions which have been proposed. The most commonly used is the "TATB assumption" stating that the cation and the anion of tetraphenylarsonium tetraphenylborate ($TPAs^+TPB^-$) have equal standard Gibbs transfer energies for any pair of solvent (25, 26) (see Figure 17.3.2). That is:

$$\Delta G_{tr,TPAs^+}^{0,w\to o} = \Delta G_{tr,TPB^-}^{0,w\to o} = \frac{1}{2}\Delta G_{tr,TPAsTPB}^{0,w\to o} \tag{17.3.2.9}$$

On the basis of this assumption, a scale for standard Gibbs energies of transfer of individual ions from one solvent to another can be obtained using standard Gibbs energy of transfer of a salt which can be calculated from partition coefficients, solubility and voltammetric measurements (9, 10, 33). Similarly, the standard potential difference for individual ions between phase w and o can be evaluated from equation (17.3.2.8). For example, the standard Gibbs energies of transfer of $TPAs^+$ and $TPB^-$ between water and

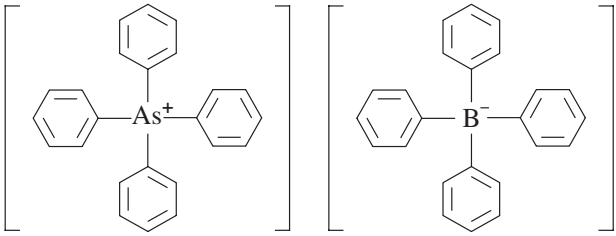


**Figure 17.3.2** The structure of TPAsTPB.

1,2-dichloroethane (DCE) are both equal to −35.2 KJ/mol, their corresponding standard potential differences are −365 and 365 mV, respectively (33). Girault and Schiffrin (35) have proposed another way to define the absolute potential scale by using the potential of zero charge (PZC) as the absolute zero point.

It should be noticed that the standard Gibbs transfer energy data commonly used are related to ion transfer between mutually saturated solvents (known as the Gibbs energy of partition), which are different from the data for transfer between pure solvents (known as the Gibbs energy of transfer). These values are in agreement only under circumstances where the ion transferred from water to an organic solvent not hydrated by water present in that solvent (34).

Updated lists of the values of standard Gibbs energies of transfer for various individual ions are given in Professor Hubert H. Girault's website at the EPFL of Switzerland (36). More values can be found in a data survey of Gibbs energy of ion transfer for 57 different solvents published by IUPAC (37). Table 17.3.1 lists some data for W/NB and W/DCE systems.

Liquid/liquid interfaces have been classified as ideal-polarizable interfaces and non-polarizable interfaces (25–27). Let us first discuss the system in which a strongly hydrophilic 1:1 electrolyte $B_1A_1$ is dissolved in water (e.g., LiCl in water) and a strongly hydrophobic 1:1 electrolyte $B_2A_2$ is dissolved in an organic solvent [e.g., tetrabutylammonium tetraphenylborate (TBATPB) in NB], as shown in Cell 1:

$$r_1/B_1A_1(w)//B_2A_2(o)/r_2 \qquad \text{Cell 1}$$

where $r_1$ and $r_2$ represent the reference electrodes which are reversible to either cation ($B_1$ or $B_2$) or anion ($A_1$ or $A_2$). The situation can be described by the following equations:

$$\Delta_o^w\phi_{B_1}^0 \gg 0 \text{ and } \Delta_o^w\phi_{A2}^0 \gg 0 \qquad (17.3.2.10)$$

$$\Delta_o^w\phi_{B2}^0 \ll 0 \text{ and } \Delta_o^w\phi_{A_1}^0 \ll 0 \qquad (17.3.2.11)$$

It has been demonstrated by Koryta (25, 26) that for such cases, there exists a range of potential differences (potential window) in which $\Delta_o^w\phi$ is controlled by the charge in the double layer rather than by the ion activities (see Figure 17.3.5A). This situation is completely analogous to that of an ideal-polarizable metal/electrolyte interface. We call this case the ideal-polarizable liquid/liquid interface. One of such example is the following

**Table 17.3.1**

Standard Gibbs energies of transfer and standard potential differences for some ions at the W/NB and the W/DCE interfaces (9, 10, 33)

| Ion | $\Delta_o^w G_{tr}^{0,W\to NB}$ (KJ/mol) | $\Delta_o^w \phi^0$ (mV) W/NB system | $\Delta_o^w G_{tr}^{0,W\to DCE}$ (KJ/mol) | $\Delta_o^w \phi^0$ (mV) W/DCE system |
|---|---|---|---|---|
| $Li^+$ | 38.4 | 398 | 55.6 | 576 |
| $Na^+$ | 34.4 | 358 | 55.9 | 579 |
| $H^+$ | 32.5 | 337 | 53 | 549 |
| $K^+$ | 24.3 | 252 | 51.9 | 538 |
| $Rb^+$ | 19.9 | 206 | 45.8 | 475 |
| $Cs^+$ | 15.5 | 161 | 37.3 | 386 |
| $TMA^{+a}$ | 3.4 | 35 | 15.4 | 160 |
| $TEA^{+a}$ | −5.8 | −60 | 1.8 | 19 |
| $TPA^{+a}$ | −15.5 | −161 | −8.8 | −91 |
| $TBA^{+a}$ | −24.2 | −248 | −22.2 | −230 |
| $TPAs^+$ | −35.9 | −372 | −35.2 | −365 |
| $F^-$ | 44.0 | −454 | 58 | −601 |
| $Cl^-$ | 30.5 | −316 | 51 | −528 |
| $Br^-$ | 28.5 | −295 | 39 | −404 |
| $I^-$ | 18.8 | −195 | 26 | −269 |
| $ClO_4^-$ | 8.0 | −83 | 17.0 | −176 |
| $SCN^-$ | 16.0 | −176 | 26 | −269 |
| $BF_4^-$ | 11.0 | −121 | −17.9 | 185 |
| $NO_3^-$ | 24.4 | −253 | 34 | −352 |
| $TPB^-$ | −35.9 | 372 | −35.2 | 365 |

[a]$TMA^+$, $TEA^+$, $TPA^+$, and $TBA^+$ are abbreviations of tetramethylammonium, tetraethylammonium, tetrapropylammonium, and tetrbutylammonium, respectively.

electrochemical cell: Ag/AgTPBCl/0.01 M TBATPBCl//0.01 M LiCl + 0.3 M $Li_2SO_4$/Ag/AgCl (dichloromethane is the organic phase, $TPBCl^-$ is tetrakis[4-chlorophenyl]borate), it has an approximately 500 mV potential window, in which other charge transfer processes can be studied electrochemically.

Let us discuss another case shown in Cell 2:

$$r_1/B_3A_1(w)//B_3A_2(o)/r_2 \qquad \text{Cell 2}$$

Both phases have a common ion $B_3$ which is transferable across this interface. However, the transfer of the ion $A_1$ from w to o and that of ion $A_2$ in the opposite direction are negligible in the potential window. This system is described by the following inequalities:

$$\Delta_o^w \phi_{A_1}^0 \ll 0 \text{ and } \Delta_o^w \phi_{A2}^0 \gg 0 \qquad (17.3.2.12)$$

$$\Delta_o^w \phi_{A_1}^0 \ll \Delta_o^w \phi_{B3}^0 \ll \Delta_o^w \phi_{A2}^0 \qquad (17.3.2.13)$$

Under these conditions, the potential difference between w and o is determined practically only by the activities of ion $B_3$ in both phases according to equation (17.3.2.14), if the concentrations of ion $B_3$ in both phases have suitable values.

$$\Delta_o^w \phi = \Delta_o^w \phi_{B_3}^0 + (RT/z_{B_3}F)\ln(\alpha_{B_3}^o/\alpha_{B_3}^w) \qquad (17.3.2.14)$$

We call this case the non-polarizable liquid/liquid interface. One example is as follows: Ag/AgTPB/0.01 M TBATPB//0.01 M TBACl/Ag/AgCl. Here $TBA^+$ is the common ion in both phases. Usually one studies the charge transfer across the ideal-polarizable liquid/liquid interface and employs a non-polarizable liquid/liquid interface as a reference electrode.

There are over 20 organic solvents which have been tested so far. As pointed out by Koryta (38), the following three requirements have been commonly employed to select the organic solvent:

(1) The solubilities of solvent in water and water in the solvent must be very small.
(2) The solvent must be polar to promote sufficient dissociation of the supporting electrolyte and thus maintaining conductivity of the solution.
(3) The density of the solvent should differ significantly from that of aqueous phase in order to obtain a physically stable liquid/liquid interface.

At present, the most commonly used solvents are NB and DCE. Other solvents which have been considered include, for example, propiophenone (39), 4-isopropyl-1-methyl-2-nitrobenzene (40), dichloromethane (41), *o*-nitrophenyloctyl ether (42). In order to have more flexible choices, organic solvent mixtures have also been employed; for example, NB with chlorobenzene (43), benzonitrile, benzene (44), and tetrachloromethane (45).

During the early days of electrochemical measurements of charge transfer reactions at liquid/liquid interfaces, TBATPB was the most commonly used supporting electrolyte in the organic phase, which usually determined the potential window. In order to widen the potential window, more hydrophobic salts were studied, including:

CVTPB (crystal violet tetraphenylborate) (46);
BTPPATPB (Bis[triphenylphosphoranylidene]ammonium tetraphenylborate) (47);
TPAsDCC (tetraphenylarsonium3,3'-commo-bis[undecahydro-1,2-dicarba-3-cobaltachosododecarborate]) (48);
TBATPBCl (tetraphenylammonium tetrakis[4-chlorophenyl]borate) (47);
TBATPBF (tetraphenylammonium tetrakis[pentafluorophenyl]borate) (47);
BTPPATPBCl (Bis[triphenylphosphoranylidene]ammonium tetrakis [4-chlorophenyl] borate) (49);
BTPPATPBF (Bis[triphenylphosphoranylidene]ammonium tetrakis[pentafluorophenyl] borate) (49)

have been successfully used recently. Now the limitations of the potential window are mostly due to the transfers of the supporting electrolytes in the aqueous phases while the salts such as BTPPATPBCl is used as the supporting electrolyte in DCE.

#### *17.3.2.2 Interfacial structure*

The distribution of the potential at the interfacial region is related to the structure of the interface. Although charge transfer reactions at liquid/liquid interfaces have been studied experimentally using modern electrochemical and spectroscopic methodologies (2, 6), the interpretation of the results has not yet allowed a complete understanding of the kinetic

mechanism. This is due to the fact that any theoretical approach of charge transfer kinetics across the liquid/liquid interface is mainly dependent upon the physical model of the interface considered. The interface between two phases is by nature a molecular interface with its own dynamics. It is obviously hard to define an interfacial structure or thickness. Is the interface sharp or diffuse? The answer to this question is timescale dependent (6). Unlike solid electrodes, the microscopic aspects of the structure of a liquid/liquid interface are not amenable to scanning probing microscopes with atomic resolution. This drawback can be turned into an advantage. Because of interfacial dynamics, the macroscopic properties of liquid/liquid interface are indeed highly reproducible (6). The current views of such interfaces have come from molecular dynamic simulations (50–52). However, it is crucial to point out that the mechanism and kinetics of charge transfer reactions at these interfaces are still not well understood and two of the most commonly used models will be described below.

***(a) MVN (Modified Verwey–Niessen) model***

The first model of interfacial structure was introduced by Verwey and Niessen (14). It was represented by a space charge region in each phase, one containing an excess of positive charge and the other an equal excess of negative charge. The space charge distribution was described by the Gouy–Chapman theory (20, 53). Gavach et al. (20) in 1977 proposed a modified version of this model assuming the presence of an ion-free layer composed of oriented solvent molecules separating two diffuse layers, as shown in Figure 17.3.3.

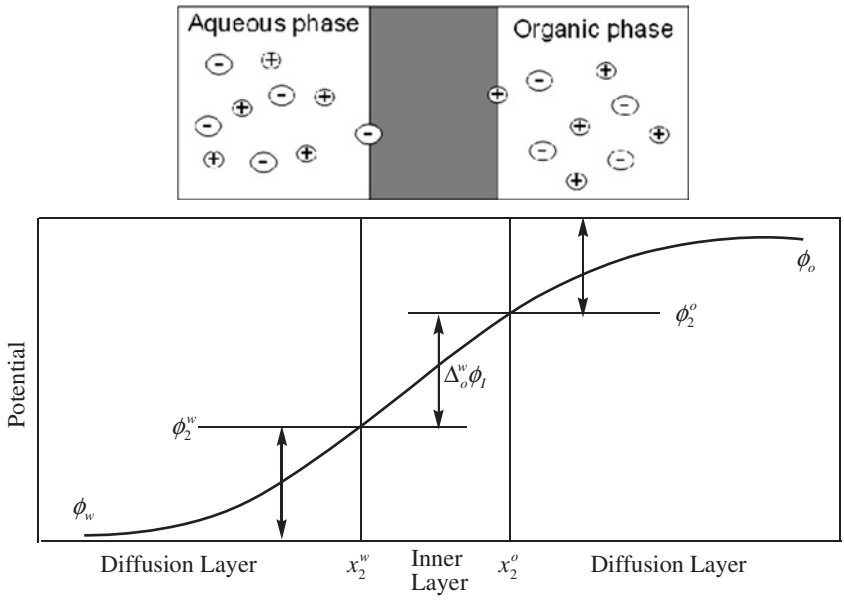


**Figure 17.3.3** The modified Verwey–Niessen model and potential distribution. (Reprinted with permission from (20). Copyright 1977 Elsevier Science).

In this MVN model, the Galvani potential difference $\Delta_o^w\phi$ was split into three parts

$$\Delta_o^w\phi = \phi^w - \phi^o = \Delta_o^w\phi_i + \phi_2^o - \phi_2^w \tag{17.3.2.15}$$

where $\Delta_o^w\phi_i = \phi(\chi_2^w) - \phi(\chi_2^o)$ is the potential difference across the inner layer and $\phi_2^o = \phi(\chi_2^o) - \phi^o$ or $\phi_2^w = \phi(\chi_2^w) - \phi^w$ are the potential differences across the diffuse layers in the phases o or w, respectively.

The variation of $d\phi/d\mathrm{x}$ in each diffuse layer is given by the classical Poisson–Boltzmann equation, which in case of a 1:1 electrolyte is

$$\left(\frac{d\phi}{d\mathrm{x}}\right)_{\mathrm{x}_2<\mathrm{x}<\mathrm{x}_\infty} = \pm\sqrt{\frac{8RTc}{\varepsilon}}\sinh\left[\frac{F}{2RT}(\phi_\chi - \phi_\infty)\right] \tag{17.3.2.16}$$

Since the model assumes the existence of a physical barrier between the two phases, it is possible to define the charge of the diffuse layer by

$$\sigma = \pm\sqrt{8RTc\varepsilon}\sinh\left[\frac{F}{2RT}(\phi_2 - \phi_\infty)\right] \tag{17.3.2.17}$$

The electroneutrality of the interface $\sigma^\circ = -\sigma^w$ leads to two important relations

$$\varepsilon^o\left(\frac{d\phi}{d\mathrm{x}}\right)_{\mathrm{x}=\chi_2^0} = \varepsilon^w\left(\frac{d\phi}{d\mathrm{x}}\right)_{\mathrm{x}=\chi_2^w} \tag{17.3.2.18}$$

and

$$\frac{\sinh[F(\phi_2^w - \phi_\infty^w)/2RT]}{\sinh[F(\phi_2^o - \phi_\infty^o)/2RT]} = -\sqrt{\frac{\varepsilon^o c^o}{\varepsilon^w c^w}} \tag{17.3.2.19}$$

From equation (17.3.2.19), the potential drop in each diffuse layer can be calculated as a function of the difference $\Delta_o^w\phi - \Delta\phi_i$. Furthermore, the potential drop in the inner layer can also be calculated. The interesting conclusion of this work is that the potential drop across the inner layer was found to be negligible.

***(b) GS (Girault–Schiffrin) model***

Girault and Schiffrin (54) proposed a new model to explain the interfacial structure according to surface tension (32) and capacitance measurements (55), which have given access to important interfacial quantities such as surface excess concentrations and have shown that there is no inner layer of oriented solvent molecules and consequently no interfacial potential drop (54, 56, 57). They suggested that the interface could be regarded as a mixed solvent layer, no more than of two or three molecular diameter thickness. The model is illustrated in Figure 17.3.4, and shows that the penetration of the ions in the interfacial region depends on their hydrophobicity or hydrophilicity. Hydrophilic ions like potassium or chloride tend not to enter the interfacial region as shown by positive excess concentration of water (Figure 17.3.4A) (54). On the other hand, at the interface between two electrolytes having a common hydrophobic cation (e.g., TBACl/TBATPB), this cation

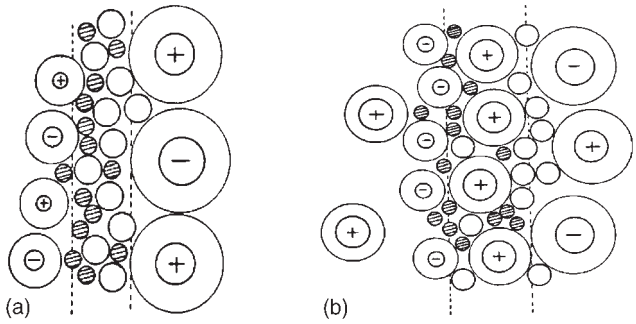


**Figure 17.3.4** Mixed solvent model. (A) KCl/TBATPB system (polarizable interface); (B) TBACl/TBATPB system (non-polarizable interface). (Reprinted with permission from (54). Copyright 1985 Elsevier Science).

will freely penetrate the interface to such an extent as to be specifically adsorbed (Figure 17.3.4B). It is expected that the variation of standard chemical potential which represents the Gibbs energy of transfer takes place within this mixed solvent layer.

### 17.3.3 Charge transfer reactions at liquid/liquid interfaces

One of the characteristics of electrochemistry at liquid/liquid interfaces is the diversity of charge transfer reactions which can be studied by electrochemical methodologies (6). These charge transfer reactions can be classified into three main categories: (a) ion transfer (IT) reaction; (b) facilitated ion transfer (FIT) reaction; (c) electron transfer (ET) reaction.

#### *17.3.3.1 Ion transfer reactions*

Ion transfer reactions are perhaps the easiest to investigate. When an ion has a relatively low Gibbs energy of transfer and its value is within the potential window of the experimental system, its transfer can occur while the liquid/liquid interface is polarized. Figure 17.3.5 shows one example. The potential window is about 500 mV (Figure 17.3.5A) and the transfer of acetylcholine ($Ac^+$) is at the middle of the potential window (Figure 17.3.5B). In contrast to ET reactions at a solid/electrolyte interface, the valence state of the ion does not change so that only the solvation is varied while the transfer is occurring. Since the first report by Gavach *et al*. in 1974 describing the observation of $TBA^+$ transfer at the polarized W/NB interface, there have been numerous investigations on this subject, ranging from simple inorganic and organic ions to drugs and biomolecules (2, 3, 34, 58, 59). Most of the IT reactions are fast and can be considered as reversible (6).

Equation (17.3.2.7) is the Nernst equation for ion transfer reactions at equilibrium. The resemblance with the classical Nernst equation for redox reactions implies that all of the electrochemical methods for reversible reactions where the Nernst equation is used as a boundary condition for the resolution of Fick's diffusion equations can be directly transposed (6).

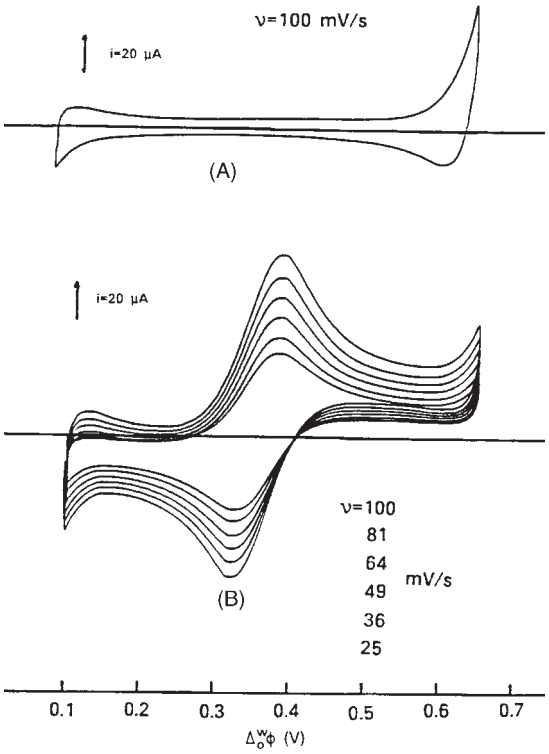


**Figure 17.3.5** Voltammograms of the following systems: (A) Aqueous phase: 0.01 M LiCl + 0.3 M $Li_2SO_4$; (B) aqueous phase: 0.4 mM AcCl + 0.01 M LiCl + 0.3 M $Li_2SO_4$. Dichloromethane phase: 0.01 M TBATPBCl ((33), page 94).

Determination of the rate constant of IT reactions has been a focus in the past 20 years (2, 3, 6). From a phenomenological point of view, an IT reaction includes three major steps:

(1) Mass transfer in one phase to the interface (mainly diffusion);
(2) Ion transfer reaction;
(3) Mass transfer in the other phase away from the interface.

Scanning electrochemical microscopy (SECM) (Chapter 12) is one method that can provide reliable and precise measurement of rate constants of IT reactions (60). Marcus recently formulated the theory for ions transfer reaction at a L/L interface and proposed a mechanism involving initial desolvation of an ion from the first phase, A, and concerted solvation by the second phase, B (61). Although there has been significant experimental progress in this area, the mechanism is still uncertain. Regardless of these mechanistic uncertainties, IT reactions can be used in many applications as will be discussed below.

### *17.3.3.2 Facilitated ion transfer reactions*

When an ion has relatively higher (or lower) Gibbs energy of transfer at a liquid/liquid interface, its transfer wave normally appears outside of the potential window or very near the positive or negative end of the potential window, so that it is difficult to study the simple IT reaction directly. In order to solve such a problem, a ligand which can complex with the ion can be chosen to be put into either phase to lower the Gibbs energy of transfer. Thus, its transfer can be adjusted to be within the potential window. Such a process is called facilitated IT reaction and can be expressed as follows:

$$M^{z+}(w) + nL(o) \rightleftarrows ML_n^{z+}(o) \qquad (17.3.3.1)$$

Koryta reported the first FIT reaction in 1979 (25), and this method can not only provide the stoichiometric information between the ion and the ligand, thermodynamic and kinetic parameters, but can also have applications in selective amperometric ion sensors, and in electro-assisted solvent extraction across liquid membranes (1, 2, 6, 62). Various ionophores, such as crown ethers, antibiotics, ETH series ionophores and calixarenes, have been used to facilitate cations transfer (1–6). Recently anion transfers facilitated by ionophores have also been observed (63, 64).

In 1991 Girault *et al*. (65) proposed a mechanism for FIT reactions (see Figure 17.3.6). Depending upon the distribution coefficient of the ligand, four possible mechanisms can be outlined as follows:

(1) Transfer by interfacial complexation (TIC);
(2) Transfer by interfacial dissociation (TID);
(3) Transfer followed by organic phase complexation (TOC);
(4) Aqueous complexation followed by the transfer of the complex (ACT).

In the case of TIC, one has to consider the mass transport of the different reactants to the interface. For a 1:1 complexation reaction with the TIC mechanism where either the ion in

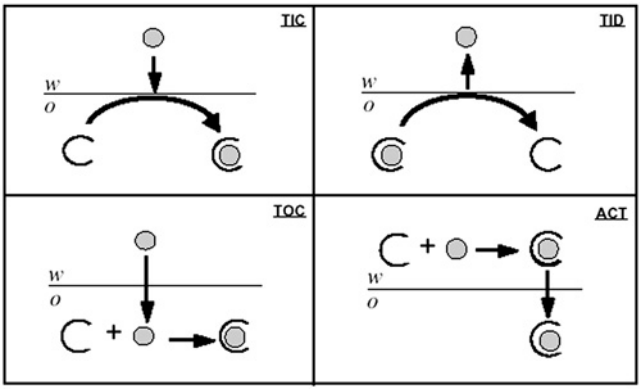


**Figure 17.3.6** Mechanisms of the FIT reaction at a liquid/liquid interface. (Reprinted with permission from (65). Copyright 1991 Elsevier Science).

one phase or the ligand in the other phase is in excess with respect to the other, the mass transport problem is equivalent to that of a redox reaction on a solid electrode. For the remaining cases, either numerical simulations or simplifying approximations are required to understand the mass transport problem.

In 1991, Matsuda *et al*. (66) developed the general theory for a FIT reaction. The equations obtained are too complicated to be applied directly even for the simplest case of 1:1 complexation. However, under the following two limiting conditions, i.e., $C_M \gg C_L$ and $C_L \gg C_M$ (*C*s are the bulk concentration of metal ion and ligand), the current–potential relationship can be simplified for 1:1 complexation (the following two equations respond to the $C_M \gg C_L$, and a TIC process)

$$\Delta_o^w\phi = \Delta_o^w\phi^{1/2} + \frac{RT}{zF}\ln\left(\frac{I}{I_l - I}\right) \tag{17.3.3.2}$$

where

$$\Delta_o^w\phi^{1/2} = \Delta_o^w\phi^{0'} - \frac{RT}{zF}\ln\xi + \frac{RT}{zF}\ln\left(\frac{1+\xi K_{P,L} + K_a^w C_M^w}{K_{P,L}K_a^o C_M^w}\right) \tag{17.3.3.3}$$

In these equations, $I_l$ is the diffusion limited current, the diffusion coefficients of all transferred species in the aqueous (or in the organic) phase are assumed to be equal to $D_W(D_O)$, and $\xi = (D_O / D_W)^{1/2}$. $K_{P,L}$ and $K_a$ are respectively the distribution coefficient of the ligand and the complexation constants in both phases.

The relationship between the cation concentration and the half-wave potential can be discussed based on the following three regions:

(1) If $1+\xi K_{P,L} > 20K_a^w C_M^w$, the half-wave potential will shift about 59 mV when the concentration of cation varies 10-folds. This inequality usually corresponds to the TIC mechanism.

(2) If $1+\xi K_{P,L} < 20K_a^w C_M^w$, the half-wave potential is independent of the concentration of the cation. The complexation constant in the aqueous phase is large and corresponds to the ACT case.

(3) If $1+\xi K_{P,L} \sim 20K_a^w C_M^w$, then the region is a mixture of the preceding two processes and is difficult to be analyzed quantitatively. Matsuda *et al*. further defined another function $F_A$ (65).

$$\begin{aligned} F_A &= \exp[(zF/RT)(\Delta\phi^{1/2} - \Delta\phi^{0'})] \\ &= (K_a^w / \xi K_a^o K_{P,L}) + [(1+\xi K_{P,L})/\xi K_a^o K_{P,L}](1/C_M^w) \end{aligned} \tag{17.3.3.4}$$

If $K_{PL}$ is known, then $K_a^w$ and $K_a^o$ can be evaluated from a plot of $F_A$ vs. $1/C_M^w$. Under the condition of $1+\xi K_{P,L} > 20K_a^w C_M^w$, the plot will pass through the origin and $K_a^o$ can be calculated from the slope. For $1+\xi K_{P,L} < 20K_a^w C_M^w$, the plot is a straight line and parallel to the abscissa. The intercept on the ordinate is $K_a^w / \xi K_a^o K_{P,L}$. Thus the majority of the thermodynamic parameters can be obtained from a simple liquid/liquid interface experiment.

Molecules with acid–base properties can also be classified as a FIT reaction. For instance, the protonated base $BH^+$ (neutral B) can be regarded either as a simple cation transfer reaction or as a proton transfer facilitated by the conjugated acid (67, 68). Finally, the FIT by ion-pair formation can also be classified into this category (6).

### *17.3.3.3 Electron transfer reactions*

Electron transfer at a liquid/liquid interface is an example of an interfacial heterogeneous ET reaction occurring between a redox couple in an aqueous phase and another redox couple in an organic phase. The ET occurs either by external polarization of the interface or by the interfacial potential difference represented in equation (17.3.3.5) and schematically shown in Figure 17.3.7 (2, 6).

$$n_2\mathrm{O}_1(\mathrm{w}) + n_1\mathrm{R}_2(\mathrm{o}) \rightleftarrows n_2\mathrm{R}_1(\mathrm{w}) + n_1\mathrm{O}_2(\mathrm{o}) \tag{17.3.3.5}$$

At equilibrium, the Galvani potential difference is

$$\Delta_{\mathrm{o}}^{\mathrm{w}}\phi = \frac{\mu_{\mathrm{R}_1}^0 - \mu_{\mathrm{O}_1}^0}{n_2F} + \frac{\mu_{\mathrm{O}_2}^0 - \mu_{\mathrm{R}_2}^0}{n_1F} + RT\ln\frac{a_{\mathrm{R}_1}a_{\mathrm{O}_2}}{a_{\mathrm{O}_1}a_{\mathrm{R}_2}} \tag{17.3.3.6}$$

In contrast to IT reactions, it is experimentally difficult to study ET reactions at a liquid/liquid interface because there are very few ideal systems. There are normally two requirements for such systems

(1) The potentials of the redox couples in both phases cannot be very different;
(2) The reactants and the products in the organic phase cannot be dissolved in the aqueous phase, and will not be transferred across the interface in their ionic forms.

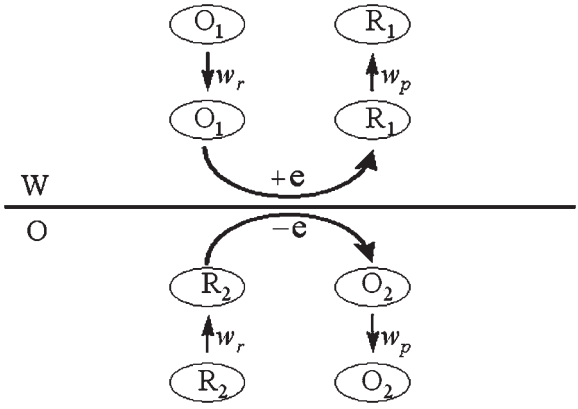


**Figure 17.3.7** The schematic diagram of a heterogeneous ET reaction at a liquid/liquid interface.

Guaninazzi *et al*. found in 1975 that copper could be formed at the W/DCE interface under constant-current electrolysis and with $CuSO_4$ in the aqueous and tetrabutylammonium hexacarbonylvanadate in the organic phase (40). This was the first report of heterogeneous ET reaction at a liquid/liquid interface. Later on, Samec *et al*. and Schiffrin *et al*. investigated this subject systematically (69–73). Bard *et al*. studied heterogeneous ET reactions at a non-polarizable interface by varying concentration ratios of the common ion in both phases using SECM (the ET reactions are driven by the interfacial potential difference) (7, 60, 74–78). Recently, Shao *et al*. combined the three-electrode setup and SECM to probe the heterogeneous ET reactions at a polarizable interface (the interface is polarized by externally applied potential) (79, 80). In the past decade, interest in ET reactions at a liquid/liquid interface has been steadily increasing and many experimental problems have been solved (6, 7, 80).

Key issues in these developments are focused on the dynamics of heterogeneous ET as well as on the effect of the Galvani potential difference. Marcus proposed the theory for ET reactions at the interface between two dielectric media (81–84). Figure 17.3.7 shows the elementary steps involved in interfacial ET processes. The reduction of the species in phase w by the redox couple in phase o requires the diffusion of both species to the interface. The activation energy $\Delta G_{act}$ for the overall process is determined by the reorganization energy term $\lambda$, the formal Gibbs energy for the elementary ET, $\Delta G^{0\prime}$, and the work terms for the approach of the reactants, $w_r$, to the interface and the departure of the product, $w_p$, away from the interface (6).

$$\Delta G_{act} = (\lambda + \Delta G^{0'} + w_p - w_r)/4\lambda \qquad (17.3.3.7)$$

For outer-sphere ET reactions where no substantial changes in the structure of the redox species are involved, the reorganization energy is dominated by the solvent contribution $\lambda_s$. In the case of W/DCE, Girault has solved the expression for $\lambda_s$ (85).

The dependence of the activation energy on the Galvani potential difference arises mainly from the three remaining parameters in equation (17.3.3.7). $\Delta G^{0\prime}$ can be obtained from the difference of the electrochemical potential of the redox couples. $w_r$ and $w_p$ depend upon the changes of the solvation energy and ionic atmosphere of the reactants and products. The Galvani potential difference across the interface can effectively induce changes in all these parameters. Therefore, the observed potential dependence of the ET rate constant can arise from two phenomena:

(1) Variations in the interfacial concentration of the reactants;
(2) Changes in the free energy of the elementary step (6).

Shao *et al*. recently demonstrated that the dependence of the heterogeneous ET rate constant on the interfacial potential difference (also called driving force) follows the Marcus theory and observed the Marcus inverted region (79, 80).

Another very interesting type of heterogeneous ET reaction involves photo-excitable dye molecules adsorbed at liquid/liquid interfaces. Such reactions are important for fundamental aspects of photosynthesis and solar energy conversion (86–88).

### 17.3.4 Methodologies and techniques

From an experimental point of view, the difficulties encountered for electrochemical measurements at a liquid/liquid interface are even more severe than that at a solid/electrolyte interface. This is because of the inherent problems of using organic solvents, such as high *iR* drop and the difficulty in separating the faradaic and charging currents. Despite these problems, almost all modern electrochemical techniques have been applied to study charge transfer reactions at liquid/liquid interfaces (2). For example, methods including cyclic voltammetry and techniques incorporating novel dropping (or ascending) water electrodes have all been employed (1, 2). Various spectroscopic techniques (87, 89, 90) and computer simulations (50–52) have been used in solving problems in this field in the past decade. SECM has emerged as a popular and powerful technique for obtaining reliable heterogeneous rate constants at a L/L interface (60).

#### *17.3.4.1 Four-electrode system*

For all experiments at a large planar liquid/liquid interface (mm- to cm-sized) a four-electrode system is usually adopted. A four-electrode potentiostat must be used in order to compensate the *iR* drop from both phases. The cell design used is shown in Figure 17.3.8. The interface is not fully planar because of curvature due to surface tension effects. The position of the interface is adjusted close to the organic and aqueous reference Luggin capillaries in order to minimize the influence of *iR* drop. Two counter electrodes made of platinum

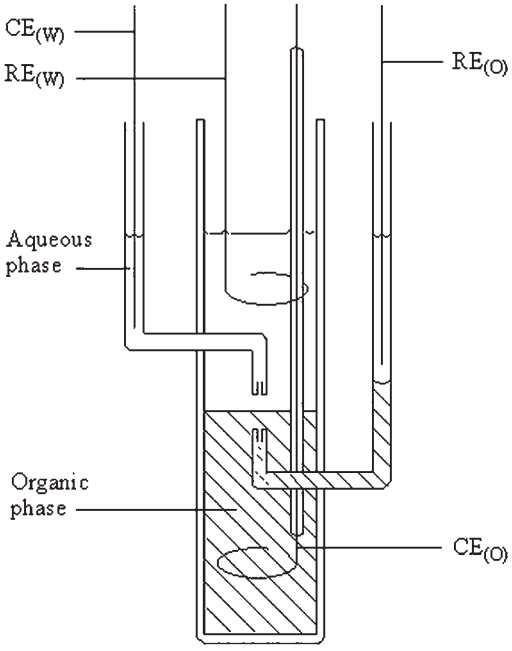


**Figure 17.3.8** Schematic diagram of the four-electrode cell.

(wire or plate) are used for passing the current. The two reference electrodes are usually Ag/AgCl or one Ag/AgCl and another Ag/AgX (X = big anion, e.g., $TPB^-$) and can be employed to control the external polarization. The majority of early thermodynamic and kinetic data gathered were from such a setup (1, 34).

### *17.3.4.2 Two-electrode system*

A micro–liquid/liquid (μ-L/L) interface is usually formed either at the tip of a pulled glass micropipet or within a small hole made in a thin membrane (8, 91, 92). Unlike solid ultramicroelectrodes (UMEs), such pipets or holes are easily made. Pipets as small as a few nanometer radii have recently been fabricated using a laser puller (93). Dual-pipets (or $\theta$-pipets) can also be prepared by pulling $\theta$-glass tubing (94–96). Another simple way of producing a μ-L/L interface in a microcavity is to chemically dissolve microwire encapsulated within a glass tube (97).

In 1986, Taylor and Girault introduced the μ-L/L interface supported at the tip of a micropipet (91). Under certain experimental conditions, the μ-L/L interface behaves like an UME. As in classical electrochemistry, which was revolutionized by the development of UMEs, many advantages can be obtained by replacing a large L/L interface with a μ-L/L interface. These advantages include minimization of charging current and *iR* drop, and a significantly increased mass transport rate. Micropipets can also be employed as probes for electrochemical imaging in SECM. The theory and application of electrochemistry at a μ-L/L interface has been reviewed (8).

Since the current passed at a μ-L/L interface is normally at nA to pA levels, electrochemical measurements can be simplified and a two-electrode system is usually employed. Figure 17.3.9 shows the typical electrochemical cell of a glass U-tube, which contains the organic reference solution in contact with the organic phase. The organic phase is covered with an aqueous layer to limit evaporation of the organic solvent during the experiment.

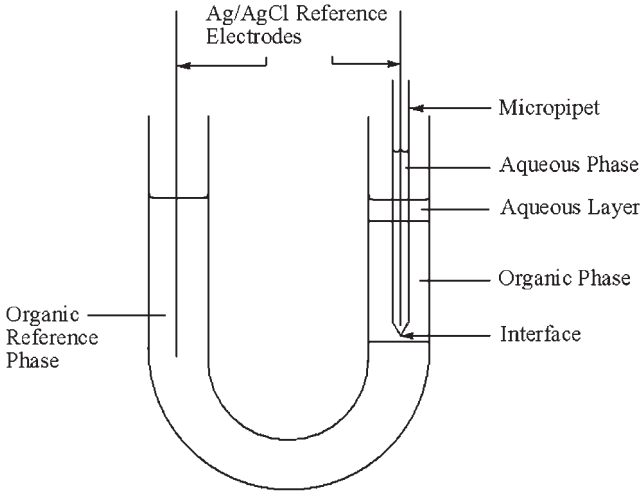


**Figure 17.3.9** Schematic diagram of the two-electrode cell.

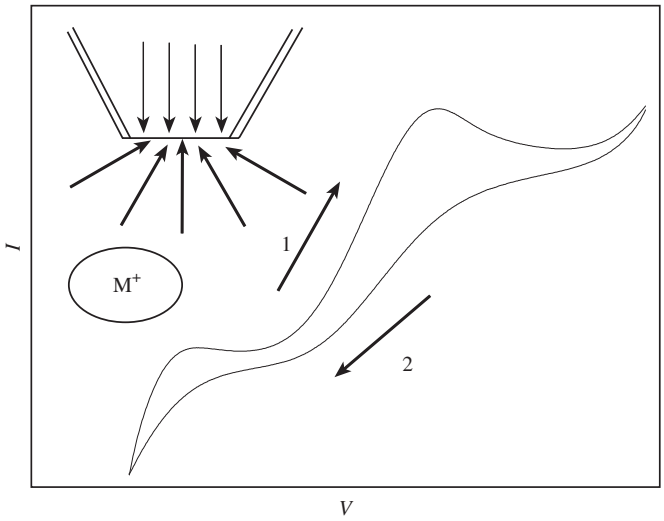


**Figure 17.3.10** The asymmetric diffusion field (see the inset) and its corresponding asymmetric cyclic voltammogram at a μ-L/L interface supported at a micropipet. 1 corresponds to linear diffusion and 2 shows the steady-state voltammogram corresponding to hemispherical diffusion.

The specific geometry of the micropipet produces an asymmetric diffusion field, i.e., ion transfer from inside the pipet to outside is confined to a linear diffusion field which can produce a peak-shaped wave in cyclic voltammetry. In the reverse process, the diffusion field is hemispherical, which produces a steady-state wave in cyclic voltammetry (see the inset in Figure 17.3.10). This unique characteristic of micropipets has been used to identify species responsible for limiting the potential window as well as in the development of mechanisms for FIT reactions (47, 65). Dual-pipets have been used in the generation/collection mode for ionic processes, and these have employed to study complicated ET-IT and IT-IT coupling reactions (96).

### *17.3.4.3 Three-electrode system*

Unlike the situation at a solid/electrolyte interface where a three-electrode system is used, four- and two-electrode systems have been widely employed for large and small liquid/liquid interfaces. Most of the four-electrode potentiostats are homemade and only a few instruments with such functions have been commercialized (98). This is probably one of the reasons why this field has not been very popular since most electrochemical laboratories are equipped with a three-electrode potentiostat. In 1998, Anson *et al*. reported that charge transfer reactions at a liquid/liquid interface could also be studied by a three-electrode system with a thin-layer cell (99, 100). Later, Scholz *et al*. reported a three-phase junction setup (101, 102). Shao *et al*. supported a small droplet of aqueous solution (μL) containing a certain concentration ratio of redox couples on a Pt surface and demonstrated that charge transfer could be studied by a three-electrode setup (103). Girault *et al*. extended this to a supported small droplet of aqueous (organic) phase on the surface of

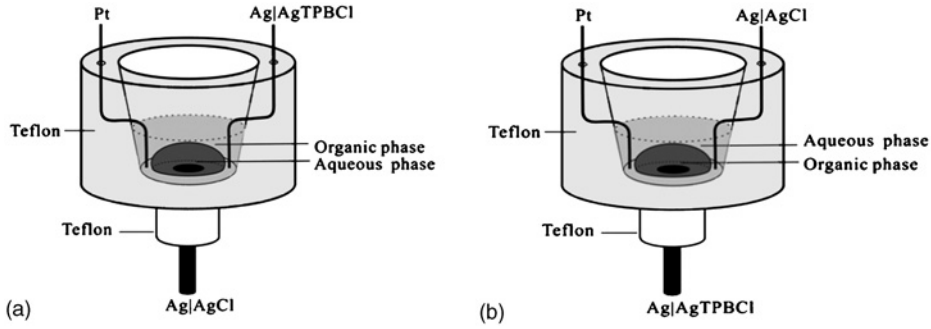


**Figure 17.3.11** Schematic presentations of the electrochemical cells for the cases in which $r$ is large (A) or small (B). (Reprinted with permission from (105). Copyright 2003 American Chemical Society).

Ag/AgCl (Ag/AgTPBCl) (104). Figure 17.3.11 shows the schematic representations of electrochemical cells, which can be used to study the phase volume ratio ($r = V_o/V_w$, $V_o$ and $V_w$ are respective organic and aqueous phase volume) effect (105).

For an aqueous droplet supported on a solid (Pt or C) electrode surface, the potential difference at the solid/liquid interface is fixed because the concentration ratio of the redox couples in the droplet is constant and it can be used as a pseudo-reference electrode. It forms a W/O interface when the assembly is immersed in an organic solution. The W/O interface formed between the aqueous droplet and the organic phase can be studied with a three-electrode system. The ET process at the solid/liquid interface and the charge transfer processes at the liquid/liquid interface are coupled as reactions in series. The disadvantage of this setup is the cations associated with the redox couples usually limit the potential window and very few redox couples can be chosen (103). The droplet supported on Ag/AgCl or Ag/AgX (X is a big anion) can function similarly and only needs $Cl^-$ (or $X^-$) to be present in the aqueous (organic) droplet to fix the potential difference at the solid/liquid interface. In this way one can obtain a wider potential window and study the effect of the phase volume ratio on charge transfer reactions at a L/L interface.

## 17.3.5 Applications

In the past 10 years, more and more applications of charge transfer reactions at liquid/liquid interfaces have been demonstrated (1–10). The following are some examples.

### *17.3.5.1 Pharmacokinetics*

In pharmaceutical sciences, log $P$ is an important parameter, which is defined as $\log P = \log(a_i^o/a_i^w)$ (where $\alpha$ is the activity of species $i$ in both phases). Lipophilicity represents the affinity of a compound for a lipidic environment, and has been widely used to design drugs and to assess their performances. It is commonly measured by its partition coefficient in a biphasic system, $P$. Therefore, log $P$ is actually related to the difference in

solvation energy between water and the adjacent organic phase, and is then directly related to the Gibbs energy of transfer (6).

Since the Gibbs energy of transfer of a species can be easily determined by cyclic voltammetry at a liquid/liquid interface, numerous compounds of biological interest have been studied in the past 20 years (2). In pharmaceutical sciences, a commonly used log *P* is based on an interface between water and *n*-octanol. However, many compounds have very low solubility in *n*-octanol and hydrogen-bonding between water and *n*-octnaol exists. These factors make direct electrochemical measurements difficult (107, 108). Girault *et al*. demonstrated that the water/DCE system could be used to replace the water/*n*-octanol system. They transposed the Pourbaix's pH–potential diagrams to include biphasic systems and established the ionic partition diagram which can be used to predict and interpret the transfer mechanism of ionizable species (6, 106, 109). This method consists of measurements of equiconcentration boundaries as a function of the interfacial Galvani potential difference $\Delta_o^w\phi$ and aqueous pH by taking account of the thermodynamic equilibria governing the distribution of the various acid–base forms of the molecule involved in the transfer. Figure 17.3.12 shows the particular case of the anti-arrythmic drug quinidine. The ionic partition diagram defines the domains of predominance of each species either in the aqueous or in the organic phase and it offers a general and direct visualization of all the transfer mechanisms. The amperometric determination of the pH-lipophilicity profile of drugs by electrochemistry at liquid/liquid interfaces will become an important competitor to the potentiometric two-phase titration which is the most popular technique to date (109).

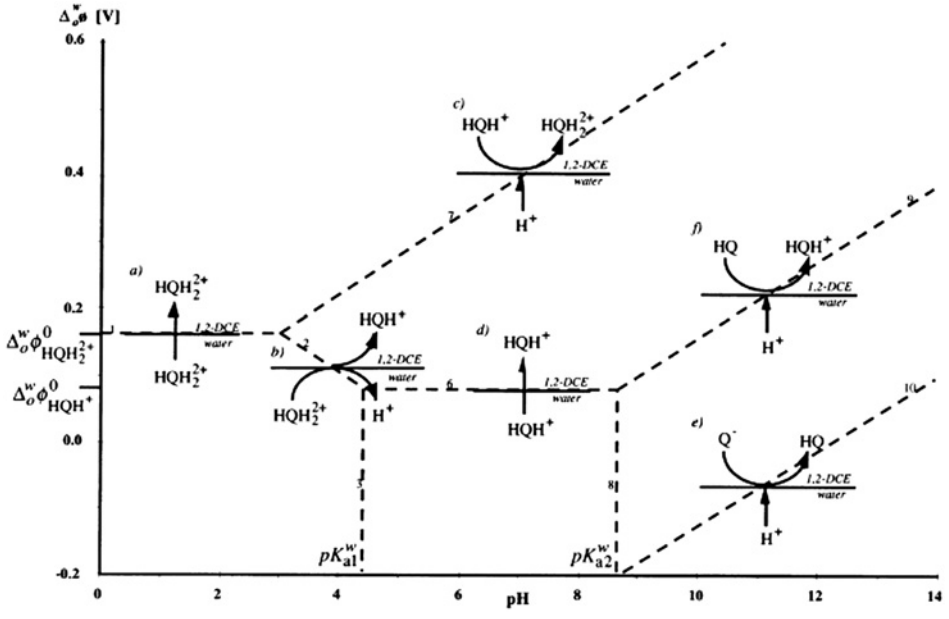


**Figure 17.3.12** Ionic partition diagram of quinidine in water/DCE interface at 21°C. (Reprinted with permission from (106). Copyright 1996 American Chemical Society).

### *17.3.5.2 Amperometric sensors*

Since most IT and FIT reactions are reversible and the currents resulting from them are proportional to their concentrations, they can be used to design amperometric ion sensors (5, 6). The main advantage of such an approach is that selectivity may be tailored by the choice of the ionophore and by the polarization potential. The main disadvantages are (1) the mechanical instability of the interface and (2) the large *iR* drop resulting from the toxic organic phase. It is possible to adopt gel electrolytes to overcome the former and charge transfer reactions at liquid/polymer-gel and agar-gel/liquid interfaces have been successfully applied in designing such amperometric sensors (110–114).

Minimization is the way to circumvent the problems caused by *iR* drop. One good example is the iondes, which consist of a thin inert polymer layer. They are microperforated and covered by a polyvinylchloride-2-nitrophenyloctylether (PVC-NPOE) electrolyte gel and can be incorporated in a flowing cell (Figure 17.3.13). Various ionophores have been put into the gel matrix in order to fabricate amperometric detectors for the measurements of different ions (115–118). Less toxic solvents such as NPOE have been employed to replace toxic NB or DCE (118).

The amperometric sensors based on FIT reactions can determine either ionophore (when metal ion is in excess) or metal ion (when ionophore is in excess). One example is the determination of trace Hg(II) and Pb(II) in water at a macro-L/L interface using stripping voltammetry where the organic phase has excess concentration of suitable ionophore with detection limits as low as 1.6 and 1 ppb, respectively (119).

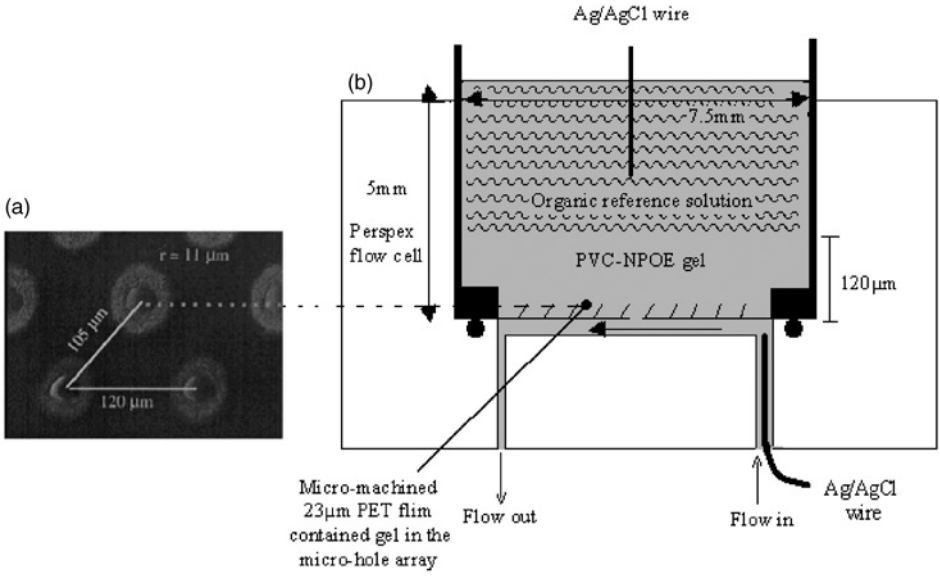


**Figure 17.3.13** (a) SEM of the entrance-side holes in an array with PVC-NPOE gel cast at 70 °C. (b) Simplified diagram of the setup for flow experiment. (Reprinted with permission from (118). Copyright 1997 Elsevier Science).

### *17.3.5.3 Electrochemical imaging*

Another important aspect of charge transfer reactions at a L/L interface is that all three types of transfer reactions can be employed to obtain imaging of various kinds of substrates and information about reactivity (5, 60). In a SECM imaging experiment, a micropipet can replace a solid tip and serve as a probe or tip. SECM imaging is obtained by rastering the tip above the substrate, either solid or liquid, and recording the variations in the tip current.

Solomon and Bard reported the first such application (74). The ET between aqueous ferrocyanide inside a micropipet and TCNQ in the outer DCE phase was used for SECM imaging. TCNQ was reduced by ferrocyanide to form $TCNQ^-$ at the tip. The images of surface topography and redox reactivity of parallel platinum bands on the silicon surface were obtained by scanning a micropipet in a horizontal x-y plane just a few micrometers above the substrate surface.

IT-based SECM imaging can be performed with a micropipet containing the same ion ($M^+$) as that in another phase (120). The IT reaction at the L/L interface can be induced by the depletion of the concentration of this ion in the top solution near the interface caused by the polarization of the micropipet, which can provide positive feedback if the bottom phase has a sufficiently high concentration of $M^+$. The images of a 5 μm pore in a polycarbonate membrane were obtained by a 3 μm diameter pipet based on the transfer of tetraethyammonium ($TEA^+$) across the W/DCE interface.

The SECM positive–negative feedback mode can also be achieved based on FIT reactions at the L/L interface (121). Figure 17.3.14 illustrates the principle. The tip current can be produced by transferring $K^+$, facilitated by DB18C6, from the aqueous phase inside the micropipet to the outer DCE phase. When the tip is biased at a sufficiently positive potential, the tip current is limited by the diffusion of DB18C6 to the interface. As the tip approaches the bottom aqueous phase, $K^+$ is released from the complex and transferred to

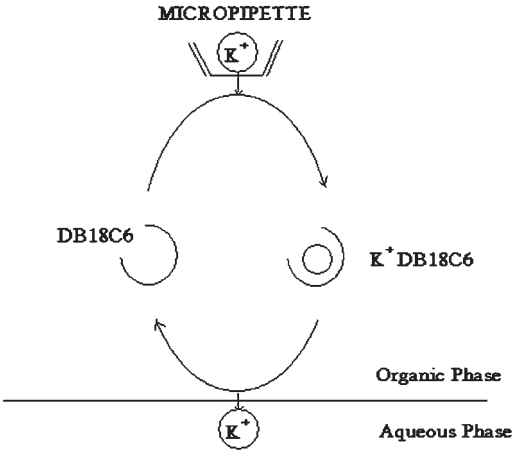


**Figure 17.3.14** Schematic diagram of SECM operating in the FIT mode. (Reprinted with permission from (121). Copyright 1997 Elsevier Science).

the aqueous phase. Here DB18C6 serves just as a mediator in the conventional SECM feedback experiments and is regenerated via an interfacial dissociation mechanism. Therefore, the tip current can be enhanced and a positive feedback can be produced. If a solid substrate is probed by this approach, a negative feedback will occur.

This approach has been used to probe $K^+$ transfer through gramicidin channels in a BLM (77), and to fabricate micro-patterns on a solid surface (122).

As mentioned in a recent review article by Girault *et al*. (6), potential applications can also be found in the areas of electrocatalysis and solar energy conversion, Marangoni pumps, electro-assisted solvent extraction and thermoelectricity, and phase transfer catalysis (123).

### 17.3.6 Prospects

Electrochemistry at liquid/liquid interfaces has progressed markedly in the past 30 years. Excellent work on modified liquid/liquid interface with lipids and nanoparticles have been reported (75, 78, 124–127). Droplet electrodes and three-phase junctions have made this field more popular and versatile (102, 103, 128). The ET induced IT reactions at three-phase junction have been employed to obtain the log *P* of different drugs at W/*n*-octanol interfaces (102, 129, 130). New and less toxic solvents, such as room temperature ionic liquids (RTILs) have replaced organic solvents to form W/RTIL interfaces (131, 132). However, from a theoretical point of view, the key aspects of potential distribution remain the major challenge. Only a few biological applications have been so far reported based on the techniques developed from this field.

### Acknowledgments

This work is supported by the National Natural Science foundation of China (#20235010, #20475003, #20173058, and #20420130137) and special 985 project of Peking University. I appreciate the help of my students Zhong Chen, Zhongwei Liang, Meiqin Zhang in drawing the Figures.

## REFERENCES

1. A. G. Volkov, D. W. Deamer, Eds., *Liquid-liquid Interfaces: Theory and Methods*, CRC Press: Boca Raton, FL, 1996.
2. A. G. Volkov, Ed., *Liquid Interfaces in Chemical, Biological, and Pharmaceutical Applications*, Marcel Dekker: New York, 2001.
3. H. H. Girault in *Modern Aspects of Electrochemistry*, J. O' M. Bockris, B. E. Conway, R. E. White, Eds., Plenum: New York, 1993, Vol. 25.
4. P. Vanysek in *Modern Electroanalytical Techniques*, *Chemical Analysis Series*, P. Vanysek, Ed., John Wiley: New York, 1996, Vol. 139.
5. B. Liu, M. V. Mirkin, *Anal. Chem*. **73**, 670A (2001).
6. F. Reymond, D. Fermin, H. J. Lee, H. H. Girault, *Electrochim. Acta* **45**, 2647 (2000).

7. S. Amemiya, Z. Ding, J. Zhou, A. J. Bard, *J. Electroanal. Chem*. **483**, 7 (2000).
8. B. Liu, M. V. Mirkin, *Electroanalysis* **12**, 1433 (2000).
9. Z. Samec, *Pure Appl. Chem*. **76**, 2147 (2004).
10. P. Vanysek, *Electrochemistry at Liquid-Liquid Interfaces*, *Lecture Notes in Chemistry*, Springer: Berlin, 1985, Vol. 39.
11. W. Nernst, E. H. Risenfield, *Ann. Phys*. **8**, 600 (1902).
12. M. Cremer, *Z. Biol*. **47**, 562 (1906).
13. W. Ostwald, *Z. Phys. Chem*. **6**, 71 (1890).
14. E. L. W. Verwey, K. F. Niessen, *Phil. Mag*. **28**, 435 (1939).
15. J. Guastalla, *Proc. 2nd Int. Congr. Sur. Act*. **3**, 112 (1957).
16. M. Blank, *J. Colloid. Interface Sci*. **22**, 51 (1966).
17. C. Gavach, T. Mlodnicka, J. Guastalla, *C. R. Acad. Sci*. **C266**, 1196 (1968).
18. C. Gavach, F. Henry, *C. R. Acad. Series C*. **274**, 1545 (1972).
19. C. Gavach, F. Henry, *J. Electroanal. Chem*. **54**, 361 (1974).
20. C. Gavach, P. Seta, B. D'Epenoux, *J. Electroanal. Chem*. **83**, 225 (1977).
21. Z. Samec, V. Marecek, J. Koryta, M. W. Khalil, *J. Electroanal. Chem*. **83**, 393 (1977).
22. Z. Samec, V. Marecek, J. Weber, *J. Electroanal. Chem*. **100**, 841 (1979).
23. J. Koryta, P. Vanysek, M. Brazina, *J. Electroanal. Chem*. **67**, 263 (1976).
24. J. Koryta, P. Vanysek, M. Brezina, *J. Electroanal. Chem*. **75**, 211 (1977).
25. J. Koryta, *Electrochim. Acta* **24**, 293 (1979).
26. J. Koryta, *Electrochim. Acta* **29**, 445 (1984).
27. J. Koryta, *Electrochim. Acta* **33**, 189 (1988).
28. O. R. Melroy, B. P. Buck, *J. Electroanal. Chem*. **136**, 19 (1982).
29. Z. Yoshida, H. Freiser, *J. Electroanal. Chem*. **162**, 307 (1984).
30. M. Senda, T. Kakutani, *Hyomen* **18**, 535 (1980).
31. S. Kihara, Z. Yoshida, T. Fujinaga, *Bunseki Kagaku* **31**, E297 (1982).
32. H. H. Girault, D. J. Schiffrin, *J. Electroanal. Chem*. **150**, 43 (1983).
33. Y. Shao, Ph. D. Thesis, Edinburgh University, 1991.
34. H. H. Girault, D. J. Schiffrin in *Electroanalytical Chemistry*, A. J. Bard, Ed., Marcell Dekker: New York, 1989, Vol. 15.
35. H. H. Girault, D. J. Schiffrin, *Electrochim. Acta* **31**, 1341 (1986).
36. http://lepa.epfl.ch/cgi/DB/InterrDB.pl.
37. Y. Marcus, *Pure Appl. Chem*. **55**, 977 (1983).
38. J. Koryta, P. Vanysek in *Advances in Electrochemistry and Electrochemical Engineering*, H. Gerischer, C. W. Tobias, Eds., John Wiley: New York, 1981, Vol. 12.
39. J. Guastalla, *J. Chim. Phys*. **53**, 470 (1956).
40. M. Guainazzi, G. Silversti, G. Serravalle, *J. Chem. Soc. Chem. Commun*. **6**, 200 (1975).
41. Z. Samec, D. Homolka, V. Marecek, L. Kavan, *J. Electroanal. Chem*. **145**, 213 (1983).
42. O. Valent, J. Koryta, *J. Electroanal. Chem*. **226**, 1 (1987).
43. P. Vanysek, *Anal. Chem*. **62**, 827A (1990).
44. Z. Koczorowski, I. Paleska, G. Geblewicz, *J. Electroanal. Chem*. **164**, 201 (1984).
45. Y. Shao, J. A. Campbell, H. H. Girault, *J. Electroanal. Chem*. **300**, 415 (1991).
46. D. Homolka, L. Hung, A. Hofmanova, M. W. Khalil, J. Koryta, V. Marecek, Z. Samec, S. K. Sen, P. Vanysek, J. Weber, M. Janda, I. Stiber, *Anal. Chem*. **52**, 1606 (1980).
47. A. A. Stewart, Y. Shao, C. M. Pereira, H. H. Girault, *J. Electroanal. Chem*. **305**, 135 (1991).
48. T. Wandlowski, V. Marecek, K. Holub, Z. Samec, *J. Phys. Chem*. **93**, 8204 (1989).
49. A. Brown, Ph.D. Thesis, Edinburgh University, 1992.
50. I. Benjamin, *J. Chem. Phys*. **97**, 1432 (1992).
51. I. Benjamin, *Chem. Rev*. **96**, 1449 (1996).

52. I. Benjamin, *Annu. Rev. Phys. Chem*. **48**, 407 (1997).
53. M. Gros, S. Gromb, C. Gavach, *J. Electroanal. Chem*. **89**, 29 (1978).
54. H. H. Girault D. J. Schiffrin, *J. Electroanal. Chem*. **195**, 213 (1985).
55. Z. Samec, V. Marecek, D. Homolka, *Faraday Discuss. Chem. Soc*. **77**, 197 (1984).
56. H. H. Girault, *Electrochim. Acta* **32**, 383 (1987).
57. H. H. Girault, *J. Electroanal. Chem*. **257**, 47 (1988).
58. M. Senda, *Anal. Sci. Technol*. **8**, 95A (1995).
59. S. Amemiya, X. Yang, T. L. Wazenegger, *J. Am. Chem. Soc*. **125**, 11832 (2003).
60. A. J. Bard, M. V. Mirkin, Eds., *Scanning Electrochemical Microscopy*, Marcel Dekker: New York, 2001.
61. R. A. Marcus, *J. Chem. Phys*. **113**, 1618 (2000).
62. M. Senda, T. Kakiuchi, T. Osakai, *Electrochim. Acta* **36**, 253 (1991).
63. Y. Shao, B. Linton, A. D. Hamilton, S. W. Weber, *J. Electroanal. Chem*. **441**, 33 (1998).
64. T. Shioya, S. Nishizawa, N. Teramae, *J. Am. Chem. Soc*. **120**, 11534 (1998).
65. Y. Shao, M. Osborne, H. H. Girault, *J. Electroanal. Chem*. **308**, 101 (1991).
66. H. Matsuda, Y. Yamada, K. Kanamori, Y. Kudo, Y. Takeda, *Bull. Chem. Soc. Jpn*. **64**, 1497(1991).
67. E. Wang, Z. Sun, *J. Electroanal. Chem*. **220**, 235 (1987).
68. K. Kontturi, L. Murtomaki, *J. Pharm. Sci*. **81**, 970 (1992).
69. Z. Samec, V. Marecek, J. Weber, *J. Electroanal. Chem*. **96**, 245 (1977).
70. Z. Samec, V. Marecek, J. Weber, *J. Electroanal. Chem*. **103**, 11 (1979).
71. Z. Samec, V. Marecek, J. Hovorka, *J. Electroanal. Chem*. **216**, 303 (1987).
72. G. Geblewicz, D. J. Schiffrin, *J. Electroanal. Chem*. **244**, 27 (1988).
73. V. J. Cunnane, D. J. Schiffrin, C. Beltran, G. Geblewicz, T. Solomon, *J. Electroanal. Chem*. **247**, 203 (1988).
74. T. Solomon, A. J. Bard, *Anal. Chem*. **67**, 2787 (1995).
75. M. Tsionsky, A. J. Bard, M. V. Mirkin, *J. Am. Chem. Soc*. **119**, 10785 (1997).
76. C. Wei, A. J. Bard, M. V. Mirkin, *J. Phys. Chem*. **99**, 16033 (1995).
77. M. Tsionsky, A. J. Bard, M. V. Mirkin, *J. Phys. Chem*. **100**, 17881 (1996).
78. M. Tsionsky, J. F. Zhou, S. Amemiya, F. Fan, A. J. Bard, R. A. W. Dryfe, *Anal. Chem*. **71**, 4300 (1999).
79. Z. Zhang, Y. Yuan, P. Sun, B. Su, J. Guo, Y. Shao, H. H. Girault, *J. Phys. Chem. B* **106**, 6713 (2002).
80. P. Sun, F. Li, Y. Chen, M. Zhang, Z. Zhang, Z. Gao, Y. Shao, *J. Am. Chem. Soc*. **125** , 9600 (2003).
81. R. A. Marcus, *J. Phys. Chem*. **94**, 1050 (1990).
82. R. A. Marcus, *J. Phys. Chem*. **94**, 4152 (1990).
83. R. A. Marcus, *J. Phys. Chem*. **94**, 7742 (1990).
84. R. A. Marcus, *J. Phys. Chem*. **95**, 2010 (1991).
85. H. H. Girault, *J. Electroanal. Chem*. **388**, 93 (1995).
86. D. J. Fermin, Z. Ding, H. D. Duong, P. F. Brevet, H. H. Girault, *Chem. Comm*. 1125 (1998).
87. D. J. Fermin, Z. Ding, H. D. Duong, P. F. Brevet, H. H. Girault, *J. Phys. Chem. B* **102**, 10334 (1998).
88. D. J. Fermin, Z. Ding, H. D. Duong, P. F. Brevet, H. H. Girault, *Phys. Chem. Chem. Phys*. **1**, 1461 (1999).
89. P. S. Pershan, *J. Chem. Soc. Faraday Discuss*. **89**, 231 (1990).
90. J. Penfold, R. K. Thomas, *J. Phys. A*. **2**, 1369 (1990).
91. G. Taylor, H. H. Girault, *J. Electroanal. Chem*. **208**, 179 (1986).
92. J. A. Campbell, H. H. Girault, *J. Electroanal. Chem*. **266**, 465 (1989).

93. Y. Shao, M. V. Mirkin, *J. Am. Chem. Soc*. **119**, 8103 (1997).
94. Y. Shao, B. Liu, M. V. Mirkin, *J. Am. Chem. Soc*. **120**, 12700 (1998).
95. B. Liu, Y. Shao, M V. Mirkin, *Anal. Chem*. **72**, 510 (2000).
96. Y. Chen, Z. Gao, F. Li, L. H. Ge, M. Q. Zhang, D. P. Zhan, Y. Shao, *Anal. Chem*. **74**, 6593 (2003).
97. V. J. Cunnane, D. J. Schiffrin, D. E. Williams, *Electrochim Acta* **40**, 2943 (1995).
98. Y. Shao, S. N. Tan, V. Devaud, H. H. Girault, *J. Chem. Soc. Faraday Trans*. **89**, 4307 (1993).
99. C. Shi, F. C. Anson, *J. Phys. Chem. B* **102**, 9850 (1998).
100. T. Chung, F. C. Anson, *Anal. Chem*. **73**, 337 (2001).
101. F. Scholz, S. Komorsky-Lovric, M. Lovric, *Electrochem. Commun*. **2**, 112 (2000).
102. R. Gulaboski, V. Mirceski, F. Scholz, *Electrochem. Commun*. **4**, 277 (2002).
103. S. Ulmeanu, H. Lee, D. J. Fermin, H. H. Girault, Y. Shao, *Electrochem. Commun*. **3** , 219 (2001).
104. V. Gobry, S. Ulmeanu, F. Reymond, G. Bouchard,P. Carrupt, B. Testa, H. H. Girault, *J. Am. Chem. Soc*. **123**, 10684 (2001).
105. M. Zhang, P. Sun, Y. Chen, F. Li, Z. Gao, Y. Shao, *Anal. Chem*. **75**, 4341 (2003).
106. F. Reymond, G. Steyaert, A. Pagliara, P. A. Carrupt, B. Testa, H. H. Girault, *J. Am. Chem. Soc*. **118**, 19511 (1996).
107. G. Caron, A. Pagliara, P. Guillard, P. A. Carrupt, B. Testa, *Helv. Chim. Acta* **79**, 1683 (1996).
108. R. N. Smith, C. Hansch, M. M. Ames, *J. Pharm. Sci*. **64**, 599 (1975).
109. F. Reymond, P. A. Carrupt, B. Testa, H. H. Girault, *Chem. Eur. J*. **5**, 39 (1999).
110. T. Osakai, T. Kakutani, M. Senda, *Bunseki Kagaku* **33**, E371 (1984).
111. T. Kakutani, T. Ohkouchi, T. Osakai, T. Kakiuchi, M. Senda, *Anal. Sci*. **1**, 219 (1985).
112. E. Wang, Z. Sun, *Trends Anal. Chem.* **7**, 99 (1988).
113. V. Marecek, H. Janchenova, M. P. Colombini, P. Papoff, *J. Electroanal. Chem*. **217**, 213 (1987).
114. V. Marecek, M. P. Colombini, *J. Electroanal. Chem*. **241**, 133 (1988).
115. H. J. Lee, C. Beriet, H. H. Girault, *J. Electroanal. Chem*. **453**, 211 (1998).
116. F. Silva, M. J. Sousa, C. M. Pereira, *Electrochim. Acta* **42**, 3095 (1997).
117. H. J. Lee, H. H. Girault, *Anal. Chem*. **70**, 4280 (1998).
118. H. J. Lee, P. D. Beattie, B. J. Seddon, M. D. Osborne, H. H. Girault, *J. Electroanal. Chem*. **440**, 73 (1997).
119. H. Ketano, M. Senda, *Anal. Sci*. **14**, 63 (1998).
120. Y. Shao, M. V. Mirkin, *J. Phys. Chem. B* **102**, 9915 (1998).
121. Y. Shao, M. V. Mirkin, *J. Electroanal. Chem*. **439**, 137 (1997).
122. Y. Yatziv, I. Turyan, D. Mandler, *J. Am. Chem. Soc*. **124**, 5618 (2002).
123. Y. Uchiyama, M. Fujinami, .T. Sawada, I. Tsuyumoto, *J. Phys. Chem. B* **104**, 4699 (2000).
124. B. M. Quinn, P. Liljeroth, K. Kontturi, *J. Am. Chem. Soc*. **124**, 12915 (2002).
125. B. M. Quinn, K. Kontturi, *J. Am. Chem. Soc*. **126**, 7168 (2004).
126. R. A. W. Dryfe, A. O. Simm, B. Kralj, *J. Am. Chem. Soc*. **125**, 13014 (2003).
127. B. Su, J. P. Abid, D. J. Fermin, H. H. Girault, H. Hoffmannova, P. Krtil, Z. Samec, *J. Am. Chem. Soc*. **126**, 915 (2004).
128. P. Sun, Z. Zhang , Z. Gao, Y. Shao, *Angew. Chem. Int. Ed*. **41**, 3445 (2002).
129. R. Gulaboski, A. Galland, G. Bouchard, K. Caban, A. Kretschmer, P. A. Carrupt, Z. Stojek, H. H. Girault, F. Scholz, *J. Phys. Chem. B* **108**, 4565 (2004).
130. R. Gulaboski, F. Scholz, *J. Phys. Chem. B* **107**, 5650 (2003).
131. T. Kakiuchi, N. Tsujioka, S. Kurita, Y. Iwami, *Electrochem. Commun*. **5**, 159 (2003).
132. T. Kakiuchi, N. Tsujioka, *Electrochem. Commun*. **5**, 253 (2003).

This page intentionally left blank

# Part Five

## DATA

This page intentionally left blank

# – 18 –

# Electrode Potentials

**Melissa D. Arning and Shelley D. Minteer**

Department of Chemistry, Saint Louis University,
3501 Laclede Ave., St. Louis, MO 63103, USA

## 18.1 OVERVIEW

The beginning of the chapter is dedicated to charts of operating potential ranges for different solvent/electrolyte/electrode combinations. Operating potentials can act as a guide for determining the maximum and minimum potential to apply to a system. The second half of the chapter includes tables of electrode potentials of organic redox couples, inorganic redox couples, biological redox couples, drugs, vitamins, and neurochemicals. Electrode potentials can be used in conjunction with operating potential ranges to determine the optimal solution/electrode for monitoring a given redox species.

## 18.2 ESTIMATED POTENTIAL RANGES: AQUEOUS AND NON-AQUEOUS SOLUTIONS

Figure 18.1 shows potential ranges (operating windows) for carbon, platinum, and mercury electrodes in aqueous solutions of common electrolytes. Figure 18.2 shows potential ranges (operating windows) for common organic solvents. Potential ranges are merely a guide and will vary with purity of solvent and electrolyte.

## 18.3 STANDARD ELECTRODE POTENTIALS: AQUEOUS SOLUTIONS

Table 18.1 contains a selected list of standard electrode potentials of common redox species in aqueous solutions. A more complete list can be found in reference (3) and a discussion on fundamental standard electrode potential concepts can be found in Chapter 1 of this handbook. All standard electrode potentials are vs. NHE and for solutions at room temperature.

## 18.4 FORMAL ELECTRODE POTENTIALS: APROTIC SOLVENTS

Table 18.2 lists formal electrode potentials for a series of organic redox species in common aprotic solvents. Due to variations in formal potentials with solvent and electrolyte


**Handbook of Electrochemistry**
**Edited by C.G. Zoski**

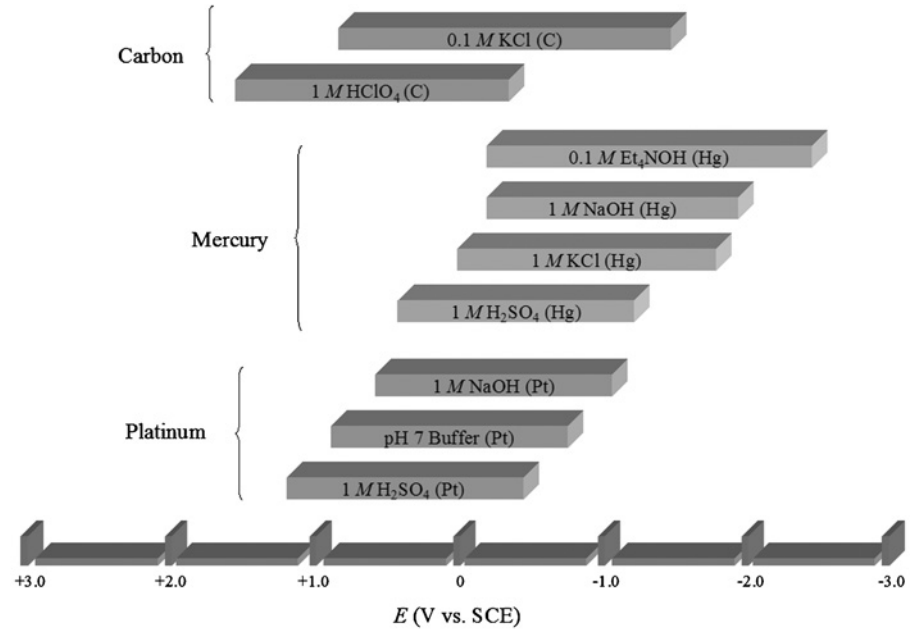


**Figure 18.1** Estimated potential ranges in aqueous solutions at 25 °C. (for colour version: see colour section at the end of the book).

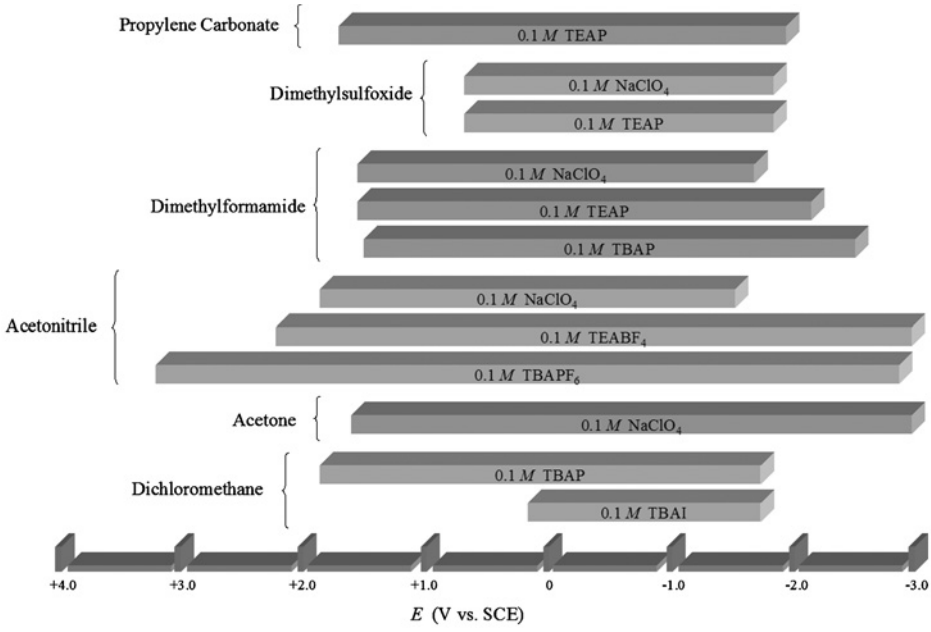


**Figure 18.2** Estimated potential ranges at Pt electrodes for non-aqueous solvent/electrolyte solutions. Data from reference (1). (for colour version: see colour section at the end of the book).

**Table 18.1**

Selected standard electrode potentials (V vs. NHE ) in aqueous solution at 25 °C. Data from references (2–4)

| Reaction | $E^0$ (V vs. NHE) |
|---|---|
| $Ag^+ + e \rightleftharpoons Ag$ | 0.799 |
| $Ag^{2+} + e \rightleftharpoons Ag^+$ | 1.980 |
| $AgBr + e \rightleftharpoons Ag + Br^-$ | 0.071 |
| $AgCl + e \rightleftharpoons Ag + Cl^-$ | 0.222 |
| $AgI + e \rightleftharpoons Ag + I^-$ | −0.152 |
| $Ag_2O + H_2O + 2e \rightleftharpoons 2Ag + 2OH^-$ | 0.342 |
| $Al^{3+} + 3e \rightleftharpoons Al$ | −1.676 |
| $As + 3H^+ + 3e \rightleftharpoons AsH_3$ | −0.230 |
| $As(OH)_3 + 3H^+ + 3e \rightleftharpoons As + 3H_2O$ | 0.240 |
| $AsO(OH)_3 + 2H^+ + 2e \rightleftharpoons As(OH)_3 + H_2O$ | 0.560 |
| $Au^+ + e \rightleftharpoons Au$ | 1.830 |
| $Au^{3+} + 2e \rightleftharpoons Au^+$ | 1.360 |
| $Ba^{2+} + 2e \rightleftharpoons Ba$ | −2.920 |
| $Be^{2+} + 2e \rightleftharpoons Be$ | −1.970 |
| *p*-Benzoquinone + $2H^+ + 2e \rightleftharpoons$ hydroquinone | 0.699 |
| $Br_2(l) + 2e \rightleftharpoons 2Br^-$ | 1.060 |
| $Br_2(aq) + 2e \rightleftharpoons 2Br^-$ | 1.087 |
| $BrO^- + H_2O + 2e \rightleftharpoons Br^- + 2OH^-$ | 0.760 |
| $2HOBr + 2H^+ + 2e \rightleftharpoons Br_2 + 2H_2O$ | 1.600 |
| $2BrO^{3-} + 12H^+ + 10e \rightleftharpoons Br_2 + 6H_2O$ | 1.480 |
| $2BrO^{4-} + 2H^+ + 2e \rightleftharpoons BrO^{3-} + H_2O$ | 1.850 |
| $CO_2 + 2H^+ + 2e \rightleftharpoons CO + H_2O$ | −0.110 |
| $CO_2 + 2H^+ + 2e \rightleftharpoons HCOOH$ | −0.200 |
| $2CO_2 + 2H^+ + 2e \rightleftharpoons H_2C_2O_4$ | −0.480 |
| $Ca^{2+} + 2e \rightleftharpoons Ca$ | −2.840 |
| $Cd(OH)_2 + 2e \rightleftharpoons Cd + 2OH^-$ | −2.840 |
| $Cd^{2+} + 2e \rightleftharpoons Cd$ | −0.403 |
| $Cd^{2+} + 2e \rightleftharpoons Cd(Hg)$ | −0.352 |
| $Ce^{4+} + e \rightleftharpoons Ce^{3+}$ | 1.720 |
| $Cl_2(g) + 2e \rightleftharpoons 2Cl^-$ | 1.358 |
| $HClO_2 + 2H^+ + 2e \rightleftharpoons HOCl + H_2O$ | 1.680 |
| $HClO + H^+ + e \rightleftharpoons ½Cl_2 + H_2O$ | 1.630 |
| $ClO_3^- + 3H^+ + 2e \rightleftharpoons HClO_2 + H_2O$ | 1.180 |
| $ClO_3^- + 2H^+ + e \rightleftharpoons ClO_2 + H_2O$ | 1.170 |
| $ClO_4^- + 2H^+ + 2e \rightleftharpoons CO_3^- + H_2O$ | 1.200 |
| $Co^{2+} + 2e \rightleftharpoons Co$ | −0.277 |
| $Co^{3+} + e \rightleftharpoons Co^{2+}$ | 1.920 |
| $Co(NH_3)_6^{3+} + e \rightleftharpoons Co(NH_3)_6^{2+}$ | 0.060 |
| $Co(phen)_3^{3+} + e \rightleftharpoons Co(phen)_3^{2+}$ | 0.330 |
| $Co(C_2O_4)_3^{3-} + e \rightleftharpoons Co(C_2O_4)_3^{4-}$ | 0.570 |
| $Cr^{2+} + 2e \rightleftharpoons Cr$ | −0.900 |
| $Cr^{3+} + 3e \rightleftharpoons Cr$ | −0.740 |
| $Cr^{3+} + e \rightleftharpoons Cr^{2+}$ | −0.424 |
| $Cr_2O_7^{2-} + 14H^+ + 6e \rightleftharpoons 2Cr^{3+} + 7H_2O$ | 1.360 |
| $Cs^+ + e \rightleftharpoons Cs$ | −2.920 |
| $Cu^+ + e \rightleftharpoons Cu$ | 0.520 |

(*Continued*)

**Table 18.1 (Cont.)**

| Reaction | $E^0$ (V vs. NHE) |
|---|---|
| $Cu^{2+} + 2CN^- + e \rightleftharpoons Cu(CN)_2^-$ | 1.120 |
| $Cu^{2+} + e \rightleftharpoons Cu^+$ | 0.159 |
| $Cu^{2+} + 2e \rightleftharpoons Cu$ | 0.340 |
| $Cu^{2+} + 2e \rightleftharpoons Cu(Hg)$ | 0.345 |
| $CuCl + e \rightleftharpoons Cu + Cl^-$ | 0.120 |
| $Cu(NH_3)_4^{2+} + 2e \rightleftharpoons Cu + 4NH_3$ | 0.000 |
| $Eu^{3+} + e \rightleftharpoons Eu^{2+}$ | −0.350 |
| $½F_2 + H^+ + e \rightleftharpoons HF$ | 3.053 |
| $Fe^{2+} + 2e \rightleftharpoons Fe$ | −0.440 |
| $Fe^{3+} + 3e \rightleftharpoons Fe$ | −0.040 |
| $Fe^{3+} + e \rightleftharpoons Fe^{2+}$ | 0.771 |
| $Fe(phen)^{3+} + e \rightleftharpoons Fe(phen)^{2+}$ | 1.130 |
| $Fe(CN)_6^{3-} + e \rightleftharpoons Fe(CN)_6^{4-}$ | 0.361 |
| $Fe(CN)_6^{4-} + e \rightleftharpoons Fe + 6CN^-$ | −1.160 |
| $2H^+ + 2e \rightleftharpoons H_2$ | 0.000 |
| $2H_2O + 2e \rightleftharpoons H_2 + 2OH^-$ | −0.828 |
| $H_2O_2 + H^+ + e \rightleftharpoons HO\bullet + H_2O$ | 0.710 |
| $H_2O_2 + 2H^+ + 2e \rightleftharpoons 2H_2O$ | 1.763 |
| $2Hg^{2+} + 2e \rightleftharpoons Hg_2^{2+}$ | 0.911 |
| $Hg_2^{2+} + 2e \rightleftharpoons 2Hg$ | 0.796 |
| $Hg_2Cl_2 + 2e \rightleftharpoons 2Hg + 2Cl^-$ | 0.268 |
| $Hg_2Cl_2 + 2e \rightleftharpoons 2Hg + 2Cl^-$ (sat'd KCl) | 0.242 |
| $HgO + H_2O + 2e \rightleftharpoons Hg + 2OH^-$ | 0.098 |
| $Hg_2SO_4 + 2e \rightleftharpoons 2Hg + SO_4^{2-}$ | 0.613 |
| $I_2 + 2e \rightleftharpoons 2I^-$ | 0.536 |
| $I_3^- + 2e \rightleftharpoons 3I^-$ | 0.536 |
| $2HOI + 2H^+ + 2e \rightleftharpoons I_2 + 2H_2O$ | 1.440 |
| $2IO_3^- + 12H^+ + 10e \rightleftharpoons I_2 + 6H_2O$ | 1.200 |
| $IO(OH)_5 + H^+ + e \rightleftharpoons IO_3^- + 3H_2O$ | 1.600 |
| $In^+ + e \rightleftharpoons In$ | −0.130 |
| $In^{3+} + 2e \rightleftharpoons In^+$ | −0.440 |
| $In^{3+} + 3e \rightleftharpoons In$ | −0.340 |
| $K^+ + e \rightleftharpoons K$ | −2.925 |
| $Li^+ + e \rightleftharpoons Li$ | −3.045 |
| $Mg^{2+} + 2e \rightleftharpoons Mg$ | −2.356 |
| $Mn^{2+} + 2e \rightleftharpoons Mn$ | −1.180 |
| $Mn^{3+} + e \rightleftharpoons Mn^{2+}$ | 1.500 |
| $MnO_2 + 2H^+ + 2e \rightleftharpoons Mn^{2+} + 2H_2O$ | 1.230 |
| $MnO_4^- + 8H^+ + 5e \rightleftharpoons Mn^{2+} + 4H_2O$ | 1.510 |
| $MnO_4^- + e \rightleftharpoons MnO_4^{2-}$ | 0.560 |
| $MoO_4^{2-} + 4H_2O + 6e \rightleftharpoons Mo + 8OH^-$ | −0.910 |
| $NO_3^- + 2H^+ + e \rightleftharpoons NO_2 + H_2O$ | 0.800 |
| $NO_3^- + 4H^+ + 3e \rightleftharpoons NO + 2H_2O$ | 0.960 |
| $NO_3^- + H_2O + 2e \rightleftharpoons NO_2^- + 2OH^-$ | 0.010 |
| $Na^+ + e \rightleftharpoons Na$ | −2.714 |
| $Ni^{2+} + 2e \rightleftharpoons Ni$ | −0.257 |
| $Ni(OH)_2 + 2e \rightleftharpoons Ni + 2OH^-$ | −0.720 |
| $NiO_2 + 2e \rightleftharpoons Ni^{2+} + 2H_2O^-$ | 1.590 |
| $O_2 + 2H^+ + 2e \rightleftharpoons H_2O_2$ | 0.695 |

**Table 18.1 (Cont.)**

| Reaction | $E^0$ (V vs. NHE) |
|---|---|
| $O_2 + 4H^+ + 4e \rightleftharpoons 2H_2O$ | 1.229 |
| $O_2 + 2H_2O + 4e \rightleftharpoons 4OH^-$ | 0.401 |
| $O_2 + e \rightleftharpoons O_2^-$ | −0.330 |
| $O_2 + H_2O + 2e \rightleftharpoons HO_2^- + OH$ | −0.080 |
| $O_2 + H^+ + e \rightleftharpoons HO_2$ | −0.130 |
| $O_3 + 2H^+ + 2e \rightleftharpoons O_2 + H_2O$ | 2.075 |
| $P + 3H^+ + 3e \rightleftharpoons PH_3$ | −0.060 |
| $HPO(OH)_2 + 3H^+ + 3e \rightleftharpoons P + 3H_2O$ | −0.500 |
| $HPO(OH)_2 + 2H^+ + 2e \rightleftharpoons H_2PO(OH) + H_2O$ | −0.500 |
| $PO(OH)_3 + 2H^+ + 2e \rightleftharpoons HPO(OH)_2 + H_2O$ | −0.280 |
| $Pb^{2+} + 2e \rightleftharpoons Pb$ | −0.125 |
| $Pb^{2+} + 2e \rightleftharpoons Pb(Hg)$ | −0.121 |
| $PbO_2 + 4H^+ + 2e \rightleftharpoons Pb^{2+} + 2H_2O$ | 1.468 |
| $PbO_2 + SO_4^{2-} + 2H^+ + 2e \rightleftharpoons PbSO_4 + 2H_2O$ | 1.698 |
| $PbSO_4 + 2e \rightleftharpoons Pb + SO_4^{2-}$ | −0.351 |
| $Pd^{2+} + 2e \rightleftharpoons Pd$ | 0.915 |
| $Pt^{2+} + 2e \rightleftharpoons Pt$ | 1.188 |
| $PtCl_4^{2-} + 2e \rightleftharpoons Pt + 4Cl^-$ | 0.758 |
| $PtCl_6^{2-} + 2e \rightleftharpoons PtCl_4^{2-} + 2Cl^-$ | 0.726 |
| $Ru(NH_3)_6^{3+} + e \rightleftharpoons Ru(NH_3)_6^{2+}$ | 0.100 |
| $Rb^+ + e \rightleftharpoons Rb$ | −2.930 |
| $S + 2e \rightleftharpoons S^{2-}$ | −0.447 |
| $2SO_2(aq) + 2H^+ + 4e \rightleftharpoons S_2O_3^{2-} + H_2O$ | −0.400 |
| $SO_2(aq) + 4H^+ + 4e \rightleftharpoons S + 2H_2O$ | 0.500 |
| $S_4O_6^{2-} + 2e \rightleftharpoons 2S_2O_3^{2-}$ | 0.080 |
| $2SO_4^{2-} + H_2O + 2e \rightleftharpoons SO_3^{2-} + 2OH^-$ | −0.940 |
| $2SO_4^{2-} + 4H^+ + 2e \rightleftharpoons S_2O_6^{2-} + 2H_2O$ | −0.250 |
| $S_2O_8^{2-} + 2e \rightleftharpoons 2SO_4^{2-}$ | 1.960 |
| $Sn^{2+} + 2e \rightleftharpoons Sn$ | −0.138 |
| $Sn^{4+} + 2e \rightleftharpoons Sn^{2+}$ | 0.150 |
| $Sr^{2+} + 2e \rightleftharpoons Sr$ | −2.890 |
| $Ti^{2+} + 2e \rightleftharpoons Ti$ | −1.630 |
| $Ti^{3+} + e \rightleftharpoons Ti$ | −0.370 |
| $TiO^{2+} + e \rightleftharpoons Ti^{3+}$ | 0.100 |
| $Tl^+ + e \rightleftharpoons Tl$ | −0.336 |
| $Tl^+ + e \rightleftharpoons Tl(Hg)$ | −0.334 |
| $Tl^{3+} + 2e \rightleftharpoons Tl^+$ | 1.250 |
| $U^{3+} + 3e \rightleftharpoons U$ | −1.660 |
| $U^{4+} + e \rightleftharpoons U^{3+}$ | −0.520 |
| $UO_2^+ + 4H^+ + e \rightleftharpoons U^{4+} + 2H_2O$ | 0.273 |
| $UO_2^{2+} + e \rightleftharpoons UO_2^+$ | 0.163 |
| $V^{2+} + 2e \rightleftharpoons V$ | −1.130 |
| $V^{3+} + e \rightleftharpoons V^{2+}$ | −0.255 |
| $VO^{2+} + 2H^+ + e \rightleftharpoons V^{3+} + H_2O$ | 0.337 |
| $VO_2^+ + 2H^+ + e \rightleftharpoons VO^{2+} + H_2O$ | 1.000 |
| $Zn^{2+} + 2e \rightleftharpoons Zn$ | −0.763 |
| $ZnO_2^{2-} + 2H_2O + 2e \rightleftharpoons Zn + 4OH^-$ | −1.285 |

**Table 18.2**

Formal electrode potentials (V vs. aq SCE) at 25 °C for hydrocarbons in solvents. Data from references (2, 7)

| Compound | Reaction | Solvent | Medium | $E^{0\prime}$ (V vs. SCE) |
|---|---|---|---|---|
| Anthracene | $An + e \rightleftharpoons An^{\bullet -}$ | DMF | 0.1 M TBAI | −1.920 |
| | $An + e \rightleftharpoons An^{\bullet -}$ | MeOH | 0.1 M TEAI | −1.920 |
| | $An^{\bullet -} + e \rightleftharpoons An^{2-}$ | DMF | 0.1 M TBAI | −2.500 |
| | $An^{\bullet +} + e \rightleftharpoons An$ | MeCN | 0.1 M TBAP | 1.300 |
| Azobenzene | $AB + e \rightleftharpoons AB^{\bullet -}$ | DMF | 0.1 M TBAP | −1.360 |
| | $AB^{\bullet -} + e \rightleftharpoons AB^{2-}$ | DMF | 0.1 M TBAP | −2.000 |
| | $AB + e \rightleftharpoons AB^{\bullet -}$ | MeCN | 0.1 M TEAP | −1.400 |
| | $AB + e \rightleftharpoons AB^{\bullet -}$ | PC | 0.1 M TBAP | −1.400 |
| Benzophenone | $BP + e \rightleftharpoons BP^{\bullet -}$ | MeCN | 0.1 M TBAP | −1.880 |
| | $BP + e \rightleftharpoons BP^{\bullet -}$ | THF | 0.1 M TBAP | −2.060 |
| | $BP + e \rightleftharpoons BP^{\bullet -}$ | $NH_3$ | 0.1 M KI | −1.230 |
| | $BP^{\bullet -} + e \rightleftharpoons BP^{2-}$ | $NH_3$ | 0.1 M KI | −1.760 |
| 1,4−Benzoquinone | $BQ + e \rightleftharpoons BQ^{\bullet -}$ | MeCN | 0.1 M TEAP | −0.540 |
| | $BQ^{\bullet -} + e \rightleftharpoons BQ^{2-}$ | MeCN | 0.1 M TEAP | −1.400 |
| Chrysene | $Ch^{\bullet +} + e \rightleftharpoons Ch$ | MeCN | 0.1 M TEAP | 1.220 |
| Ferrocene | $Cp_2Fe^{+} + e \rightleftharpoons Cp_2Fe$ | MeCN | 0.2 M $LiClO_4$ | 0.310 |
| Naphthalene | $N + e \rightleftharpoons N^{\bullet -}$ | MeCN | 0.1 M TEAP | −2.600 |
| Nitrobenzene | $NB + e \rightleftharpoons NB^{\bullet -}$ | MeCN | 0.1 M TEAP | −1.150 |
| | $NB + e \rightleftharpoons NB^{\bullet -}$ | DMF | 0.1 M $NaClO_4$ | −1.010 |
| | $NB + e \rightleftharpoons NB^{\bullet -}$ | $NH_3$ | 0.1 M KI | −0.420 |
| | $NB^{\bullet -} + e \rightleftharpoons NB^{2-}$ | $NH_3$ | 0.1 M KI | −1.241 |
| Oxygen | $O_2 + e \rightleftharpoons O_2^{\bullet -}$ | DMF | 0.2 M TBAP | −0.870 |
| | $O_2 + e \rightleftharpoons O_2^{\bullet -}$ | MeCN | 0.2 M TBAP | −0.820 |
| | $O_2 + e \rightleftharpoons O_2^{\bullet -}$ | DMSO | 0.1 M TBAP | −0.730 |
| Perylene | $P^{\bullet +} + e \rightleftharpoons P$ | MeCN | 0.1 M TEAP | 0.850 |
| Phenanthrene | $Ph^{\bullet +} + e \rightleftharpoons Ph$ | MeCN | 0.1 M TEAP | 1.280 |
| Pyrene | $Py^{\bullet +} + e \rightleftharpoons Py$ | MeCN | 0.1 M TEAP | 1.360 |
| $Ru(bpy)_3^{n+}$ ($RuL_3^{n+}$) | $RuL_3^{3+} + e \rightleftharpoons RuL_3^{2+}$ | MeCN | 0.1 M $TBABF_4$ | 1.320 |
| | $RuL_3^{2+} + e \rightleftharpoons RuL_3^{+}$ | MeCN | 0.1 M $TBABF_4$ | −1.300 |
| | $RuL_3^{+} + e \rightleftharpoons RuL_3$ | MeCN | 0.1 M $TBABF_4$ | −1.490 |
| | $RuL_3 + e \rightleftharpoons RuL_3^{-}$ | MeCN | 0.1 M $TBABF_4$ | −1.730 |
| Stilbene | $St^{\bullet +} + e \rightleftharpoons St$ | MeCN | 0.1 M $NaClO_4$ | 1.430 |
| Tetracene | $T^{\bullet +} + e \rightleftharpoons T$ | MeCN | 0.1 M $NaClO_4$ | 0.770 |
| Tetracyanoquinodimethane | $TCNQ + e \rightleftharpoons TCNQ^{\bullet -}$ | MeCN | 0.1 M $LiClO_4$ | 0.130 |
| | $TCNQ^{\bullet -} + e \rightleftharpoons TCNQ^{2-}$ | MeCN | 0.1 M $LiClO_4$ | −0.290 |
| *N*,*N*,*N*′,*N*′-Tetramethyl-*p*-phenylenediamine | $TMPD^{\bullet +} + e \rightleftharpoons TMPD$ | DMF | 0.1 M TBAP | 0.210 |
| Tetrathiafulvalene | $TTF^{\bullet +} + e \rightleftharpoons TTF$ | MeCN | 0.1 M TEAP | 0.300 |
| | $TTF^{2+} + e \rightleftharpoons TTF^{\bullet +}$ | MeCN | 0.1 M TEAP | 0.660 |
| Thianthrene | $TH^{\bullet +} + e \rightleftharpoons TH$ | MeCN | 0.1 M $TBABF_4$ | 1.230 |
| | $TH^{2+} + e \rightleftharpoons TH^{\bullet +}$ | MeCN | 0.1 M $TBABF_4$ | 1.740 |
| | $TH^{\bullet +} + e \rightleftharpoons TH$ | $SO_2$ | 0.1 M TBAP | 0.300 |
| | $TH^{2+} + e \rightleftharpoons TH^{\bullet +}$ | $SO_2$ | 0.1 M TBAP | 0.880 |
| Tri-*N*-*p*-tolylamine | $TPTA^{\bullet +} + e \rightleftharpoons TPTA$ | THF | 0.1 M TBAP | 0.980 |

(see Chapter 1 of this handbook), this table should only be used as a guide. All potentials are for solutions at room temperature and vs. SCE. Table 18.3 lists electrode potentials of common redox species in aprotic solvents. These lists are not comprehensive and additional redox potentials can be found in reference (7). If an exact formal potential value is not needed, then Figure 18.3, a chart of potential ranges for the oxidation and reduction of

**Table 18.3**

Formal electrode potentials (V vs. aq SCE) at 25 °C for common redox species in solvents. Data from reference (7)

| Redox species | Solvent | Electrolyte | $E^{0\prime}$ (V) |
|---|---|---|---|
| Theophylline | $H_2O$ | $HCOONH_4$ | 0.765 |
| Methyl viologen | $H_2O$ | PBS | 0.700 |
| Phenanthrene quinone | 2-Propanol | PBS | −0.280 |
| Catechol | $H_2O$ | PBS | 0.600 |
| Hydroquinone | $H_2O$ | PBS | 0.035 |
| Aspirin/acetylsalicylic acid | MeCN | TBAI | −1.640 |
| Salicylic acid | MeCN | TBAI | −1.540 |
| L-DOPA | DMSO | TEAP | −2.500 |
| Alizarin red S | $H_2O$ | MB | 0.410 |
| Ferrocenemethanol | MeOH | $HClO_4$ | 0.200 |

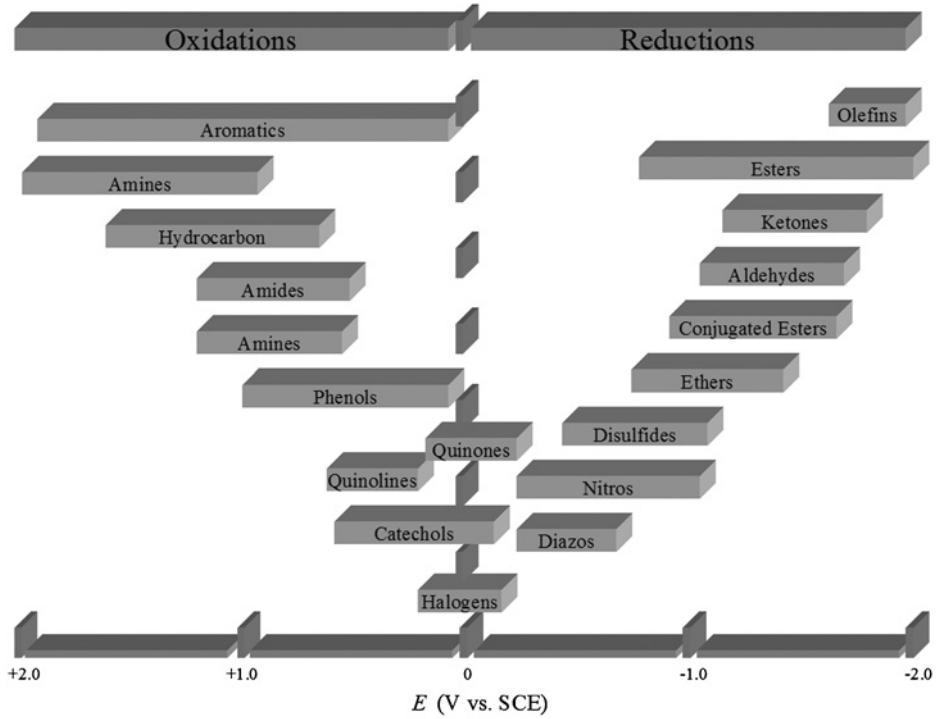


**Figure 18.3** Estimated potential range of organic functional groups at 25 °C. Data from references (5, 6). (for colour version: see colour section at the end of the book).

various organic functional groups, can be used to find an approximate potential range for a specific organic functional group.

## 18.5 FORMAL ELECTRODE POTENTIALS: COMMON ORGANIC MEDIATORS

Table 18.4 is a list of formal electrode potentials (vs. NHE) for common organic mediators at room temperature in aqueous solution of pH = 7. These are popular organic mediators that are often used for sensors and biosensors.

## 18.6 ELECTRODE POTENTIALS: INORGANIC ONE-ELECTRON COMPLEXES

Table 18.5 lists electrode potentials for common one-electron processes. These redox species are also frequently used as electron transfer mediators in sensors and biosensors.

**Table 18.4**

Electrode potentials (V vs. NHE) at 25 °C for common organic mediators at pH 7.0. Data from reference (8)

| Organic mediator | $E^{0\prime}$ (V vs. NHE) |
|---|---|
| *N*,N′-Dimethyl-*p*-phenylenediamine | 0.380 |
| 1,4-Benzoquinone | 0.280 |
| *N*,*N*,*N*′,*N*′-Tetramethyl-*p*-phenylenediamine | 0.270 |
| 2,6-Dichlorophenol indophenol | 0.217 |
| 1,2-Naphthoquinone-4-sulfonic acid | 0.217 |
| Toluylene blue | 0.115 |
| Phenazine methosulfate | 0.060 |
| Rosinduline 2G | 0.080 |
| Phenazine ethosulfate | 0.055 |
| Cresyl blue | 0.047 |
| Toluidine blue | 0.027 |
| Methylene blue | 0.011 |
| Tetramethyl-*p*-benzoquinone | 0.005 |
| Indigo-disulfonate | −0.125 |
| Safranine T | −0.289 |
| Neutral red | −0.325 |
| 1,1′-Dibenzyl-4,4′-bipyridyl salt | −0.350 |
| 1,1′-Ethylene-2,2′-bipyridyl dichloride | −0.350 |
| 1,1′-Bis(hydroxyethyl)-4,4′-bipyridyl salt | −0.408 |
| 1,1′-Dimethyl-4,4′-bipyridyl dichloride | −0.430 |

**Table 18.5**

Formal and standard electrode potentials (V vs. NHE) at 25 °C for inorganic complexes in aqueous solution

| Inorganic complexes | $E$ (V vs. NHE) | Reference |
|---|---|---|
| $Ni(bpy)_3^{3+}$ | $E^0 = 1.720$ | 9 |
| $Ru(bpy)_3^{2+}$ | $E^0 = 1.272$ | 10 |
| $Ru(phen)_3^{2+}$ | $E^0 = 1.220$ | 11 |
| $Fe(phen)_3^{2+}$ | $E^0 = 1.107$ | 10 |
| $Fe(bpy)_3^{2+}$ | $E^0 = 1.074$ | 10 |
| $IrCl_6^{2-}$ | $E^0 = 0.892$ | 12 |
| $Os(bpy)_3^{2+}$ | $E^0 = 0.844$ | 10 |
| $Mo(CN)_8^{4-}$ | $E^0 = 0.798$ | 10 |
| $Co(oxalate)_3^{3-}$ | $E^0 = 0.570$ | 13 |
| $Ru(NH_3)_4(bpy)^{2+}$ | $E^0 = 0.520$ | 14 |
| $W(CN)_8^{3-}$ | $E^0 = 0.510$ | 15 |
| $Ru(NH_3)_5Pz^{3+}$ | $E^{0\prime} = 0.490$,1 M NaCl | 16 |
| $Co(EDTA)^-$ | $E^0 = 0.380$ | 13 |
| $Co(phen)_3^{3+}$ | $E^0 = 0.370$ | 10 |
| $Co(bpy)_3^{3+}$ | $E^0 = 0.315$ | 17 |
| $Ru(NH_3)_5(py)^{2+}$ | $E^{0\prime} = 0.299$,1 M $CF_3SO_3H$ | 18 |
| $Fe(dipic)_2$ | $E^{0\prime} = 0.278$, pH = 5.15 | 19 |
| $Co(terpy)_2^{3+}$ | $E^0 = 0.270$ | 17 |
| $Ru(en)_3^{3+}$ | $E^{0\prime} = 0.184$, 0.1 M $KPF_6$ | 20 |
| $Fe(EDTA)^-$ | $E^0 = 0.120$ | 21 |
| Toluylene blue | $E^{0\prime} = 0.115$, pH = 7 | 22 |
| Thionine | $E^{0\prime} = 0.056$, pH = 7 | 22 |
| $Ru(NH_3)_6^{3+}$ | $E^{0\prime} = 0.051$, 0.1 M $NaBF_4$ | 23 |
| Cresyl blue | $E^{0\prime} = 0.047$, pH = 7 | 22 |
| Methylene blue | $E^{0\prime} = 0.011$, pH = 7 | 22 |
| $Co(en)_3^{3+}$ | $E^{0\prime} = -0.216$, 1 M $NaClO_4$ | 20 |
| $Cr(bpy)_3^{3+}$ | $E^0 = -0.250$ | 24 |
| $Co(sepalchrate)^{3+}$ | $E^0 = -0.300$ | 25 |
| Neutral red | $E^{0\prime} = -0.325$, pH = 7 | 22 |
| Benzylviologen | $E^0 = -0.352$ | 26 |

## 18.7 FORMAL ELECTRODE POTENTIALS: BIOLOGICAL REDOX SPECIES

Table 18.6 lists formal potentials for common protein electron transfer reactions in biologically related systems. Table 18.7 lists standard reduction potentials for biochemical reduction reactions.

## 18.8 FORMAL ELECTRODE POTENTIALS: COMMON VITAMINS, DRUGS, NEUROCHEMICALS

Table 18.8 lists half-wave potentials or peak potentials for selected vitamins, drugs, and neurochemicals. These potentials are dependent on solvent, solvent purity, and electrolyte and thus should serve only as a guide.

**Table 18.6**

Reduction potentials (V vs. SCE) for selected biological redox systems at 25 °C in aqueous solution at pH 7. Data from reference (27)

| Redox couples | $E^{0\prime}$ (V vs. SCE) |
|---|---|
| Laccase $Cu^{2+}/Cu^{+}$ | 0.165 |
| Cytochrome f $Fe^{3+}/Fe^{2+}$ | 0.125 |
| Cytochrome a (mammalian) $Fe^{3+}/Fe^{2+}$ | 0.100 |
| $O_2/H_2O_2$ | 0.055 |
| Cytochrome c (mammalian) $Fe^{3+}/Fe^{2+}$ | 0.020 |
| Hemoglobin $Fe^{3+}/Fe^{2+}$ | −0.070 |
| Ubiquinone ox/red | −0.140 |
| Cytochrome b (mammalian) $Fe^{3+}/Fe^{2+}$ | −0.210 |
| Methylene blue/leukomethylene blue | −0.230 |
| Myoglobin $Fe^{3+}/Fe^{2+}$ | −0.236 |
| Cytochrome b3 (mammalian) $Fe^{3+}/Fe^{2+}$ | −0.240 |
| Glucose oxidase ox/red (pH 5.3) | −0.305 |
| Horseradish peroxidase $Fe^{3+}/Fe^{2+}$ | −0.310 |
| FMN (old yellow enzyme)/FMNH3 | −0.360 |
| Riboflavin/dehydroriboflavin | −0.448 |
| Glutathione ox/red | −0.470 |
| Adrenodoxin $Fe^{3+}/Fe^{2+}$ | −0.515 |
| Xanthine oxidase ox/red | −0.534 |
| Flavodoxin ox/red | −0.550 |
| $NAD^{+}$/NADH | −0.560 |
| $NADP^{+}$/NADPH | −0.564 |
| $H^{+}/½H_2$ | −0.660 |
| Ferredoxin (spinach) $Fe^{3+}/Fe^{2+}$ | −0.668 |

## 18.9 ABBREVIATIONS

| | |
|---|---|
| PBS | phosphate buffer |
| TBAI | tetrabutylammonium iodide |
| TBAP | tetrabutylammonium perchlorate |
| TEAP | tetraethylammonium perchlorate |
| $TEABF_4$ | tetraethylammonium tetrafluoroborate |
| $TBAPF_6$ | tetrabutylammonium hexafluorophosphate |
| TEAI | tetraethylammonium iodide |
| MeCN | acetonitrile |
| DMF | dimethylformamide |
| DMSO | dimethylsulfoxide |
| THF | tetrahydrofuran |
| MeOH | methanol |
| PC | propylene carbonate |
| EtOH | ethanol |

**Table 18.7**

Standard electrode potentials (V vs. NHE) at 25 °C for half-cell reactions of selected biochemical reductions. Data from reference (28)

| | $E^0$ |
|---|---|
| *Reduction of carbonyl to aldehyde* | |
| 1,3-Diphosphoglycerate + $2e^-$ → 3-phosphoglyceraldehyde + $HPO_4^{2-}$ | −0.286 |
| Acetyl-CoA + $2H^+$ + $2e^-$ → acetaldehyde + coenzyme A | −0.412 |
| Oxalate + $3H^+$ + $2e^-$ → ascorbate | −0.462 |
| Gluconate + $3H^+$ + $2e^-$ → glucose | −0.470 |
| Acetate + $3H^+$ + $2e^-$ → acetaldehyde | −0.598 |
| *Reduction of carbonyl to alcohol* | |
| Dehydroascorbic acid + $H^+$ + $2e^-$ → ascorbate | 0.077 |
| Glyoxylate + $2H^+$ + $2e^-$ → glycolate | −0.090 |
| Hydroxypyruvate + $2H^+$ + $2e^-$ → glycerate | −0.158 |
| Oxaloacetate + $2H^+$ + $2e^-$ → malate | −0.166 |
| Pyruvate + $2H^+$ + $2e^-$ → lactate | −0.190 |
| Acetaldehyde + $2H^+$ + $2e^-$ → ethanol | −0.197 |
| Acetoacetate + $2H^+$ + $2e^-$ → b-hydroxybutyrate | −0.349 |
| *Carboxylation* | |
| Pyruvate + $CO_2$(g) + $H^+$ + $2e^-$ → malate | −0.330 |
| a-Ketoglutarate + $CO_2$(g) + $H^+$ + $2e^-$ → isocitrate | −0.363 |
| Succinate + $CO_2$(g) + $H^+$ + $2e^-$ → a-ketoglutarate + $H_2O$ | −0.673 |
| Acetate + $CO_2$(g) + $H^+$ + $2e^-$ → pyruvate + $H_2O$ | −0.699 |
| *Reduction of carbonyl with amino* | |
| Oxaloacetate + $NH_4^+$ + $2H^+$ + $2e^-$ → aspartate + $H_2O$ | −0.107 |
| Pyruvate + $NH_4^+$ + $2H^+$ + $2e^-$ → alanine + $H_2O$ | −0.132 |
| a-Ketoglutarate + $NH_4^+$ + $2H^+$ + $2e^-$ → glutamate + $H_2O$ | −0.133 |
| *Reduction of C=C* | |
| Crotonyl-CoA + $2H^+$ + $2e^-$ → butyryl-CoA | 0.187 |
| Fumarate + $2H^+$ + $2e^-$ → succinate | 0.031 |
| *Reduction of disulfide* | |
| Cystine + $2H^+$ + $2e^-$ → 2–cysteine | −0.340 |
| Glutathione dimer + $2H^+$ + $2e^-$ → 2–glutathione | −0.340 |
| *Others* | |
| $FAD^+$ + $H^+$ + $2e^-$ → FADH | −0.200 |
| $NAD^+$ + $H^+$ + $2e^-$ → NADH | −0.320 |

**Table 18.8**

Half-wave and peak potentials for common vitamins, drugs, and neurochemicals at room temperature

| | Solvent | Electrolyte or reference | $E^{1/2}$ (or $E_p$) | Reference |
|---|---|---|---|---|
| *Vitamins* | | | | |
| Vitamin A/retinol | DMF | TEAI | −2.400 | 7 |
| Vitamin B2/riboflavin | DMSO | $NaClO_4$ | −1.020 | 7 |
| Vitamin B3/Niacin/nicotinic acid | $H_2O$ | TEAP | −1.440 | 7 |
| Folate/folic acid | $H_2O$ | NaOH | 0.560 | 7 |
| Vitamin B12/cyanocobalamin | $H_2O$ | 0.1 M KCN, vs. SCE | −1.120 | 27 |
| Vitamin C/ascorbic acid | $H_2O$ | PBS | $E_p$ = 0.020 | 7 |
| *Neurochemicals* | | | | |
| Aspartic acid | DMSO | TEAP | −2.400 | 7 |
| Glutamic acid | DMSO | TEAP | −2.120 | 7 |
| Epinephrine/L-adrenaline | $H_2O$ | $H_2SO_4$ | $E_p$ = 0.550 | 7 |
| Progesterone | MeCN | TBAI | −1.850 | 7 |
| Hydrocortisone | EtOH | PBS | −1.300 | 7 |
| Catechol | $H_2O$ | pH = 0 | 0.792 | 27 |
| Epinephrine | $H_2O$ | pH = 0 | 0.809 | 27 |
| Dopamine | $H_2O$ | pH = 0, vs. SCE | 0.580 | 27 |
| Dihydroxyphenylalanine | $H_2O$ | pH = 0 | 0.800 | 27 |
| Epinine | $H_2O$ | pH = 0 | 0.788 | 27 |
| Norhomoepinephrine | $H_2O$ | pH = 0 | 0.822 | 27 |
| Adrenalone | $H_2O$ | pH = 0 | 0.909 | 27 |
| Protocatechnic acid | $H_2O$ | pH = 0 | 0.883 | 27 |
| 6-Hydroxydopamine | $H_2O$ | pH = 6.87, vs. SCE | −0.159 | 27 |
| 6-Methoxydopamine | $H_2O$ | pH = 6.87, vs. SCE | −0.070 | 27 |
| *Drugs* | | | | |
| Sertraline | $H_2O$ | pH = 8, vs. Ag/AgCl | −1.750 | 29 |
| THC | $H_2O$ | PH = 7.02, vs. Ag | 1.500 | 30 |
| Caffeine | $H_2O$ | $HCOONH_4$ | 0.850 | 7 |
| $\beta$-Carotene | $H_2O$ | vs. Ag wire | 0.600 | 32 |
| Celecoxib | $H_2O$ | pH = 7, vs. Ag/AgCl | −1.540 | 33 |
| Azithromycin | $H_2O$ | PH = 6.0 PBS, vs. $Ag/AgNO_3$ | 0.800 | 34 |
| Acetaminophen | $H_2O$ | Acetate buffer, vs. SCE | 0.500 | 35 |
| Ciprofloxacin | $H_2O$ | pH = 7.3 PBS, vs. SCE | −1.410 | 31 |
| Enoxacin | $H_2O$ | pH = 7.3 PBS, vs. SCE | −1.350 | 31 |
| Norfloxacin | $H_2O$ | pH = 7.3 PBS, vs. SCE | −1.405 | 31 |
| Ofloxacin | $H_2O$ | pH = 7.3 PBS, vs. SCE | −1.403 | 31 |
| Pefloxacin | $H_2O$ | pH = 7.3 PBS, vs. SCE | −1.435 | 31 |

## 18.10 CHEMICAL STRUCTURES

**Anthracene**

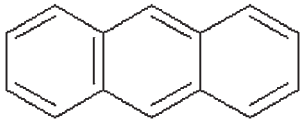

**Azobenzene**

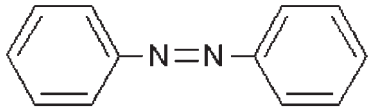


**1,4-Benzoquinone**

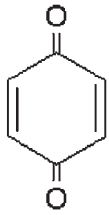


**Benzophenone**

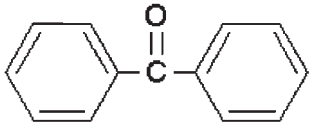


**Chrysene**

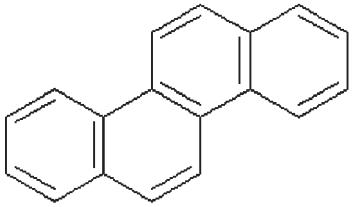

**Ferrocene**

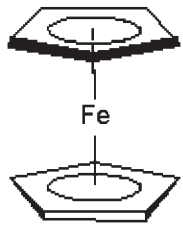


**Nitrobenzene**

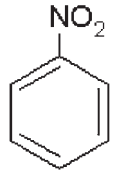


**Naphthalene**

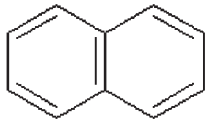

**Perylene**

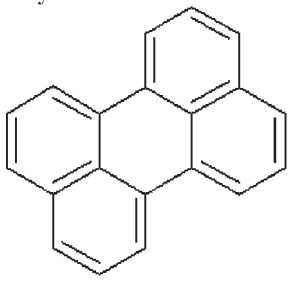

**Phenanthrene**

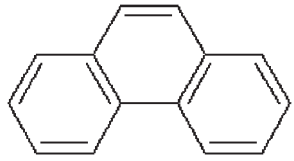

**Pyrene**

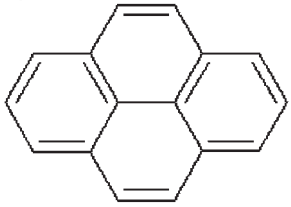

**Stilbene**

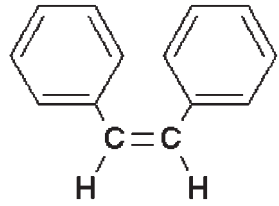


**Tetracene**

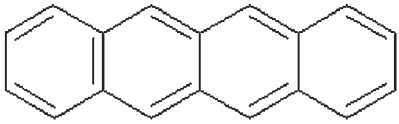

**Tetracyanoquinodimethane**

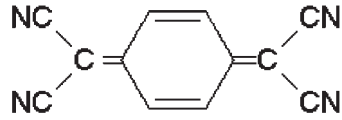


**Tetramethylphenylenediamine**

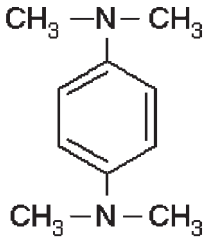


**Tetrathiafulvalene**

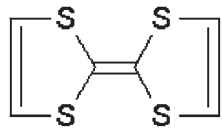


**Tri-*N*-*p*-tolylamine**

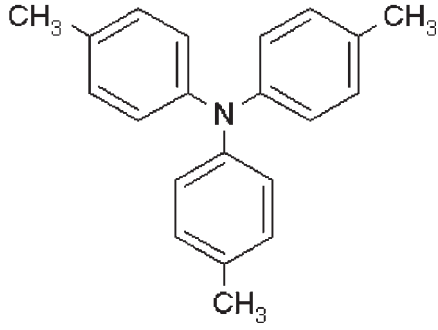


**Thianthrene**

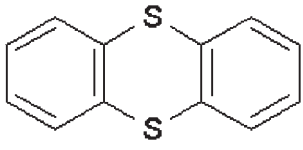

## REFERENCES


1. C. K. Mann, *Electroanal. Chem.* **3**, 57 (1969).
2. A. J. Bard, L. R. Faulkner, *Electrochemical Methods: Fundamentals and Applications*, 2nd ed., Wiley: New York, 2001.
3. A. J. Bard, R. Parsons, J. Jordan, *Standard potentials in aqueous solution*, Dekker: New York, 1985.
4. C. M. A. Brett, A. M. O. Brett, *Electrochemistry: Principles, Methods and Applications*, Oxford: Oxford, 1993.
5. D. A. Skoog, F. J. Holler, T. A. Nieman, *Principles of Instrumental Analysis*, 5th ed., Harcourt: Philadelphia, 1998.
6. S. G. Weber, "Chem. Analysis," in *Detectors for Liquid Chromatography*, E. S. Yeung, Ed., Wiley: New York, 1986, Vol. 89.
7. L. Meites, P. Zuman, *Handbook Series in Organic Electrochemistry*, CRC Press: Cleveland, 1977, Vol. 1–2.
8. M. L. Fultz, R. A. Durst, *Anal. Chem. Acta* **140**, 1 (1982).
9. D. H. Macartney, N. Sutin, *Inorg. Chem.* **22**, 3530 (1983).
10. T. Kuwana, in *Electrochemical Studies of Biological Systems*, D. T. Sawyer, Ed., ACS Symposium Series #38, ACS, 1977.
11. A. A. Schilt, *Analytical Applications of 1,10-Phenathroline and Related Compounds*, Pergamon Press: New York, 1969.
12. F. P. Bossu, K. L. Chellappa, D. W. Margerum, *J. Am. Chem. Soc.* **99**, 2195 (1977).
13. L. Hin-Fat, W. C. E. Higginson, *J. Chem. Soc. A* **2**, 298 (1967).
14. G. M. Brown, N. Sutin, *J. Am. Chem. Soc.* **83**, 3357 (1961).
15. H. Baadsgaard, W. D. Treadwell, *Helv. Chim. Acta.* **38**, 1669 (1955).
16. H. S. Lim, D. J. Barclay, F. C. Anson, *Inorg. Chem.* **11**, 1460 (1972).
17. D. Cummins, H. B. Gray, *J. Am. Chem. Soc.* **99**, 5158 (1977).
18. G. M. Brown, H. J. Krentzien, M. Abe, H. Taube, *Inorg. Chem.* **18**, 3374 (1979).
19. G. Anderegg, *Helv. Chim. Acta.* **43**, 1530 (1960).
20. E. L. Yee, R. J. Cave, K. L. Guyer, P. D. Tyma, M. J. Weaver, *J. Am. Chem. Soc.* **101**, 1131 (1979).
21. H. J. Schugar, A. T. Hubbard, F. C. Anson, H. B. Gray, *J. Am. Chem. Soc.* **91**, 71 (1969).
22. W. Clark, *Oxidation-Reduction Potentials of Organic Systems*, Williams & Wilkins Co.: Baltimore, 1960.
23. T. Matsubara, P. C. Ford, *Inorg. Chem.* **15**, 1107 (1976).
24. B. S. Brunschwig, N. Sutin, *J. Am. Chem. Soc.* **100**, 7568 (1978).
25. A. M. Sargeson, *Chem. Br.* **15**, 23 (1979).
26. R. C. Prince, S. J. G. Linkletter, P. L. Dutton, *Biochem. Biophys. Acta* **635**, 132 (1981).
27. G. Dryhurst, K. M. Kadish, F. Scheller, R. Renneberg, *Biological Electrochemistry*, Academic Press: New York, 1982.
28. H. A. Krebs, H. L. Kornberg, K. Burton, *Erg. Physiol.* **49**, 212 (1957).
29. M. H. Vela, M. B. Quinaz Garcia, M. C. Montenegro, *Fresenius J. Anal. Chem.* **369**, 563 (2001).
30. U. Backofed, W. Hoffmann, F. Matysik, *Biomed. Chromatogr.* **14**, 49 (2000).
31. M. Warowna-Grzeskiewicz, J. Chodkowski, Z. Fijalik, *Acta Poloniae Pharm.* **52**, 442 (1995).
32. A. L. Suarez-Fernandez, G. Alarnes-Varela, A. Costa-Garcia, *Electrochim. Acta* **44**, 4489 (1999).
33. M. M. Ghoneim, A. M. Beltagi, *Talanta* **60**, 911 (2003).
34. O. A. E. Farghaly, N. A. L. Mohamed, *Talanta* **62**, 531 (2004).
35. C. M. Shearer, K. Christenson, A. Mukherji, G. J. Papariello, *J. Pharm. Sci.* **61**, 1627 (1972).

This page intentionally left blank

# – 19 –

# Diffusion Coefficients

**John E. Baur**

Department of Chemistry, Illinois State University,
Normal, IL 61790-4160, USA

## 19.1 INTRODUCTION

Electrochemical experiments are often designed so that diffusion is the sole form of mass transport. Even in cases where convection and migration occur, diffusion can rarely be ignored as a significant contributor to the overall mass transport. Therefore, theoretical treatments of electrochemical systems that involve mass transport normally require that the diffusion coefficient of the redox species of interest, $D$, is known. A quick perusal of this or any other electrochemistry text reveals that $D$ is a term in most important equations relating current to solution conditions. Only current arising from non-transport related sources (e.g., double-layer charging and redox reactions of adsorbate layers) are independent of the diffusion coefficient.

Yet despite its importance, values of $D$ are not readily found. This is because the diffusion coefficient of a species in solution depends upon several factors (e.g., temperature, viscosity, electrolyte, etc.), so comprehensive tabulation is impractical. When the diffusion coefficient must be known for a new compound or a new set of conditions, the usual approach is to measure $D$ for the particular species of interest under specified experimental conditions. Making such measurements accurately requires careful characterization and calibration of the measurement system using a species with a known diffusion coefficient under well-defined conditions. Methods for measuring diffusion coefficients are described in this chapter. A tabulation of values of $D$ for commonly used redox species is included at the end of the chapter.

## 19.2 FUNDAMENTAL EQUATIONS

Simply stated, the diffusion coefficient is the proportionality between flux, $J(x,t)$, and concentration gradient, $\partial C(x,t)/\partial x$, which is mathematically expressed by Fick's first law


**Handbook of Electrochemistry**
**Edited by C.G. Zoski**

(for one dimension):

$$J(x,t) = -D\frac{\partial C(x,t)}{\partial x} \tag{19.1}$$

where $x$ is the distance measured from the electrode surface and $t$ is time. In electrochemistry, flux commonly has units of mol $cm^{-2}$ $sec^{-1}$ and the concentration gradient has units of mol $cm^{-4}$, so the diffusion coefficient has units of $cm^2$ $sec^{-1}$. Faradaic current is proportional to flux at the electrode surface, $J(0,t)$:

$$i(t) = -nFAJ(0,t) \tag{19.2}$$

where $F$ is Faraday's constant. Most electrochemical measurements of the diffusion coefficient rely on a measurement of the faradaic current.

Equations (19.1) and (19.2) reveal that at least three other quantities must be accurately known in order to make a reliable measurement of $D$. These critical variables are the electrode area $A$ (or in the case of ultramicroelectrodes (UMEs) (Chapter 6), the electrode radius $r_0$), the stoichiometric number of electrons, $n$, involved in the electron transfer reaction, and the bulk concentration of the redox species, $C^*$.[1] The electrode area is normally determined electrochemically with equations equivalent to equation (19.2) and using a redox couple having a known diffusion coefficient. This is done because calculations based on manufacturers' nominal dimensions or on optically measured dimensions ignore imperfections in the manufacture, geometry, and local reactivity of the electrode. For existing redox couples the value of $n$ is often known, but for the characterization of a new species $n$ must be experimentally determined. To avoid techniques that in turn rely on knowledge of the diffusion coefficient, coulometric or thin layer methods are preferred for such determinations. Finally, care must be taken to ensure that the redox species, supporting electrolyte, and solvent are of high purity, and that proper volumetric technique is used in preparing solutions so that $C^*$ is accurately known. Because a measured value of $D$ will contain errors associated with each of these experimental variables in addition to the current, without very careful measurements and precisely calibrated instruments and electrodes, it is difficult to accurately determine diffusion coefficients to more than two significant figures.

## 19.3 GENERAL CONSIDERATIONS

### 19.3.1 Selection of a technique

The techniques described in this chapter (see Chapter 11 for detailed description of techniques) for the determination of diffusion coefficients are summarized in Table 19.1. Each of these techniques has its own strengths and weaknesses that should be evaluated before selecting a method. One important consideration is the dependence of $D$ on the experimentally measured quantities (e.g., current or electrode dimensions). Under conditions of

[1] $C^*$ does not appear in equation (19.1) or equation (19.2), but the flux at the surface depends on $C^*$.

**Table 19.1**

Summary of electrochemical methods for measuring diffusion coefficients

| Method | Procedure | Equation | Comments |
|---|---|---|---|
| Methods with $D \propto i$ | | | |
| Chronoamperometry at disk UME | Measure steady-state current | $D = \frac{i_{ss}}{4nFC^* r_0}$ | RG $\gtrsim$ 100, $4Dt/{r_0}^2 > 500$ for <2% planar diffusion contribution to $i_{ss}$ |
| Chronoamperometry at hemispherical UME | Measure steady-state current | $D = \frac{i_{ss}}{2\pi nFC^* r_0}$ | RG $\gtrsim$ 100, $Dt/{r_0}^2 > 800$ for <2% planar diffusion contribution to $i_{ss}$ |
| Linear scan voltammetry at disk UME | Measure steady-state current | $D = \frac{i_{ss}}{4nFC^* r_0}$ | RG $\gtrsim$ 100, same time criterion as chronoamperometry, but use $t \approx \lvert E_f - E_{1/2}\rvert / v$ |
| Linear scan voltammetry at hemispherical UME | Measure steady-state current | $D = \frac{i_{ss}}{2\pi nFC^* r_0}$ | RG $\gtrsim$ 100, same time criterion as chronoamperometry, but use $t \approx \lvert E_f - E_{1/2}\rvert / v$ |
| Methods with $D \propto i^{3/2}$ | | | |
| Rotating disk electrode | Measure limiting current, $i_l$ as a function of rotation rate $\omega$ and plot $i_l$ vs. $\omega^{1/2}$ | $D = \left(\frac{\text{slope}}{0.62nFAC^* v^{-1/6}}\right)^{3/2}$ | Use with $10 < \omega < 10{,}000$ |
| Methods with $D \propto i^2$ | | | |
| Chronoamperometry at planar electrode | Measure current as a function of time, plot $i(t)$ vs. $t^{-1/2}$ | $D = \frac{(\text{slope})^2 \pi}{(nFAC^*)^2}$ | Avoid charging current measurements at short times ($t \lesssim 10R_sC_d$), avoid long times (convection, edge effects) |
| Normalized chronoamperometry at disk UME | Measure current as a function of time and normalize by steady-state current. Plot normalized current vs. $t^{-1/2}$ | $D = \frac{4r_0^2}{(\text{slope})^2 \pi^3}$ | Requires only $r_0$; avoid charging current measurements at short times ($t \lesssim 10R_sC_d$) |

(*Continued*)

**Table 19.1 (Cont.)**

| Method | Procedure | Equation | Comments |
|---|---|---|---|
| Chronopotentiometry at planar electrode | Measure transition time at several current densities, find average value of $\tau$ | $D = \frac{4i_0^2\tau}{\pi(nFC^*)^2}$ | Avoid conditions with long transition times (convective effects); less accurate when there are large relative background contributions to the overall current (i.e., low $C^*$, large $C_d$, short $\tau$) |
| Linear scan voltammetry at a planar electrode | Measure peak current as a function of scan rate, plot $i_p$ vs. $v^{1/2}$ | $D = \frac{(\text{slope})^2}{n^3(2.69\times10^5 AC^*)^2}$ | Nernstian systems only; avoid scan rates with appreciable nonlinear diffusion; should be considered an approximate method |

linear diffusion, the current is typically proportional to $D^{1/2}$ (e.g., in chronoamperometry, equation (19.8), and in linear scan voltammetry (LSV), equation (19.17), Chapter 11), or in other words $D$ is proportional to $i^2$. Any errors in $i$ (or $C^*$, $A$, or $n$) are thus amplified because of the second-order dependence of the diffusion coefficient on these variables. For the rotating disk electrode (RDE) (Chapter 11), current is proportional to $D^{2/3}$ (equation (19.12)), so $D$ depends on $i^{3/2}$. For steady-state UME techniques (Chapters 6 and 11), the current is directly proportional to $D$ (equations (19.3) and (19.4)). Because of this linear relationship, errors in $i$ (or $C^*$, $A$, or $n$) produce the smallest error in $D$. Therefore, in most situations, steady-state UME techniques are preferred for determinations of diffusion coefficients. One caveat is that with UMEs it is often more difficult to make accurate measurements of the electrode dimensions (because they are so small), but calibration of the electrode with a system having a known diffusion coefficient can compensate for this uncertainty. Certainly the application of more than one technique will also improve the confidence in the measured value of $D$.

### 19.3.2 Electrode

The electrode is a critical component in the electrochemical measurement of diffusion coefficients. The general type of electrode to be used (i.e., UME or conventional electrode, see Chapters 5, 6, and 11 for more detail) has a fundamental impact on the type of measurement to be made. As shown in Figure 19.1*a*, at a conventional electrode diffusion normally is planar (i.e., comes from essentially one direction toward the electrode surface). With planar diffusion there is a depletion of the redox species close to the surface, resulting in a current that decays with time. As such, under planar diffusion control the current is measured as a function of time. With an RDE, forced convection causes efficient, steady-state transport of species to the electrode surface (Figure 19.1*b*) and time-independent current results. With

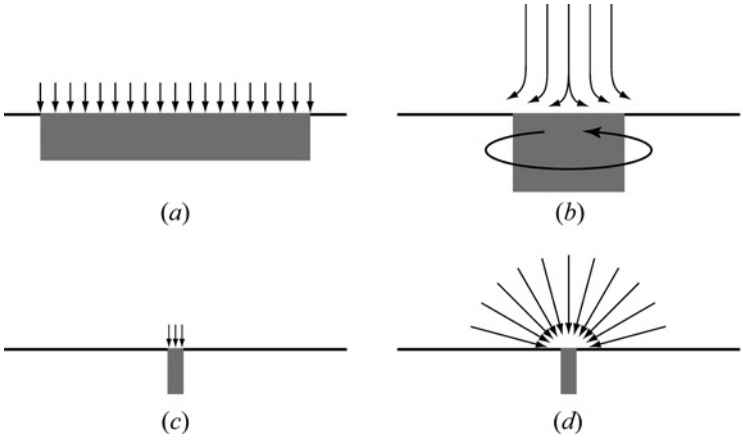


**Figure 19.1** Mass transport to electrodes of different types. (*a*) Planar diffusion to a macroelectrode, (*b*) convection to a rotating disk electrode, (*c*) planar diffusion to a microdisk electrode at short times, (*d*) radial diffusion to a microdisk electrode at long times.

UMEs, planar diffusion occurs at short times because the diffusion distance is small compared to the electrode dimensions (Figure 19.1*c*). At longer times the current becomes time-independent as radial diffusion dominates (Figure 19.1*d*). For diffusion coefficient measurements with UMEs, the steady-state current is normally measured, although some techniques utilize both short- and long-time current measurements.

The electrode selected for the measurement of a diffusion coefficient should be closely inspected for defects and non-idealities. Figure 19.2 depicts several possible non-idealities: poor electrode seals, irregular geometry, thin insulators, eccentricities, and protrusions, all of which contribute to errors in the measured current. If the electrode is poorly sealed (Figure 19.2*a*), solution can creep between the conductor and insulator, increasing both the apparent electrode capacitance ($C_d$) and the geometric area. Because the ratio of perimeter to surface area for a UME is large, this type of defect is typically more problematic for a UME than for a conventional electrode. Irregular or elongated geometries (Figure 19.2*b*) are also problematic for UMEs because the current is dependent on electrode radius and a true circular or spherical geometry is assumed. In contrast, for pure planar diffusion the

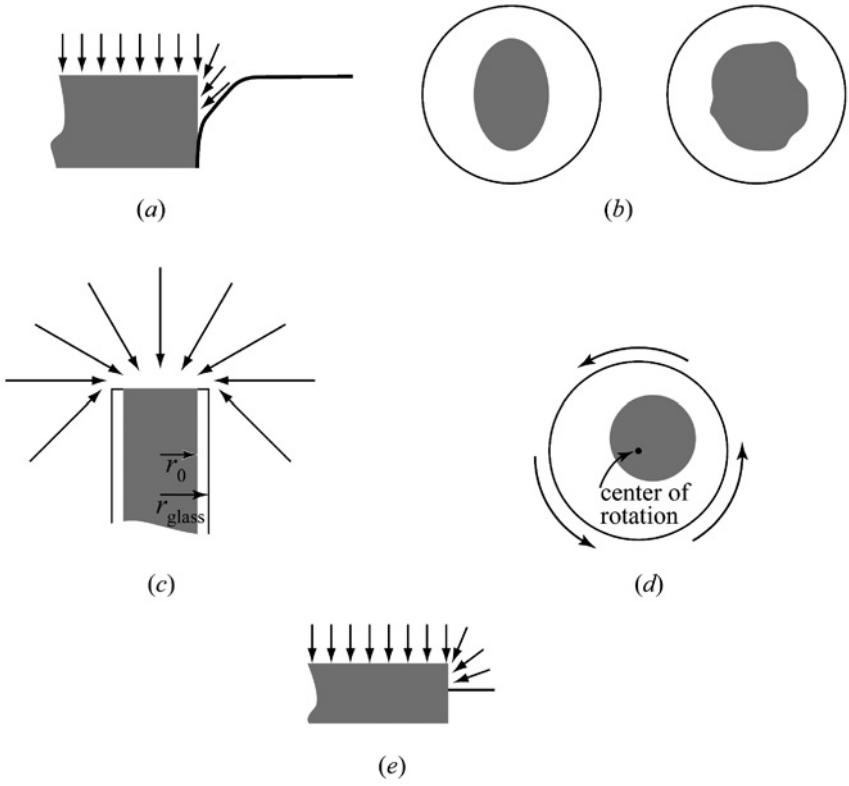


**Figure 19.2** Electrode features causing deviations from theoretical behavior. (*a*) Crack or poor seal at electrode-insulator boundary, (*b*) elongated and irregular electrode geometries, (*c*) UME with a thin insulator, (*d*) RDE in which the disk is not centered on the axis of rotation, (*e*) electrode protrusion from the plane of the insulator.

current is only dependent on area (not geometry), so such irregularities are typically not important. Thin insulators (Figure 19.2*c*) are especially problematic for UMEs at long times because molecules can diffuse from behind the plane of the electrode, causing the measured current to be higher than the theoretical current. Eccentricities (Figure 19.2*d*) are most problematic for RDEs; an electrode not centered on the axis of rotation will exhibit a positive deviation from the theoretical current. Protrusions (Figure 19.2*e*) are problematic for any type of electrode, as they give increased areas and can have unusual diffusional or hydrodynamic behaviors near the edges. While electrochemical measurements of electrode areas can correct some of these non-idealities, the presence of such defects can potentially cause measurements to deviate significantly from theory. It is therefore of vital importance that electrodes used for measurements of diffusion coefficient are free of such defects.

### 19.3.3 Electrochemical system

Before attempting to measure diffusion coefficients, some basic information regarding the electrochemical behavior of the redox species must be known. This is particularly important for newly prepared compounds. First, one should evaluate the reversibility of the electron transfer reaction. Certain techniques, such as LSV, can only be applied to measure diffusion coefficients for nernstian systems. Second, the presence of any coupled homogeneous reactions should be established. The current for each technique is often dependent on such reactions, thus making measurements of the diffusion coefficient unreliable. Finally, the adsorption of reactants or products can produce faradaic current that can greatly affect the measurement of the diffusion coefficient. For example, measurement of the critical time in chronopotentiometry is less reliable when adsorption is present. For these reasons, the electrochemical behavior of the compound must be factored into the selection of a technique.

Background measurements of blanks should always be subtracted when making careful diffusion coefficient measurements. Such corrections can often minimize charging current, instrumental offsets, and other background contributions to the measured current. Care must be taken, however, that the condition of the electrode does not change between measurements of the blank and the redox species.

Finally, before measuring the diffusion coefficient of a new compound, the technique and equipment should be tested using at least one standard compound (see tables of $D$ at the end of this chapter for common test compounds). In this way an estimate of the accuracy can be made before measuring the diffusion coefficient of an unknown. If accuracy is a particular concern, the use of more than one technique will improve the reliability of the measurement.

### 19.3.4 Instrumentation

For the most reliable measurements of $D$, some general instrumental conditions must be controlled. When using a technique that requires the measurement of a diffusion-limited current (i.e., those described in this chapter with the exception of the RDE technique), all other modes of mass transport must be eliminated. Convection from vibrational agitation of the solution is minimized by conducting the experiment on a vibrationally isolated

workstation. The temperature should be carefully controlled by using a water-jacketed cell to avoid convection due to thermal gradients. Since the diffusion coefficient is a function of temperature, such thermostatic control is also important for calibration. To avoid migration, sufficient supporting electrolyte must be present in solution.[2] A rule of thumb is that supporting electrolyte concentration should be 100× the concentration of the redox couple. Finally, the amplification factor of the potentiostat (or galvanostat) must be carefully calibrated to minimize errors in the current measurement.

## 19.4 ELECTROCHEMICAL METHODS

In the following discussion, the specific techniques for measuring diffusion coefficients are listed in order of preference. The selection of a technique will depend on the individual situation and the equipment available to the researcher.

### 19.4.1 Potential step techniques (chronoamperometry)

Techniques based upon the application of a large amplitude potential step (see Chapter 11) are probably the simplest and most widely applicable methods for measuring $D$. When using these techniques, it is of vital importance that the potential is stepped from a value where the species of interest is not reduced (or oxidized) to a value where the current is diffusion-controlled (Figure 19.3). Furthermore, the step potential must be selected so that only the redox species is electrolyzed. Cyclic voltammetry (CV) (see Chapter 11) is useful for selecting these potentials. By conducting the experiment in a blank solution, any contributions to the current from extraneous sources can be identified and subtracted from the current measured due to the redox couple. An advantage of chronoamperometric techniques is that species with slow heterogeneous kinetics (see Chapter 15) are amenable to the determination of $D$, as long as the potential can be stepped to a value where the rate of the electron transfer reaction is large and therefore the process is under diffusion control.

There are limitations to this approach. First, very short and very long times must be avoided. At short times, current arising from the charging of the double layer can cause deviations from theoretical behavior (Figures 19.3*a* and *b*). This charging current decays exponentially, so it is normally negligible after several time constants (the product of the uncompensated resistance $R_u$ and the electrode double layer capacitance $C_d$). In most situations, this corresponds to a few milliseconds (for macroelectrodes) or microseconds (UMEs), and these problems can be avoided by not collecting data during the first 5–10 time constants after the potential step. At long times, convection develops in the solution (from vibrations and/or by density gradients arising from the electrolysis products), causing positive deviations from the theoretical current. These effects can become noticeable in as short as 20–30 seconds, but the exact time depends on the experimental conditions.

[2]UME techniques have been developed to measure $D$ in solutions with low or no supporting electrolyte. See references (2) and (3).

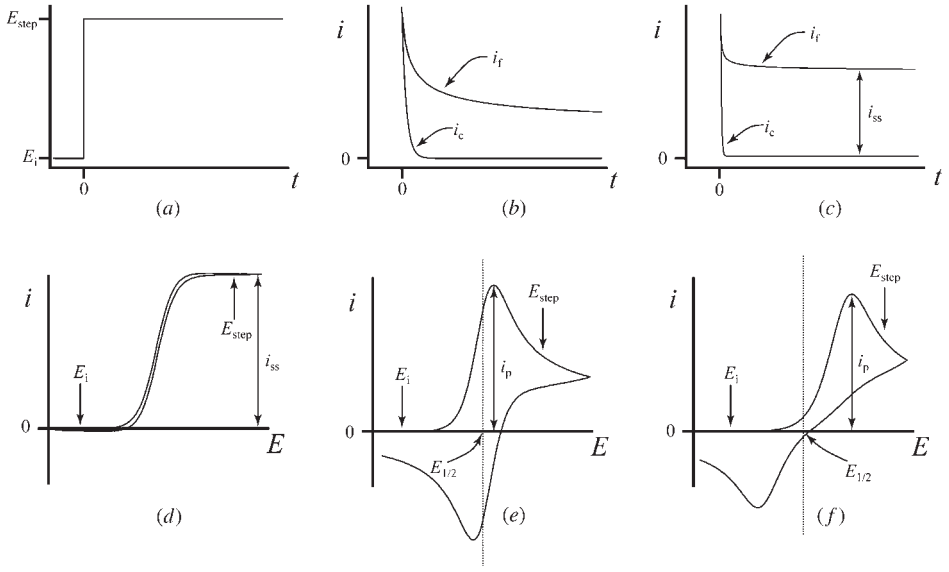


**Figure 19.3** Charging current and selection of step potential for chronoamperometry. (*a*) Potential waveform applied to the electrode in chronoamperometry. At $t = 0$, the potential is stepped from the initial value $E_i$ to a constant value $E_{step}$. (*b*) Dependence of faradaic current ($i_f$) and charging current ($i_c$) on time for a planar macroelectrode. (*c*) Dependence of $i_f$ and $i_c$ on time for a UME. (*d*) Cyclic voltammogram at a UME showing $i_{ss}$ and selection of $E_i$ and $E_{step}$. (*e*) Cyclic voltammogram of a reversible redox couple at a macroelectrode showing $i_p$ and $E_{1/2}$ and selection of $E_i$ and $E_{step}$. (*f*) Cyclic voltammogram of a quasi-reversible redox couple at a macroelectrode showing $i_p$ and $E_{1/2}$ and selection of $E_i$ and $E_{step}$.

Convective effects are most notable in solvents with low viscosity such as acetonitrile and dimethylformamide (see Chapter 3).

#### *19.4.1.1 Chronoamperometry at UMEs*

Steady-state conditions are typically attained within a few seconds after application of the potential step to a UME (see Chapter 6 for detailed discussions of UMEs). The resulting limiting current, $i_{ss}$ (Figure 19.3*c*), is linearly dependent on the diffusion coefficient. Rearranging the equations for $i_{ss}$ at hemispherical electrodes (equations (6.1.4.5) and (11.2.64)) and disk electrodes (equations (6.1.4.5) and (11.2.65)) gives expressions for the diffusion coefficient in terms of the experimental variables:

$$D = \frac{i_{ss}}{2\pi nFC^* r_0} \quad \text{(hemispherical UME)} \tag{19.3}$$

$$D = \frac{i_{ss}}{4nFC^* r_0} \quad \text{(circular disk UME)} \tag{19.4}$$

It is important to note that these equations only hold for an electrode embedded in an infinite insulating plane (Figures 19.1*c* and *d*). Electrodes having thin insulators (such as those used for *in vivo* voltammetry (see Chapter 17) or as SECM tips (see Chapters 6 and 12)) are susceptible to significant diffusion from behind the plane of the electrode (Figure 19.2*c*), resulting in appreciably larger steady-state currents. Therefore only UMEs having large values of RG (RG = $r_{glass}/r_0$, where $r_{glass}$ is the radius of the insulation) should be used for diffusion coefficient measurements. Electrodes with $RG \gtrsim 100$ can be assumed to behave as if they are embedded in infinite insulators. For an electrode radius of 5 μm, this means that the overall tip radius should be no less than 0.5 mm.

For careful measurements of the diffusion coefficient, it is critical that the measured current be truly at steady state, otherwise the current will contain a planar diffusion contribution that will produce a larger apparent value of *D*. At a hemispherical electrode, the Cottrell equation is used to determine the relative contributions of planar and spherical diffusion:

$$i(t) = nFADC^* \left[ \frac{1}{(\pi Dt)^{1/2}} + \frac{1}{r_0} \right] \tag{19.5}$$

Steady-state conditions are reached when the planar diffusion term of the Cottrell equation (equation (19.5)) is insignificant compared to the spherical diffusion term:

$$\frac{1}{(\pi Dt)^{1/2}} \ll \frac{1}{r_0} \tag{19.6}$$

The dimensionless parameter $Dt/r_0^2$ is a convenient measure of the degree of spherical diffusion and can be used for estimating errors that arise from assuming the measurement is at steady state. For a 1% error (i.e., the spherical diffusion is 100 times the planar contribution), $Dt/r_0^2$ must be greater than 3200. For a hemispherical electrode with a radius of 5 μm ($5 \times 10^{-4}$ cm) and a molecule with a diffusion coefficient of $1 \times 10^{-5}$ cm$^2$ sec$^{-1}$, this corresponds to 80 sec, a time where appreciable convective effects might be present. If a 2% error is acceptable, $Dt/r_0^2$ must exceed 800, corresponding to a time of only 20 sec, well before convective effects are likely to be significant. A modest decrease in the electrode size greatly reduces the time required to reach steady state; an electrode with a radius of 2.5 μm would have a 1% error at 20 sec and 2% at 5 sec.

Disk UMEs are easier to fabricate than hemispherical UMEs, and are therefore much more commonly used. The Shoup and Szabo equation (1) for chronoamperometry at a disk UME

$$i(\tau) = 0.7854 + 0.8862\tau^{-1/2} + 0.2146 \exp(-0.7823\tau^{-1/2}) \tag{19.7}$$

where $\tau = 4Dt/r_0^2$ and $i(\tau)$ is ratio of the current at time $\tau$ to the steady-state current ($i_{ss}$), can be used to estimate the time required to reach steady state within a given error level. A value of $\tau = 2000$ gives a 1% error and $\tau = 500$ gives a 2% error. For a disk with a radius of 5 μm and a compound with a diffusion coefficient of $1 \times 10^{-5}$ cm$^2$ sec$^{-1}$, this corresponds to 50 and 12 sec, respectively. As with the spherical electrode, a decrease of the electrode radius by a factor of 2 (to 2.5 μm) gives a fourfold reduction of these times to 12.5 and 3 sec, respectively.

Another advantage of UME determinations of the diffusion coefficient is that measurements can be made in solutions of low conductivity, i.e. low or no supporting electrolyte (2, 3). Furthermore, double potential step techniques can be useful for determining diffusion coefficients of both $D_O$ and $D_R$ (4). Although these methods are beyond the scope of this chapter, the interested reader is referred to the original literature.

#### *19.4.1.2 Chronoamperometry at macroelectrodes*

At a large planar electrode, the diffusion-limited current following the application of a potential step follows the familiar Cottrell equation:

$$i(t) = \frac{nFAD^{1/2}C^*}{\pi^{1/2}t^{1/2}} \tag{19.8}$$

For electrodes with pure linear diffusion, the diffusion coefficient can be calculated from a plot of $i$ vs. $t^{-1/2}$ (Figure 19.4). The slope of the best-fit line is then $nFAD^{1/2}C^*/\pi^{1/2}$, and $D$ can be found from

$$D = \frac{(\text{slope})^2\pi}{(nFAC^*)^2} \tag{19.9}$$

This is an excellent technique for measuring diffusion coefficients, and it has long been used for this purpose. The classic work of von Stackelberg (5) represents perhaps the most careful study of diffusion coefficients using this method.

The Cottrell equation assumes that planar diffusion is the only contribution to the overall current. However, purely planar diffusion is only achievable with very large electrodes or with shielded electrodes. The current measured with small, unshielded electrodes can exhibit appreciable edge effects, resulting in positive deviations from the Cottrell equation and thus positive errors in the diffusion coefficient. Edge effects are normally manifested at long times (i.e., small values of $t^{-1/2}$). The presence of convection at long times will also be evidenced by a positive deviation of the current. For these reasons, only those data points from the linear portion of the $i$ vs. $t^{-1/2}$ curve should be used for the analysis of $D$.

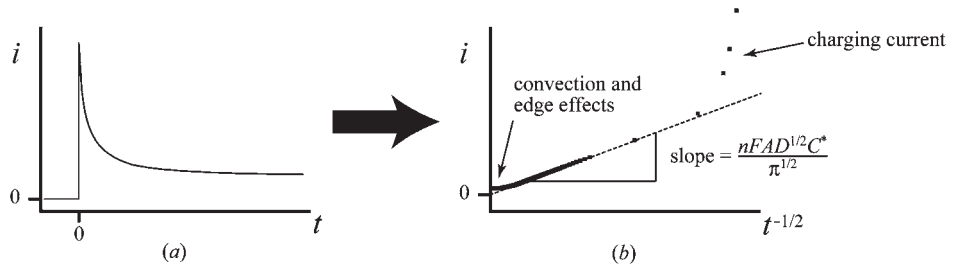


**Figure 19.4** Analysis of data for chronoamperometry at a macroelectrode. (*a*) Raw data, (*b*) current plotted as a function of $t^{-1/2}$. Note the positive deviations arising from charging current and convection/edge effects.

In theory, spherical macroelectrodes (e.g., mercury drops) could be used to measure the diffusion coefficient. The advantage of mercury drops is that the surface is renewable and therefore electrode fouling can normally be avoided. However, these electrodes are of limited utility because they exhibit both planar diffusion, which predominates at short times, and spherical diffusion, which predominates at very long times. The time required to reach steady state with large spherical electrodes exceeds the time at which convection occurs. Likewise, the time frame for purely planar diffusion is short enough (~30 msec for $r_0$ = 0.1 cm, $D = 1 \times 10^{-5}$ cm$^2$ sec$^{-1}$, and $\leq$1% contribution from spherical diffusion) that no particular advantage is realized by using spherical macroelectrodes to measure $D$. Hemispherical UMEs, however, are well-suited to steady-state measurements of diffusion coefficients (see above).

#### *19.4.1.3 Normalized chronoamperometry techniques*

By normalizing the chronoamperometric response of a UME to the limiting current at steady state, an equation depending only on $r_0$, $D$, and $t$ results (6, 7):

$$\frac{i(t)}{i_{ss}} = 1 + \frac{2r_0}{\pi(\pi D_O t)^{1/2}} \tag{19.10}$$

A plot of the normalized current as a function of $t^{-1/2}$ gives a straight line with an intercept of 1 and a slope of $2r_0/\pi(\pi D)^{1/2}$. The diffusion coefficient can then be calculated from this slope:

$$D = \frac{4r_0^2}{(\text{slope})^2 \pi^3} \tag{19.11}$$

Note that $D$ is now dependent on the square of the radius, so careful characterization of the UME's dimensions using a test compound is particularly important. An additional advantage of this normalization technique is that because the measurement of $i_{ss}$ and $i(t)$ can occur in the same experiment, calibration errors in the current amplifier are essentially eliminated. An alternative approach is to fit the normalized chronoamperometry data to the Shoup and Szabo equation (equation (19.7)), which only requires knowledge of $r_0$.

### 19.4.2 Rotating disk electrode techniques

The advantage of using the RDE for determining diffusion coefficients is that the measured current is steady state (see Chapter 11). The Levich equation relates the measured current to the experimental parameters:

$$i_l = 0.62nFAC^* D^{2/3} \omega^{1/2} \nu^{-1/6} \tag{19.12}$$

where $v$ is the kinematic viscosity. In the determination of diffusion coefficients with an RDE, it is common to change the rotation rate[3] ($\omega$ in $sec^{-1}$) and plot $i_l$ vs. $\omega^{1/2}$. The slope of the resulting best-fit line can be used to determine $D$:

$$D = \left( \frac{\text{slope}}{0.62nFAC^* v^{-1/6}} \right)^{3/2} \tag{19.13}$$

As with chronoamperometry, there are limits to the range of experimental conditions under which equation (19.12) applies, but with the RDE the important parameter is the rotation rate $\omega$. At low values of $\omega$, the hydrodynamic boundary layer becomes large and the assumptions used to derive the Levich equation no longer hold. The lower limit for $\omega$ can be found from

$$\omega > 10 \frac{v}{r_1^2} \tag{19.14}$$

where $r_1$ is the electrode radius. At large values of $\omega$, laminar flow is overcome by turbulent flow and again the Levich equation no longer holds. This occurs with Reynolds number Re

$$\text{Re} = \frac{\omega r_1^2}{v} \tag{19.15}$$

greater than about $10^5$. Thus for a solution with $v = 0.009$ $cm^2$ $sec^{-1}$ and $r_1 = 0.15$ cm, the Levich equation can in theory be applied over the range of $\omega$ = 4–40,000 $sec^{-1}$, or 40–400,000 rpm. Practically, however, the upper limit is more on the order of 10,000 rpm for real RDEs (8).

Two additional experimental factors are important when the RDE is used to determine diffusion coefficients. First, the Levich equation assumes that the disk is centered on the axis of rotation. Any non-idealities in the construction of the RDE will result in an increase in the measured current, and thus lead to an overestimation of $D$. Second, edge effects can be present, particularly at very low rotation rates and/or with very small electrodes. These effects will be apparent as non-linearities in the $i_l$ vs. $\omega^{1/2}$ plot, and therefore rotation rates at which these non-linearities occur should not be used for the determination of the diffusion coefficient.

For more accurate determinations of diffusion coefficients with the RDE, one can apply the Riddiford correction (9), where the constant 0.62 in the Levich equation is replaced by

$$\frac{0.554}{0.8934 + 0.316(D/v)^{0.36}} \tag{19.16}$$

For a diffusion coefficient of $1 \times 10^{-5}$ $cm^2$ $sec^{-1}$ and a kinematic viscosity of 0.009 $cm^2$ $sec^{-1}$, the coefficient becomes 0.60, corresponding to a 3% difference from the Levich equation. The application of this correction is problematic, however, because an

[3] $\omega$ is an angular velocity, so the one revolution is actually $2\pi$, or 1 revolution per second corresponds to $\omega = 2\pi$ $sec^{-1}$.

approximate value of $D$ must be known to calculate the coefficient, which is then used to calculate $D$. Because of this uncertainty, one should expect an error of a few percent in the calculated value of the diffusion coefficient even with the most careful RDE experiment.

### 19.4.3 Potential sweep techniques

Linear scan voltammetry (LSV) and cyclic voltammetry (CV) (see Chapter 11) are among the most common electrochemical techniques employed in the laboratory. Despite their utility, however, they are not particularly well suited to careful measurements of diffusion coefficients when using electrodes of conventional size. We will briefly discuss techniques for measuring $D$ with LSV and CV, but the reader should be cautioned that these measurements under conditions of planar diffusion (i.e., at conventional electrodes) are probably useful to only one significant digit, and then only for nernstian systems with no coupled homogeneous reactions and with no adsorption. For more reliable results with LSV and CV, UMEs should be used.

For a reversible redox reaction (Figure 19.3*e*), the diffusion-controlled peak current at a planar electrode (Figure 19.3) is given by (10)

$$i_p = 2.69\times10^5 n^{3/2} A C^* D^{1/2} v^{1/2} \tag{19.17}$$

The most straightforward method for determining the diffusion coefficient is to measure the peak current ($i_p$) at several scan rates ($v$) and then plot $i_p$ as a function of $v^{1/2}$. The slope of the best-fit line can then be used to calculate $D$:

$$D = \frac{(\text{slope})^2}{n^3 (2.69\times10^5 A C^*)^2} \tag{19.18}$$

It is important to re-emphasize that this equation applies only to reversible reactions. If one wishes to use this method, then steps should be taken to ensure that the system is in fact reversible and has no coupled homogeneous reactions. CV is useful for this purpose (see Chapters 11 and 15).

For irreversible systems ($O + e \xrightarrow{k_f} R$), $D$ could also (in theory) be calculated from an analogous equation (10):

$$i_p = 2.99\times10^5 \alpha^{1/2} n^{3/2} A C^* D^{1/2} v^{1/2} \tag{19.19}$$

This equation requires knowledge of the transfer coefficient $\alpha$, which can be estimated from

$$\left|E_p - E_{p/2}\right| = \frac{1.857RT}{\alpha F} \tag{19.20}$$

However, the errors associated with this determination of $\alpha$ will further decrease the reliability of the measured $D$. This fact, combined with the limitations of LSV discussed for the

reversible case, means that this technique should not be used other than for an estimation of the diffusion coefficient. For quasi-reversible systems (Figure 19.3*f*), the peak current is a complex function of the heterogeneous rate constant, and therefore a reliable value of the diffusion coefficient cannot be obtained.

Much more accurate measurements of diffusion coefficients can be obtained with LSV or CV using UMEs. These measurements are much less dependent on the electrochemical reversibility of the redox couple. Measurement of the diffusion-limited current from a voltammogram recorded at a microelectrode is demonstrated in Figure 19.3*c*. The concept is identical to that already discussed for chronoamperometry at UMEs; at slow scan rates (i.e., long times) the current becomes steady state as long as the potential is well past $E_{1/2}$. The dependence of $D$ on the steady-state current $i_{ss}$ is given by equation (19.3) for a hemispherical UME and equation (19.4) for a disk UME. The time considerations for CV are the same as those discussed above for chronoamperometry, except that the time is estimated from the scan rate and the difference between the final potential $E_f$ and $E_{1/2}$:

$$t \approx \frac{|E_f - E_{1/2}|}{v} \tag{19.21}$$

Thus for a UME with a radius of 5 μm and $|E_f - E_{1/2}| = 0.3$ V, planar diffusion contributes $<2\%$ to the measured current at a scan rate of $<20$ mV sec$^{-1}$.

### 19.4.4 Current step techniques (chronopotentiometry)

In chronopotentiometry, a current is applied to the electrode and the potential changes to a value at which the flux of the electroactive species is sufficient to supply the applied current. After a certain time, the flux of redox species to the surface cannot sustain this current and the potential changes rapidly to a new value at which another species (often solvent or electrolyte) is reduced (or oxidized). This time, termed the transition time $\tau$, follows the Sand equation:

$$\tau^{1/2} = \frac{\pi^{1/2} nFD^{1/2} C^*}{2i_0} \tag{19.22}$$

where $i_0$ is the current density ($i/A$). To calculate diffusion coefficients, the transition times are measured at several current densities, and an average value of $D$ can be calculated from

$$D = \frac{4i_0^2 \tau}{\pi (nFC^*)^2} \tag{19.23}$$

The two primary advantages of chronopotentiometry are that the measured quantity ($\tau$) is directly proportional to D, and that $\tau$ is the same regardless of heterogeneous electrode kinetics (although the break in the $E$–$t$ curve is less sharp when the reaction is not reversible). The primary disadvantages of chronopotentiometry include some of those

discussed previously for planar electrodes—convection at long times and complications by charging current contributions to the overall current. Convective effects can be minimized as before by choosing current densities such that transition times are no longer than 30–60 sec. The charging current issue is more troublesome, especially under conditions where short transition times occur. The current that flows to charge the double-layer means that the faradaic current differs from the applied current, thus introducing inaccuracies in the measurement of $\tau$. Short transition times, low concentrations, and electrodes having a large capacitance contribute to a higher fraction of the applied current going towards charging current and thus a less accurate determination of diffusion coefficient. Furthermore, the oxidation of the electrode surface or the presence of adsorbed electroactive material can complicate the measurement of the transition times. For these reasons, chronopotentiometry is not commonly used for accurate measurements of diffusion coefficients.

### 19.4.5 Scanning electrochemical microscopy (SECM) techniques

Scanning electrochemical microscopy (SECM) (see Chapter 12) has unique capabilities that can be exploited for measurements of the diffusion coefficient. Bard introduced a transient SECM technique that allows the determination of $D$ without knowledge of $C^*$ or $n$ (11). The only parameter that must be known is the tip radius $a$. This technique uses an approximate analytical expression relating a characteristic transition time $t_c$ to the change in tip position above a substrate. From plots of the normalized tip current vs. $t^{-1/2}$, $t_c$ can be determined, and then a working curve is used to calculate $D$. Although this technique has relatively low precision, it is useful for measuring diffusion coefficients in situations where the concentration is not known or cannot be independently measured. For example, it has been used for measuring diffusion coefficients in non-traditional media such as gels (12).

The diffusion coefficient ratio of a redox couple can also be measured with SECM using an approach developed by Unwin (13, 14). With this technique, the ratio of the steady-state collector current for the substrate generation/tip collection (SG/TC) mode to the steady-state collector current measured in the feedback mode (at the same tip-substrate separation) gives directly the ratio of diffusion coefficients for the redox couple. The advantage of this approach is that no knowledge of the tip-substrate separation, the electrode sizes, or the mediator concentration is required.

Beyond these applications, SECM can also be used to probe diffusional transport in unusual samples because the UME can be placed precisely in the microenvironment of interest. For example, lateral proton diffusion in Langmuir monolayers (15), diffusional transport through porous membranes and dentin (16), and the contribution of diffusion to iontophoretic transport in skin (17) have been investigated using the SECM.

## 19.5 TABLES OF DIFFUSION COEFFICIENTS

Diffusion coefficients for common test compounds (see Tables 19.2 –19.4).

**Table 19.2**

Diffusion coefficients of selected inorganic and organometallic compounds. Unless otherwise indicated, data are for 25 °C or room temperature

| Compound | Solvent system | $D \times 10^5$ ($cm^2\ sec^{-1}$) | Method[a] | Reference |
|---|---|---|---|---|
| $Ag^+$ | 0.1 M $KNO_3$ | 1.55 | 1 | 5 |
| $Cd^{2+}$ | 1.0 M KCl | 0.808 | 1 | 5 |
| $Tl^+$ | 0.5 M $KNO_3$ | 1.9 | 5 | 18 |
| | 0.9 M $NaNO_3$ | 1.6 | 5 | 18 |
| $Fe(CN)_6^{3-}$ | 0.05 M KCl | 0.765 | 1 | 5 |
| | 0.1 M KCl | 0.763 | 1 | 5 |
| | 0.5 M KCl | 0.770 | 1 | 5 |
| | 1.0 M KCl | 0.763 | 1 | 5 |
| | 0.5 M KCl, pH 3.0 | 0.72 | 2, 3 | 19 |
| $Fe(CN)_6^{4-}$ | 0.05 M KCl | 0.662 | 1 | 5 |
| | 0.1 M KCl | 0.650 | 1 | 5 |
| | 0.5 M KCl | 0.639 | 1 | 5 |
| | 1.0 M KCl | 0.632 | 1 | 5 |
| $Ru(NH_3)_6^{3+}$ | Phosphate buffer, pH 7.0 | 0.55 | 1 | 19 |
| | 0.1 M NaTFA | 0.67 | 2 | 20 |
| Ferrocene (Fc) | 0.5 M $TBABF_4$ in $CH_3CN$ | 1.7 | 2 | 21 |
| | 0.2 M $TBAClO_4$ in $CH_3CN$ | 2.2 | 2, 3 | 19 |
| | 0.2 M $LiClO_4$ in $CH_3CN$ | 2.4 | 4 | 22 |
| | 0.1 M $TBAClO_4$ in $CH_3CN$ | 2.2 | 6 | 23 |
| | 0.1 M $TBAClO_4$ in $CH_3CN$ | 2.7 (40 °C) | 2 | 24 |
| | 0.1 M $TBAClO_4$ in $CH_3CN$ | 3.0 (50 °C) | 2 | 24 |
| | 0.1 M $TBAClO_4$ in $CH_3CN$ | 3.2 (60 °C) | 2 | 24 |
| $Fc^+$ | 0.1 M $TBAClO_4$ in $CH_3CN$ | 1.6 | 6 | 14 |
| $Fc(CO_2H)$ | 0.2 M $LiClO_4$ in $CH_3CN$ | 1.1 | 4 | 22 |
| | 0.1 M $NaClO_4$ (aqueous) | 0.67 | 2 | 12 |
| $Fc(CH_2CO_2^-)$ | 0.1 M $LiClO_4$ (aqueous) | 0.51 | 2 | 2 |
| $FcTMA^+$ | 0.1 M $NaClO_4$ (aqueous) | 0.66 | 2 | 12 |
| $FcMeTMA^+$ | 0.1 M $TBAClO_4$ | 1.4 | 2 | 2 |
| $Fc(CH_2OH)_2$ | 0.1 M $NaClO_4$ (aqueous) | 0.65 | 2 | 12 |
| | 0.1 M $LiClO_4$ (aqueous) | 0.63 | 3 | 25 |
| | 0.050 M $TMAClO_4$ (aqueous) | 0.78 | 2 | 26 |
| $IrCl_6^{2-}$ | 0.5 M $K_2SO_4$ | 0.64 | 5 | 27 |
| Osmocene | 0.2 M $LiClO_4$ in $CH_3CN$ | 2.2 | 4 | 22 |
| Ruthenocene | 0.2 M $LiClO_4$ in $CH_3CN$ | 2.2 | 4 | 22 |
| $Ru(bpy)_3^{2+}$ | 0.1 M $TEABF_4$ in $CH_3CN$ | 2.1 | 7 | 28 |
| $Fe(bpy)_3^{2+}$ | 0.1 M $TEABF_4$ in $CH_3CN$ | 2.1 | 7 | 28 |
| $Ru(acac)_3$ | 0.1 M $TEABF_4$ in $CH_3CN$ | 2.3 | 7 | 28 |

*Abbreviations:* TFA, trifluoroacetate; TBA, tetra-*n*-butylammonium; TEA, tetraethylammonium; TMA, trimethylammonium; bpy, 2,2′-bipyridine; acac, acetylacetone.

[a]1, chronoamperometry at a shielded planar electrode; 2, steady-state current at a disk UME; 3, normalized chronoamperometry; 4, chronopotentiometry; 5, chronoamperometry at unshielded, planar electrode; 6, scanning electrochemical microscopy (method from reference (23)); 7, rotating disk electrode.

**Table 19.3**

Diffusion coefficients of selected organic compounds. Unless otherwise indicated, data are for 25 °C or room temperature

| Compound | Solvent system | $D \times 10^5$ ($cm^2\ sec^{-1}$) | Method[a] | Reference |
|---|---|---|---|---|
| *p*-benzoquinone | 0.25 M $TEAClO_4$ in $CH_3CN$ | 2.7 | 1 | 23 |
| Hydroquinone | 0.1 M $H_2SO_4$ | 0.73 | 2 | 29 |
| Anthracene | 0.1 M $TEAClO_4$ in $CH_3CN$ | 2.55 | 3 | 30 |
| | 0.1 M $TBABF_4$ in DMF | 1.1 | 4 | 31 |
| Anthraquinone | 0.1 M $TBABF_4$ in DMF | 1.0 | 4 | 31 |
| Benzophenone | 0.1 M $TBABF_4$ in DMF | 1.0 | 4 | 31 |
| Biphenyl | 0.1 M $TEAClO_4$ in $CH_3CN$ | 2.48 | 3 | 30 |
| Fullerene (C60) | 0.5M TBABr in *o*-dichlorobenzene | 0.11 | 4 | 32 |
| Fullerene (C70) | | 0.11 | 4 | 32 |
| Napthalene | 0.1 M $TEAClO_4$ in $CH_3CN$ | 2.74 | 3 | 30 |
| Perylene | 0.1 M $TBABF_4$ in DMF | 0.84 | 4 | 31 |
| TMPD (*N,N,N′,N′*-tetramethylphenylene diamine) | 0.1 M $TBAClO_4$ | 2.4 | 5 | 24 |
| Ascorbic acid | 0.1 M Phosphate, pH 7.4 | 0.53 | 6 | 33 |
| Catechol | 0.1 M $H_2SO_4$ | 0.66 | 2 | 29 |
| (−)-3,4-dihydroxy-norephedrine | 0.1 M $H_2SO_4$ | 0.66 | 7 | 33, 34 |
| 3,4-dihydroxy-hydrocinnamic acid | 0.1 M $H_2SO_4$ | 0.69 | 7 | 34 |
| L-DOPA | 0.1 M $H_2SO_4$ | 0.55 | 7 | 33, 34 |
| L-DOPA methyl ester | 0.1 M $H_2SO_4$ | 0.70 | 7 | 34 |
| DOPAC (3,4-dihydroxy-phenylacetic acid) | 0.1 M Phosphate, pH 7.4 | 0.59 | 6 | 33 |
| Dopamine | 0.1 M Phosphate, pH 7.4 | 0.60 | 6 | 33 |
| | 0.1 M $H_2SO_4$ | 0.67 | 7 | 34 |
| Epinephrine | 0.1 M Phosphate, pH 7.4 | 0.52 | 6 | 33 |
| | 0.1 M $H_2SO_4$ | 0.61 | 7 | 34 |
| 4-methylcatechol | 0.1 M Phosphate, pH 7.4 | 0.66 | 6 | 33 |
| Norepinephrine | 0.1 M Phosphate, pH 7.4 | 0.55 | 6 | 33 |
| | 0.1 M $H_2SO_4$ | 0.62 | 7 | 34 |
| Serotonin (5-hydroxy-tryptamine) | 0.1 M Phosphate, pH 7.4 | 0.54 | 6 | 33 |

*Abbreviations:* TBA, tetra-*n*-butylammonium; TEA, tetraethylammonium.

[a]1, scanning electrochemical microscopy (method from reference (23)); 2, hydrodynamic voltammetry with a tubular electrode; 3, tracer diffusion from capillaries; 4, rotating disk electrode; 5, steady-state current at a disk UME; 6, flow injection analysis (a non-electrochemical method); 7, chronoamperometry at unshielded planar electrode.

**Table 19.4**

Diffusion coefficients of other species of interest. Unless otherwise indicated, data are for 25 °C or room temperature

| Compound | Solvent system | $D \times 10^5$ ($cm^2\ sec^{-1}$) | Method[a] | Reference |
|---|---|---|---|---|
| $H^+$ | 0.1 M $KNO_3$ | 7.9 | 1 | 35 |
| | 1.0 M KCl | 7.3 | 2 | 36 |
| | 0.1 M $NaClO_4$ in 0.010–0.060 M $HClO_4$ | 7.1 | 1 | 37 |
| $OH^-$ | 0.1 M $Na_2SO_4$ | 5.6 | 3 | 38 |
| | 1 M $KNO_3$ | 4.4 | 3 | 39 |
| | 0.1 M $Na_2SO_4$ in 0.2–25 mM $OH^-$ | 4.9 | 1 | 40 |
| $H_2$ | 0.1 M $KNO_3$ | 5.0 | 1 | 35 |
| $O_2$ | 1.0 M KOH | 1.6 | 3 | 41 |
| | 0.025 M $H_2SO_4$ | 1.9 | 3 | 42 |
| | 0.1 M $Na_2SO_4$ | 2.5 | 4 | 43 |

[a]1, steady-state current at a disk UME; 2, chronoamperometry at a shielded planar electrode; 3, rotating disk electrode; 4, diaphragm diffusion cell.

## REFERENCES


1. D. Shoup, A. Szabo, *J. Electroanal. Chem*. **140**, 237 (1982).
2. W. Hyk, A. Nowicka, Z. Stojek, *Anal. Chem*. **74**, 149 (2002).
3. W. Hyk, Z. Stojek, *Anal. Chem*. **74**, 4805 (2002).
4. H. Ikeuchi, M. Kanakubo, *J. Electroanal. Chem*. **493**, 93 (2000).
5. M. von Stackelberg, M. Pilgram, V. Toome, *Z. Elektrochem*. **57**, 342 (1953).
6. S. C. Petrovic, R. H. Hammericksen, *Electroanalysis* **14**, 599 (2002).
7. G. Denuault, M. V. Mirkin, A. J. Bard, *J. Electroanal. Chem*. **308**, 27 (1991).
8. A. J. Bard, L. R. Faulkner, *Electrochemical Methods: Fundamentals and Applications*, 2nd ed., John Wiley & Sons, Inc.: New York, 2001.
9. D. P. Gregory, A. C. Riddiford, *J. Chem. Soc*., 3756 (1956).
10. R. S. Nicholson, I. Shain, *Anal. Chem*. **36**, 706 (1964).
11. A. J. Bard, G. Denuault, R. A. Friesner, B. C. Dornblaser, L. S. Tuckerman, *Anal. Chem*. **63**, 1282 (1991).
12. F.-R. F. Fan, *J. Phys. Chem*. **102**, 9777 (1998).
13. R. D. Martin, P. R. Unwin, *Anal. Chem*. **70**, 276 (1998).
14. R. D. Martin, P. R. Unwin, *J. Electroanal. Chem*. **439**, 123 (1997).
15. J. Zhang, P. R. Unwin, *Phys. Chem. Chem. Phys*. **4**, 3814 (2002).
16. S. Nugues, G. Denuault, *J. Electroanal. Chem*. **408**, 125 (1996).
17. B. D. Bath, E. R. Scott, J. B. Phipps, H. S. White, *J. Pharm. Sci*. **89**, 1537 (2000).
18. M. Kakihana, H. Ikeuchi, G. P. Sato, K. Tokuda, *J. Electroanal. Chem*. **108**, 381 (1980).
19. J. E. Baur, R. M. Wightman, *J. Electroanal. Chem*. **305**, 73 (1991).
20. D. O. Wipf, E. W. Kristensen, M. R. Deakin, R. M. Wightman, *Anal. Chem.* **60**, 306 (1988).
21. M. V. Mirkin, T. C. Richards, A. J. Bard, *J. Phys. Chem.* **97**, 7672 (1993).
22. T. Kuwana, D. E. Bublitz, G. Hoh, *J. Am. Chem. Soc*. **82**, 5811 (1960).
23. R. D. Martin, P. R. Unwin, *Anal. Chem*. **70**, 276 (1998).
24. S. R. Jacob, Q. Hong, B. A. Coles, R. G. Compton, *J. Phys. Chem*. **103**, 2963 (1999).

25. S. C. Petrovic, W. Zhang, M. Ciszkowska, *Anal. Chem*. **72**, 3449 (2000).
26. W. Miao, Z. Ding, A. J. Bard, *J. Phys. Chem. B* **106**, 1392 (2002).
27. M. R. Deakin, K. J. Stutts, R. M. Wightman, *J. Electroanal. Chem*. **182**, 113 (1985).
28. M. Morita, Y. Tanaka, K. Tanaka, Y. Matsuda, T. Matsumura-Inoue, *Bull. Chem. Soc. Japan* **61**, 2711 (1988).
29. L. R. Sharma, R. K. Kalia, *J. Chem. Eng. Data* **22**, 39 (1977).
30. T. A. Miller, B. Prater, J. K. Lee, R. N. Adams, *J. Am. Chem. Soc.* **87**, 121 (1965).
31. S. U. Pedersen, T. B. Christensen, T. Thomasen, K. Daasbjerg, *J. Electroanal. Chem.* **454**, 123 (1998).
32. B. Miller, J. M. Rosamilia, G. Dabbagh, A. J. Muller, R. C. Haddon, *J. Electrochem. Soc*. **139**, 1941 (1992).
33. G. Gerhardt, R. N. Adams, *Anal. Chem*. **54**, 2618 (1982).
34. S. A. Nowinski, D. M. Anjo, *J. Chem. Eng. Data* **34**, 265 (1989).
35. J. V. Macpherson, P. R. Unwin, *Anal. Chem*. **69**, 2063 (1997).
36. M. von Stackelberg, M. Pilgram, *Coll. Czech. Chem. Commun*. **25**, 2974 (1960).
37. J. Zhou, Y. Zu, A. J. Bard, *J. Electroanal. Chem*. **491**, 22 (2000).
38. M. Breiter, K. Hoffmann, *Z. Elektrochem*. **64**, 462 (1960).
39. R. Landsberg, W. Geissler, S. Mueller, *Z. Chem*., **1**, 169 (1961).
40. B. Liu, A. J. Bard, *J. Phys. Chem. B* **106**, 12801 (2002).
41. C. P. Winlove, K. H. Parker, R. K. C. Oxenham, *J. Electroanal. Chem*. **170**, 293 (1984).
42. V. G. Levich, *Physiochemical Hydrodynamics*, Prentice-Hall: Englewood Cliffs, NJ, 1962.
43. G. W. Hung, R. H. Dinius, *J. Chem. Eng. Data* **17**, 449 (1972).

# – 20 –

# Liquid Junction Potentials

**Robert A. W. Dryfe**

School of Chemistry, University of Manchester, Oxford Road,
Manchester M13 9PL, UK

## 20.1 TYPES OF LIQUID JUNCTIONS

### 20.1.1 Interfacial potentials without electrolyte transport

Potentiometric methods of electroanalysis (see Chapter 7 of this handbook) depend on the ability of a membrane material to transport either cations or anions selectively. This selective behaviour results in an imbalance of concentrations on either side of the membrane which, in turn, leads to the establishment of a measurable potential difference across the membrane. In the simplest possible analysis, if we consider our membrane to be infinitely thin, or alternatively to have some kind of electrolyte boundary that is infinitely thin, then the equality of electrochemical potential, $\overline{\mu}_i$, in either of the solution phases, $\alpha$ and $\beta$, implies that

$$\overline{\mu}_{\alpha,i} = \overline{\mu}_{\beta,i} \tag{20.1.1-1}$$

where $i$ is the ion which is able to partition between the two phases. Thus, from the definition of the electrochemical potential:

$$\mu^0_{\alpha,i} + RT \ln a_{\alpha,i} + z_i F \phi_\alpha = \mu^0_{\beta,i} + RT \ln a_{\beta,i} + z_i F \phi_\beta \tag{20.1.1-2}$$

where $\mu_i^0$ is the standard chemical potential of the ion in a given phase, $a$ is the ion activity, $\phi$ is the electrical potential of the phase, $z$ is the charge number of the ion, $F$ is Faraday's constant, $R$ is the universal gas constant and $T$ is the absolute temperature.

Hence, the potential difference established across the membrane depends on the ratio of the activities of the ions in phases $\alpha$ and $\beta$:

$$\Delta\phi \equiv \phi_\beta - \phi_\alpha = \frac{RT}{zF} \ln\left(\frac{a_{\alpha,i}}{a_{\beta,i}}\right) \tag{20.1.1-3}$$


**Handbook of Electrochemistry**
**Edited by C.G. Zoski**

where $\Delta\phi$ is the potential difference between phase $\beta$ and phase $\alpha$. Towards the end of the chapter, methods to establish stable interfacial potentials between phases that are physically distinct (i.e. do not require separation via a membrane) will be discussed.

The establishment of such interfacial potentials is readily envisaged for cases where the net transport of an electrolyte is prevented because one of its constituents cannot partition. What is perhaps less obvious is that such potentials arise continually within solution phases, even where there is no physical separation into distinct phases. These so-called liquid junction potentials or diffusion potentials play an important role in electrochemical experiments, but because there is no well-defined phase boundary, they are intrinsically more difficult to measure. This chapter discusses how these potentials arise, how they may be calculated, what quantities are associated with them, and how they may be minimised. Finally, interfaces *between* electrolytes (i.e. those interfaces between immiscible electrolyte solutions (ITIES)) and the application of some of the concepts developed earlier in the chapter to "non-standard" electrolyte systems, such as polymer electrolytes and room-temperature ionic liquids, will be discussed.

### 20.1.2 Interfacial potentials with electrolyte transport

The starting point for the discussion of the potentials that arise within a given electrolyte solution is to return to the Nernst–Planck equation, describing the flux of charge $J$ within an electrolyte (1):

$$J = -\frac{F}{RT}\nabla\phi\sum_j z_j D_j C_j - \sum_j D_j \nabla C_j + v\sum_j C_j \qquad (20.1.2\text{-}1)$$

which reduces to

$$J = -\frac{F}{RT}\frac{\partial\phi(x)}{\partial x}\sum_j z_j D_j C_j - \sum_j D_j \frac{\partial C_j(x)}{\partial x} + v(x)\sum_j C_j \qquad (20.1.2\text{-}2)$$

for the one-dimensional case, where $x$ is the relevant spatial co-ordinate. Of the symbols, $D_j$ and $C_j$ are the diffusion coefficient and concentration of ion $j$, respectively, and $v$ is the velocity of the solution. The terms on the right-hand side of these equations represent fluxes due to migration, diffusion, and convection, respectively.

Equation (20.1.2-1) can be written in terms of the current density, since this quantity is defined as the flux multiplied by $-z_i F$:

$$I = F\nabla\phi\sum_j z_j u_j C_j + F\sum_j z_j D_j \nabla C_j - Fv\sum_j z_j C_j \qquad (20.1.2\text{-}3)$$

where $I$ is the current density ($i/A$, where $A$ represents electrode area), and $u_j$ is the mobility of each ion. In the limit of infinite dilution, the ionic mobility is related to its diffusion coefficient via the Einstein law (2):

$$u_i = \frac{z_i F D_i}{RT} \qquad (20.1.2\text{-}4)$$

Note that there is some inconsistency in prior literature regarding the precise definition of ionic mobility, with some authors distinguishing between the competing definitions by referring to an "absolute" and a "conventional" mobility (2). Here, the term mobility refers to the latter quantity, which has dimensions of the form $cm^2\ s^{-1}\ V^{-1}$, which is positive (for cations) or negative (for anions).[1] Even if the solution is flowing, the convective term in the above equation will not contribute to the overall current because of the requirement for local electroneutrality. Hence, equation (20.1.2-3) may be re-arranged to give

$$\nabla\phi = \frac{I}{\kappa} - \frac{F}{\kappa}\sum_j z_j D_j \nabla C_j \tag{20.1.2-5}$$

where $\kappa$ represents the electrolyte conductivity, defined as

$$\kappa = F\sum_j z_j u_j C_j \tag{20.1.2-6}$$

Equation (20.1.2-2) is important because it states that even when no current flows, a potential gradient arises *within* a given solution when the diffusion coefficients of the ions of the electrolyte differ. This condition, which is almost certain to be met for ions of even slightly differing size, means that the summation term in equation (20.1.2-5) is non-zero, so that a potential gradient exists in solution. Physically, the reason for the establishment of the gradient can be understood if we question the assumption made in arriving at equation (20.1.2-5), namely that the solution must be locally electroneutral. Clearly, electroneutrality will be rapidly violated if the ions diffuse through the solution at different rates. However, this imbalance in transport rates sets up the electric field in solution if, for example, the cations move ahead of the anions. The diffusion potential then arises since electroneutrality is, therefore, the brake that acts to restore parity to the solution. Lingane has delineated three types of diffusion potential, depending on the differences between the constituent parts of the electrolyte solution (3). The first potential is considered to arise when the entire solution consists of the same electrolyte, but a difference in activities exists within the solution. If electrodes reversible to one of the ions are introduced, this becomes a "concentration cell", discussed in Section 20.2.1. The second type of boundary arises where two solutions containing a common ion meet; the common-ion activities in both halves are identical, but each half of the cell contains a different counter-ion. Finally, the third type of diffusion potential, according to the Lingane classification, is established when neither of the conditions of the first and second type is met.

A consequence of this phenomenon arises from further consideration of equation (20.1.2-1). Neglecting the third (convective) term, for the reasons stated above, the current is given by the sum of the migratory and diffusive fluxes. In the case of the bulk electrolyte

[1]Allowing mobilities to take negative, or positive, values (dependent on the ionic charge) accounts for the opposing displacements of ions of opposite charge in the presence of an electric field. Although this deviates from the notation adopted in some texts, this approach means equation (20.1.2-6) follows directly from the Nernst–Planck equation. Further, there is no need to introduce the absolute value of the charge number in the definition of the conductivity, since the product $z_i u_i$ will always be positive. The consequence of this is that definitions of parameters such as ionic conductivity and, in turn, transference number must use $z_i u_i$, rather than $u_i$.

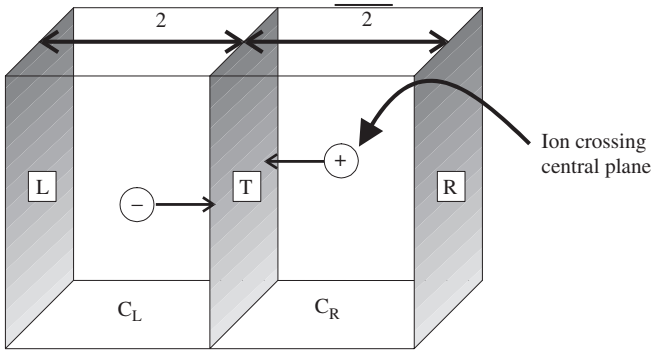


**Figure 20.1** Schematic description of charge transport in the bulk of a cell: electroneutrality can be maintained by cations moving from electrode "R" to "L", or via anions moving in the reverse direction, or by a combination of both processes. The transference number is, essentially, the fraction of charge passed across a virtual reference plane, "T", in the solution due to a given ion.

solution on addition of an excess of supporting electrolyte (see Chapter 3 of this handbook), the flux of this electrolyte is essentially due to migration alone. Hence, the current density within a region of the bulk solution is given solely by the first term of equation (20.1.2-3). This equation reveals that the fluxes carried by the components of a binary electrolyte will only be equal (or, rather equal and opposite, given their response to an electric field) if the mobilities of the constituent ions are of the same magnitude. As with the discussion of diffusion coefficients, it is extremely unlikely that this condition will be met. Thus, in almost all cases, it is clear that differing fractions of charge will be carried by the components of a given electrolyte solution. This situation may be illustrated schematically for a two-electrode cell illustrated in Figure 20.1. For a given electrolysis process, the excess negative charge generated by the reduction of one equivalent of reactant at the cathode may be compensated by (a) a movement of one equivalent of cations from the bulk of the solution *towards* the cathode; or (b) by movement of one equivalent of anions *away* from the cathode, into the bulk solution. Analogous arguments would hold for the oxidation reaction occurring at the anode. However, a third possibility exists, which will be the more general case: namely that some fraction of the charge balance will be carried out by movement of the cations in one direction *and* the remaining fraction will arise from movement of the anions in the other direction. The important point is, based on the statement about mobilities, that these fractions will *not* necessarily be equal (i.e. the fraction of charge transported by each ion will *not* usually be one-half) but nor will it normally approach zero (or one). This gives rise to the concept of the transference number, defined algebraically below, which is simply the fraction of the current flowing attributable to a particular ion. In summary, the origin of the transference number can be understood by paraphrasing Orwell: "all ions are mobile, but some are more mobile than others".

The conclusion that charge transport is unequally shared between the constituent ions of an electrolyte may appear to be at odds with the underlying assumption that the solutions remain locally electroneutral, but one can again resolve this objection by consideration of the "membrane" case alluded to in the opening section. If one considers ion transport

within a cation-exchange membrane (e.g. an organic ionomer such as "Nafion" or an inorganic ion-exchanger such as a zeolite (see Section 20.5)), then for an ideal membrane the fraction of charge transported by the cation should approach one. This does not mean that electroneutrality is violated, merely that the anions (or rather the framework charges) are bystanders with zero mobility. The converse case applies to electronic conduction within metals in the case where charge is transported solely by the mobile electrons; again, this does not violate the principle of electroneutrality within the bulk of the metal.

The transference number was defined above as the fraction of current (or current density) attributable to a particular ion:

$$t_i = \frac{I_i}{I} = \frac{I_i}{\sum_j I_j} \tag{20.1.2-7}$$

By definition,

$$\sum_j t_j = 1 \tag{20.1.2-8}$$

As discussed above for the bulk solution where there is no concentration gradient, the current density will arise solely from the first term of equation (20.1.2-3). Combination with equation (20.1.2-7) leads to (2)

$$t_i = \frac{z_i C_i u_i}{\sum_j z_j C_j u_j} \tag{20.1.2-9}$$

Recall that the mobility terms are, by definition, positive for cations and negative for anions. Some further relations are required to complete our definitions of transference numbers (4). The molar conductivity, $\Lambda$, of a solution is defined as

$$\Lambda = \frac{\kappa}{C} \tag{20.1.2-10}$$

where $C$ is the electrolyte concentration.

Kohlrausch's law of independent ionic migration states that the molar conductivity at infinite dilution, $\Lambda^0$, is given by the sum of the values for its ionic components, $A^{a+}$ and $B^{b-}$.

$$\Lambda^0 = \nu_A \lambda_A^0 + \nu_B \lambda_B^0 \tag{20.1.2-11}$$

where $\lambda_A^0$ is the limiting ionic molar conductivity for ion A and $\nu_A$ defines its stoichiometry in the electrolyte.

By definition,

$$\lambda_i = z_i u_i F \tag{20.1.2-12}$$

Combining equations (20.1.2-7) and (20.1.2-10) yields

$$t_i = \frac{C_i \lambda_i}{\sum_j C_j \lambda_j} \tag{20.1.2-13}$$

For a binary electrolyte, a combination of equations (20.1.2-11) and (20.1.2-13) leads to

$$t_A = \frac{C_A \lambda_A^0}{C_A \lambda_A^0 + C_B \lambda_B^0} = \frac{v_A \lambda_A^0}{\Lambda^0} \tag{20.1.2-14}$$

Note that the transference numbers defined in terms of ionic conductivity apply, strictly speaking, to infinite dilution where ion–ion interactions are minimal and Kohlrausch's law holds.

Having defined the relevant quantities, methods of measuring them and appropriate sample calculations are given in the next sections. Note that the subsequent sections are solely concerned with transference parameters of electrolyte solutions. The measurement of transference numbers in ionic crystals is subject to some quite different constraints and is not considered here. This area has been reviewed in reference (5).

## 20.2 TRANSFERENCE NUMBERS AND CONDUCTIVITY

### 20.2.1 Experimental methods of determining transference number

The molar conductivity of an electrolyte is the more generally useful quantity since the Kohlrausch law allows its limiting value to be resolved into those of its constituent ions. Comparison between different electrolytes with a common ion therefore allows the determination of an unknown molar conductivity. However, the quantity typically measured is the overall electrolytic conductivity. A way to apportion the conductivity (and hence mobility) to the individual ions of the electrolyte is required. Equation (20.1.2-11) shows that resolution of the molar conductivity into the terms arising from its constituent ions is possible if the transference number of the ion is found. Although this property and the methods developed to measure it may seem rather arcane, it has been of fundamental importance in the understanding of the conductivity and diffusion potentials developed within electrolyte solutions. Experimentally, a number of ways of measuring transference numbers have been developed; these are summarised below.

One important point to make is that the quantity accessed experimentally, in general, is the net transference number for a given species regardless of its exact speciation (6). For complex ions, if the Hittorf method (see below) is used to measure the transport of chloropalladate ions for example, by analysis of the amount of Pd accumulated on an electrode surface, one has no way of distinguishing between the transfer of $[PdCl_4]^{2-}$ and $[PdCl_3]^-$, both of which occur in solution. The existence of rapidly occurring equilibria, which will typically interconvert on time-scales much shorter than the measurement time-scale, means that the net transference of anionic palladium species of whatever form is

measured rather than the transport of a particular species. This general point must be borne in mind for all measurements other than those in simple binary electrolytes (e.g. for aqueous sodium chloride solutions).

The classical methods of experimental transference number determination can be divided into three general groups. The first (the Hittorf method) is essentially an analytical approach, which relates changes in cell composition to the transference numbers of the electrolyte solution. The second group of methods relates the motion of the boundary separating zones of different composition to the transference numbers. The final approach relates the cell potential, which arises from the diffusion potential, to the transference number. Each of these methods is summarised, in turn, below.

#### *20.2.1.1 The Hittorf method*

This approach uses a three-compartment cell and relates the change in composition of the anodic and cathodic parts of the cell to the experimental transference number. The crucial assumption is that the composition within the central compartment is not affected by the electrolytically induced changes within the outer compartments. The cell can thus be represented as shown in Figure 20.2.

If, for example, two silver/silver chloride electrodes are bathed in a sodium chloride solution, reduction of an equivalent of silver chloride to silver will be compensated, as explained above, by the ingress of $t_+$ equivalents of sodium ions and the egress of $t_-$ equivalents of chloride ion. However, one equivalent of chloride has also been gained by electrolysis, so the net change in chloride composition is $(1 - t_-)$, which equals $t_+$ by equation (20.1.2-8). The reaction will be driven in reverse at the anode. Hence, there will be a net loss of $t_+$ equivalents of chloride, accompanied by an egress of $t_+$ ions of sodium. The situation can be extended to more complex electrolyte solutions but the principle remains the same. Key to the method is the analysis of the compositional changes within the outer (electrode) compartments of the cell. The method dates back to 1863; the classical approach to the analysis involved cell designs where outer compartments could be isolated from the inner part of the cell (via stopcocks; see Figure 20.3) and, originally, compositional changes

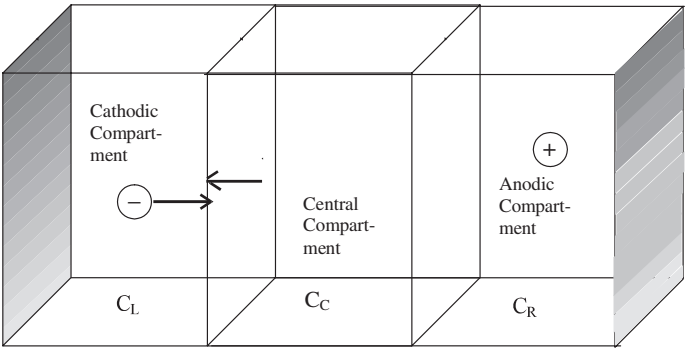


**Figure 20.2** Schematic representation of the Hittorf cell. The basis of the method is that the composition of the central compartment is uniform.

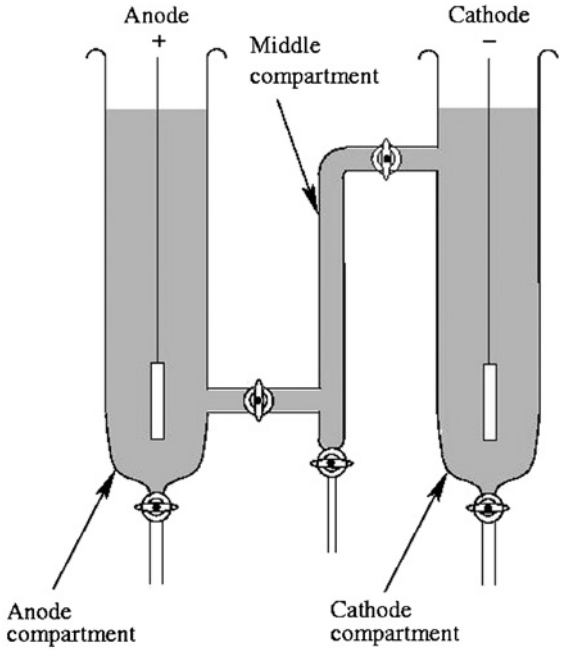


**Figure 20.3** Schematic diagram of the Hittorf apparatus for experimental determination of transference numbers. (for colour version: see colour section at the end of the book).

were determined from the net weight change within the outer solutions. *In situ* analytical methods of compositional change, including spectrophotometric and conductometric detection, were subsequently introduced (6), although questions then arise about the locus of the detection process and how representative it may be of the electrolyte concentration within the compartment as a whole.

Much of the early 20th century data on transference numbers, and hence on ionic mobilities, was obtained via this route. One general drawback of the Hittorf method is the requirement, for transference measurements, that all of the charge transfer reported be due to migration. This condition is difficult to satisfy for the Hittorf approach; it is extremely difficult to exclude diffusive (and convective) contributions from the cell. This need highlights a general feature of transference measurements: a compromise often has to be made to achieve maximum possible accuracy. On one hand, passage of a large current in a Hittorf cell maximises compositional changes and hence minimises the error in determining those changes. However, the perturbation imposed on the cell is likely to mean that the parameters extracted correspond in part to the movement of ions through a substantially electrolysed solution of electrolyte rather than through the pristine electrolyte solution.

#### *20.2.1.2 The moving boundary method*

This approach requires an observable boundary between the "front" of differing composition and the rest of the cell. The front is established by gravitational stratification between

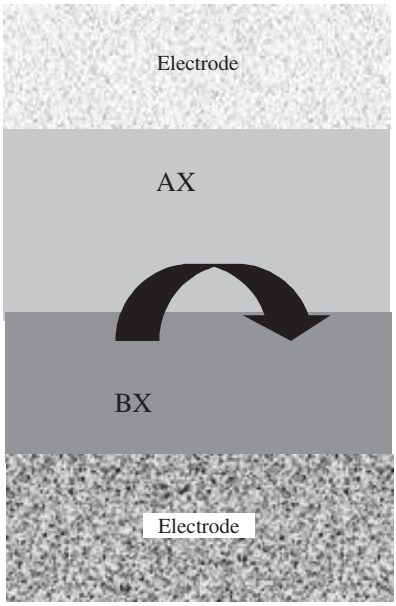


**Figure 20.4** Schematic of the moving boundary method. Two stratified solutions retain their compositional boundary because of the differences in mobility of ions A and B.

two compartments of electrolyte solutions, AX and BX. The front is maintained because of the differing mobilities of ions A and B under the applied electric field (see equation (20.1.2-3) and Figure 20.4).

If one equivalent of charge is passed, driving solution AX towards the upper electrode, the boundary will move forward through a volume $V_{A,0}$ and the number of moles of solution displaced is

$$C_A V_{A,0} = \frac{t_A}{z_A} \tag{20.2.1-1}$$

where $t_A$ is the transference number of ion A in electrolyte AX. The above equality holds because of the presence of the common ion, X, on either side of the boundary (i.e. the net movement of the boundary is due to A). The ratio of the volume advanced under passage of one equivalent of charge to the volume generally swept out ($V_A$) is

$$V_{A,0} = \frac{V_A F}{It} \tag{20.2.1-2}$$

where $t$ is the duration of the experiment. The transference number found from equations (20.2.1-1) and (20.2.1-2) is

$$t_A = \frac{z_A C_A V_A F}{It} \tag{20.2.1-3}$$

The key issue here is the extent to which a stable, moving boundary can be obtained and how accurately its progress can be monitored. Boundary observation methods have often employed optical methods. Either the change in absorbance (where an indicator solution may be added at low concentration to one of the solutions) or the change in refractive index can be used to monitor the front. Solution resistance can also be used to probe the moving boundary (by definition, the leading ion A has a mobility higher than that of B). Another analytical route is presented by the thermal gradient arising from the difference in conductivities, due to Joule heating, from the following solution (6).

The Joule heating effect is one of a number of instabilities, including other convective and diffusive interferences, which can disturb the boundary and interfere with measurements. The use of this method is, therefore, complicated in solutions of poor conductivity and requires measurement of transference numbers over a range of electrolysis conditions, with extrapolation to zero current. The general issue of the extent of the perturbation, discussed for the Hittorf technique, also arises here. Errors are minimised by prolonging the measurement time, but the perturbation to the cell (noted above, but also arising from differences in molar volume between the products of the electrolysis reaction) will be maximised therefore raising questions over the extent to which the parameter actually measured corresponds to the parameter sought. The general solution to this problem is the measurement of transference numbers at a variety of electrolysis currents (or electrolysis times) with extrapolation of the variation to zero charge.

Other methods related to the moving boundary method include the indirect moving boundary method (where the concentration in the "trailing edge" behind the boundary is monitored) and the analytical boundary method. The latter approach involves analysis of the compositional change within the moving boundary zone and is a hybrid of the Hittorf and standard moving boundary techniques.

#### *20.2.1.3 Measurements of cell potential*

This approach avoids some of the difficulties associated with methods (a) and (b). In contrast to the other methods, which utilise the effect of a charge passed on the composition of the electrode compartments, or on the bulk of the solution, this method relates the cell potential observed in concentration cells to the transference number of the constituent ions. Experimentally, a concentration cell is made by opening the inter-connecting valve between the two solution compartments. Each compartment must contain an electrode that is reversible to one of the ions in the solution. Diffusion will blur the distinction between the solutions once they come into contact and will ultimately homogenize them. However, as explained at the outset of this chapter, diffusion of the more concentrated electrolyte into the more dilute solution will set up a diffusion potential which will essentially act as a brake on the transport of the more mobile ion. If there were no difference in the magnitude of the cationic and anionic mobility, no diffusion potential would arise. Hence, the value of the cell potential reflects the transference numbers of the electrolytes in solution. A way to relate the observed cell potential to the transference number is necessary. A rigorous derivation of the inter-relationship between the two quantities requires recourse to Onsager's equation for the thermodynamics of irreversible systems, which is beyond the scope of this chapter (4). An approximate derivation, which gives the identical final result, can be

obtained by imposing a pseudo-steady-state condition on the electrolyte transport (7). This implies that the diffusive flux balances the migratory flux developed. Another form of the one-dimensional Nernst–Planck equation (20.1.2-2) can be written to describe the counteracting fluxes in the pseudo-steady-state:

$$\mathrm{d}\mu_i = RT \ln a_i \approx -F\mathrm{d}\phi \tag{20.2.1-4}$$

where the forces are assumed to apply in one dimension only. Each term can be written as the sum of its ionic components. For every mole passed, the diffusive flux must include the transference number of each ion (normalised for its charge since this is by definition the fraction of current carried by a given ion in response to the electric field see equation (20.1.2-7)). Hence,

$$RT \sum_i \frac{t_i}{z_i} \ln a_i \approx -F\,\mathrm{d}\phi \tag{20.2.1-5}$$

Therefore,

$$\mathrm{d}\phi = \frac{-RT}{F} \sum_i \frac{t_i}{z_i} \ln a_i \tag{20.2.1-6}$$

which is the equation resulting from the full Onsager analysis. Equation (20.2.1-6) relates to a differential potential within the solution and must be integrated with respect to the cell length ($l$) to equal the (measurable) potential difference between the electrodes resulting from the diffusion potentials within the cell. Consequently,

$$\Delta\phi = \frac{-RT}{F} \sum_i \int_0^l \frac{t_i}{z_i} \frac{\mathrm{d}(\ln a_i)}{\mathrm{d}x} \mathrm{d}x = \frac{-RT}{F} \sum_i \int_0^l \frac{t_i}{z_i a_i} \frac{\mathrm{d}a_i}{\mathrm{d}x} \mathrm{d}x \tag{20.2.1-7}$$

Deriving the exact solution of this integral requires that a number of assumptions be made. The most general assumption is that solution activities can be replaced by the ionic concentrations, that the transference number is concentration independent and that the concentration varies linearly across the cell. Thus

$$\Delta\phi = \frac{-RT}{F} \sum_i \frac{t_i}{z_i} \ln \frac{C_i(l)}{C_i(0)} \tag{20.2.1-8}$$

which, for a symmetrical ($z$:$z$) electrolyte, reduces to

$$\Delta\phi = \frac{-RT}{z_i F} (t_+ - t_-) \ln \frac{C_i(l)}{C_i(0)} = \frac{-RT}{z_i F} (2t_+ - 1) \ln \frac{C_i(l)}{C_i(0)} \tag{20.2.1-9}$$

by combination with equation (20.1.2-8). Equation (20.2.1-9) is known as the Planck–Henderson equation. It predicts that when the charge is transported equally by both ions, the cell potential from equation (20.2.1-9) reduces to zero. Likewise, if some part of the solution is only permeable to one ion, there is no net transference and the measured potential collapses to the membrane case discussed in Section 20.1.1.

The above analysis provides a simple route to the measurement of transference numbers from readily measurable quantities. The method may be applied to a wide range of electrolyte solutions (hence a large working range of electrolyte concentrations). The drawback is the rather severe set of approximations made in the derivation of equation (20.1.2-10) which limits the accuracy of the transference numbers derived. More accurate results can be obtained by considering the non-ideality of the electrolytes, to a first approximation by use of the Debye–Hückel limiting law. The fact that the potentials respond to the logarithm of the concentration ratio also reduces the accuracy of this method.

Distinct from the preceding methods is a crude approach to transference number determination. This method relies on the relationship between the mobilities and diffusion coefficients of ions, the Einstein law:

$$u_i = \frac{z_i F D_i}{RT} = \frac{\lambda_i}{z_i F} \qquad (20.2.1\text{-}10)$$

If the ions' diffusion coefficients are measured independently, the ratio of mobilities and transference numbers can be found (equation (20.1.2-9)). The problem is that the Einstein law is only valid at infinite dilution. This approach to transference number determination is substantially more limited than the schemes detailed above.

### 20.2.2 Sample calculations of ionic transference numbers

Some reported values of cationic transference numbers are listed in Table 20.3. Conductivity data from Table 20.1 can be used to calculate transference numbers for protons in aqueous nitric acid, for example, from equations (20.1.2-9) and (20.1.2-12):

$$t_{H^+} = \frac{3.62\times10^{-3}\times[1\times C_{H^+}]}{3.62\times10^{-3}\times[1\times C_{H^+}] - 7.40\times10^{-4}\times[(-1)\times C_{NO_3^-}]} = 0.83 \qquad (20.2.2\text{-}1)$$

since the concentrations of both ions must be equal. Likewise, the transference number for protons in dilute sulphuric acid can be found from

$$t_{H^+} = \frac{3.62\times10^{-3}\times[1\times C_{H^+}]}{3.62\times10^{-3}\times[1\times C_{H^+}] - 8.29\times10^{-4}\times[(-2)\times C_{SO_4^{2-}}]} = 0.81 \qquad (20.2.2\text{-}2)$$

since the concentration of protons is twice the sulphate concentration. Note that the anomalously high proportion of the current carried by the proton in aqueous solution is evidence of the veracity of the Grotthus mechanism of proton transport.

An illustration of the Hittorf method can be found in an early experimental report of the technique for barium chloride solutions, electrolysed using silver/silver chloride electrodes (8). The 18th run in this study reportedly passed 0.0194 F across the cell, which is schematically described in Figure 20.5.

The composition of the anode compartment following electrolysis was 1.366 wt% of barium chloride, where the compartment contained 120.37 g of solution. The product of

**Table 20.1**

Selected limiting ionic conductivities in aqueous solution at 298 K. The values are tabulated with cations (left-hand half of table) and anions (right-hand half of table) listed separately. Elemental ions are listed first, in order of increasing atomic mass, with molecular ions following, also in order of increasing mass

| Cation | $\lambda^0$ (S cm$^2$ mol$^{-1}$) | Reference | Anion | $\lambda^0$ (S cm$^2$ mol$^{-1}$) | Reference |
|---|---|---|---|---|---|
| $H^+$ | 349.8 | (11) | $F^-$ | 55.4 | (11) |
| $Li^+$ | 38.6 | (11) | $Cl^-$ | 76.4 | (11) |
| $Be^{2+}$ | 90.0 | (11) | $Br^-$ | 78.1 | (11) |
| $Na^+$ | 50.1 | (11) | $I^-$ | 76.8 | (11) |
| $Mg^{2+}$ | 106.0 | (11) | $OH^-$ | 198.3 | (11) |
| $K^+$ | 73.5 | (11) | $N_3^-$ | 69.0 | (11) |
| $Ca^{2+}$ | 119.0 | (11) | $CH_3CO_2^-$ | 40.9 | (11) |
| $Co^{2+}$ | 110.0 | (11) | $CO_3^{2-}$ | 138.6 | (11) |
| $Cu^{2+}$ | 107.2 | (11) | $NO_3^-$ | 71.5 | (11) |
| $Zn^{2+}$ | 105.6 | (11) | $C_2H_5CO_2^-$ | 35.8 | (11) |
| $Rb^+$ | 77.8 | (11) | $FCH_2CO_2^-$ | 44.3 | (11) |
| $Sr^{2+}$ | 118.8 | (11) | $ClO_3^-$ | 64.6 | (11) |
| $Ag^+$ | 61.9 | (11) | $CNCH_2CO_2^-$ | 43.4 | (11) |
| $Cs^+$ | 77.2 | (11) | $C_3H_7CO_2^-$ | 32.6 | (11) |
| $Ba^{2+}$ | 127.2 | (11) | $C_2O_4^{2-}$ | 148.2 | (11) |
| $La^{3+}$ | 209.1 | (11) | $ClCH_2CO_2^-$ | 42.2 | (11) |
| $Ce^{3+}$ | 209.4 | (11) | $SO_4^{2-}$ | 160.0 | (11) |
| $Pr^{3+}$ | 208.8 | (11) | $H_2PO_4^-$ | 32.3 | (21) |
| $Nd^{3+}$ | 208.2 | (11) | $ClO_4^-$ | 67.3 | (11) |
| $Sm^{3+}$ | 205.5 | (11) | $C_5H_{11}CO_2^-$ | 27.4 | (22) |
| $Eu^{3+}$ | 203.4 | (11) | $C_6H_5CO_2^-$ | 32.3 | (11) |
| $Gd^{3+}$ | 201.9 | (11) | $BrO_3^-$ | 55.7 | (11) |
| $Dy^{3+}$ | 196.8 | (11) | $BrCH_2CO_2^-$ | 39.2 | (11) |
| $Ho^{3+}$ | 198.9 | (11) | $C_7H_{15}CO_2^-$ | 23.1 | (23) |
| $Tl^+$ | 74.7 | (11) | $P_2O_7^{4-}$ | 380.0 | (11) |
| $Pb^{2+}$ | 139 | (11) | $IO_3^-$ | 40.5 | (11) |
| $Am^{3+}$ | 193.2 | (15) | $ICH_2CO_2^-$ | 40.6 | (11) |
| $Cf^{3+}$ | 191.1 | (15) | $IO_4^-$ | 54.5 | (11) |
| $NH_4^+$ | 73.5 | (11) | $Fe(CN)_6^{3-}$ | 302.7 | (11) |
| $NCH_3H_3^+$ | 58.7 | (11) | $Fe(CN)_6^{4-}$ | 440.0 | (11) |
| $N(C_2H_5)H_3^+$ | 46.6 | (16) | $C_6H_2(NO_2)_3O^-$ | 30.4 | (11) |
| $N(CH_3)_2H_2^+$ | 51.8 | (11) | $P_3O_9^{3-}$ | 250.8 | (11) |
| $N(CH_3)_3H^+$ | 47.2 | (11) | $P_3O_{10}^{5-}$ | 545.0 | (11) |
| $N(CH_3)_4^+$ | 44.9 | (11) | $P_4O_{12}^{3-}$ | 279 | (11) |
| $N(C_2H_5)_2H_2^+$ | 36.8 | (16) | $(C_6H_5)_4B^-$ | 19.7 | (19) |
| $N(C_2H_5OCH_3)H_3^+$ | 39.1 | (16) | | | |
| Piperidinium | 37.5 | (16) | | | |
| $N(C_3H_7OCH_3)H_3^+$ | 41.8 | (16) | | | |
| Cyclohexylammonium | 35.0 | (16) | | | |
| $N(C_2H_5)_3H^+$ | 31.3 | (16) | | | |
| $N(C_2H_5)_4^+$ | 32.6 | (11) | | | |
| $N(C_2H_5OCH_3)_2H_2^+$ | 29.3 | (16) | | | |
| $N(CH_3)_3C_6H_5^+$ | 34.6 | (11) | | | |

(*Continued*)

**Table 20.1 (Cont.)**

| Cation | $\lambda^0$ (S cm$^2$ mol$^{-1}$) | Reference | Anion | $\lambda^0$ (S cm$^2$ mol$^{-1}$) | Reference |
|---|---|---|---|---|---|
| $Co(NH_3)_6^{3+}$ | 305.7 | (11) | | | |
| $N(C_3H_7)_4^+$ | 23.4 | (11) | | | |
| $N(C_4H_9)_4^+$ | 19.4 | (11) | | | |
| $UO_2^{2+}$ | 114.0 | (17) | | | |
| $PuO_2^{2+}$ | 118.0 | (18) | | | |
| $N(C_5H_{11})_3C_4H_9^+$ | 20.7 | (19) | | | |
| $(C_6H_5)_4P^+$ | 19.9 | (20) | | | |
| $(C_6H_5)_4As^+$ | 19.4 | (20) | | | |
| $(C_6H_5)_4Sb^+$ | 19.1 | (20) | | | |

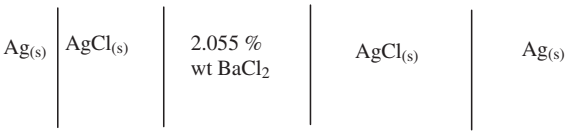


**Figure 20.5** Cell used by Jones and Dole (8) for calculation of transference numbers by the Hittorf method. The solution compartment is further sub-divided into sub-compartments (see Figure 20.3), although the composition of each sub-compartment is initially identical.

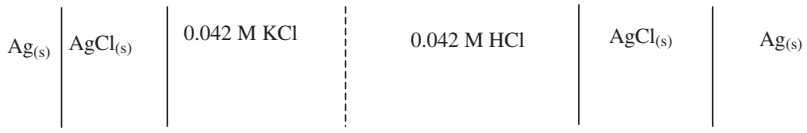


**Figure 20.6** Example cell for calculation of transference number by the moving boundary method.

this weight percentage and the weight of solution (g), divided by the molecular mass of the salt (208.27 g mol$^{-1}$), gives the number of moles of salt remaining in the anode compartment following electrolysis. Hence $7.89 \times 10^{-3}$ moles of $Ba^{2+}$ ions remained in the anode compartment of the cell after electrolysis. The original $Ba^{2+}$ content, calculated as the product of the weight of solution and its weight percentage pre-electrolysis (2.055 wt%), was 2.47 g. Since this initial $BaCl_2$ content corresponded to 0.0119 moles, the loss of $Ba^{2+}$ induced by electrolysis was, therefore: $0.0119 - 7.89 \times 10^{-3} = 4.06 \times 10^{-3}$ moles. As explained in the preceding section, the net loss from the anode compartment will be $t_+$ moles of univalent cation per unit charge passed. For a divalent cation, only half the number of moles need be lost to compensate the charge (compare equation (20.1.2-9)). Thus, the transference number is twice the ratio of moles lost per Faraday passed. In this case,

$$t_{Ba^{2+}} = \frac{2 \times 4.06 \times 10^{-3}\,\text{F}}{1.94 \times 10^{-2}\,\text{F}} = 0.419 \qquad (20.2.2\text{-}3)$$

Likewise, a simple illustration of the moving boundary method can be provided, for example, for the case of electrolysis of the cell denoted in Figure 20.6.

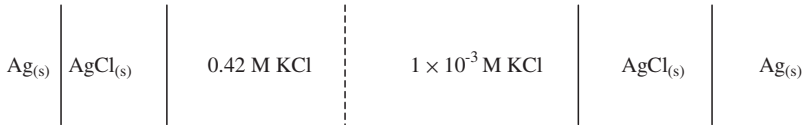


**Figure 20.7** Example cell for calculation of transference number by the measurement of cell potential.

The advance of the moving boundary marking the denser, less mobile KCl solution allows the transference number of the potassium ion to be found from equation (20.2.1-3). For a capillary of 0.209 cm inner radius, the displacement of the boundary after 200, 400 and 600 sec was found to be 6.4, 12.9 and 19.2 cm. A constant current of 36.4 mA was maintained. Using the first pair of data, the volume displaced (the cross-sectional area multiplied by the distance the boundary has moved through) is 0.88 $cm^3$:

$$t_{K^+} = \frac{1 \times 4.2 \times 10^{-5}\,\text{mol cm}^{-3} \times 0.88\ \text{cm}^3\ \times 9.648 \times 10^4\ \text{C mol}^{-1}}{(0.0364 \times 200)\,\text{C}} = 0.49 \qquad (20.2.2\text{-}4)$$

Finally, a simple measurement of a diffusion potential allows us to determine the potassium ion transference number as shown in the cell of Figure 20.7.

The measured cell potential was −3.0 mV. Re-arrangement of equation (20.2.1-9) gives

$$t_{K^+} = \frac{1}{2} - \frac{zF\Delta\phi}{2RT\ln\left(\dfrac{C_i(l)}{C_i(0)}\right)}$$

$$= 0.5 - \left(\frac{[1 \times 9.64 \times 10^4 \times (-3) \times 10^{-3}]\,\text{J mol}^{-1}}{2 \times (8.314 \times 298)\ \text{J mol}^{-1} \times (-6.04)}\right) = 0.49 \qquad (20.2.2\text{-}5)$$

where the cell potential is defined, following convention, as the potential difference between the right-hand electrode (located at *l*) and the left-hand electrode.

### 20.2.3 Experimental methods of determining electrolytic conductivity

The electrolyte conductivity can be measured using a conductivity cell which consists of a pair (or pairs) of electrode(s) of known area separated by a constant distance. A simple two-electrode cell can be used. For small excursions of potential, the current response of the cell is proportional to the electrolytic conductance, *L*. The conductivity, $\kappa$ (see equation (20.1.2-3)) is related to *L* via (4, 9)

$$\kappa = L\left(\frac{l}{A}\right) \qquad (20.2.3\text{-}1)$$

where the quantity in brackets is known as the cell constant and is the ratio of electrode separation, *l*, to the surface area, *A*. The cell constant is initially determined by measuring

the conductance of a solution of known conductivity (dilute aqueous solutions of potassium chloride, for example) before proceeding to measurements on solutions of unknown conductivity. The reciprocal quantities of $L$ and $\kappa$ are the electrolyte resistance ($R$) and resistivity, respectively. To minimise the effects of electrolysis, a sinusoidally alternating voltage is imposed upon the cell. An ac bridge arrangement can be employed to determine the resistance of the electrolyte. The resistance is the purely in-phase component of the frequency-dependent complex impedance of the cell, $Z(\omega)$, which is defined as

$$Z(\omega) = R_c - jX_c \tag{20.2.3-2}$$

where $R_c$ and $X_c$ are the resistance and capacitative reactance of the cell, respectively (10). Care must be taken to ensure that the out-of-phase capacitative response does not contribute to the measured signal. Also, the conductivity cell must be designed such that the dominating resistance is that of the electrolyte rather than any interfering resistances due to electrode processes or extraneous resistances from the external circuitry. Electrodes of platinum black electrodes are almost always used. Conductance should be determined at a range of frequencies to ensure that the value derived is constant and therefore free of any artefacts due to capacitative effects.

The essential point with regard to the interpretation of data is that the molar conductivity (see equation (20.1.2-10)) at infinite dilution can be broken down into terms due to the constituent ions. Some knowledge of the transference properties of the individual ions can be used to determine the fraction of electrolyte conductivity attributable to each ion.

### 20.2.4 Sample calculations relating to electrolytic conductivity

To illustrate the relation between transference numbers and conductivity, the transport number of potassium in dilute potassium chloride solution is used to find the limiting ionic conductivity. On extrapolation to infinite dilution, the molar conductivity of aqueous potassium chloride solution is found to be 149.85 S cm$^2$ mol$^{-1}$ (11). From equation (20.1.2-14) and the value for $t_{K^+}$ found in Section 20.2.3:

$$\begin{aligned}\lambda^0_{K^+} &= t_{K^+}\Lambda^0_{KCl} = t_{K^+}\left(\lambda^0_{K^+} + \lambda^0_{Cl^-}\right) \\ &= 0.49 \times 149.9 = 73.45 \text{ S cm}^2 \text{ mol}^{-1}\end{aligned} \tag{20.2.4-1}$$

The remaining molar conductivity of the potassium chloride solution can be attributed to the chloride anion if one neglects the contribution arising from the auto-ionisation of water. Hence, the limiting ionic conductivity of the chloride anion is 76.42 S cm$^2$ mol$^{-1}$.

The values of individual ionic conductivities can also be found by comparison between the extrapolated values. For example, the limiting molar conductivity of magnesium chloride is found to be 258.7 S cm$^2$ mol$^{-1}$. Comparison with the potassium chloride value yields the limiting ionic conductivity of magnesium:

$$\lambda^0_{Mg^{2+}} = \Lambda^0_{MgCl_2} - \Lambda^0_{KCl} + \lambda^0_{K^+} - \lambda^0_{Cl^-} = 105.9 \text{ S cm}^2 \text{ mol}^{-1} \tag{20.2.4-2}$$

A list of representative limiting ionic conductivity values and related parameters is given in the next section.

The concentration dependence of ionic conductivity has been discussed briefly above. Due to ion–ion interactions, the conductivity per ion falls as the ion concentration is increased. Two specific interactions have been identified: the electrophoretic effect due to the tendency of the ion atmosphere to move in the opposite direction of the ion; and the relaxation effect due to the finite time required for the ion atmosphere to re-arrange itself due to the asymmetry imposed by the electric field. Onsager produced a limiting law that showed that the molar electrolytic conductivity fell with the square root of the ion concentration:

$$\Lambda = \Lambda^0 - (A + B\Lambda^0)C_i^{1/2} \tag{20.2.4-3}$$

The constants $A$ and $B$ are related to the above retarding effects. Exact expressions have been presented for these terms (12, 13). In aqueous solutions at room temperature, the values of $A$ and $B$ are 59.86 S cm$^2$ mol$^{-1}$ M$^{-1/2}$ and 0.2296 M$^{-1/2}$, respectively. Values for these parameters have also been presented for non-aqueous solutions (7).

With regard to calculation in aqueous solution (for example, using a $1 \times 10^{-3}$ M aqueous solution of potassium chloride), equation (20.2.4-3) predicts a molar conductivity of 148.87 S cm$^2$ mol$^{-1}$. This compares with the experimentally observed value of 146.95 S cm$^2$ mol$^{-1}$. The agreement diverges increasingly as the ionic concentration is increased. The Onsager equation predicts KCl molar conductivity values of 140.42 and 120.04 S cm$^2$ mol$^{-1}$ for 0.01 and 0.1 M concentrations, respectively. The experimentally observed values are higher than these values.

Determination of the degree of dissociation of weak electrolytes is a common application of conductivity measurements. This approach will be briefly outlined here with a sample calculation illustrating the utility of the method. From the data presented in the next section, the limiting molar conductivity of acetic acid can be seen to be 389.9 S cm$^2$ mol$^{-1}$ (from addition of the limiting values for the proton and the acetate ion). At finite concentrations, this weak acid will only be partially deprotonated. The ratio of observed to predicted electrolytic conductivity can be used to determine the degree of dissociation, $\alpha$. At 0.01 M, the observed molar conductivity of acetic acid was found to be 14.30 S cm$^2$ mol$^{-1}$. Thus

$$\alpha = \frac{\Lambda_{\text{expt}}}{\Lambda} \approx \frac{\Lambda_{\text{expt}}}{\Lambda^0} = \frac{14.30\,\text{S cm}^2\text{mol}^{-1}}{389.9\,\text{S cm}^2\text{mol}^{-1}} = 0.0367 \tag{20.2.4-4}$$

The assumption made here is that the solution is sufficiently dilute for the molar conductivity, on complete dissociation at this concentration, to approximate the limiting molar conductivity. Equation (20.2.4-1) can be used to adjust the molar conductivity for ion–ion interactions but this requires knowledge of the ionic concentration, $C_i$. One approach is to use the initial approximation to $\alpha$ to give an initial $C_i$ value; substitution of the aqueous phase constants into equation (20.2.4-3) gives

$$\Lambda = \{389.9 - [59.8 + (0.2296 \times 389.9)](\alpha C)^{1/2}\}\,\text{S cm}^2\ \text{mol}^{-1} \tag{20.2.4-5}$$

The $\alpha C$ term is initially approximated to $0.0367 \times 0.01$ M, thus

$$\Lambda = 389.9 - [149.32 \times (3.67 \times 10^{-4})^{1/2}] = 387.0 \text{ S cm}^2 \text{ mol}^{-1} \qquad (20.2.4\text{-}6)$$

Hence, $\alpha$ can be re-computed and is found to be 0.0369. Repetition of the iteration procedure does not significantly change the value of $\alpha$ indicating that convergence has occurred. More accurate functional forms of the factor relating $\Lambda^0$ to $\Lambda$ have been given (12). The ease with which conductometric titrations can be applied to follow acid–base neutralisation reactions is notable.

The models discussed above hold for aqueous solutions. More complex behaviour is observed in non-aqueous solutions, particularly in media of low polarity. In such cases, extensive ion-pairing is observed. That is, electrically neutral ion-pairs will not contribute to solution conductivity. Conversely, under some conditions charged "triple ions" can form. The formation of such species is clearly favoured by higher concentrations. Thus, in some cases, molar conductivity can increase with ionic activity due to triple ion formation. Theories have been developed to predict the formation constants of such species (14).

### 20.2.5 Tabulation of parameters related to electrolyte conductance

The limiting values of various ionic conductivities, $\lambda^0$, are given in Table 20.1 for aqueous solutions. Transference numbers for any given electrolyte, for solutions of infinite dilution, can be determined from the data in this table, using equation (20.1.2-13). Similarly, the mobility of an ion can be found by combining data from this table with equation (20.1.2-12).

The temperature and concentration dependence of the transport properties of a number of aqueous electrolytes can be assessed via Tables 20.2 and 20.3. Table 20.2 reports the temperature dependence of limiting ionic conductivities of a number of ions in aqueous solution whereas Table 20.3 gives the concentration dependence of a number of aqueous phase transference numbers.

Parameters for ionic transport in non-aqueous solutions (including pure sulphuric acid) and solvent mixtures are provided below (Tables 20.4–20.9).

**Table 20.2**

Temperature variation of the limiting ionic conductivities for selected ions in aqueous solution (24)

| Cation | $\lambda^0$(S cm$^2$ mol$^{-1}$) | | | |
|---|---|---|---|---|
| | 288 K | 298 K | 308 K | 313 K |
| $H^+$ | 300.6 | 349.8 | 397 | 441.4 |
| $Na^+$ | 39.8 | 50.1 | 61.5 | 73.8 |
| $K^+$ | 59.7 | 73.5 | 88.2 | 103.5 |
| $Cl^-$ | 61.4 | 76.4 | 92.2 | 108.9 |
| $Br^-$ | 63.1 | 78.1 | 94 | 110.7 |

**Table 20.3**

Cationic transference numbers of selected electrolytes in aqueous solution at 298 K (9, 24)

| Cation | $t_+$ | | | | | | |
|---|---|---|---|---|---|---|---|
| | 0.01 M | 0.02 M | 0.05 M | 0.1 M | 0.2 M | 0.5 M | 1.0 M |
| $H^+$ (in HCl) | 0.825 | 0.827 | 0.829 | 0.831 | 0.834 | – | – |
| $Li^+$(in LiCl) | 0.329 | 0.326 | 0.321 | 0.317 | 0.311 | 0.300 | 0.287 |
| $Na^+$ (in NaCl) | 0.392 | 0.390 | 0.388 | 0.385 | 0.382 | – | – |
| $K^+$(in KCl) | 0.490 | 0.490 | 0.490 | 0.490 | 0.489 | 0.489 | 0.488 |

**Table 20.4**

Limiting ionic conductivities of selected ions in methanol at 298 K

| Cation | $\lambda^0$ (S cm$^2$ mol$^{-1}$) | Reference | Anion | $\lambda^0$ (S cm$^2$ mol$^{-1}$) | Reference |
|---|---|---|---|---|---|
| $Li^+$ | 39.1 | (25) | $Cl^-$ | 52.1 | (25) |
| $Na^+$ | 45.1 | (25) | $Br^-$ | 56.4 | (25) |
| $Mg^{2+}$ | 115.2 | (26) | $I^-$ | 62.6 | (25) |
| $K^+$ | 47.8 | (25) | $CH_3O^-$ | 53.0 | (24) |
| $Ca^{2+}$ | 120.0 | (26) | $NO_3^-$ | 61.1 | (25) |
| $Zn^{2+}$ | 96.0 | (25) | $ClO_4^-$ | 71.0 | (25) |
| $Rb^+$ | 56.1 | (25) | $C_6H_2(NO_2)_3O^-$ | 47.1 | (25) |
| $Sr^{2+}$ | 118 | (26) | $(C_6H_5)_4B^-$ | 37.1 | (25) |
| $Ag^+$ | 50.1 | (25) | | | |
| $Cs^+$ | 61.3 | (25) | | | |
| $N(CH_3)_4^+$ | 68.7 | (25) | | | |
| $N(C_2H_5)_4^+$ | 59.6 | (27) | | | |
| $N(C_3H_7)_4^+$ | 45.3 | (27) | | | |
| $N(C_4H_9)_4^+$ | 38.9 | (27) | | | |
| $N(C_5H_{11})_4^+$ | 34.8 | (27) | | | |
| $N(C_6H_{13})_4^+$ | 30.8 | (27) | | | |
| $N(C_7H_{15})_4^+$ | 28.8 | (27) | | | |

## 20.3 MINIMIZATION OF LIQUID JUNCTION POTENTIAL

### 20.3.1 Balancing ionic mobilities

Equations (20.1.2-2) and (20.2.1-7) relate the diffusion potential to mass-transport within the electrolyte and to transference numbers, respectively. If both the transference numbers are equal to one-half in the latter equation, then the diffusion potentials in solution arising from contact of solutions with differing concentrations will be eliminated. The limiting values of the ionic diffusion coefficient are related to their mobility by the Einstein law, equation (20.2.1-10), which provides justification for the argument that balancing the mobilities of the electrolyte's constituent ions will nullify any diffusion potential. This approach to eliminating diffusion potentials clearly suffers from the severe restriction that

**Table 20.5**

Limiting ionic conductivities of selected ions in ethanol at 298 K

| Cation | $\lambda^0$ (S cm$^2$ mol$^{-1}$) | Reference | Anion | $\lambda^0$ (S cm$^2$ mol$^{-1}$) | Reference |
|---|---|---|---|---|---|
| $Li^+$ | 17.1 | (25) | $Cl^-$ | 21.9 | (25) |
| $Na^+$ | 20.4 | (25) | $Br^-$ | 23.9 | (25) |
| $Mg^{2+}$ | 101.8 | (25) | $I^-$ | 27.0 | (25) |
| $K^+$ | 22.2 | (25) | $C_2H_5O^-$ | 25.4 | (24) |
| $Rb^+$ | 25.0 | (26) | $ClO_4^-$ | 33.6 | (24) |
| $Cs^+$ | 26.5 | (25) | $C_6H_2(NO_2)_3O^-$ | 26.3 | (24) |
| $N(CH_3)_4^+$ | 29.7 | (25) | | | |
| $N(C_2H_5)_4^+$ | 29.3 | (25) | | | |
| $N(C_3H_7)_4^+$ | 23.0 | (25) | | | |
| $N(C_4H_9)_4^+$ | 19.7 | (25) | | | |
| $N(C_7H_{15})_4^+$ | 14.0 | (25) | | | |

**Table 20.6**

Limiting ionic conductivities of selected ions in acetonitrile at 298 K

| Cation | $\lambda^0$ (S cm$^2$ mol$^{-1}$) | Reference | Anion | $\lambda^0$ (S cm$^2$ mol$^{-1}$) | Reference |
|---|---|---|---|---|---|
| $Li^+$ | 79.9 | (26) | $Cl^-$ | 91.6 | (28) |
| $Na^+$ | 76.9 | (25) | $Br^-$ | 100.7 | (25) |
| $Mg^{2+}$ | 189.6 | (26) | $I^-$ | 102.1 | (25) |
| $K^+$ | 83.6 | (25) | $NO_3^-$ | 106.4 | (25) |
| $Zn^{2+}$ | 189.6 | (26) | $BF_4^-$ | 108.5 | (25) |
| $Ag^+$ | 86.0 | (25) | $ClO_4^-$ | 103.7 | (25) |
| $Cs^+$ | 87.3 | (25) | $PF_6^-$ | 104.0 | (25) |
| $N(CH_3)_4^+$ | 94.5 | (25) | $BCl_4^-$ | 95.2 | (28) |
| $N(C_2H_5)_4^+$ | 85.5 | (27) | $C_6H_2(NO_2)_3O^-$ | 77.0 | (25) |
| $N(C_3H_7)_4^+$ | 71.1 | (27) | $BPh_4^-$ | 58.1 | (25) |
| $N(C_4H_9)_4^+$ | 62.1 | (27) | | | |
| $N(C_5H_{11})_4^+$ | 56.5 | (27) | | | |
| $N(C_6H_{12})_4^+$ | 51.4 | (27) | | | |
| $N(C_7H_{15})_4^+$ | 47.9 | (27) | | | |
| $(C_6H_5)_4As^+$ | 55.8 | (25) | | | |

the experimentalist be limited to combinations of ions with equal and opposite mobility values (or, equivalently, identical ionic conductivities). The data in the preceding section can be used to identify appropriate pairs of ions. The similar limiting ionic conductivities of potassium and chloride explain why this pair of ions is often used to eliminate diffusion potentials (see Section 20.3.2). Likewise, aqueous solutions of potassium nitrate and lithium acetate ought to exhibit minimal diffusion potentials. For non-aqueous media, Table 20.6 shows that diffusion potentials should be negligible in acetonitrile solutions of tetramethylammonium tetrachloroborate or solutions of tetraphenylarsonium tetraphenylborate in the same solvent. The latter observation implies that the effective diameter of the

**Table 20.7**

Limiting ionic conductivities of selected ions in sulphuric acid at 298 K

| Cation | $\lambda^0$ (S cm$^2$ mol$^{-1}$) | Reference | Anion | $\lambda^0$ (S cm$^2$ mol$^{-1}$) | Reference |
|---|---|---|---|---|---|
| $H^+$ | 1.08 | (29) | $HSO_4^-$ | 170 | (29) |
| $Li^+$ | 0.64 | (29) | | | |
| $Na^+$ | 0.80 | (29) | | | |
| $K^+$ | 1.20 | (29) | | | |
| $Ag^+$ | 1.59 | (29) | | | |
| $NH_4^+$ | 1.06 | (29) | | | |
| $H_3SO_4^+$ | 245 | (29) | | | |

**Table 20.8**

Limiting ionic conductivities of cations in nitrobenzene at 298 K

| Cation | $\lambda^0$ (S cm$^2$ mol$^{-1}$) | Reference |
|---|---|---|
| $Li^+$ | 16.3 | (26) |
| $Na^+$ | 17.8 | (26) |
| $N(CH_3)_4^+$ | 17.1 | (30) |
| $N(C_2H_5)_4^+$ | 16.2 | (30) |
| $N(C_3H_7)_4^+$ | 13.3 | (30) |
| $N(C_4H_9)_4^+$ | 11.7 | (30) |

**Table 20.9**

Cationic transference numbers for sodium chloride and potassium chloride in equimolar mixtures 50:50 of methanol and water (24)

| Cation | $T_+$ | | | | | | |
|---|---|---|---|---|---|---|---|
| | Limiting value | 0.001 M | 0.002 M | 0.005 M | 0.01 M | 0.02 M | 0.05 M |
| $Na^+$ (in NaCl) | 0.4437 | 0.4425 | 0.4421 | 0.4415 | 0.4412 | 0.4412 | 0.4398 |
| $K^+$(in KCl) | 0.5068 | 0.5070 | 0.5071 | 0.5074 | 0.5077 | 0.5085 | 0.5105 |

latter pair of ions in non-aqueous solutions is similar and is the basis of the Grunwald assumption used as a reference scale for ion transfer energies (see Section 20.4.1). This approach, while feasible if the experimentalist can tolerate the restriction on electrolytes, is also weakened since it implicitly assumes that the concentration (and temperature) dependencies of the transference numbers are identical. While this may be true for a first approximation, the data of Table 20.9 show that the cationic transference numbers of sodium chloride and potassium chloride display opposite dependencies on concentration in water/methanol mixtures, for example.

### 20.3.2 The salt bridge

A more general approach to minimising liquid junction potentials is to connect two electrolyte solutions via a salt bridge. The salt bridge is a solution of ions of balanced mobility, such as aqueous phase potassium chloride (see Section 20.3.1). The two solutions are either separated by some kind of "frit" or the salt bridge can consist of a gel of the ions of balanced mobility which should ideally minimise mutual solution contamination. If potassium chloride is used, an excess of this salt over the electrolyte(s) in the other compartments of the cell means the (limited) ion transport at each end of the salt bridge will be dominated by the potassium and chloride ions. This situation is analogous to the use of a supporting electrolyte in voltammetric measurements to ensure that migratory transport in bulk solution has a negligible contribution from the species of interest (see Chapter 3 of this handbook). In the conventional voltammetric case, a concentration ratio of supporting electrolyte to analyte in excess of 100 is normally maintained. The definition of the transference number, equation (20.1.2-9), means that under such conditions at least 99% of the migratory flux will be due to the supporting electrolyte. The establishment of such experimental conditions is important for the analysis of voltammetric data since it is generally assumed that the analyte is transported solely by diffusion. Since the transference number of each end of the salt bridge will be dominated by the potassium and chloride ions and since their mobilities almost cancel, a very low liquid junction potential should be established between the two solutions. Given that the limiting ionic mobilities of potassium and chloride do not sum to zero in aqueous solution, a finite liquid junction potential will be established. Equation (20.2.1-9) can be used to determine the magnitude of this potential, but it is typically of the order of 1–2 mV for most practical KCl salt bridges.

## 20.4 JUNCTIONS OF IMMISCIBLE LIQUIDS

### 20.4.1 The non-polarisable liquid/liquid interface

We now return to the example introduced in Section 20.1.1, where two electrolyte solutions $\alpha$ and $\beta$ were placed in contact and a hypothetical barrier was invoked that prevented the transfer of one of the ions between the phases. Although this example may have seemed obscure, such a system may readily be constructed for the interface between two immiscible electrolyte solutions (ITIES). Such a system can be formed by contacting water with an immiscible organic solvent such as nitrobenzene or 1,2-dichloroethane, as discussed in Section 17.3 in Chapter 17 of this handbook. The two solvents possess a slight mutual solubility. Once the two phases are equilibrated, the system is composed of an organic saturated aqueous phase in contact with a water saturated organic phase. For this reason, measurement of any transport property should always be performed on mutually pre-saturated solutions.

The choice of the organic phase also requires some care. The solubility characteristics with water must be such that two distinct phases form; typically this means that non-polar organic solvents must be employed. However, if the polarity of the organic solvent is too low (such as long-chain alkanes or alcohols), it becomes impossible to dissolve appreciable

amounts of any electrolyte in the organic phase, thus precluding use of these solvents to form electrolyte phases. The choice of organic solvents for liquid/liquid studies is therefore dictated by the need to compromise between the above two opposing factors. A further requirement is that the interface is gravitationally stable. Thus, there must be an appreciable difference in density to form a single stable interface, particularly for measurements at the polarised interface (see next section). A final requirement is that the interface should be chemically stable. This often restricts the usable pH range of the aqueous phase because many of the organic electrolytes are unstable.

To return to the case where one ion is readily solvated by both phases, the equality of the electrochemical potential leads to equation (20.1.1-2). However, equation (20.1.1-3) does not follow from this equation because phases $\alpha$ and $\beta$ are not composed of the same solvent. Hence, the standard chemical potentials of the partitioning ion in the two phases differ. Thus, equation (20.1.1-3) is replaced by

$$\Delta\phi \equiv \phi_\beta - \phi_\alpha = \frac{\mu^0_{i,\alpha} - \mu^0_{i,\beta}}{zF} + \frac{RT}{zF}\ln\left(\frac{a_{\alpha,i}}{a_{\beta,i}}\right) \tag{20.3.1-1}$$

By analogy with the Nernst equation, one can define the first term on the right-hand side of equation (20.3.1-1) as the standard potential of transfer of the ion, $i$, between phases $\alpha$ and $\beta$:

$$\Delta\phi^0_i = \frac{\Delta G^0_i}{zF} = \frac{\mu^0_{i,\alpha} - \mu^0_{i,\beta}}{zF} \tag{20.3.1-2}$$

The above equations state that when an ion readily partitions, the interfacial potential established is determined, in the first instance, by the standard Gibbs energy of transfer for the ion between the two phases. The second term in equation (20.3.1-1) makes it clear that this potential can be modified by "perturbing" the distribution potential established by the ion from its standard value. This can be achieved by establishing significantly different activities of ion $i$ in the aqueous and organic phases by using differing concentrations of extremely hydrophilic and extremely hydrophobic counter-ions, respectively. An example of such an approach is the use of the tetraphenylarsonium cation as the common-ion in a water/1,2-dichloroethane electrolyte system, with chloride and tetraphenylborate as the respective counter-ions in the aqueous and organic phases (31). In all such cases, the interface is non-polarisable since any attempt to impose an external potential difference (see next section), which is not equal to the distribution potential of the common ion, will be opposed by the common-ion readjusting its relative activities to return the system to equilibrium.

Where both ions of a given univalent electrolyte, AB, have appreciable solubility in phases $\alpha$ and $\beta$, an equilibrium salt distribution coefficient, $K_{AB}$, can be defined as

$$K_{AB} = \frac{a_{\alpha,AB}}{a_{\beta,AB}} = \sqrt{\frac{a_{\alpha,A^+}a_{\alpha,B^-}}{a_{\beta,A^+}a_{\beta,B^-}}} = \sqrt{K_{A^+}K_{B^-}} \tag{20.3.1-3}$$

where the $K_i$ terms on the right-hand side refer to the distribution of the ions. Relating the equilibria for the salt and ions to the free energy changes for transfer of these species:

$$\begin{aligned} -RT\ln K_{AB} &= \frac{-RT}{2}\ln K_{A^+} - \frac{RT}{2}\ln K_{B^+} \\ \Rightarrow \Delta G^0_{AB} &= \tfrac{1}{2}(\Delta G^0_{A^+} + \Delta G^0_{B^-}) \end{aligned} \qquad (20.3.1\text{-}4)$$

The definition of the standard Gibbs energy of transfer (equation (20.3.1-2)):

$$\Delta\phi = \tfrac{1}{2}(\Delta\phi^0_{A^+} + \Delta\phi^0_{B^-}) \qquad (20.3.1\text{-}5)$$

(i.e., the distribution potential) established by the salt is the mean of the potentials of the individual ions (32).

It is also important to note that the distribution of the common ion(s) accounts for the potential difference established at the liquid/liquid interface. Diffusion potentials can also play a part, but the potential differences derived in the above expressions are equilibrium values arising because of the differences in solvation of the participating ions. As a historical note, some of the earliest experiments on immiscible electrolyte phases were performed with the aim of establishing transport numbers of ions, using a variant of the concentration cell, with an immiscible liquid separating the two aqueous phases (33).

Expressions (20.3.1-4) and (20.3.1-5) show that measurement of the interfacial potential, or alternatively, determination of the distribution coefficient of a salt, can be used to find the standard potential of transfer of a given ion between the immiscible phases in question. As with the determination of the standard potential for redox processes, the issue of the reference scale arises. The potentiometric approach (equation (20.3.1-1)) is straightforward, but requires a way of relating the potential of an appropriate reference electrode in phase $\alpha$ to the potential of the second reference electrode immersed in phase $\beta$. The distribution approach (equation (20.3.1-4)) relies on an extra-thermodynamic assumption to resolve the measured salt distribution potential to that of the constituent ions. One of the most commonly used assumptions is that due to Grunwald (34) which states that the standard Gibbs energy of transfer of the tetraphenylarsonium cation is equal to the value for the tetraphenylborate anion (see Section 17.3 in Chapter 17 of this handbook for further details). Given that the transfer potentials are additive (equation (20.3.1-5)), this assumption permits the transfer potentials of other ions to be determined. Although arbitrary, such assumptions are analogous to the assignment of 0.0 V for the standard reduction potential of the proton. Assumptions with a better physical grounding have been presented more recently on the basis of experiments performed using polarised liquid/liquid interfaces (see next section).

Standard Gibbs energies of ion transfer are reported for various ions in Tables 20.10 and 20.11. Values are given for the two most common solvents used with water to form immiscible electrolyte boundaries, namely nitrobenzene and 1,2-dichloroethane.

### 20.4.2 The polarisable liquid/liquid interface

In contrast to the cells discussed in the previous section, addition of electrolytes CD and EF to phases $\alpha$ and $\beta$, respectively, leads to the formation of a polarised liquid/liquid interface

**Table 20.10**

Standard Gibbs energies of transfer for ions from water to nitrobenzene

| Cation | $\Delta G^0$ (kJ mol$^{-1}$) | Reference | Anion | $\Delta G^0$ (kJ mol$^{-1}$) | Reference |
|---|---|---|---|---|---|
| $H^+$ | +32.5 | (35) | $Cl^-$ | +37.0 | (36) |
| $Li^+$ | +38.4 | (35) | $Br^-$ | +28.5 | (35) |
| $Na^+$ | +34.5 | (35) | $I^-$ | +18.8 | (35) |
| $Mg^{2+}$ | +71.4 | (35) | $NO_3^-$ | +24.4 | (35) |
| $K^+$ | +24.3 | (35) | $ClO_4^-$ | +8.7 | (35) |
| $Ca^{2+}$ | +68.3 | (35) | $B(C_6H_5)_4^-$ | −35.9 | (35) |
| $Rb^+$ | +19.9 | (35) | | | |
| $Sr^{2+}$ | +67.2 | (35) | | | |
| $Cs^+$ | +15.5 | (35) | | | |
| $Ba^{2+}$ | +63.3 | (35) | | | |
| $NH_4^+$ | +27.4 | (35) | | | |
| $N(CH_3)_4^+$ | +3.4 | (35) | | | |
| $N(C_2H_5)_4^+$ | −5.8 | (35) | | | |
| $N(C_3H_7)_4^+$ | −15.5 | (35) | | | |
| $N(C_4H_9)_4^+$ | −24.2 | (35) | | | |
| $As(C_6H_5)_4^+$ | −35.9 | (35) | | | |

**Table 20.11**

Standard Gibbs energies of transfer for ions from water to 1,2-dichloroethane

| Cation | $\Delta G^0$ (kJ mol$^{-1}$) | Reference | Anion | $\Delta G^0$ (kJ mol$^{-1}$) | Reference |
|---|---|---|---|---|---|
| $H^+$ | +53 | (37) | $Cl^-$ | +45.4 | (36) |
| $Li^+$ | +55.6 | (38) | $Br^-$ | +38.3 | (35) |
| $Na^+$ | +55.9 | (38) | $I^-$ | +26.4 | (35) |
| $K^+$ | +51.9 | (38) | $ClO_4^-$ | +17.2 | (35) |
| $Rb^+$ | +45.8 | (38) | $B(C_6H_5)_4^-$ | −33.0 | (38) |
| $Cs^+$ | +37.3 | (38) | | | |
| $N(CH_3)_4^+$ | +17.6 | (35) | | | |
| $N(C_2H_5)_4^+$ | +4.2 | (35) | | | |
| $N(C_3H_7)_4^+$ | −8.8 | (35) | | | |
| $N(C_4H_9)_4^+$ | −21.8 | (35) | | | |
| $As(C_6H_5)_4^+$ | −32.5 | (38) | | | |

if none of the constituent ions transfer readily to the other phase. In terms of equation (20.3.1-2), the standard Gibbs energy of transfer for each ion from its initial phase to the other phase must be considerable (at least 10 kJ mol$^{-1}$ in practice). The four ions thus function as supporting electrolytes defining a "potential window" with a size determined at the positive end by the lower of the transfer energies of $C^+$ or $B^-$ and at the negative end by the lower of the transfer energies of $D^-$ or $A^+$. Suitable candidates for aqueous and organic phase supporting electrolytes may be identified from Table 20.10. For example, a large potential window can be obtained using lithium sulfate as the aqueous phase salt and tetrapentylammonium tetrakis(4-chlorophenyl)borate as the organic phase salt.

The defined potential window can be used to investigate ion and electron transfer processes as discussed in Section 17.3 in Chapter 17 of this handbook where the potential of the ion/electron transfer process must fall within the available window. Experiments can be performed with a two-electrode configuration where currents are sufficiently small, but more generally a four-electrode potentiostat (two reference and two counter electrodes) is required. The experimental procedures required for this type of experiment are discussed in more detail in Section 17.3 in Chapter 17 of this handbook.

## 20.5 NON-CLASSICAL ELECTROLYTES: POLYMER-BASED ELECTROLYTES AND IONIC LIQUIDS

The preceding sections give an overview of the theoretical framework and experimental techniques required to determine transference numbers and associated properties in electrolyte solutions. The bulk of theoretical developments belong to the early twentieth and even late nineteenth centuries with much of the accurate experimentation being performed during the early/mid twentieth century (aqueous solutions) and mid/late twentieth century (non-aqueous solutions). Although experimental data for what might be termed "classical electrolyte" solutions is still being collected and refined, much of the thrust of current research in this area is in the understanding of ion transport in less conventional electrolyte media. Much of the impetus for this work has stemmed from recent successes in the processing of ionomeric materials for power applications, specifically fuel cells. Polymeric electrolytes, in general, present challenges for the accurate determination of conductivity parameters. Another stimulus for research in non-classical electrolytes has come from successes in the synthesis of air- and water-stable room-temperature ionic liquids. Since these areas are still developing rapidly, it is impossible to present an authoritative statement of the relevant transport parameters. However, a flavour of the recent work in these areas and an indication of likely future developments will be presented.

Polymer electrolytes can be formed by the dissolution of salts within high molecular weight polymers such as polyethylene oxide and its derivatives. This area has been studied widely since their initial discovery in the 1970s because of practical applications deriving from all solid-state electrochemical devices. The low intrinsic conductivity of many polymer electrolytes (ca. $10^{-4}$ S cm$^{-1}$ is common, two orders of magnitude lower than moderately concentrated aqueous electrolyte solutions) has hampered their development and considerable effort has been expended towards understanding and ultimately improving on these values. There are various differences that should be considered when comparing ion transport in polymer systems with that in liquid phase electrolytes. One important distinction is the structural heterogeneity intrinsic to many polymers. A thorough knowledge of the phase diagram of the polymer is required to offer a meaningful interpretation of conductivity data. Ionic conductivity has been attributed to the amorphous regions of the polymer. Likewise, the sample history may affect its ion transport properties (39). Two important contrasts with liquid state migratory fluxes have been identified. First, the ion cannot move with a solvation sheath since the (largely translationally immobile) polymer is the solvent. Second, enhanced ion–ion and ion–polymer interactions mean the sensitivity of molar conductivity to concentration changes is enhanced in polymer

electrolytes. Despite the structural complexity of polymer electrolytes compared to liquid electrolyte solutions, one advantage with regard to the experimental determination of transference numbers is that the Hittorf method (Section 20.2.1) can be applied to polymeric species without some of the objections that compromise this method in liquids. Specifically, the low rates of diffusion and absence of convective fluxes in the polymer mean that these factors will exert minimal interferences on the transference numbers determined. Experimental determinations of transference numbers within polymer electrolytes have shown that the bulk of the charge is carried by the anionic species. This is expected from the stronger interactions anticipated between cations and the polymer chain although there are some discrepancies between numbers determined by different techniques. Electrochemical methods can also be employed to deposit conducting polymers, such as polypyrrole and polyaniline, whose charge transfer behaviour is often dictated by the uptake of ions into the polymer framework to re-establish electroneutrality (40, 41).

A related "non-classical" electrolyte system where ion transport properties have received much recent attention are ionomeric materials. The best-known example of this class of materials are the perfluorinated sulphonates which have an anionic backbone and possess a high exchange capacity for protons and alkali metal cations. Recent interest in these particular ionomers stems from potential applications in fuel cells and battery devices. For the anionic polymers, the transference number of the cation tends towards one since anions ought to be charge-excluded (42). The conductivity of these materials towards various ions, notably the proton and alkali metals, has been extensively studied in various solvents (43). Proton-conducting membranes displaying proton conductivities approaching values of $10^{-2}$ S cm$^{-1}$ have been reported (44). Correlations have been made of conductivity with various parameters spanning both the structure of the polymer, polymer–solvent interactions and the resultant solvation of the ion under investigation. A general conclusion is that a weakly basic polymer backbone aids conductivity, since it prevents the ions from being held too tightly by the framework (42). Smaller ions (e.g. monovalent metallic cations) generally display much higher conductivity than organic cations, for example (43). Conductivities can be determined using a standard cell of similar design to that employed for liquid electrolytes.

Numerous research groups have investigated the electrochemical properties of room-temperature ionic liquids, an activity driven by their perceived "environmentally friendly" nature and the large potential window they frequently display (45). Although a phase consisting solely of ions may be expected to display high conductivity, the high concentration of charge carriers is offset by the relatively low mobility that arises from the high viscosity of these liquids. Accordingly, conductivity values of the order of $10^{-3}$ S cm$^{-1}$ are common, which makes these media closer to electrolyte solutions in nitrobenzene (see Table 20.8) in terms of conductivity. A recent reference has observed proton conductivity in excess of 0.1 S cm$^{-1}$ in a solvent-free ionic liquid which bodes well for future energy storage applications (46). The temperature dependence of the ionic conductivity has been investigated for imidazolium-based ionic liquids but detailed studies of the relationship between ion transport and other liquid properties are still being elucidated (47). High-temperature ionic liquids, such as molten alkali halides, generally have high specific conductivities (greater than 1 S cm$^{-1}$) although ionic mobility will clearly be enhanced at temperatures of ca. 1000 K (48).

In measuring transport numbers, one point noted in high-temperature ionic liquids (molten salts) is that an appreciable electrolysis of the molten salt leads to a significant change in the liquid's centre of mass due to its pure nature. Attempts to determine transport numbers via the Hittorf approach will generally be highly susceptible to gravitational instabilities in contrast to the situation for polymer electrolytes. An alternative approach is to use the Nernst–Einstein equation (20.2.1-10) to determine ionic mobility from diffusion coefficient measurements and then to find the transport number for the electrolyte (equation (20.1.2-9)). In high-temperature molten salts such as the alkali metal chlorides, cationic transport numbers of 0.7–0.8 have been reported (48).

There will be considerable activity in the optimisation of ion transport parameters within the "non-classical" electrolyte systems discussed in this section. Future prospects for research in this area are likely to involve combination of aspects of the systems referred to above (e.g. the use of room-temperature ionic liquids in conjunction with ionomers) to achieve improvements in performance of energy storage systems.

## REFERENCES


1. A. J. Bard, L. R. Faulkner, *Electrochemical Methods: Fundamentals and Applications*, 2nd ed., Wiley: New York, 2001, Chap. 1.
2. J. Newman, in *Advances in Electrochemistry and Electrochemical Engineering*, C. W. Tobias, Ed., Wiley: New York, 1967, Vol. V.
3. J. J. Lingane, *Electroanalytical Chemistry*, 2nd ed., Wiley: New York, 1958.
4. H. H. Girault, *Analytical and Physical Electrochemistry*, EPFL Press: Lausanne, 2004, Chap. 4.
5. F. Bénière, in *Physics of Electrolytes*, J. Hladik, Ed., Academic Press: London, 1972, Vol. I, Chap. 6.
6. M. Spiro, in *Techniques of Chemistry Vol I: Physcial Methods of Chemistry*, A. Weissberger, B. W. Rossiter, Eds., Wiley: New York, 1971, Part IIA, Chap. 4.
7. J. O. Bockris, A. K. N. Reddy, *Modern Electrochemistry Part 1: Ionics*, 2nd ed., Plenum Press: New York, 1998, Chap. 4.
8. G. Jones, M. Dole, *J. Am. Chem. Soc*. **51**, 1073 (1929).
9. A. J. Bard, L. R. Faulkner, *Electrochemical Methods: Fundamentals and Applications*, 2nd ed., Wiley: New York, 2001, Chap. 4.
10. A. J. Bard, L. R. Faulkner, *Electrochemical Methods: Fundamentals and Applications*, 2nd ed., Wiley: New York, 2001, Chap. 10.
11. R. A. Robinson, R. H. Stokes, *Electrolyte Solutions*, 2nd ed., Butterworths: London, 1959, p. 465.
12. T. Shedlovsky, *J. Am. Chem. Soc.* **54**, 1405 (1932).
13. R. A. Robinson, R. H. Stokes, *Electrolyte Solutions*, 2nd ed., Butterworths: London, 1959, Chap. 7.
14. R. M. Fuoss, *J. Am. Chem. Soc.* **80**, 5059 (1958).
15. B. Fourest, L. R. Morss, G. Blain, F. David, J. M'Halla, *Radiochim. Acta* **69**, 215 (1995).
16. S. T. Lobo, R. E. Robertson, *Can. J. Chem.* **55**, 3850 (1977).
17. G. Marx, W. D. Wittke, *Zeitschrift für Naturforschung A* **32A**, 186 (1977).
18. F. Arndt, G. Marx, *Zeitschrift für Naturforschung A* **36A**, 1019 (1981).
19. J. F. Skinner, R. M. Fuoss, *J. Phys. Chem.* **68**, 1882 (1964).
20. G. Kalfoglou, L. H. Bowen, *J. Phys. Chem.* **73**, 2728 (1969).
21. M. Selvaratnam, M. Spiro, *Trans. Farad. Soc.* **61**, 360 (1965).

22. A. N. Campbell, J. I. Friesen, *Can. J. Chem.* **38**, 1939 (1960).
23. A. N. Campbell, E. M. Kartzmark, G. R. Lakshminarayanan, *Can. J. Chem.* **40**, 839 (1962).
24. B. E. Conway, *Electrochemical Data*, Elsevier: Amsterdam, 1952, Chap. 4.
25. J. I. Padova, in *Modern Aspects of Electrochemistry*, B. E. Conway, J. O. Bockris, Eds., Plenum Press, New York, 1972, Vol. VII, Chap. 1.
26. J. Burgess, *Metal Ions in Solution*, Wiley, New York, 1978, Chap. 4.
27. B. Das, M. Sama, D. K. Hazra, *J. Chem. Eng. Data* **45**, 353 (2000).
28. I. Y. Ahmed, C. D. Schulbach, *Can. J. Chem.* **71**, 2358 (1967).
29. D. P. Sidebottom, M. Spiro, *J. Phys. Chem.* **79**, 943 (1975).
30. M. Della Monica, L. Senatore, *J. Phys. Chem.* **74**, 205 (1970).
31. T. Solomon, A. J. Bard, *J. Phys. Chem.* **99**, 17487 (1995).
32. H. H. J. Girault, D. J. Schiffrin, *Electroanal. Chem.* **15**, 1 (1989).
33. E. H. Riesenfeld, *Ann. Phys.* **8**, 609 (1902).
34. E. Grunwald, G. Baughman, G. Kohnstam, *J. Am. Chem. Soc.* **82**, 5801 (1960).
35. J. Koryta, *Electrochim. Acta* **29**, 445, (1984).
36. Y. Shao, S. G. Weber, *J. Phys. Chem.* **100**, 14714 (1996).
37. A. Sabela, V. Maraček, Z. Samec, R. Fuoco, *Electrochim. Acta* **37**, 231 (1992).
38. Y. Shao, A. A. Stewart, H. H. Girault, *J. Chem. Soc. Farad. Trans*. **87**, 2593 (1991).
39. P. G. Bruce, C. A. Vincent, *J. Chem. Soc. Farad. Trans*. **89**, 3187 (1993).
40. A. J. Bard, L. R. Faulkner, *Electrochemical Methods: Fundamentals and Applications*, 2nd ed., Wiley: New York, 2001, Chap. 14.
41. R. W. Murray, *Acc. Chem. Res*. **13**, 135 (1980).
42. M. Doyle, M. E. Lewittes, M. G. Roelofs, S. A. Perusich, *J. Phys. Chem. B* **105**, 9387 (2001).
43. M. Doyle, M. E. Lewittes, M. G. Roelofs, S. A. Perusich, R. E. Lowrey, *J. Membr. Sci.* **184**, 257 (2001).
44. K. D. Kreuer, A. Fuchs, M. Ise, M. Spaeth, J. Maier, *Electrochim. Acta* **43**, 1281 (1998).
45. M. C. Buzzeo, R. G. Evans, R. G. Compton, *Chem. Phys. Chem*. **5**, 1106 (2004).
46. W. Xu, C. A. Angell, *Science* **302**, 422 (2003).
47. A. B. McEwen, H. L. Ngo, K. LeCompte, J. L. Goldman, *J. Electrochem. Soc*. **146**, 1687 (1999).
48. J. O. Bockris, A. K. N. Reddy, *Modern Electrochemistry Part 1: Ionics*, 2nd ed., Plenum Press: New York, 1998, Chap. 5.

This page intentionally left blank

# Subject Index

# COLOUR SECTION

This page intentionally left blank

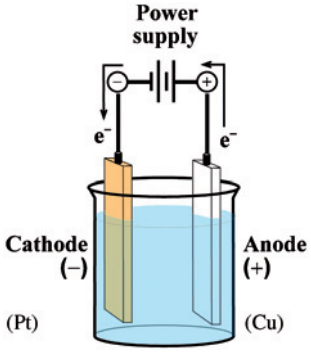


**Plate 1** An electrolytic electrochemical cell. (see page 20)

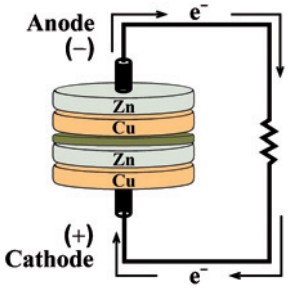


**Plate 2** A galvanic electrochemical cell. (see page 21)

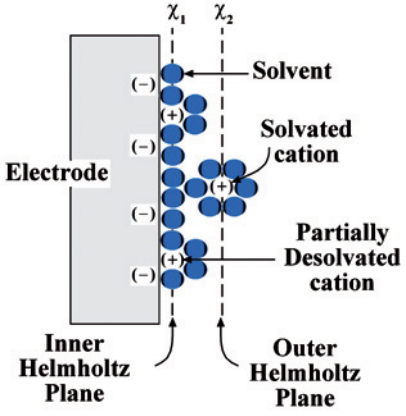


**Plate 3** The electrical double layer (adapted from reference (3), with permission). (see page 23)

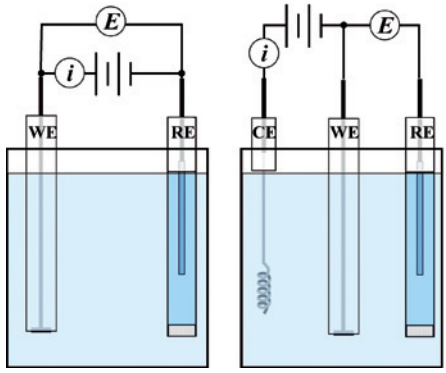


**Plate 4** Schematic representation of two-electrode (left) and three-electrode (right) electrochemical cells. (see page 24)

**Plate 5** Two-electrode cell for solid-state conductivity measurements. (see page 35)

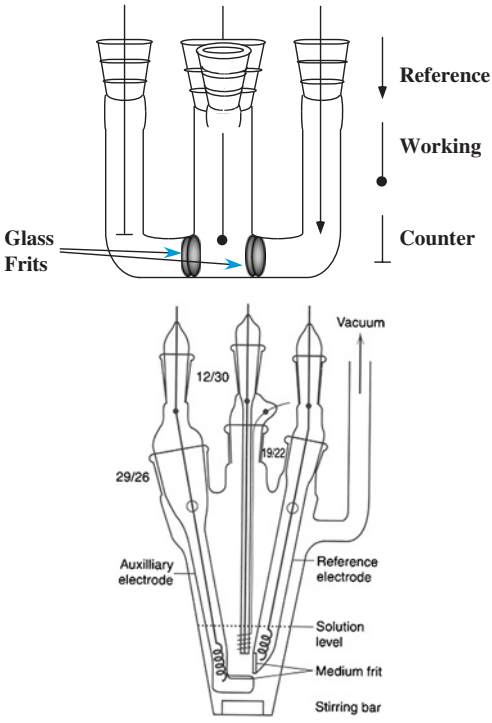


**Plate 6** Three-electrode electrochemical cells. Three-compartment cell with (top panel) and without (bottom panel) glass frits (3, 4). (see page 36)

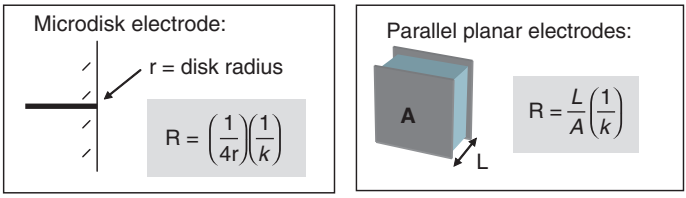


**Plate 7** Relationships between solution resistance and cell geometry for two limiting cases of electrodes in contact with electrolytes. (see page 61)

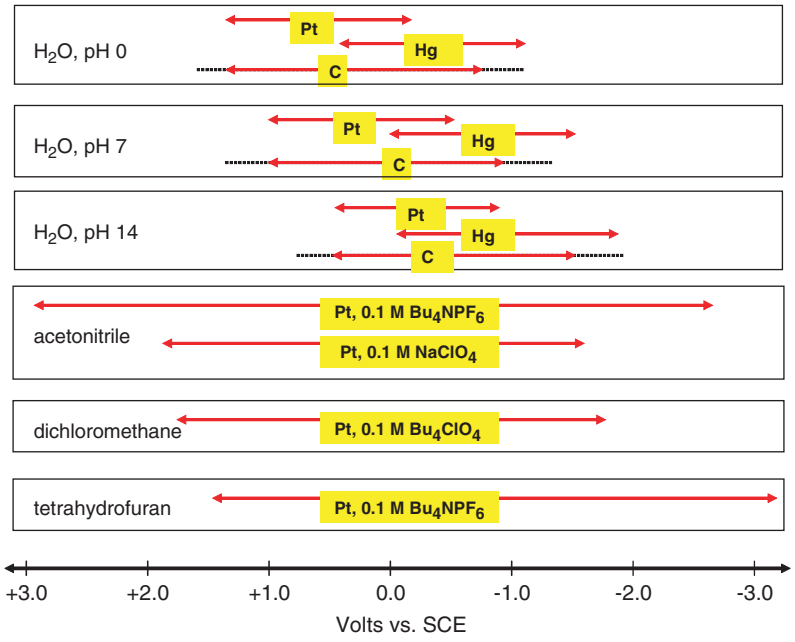


**Plate 8** Potential limits for some selected combinations of solvent, electrolyte, and working electrode. Data compiled from Rieger, Electrochemistry, 2nd edition, Chapman & Hall, New York, 1994; Bard and Faulkner, "Electrochemical Methods", Wiley, New York, 1980; and Rocklin, in "A Practical Guide to HPLC Detection", D. Parriott, Ed., Academic Press, San Diego, 1993, Chapter 6. (see page 63)

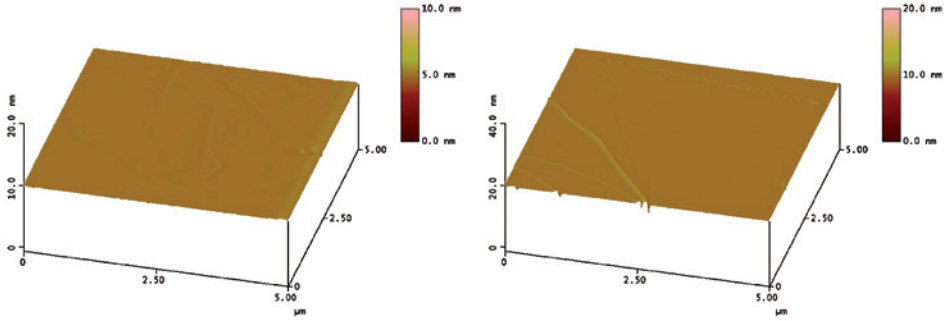


**Plate 9** Atomic force micrographs of the basal plane of HOPG after (left) careful layer plane cleavage and (right) damaging cleavage leaving a fracture plane. (see page 117)

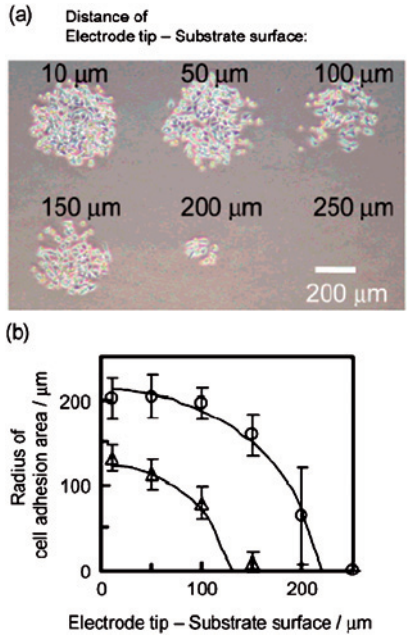


**Plate 10** Size of cellular adhesion area at various distances between the electrode tip and the substrate surface during the electrochemical treatment. (a) Phase contrast micrograph of HeLa cells cultured for 24 h on the BSA-coated glass substrate, which was pretreated by a Br – oxidation pulse of 30 sec at the tip–surface distance indicated in the micrograph. (b) Plots of the radius of the cell adhesion area versus the distance of electrode tip–substrate surface for the electrolysis periods of 10 sec (4) and 30 sec (O). Error bars for the plots were calculated from the standard deviation of at least four cellular patterns. Solid curves were calculated assuming a diffusion-limited surface reaction. [Reproduced with permission from H. Kaji, K. Tsukidate, T. Matsue, M. Nishizawa, *J. Am. Chem. Soc*. **126**, 15026 (2004). Copyright 2004, American Chemical Society.] (see page 178)

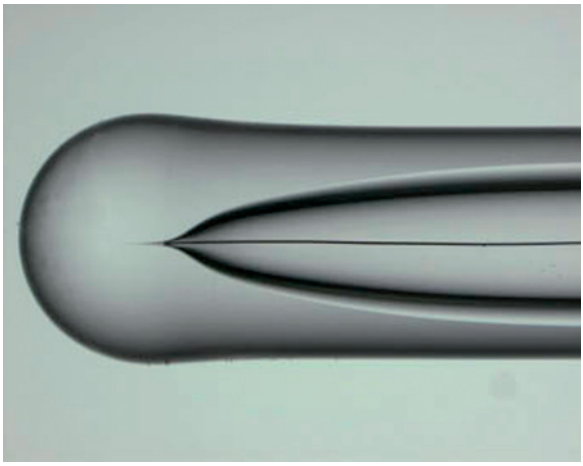

**Plate 11** The 25 μm Pt wire is inserted at the base of the cone and remains straight. (see page 191)

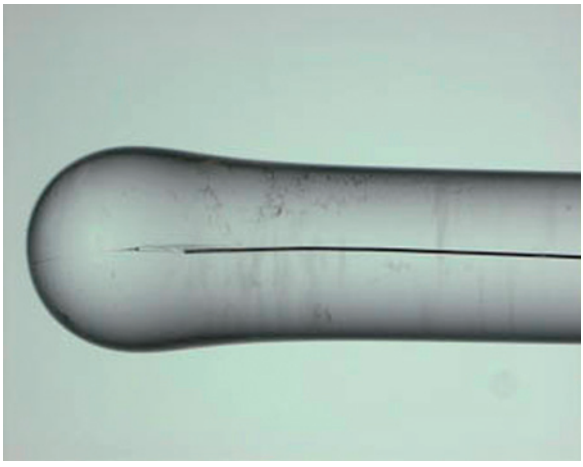

**Plate 12** Sealed 25 μm Pt wire in a Pyrex capillary. A small air-pocket is observed at the beginning of the wire but the rest of the body is properly sealed. This is not unusual and can be shaved off during the polishing steps. (see page 193)

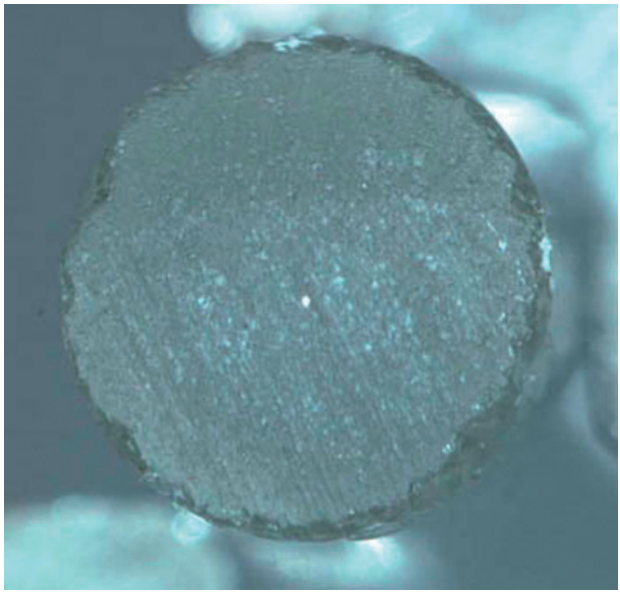

**Plate 13** Polished capillary exposing the 25 μm Pt wire at the center. (see page 194)

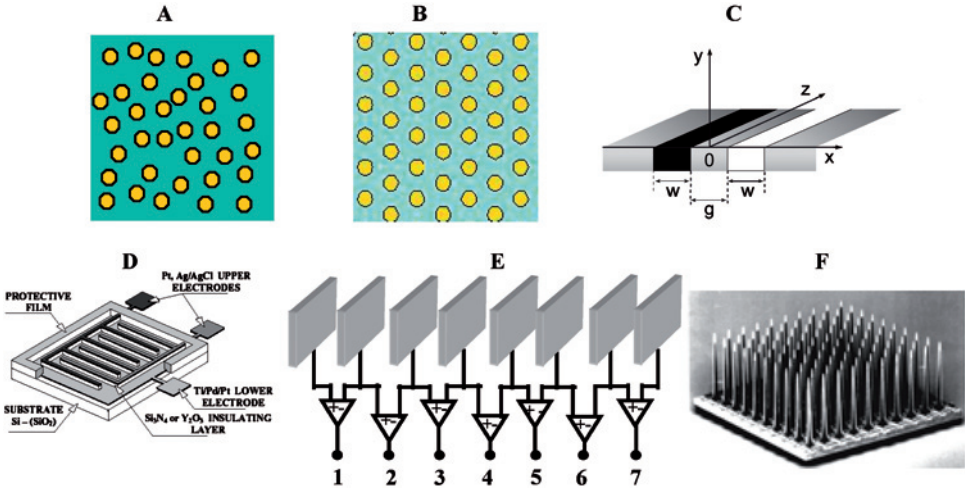


**Plate 14** Classification of microelectrodes: (A) random array, (B) ordered array, (C) paired electrode, schematic representation of a double band assembly, (D) interdigitated array, schematic presentation of IDA electrodes vertically arranged (E) linear array, (F) three-dimensional array, Utah electrode array (reprints from reference (28)). (see page 393)

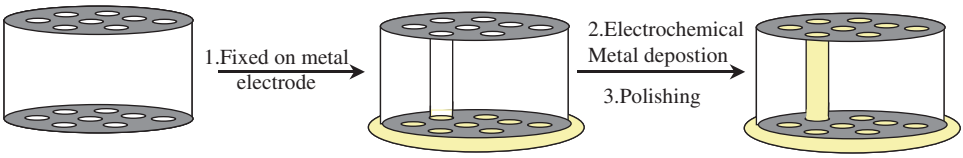


**Plate 15** Schematic diagram of the procedure used to prepare the microelectrode array using templates. (see page 407)

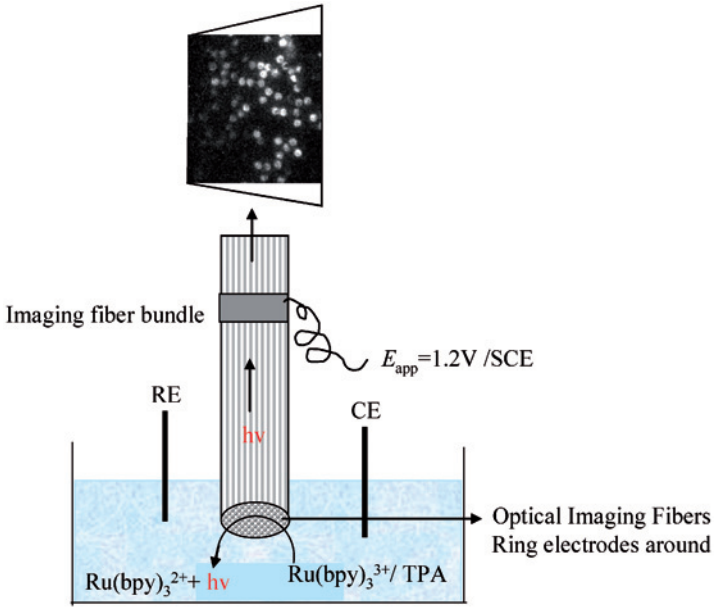


**Plate 16** Electrochemiluminescence (ECL) imaging using an opto-electrochemical microring array. (see page 411)

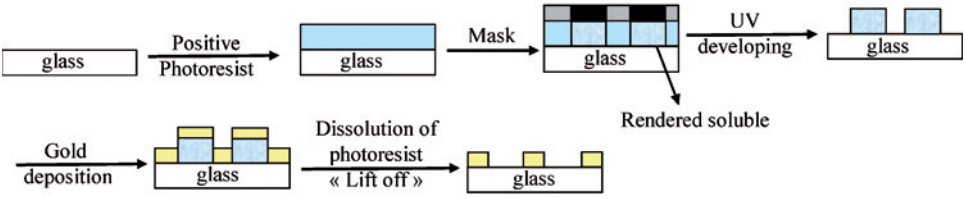


**Plate 17** Gold microelectrode array made using photolithography (positive resin) and lift off. (see page 413)

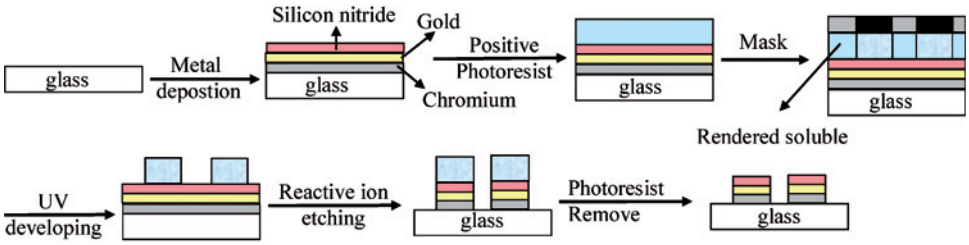


**Plate 18** Photolithography and reactive ion etching. (see page 413)

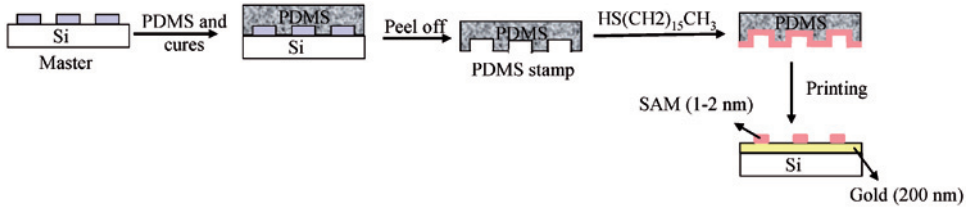


**Plate 19** Schematic procedure for micro-contact printing. (see page 415)

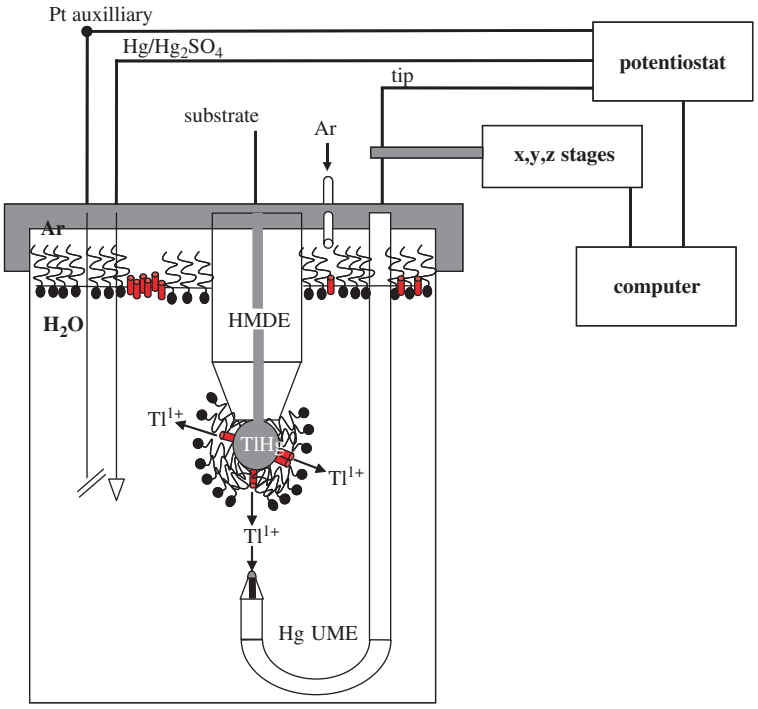


**Plate 20** Schematic diagram of an ion channel SECM experiment where a submarine UME is used. (Adapted from reference (20)). (see page 531)

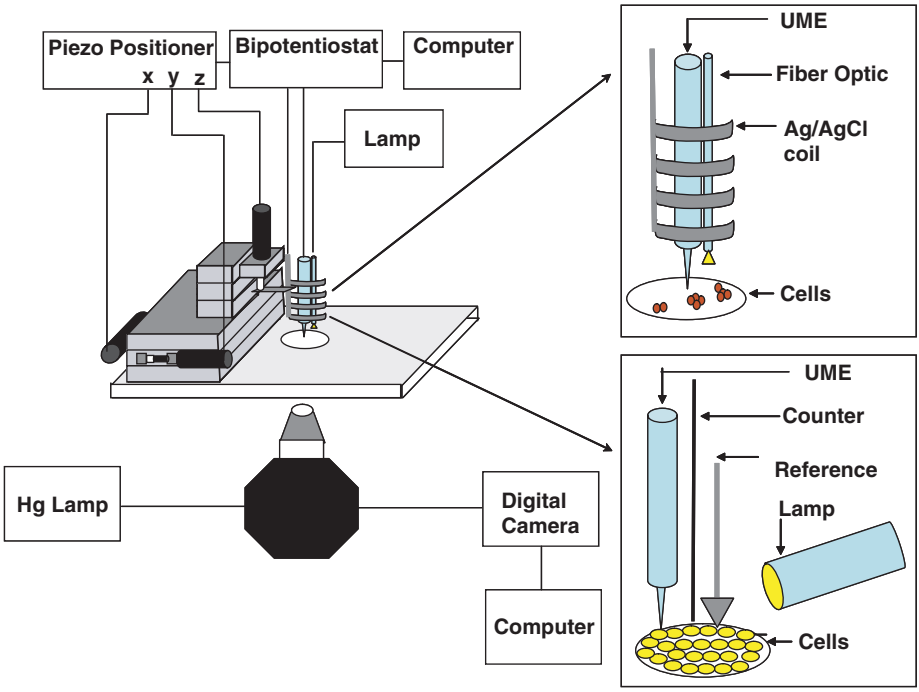


**Plate 21** Schematic representation of a combined SECM and inverted microscope setup. (see page 533)

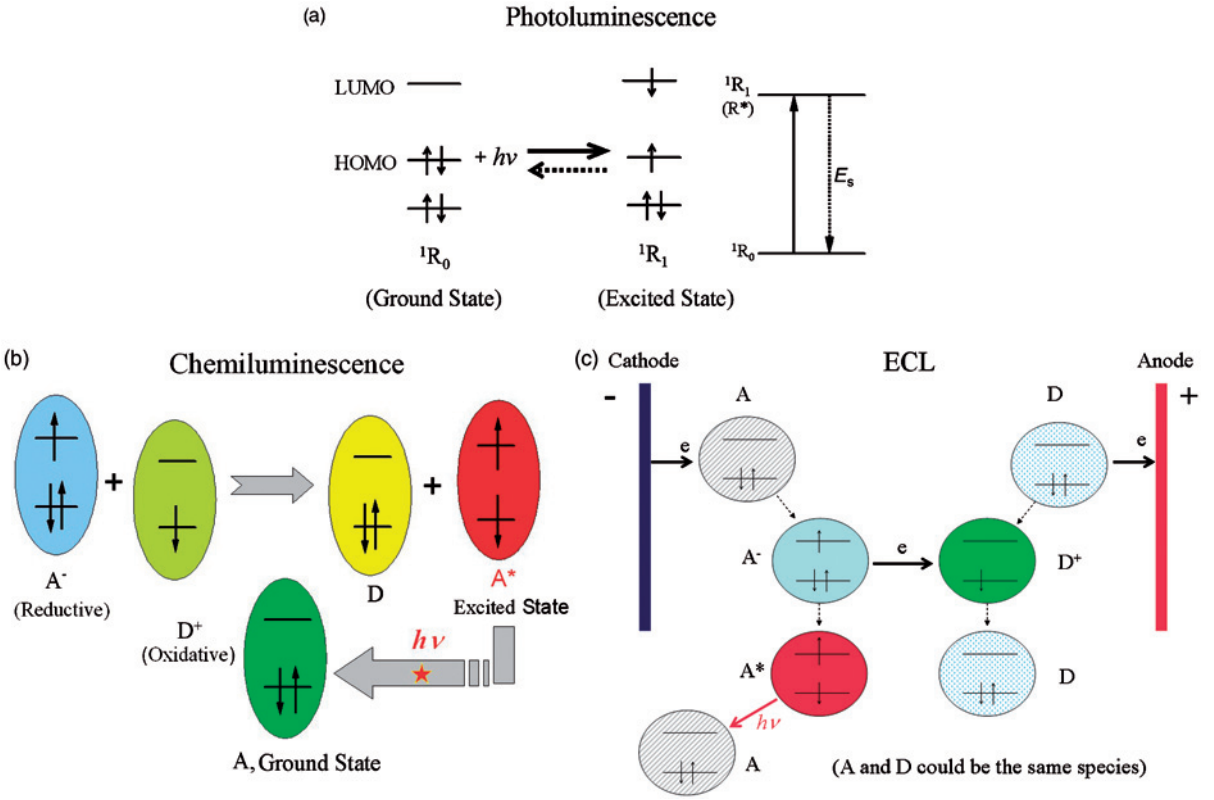


**Plate 22** Schematic diagrams showing the general principles of (a) Photoluminescence, (b) Chemiluminescence, (c) ECL. (see page 543)

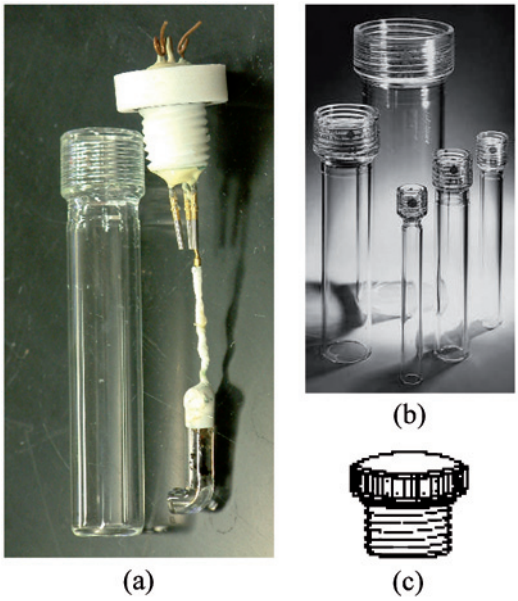


**Plate 23** (a) Commonly used cell for annihilation ECL study, (b) which can be fabricated from ACE glass internal threaded connectors, (c) Teflon or PTFE plugs. (see page 557)

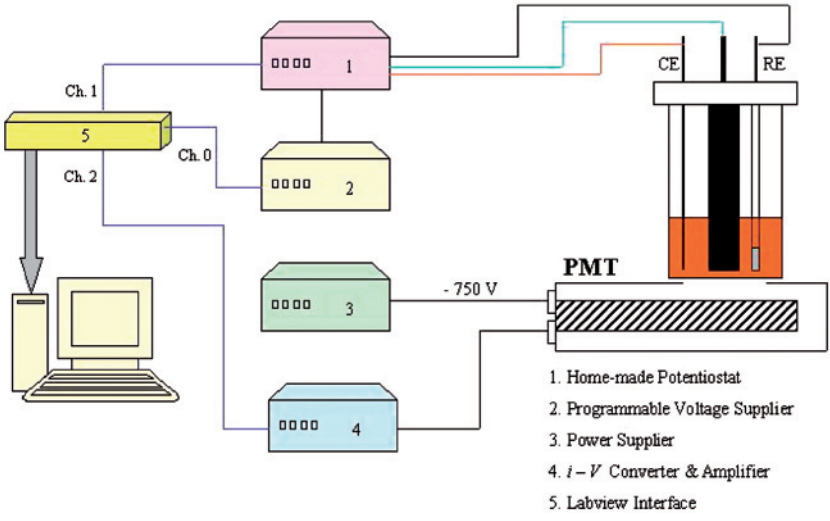


**Plate 24** Schematic diagram of an ECL instrumental setup. (see page 566)

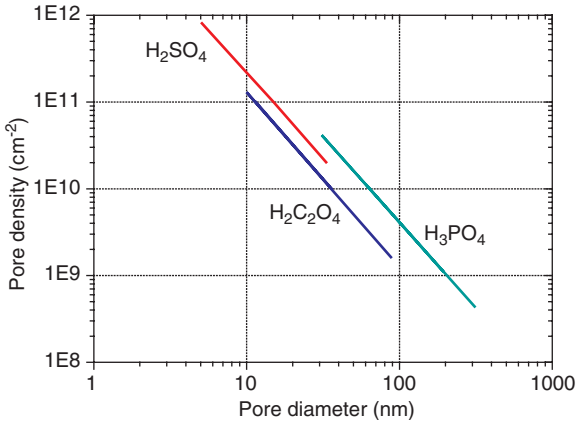


**Plate 25** Pore density vs. pore diameter in alumina nanoporous membranes prepared in the three electrolytes indicated. Reproduced with permission from http://www.synkera.com/. (see page 680)

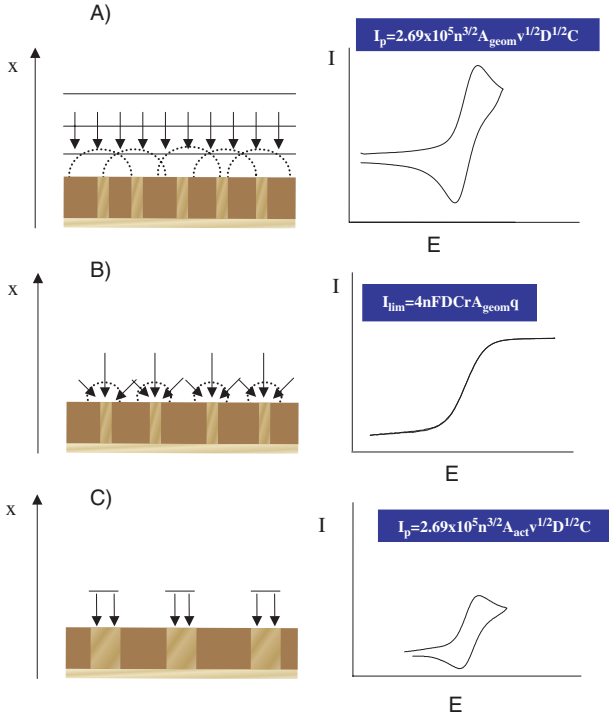


**Plate 26** Schematic drawing of the different diffusional regimes at NEE: (A) Total Overlap; (B) Pure Radial; (C) Linear active. The scan rate or the distance between the nanodisk elements increases from (A) to (C). Relevant equations for peak currents (A and C) and plateau current (B) refer to reversible redox systems. $A_{act}$ is the active area (nanodisk surface), $A_{geom}$ is the total geometric area of the ensemble (nanodisks and insulator), $q$ is the nanodisk density (disk $cm^{-2}$), and all other symbols have their usual meaning. Reprinted with permission from reference (86). (see page 700)

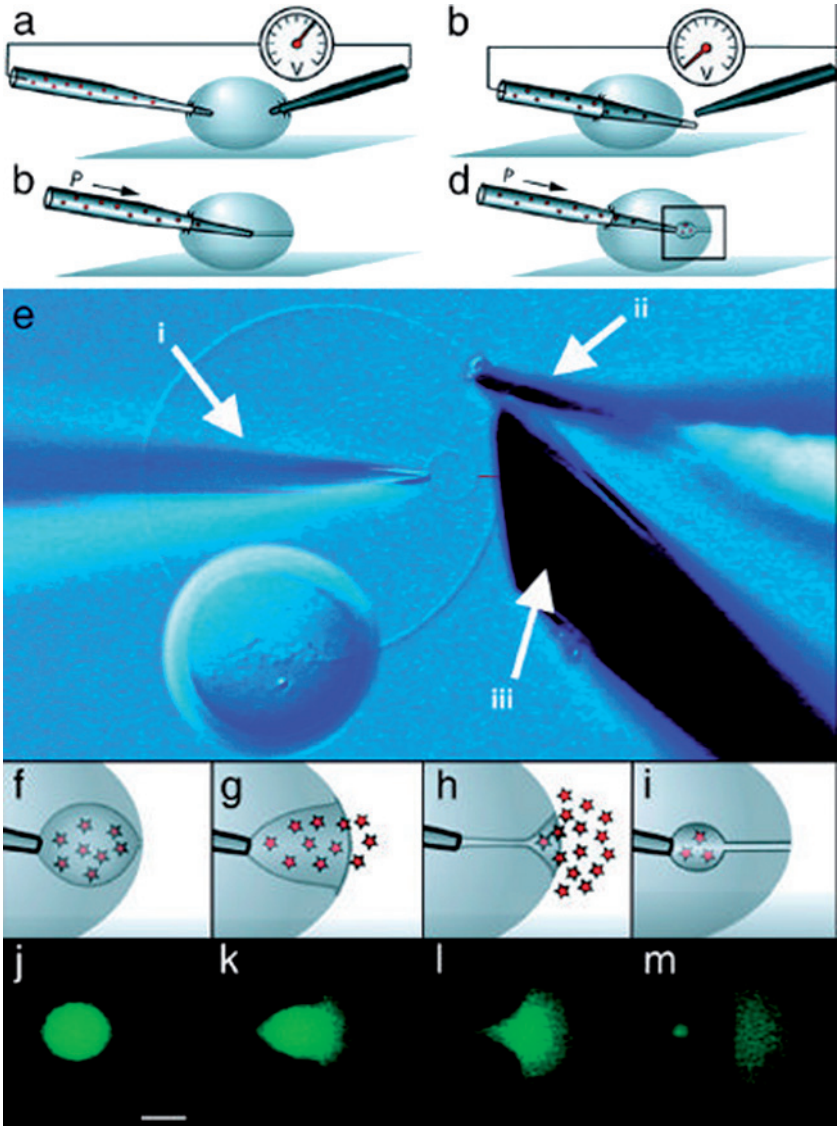


**Plate 27** Formation and release of vesicles in an artificial cell. (A–D) Schematics of a microinjection pipette electroinserted into the interior of a unilamellar liposome and then through the opposing wall, pulled back in to the interior, followed by spontaneous formation of a lipid nanotube and formation of a vesicle from flow out of the tip of the micropipette. (E) Nomarski image of a unilamellar liposome, with a multilamellar liposome attached as a reservoir of lipid, microinjection pipette (i), electrode for electroinsertion (ii), and 30-μm diameter amperometric electrode beveled to a 45° angle (iii). A small red line depicts the location of the lipid nanotube, which is difficult to observe in the computer image with a 20× objective, illustrating a vesicle with connecting nanotube inside a liposome. (F–I) Fluid injection at a constant flow rate results in growth of the newly formed vesicle with a simultaneous shortening of the nanotube until the final stage of exocytosis takes place spontaneously and a new vesicle is formed with the attached nanotube. (J–M) Fluorescence microscopy images of fluorescein-filled vesicles showing formation and final stage of exocytosis matching the events in F–I. (Scale bar represents 10 μm.) Reproduced with permission from reference (79). (see page 728)

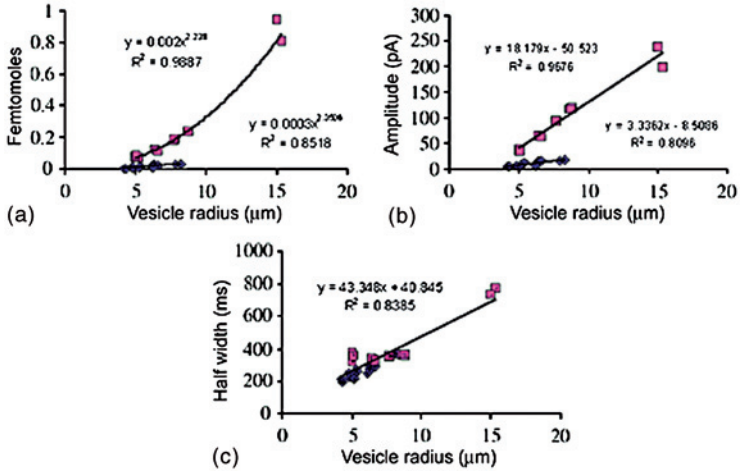


**Plate 28** Amperometric data for fusion of vesicles of varying size at beveled 5- (◆) and 33-μm (■) electrodes: (A) the amount of catechol observed at each electrode, (B) the amplitude of each current transient, and (C) the half-width of each transient vs. the radius of vesicles undergoing exocytosis. Each data set has been curve fit to observe the trend in the data as indicated. Reproduced with permission from reference (80). (see page 732)

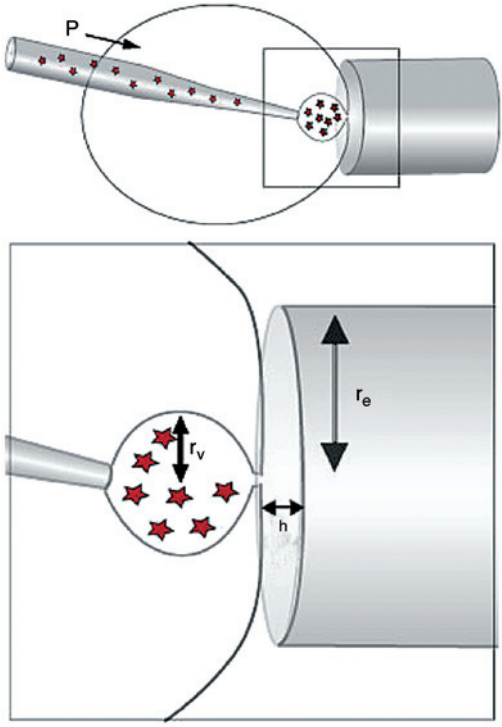


**Plate 29** Simple model of coulometric efficiency for artificial exocytosis. This first-stage model assumes that the efficiency of oxidation for material released is simply the ratio of the membrane–electrode space (calculated as $\pi r_e^2 h$) over the volume of the vesicle ($4\ \pi r_v^3/3$). This assumes that all the catechol that is present in the membrane–electrode space after exocytosis will be oxidized, but also that only catechol in the solution that fits in this volume will be oxidized. Reproduced with permission from reference (80). (see page 733)

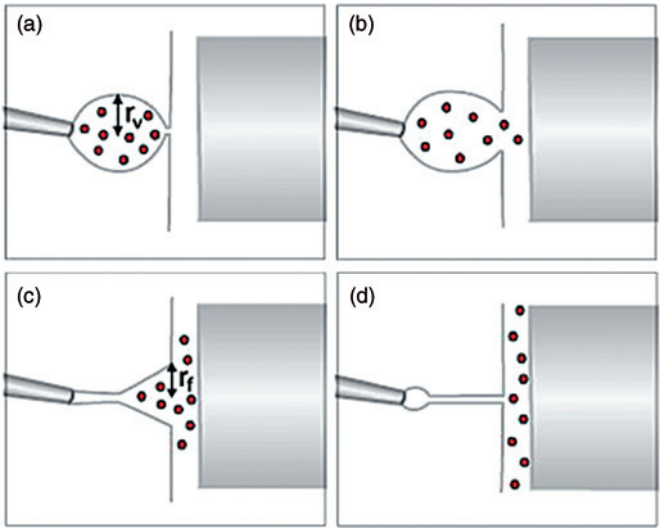


**Plate 30** A more complete model of the release process during exocytosis based on the fluorescence observations. This model assumes that as the vesicle opens, it has a transitory period where mass transport of catechol to the electrode is via diffusion from a frustum with opening $r_f$ defined the value of $r_v$. Catechol diffusing to the electrode is oxidized. After exocytosis is complete, the membrane–electrode space is filled with solution from the inside of the vesicle and catechol present continues to be oxidized as in the thin-layer representation of Figure 17.1.9. Reproduced with permission from reference (80). (see page 734)

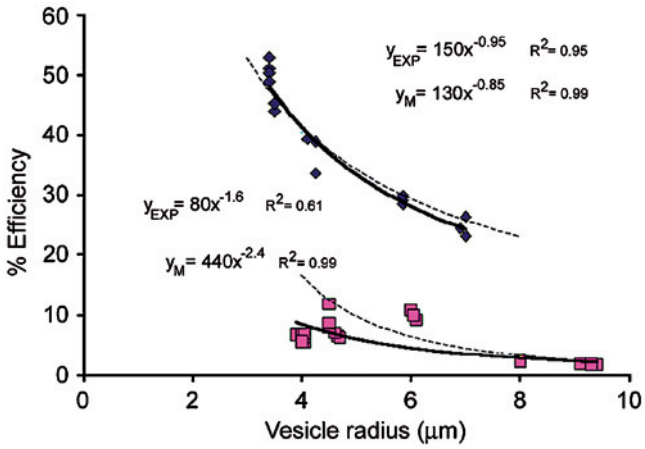


**Plate 31** Coulometric efficiencies for a data set obtained with a beveled 33-µm electrode (◆) compared to data obtained with a 5-µm electrode (■) for release of catechol measured from a range of vesicle sizes. This is compared to the theoretical coulometric efficiencies for these electrode dimensions calculated with the conditions outlined in Figure 17.1.6 and with the model discussed in the text (dashed lines). These are compared to each set of experimental data, which are shown with best-fit equations (thick lines). The equations for all lines, and their correlation coefficients, are given with the symbols $y_{exp}$ for experimental data sets and $y_m$ for the modeled efficiencies with that for the 5-µm electrode to the left and that for the 33-µm electrode to the right. Reproduced with permission from reference (80). (see page 736)

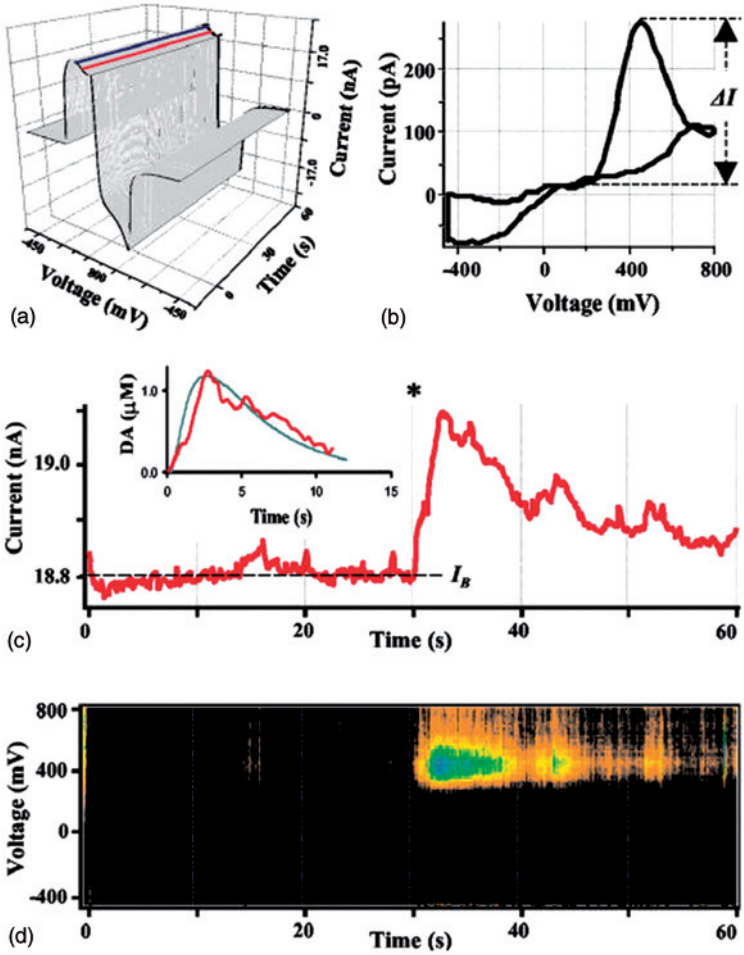


**Plate 32** Analysis of cyclic voltammetry recordings from a single rat chromaffin cell. (A) A representative recording shown as a three-dimensional matrix of data. Red and blue lines represent samplings of the current at 400 and 0 mV, respectively. (B) Voltammogram of catecholamines released during the same recording. A subtraction was made between 10 consecutive averaged I–V profiles at 10 sec from those at 33 sec. Dashed line indicates ΔI, the height of DA oxidation peak. (C) Current sampled at 400-mV oxidation potential. The asterisk indicates a time when the patch was disrupted by suction and a whole-cell configuration was attained. The inset shows a random walk fit (green) of the sampled current trace (red) using 15 MΩ access resistance, 8 μm cell radius, 60 μm distance between the CFE and the pipette tip, and 6.7 μM cytosolic catecholamine concentration. (D) Pseudo-three-dimensional representation of approximate voltammograms of intracellular metabolites encountering the CFE during the recording, in which the intensity of color ("Planet Earth" color table) indicates the current at a given voltage and time. Reproduced with permission from reference (120). (see page 745)

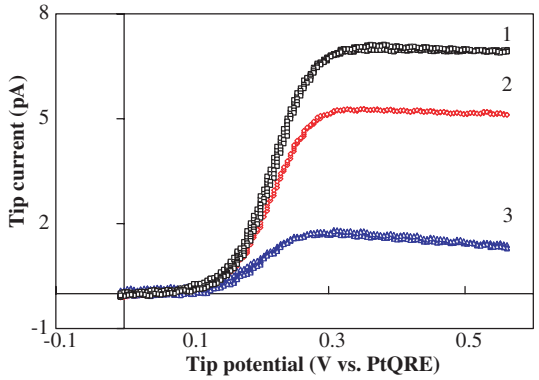


**Plate 33** SECM tip cyclic voltammograms of 2 mM $Cp_2FeTMA^+$ in an aqueous solution containing no supporting electrolyte at a Pt tip ($a \sim 18$ nm) at three different gap separations. Curve 1: Tip held far away from the substrate (ITO) surface. Curve 2: Tip at a distance within the range where the tip current started to decrease with decreasing distance. Curve 3: Tip closer to the surface as compared with curve 2. Tip potential scan rate 5 mV/sec for all cases. $E_S = -0.3$ V vs. PtQRE. (see page 766)

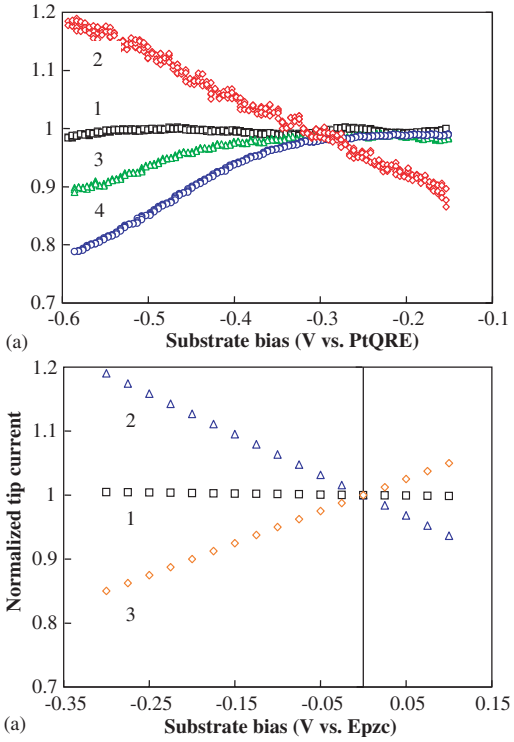


**Plate 34** (A) Tip limiting current at $E_T = 0.6$ V vs. PtQRE as a function of the substrate potential, $E_S$, for different charged species. Curve 1: 2 mM $C_pFeC_pCOO^-$ in 1.0 M $NaNO_3$. Curve 2: 2 mM $Cp_2FeTMA^+$, no supporting electrolyte. Curve 3: 2 mM $C_pFeC_pCOO^-$, no supporting electrolyte. Curve 4: 2 mM $Fe(C_pCOO^-)_2$, no supporting electrolyte. All limiting currents are normalized with respect to the limiting tip current of curve 1 at $E_S = -0.3$ V vs. PtQRE. Substrate potential scan rate: 5 mV/sec. (B) Normalized theoretical tip current as a function of $E_S$, with respect to the tip current at $E_S = E_{pzc}$ (the potential of zero charge) of ITO. Curve 1: 1 mM $Cp_2FeTMA^+$ in 1.0 M $NaNO_3$. Curve 2: 1 mM $Cp_2FeTMA^+$ only. Curve 3: 1 mM $C_pFeC_pCOO^-$ only. (see page 767)

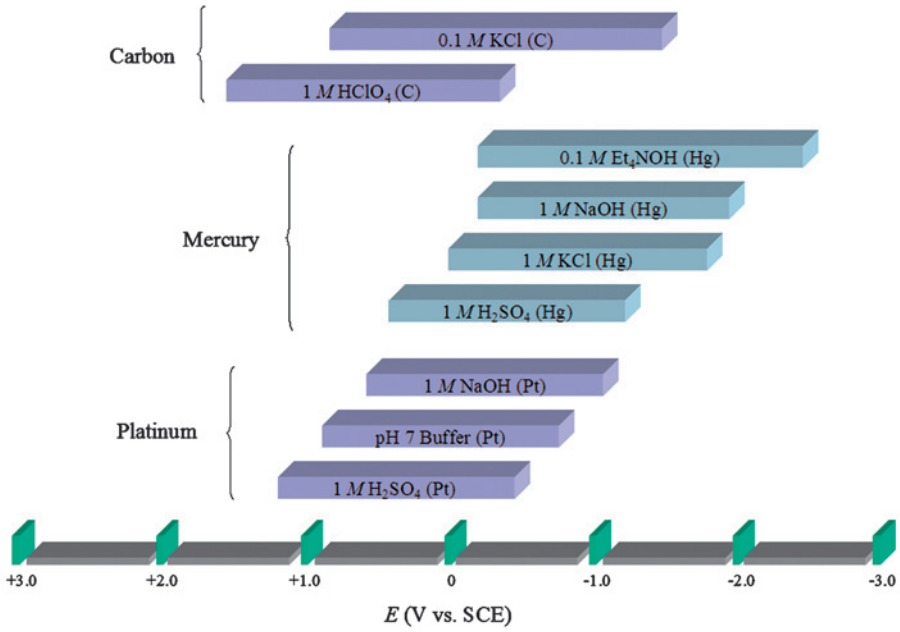


**Plate 35** Estimated potential ranges in aqueous solutions at 25 °C. (see page 814)

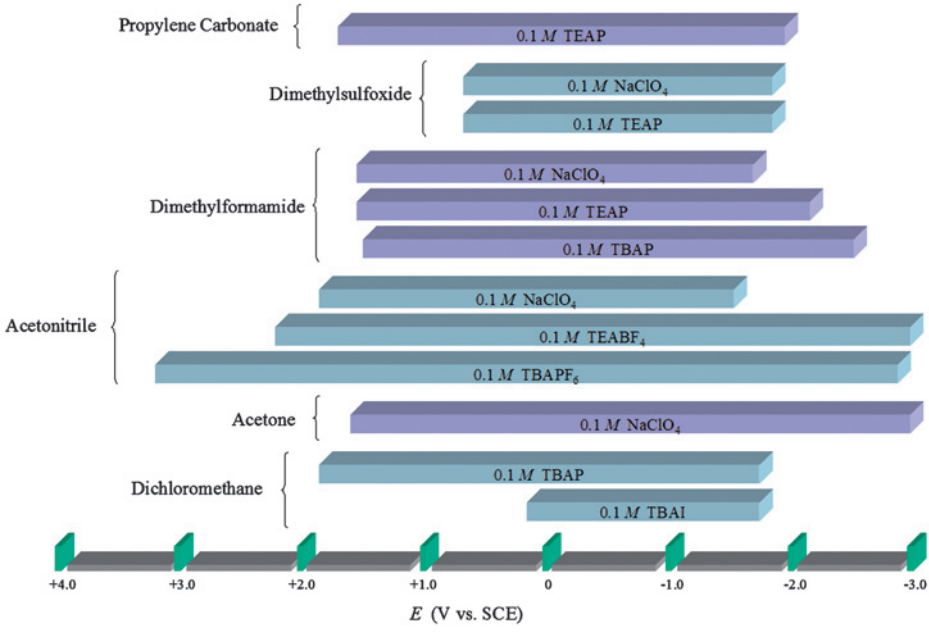


**Plate 36** Estimated potential ranges at Pt electrodes for non-aqueous solvent/electrolyte solutions. Data from reference (1). (see page 814)

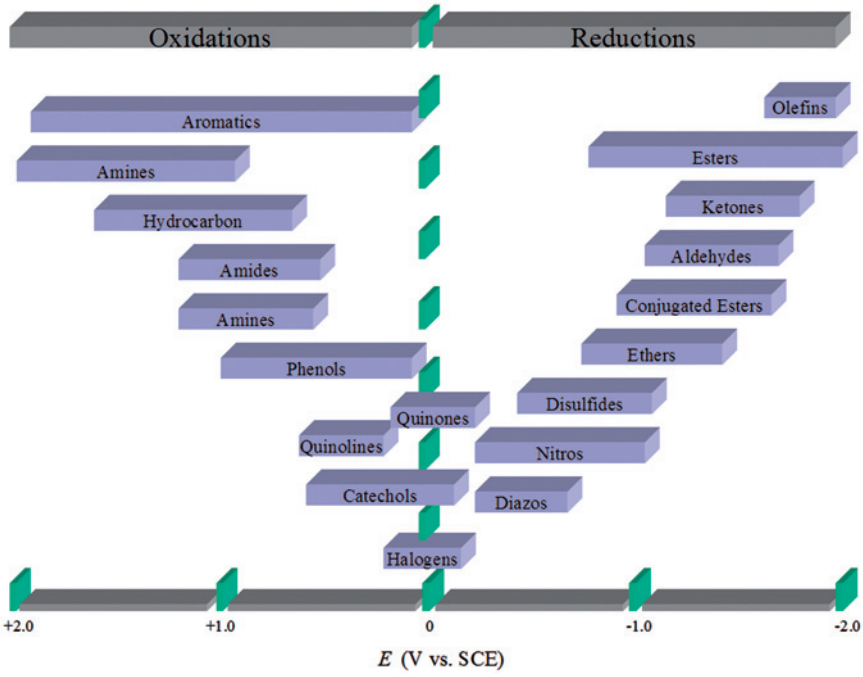


**Plate 37** Estimated potential range of organic functional groups at 25 °C. Data from references (5, 6). (see page 819)

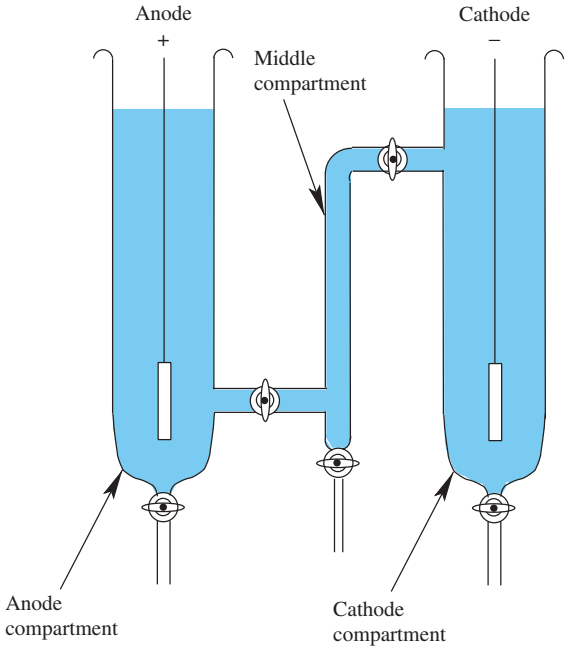


**Plate 38** Schematic diagram of the Hittorf apparatus for experimental determination of transference numbers. (see page 856)

This page intentionally left blank